Experimental Investigation and Optimization of Cutting Parameters in Plasma Arc Cutting

Thesis submitted in partial fulfilment of the requirements for the degree of

Master of Technology (Research)

In

Production Engineering

By

DILIP KUMAR BAGAL

Roll No. 612ME104

DEPARTMENT OF MECHANICAL ENGINEERING

NATIONAL INSTITUTE OF TECHNOLOGY, ROURKELA

2015

Experimental Investigation and Optimization of Cutting Parameters in Plasma Arc Cutting

Thesis submitted in partial fulfilment of the requirements for the degree of

Master of Technology (Research)

In

Production Engineering

By

DILIP KUMAR BAGAL

Roll No. 612ME104

Under the Supervision of

Prof. K. P. MAITY

DEPARTMENT OF MECHANICAL ENGINEERING

NATIONAL INSTITUTE OF TECHNOLOGY, ROURKELA

2015

Department of Mechanical Engineering
National Institute of Technology, Rourkela
Odisha-769008

CERTIFICATE

This is to certify that M. Tech. (Research) thesis entitled, "Experimental Investigation and Optimization of Cutting Parameters in Plasma Arc Cutting" submitted by **Dilip Kumar Bagal** in partial fulfillment for the requirements of the award of Master of Technology (Research) degree in Mechanical Engineering with specialization in **Production Engineering** at **National Institute of Technology, Rourkela** is an authentic work carried out by him under my supervision and guidance. He has fulfilled all the prescribed requirements and the thesis, which is based on candidate's own work, has not been submitted elsewhere for a degree.

Dr. Kalipada Maity
Supervisor
Department of Mechanical Engineering
National Institute of Technology, Rourkela,
Odisha, India

Acknowledgement

I place on record and warmly acknowledge the continuous encouragement, invaluable supervision, timely suggestion and inspiring guidance offered by my supervisor ***Dr. Kalipada Maity,*** *Professor, National Institute of Technology, Rourkela*, for bringing this research to a successful completion.

I also admire his profound knowledge and expertise in the field of Optimization Techniques which served as an inspiration and provided a sound foundation on which the research work was carried out. Amidst the busy schedule, his sincere directives and timely help has comprehended this research in stipulated time. I also wish to express my deep sense of gratitude to ***Dr. S. S. Mahapatra,*** *HOD, Mechanical Engineering, National Institute of Technology, Rourkela* for giving me an opportunity to work on this project with valuable departmental facilities.

I also express my sincere gratitude to the Mechanical Engineering Department, National Institute of Technology-Rourkela and Larsen & Toubro, Kansbahal Works-Rourkela for providing me the entire facilities requisite for the research work. My special thanks to ***Dr. S. K. Patel****, HOD, Department of Workshops* and ***Dr. M. Masanta****, Person In Charge, Engineering Welding & Foundry Shop,* for his support and help rendered by giving me the permission to utilize the laboratory for carrying out my research work. I would also like to express my special thanks to *Mr. Soma Tigga, Technician of central workshop, NIT Rourkela*, for helping me with my experiments in our institute. I do extend my gratefulness to all my beloved friends who are directly or indirectly involved in the successful completion of this research work.

Dilip Kumar Bagal
612ME104

Abstract

Experimental investigation of plasma arc cutting has been carried out using AISI 4140 and AISI 304 stainless steel as work-piece. The process parameters were considered as follows: feed rate, cutting current, cutting speed, gas pressure, voltage and torch height. The response parameters were chosen as follows: material removal rate (MRR), surface roughness (SR), right bevel angle (RBA), chamfer, dross, kerf width and heat affected zone (HAZ) which are the main cut quality characteristics of plasma arc cutting operation. The optimization of the process parameters have been carried out using desirability function, grey based principal component analysis (PCA) hybrid approach, genetic algorithm (GA), particle swarm optimization (PSO), simulated annealing (SA) and teaching-learning-based-optimization (TLBO) algorithm coupled with response surface methodology (RSM). A regression model was developed that represents the relationship between independent and dependent variables based on RSM. This type of novel approach has been proposed to evaluate and estimate the influence of plasma arc machining parameters on the quality of cut. This user-friendly mathematical approach is straight forward and the results thus obtained have also been validated by running confirmatory tests. The premise attributes provide beneficial knowledge for managing the machining parameters to enhance the preciseness of machined parts by plasma arc cutting. The obtained results indicate that the TLBO approach was significantly affected by the machining parameters directly with easy operability and economically.

Key words: Desirability; GA; Grey; HAZ; MRR; PAC; PCA; PSO; RBA; SA; SR; TLBO

Table of Contents

List of Figures

List of Tables

Abbreviations

2D Two Dimensional

3D Three Dimensional

A First Input Variable

Adj. MS Adjacent Mean of Squares

Adj. SS Adjacent Sum of Squares

AHP Analytic Hierarchy Process

AISI American Iron and Steel Institute

ANN Artificial Neural Network

ANOVA Analysis of Variance

AWJ Abrasive Water Jet

AWJC Abrasive Water Jet Cutting

B Second Input Variable

BBD Box-Behnken Design

BPH Benign Prostatic Hyperplasia

C Third Input Variable

CCD Central composite design

CCR Cooper and Rhodes

CI Confidence Interval

Cis Confidence Intervals

CO_2 Carbon Dioxide

CNC Computer Numerical Control

Coef. Coefficient

CT Computed Tomography

D Fourth Input Variable

$\widetilde{D}$ Desirability Function Value

D_m Total mean of the desirability function value at the optimal level

DEA Data Envelopment Analysis

DoF Degree of Freedom

DMUs Decision-Making Units

EBM Electron Beam Machining

EDM Electrical Discharge Machining

EN European Standard Steel Number

F Statistic Test Value

Fig. Figure Number

GA Genetic Algorithm

GRA Grey Relational Analysis

Grey-PCA Grey based Principal Component Analysis

GRG Grey Relational Grade

H_α Hypothesis

Hardox Abrasion Resistant Steel Grade

HAZ Heat-Affected Zone

HB Higher-The-Better

HV Vickers Hardness

i.e. That is

IHSA Improved Harmony Search Algorithm

ISO International Organization for Standardization

L (1) Lowest Level

L (2) Medium Level

L (3) Highest Level

LB Lower-The-Better

LBC Laser Beam Cutting

LP Linear Programming

L & T Larsen & Tourbo Company

K Kelvin

MATLAB MATrix LABoratory

MC Milling Cutting

MRR Material Removal Rate

MS Means of squares

NB Nominal-The-Best

NC Numerical Control

Norm. Normalization

NPJ Nitrogen Cold Plasma Jet

NSGA-II Non-Dominated Sorting GA-II

OFC Oxygen Flame Cutting

P Probability value

PAC Plasma Arc Cutting

PBC Plasma Beam Cutting

PCA Principal Component Analysis

PET Positron Emission Tomography

PKRP Plasma Kinetic Resection of the Prostate

PSO Particle Swarm Optimization

QstE High-Strength Steel Grade

R_a Surface Roughness

RBA Right Bevel Angle

RCGA Real Coded Genetic Algorithm

RSM Response Surface Methodology

S235JR Steel Grade

S/N Ratio Signal to Noise Ratio

SA Simulated Annealing

SC Saw Cutting

Seq. SS Sequential Sum of Squares

Sl. No. Serial Number

SPS Spark Plasma Sinter

SR Surface Roughness

SS Sums of Squares

St. German Steel Grade

Std. Err. Standard Error

T Statistical Value

TIG Tungsten Inert Gas

TOPSIS Technique for Order of Preference by Similarity to Ideal Solution

TLBO Teacher-Learning-Based-Optimization

UAT User Acceptance Testing

USM Ultra-Sonic Machining

vs. Versus

W Watt

WEDC Wire Electrical Discharge Cutting

WEDM Wire Electo-Discharge Machining

WSPC Water Shield Plasma Cutting

ZTA Zirconia Toughened Alumina

Nomenclature

L_9 Orthogonal Array of 9 Runs

L_{18} Orthogonal Array of 18 Runs

L_{27} Orthogonal Array of 27 Runs

L_{30} Orthogonal Array of 30 Runs

2^1X3^7 One Parameter with Two Levelled and Seven Parameters with Three Levelled

ΔH Value of Enthalpy

Y Response Parameter

X_i Singular Term of Input Variable

X_{ii} Square Term of Input Variable

X_iX_j Interaction Term of Input Variable

b_o Regression Coefficient of Constant Term

b_i Regression Coefficient of Singular

b_{ij} Regression Coefficients of Interaction

b_{ii} Regression Coefficients of Square

Ψ Regression Error Coefficient

$X_i*(k)$ Normalized Value of the k^{th} Element

K^{th} Element Number

I^{th} Sequence Number

$X_{0b}(k)$ Desired Value

$\max X_i*(k)$ Largest Value of $X_i(k)$

$\min X_i*(k)$ Smallest Value of $X_i(k)$

$X_i(k)$ Sequence

$X_0(k)$ Reference Sequence

m Number of Experiment

n Number of the Response

R_{jl} Correlation Coefficient Array

ζ Distinguishing Coefficient

β_k Weighting Value of the k^{th} Performance

$Cov(x_i(j))$ Covariance of Sequence

$\sigma x_i(j)$ Standard Deviation of Sequence $x_i(j)$

$\sigma x_i(l)$ Standard Deviation of Sequence $x_i(l)$

λ Eigen Value

λ_k Eigen Value

V_{ik} Eigen Vector

K Boltzmann Constant

T Temperature

ΔE Energy Function Value

v[]=Particle Velocity

p[]=New Particle Position

persent[]=Current Particle (Solution)

pbest[]=Best Solution Among the Each Particle

gbest[]=Best Among Defined as Stated Before

rand()=Random Numbers

ω=Inertia Weights

C_1, C_2=learning Factors

L Number of Learners

J Number of Subjects

I Number of Iterations

(-1) Lowest Level of Input Variable

(0) Middle Level of Input Variable

(-1) Highest Level of Input Variable

L(1) Lowest Level of Input Variable

L(2) Middle Level of Input Variable

L(3) Highest Level of Input Variable

µm Micro-meter

A^2 Square Term of 1^{st} Input Variable

B^2 Square Term of 2^{nd} Input Variable

C^2 Square Term of 3^{rd} Input Variable

D^2 Square Term of 4^{th} Input Variable

A×B Interaction Term of 1^{st} and 2^{nd} Variable

A×C Interaction Term of 1^{st} and 3^{rd} Variable

A×D Interaction Term of 1^{st} and 4^{th} Variable

B×C Interaction Term of 2^{nd} and 3^{rd} Variable

B×D Interaction Term of 2^{nd} and 4^{th} Variable

C×D Interaction Term of 3^{rd} and 4^{th} Variable

W_i Initial Weight of Work Piece

W_f Final Weight of Work Piece

ρ Density

t_m Machining Time

Y_{m1} First Principal Component

Y_{m2} Second Principal Component

Y_{m3} Third Principal Component

Y_{m4} Fourth Principal Component

Chapter 1

INTRODUCTION

1 INTRODUCTION

1.1 Overview

Modern industries depend on the manipulation of heavy metal with alloys. Different cutting methods are used to machine raw materials into specified pieces for making infrastructure and machine tools. Plasma arc cutting (PAC), developed in the mid 1950's was predominantly used to cut stainless steel and aluminium alloys. Plasma is the fourth and the most highly energized state of matter. In fact, plasma appears and behaves like a high temperature gas but with the capability to conduct electricity [1]. The Plasma is generally defined as the gas that is partially or fully ionized containing electrons, ions, neutral atoms and/or molecules. There are two possible states of plasma, thermal and non-thermal. Non-thermal plasmas are characterized by their low temperature while thermal plasmas have relatively very high temperatures and very high energy content. Partial thermal equilibrium is attained between the electrons and the heavy particles of the plasma plume. In the mid to late twentieth century, thermal plasmas have been tested and used extensively in many applications such as extractive metallurgy, process metallurgy, plasma spray coatings, plasma welding and cutting, synthesis of advanced materials and toxic and hazardous waste treatment. In the mid to late twentieth century, thermal plasmas have been tested and used extensively in many applications such as extractive metallurgy, process metallurgy, plasma spray coatings, plasma welding and cutting, synthesis of advanced materials and hazardous waste treatment [2].

The basic principle is that the arc formed between the electrode and the work piece is constricted by a fine bore, copper nozzle. This increases the temperature and velocity of the plasma emanating from the nozzle. The temperature of the plasma can be raised up to

20,000 °C and the velocity can approach the speed of sound. When used for cutting, the plasma gas flow is increased so that the deeply penetrating plasma jet cuts through the material and molten material is removed in the efflux plasma [3]. Since the introduction of the PAC process in the mid-1950, there has been a steady growth in its application in the metal fabrication industries for profile cutting of metallic sheets and plates. Despite superior industrial developments, the process has received very little attention from the research community on any of the scientific aspects of the process, including thermal plasma generation, plasma- material interaction, liquid metal removal and process control [4].

In PAC, the outlet of nozzle is very small in size to create a continuous flame to work material at a constant range of current density. The high rate of plasma jet is due to its tremendous thermal energy and momentum which tends in melting, vaporizing and removal of the material of the nozzle. Similarly, when the flow rate of plasma jet becomes very slow then unwanted dross is formed at bottom of work piece. So, a well optimized plasma cutting system is required for effective machining in industries. The practicability and efficacy is required to be established through experimentation and optimization using statistical and nature inspired algorithms based optimization approach for the processing parameters of PAC in order to achieve the best optimal setting.

Experimentation and making inferences are the complimentary features of general scientific methodology. Statistics as a scientific discipline is mainly designed to achieve these objectives. Planning of experiments is very useful in deriving clear and accurate conclusions from the experimental observations. On this basis the inferences have three main aspects. Firstly, it establishes methods for drawing inferences from observations

when these are not exact and probabilistic in nature. Secondly, it specifies methods for collection of data appropriately, so that assumptions for the application of appropriate statistical methods can be successfully implemented. Lastly, techniques for proper interpretation of results are devised [5]. State of the art knowledge in PAC is defined more by the huge amount of patents literature than by journal papers; this fact induces a strong need for understanding the physical reasons behind industrially patented successful ideas that, due to patenting rules and strategies, are often not completely and correctly described [6; 7].

1.2 Literature Review

The surface roughness and material removal rate of AISI 1017 mild steel using manual PAC machining was analyzed by Taguchi methodology. *Bhuvenesh et al.* [8] observed that the relationship between average material removal rate and average surface roughness is inversely proportional to each other. *Kechagias and Billis* [9] modeled a parametric design of computer numerical controlled (CNC) plasma arc cutting process of St. 37 carbon steel and AISI steel plates by using robust design of orthogonal array L_{18} (2^1X3^7). Arc current is the most significant factor. The plate thickness is the least significant parameter in PAC process. *Madic and Radovanovic* [10] modeled a parametric design of PAC process by using artificial neural network (ANN) to predict surface roughness. It is observed that surface roughness increases with increasing cutting speed, but decreases with increasing cutting arc current. Good surface finish can be achieved by this process using 8 mm thick plate, when cutting current and cutting speeds are set nearer to their higher and lower level of the experimental range respectively.

The proficiency of a manufacturing practice to produce a desired quality of cut and material removal rate (MRR) depend on various considerations. The factors that bias output responses are machining parameters, tool and work piece material properties and cutting conditions. Therefore, it is important for the researchers to model and appraise the relationship among roughness and the parameters affecting its value. The determination of this correlation remains an open field of research, mainly on account of the advances in machining and materials technology with the feasible modeling techniques. In machinability investigations, it is reviewed that the statistical design of experiments is used quite extensively. Statistical designs were assigned to the process of design of experiment so that the adequate data can be examined by statistical methods, resulting in precise and objective conclusions [11]. *Yun and Na* [12] carried out an experiment about the real time control of PAC process using intensity measurements of ejected plasma gas. They observed that the amount of the attached dross substantially reduced by a simple controlled speed. *Zhang et al.* [13] gave the various aspects of keyhole throughout the PAC process. Their experimental results revealed that once the keyhole was established, the width of the keyhole did not change with the changes in the welding current and the welding speed. But, it changed with the variation in the flow rate of the plasma gas and the diameter of the orifice. *Asiabanpour et al*. [4] optimized the quality of 18 parts manufactured by the automated plasma cutting process using response surface method (RSM) and desirability functions. It was concluded that a high value of current and pressure are necessary for quality cut due to PAC process.

The input parameters of plasma arc cutting process using QstE-380 and Hardox 450 alloy steel plate were optimized by using RSM. *Ferreira et al.* [14] observed that there

was increase in cutting speed to 65 % from 35 % with reduction in cost around 28 %. *Hatala et al.* [15] described the effect of technological factors on roughness parameters (Ra) and heat affected zone (HAZ) of the steel surface EN ISO S355 by using planned experimentation and regression model analysis. They concluded that for achieving higher quality of cut surface it was recommended to use higher pressures of plasma gas and appropriate feed rate of plasma torch. For getting lower HAZ value, the cutting speed and power should be controlled. *Schitsin et al.* [16] developed the application of plasma cutting of metals using reversed polarity current and mixed gas supply. The high efficiency of plasma cutting with reversed polarity in both the manual and automatic cutting modes in the plant conditions is stressed.

CNC plasma cutting process by using S235JR sheet materials at different cutting speeds, amperes and arc voltages was experimented and temperature distribution, thickness of HAZ, surface roughness (SR) and hardness were measured from the material at their different values. Based on the values obtained from these measurements, the ideal cutting conditions were identified for the materials exposed to the cutting procedures [17]. *Chakravarty et al.* [18] validated the obtained results of hardness and toughness responses in spark plasma sintered zirconia toughened alumina (ZTA) machining by utilizing neural network and genetic algorithm technique. Zirconia content, spark plasma sintered (SPS) temperature and heating rate were assumed as the input variable in the entire experimentation. *Bober* [19] solved the cutting scheme of numerical controlled (NC) plasma cutting machine by employing backtracking algorithm, genetic algorithm and heuristic algorithm respectively. He discovered that the novel genetic algorithm gave predominant results among all algorithms with short interval of span in the machining.

The difficulty generated in laser beams, flame or plasma torches, water jet, and metal cutter paths of 2-Dimensional cutting operations was identified. *Lee and Kwon* [20] proposed a two-step genetic algorithm combining global search for piercing point optimization and local search for part sequencing. *Keraita and Kim* [21] examined the efficiency of a PC-based CNC pipe profile cutting machine by simultaneously managing only two axes. The manufactured CNC pipe cutting machine of plasma arc cutting process has the ability of making high precision parts by simultaneously controlling only two axes. *Mikkelsen* [22] investigated of ignition propensity of plasma cutting and other hot work processes in the nuclear industry. He found that the plasma cutting of similar sections of carbon steel led to higher relative ignition hazard than was seen for arc gouging. This design indicates that arc ampere is the most important parameter which affects the whole design of experiment by 50.89 % and the torch stand-off distance influences also right bevel angle by 15.90 % and plate thickness by about 6.20 %. *Gullu and Atici* [23] investigated the consequence of plasma arc parameters on the structure variation of AISI 304 and St. 52 steel plates by digital optic microscope (Maker: Panasonic, Model: PRIOR) and Vicker hardness measurement device for HAZ and hardness respectively. After cutting, it is seen that the areas near to our surface of the part hardness increases i.e., around 250-350 HV and decreased towards core of the material.

A Fuzzy model was developed for predicting SR in plasma cutting of AISI 4140 steel plate. It was evident from the statistical analysis that the cutting speed was the most significant factor affecting the SR [24]. *Kim et al.* [25] studied the characteristics of the plasma cutting for thick steel ship plate. They found that an increase in electric current increased the straightness and depth of heat affected zone of cutting plane. An increasing

cutting speed increased the surface roughness of cutting surface and decreased the straightness of cutting plane. Plasma cutting conditions should comprehensively be considered for cutting shape, depth of heat affected zone and surface roughness of cutting surface.

A report on the investigation of selected transient phenomena taking place in PAC that are relevant for process optimization was described and high-speed imaging diagnostics were exploited for the characterization of different technological solutions in order to provide deeper insights into torch and process design [26]. *Saravanakumar et al.* [27] applied RSM with Fuzzy ruled based approach to optimize the parameters of servo pneumatic system and analysis of variance (ANOVA) test has been carried out by Minitab software. *Ye et al.* [28] optimized the input variables of the inductive angle sensor utilizing RSM technique to test validity and accuracy of the model. *Asiltürk and Neseli* [29] modeled a mathematical design to optimize surface roughness using Taguchi based RSM. The feed rate was found to have critical effect in enhancing the surface smoothness in turning operation. RSM approach has been applied in turning process on AISI 410 steel with surface roughness as the output response and concluded that the feed rate is the most significant parameter on the SR among all chosen machining factors [11].

A model of design of experiment was developed by considering tool geometry parameters as input factors to optimize the output response i.e., SR. The results revealed that the radius of nose in tool gave dominant characteristics to the measured response [30]. *Sankar et al.* [31] used the combined approach of RSM and particle swarm optimization (PSO) technique to analyze the performance characteristics on system

identification of an orthotropic and isotropic plate along a dynamic system with 4 degree of freedom on time domain signals.

Fuzzy theory was used for the prediction of cutting parameters in PAC process of AISI 4140 steel. The parameters considered in this study were plasma arc current, cutting speed, and thickness of cut material. Fuzzy rule–based modeling was employed for prediction of surface roughness. The most convenient pipe cutting method according to the Fuzzy analytic hierarchy process (AHP) and Fuzzy technique for order of preference by similarity to ideal solution (TOPSIS) techniques for ship building industry was illustrated [32]. *Kafali et al.* [33] discovered that the plasma cutting was the most favorable pipe cutting technique for straight cut of carbon steel pipes and more productive. By this method the shipyards were able to obtain a competitive advantage in pipe cutting operation. *Todorov et al.* [34] studied the aims to preview a modular conception of building high speed sheet metal cutting machines using three different sources – laser, plasma and water jet machining. The modular principle of building opportune to develop a wide variety of variants allowing different work piece parameters with addition to the usage of the specified cutting sources covering a range of machines. They focused on a product created using virtual prototyping technology showing its advantages in the development of multiple variants design.

An electrode insulation layer was developed using oxygen plasma surface treatment for electrochemical micro-drilling. *Hung et al.* [35] suggested that the most effective improvement was to coat the insulation layer on the electrode sidewall so that current could only be accurately released from the bottom end. The innovative oxygen plasma surface treatment was used to improve film adhesion on the helical edge of electrode.

Krajcarz [36] described different ways of cutting metal, such as water jet cutting, laser and plasma cutting. He found that the water jet cutting was the most versatile method for the separation of materials. This technique can cut through almost any material such as steel, stone, ceramics, aluminium, glass, wood, plastics, laminates, etc. But laser plasma seems to be more universal because it can be used to cut materials ranging from 0.5-160 mm. *Zheng et al.* [37] examined the efficacy and safety of terazosin and plasma kinetic resection of the prostate (PKRP) in the treatment of benign prostatic hyperplasia (BPH) patients with coexisting hypertension. They concluded that PKRP combined with terazosin in treating BPH with concomitant hypertension patient was a safe and effective procedure with a good patient compliance. *King et al.* [38] investigated the plasma arc welding process for TiB2–20TiC ceramics. They concluded that the large crystals and pores present in the FZ present critical flaws that would decrease the strength of a welded joint. *Bhuvenesh et al.* [39] investigated the SR and MRR of AISI 1017 mild steel using manual plasma arc cutting machining by Taguchi methodology. They observed that the relationship between average MRR and average SR was inversely proportional to each other. *Yun and Na* [12] carried out an experiment about the real time control of PAC process by using intensity measurements of ejected plasma gas. They observed that the amount of the attached dross substantially reduced by a simple controlled speed.

The various aspects of keyhole were analyzed throughout the PAC process. The results revealed that once the keyhole is established, the width of the keyhole does not change with the changes in the welding current and the welding speed whereas, it changes with the changes in the flow rate of the plasma gas and the diameter of the orifice [40]. *Xu et al.* [41] carried out an experiment to reduce the kerf width and to improve the kerf

quality by using the hydro-magnetically confined plasma arc on engineering ceramic plates. They concluded that for a given diameter of nozzle, a high quality cut can be produced by using a lower arc current than that was usually required in conventional PAC process, while ensuring a fine arc shape and capability of cutting simply by employing hydro-magnetic constriction. *Senthilkumar et al.* [42] stated that the Non-Dominated Sorting GA-II (NSGA-II) was a fastest, elitist multi-objective genetic algorithm that was broadly used for generating the Pareto frontier. Its main advantage in solving multi-objective problems is that it leads the search toward the global Pareto front while sustaining diversity of the solution set along that front.

The advanced cutting techniques on Hardox 500 and St. 37 steel materials were compared and the effect of structural properties of the material was analyzed. *Dahil et al.* [43; 44] noticed that the plasma cutting is used to cut the work material with maximum hardness and minimum cutting damage occurs in the wire erosion process. *Salonitis et al.* [45] recently carried out an experimental investigation of the PAC process. *Kumar et al.* [46] modelled a Semi-empirical mathematical model on responses of wire electo-discharge machining (WEDM) process using RSM approach. *Ghodsiyeh et al.* [47] optimized the parameters of WEDM operation utilizing RSM technique as a multi-objective type problem on titanium alloy material. *Madić et al.* [48] optimized CO_2 laser cutting process with several optimization techniques such as ANN trained with Levenberg–Marquardt algorithm, real coded genetic algorithm (RCGA), simulated annealing (SA) and improved harmony search algorithm (IHSA) approaches. *Reddy et al.* [49] optimized the input variables of electro-discharge machining (EDM) operation using Taguchi technique on the MRR, SR, white layer thickness and surface crack density.

Further, they built a mathematical model by performing nonlinear regression analysis for predicting the responses of EDM process. *Lal et al.* [50] investigated the impact of WEDM process parameters on the kerf width while machining newly developed hybrid metal matrix composite (Al7075/SiC/Al_2O_3) material. Taguchi methodology was employed to optimize the machining parameters on the kerf width. *Molchanova et al.* [51] compared the special features of plasma, water jet and laser cutting and piercing of structural materials which are used in radio electronics. *Zhu et al.* [52] applied optical methods to analyze the effects of the rate of air flow in plasma arc machining. They concluded that the shape, height, intensity and thickness of ground-state OH distribution differ significantly with air flow rates.

The surface topology, hardness distribution, friction and wear properties were analyzed using the microstructure of the brazed parts which was strengthened by plasma arc powder [53]. *Zhang et al.* [54] studied the metallurgical, nano-mechanical and wear behaviors of (CuCoCrFeNi) 95B5 multi-element alloy coated products which were fabricated by plasma transferred arc cladding process. *Xu et al.* [55] modeled a device which generated stable cold plasma jet under the atmospheric pressure. They analyzed friction, wear and thermal tests on a mirror steel NAK80/diamond friction pair in atmospheres of air, nitrogen and nitrogen cold plasma jet (NPJ) respectively. *Xiaojie et al.* [56] explored the performances of cutting by plasma with their new arc ignition circuit. They found that the performance of plasma cutting was affected significantly by cutting current and speed.

The quality, mechanical properties and micro-structure of the cut edges of steel can be achieved by plasma, laser beam, water jet and Oxy-fuel flame cutting processes.

Weglowski and Pfeifer [57] suggested that the lowest roughness was achieved by means of plasma cutting over the water surface. *Wang et al.* [58] tested the accuracy of digital control of the plasma cutting power supply and the two power electronic building blocks. From the performance test results, they concluded that the design was rational and feasible, and the developed high power plasma cutting power supply which worked in reliably with excellent performance. *Vereshchago and Kostyuchenko* [59] designed a physical-mathematical model of source-arc system in plasma cutting which takes into account the instability of arcing at low currents.

The cutting performance, such as cutting efficiency and electrode wear of PAC were tested for casing and wellhead [60]. The results showed that cutting performance is affected significantly by cutting current and velocity. *Thiébaud et al.* [61] modelled a 3-Dimensional thermal simulated model for the flame cutting process using thick steel plates. They analyzed the metallurgical properties of steel and found the efficiency of process as 26.5 % throughout the experimentations. *Tezuka et al.* [62] studied different advanced cutting process such as plasma arc, laser and abrasive water jet machining operations to achieve the application of removing the fuel debris and the internal core of nuclear power plant. They found that both PAC and abrasive water jet (AWJ) machining economically enhanced the removal process of unwanted debris from the plant as compared to laser cutting process. *Sun et al.* [63] applied a new system in the plasma arc cutting power supply by low-frequency pilot arc technology to control the rapidity and stability of the arc. They concluded that this type of arrangement would help to achieve excellent dynamic responsibility. *Prevosto and Kelly* [64] investigated the characteristics of cutting arcs which were produced at the region of nozzle exit-anode gap and inside of

the nozzle. They carried out experiments by varying cutting torch with specific energy density.

The experiments to analyze the influence of plasma welding and cutting by varying cathode and the type of erosion have been carried out. *Nemchinsky* [65] described the role of cathode geometry and plasma flow pattern in the cathode proximity. *Mancinelli et al.* [66] analyzed a 2D model of the gas breakdown development in the space-charge layer of the double-arc cutting system which was continuous to the nozzle of a cutting arc torch operated with oxygen. They found that the flow of return electrons stops the cutting current loop of double-arcing process. *Krajcarz* [36] compared the best cutting technology for cutting purpose among AWJ, PAC and laser cutting process. He found that PAC was the appropriate machining for cutting thick steel plate. *Kavka et al.* [67] carried out experiments on PAC in the steam working medium. They found that around 20% of total available power was utilized for cutting of materials. *Jiajian et al.* [68] experimented on the dynamics of air flow rate of plasma discharge in non-equilibrium condition. It is concluded that the shape, height, intensity and thickness of ground-state OH distribution changed significantly with flow rate of air. *Ismail and Taha* [69] studied the hardness distribution of multiple passes in plasma arc surface hardening operation. They found that the value of hardness was higher at the center of the plasma arc hardening tracks and then decreased in the region adjacent to each plasma arc track. *Guo and Ueng* [70] optimized the deposition condition to increase the performance of acetylene/argon plasma in router bit and also analyzed the surface through scanning electron microscopy to enhance the quality of routing. *Gruber et al.* [71] observed the plasma arc between nozzle tip and anode in a series of duty cycles using high-speed camera. They revealed that the melting

process of hafnium at the tip of cathode caused the formation of droplet and this would reduce material loss of rate of cathode material. *Farahnakian et al.* [72] carried out experimentation the condition of turning operation by attaching plasma and ultrasonic set up on the AISI 4140 hardened steel. Results concluded a reduction in the cutting forces by hybrid machining in comparison with computed tomography (CT), positron emission tomography (PET), and user acceptance testing (UAT) process on cutting conditions. The surface roughness of work piece can be enhanced in the proposed machining. *Emmelmann et al.* [73] improved the plasma welding operation without taking any type of filler material for steel sheets. They observed the enhancement of performance of plasma welding can be improved by using a low power laser beam which was less than 500 W.

The parameters of PAC of EN 31 steel by utilizing weighted principal component analysis based on Taguchi L_{27} orthogonal array were optimized. *Das et al.* [74] revealed that gas pressure is the most significant factor which affects the responses of PAC. *Yoshihiro et al.* [75] studied the effect of magnetic arc blow in the operation of oxygen plasma arc cutting. They successfully reduced the generation of double arc on steel plates using magnetized shield cap attachments. *Akkurt* [76] examined the machining quality such as cut edge deformation, cut surface properties, cut channel geometry and metallurgical practices in various cutting methods i.e., AWJ cutting, laser beam cutting (LBC), plasma beam cutting (PBC), water shield plasma cutting (WSPC), wire electrical discharge cutting (WEDC), electrical discharge machining (EDM), oxygen flame cutting (OFC), saw cutting (SC), electron beam machining (EBM), milling cutting (MC), ultra-sonic machining (USM) and other conventional machining. He observed that the most significant changes occur with respect to metallurgical properties and hardness values

during oxygen flame cutting. In this method, the hardness values varied from the surface to the center and most part of the material is affected by the amount of heat released.

The results of inert gas cutting of stainless steel and aluminum showing that good quality cuts are achieved with more than 60 % of the maximum cutting speed. Wandera et al. [77] suggested that the parameter limits for the velocity are set to 100 and 80 % of the maximum cut speed for better accurate results. Zhou et al. [78] developed the analysis of energy balance, a new composite heat source model of the manual process of oxygen cutting, an element birth and death technique was used in the numerical analysis by using the finite element code in ANSYS. Chen [79] analyzed the effect of cut quality of mild steel on CO_2 laser machining by varying the gas composition such as oxygen, argon, nitrogen and helium, and their pressures. He found that a high concentration of oxygen was required for high performance of machining as compared to other inert gases. Ahmadi et al. [80] gave a mathematical model about oxygen assisted mild steel cutting by cw CO_2 and Yb:YAG fiber lasers. The model originated from the conservation equations of mass, momentum, and energy in a steady state. This model approached to numerical predictions of nozzle speed, cutting speed and contribution of oxidation power.

1.3 Summary

Although lot of work has been done in the field of plasma arc machining, from the literature survey it is clear that there is lack of research in stainless steel of grade AISI 304 and AISI 4140 for enhanced quality of cutting operation through plasma. Moreover, the knowledge about the fundamental parameters of plasma arc machining like cutting current, voltage, stand-off gap, feed rate and pressure of gas are incomplete. It is observed that literature in context to optimization of the quality response of plasma arc machining

based on various optimization techniques is limited. Optimization of the cutting characteristics like material removal rate, surface roughness, right bevel angle, dross, kerf and heat affected zone by various optimization techniques such as RSM, desirability, GA, PSO, SA, TLBO and DEA approach are still in its initial stages and therefore, there is scope for further development in these areas.

1.4 Objectives of the Present Work

From the summary of literature review, following objectives are outlined as:

a) Experimental investigation of plasma arc cutting operation of stainless steel AISI 304 and AISI 4140.

b) Modeling of optimization criteria of plasma cutting operation using RSM, desirability function, Grey based PCA hybrid approach, genetic algorithm, PSO, SA and TLBO algorithm approaches.

c) Developing the portable laboratorial plasma arc cutting machine set up and optimization of its process parameters.

d) Investigating the cutting characteristics of CNC Oxy-fuel gas cutting using DEA based on Taguchi approach.

Chapter 2

THEORY OF PLASMA CUTTING

2 THEORY OF PLASMA CUTTING

In this chapter, basic fundamentals of plasma and its applications are described. Further, the principle of Oxy-fuel gas cutting process and the description of stainless steel have also been explained.

2.1 What is Plasma?

- Generally, plasma is described as the fourth state of matter.
- Plasma appears and behaves like a high temperature gas but with a capability to conduct electricity [81; 82].

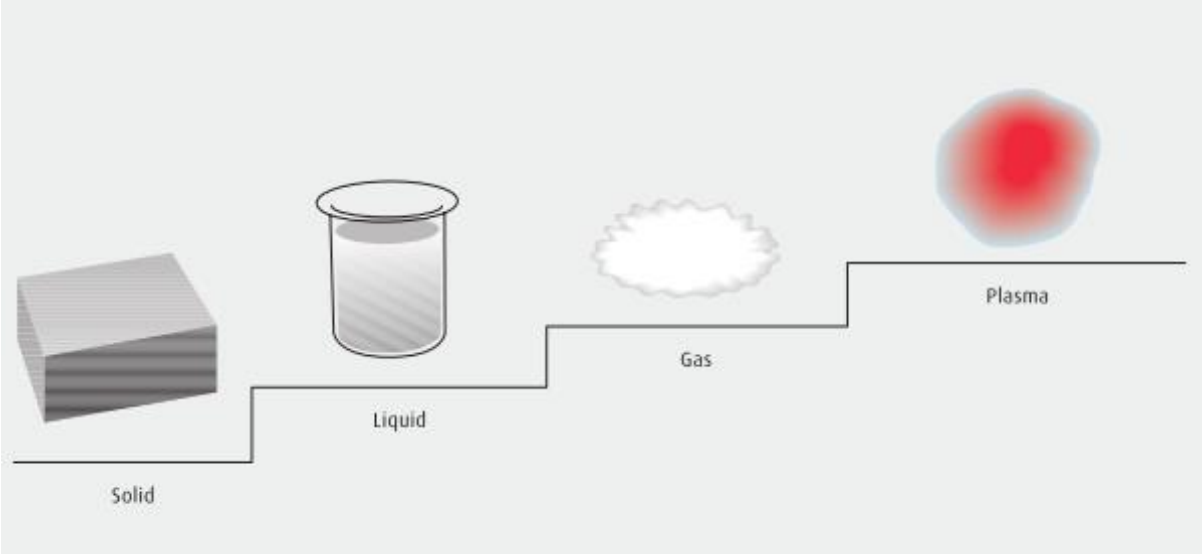

Fig. 1 States of matter [81]

2.2 Natural Plasma

Approximately 99 % of the visible universe comprises of plasma. Plasma dominates the atmosphere of earth within solar system and farther out in the interstellar space. Some natural plasma can be observed close to the earth's surface and examples are given below [83].

- Sun consists of hot plasma with magnetic field as shown in Fig. 2.

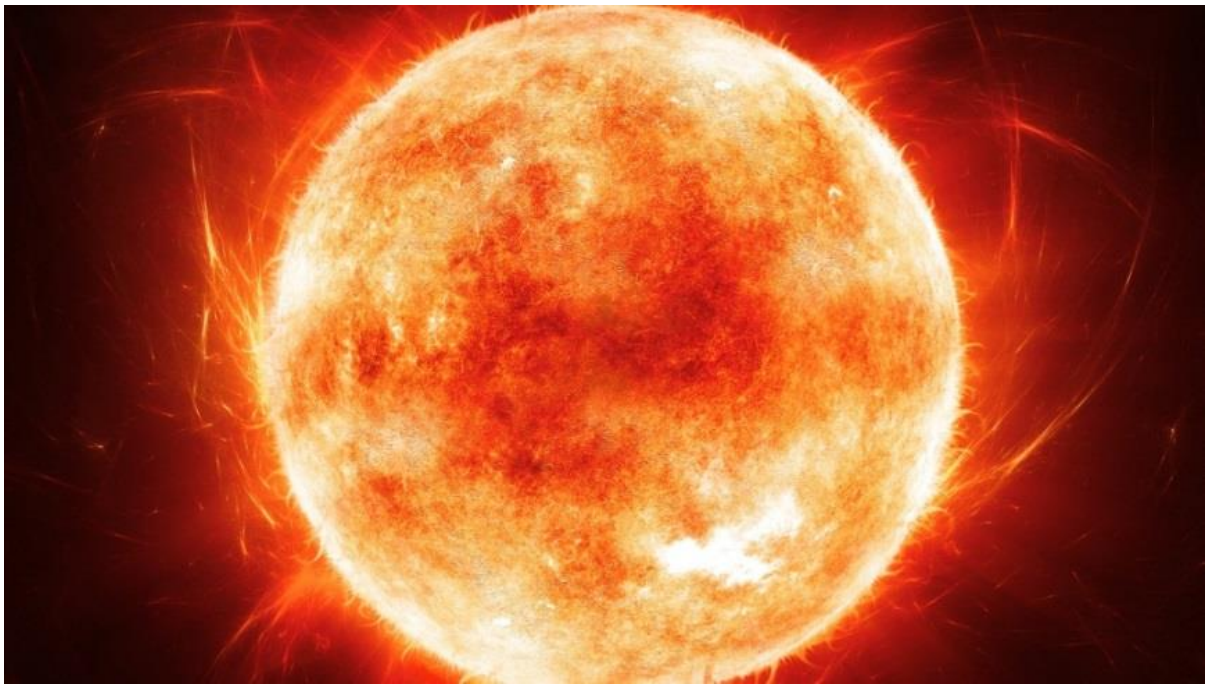

Fig. 2 Natural example hot sun [84]

- Lightning is the formation of electrically conducting plasma channel through the air in excess of 5 km distance from the ground's surface [85].

Fig. 3 Another example lightning [86]

2.3 Artificial Arc Creation

In early 1950's, the first open arc was discovered through tungsten inert gas (TIG) welding [87]. Further, the conventional plasma arc cutting process was applied in live industrial applications in 1960 [88].

2.4 How Plasma Cuts Through Metal?

The plasma cutting process, as used in the cutting of electrically conductive metals, utilizes this electrically conductive gas to transfer energy from an electrical power source through a plasma cutting torch to the material being cut [89].

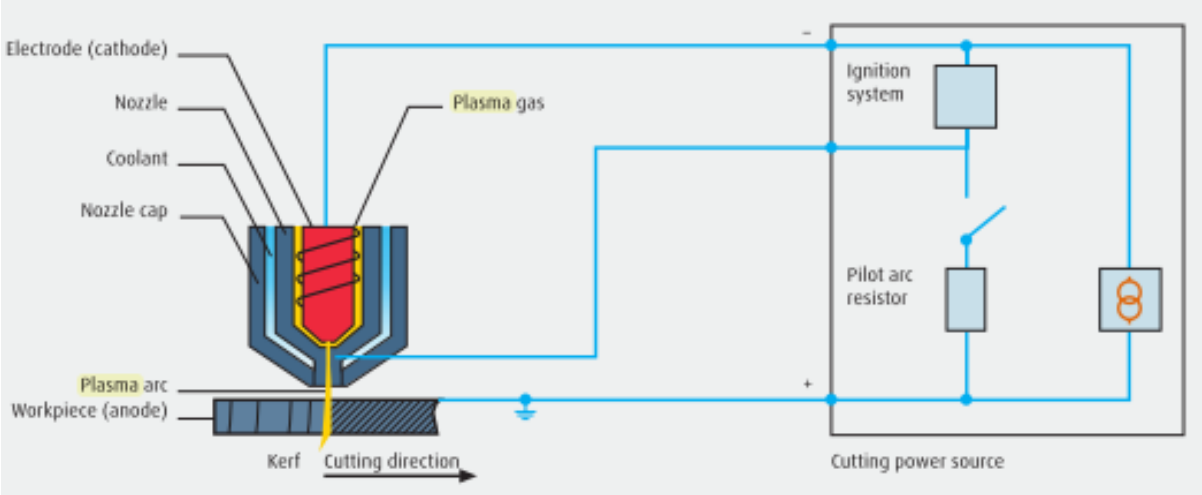

Fig. 4 Principle of plasma cutting [83]

2.5 Types of Plasma Cutting Process

In this section, the various types of the plasma cutting technologies are described.

2.5.1 Conventional plasma arc cutting

The plasma jet generated by conventional dry arc constriction techniques was introduced in 1957 by Union Carbide's Linde Division. In the same year, Dr. Robert Gage got a patent, which was a virtual monopoly for union carbide for 17 years. This technique

could be used to cut any metal at relatively high cutting speeds. The thickness of a plate could range from thin sheet metal to plates as thick as 10 inches (i.e., 250 mm).

The cut thickness was ultimately dependent on the current-carrying capacity of the torch and the physical properties of the metal. A heavy duty mechanized torch with a current capacity of 1000 Amperes could cut through 10 inches thick of stainless steel and aluminium. However, in the most industrial applications, plate thickness seldom exceeded two inches. In this thickness range, conventional plasma cuts were usually beveled and had a rounded top edge. Beveled cuts were a result of an imbalance in the heat input into the cut face.

A positive cut angle resulted because the heat energy at the top of the cut dissipated as the arc progressed through the cut. This heat imbalance was reduced by placing the torch as close as possible to the work piece and applying the arc constriction principle. Increased arc constriction caused the temperature profile of the electric arc to become more uniform and extended. Correspondingly, the cut became squarer. Unfortunately, the constriction of the conventional nozzle was limited by the tendency of increased constriction to develop two arcs in series, one arc between the electrode and nozzle, and a second arc between the nozzle and work piece. This phenomenon was known as double arcing, and damaged both the electrode and nozzle. Double arcing severely limited the extent to which plasma cut quality could be improved.

Since the introduction of the plasma arc process in the mid-1950, considerable research has been focused on increasing arc constriction without creating double arcing. Plasma arc cutting as performed then is now referred to as conventional plasma cutting. It can be cumbersome to apply if the user is cutting a wide variety of metals and different

plate thicknesses. For example, if the conventional plasma process is used to cut stainless steel, mild steel, and aluminium, it is necessary to use different gases and gas flows for optimum cut quality on all three metals. Conventional plasma cutting predominated from 1957 to 1970, and often required very expensive gas mixtures of argon and hydrogen [83].

2.5.2 Air plasma cutting

Air cutting was introduced in the early 1960s for cutting mild steel. The oxygen in the air provided additional energy from the exothermic reaction with molten steel. This additional energy increased cutting speeds by about 25 % over plasma cutting with nitrogen. Although air cutting was not pursued in the late 1960s in the United States and the western world, steady progress was made in Eastern Europe with the introduction of torch (i.e., Feinstrahl Brenner) producing a restricted arc, developed by Manfred van Ardenne. This technology was adopted in Russia and eventually in Japan. The major supplier became Mansfield of East Germany. Several shipyards in Japan were early users of air plasma cutting equipment. However, the electrode life was relatively short and studies disclosed that the cutting face of the work piece had a high percentage of nitrogen in solution which could cause porosity when subsequently welded [83].

2.5.3 Water shield plasma cutting

Water shield plasma cutting was similar to dual flow except that water was substituted for the shield gas. Cut appearance and nozzle life were improved because of the cooling effect provided by the water. Cut rectangularity, cutting speed and dross accumulation were not measurably improved over dual flow plasma cutting because the water did not provide additional arc constriction [83].

2.5.4 Water injection cutting

Earlier, it was stated that the key to improving cut quality was increasing arc constriction while preventing double arcing. In the water injection plasma cutting process, water was radially injected into the arc in a uniform manner. The radial impingement of the water at the arc provided a higher degree of arc constriction than could be achieved by just the copper nozzle alone. Arc temperatures in this region are estimated to approach 50,000 K or roughly nine times the surface temperature of the sun and more than twice the temperature of the conventional plasma arc. The net result obtained was improved cut dimension, increased cutting speeds and the elimination of dross while cutting mild steel [83].

2.5.5 Underwater cutting

Further attempts in Europe to decrease the noise level of the plasma arc and to eliminate smoke development as much as possible led to underwater cutting. This method of high power plasma cutting with cutting currents above 100 amperes has become so popular that today many high power plasma cutting systems can cut under water. For underwater plasma cutting, the work piece is immersed about 2-3 inches under water and plasma torch cut while immersed in the water. The smoke and noise level as well as the arc glare are reduced dramatically. One negative effect of this cutting method is that the work piece cannot be observed while cutting and the cutting speed is reduced by 10-20 %. Further, the operator can no longer govern the cutting process from the arc sound nor can oversee the quality of cut produced by the consumables.

Finally, while cutting in water, some water surrounding the cut zone disintegrates into oxygen and hydrogen, and the freed oxygen has a tendency to combine with the

molten metal from the cut (especially aluminium and other light metals) to form metal oxide, which leaves free hydrogen gas in the water. If this free hydrogen gets collected in a pocket under the work piece, then it creates small explosions while reignited with the plasma jet. Therefore, the water needs to be constantly agitated while cutting such metals [83; 90].

2.5.6 Precision plasma cutting set up

The set-up of the equipment being very simple, the easiness of use of the process and the quality of the components increase productivity and achieve high quality plasma cutting [83].

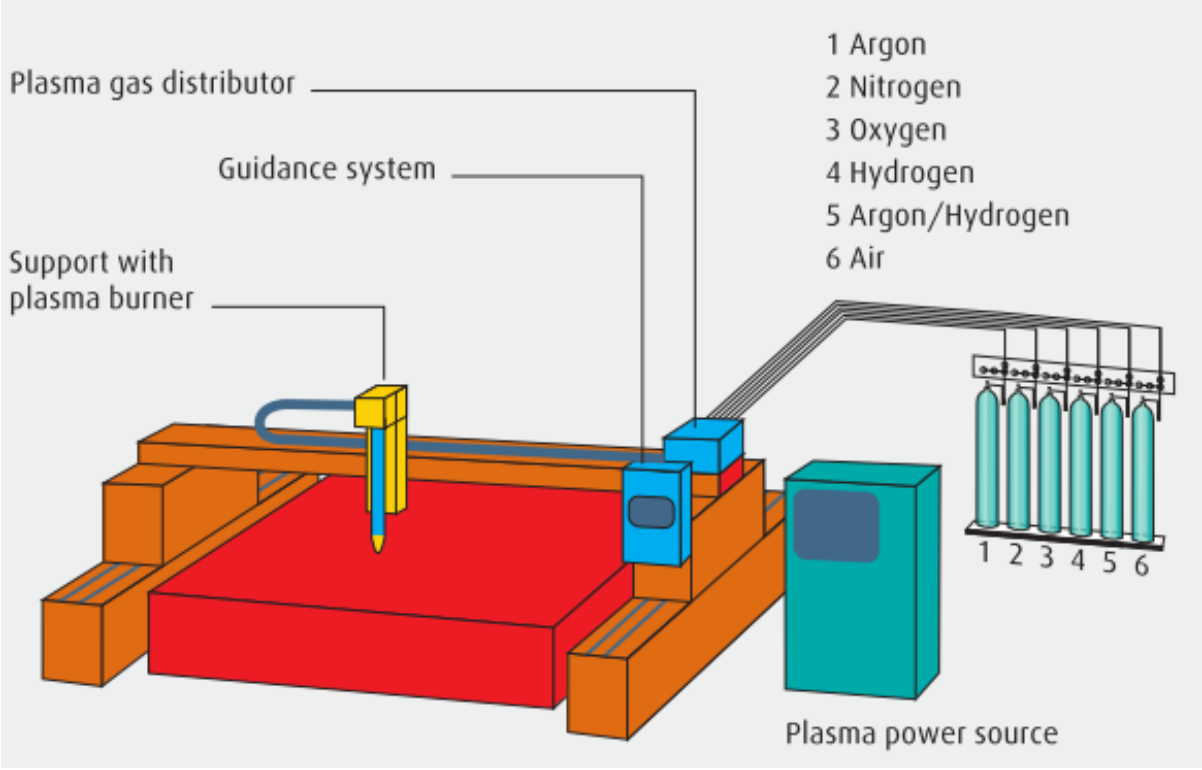

Fig. 5 Set up of plasma cutting process [83]

2.6 Computer Numerical Controlled Oxy-Fuel Gas Cutting

Cutting of thick plates is the challenging task in industrial practice. Computer Numerical controlled (CNC) profile cutting process has got advancement up to highly sophisticated and automatic operation to cut thick plates. That may be either gas i.e., Oxy-fuel cutting or plasma cutting machine. There is the requirement of variety of shapes or profiles to be cut from varying thickness of plates from 1-250 mm in industrial practice from variety of materials of plates like mild steel, stainless steel etc. Such cut shaped profiles are used in manufacturing and fabrication work [91].

In Oxy-flame cutting, a preheat flame is directed typically to the edge, or corner of the large section of steel to be cut. Once the steel becomes locally preheated to about 870 °C or higher, it is blasted with a stream of high purity oxygen to make the cut. The oxygen readily reacts with the hot iron to produce a stream of molten FeO. The molten metal is swept away by the flowing oxygen. The iron combusts approximately according to:

$$Fe\ (hot\ solid) + 1/2\ O_2\ (gas) = FeO\ (liquid) \qquad \Delta H_{298°C} = -63.8\ kcal/mole \qquad (1)$$

The enthalpy of this reaction heats and makes the molten products of combustion (i.e., FeO) so that it can flow away from the cut surface under the action of the blowing oxygen,. It heats the surrounding material so that the cut can be propagated. Iron oxide in the liquid state in actuality has an indefinite stoichiometry, which can vary depending on temperature and probably pressure. The metallurgist usually refers to molten iron oxide as Fe_xO, where x typically ranges in between 0.95-1.0, under usual conditions. From Equation 1, the value of $\Delta H_{298°C}$ is for the case where x equals 0.95. If more than stoichiometric quantities of oxygen are supplied to the iron being cut, there is the

possibility for the molten FeO to react and solidify to higher forms of oxides (Fe_3O_4 and Fe_2O_3) according to:

$$FeO + 1/6\ O_2 = 1/3\ Fe_3O_4 \quad \Delta H_{298°C} = -25.5 \text{ kcal/mole (FeO further oxidized)} \quad (2)$$

$$FeO + 1/4\ O_2 = 1/2\ Fe_2O_3 \quad \Delta H_{298°C} = -34.6 \text{ kcal/mole (FeO further oxidized)} \quad (3)$$

These additional oxidations of the iron to Fe_3O_4 and Fe_2O_3 occur from either (i) more-than-stoichiometric amounts of oxygen being dissolved into the molten FeO by the high partial pressure of gaseous oxygen surrounding the liquid FeO which pushes the oxygen concentration in the molten FeO towards saturation, or by (ii) excess free oxygen in the gas phase combining and reacting with the ejected and cooling FeO as it solidifies. It seems reasonable to presume that both mechanisms will occur. The final products of iron cutting can be a mixture of all three of these oxides together with some melted, but un-oxidized iron that was also produced by the intense heat release of the above oxidation reactions. Material discharged from the kerf (i.e., the slit or the notch) of oxygen cutting is reported of consisting about two-thirds iron oxide and one-third un-oxidized iron that was melted and carried out of the kerf by the stream of unused oxygen [91].

2.7 Stainless Steel

Stainless Steel is a steel alloy with a minimum of 10.5-11 % chromium content by mass [92]. In the 1821, French metallurgist Pierre Berthier discovered the iron-chromium alloys [93]. But in the 1912, Sheffield metallurgist Harry Brearley published it as Non-rusting Steel in The New York Times [94]. In this project, AISI 4140 and AISI 304 graded stainless steel are considered for experimentation of cutting process.

Chapter 3

EXPERIMENTATION

3 EXPERIMENTATION

The whole experiment of plasma arc cutting process of both 1st and 2nd cases was carried out by computer numerical controlled (CNC) plasma machine (Model: BURNY 1250, Maker: MESSER) where the cutting process is conducted in hypertherm environment. The parameters of plasma machining viz. oxygen supply, fuel gas supply and power supply were fixed at 20 MPa, 1.2 MPa and 400 VDC respectively. The material of AISI 4140 stainless steel of thickness 120 mm and 100 mm was selected for cutting operation in both the cases. Feed rate, cutting current, voltage and torch height were considered as the input process parameters. The quality of cut and material removal rate were measured as the major responses. Material removal rate (MRR) was measured by electronic weighing device. Surface roughness (SR) was measured using Talysurf device. The values of dross, chamfer, kerf width and heat affected zone (HAZ) were calculated with the help of Vernier caliper and the right bevel angle was measured using protractor. The industrial set up of plasma cutting operation is shown in Fig. 6 and the work piece of after cut is shown in Fig. 7. The structure of entire experimentation in this project is tabulated in Table 1.

Table 1 Structure of Experimentation

	Phase 1	Phase 2	Phase 3	Phase 4
Work piece	AISI-4140 Stainless Steel	AISI-4140 Stainless Steel	AISI-304 Stainless Steel	AISI-4140 Stainless Steel
Thickness of work piece	120 mm	100 mm	5 mm	85 mm
Process parameter	a) Feed Rate b) Cutting Current c) Voltage d) Torch Height	a) Feed Rate b) Cutting Current c) Voltage d) Torch Height	a) Cutting Current b) Cutting Speed c) Gas Pressure d) Stand-off Gap	a) Nozzle speed b) Torch height c) Oxy-fuel speed
Response	a) MRR b) SR c) Right Bevel Angle	a) MRR b) SR c) Chamfer d) Dross e) Kerf	a) MRR b) SR c) Chamfer d) Dross e) Right Bevel Angle f) Kerf g) HAZ	a) Bevel angle b) Dross width c) Dross height
Plasma cutting machine	BURNY 1250	BURNY 1250	Portable laboratorial PAC machine set up	LINDE controller profile cutter
Location of experimentation	L & T Kansbahal	L & T Kansbahal	Central Workshop of NITRKL	L & T Kansbahal
RSM (Design of Experiment)	Box-Behnken Design (L_{27})	Central Composite Design (L_{30})	Box-Behnken Design (L_{27})	Taguchi (L_9)

Fig. 6 Experimental set up used for plasma cutting process at industry

In 3rd case, AISI 304 stainless steel was selected for cutting operation with dimensions of 250×70×5 mm^3. Cutting current, cutting speed, gas pressure and stand-off gap were considered as the input process factors. MRR, SR, chamfer, dross, right bevel angle, kerf width and HAZ were measured as the output responses. MRR was measured by electronic weighing device. Surface roughness was measured using Talysurf device. The value of chamfer, dross, kerf width and HAZ were measured with Vernier caliper. The cutting process is carried out with portable plasma arc cutting system by attaching brass type of 2 mm diameter nozzle which is given in Fig. 8 (a). In plasma cutting operation, materials with high melting temperature on the cut surface of work piece are removed with the help of the flame of plasma as shown in Fig. 8 (b). The schematic diagrams of used base table and nozzle which was designed by Solid works version 12 are

shown in Fig. 8 (c) and (d). The nozzle of plasma arc machining is presented in Fig. 8 (e), which is made up of brass material. The work piece of AISI 304 stainless steel after cut by plasma is shown in Fig. 8 (f).

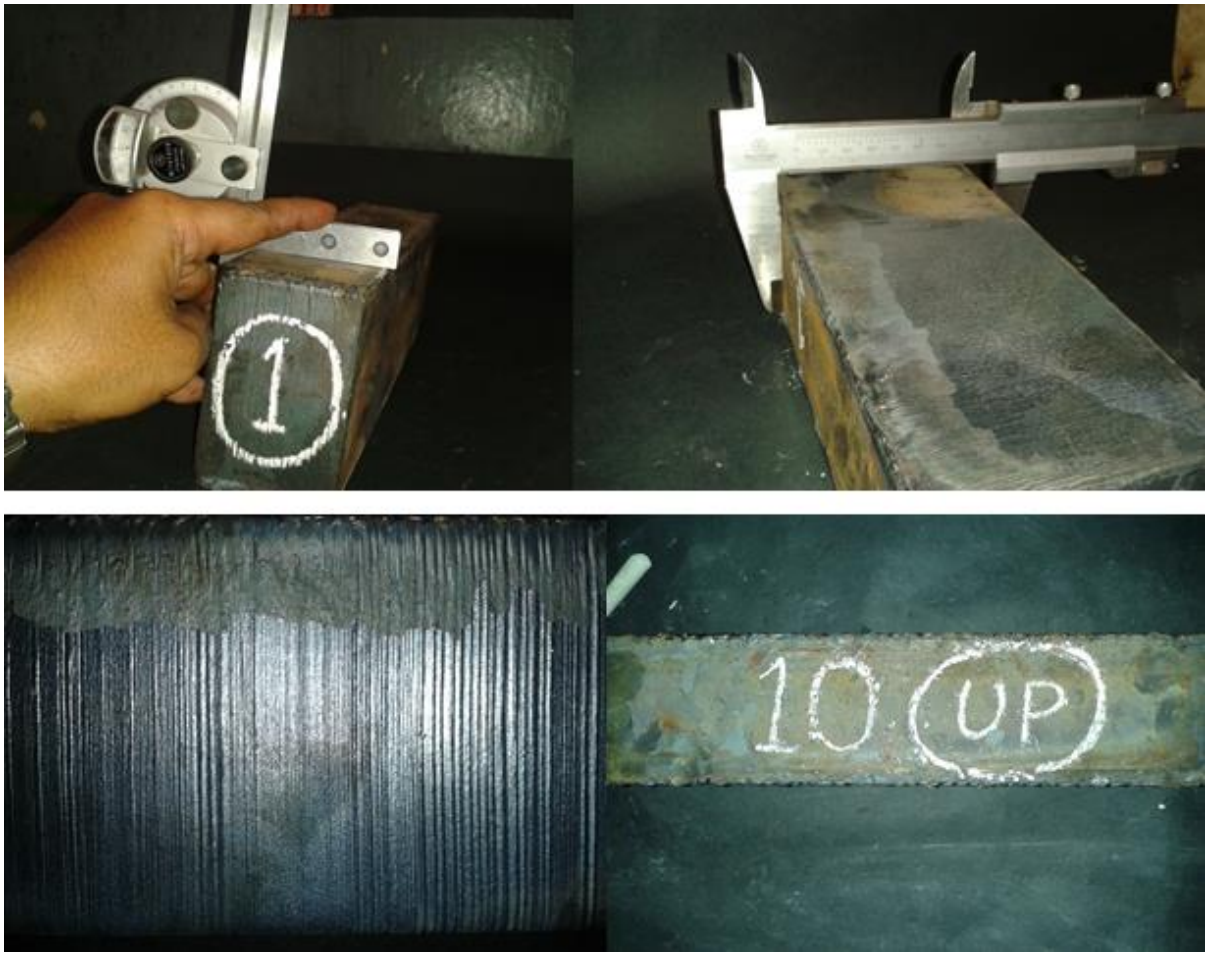

Fig. 7 Work piece of AISI 4140 steel after cut

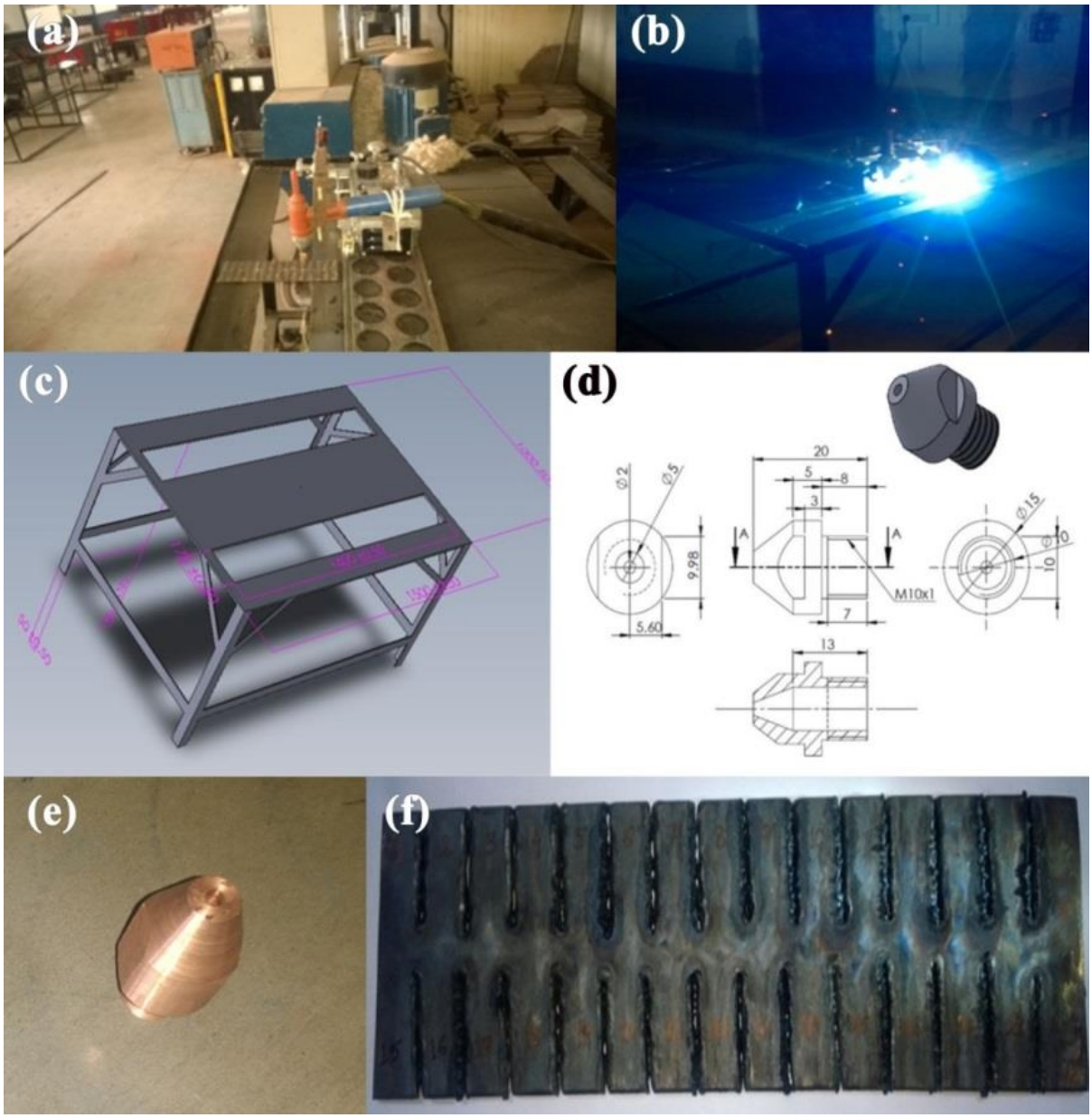

Fig. 8 (a) Experimental set-up for plasma arc cutting system, (b) During plasma arc cutting operation, (c) Schematic diagram of used table for cutting process, (d) Schematic diagram of used nozzle for cutting process, (e) Brass nozzle used in plasma cutting and (f) Work piece of AISI 304 steel after cut

The experimental setup of Oxy-fuel gas cutting process is displayed in Fig. 9. The whole experiment of CNC Oxy-fuel gas cutting process is experimented CNC profile

cutting machine (Model: LINDE, Maker: SIEMENS). AISI 4140 stainless steel is taken for investigation with thickness of 85 mm as shown in the same figure. Nozzle speed, Oxy-fuel speed and torch height were considered as the input process parameters. Bevel angle, dross breadth and dross height were measured as the output responses.

Fig. 9 Experimental set up of CNC Oxy-fuel gas cutting operation

3.1 Development of an Automated Plasma Arc Cutting System

The plasma arc cutting setup comprises mainly of following parts:

3.1.1 Speed control unit

Here, speed control unit is the movable tractors which run with a predefined speed required for cutting. Plasma arc cutting torch is fixed with it using a clamp in a particularly 90 º so that during cutting a stable and continuous arc form. Cutting speed can be changed using a regulator.

3.1.2 Rail track

Movable tractor is run in a particular speed over this rail track in a straight line. Plasma arc cutting torch: Torch is fixed with the movable tractor unit. A brass nozzle is attached in the torch and argon gas is passed through this. The torch was maintained at an angle approximate 90 º to the work piece.

3.1.3 Plasma arc cutting machine

This is the main part of plasma arc cutting setup by which controlled amount of current and voltage is supplied during cutting process. A rectifier with current range 50-400 Amperes and voltage up to 230 Volts is attached for supplying power to the system depending on the current setting.

3.1.4 Gas cylinder

For plasma arc cutting argon gas is supplied to the cutting torch with a particular flow rate so that an inert atmosphere formed and stable arc created for cutting. Gas flow is controlled by a regulator and valve.

3.1.5 Work holding table

A heavy ironed table is used for holding the work piece as well as speed controller with plasma torch, so that during cutting gap between the brass nozzle and work piece is maintained.

3.2 Cut Quality Characteristics of Plasma Cutting

3.2.1 Metal removal rate

Metal removal rate (MRR) is one of the most important criterions determining the machining operation, with a higher rate always preferred in such operations. The metal removal rate is calculated using the following expression:

$$MRR = \frac{w_i - w_f}{\rho \times t_m} \tag{4}$$

where w_i and w_f are the initial and final weight of work piece before and after cut using plasma respectively. The ρ is the density of AISI 304 and 4140 graded steel i.e., 8000 kg/mm^3 and t_m is the machining time.

3.2.2 Average surface roughness

Surface finish is another important aspect in the machining. The average surface roughness (Ra), which is mostly used in industry, was taken up for the present study. The roughness was measured with a sampling length of 10 mm. The average surface roughness was measured using a Talysurf tester (a stylus-type surface roughness meter).

3.2.3 Right bevel angle

The bevel angle is the deviation angle from the 90º of fine cut which occurred due to shape of plasma flame. This is the major quality characteristics of plasma arc cutting (PAC) operation at cut side wall.

3.2.4 Chamfer

A chamfer is a beveled edge connecting two surfaces. If the surfaces are at right angles, the chamfer will typically be symmetrical at 45 º. This is another characteristic of dimensional accuracy of the fabricated parts using plasma arc cutting operation.

3.2.5 Dross

Dross is the type of mass of solid impurities that forms on the surface of molten metal as a result of oxidation in the plasma arc cutting process.

3.2.6 Kerf

During plasma-arc cutting, the hot plasma jet melts the material and the kinetic energy of the jet removes the melt thus producing the desired kerf. This process causes a larger heat input in the material which results in a larger heat affected zone (HAZ). The dimensional accuracy largely depends on the kerf size, which in turn depends on the process variables.

3.2.7 Heat affected zone

There exists a narrow heat affected zone in PAC. The temperature of the zone will be below meting point and above recrystallization temperature. There is a change in micro-structure in heat affected zone. It is the zone of metallurgical change where the melted liquid have converted to solid form at the lowest temperature and this changes occur at the outer extremity [95].

Chapter 4

VARIOUS OPTIMIZATION METHODS

4 VARIOUS OPTIMIZATION METHODS

4.1 Response Surface Methodology

According to Montgomery, response surface method (RSM) is a collection of mathematical and statistical techniques that are helpful for modeling and analysis of problems in which response is influenced by several input variables, and the main objective is to find the correlation between the response and the variables inspected [24]. RSM has many advantages, and has effectively been applied to study and optimize the processes. It offers enormous information from a small number of experiments. In addition, it is possible to detect the interaction effect of the independent parameters on the response. The model easily clarifies the effect for binary combination of the independent process parameters. Furthermore, the empirical model that related the response to the independent variables is used to obtain information. According to Pradhan, it has been widely used in analyzing various processes, designing the experiment, building models, evaluating the effects of several factors and searching for optimum conditions to give desirable responses and reduce the number of experiments [25], [26] and [27]. RSM is an interaction of mathematical and statistical techniques for modeling and optimizing the response variables which incorporates quantitative independent variables. The behavior of the system is explained by the following second order polynomial regression model also known as a quadratic model.

$$y = b_0 + \sum_{i=1}^{n} b_i x_i + \sum_{i=1,j=1}^{n} b_{ij} x_i x_j + \sum_{i=1}^{n} b_{ii} {x_i}^2 \pm \Psi \qquad (5)$$

where y and x are out put response and input factor respectively, b_0, b_i, b_{ij} and b_{ii} are the polynomial constants and Ψ is the error constant. The coefficients of regression model can be estimated from the experimental results by Statistica 9.1 software [96].

4.2 Desirability Approach

The final aim of response surface methodology approach is to optimize the process factors on responses. Therefore, the developed models can be utilized for the simulation and optimization for any machining operation. To optimize the process with two or more output responses, it is very useful to utilize the concept of desirability function. This is one of the most widely used methods for optimization of multiple response processes in the field of science and engineering. It combines multiple responses into one response called desirability function by choosing a value from 0 (one or more characteristics are unacceptable) to 1 (all process characteristics are on target). Each of the estimated responses is transformed to an individual desirability value (d_i) ranging from 0 to 1. Mathematically, it is defined as per following equation:

$$d_i = \begin{cases} 0 \\ \left[\dfrac{\tilde{y}_i - y_{i_{min}}}{y_{i_{max}} - y_{i_{min}}}\right] \\ 1 \end{cases} \quad \begin{matrix} \tilde{y}_i \le y_{i_{min}} \\ y_{i_{min}} \le \tilde{y}_i \le y_{i_{max}} \\ \tilde{y}_i \ge y_{i_{max}} \end{matrix} \tag{6}$$

where the values $y_{i_{min}}$ and $y_{i_{max}}$ the minimum and maximum acceptable value of $\tilde{y}_i$ (each output response variable) respectively. The value of individual desirability value increases as the desirability of the corresponding response increases. The overall desirability value (D) of the process was computed as a geometric mean of the individual desirability functions and is given as following equation [97]:

$$D = (d_1 \times d_2 \times \ldots \times d_n)^{\frac{1}{n}} \tag{7}$$

All computations of desirability function were carried out utilizing Statistica 9.1 software.

4.3 Grey Relational Analysis

In the procedure of grey relational analysis (GRA), the experimental results of responses are normalized at first in the range between 0 and 1 due to different measurement units. This data pre-processing step is termed as grey relational generating. Based on the normalized experimental data, grey relational coefficient is calculated to correlate the desired and actual experimental data using Equation 11. The overall grey relational grade (GRG) is determined by averaging the grey relational coefficient corresponding to selected responses using Equation 12. This approach converts a multiple response process optimization problem into a single response optimization by calculating overall grey relational grade [65] and [66]. The normalized experimental results can be expressed as follows.

For the larger-the-better characteristic

$$x_i(k) = \frac{y_i(k) - \min y_i(k)}{\max y_i(k) - \min y_i(k)} \tag{8}$$

For the smaller-the-better characteristic

$$x_i(k) = \frac{\max y_i(k) - y_i(k)}{\max y_i(k) - \min y_i(k)} \tag{9}$$

and for the nominal-the-better characteristic

$$x_i(k) = 1 - \frac{\left| y_i(k) - y_{ob}(k) \right|}{\max y_i(k) - \min y_i(k)} \tag{10}$$

where max $y_i(k)$ and min $y_i(k)$ are the largest and smallest values of $y_i(k)$ respectively and $y_{ob}(k)$ is the target of $y_i(k)$. The Grey relational coefficient $\xi_i(k)$ for $y_i(k)$ to $y_0(k)$ is calculated as

$$\xi_i(k) = \frac{\Delta_{\min} + \psi\Delta_{\max}}{\Delta_{0i}(k) + \psi\Delta_{\max}} \tag{11}$$

where $\Delta_{0i}(k)=x_0(k)-x_i(k)$ is the difference of absolute value between $x_0(k)$ and $x_i(k)$, $\Delta_{\min}$ and $\Delta_{\max}$ are the minimum and maximum values of the absolute differences (Δ_{0i}) of all comparing sequences. Ψ is a distinguishing coefficient, $0 \leq \Psi \leq 1$, the value of Ψ is to be set to 0.5 to maintain equal weightage of all parameters. GRG, γ_i is obtained by averaging the grey relational coefficient corresponding to each experiment.

$$\gamma_i = \frac{1}{n}\sum_{i=1}^{0} \xi_i(k) \tag{12}$$

Experiments were conducted according to RSM orthogonal array of L_{27} and L_{30}.

4.4 Principal Component Analysis

Principal component analysis is a mathematical approach that converts a set of observations of probably correlated variables into a set of values of uncorrelated variables. It was invented very early and later mostly used as a tool in investigative data analysis and for the formation of predictive models. Principal component analysis can be done by Eigen value decomposition of a data covariance matrix or singular value decomposition of a data matrix. It is used for identifying patterns in data and expressing the data in such a way as to highlight their similarities and differences [34]. The main advantage of principal component analysis is that once the patterns in data have been identified, the data can be compressed i.e., by reducing the number of dimensions, without much loss of information. The explicit goals of principal component analysis are:

1. To extract the most significant information from the data,
2. To squeeze the size of the data set by keeping only the significant,
3. To simplify the explanation of the data set and
4. To analyze the structure of the observations and the variables.

The procedure is described as follows [34]:

1. The original multiple quality characteristic array

$$X = \begin{bmatrix} x_1(1) & x_1(2) & \dots & \dots & x_1(n) \\ x_2(1) & x_2(2) & \dots & \dots & x_2(n) \\ : & : & \dots & \dots & : \\ : & : & \dots & \dots & : \\ x_m(1) & x_m(2) & \dots & \dots & x_m(n) \end{bmatrix} \quad (13)$$

i=1,2,...,m; j=1,2, ...,n [35]

where m is the number of experiment and n is the number of the response. In the present work, x is the grey relational coefficient of each response.

2. Correlation coefficient array

The correlation coefficient array is evaluated as follows:

$$R_{jl} = \left(\frac{Cov(x_i(j), x_i(l))}{\sigma x_i(j) \times \sigma x_i(l)} \right) \quad (14)$$

$j = 1,2,3,\dots,m$

$l = 1,2,3,\dots,n$

where $Cov(x_i(j))$, $x_i(l)$ is the covariance of sequences $x_i(l)$ and $x_i(l)$, $\sigma x_i(j)$ is the standard deviation of sequence $x_i(j)$ and $\sigma x_i(l)$ is the standard deviation of sequence $x_i(l)$.

3. Determining the Eigen values and eigenvectors

The Eigen values and eigenvectors are determined from the correlation coefficient array:

$$(R - \lambda_k I_m) V_{ik} = 0 \quad (15)$$

where λ is the Eigen value $\sum_{k=1}^{n}\lambda_k = n, k = 1,2,3,...,n$ and $V_{ik} = [a_{k1}, a_{k2}, a_{k3}, ..., a_{km}]^T$ is the eigenvectors corresponding to the Eigen value λ_k. The Eigen values and its variation are evaluated as per Equation 15.

4. Principal components

The uncorrelated principal component is formulated as

$$Y_{mk} = \sum_{i=1}^{n} x_m(i) \cdot V_{ik} \tag{16}$$

where Y_{m1} is called the first principal component, Y_{m2} is called the second principal component and so on. The principal components are aligned in descending order with respect to variance, and therefore, the first principal component Y_{m1} accounts for the most variance in the data.

4.5 Genetic Algorithm

Genetic Algorithm is used extensively for the solution of optimization problems and was first developed by Holland in the 1970s. These algorithms are based on the biological evolution process. A similar analogy is used to evolve solutions to complex optimization problems. The notable feature of Genetic Algorithm is that it emulates the biological system's characteristics like self-repair and reproduction. A potential solution to a problem may be represented by a set of parameters known as genes. These genes are combined together to form a string which is referred to as a chromosome. It is widely believed that ideally a binary string should be used for the chromosome. The set of parameters represented by a particular chromosome is called as genotype. This genotype contains the information required to construct an organism called the phenotype. A fitness function is analogous to the objective function in an optimization problem. The fitness function

returns a single numerical fitness which is proportional to the utility or ability of the individual which that chromosome represents. During reproduction in the GA, individuals are selected from the population and recombined, producing off-springs which will comprise the next generation. Two parents are selected and their chromosomes are recombined, typically using the mechanisms of crossover and mutation. Crossover is the operation when two individuals are taken and their chromosomes are cut at some randomly chosen position, to produce two head and tail segments. These segments are swapped to produce two new full length chromosomes. The off springs inherit some genes from each parent. This is known as a single point crossover. Mutation is the technique used to randomly alter the genes with a small probability and is typically applied after crossover. Crossover is more important for rapidly exploring a search space. Mutation provides only a small amount of random search. If the GA has been implemented correctly, the population will evolve over successive generations so that the fitness of the best and the average individual in each generation increases towards the global optimum. A gene is said to have converged when 70% of the population share the same value of the fitness function [98].

4.5.1 Algorithm of GA approach

1. Initial population: Generate random population of chromo-somes.
2. Fitness: Evaluate the fitness of each chromosome in the population.
3. Test: If the end condition is satisfied, stop, and return the best solution in current population.
4. New population: Create a new population by repeating following steps until the new population is complete. Reproduction: Select two parent chromosomes from

the population according to their fitness. Crossover: With a crossover probability, crossover the parents to form a new offspring (children). If no crossover was performed, offspring is an exact copy of parents. Mutation: With a mutation probability, mutate new offspring at each locus (position in chromosome).

5. Replace: Use new generated population for a further run of algorithm.
6. Loop: Go to step 2 [99-101].

4.6 Simulated Annealing

Unlike other non-conventional optimization patterns, simulated annealing process uses single point search method. Simulated annealing method resembles the coding process of molten metals through annealing. At high temperatures, the atoms in the molten metal can travel freely with respect to each other, but as the temperature is reduced, the movement of the atoms becomes restricted. The atoms start to get ordered and finally form crystals having the minimum possible energy. However, the formation of the crystal typically depends on the cooling rate. If the temperature is reduced at a very fast rate, the crystalline state may not be attained at all; instead, the system may end up in a polycrystalline state, which may possibly have a higher energy state than the crystalline state. Therefore, in order to achieve the absolute minimum energy state, the temperature is to be reduced at a slow rate. The process of slow cooling is known as annealing in metallurgical practice. The simulated annealing procedure simulates this process of slow cooling of molten metal to achieve the minimum function value in minimization problem. The cooling phenomenon is simulated by controlling a temperature-like parameter using the concept of the Boltzmann probability distribution. According to Yang et al. a system in thermal equilibrium at a temperature T has its energy distributed probabilistically as

$$P(E) = exp(-\Delta E / KT) \quad (17)$$

where K is Boltzmann constant. By adjusting the temperature T and assuming that the search process follows the Boltzmann probability distribution, the convergence of an algorithm can be achieved [58], [59], [60] and [61]. Simulated annealing algorithm starts with an initial point and a high temperature T. A second point is generated at random in the vicinity of the initial point and the difference in the function values ΔE at these two points is calculated. If the second point has a smaller function value, the point is accepted; otherwise the point is accepted with a probability exp(−ΔE/T). This completes one cycle of the simulated annealing procedure. In the next cycle, again another point created at random in the neighborhood of the updated current point and the Metropolis algorithm is used to accept or reject the point. In order to simulate the thermal equilibrium at every temperature, a number of points (n) are usually tested at a particular temperature, before reducing the temperature. The algorithm is terminated when a sufficiently small temperature is obtained or a desirable minimal change in function value is observed. The initial temperature T and number of iterations N performed at every temperature are two important parameters, which govern the successful working of the simulated annealing procedure. The algorithm is terminated when a sufficiently small temperature is obtained or a desirable minimum change in function value is observed. The initial temperature T and number of iterations N performed at every temperature are two important parameters, which govern the successful working of the simulated annealing algorithm is given below [62], [63] and [64].

4.6.1 Algorithm of SA approach

1. Randomly generated initial point X^0 is to be chosen with a termination temperature T_{low}. Also, the set number of iterations (N) to be performed at a particular temperature and iteration counter t=0.
2. The value of objective function $E_1 = f(X^t)$ is to be evaluated.
3. A neighbourhood point X^{t+1} using random perturbation and the objective function at X^{t+1} as $E_2 = f(X^{t+1})$ is to be evaluated.
4. $\Delta E = E_2 - E_1$ IS to be determined.
5. Go to following steps:

(i) If $\Delta E < 0$, the point is accepted. That is $X^t = X^{t+1}$ and $E_1 = E_2$.

(ii) Set t = t+1 and step-6 is executed.

(iii) If $\Delta E \geq 0$, the random number r in the range (0, 1) created. It is checked whether $r \leq \exp(-\Delta E/T)$. If satisfied then t = t + 1 is set and step-6 is used. Else begin with new initial point X^t and go to step-3.

6. If t >N step-7 is executed.
7. The temperature is reduced periodically by a factor k_1 according to $T = k_1T$ and step-3 is adopted.
8. If $T \leq T_{low}$ the process is terminated.

4.7 Particle Swarm Optimization

Particle swarm optimization (PSO) is a population based stochastic optimization technique developed by Eberhart and Kennedy [14] in 1995, inspired by the social behavior of bird flocking or fish schooling. The intelligence of swarm is based on the principle of social and psychological behavior of the swarm. The optimization procedure

is initialized with a population of random solutions and searches for optima by updating generations. The potential solutions called particles fly through the problem space by following the current optimum particles. PSO is very easy to implement and there are few parameters to adjust. The algorithm can be explained based on the following scenario: a group of birds are randomly searching food in an area. There is only one piece of food in the area being searched. All the birds do not know where the food is. But they know how far the food is in their search. So the best strategy to attain the food is to simply follow the bird, which is nearest to the food. In optimization problems, each bird in the search space is referred to as particle. All the particles are evaluated by the fitness function to be optimized and have velocities for the particles. The particles fly through the problem space by following the current optimum particles. The problem is initialized with a group of random particles and then searches for optima by updating generations. In all the iterations, each particle is updated by following two best values. The best solution achieved so far among the particle is called as particle best termed as pbest and the best solution obtained so far in the population is called as global best termed as gbest. A particle takes the entire particle toward its pbest and gbest locations. After finding the two best values, the particles are updated with its velocity and positions using Eqs. (18) and (19).

$$v[] = \omega \times v[] + C1 rand() \times (pbest[] - present[]) + C2 \times rand() \times (gbest[] - present[]) \quad (18)$$

$$p[] = present[] + v[] \quad (19)$$

where

v[]=Particle velocity

p[]=New particle position

persent[]=Current particle (solution)

pbest[]=Best solution among the each particle

gbest[]=Best among defined as stated before

rand()=Random numbers between 0 and 1

ω=Inertia Weights i.e., 0.9

C1, C2=learning factors, usually C1=C2=2.

4.7.1 Algorithm of PSO approach

1. Initialize a population of n particles randomly.
2. Calculate fitness value for each particle. If the fitness value is better than the best fitness value (pbest) in history, then set current value as the new pbest.
3. Choose particle with the best fitness value of all the particles considered so far as the gbest.
4. For each particle; calculate particle velocity and position according to Eqs. (18) and (19).
5. Particle velocities on each dimension are clamped to a maximum velocity i.e., v_{max}. If the sum of acceleration would cause the velocity on that dimension to exceed v_{max} (specified by the user), the velocity on the dimension is limited to v_{max}.
6. Terminate if maximum number of iterations is reached. Else, go to Step 2.
7. End.

4.8 Teaching Learning Based Optimization

Recently, *Rao et al.* [102] proposed a new population based method known as teaching-learning-based-optimization (TLBO) algorithm. TLBO resembles the teaching-

learning process in a class room for finding out the global optimal solution. Teacher and learners are the two critical components of the algorithm and emphasizes on two basic modes of the learning, through teacher (known as teacher phase) and interacting with the other learners (known as learner phase). In this algorithm a group of learners is considered as population and different subjects taught to the learners are considered as different design variables of the optimization problem. A learner's overall result is equivalent to the value of the objective function.

4.8.1 Algorithm of TLBO approach

1. Initialize the number of learners *L* (i.e., the population size), number of subjects *J* taught to the learners (i.e., the design variables). Select maximum number of iterations *I*. Set iteration counter $i = 0$.
2. Generate a random population of results Y and calculate corresponding f(Y).
3. Calculate mean result in each subject by using;

$$M_{ji} = \frac{1}{L}\sum_{L=1}^{L} X_{ijL} \tag{20}$$

4. Identify the best learner *l-best*.
5. Calculate $dm_{ij} = r_i\,(Y_{ijl\text{-}best} - T_F M_{ij})$ for each *j*.

   Update $Y'_{ijk} = Y_{ijl} + dm_{ij}$ for all *j* and *k*.
6. If f(Y′) gives better result,

   Accept Y′

   Else

   Retain Y as Y′.
7. Randomly select two learners *L1* and *L2* such that $f(Y')_{L1} \neq f(Y')_{L2}$
8. If $f(Y_{L1})$ is better than $f(Y_{L2})$

$$Y''_{ijL1} = Y'_{ijL1} + r_i\,(Y'_{ijL1} - Y'_{ijL2}) \quad (21)$$

Else

$$Y''_{ijL1} = Y'_{ijL1} + r_i\,(Y'_{ijL2} - Y'_{ijL1}) \quad (22)$$

9. If f(Y″) is better

Accept Y″

Else

Retain Y′ as Y″

10. If $i \geq I$

Terminate and Y″ is solution

Else

$i = i+1$, Y = Y″, go to Step 3.

4.9 Data Envelopment Analysis Model

The data envelopment analysis (DEA) model is being currently used for optimization of different processes. In the present investigation, the optimization of the process parameters of the CNC Oxy-fuel gas cutting has been carried out using DEA approach. The work material was considered as AISI 4140 steel. The output responses are bevel angle, dross breadth and dross height. The input parameters are nozzle speed, Oxy-fuel speed and torch height.

Data Envelopment Analysis model initiated in the 1978. *Charnes et al.* [103] demonstrated Charnes, Cooper and Rhodes (CCR) model as the conversion of a fractional linear measure of efficiency into a linear programming (LP) format. As a result, Decision-Making Units (DMUs) could be assessed on the basis of multiple inputs and outputs, even if the objective function was unknown. This nonparametric approach solves an LP formulation

per DMU and the weights assigned to each linear aggregation are the results of the corresponding LP. The weights are chosen so as to show the specific DMU in as positive a light as possible, under the restriction that no other DMU, given the same weights, is more than 100 % efficient. Consequently, a Pareto frontier is achieved, marked by specific DMUs on the boundary envelope of input–output variable space. The frontier is considered a sign of relative efficiency, which has been achieved by at least one DMU. Adler et al. [104] described that DEA is a mathematical model that measures the relative efficiency of decision-making units with multiple inputs and outputs but with no obvious objective function to aggregate the data in its entireness. Relative efficiency is expressed as the ratio of total weighted output to total weighted input.

4.9.1 Steps of DEA approach

1. ***Normalization of input response***

It is necessary to normalize responses to ensure that all the attributes are equivalent and occurred in the domain of [0, 1]. The given response is normalized by the following equation:

$$Z_{ij} = \frac{X_{ij}}{\max X_{ij}} \tag{23}$$

For i=1,2,…,m and j=1,2,…,n

And for the bevel angle and dross breadth parameters as per the following equation:

$$Z_{ij} = \frac{\min X_{ij}}{X_{ij}} \tag{24}$$

For i=1,2,…,m and j=1,2,…,n

where X_{ij} is the mean for the i^{th} response in the j^{th} experiment.

2. *Calculation for relative efficiency*

For each experiment the relative efficiency has been computed by the aid of Lingo 14 software package. Following equation is used for the calculation of the relative efficiency:

$$\max E_{kk} = \sum_{y}^{k} O_{ky} V_{ky} \tag{25}$$

Such that,

$$\sum I_{kx} U_{kx} = 1 \tag{26}$$

$E_{ks} \leq 1$ For all the design such that,

$$U_{kx}, V_{ky} > 0 \tag{27}$$

3. ***Calculation for S/N ratio***

Applying Taguchi method to obtain relative efficiency value according to larger-the-better criterion by the help of Statistica 9.1 software as per following formula:

$$\eta = -10 \log_{10}\left(\frac{1}{n}\sum_{i=1}^{n}\frac{1}{y_i^2}\right) \tag{28}$$

Chapter 5

RESULTS AND DISCUSSION

5 RESULTS AND DISCUSSION

Cutting the stainless steel plates are still more defying than that of other steel metals due to the difference in the physical, mechanical, and metallurgical properties of the metals to be cut. Proper choice of mechanism and process variables are, therefore, obligatory to make the cuts with good quality. Therefore, plasma arc cutting of stainless steel metals has increasing demand due to the higher penetration rates and with the benefits of high cutting speed providing higher productivity. This work demonstrated a bid for development of empirical models of the plasma arc cutting process based on response surface methodology (RSM). Parameter design of RSM being simple and effective is adopted for in-depth study to understand process parameters and their interaction effects on responses like accuracy of dimensions in different directions of PAC built parts with minimum experimental runs [39]. To maintain a high production rate and admissible quality of cut devices, the machining process parameters of PAC must be optimized [40].

In the 1st case study, the entire experimentations are arranged utilizing Box-Behnken Design (BBD). From the experimental data, multiple regression models for the material removal rate, surface roughness and bevel angle are produced utilizing RSM on AISI 4140 steel. The machining parameters i.e., feed rate, cutting current, voltage and torch height are optimized utilizing proposed approach to maximizing MRR and minimizing the surface roughness and bevel angle. In general plasma arc cutting process involves a large number of response parameters. In the present investigation, a number of response parameters have been optimized with respect to number of process parameters using RSM

combined with grey relational analysis and principal component analysis. The quality of cut and material removal rate are taken as the responses.

In the present 2nd investigation experimental investigation of plasma arc cutting processes on AISI 4140 stainless steel is done using central composite design of RSM. The process parameters considered for this study are feed rate, cutting current, voltage and torch height. The responses are material removal rate, surface roughness, chamfer, dross and kerf.

In the 3rd study, a portable plasma arc cutting machine was renovated with automatic heating arrangement for micro-plasma cutting. The slots are made up of stainless steel. The whole experimentations are planned using Box-Behnken Design (BBD) on AISI 304 stainless steel material. From the experimental data, multiple regression models for the material removal rate, surface roughness, chamfer, dross, right bevel angle, kerf width and heat affected zone are developed using RSM. The machining parameters, i.e., cutting current, cutting speed, gas pressure and stand-off gap are optimized using RSM to maximize MRR and minimize the value of other cut characteristics.

5.1 Results of Case 1

The response surface methodology was utilized to study the influences of the independent factors feed rate (A), cutting current (B), voltage (C) and torch height (D) at three variation levels in the extraction procedure which is tabulated in Table 2. The whole experimentations were planned using Statistica 9.1 software (Company: Statsoft). Three levels are selected for each independent variable such as low (-1), middle (0) and high level (+1) which is shown in Table 2. The experimental design consisted of twenty seven cases or runs according to single blocked BBD. Analysis of variance (ANOVA) and F-test

are used to check significant criteria for the fitted models. The results obtained were presented as mean values with standard deviation. After getting the layout of experimental design of input factors from Statistica software, the cutting operation by plasma arc on the selected work piece have been carried out. According to the DOE, the three output quality characteristics of cut are measured and tabulated in Table 3. The design of experiment consisted of actual level value of input factors with standard order of BBD and corresponding value of output responses. After simulating the optimization approach by software to this model, the ANOVA evaluation has been carried out to each response. Similarly, the estimated coefficient of the model was calculated for each cut quality. The influences of input variables in plasma arc machining for each response is briefly described below:

Table 2 Values of Input Process Parameters

Process parameters	Units	Code	L(1)	L(2)	L(3)
Feed Rate	mm/min	A	900	950	1000
Cutting Current	Ampere	B	40	45	50
Voltage	Volt	C	100	125	150
Torch Height	mm	D	1	2	3

Table 3 RSM Design with Input Parameters

Std. Order	Run Order	Feed Rate (mm/min)	Current (Ampere)	Voltage (Volt)	Torch Height (mm)	MRR (mm^3/min)	SR (µm)	Right Bevel Angle (Degree)
8	1	950	45	150	3	0.273575	6.46	4
3	2	900	50	125	2	0.080358	4.54	3
9	3	900	45	125	1	0.276183	6.59	3
20	4	1000	45	150	2	0.115758	3.66	4
7	5	950	45	100	3	0.253758	4.83	3
23	6	950	40	125	3	0.212808	6.28	2
26	7	950	45	125	2	0.055367	4.34	4
22	8	950	50	125	1	0.102458	7.61	2
27	9	950	45	125	2	0.055367	4.44	4
2	10	1000	40	125	2	0.256292	2.94	3
10	11	1000	45	125	1	0.279733	6.79	3
15	12	950	40	150	2	0.03145	4.77	3
21	13	950	40	125	1	0.425975	6.14	3
17	14	900	45	100	2	0.057892	4.78	4
6	15	950	45	150	1	0.075092	6.54	3
24	16	950	50	125	3	0.486575	5.51	4
12	17	1000	45	125	3	0.512717	3.87	4
16	18	950	50	150	2	0.087883	5.41	4
5	19	950	45	100	1	0.076375	7.71	3
11	20	900	45	125	3	0.419067	7.86	3
1	21	900	40	125	2	0.209792	6.25	3
18	22	1000	45	100	2	0.099542	3.98	4
25	23	950	45	125	2	0.055367	4.46	4
4	24	1000	50	125	2	0.131058	5.71	3
19	25	900	45	150	2	0.060208	5.86	4
14	26	950	50	100	2	0.10515	4.19	3
13	27	950	40	100	2	0.030183	5.73	3

5.1.1 RSM with desirability function approach

5.1.1.1 For material removal rate:

The impact of estimated values of MRR was calculated and recorded in Table 4. The ANOVA evaluation for MRR has been carried out firstly and its results are tabulated in Table 5. Here, the block effect has also been considered because the levels of block are

taken as one. Due to this variation in block, there is negligible amount of effect arisen in experiment. This effect is ignored for further computation of optimization. The total degree of freedom for all input factors of plasma arc cutting is 26. From the Table 5, it is understood that the most of the terms have P-value less than 0.05 under the confidence interval of 95 %. Hence, these terms demonstrates significance within experiment. In case of individual terms, only torch height is the most significant among all parameters. Pareto chart of effects of all factors on MRR response are shown in Fig. 10 and the results indicate that the quadratic of torch height is the second most enhancing factor among all considered factors. The scatter plot between the observed and the predicted value of MRR of all 27 runs is shown in Fig. 11. It is concluded that there is a reasonable correlation between the measured and predicted values of MRR response. In Fig. 13, the histogram plot of predicted data of MRR with 95 % confidence interval of normal distribution is displayed. The surface and contour plot of this interaction terms have been considered for further analysis and are shown in Fig. 16-17 respectively. In this figure, it is clearly displayed that the value of MRR increases with increasing cutting current and torch height. In Table 6, the model of estimated coefficients of the independent variable on the MRR is presented.

Table 4 Effect of Estimated Values for MRR

Factor	Effect	Std. Err.	T	P
Constant	0.240427	0.018048	13.32148	0.000000
A (mm/min)	0.048600	0.031260	1.55470	0.145985
A^2	-0.090480	0.023445	-3.85922	0.002272
B (Ampere)	-0.028836	0.031260	-0.92246	0.374462
B^2	-0.048153	0.023445	-2.05384	0.062447
C (Volt)	0.003511	0.031260	0.11232	0.912430
C^2	0.063487	0.023445	2.70790	0.019029
D (mm)	0.153781	0.031260	4.91939	0.000354
D^2	-0.202444	0.023445	-8.63482	0.000002
A×B	0.002100	0.054144	0.03879	0.969699
A×C	0.006950	0.054144	0.12836	0.899989
A×D	0.045050	0.054144	0.83204	0.421637
B×C	-0.009267	0.054144	-0.17115	0.866955
B×D	0.298642	0.054144	5.51568	0.000133
C×D	0.010550	0.054144	0.19485	0.848770

Table 5 ANOVA Table for MRR

Factors	SS	DoF	MS	F	P
A (mm/min)	0.007086	1	0.007086	2.41708	0.145985
A^2	0.043662	1	0.043662	14.89356	0.002272
B (Ampere)	0.002495	1	0.002495	0.85094	0.374462
B^2	0.012366	1	0.012366	4.21826	0.062447
C (Volt)	0.000037	1	0.000037	0.01261	0.912430
C^2	0.021497	1	0.021497	7.33273	0.019029
D (mm)	0.070945	1	0.070945	24.20036	0.000354
D^2	0.218580	1	0.218580	74.56014	0.000002
A×B	0.000004	1	0.000004	0.00150	0.969699
A×C	0.000048	1	0.000048	0.01648	0.899989
A×D	0.002030	1	0.002030	0.69229	0.421637
B×C	0.000086	1	0.000086	0.02929	0.866955
B×D	0.089187	1	0.089187	30.42278	0.000133
C×D	0.000111	1	0.000111	0.03797	0.848770
Error	0.035179	12	0.002932		
Total SS	0.548623	26			

Table 6 Regression Coefficients of MRR

Factor	Regression Coef.	Std. Err.	T	P
Constant	39.24466	11.02705	3.55895	0.003931
A (mm/min)	-0.06972	0.01870	-3.72736	0.002888
A^2	0.00004	0.00001	3.85922	0.002272
B (Ampere)	-0.23532	0.13626	-1.72698	0.109797
B^2	0.00193	0.00094	2.05384	0.062447
C (Volt)	0.02407	0.02473	0.97351	0.349518
C^2	-0.00010	0.00004	-2.70790	0.019029
D (mm)	-2.53113	0.59271	-4.27045	0.001087
D^2	0.20244	0.02345	8.63482	0.000002
A×B	0.00000	0.00011	0.03879	0.969699
A×C	0.00000	0.00002	0.12836	0.899989
A×D	0.00045	0.00054	0.83204	0.421637
B×C	-0.00004	0.00022	-0.17115	0.866955
B×D	0.02986	0.00541	5.51568	0.000133
C×D	0.00021	0.00108	0.19485	0.848770

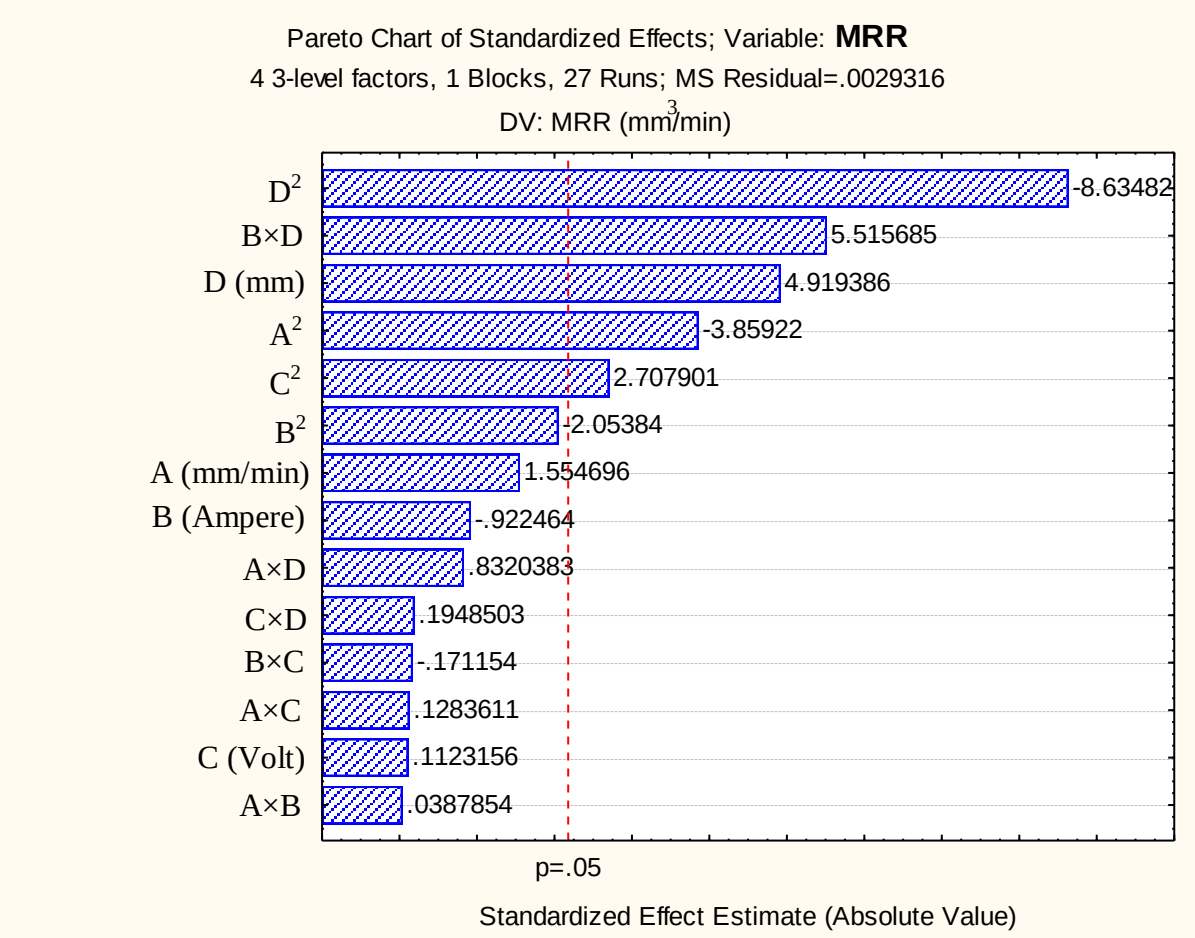

Fig. 10 Pareto chart of standardized effect of factors on MRR

In Fig. 10, the torch height factor with quadratic form had shown the most significant impact on the MRR response of plasma arc cutting operation. From this Pareto chart it can be revealed the comparison of influences among out all types of terms (i.e. individual, square and interaction terms).

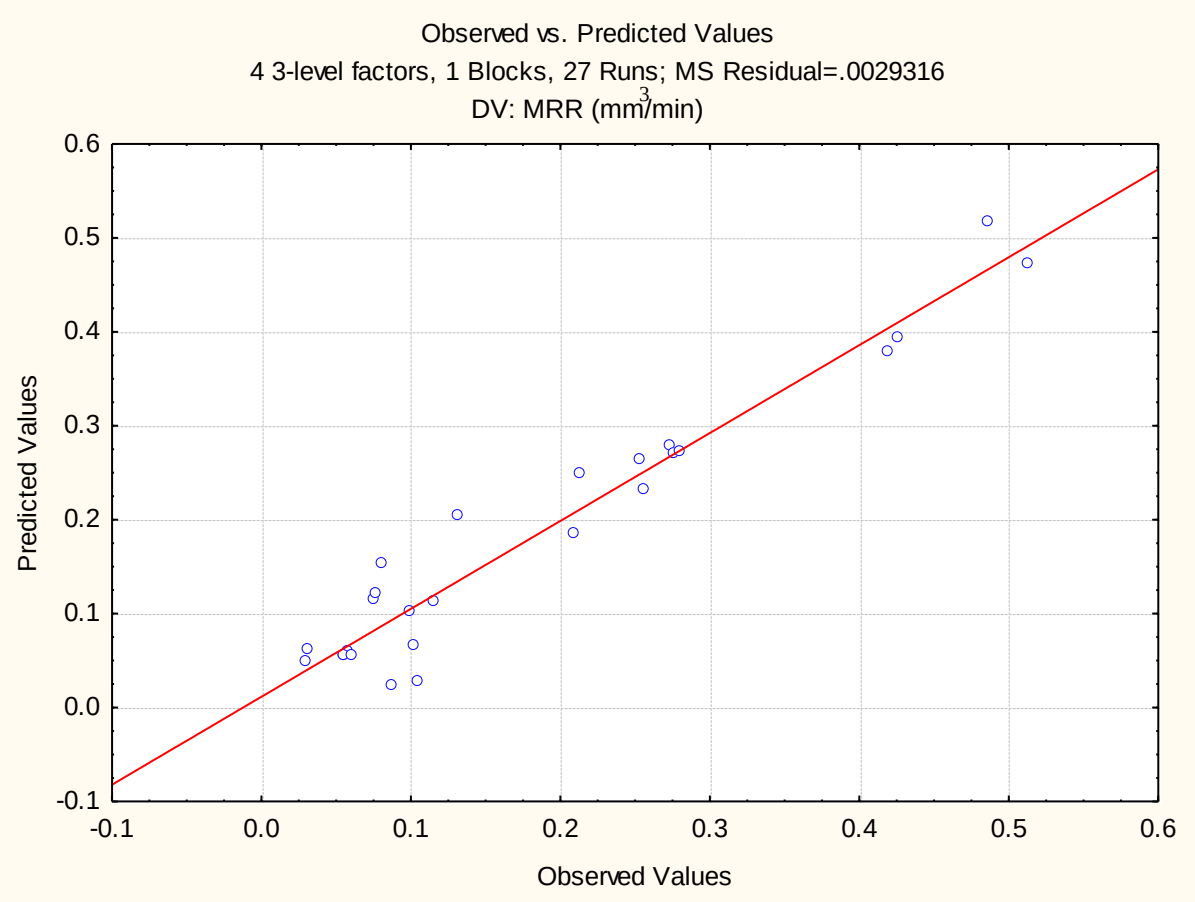

Fig. 11 Plot of observed vs. predicted values of MRR

The scatter plot between the observed and the predicted value of plasma cut responses of all 27 runs is shown in Fig. 11. This plot showed the comparison between each of the observed values with the predicted value which are calculated from the developed model. Here, the most of the points lie on the normal line of fitted values except the plot of MRR, because the uniformity lacks in the middle region. From this result it can be revealed that the response model fits best to experimental data, as the relationship between the actual and the predicted MRR is linear.

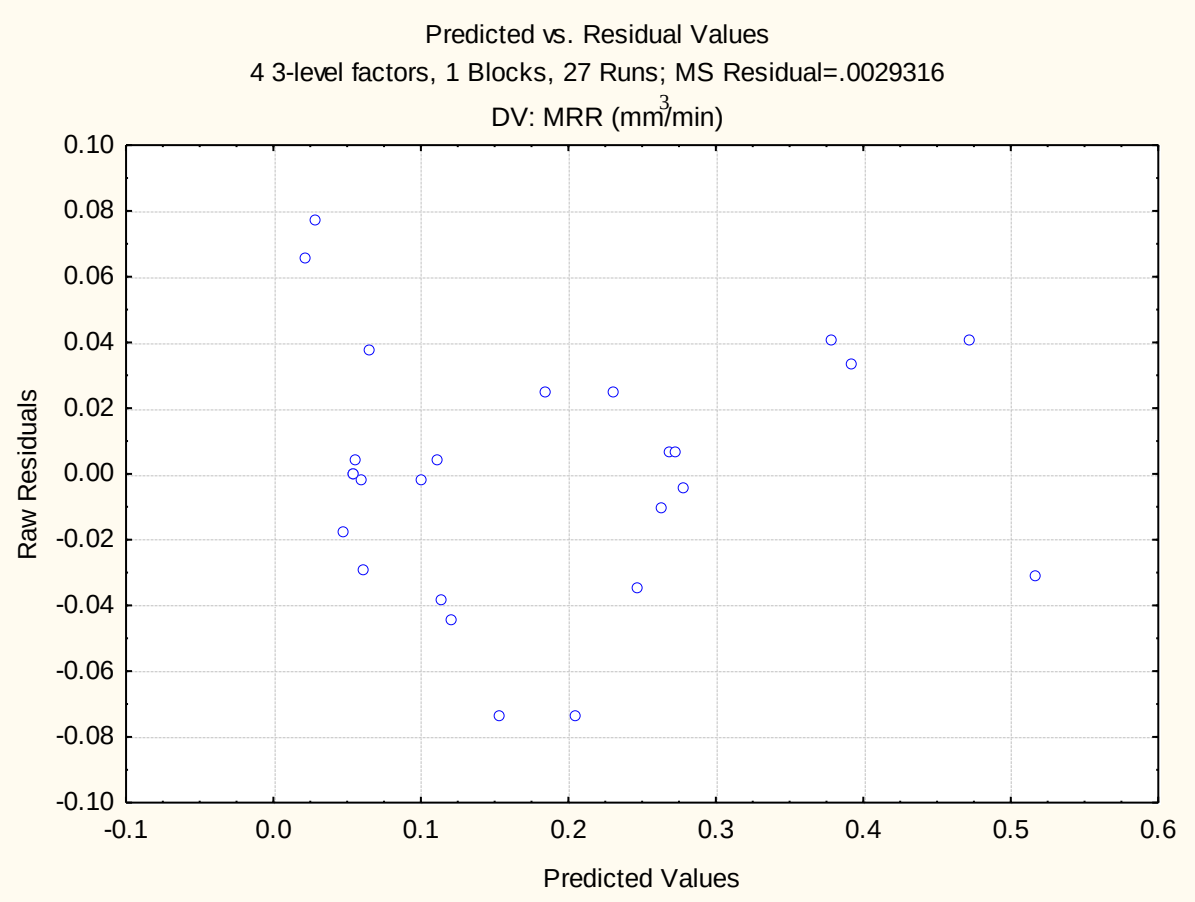

Fig. 12 Plot of predicted vs. residual values of MRR

From the Fig. 12, no standard pattern is formed in the plot of predicted vs. residual values that showed the adequacy of the fitted model for MRR. This plot displayed the variation of the raw residuals with respect to the predicted values which occurred in the analysis part of optimization.

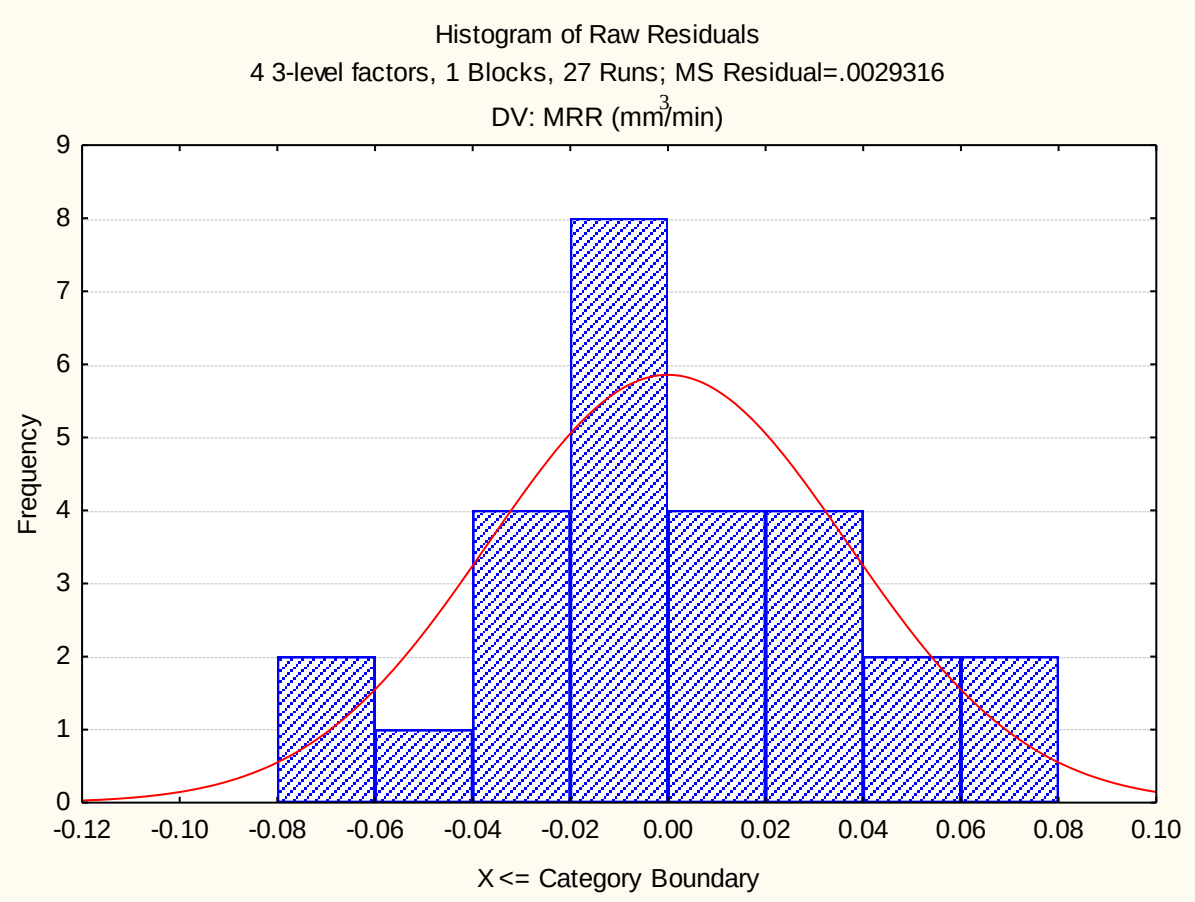

Fig. 13 Histogram plot of predicted values of MRR

The perfect normal probability distribution of the histogram plot of residuals for MRR response is shown in Fig. 13. From the above graphs, it is seen that the normal probability created in the histogram plot of residual for MRR is tolerable. The red line in the graph depicts the normality distributed curve of predicted values of MRR and here it is fitted well with 95 % confidence interval.

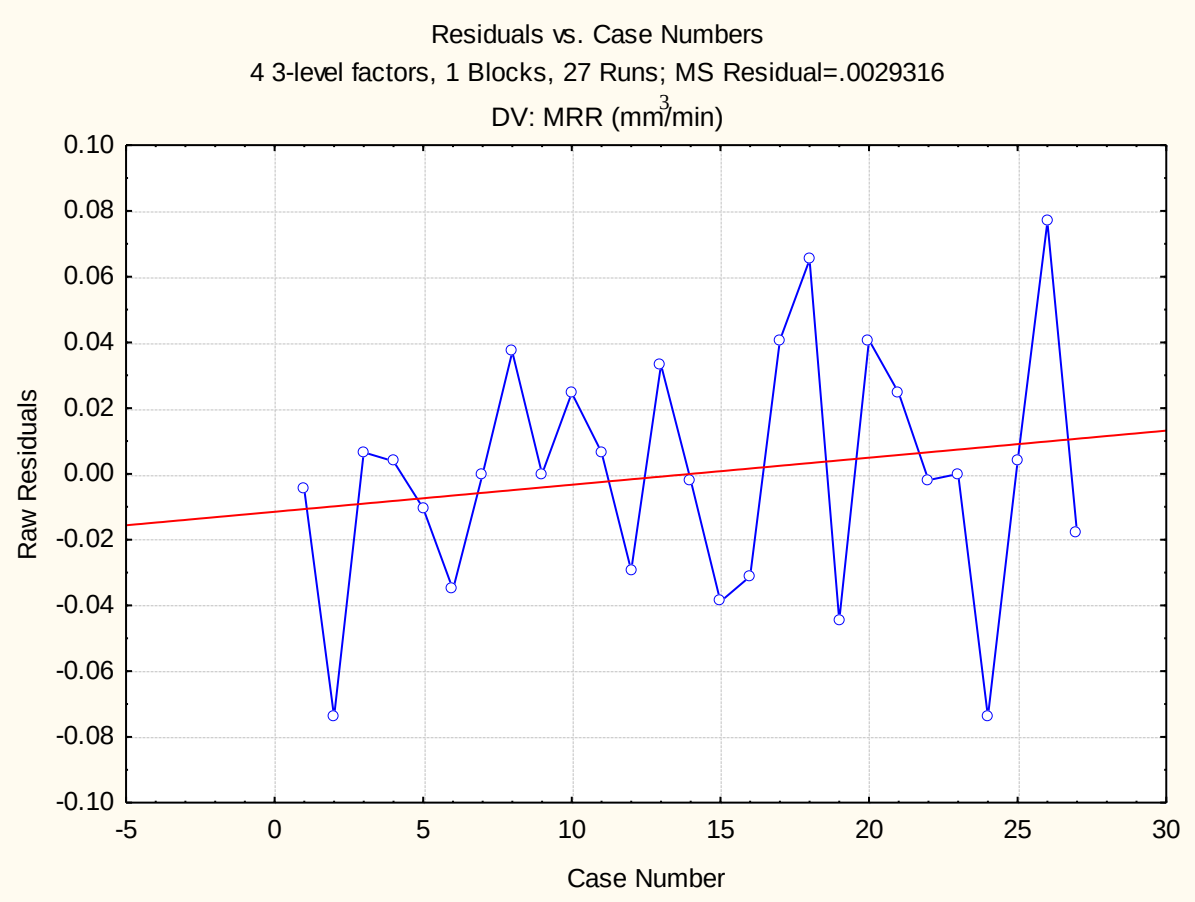

Fig. 14 Plot of residuals vs. case numbers values of MRR

From the Fig. 14, it is evident that the highest MRR value among all experimental runs is by the run number 26. The red line indicates that the value of MRR increases with increase in run order. In this figure, each point indicates the experimental run orders which are conducted as per design of experiment in plasma arc machining.

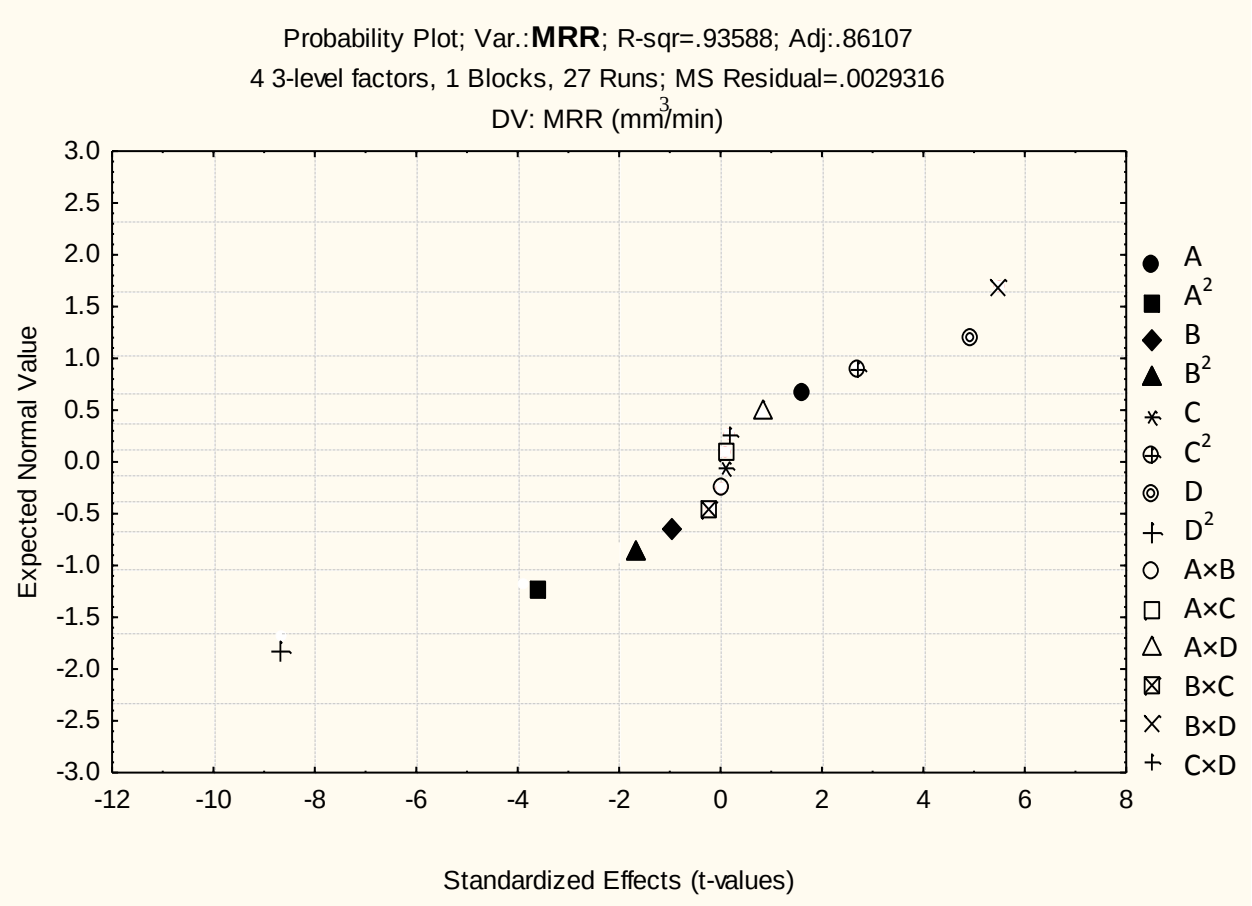

Fig. 15 Probability plot of MRR

The normal probability plot of MRR corresponding to each regression terms figured in Fig. 15. In this plot, it can be predicted the effect of the standardized T-value effect on all type of terms in normal probability plot. Here, most of the interaction terms are merged in the middle region of the plot.

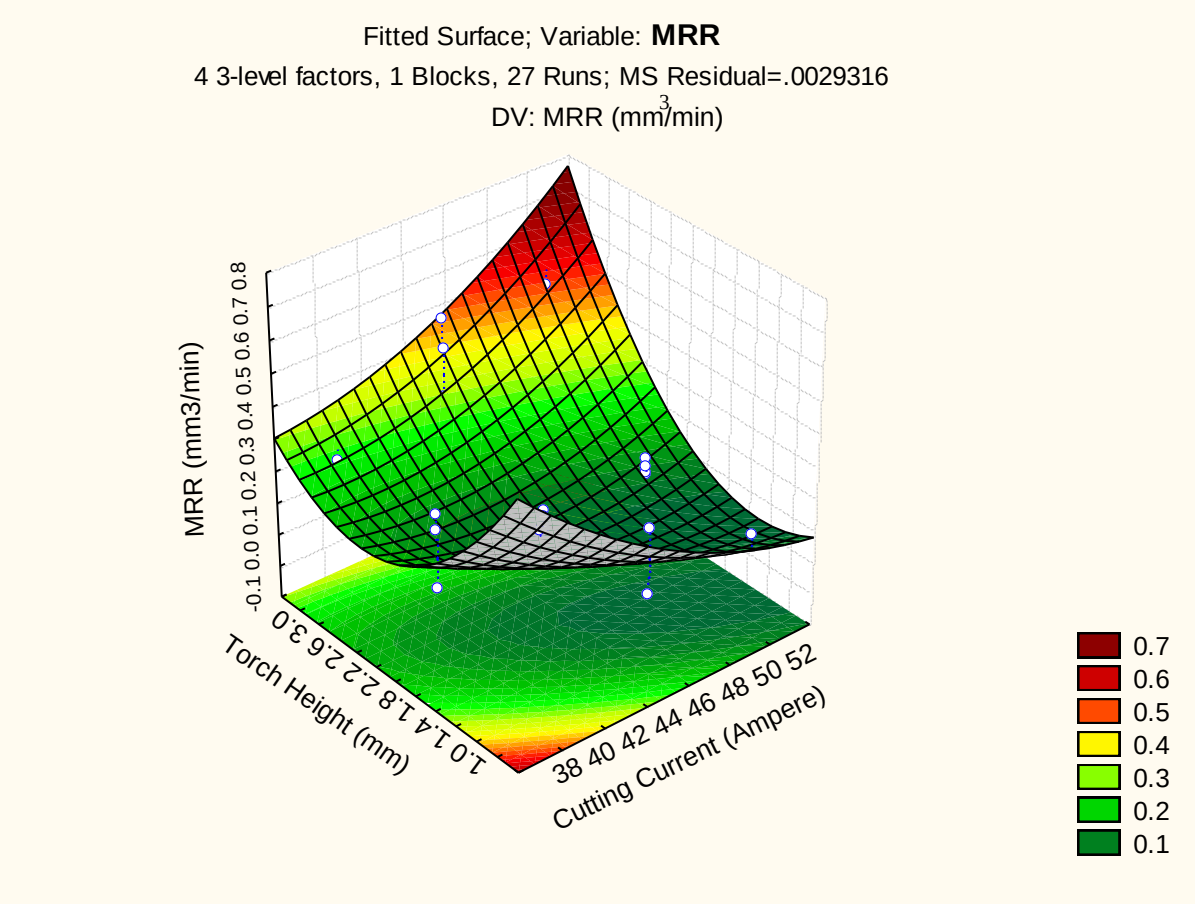

Fig. 16 3D fitted surface plot of MRR

The 3D surface plot of the significant interaction terms can be exerted in Fig. 16. It is to be noted that all other terms are taken into account at their average value. From the figure, it is evident that the interaction of cutting current and torch height influences the above mentioned output.

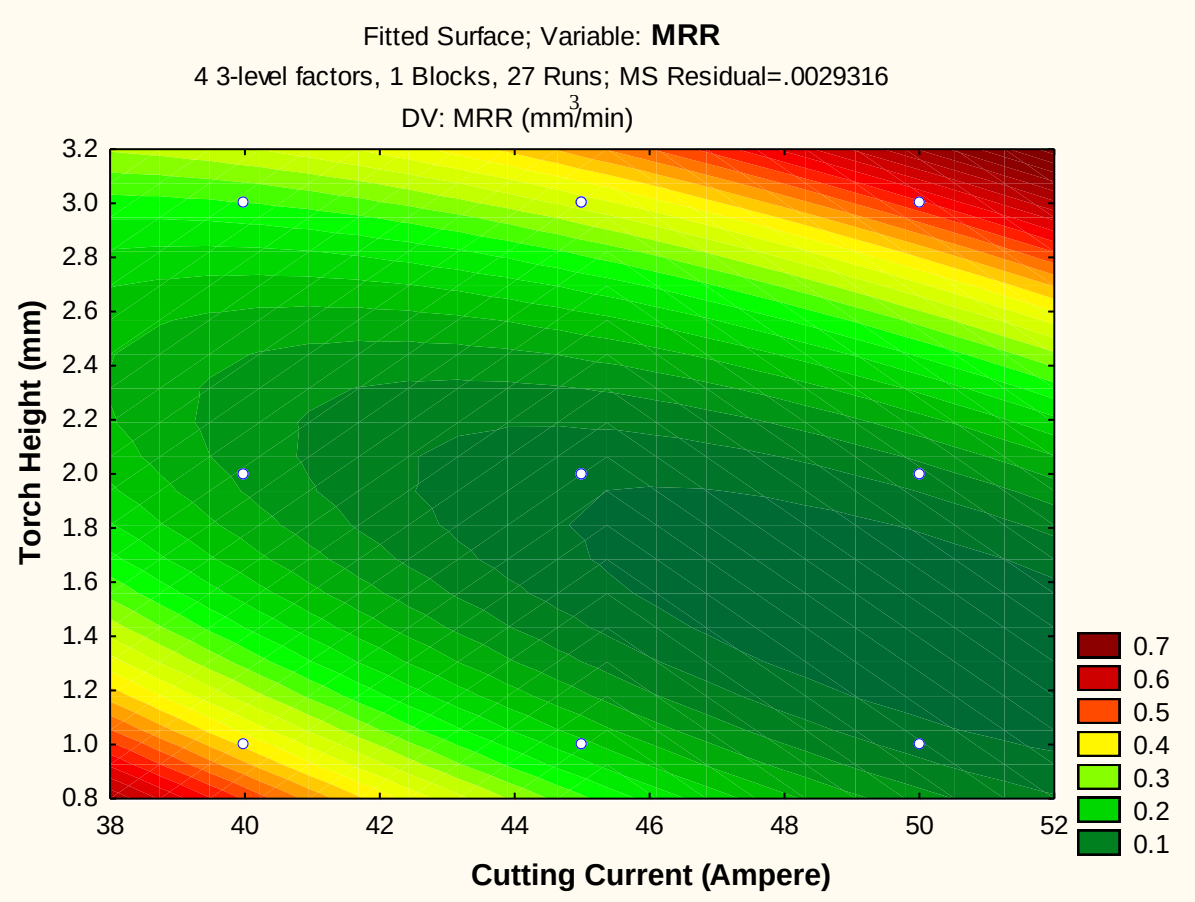

Fig. 17 2D fitted counter plot of MRR

The counter plots of interaction terms at their average level vs. MRR are found in Fig. 17. Mainly the shapes of counter plots might be elliptical or saddle form that indicates the combinations of each variable are significant except torch height vs. cutting current plot. The lowest value of MRR can thus be obtained in the maximum region of current as seen in Fig. 17.

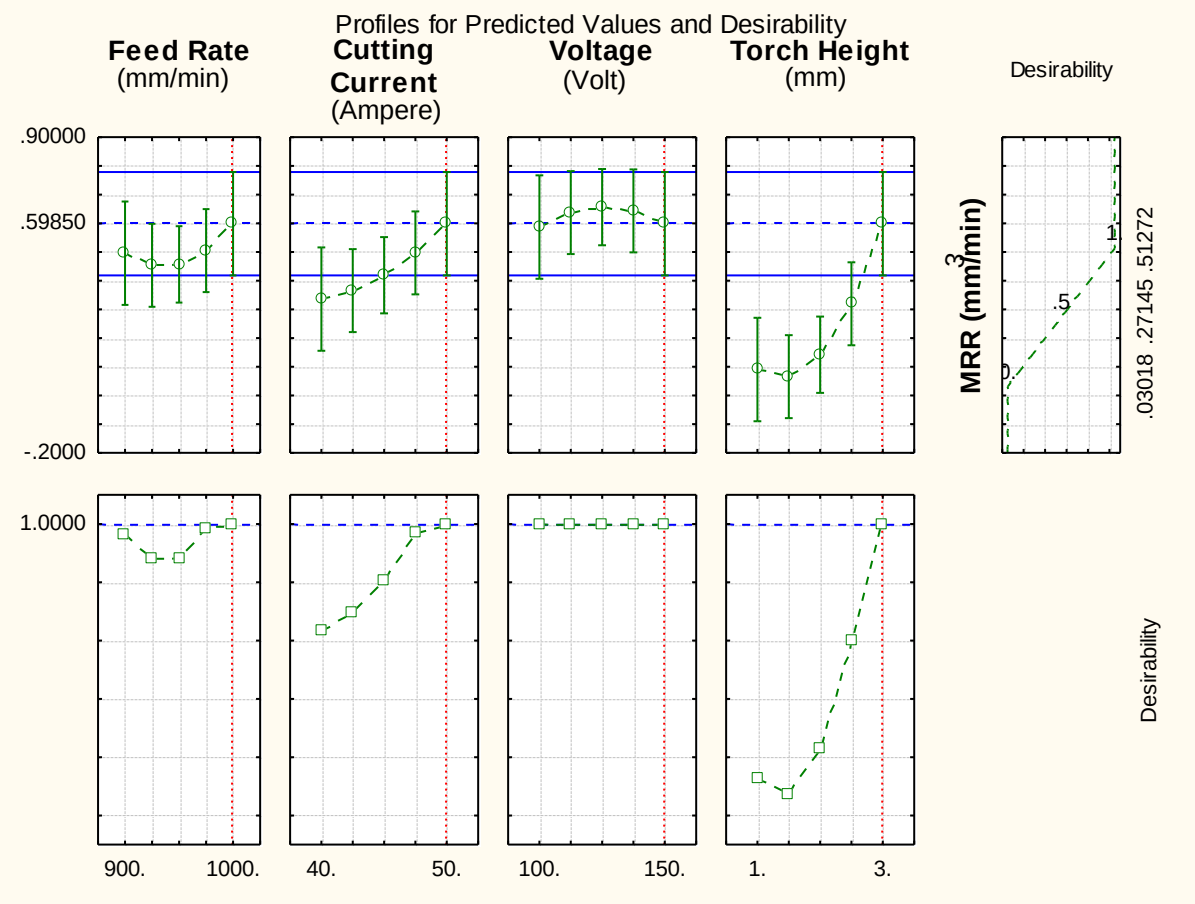

Fig. 18 Profile plot of predicted values and desirability of MRR

The noble desirability function methodology helped to find out the optimum MRR response which fits the quadratic fit model. The level of variable giving the highest desirability, i.e., 1.0000 was considered as optimum parametric setting. The optimized levels of variables (A, B, C and D) were determined using the desirability profiles that are shown in Fig. 18 for predicted values of responses and red dotted line showed desirability function value.

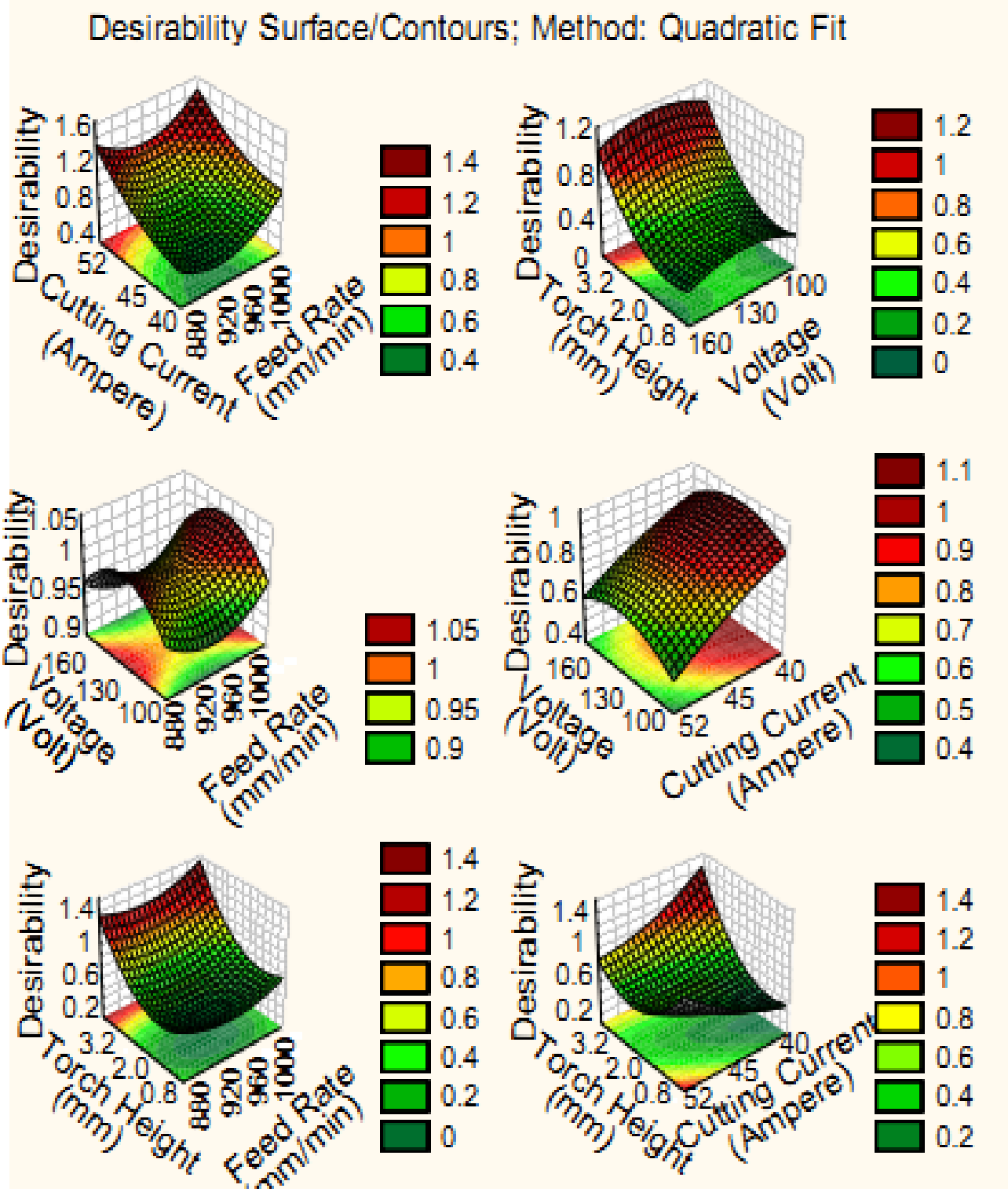

Fig. 19 Desirability 3D surface plot of MRR

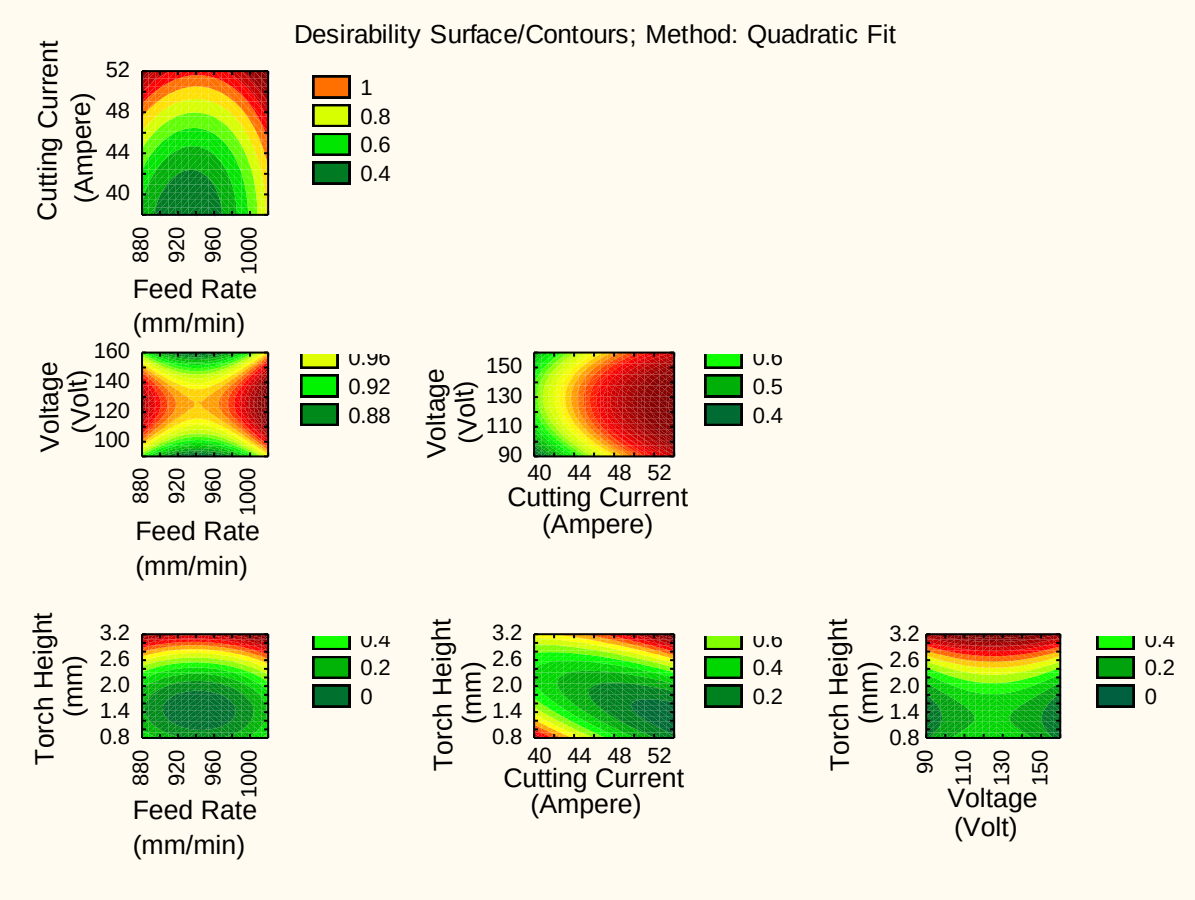

Fig. 20 Desirability 2D counter plot of MRR

The technique of desirability function helped to get optimum MRR response which was fitted by the quadratic fit model. The 3D and 2D interaction plots were determined using the desirability profiles that are shown in Fig. 19 and Fig. 20 respectively. Here, the green and red area showed the minimum and maximum influence of input variables on output response in the interaction condition.

5.1.1.2 For surface roughness:

Similarly in case of SR output response, the effect of estimated values was computed and recorded in Table 7. The ANOVA for SR has been carried out firstly and its results are given in Table 8. Here, the block effect has also been considered because the levels of block are taken as one. Due to this variation in block, there is negligible

amount of effect occurred in experiment. This effect is ignored for further calculation of optimization. The total degree of freedom for all input factors is 26. From the Table 8, it is seen that the most of the terms have P-value less than 0.05 under the confidence interval of 95 %. Hence, these terms show significance within experiment. In case of individual terms, only feed rate and torch height are the most significant among all parameters. Pareto chart of effects of all factors on SR response are shown in Fig. 21 and the results indicate that the quadratic of torch height is the second most enhancing factor among all considered factors. The scatter plot between the observed and the predicted value of SR of all 27 runs is shown in Fig. 22. It is concluded that there is a reasonable correlation between the measured and predicted values of SR response. In Fig. 24, the histogram plot of predicted data of SR with 95 % confidence interval of normal distribution is displayed. In Table 9, the model of estimated coefficients of the independent variable on the SR is obtained.

Table 7 Effect of Estimated Values for SR

Factor	Effect	Std. Err.	T	P
Constant	5.97389	0.109622	54.4952	0.000000
A (mm/min)	-1.48833	0.189871	-7.8386	0.000005
A^2	-0.06333	0.142404	-0.4447	0.664419
B (Ampere)	0.14333	0.189871	0.7549	0.464869
B^2	-0.34458	0.142404	-2.4198	0.032331
C (Volt)	0.24667	0.189871	1.2991	0.218308
C^2	-0.19958	0.142404	-1.4015	0.186385
D (mm)	-1.09500	0.189871	-5.7671	0.000089
D^2	-1.73333	0.142404	-12.1720	0.000000
A×B	2.24000	0.328867	6.8113	0.000019
A×C	-0.70000	0.328867	-2.1285	0.054699
A×D	-2.09500	0.328867	-6.3704	0.000036
B×C	1.09000	0.328867	3.3144	0.006174
B×D	-1.12000	0.328867	-3.4056	0.005215
C×D	1.40000	0.328867	4.2570	0.001113

Table 8 ANOVA Table for SR

Factors	SS	DoF	MS	F	P
A (mm/min)	6.64541	1	6.64541	61.4442	0.000005
A^2	0.02139	1	0.02139	0.1978	0.664419
B (Ampere)	0.06163	1	0.06163	0.5699	0.464869
B^2	0.63327	1	0.63327	5.8553	0.032331
C (Volt)	0.18253	1	0.18253	1.6877	0.218308
C^2	0.21245	1	0.21245	1.9643	0.186385
D (mm)	3.59707	1	3.59707	33.2590	0.000089
D^2	16.02370	1	16.02370	148.1571	0.000000
A×B	5.01760	1	5.01760	46.3933	0.000019
A×C	0.49000	1	0.49000	4.5306	0.054699
A×D	4.38902	1	4.38902	40.5815	0.000036
B×C	1.18810	1	1.18810	10.9853	0.006174
B×D	1.25440	1	1.25440	11.5983	0.005215
C×D	1.96000	1	1.96000	18.1224	0.001113
Error	1.29784	12	0.10815		
Total SS	44.11383	26			

Table 9 Regression Coefficients of SR

Factor	Regression Coef.	Std. Err.	T	P
Constant	220.9933	66.97735	3.29952	0.006346
A (mm/min)	-0.1877	0.11361	-1.65235	0.124368
A^2	0.0000	0.00006	0.44475	0.664419
B (Ampere)	-5.8032	0.82763	-7.01179	0.000014
B^2	0.0138	0.00570	2.41977	0.032331
C (Volt)	-0.0611	0.15018	-0.40685	0.691282
C^2	0.0003	0.00023	1.40153	0.186385
D (mm)	13.9617	3.60005	3.87818	0.002195
D^2	1.7333	0.14240	12.17198	0.000000
A×B	0.0045	0.00066	6.81127	0.000019
A×C	-0.0003	0.00013	-2.12852	0.054699
A×D	-0.0209	0.00329	-6.37036	0.000036
B×C	0.0044	0.00132	3.31441	0.006174
B×D	-0.1120	0.03289	-3.40563	0.005215
C×D	0.0280	0.00658	4.25704	0.001113

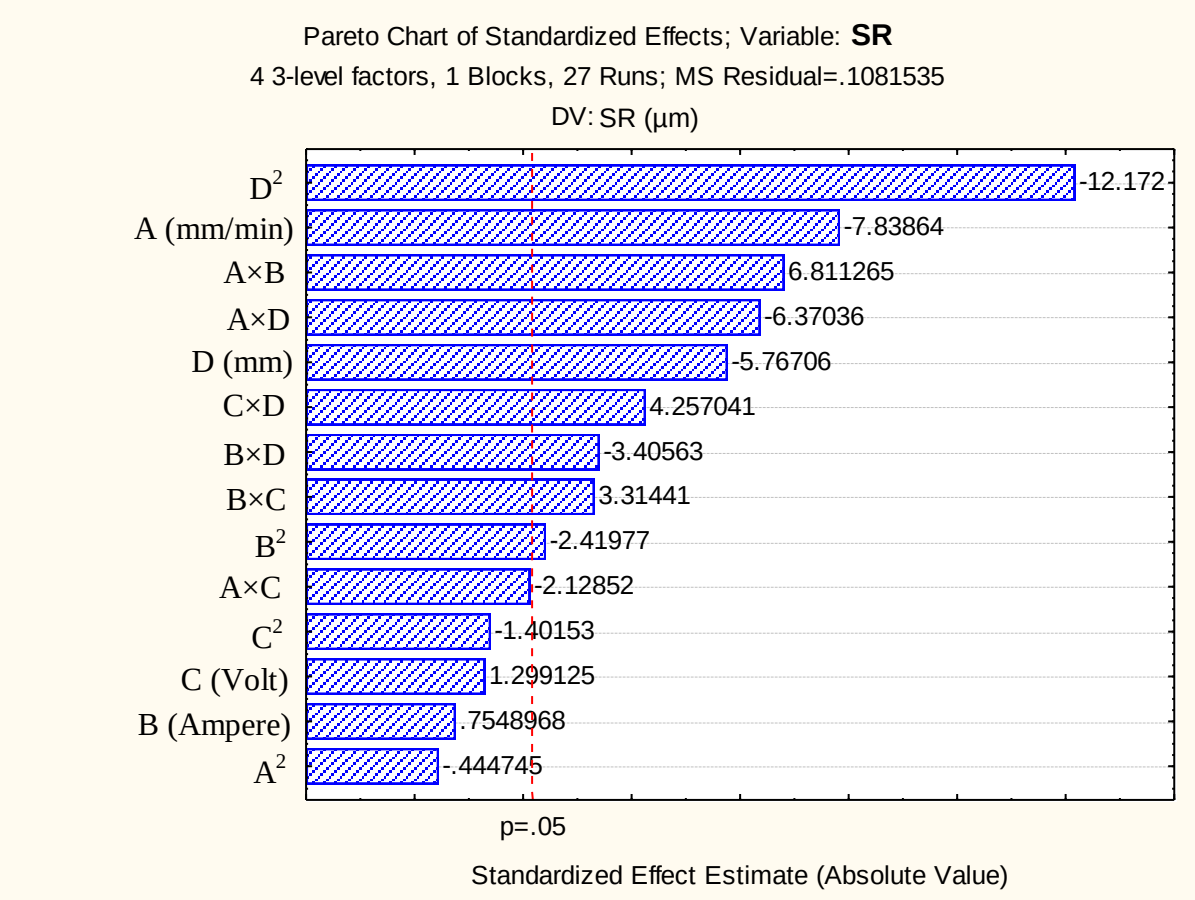

Fig. 21 Pareto chart of standardized effect of factors on SR

The quadratic form of torch height factor had the most significant influence on the SR response of plasma arc cutting process as shown in Fig. 21.

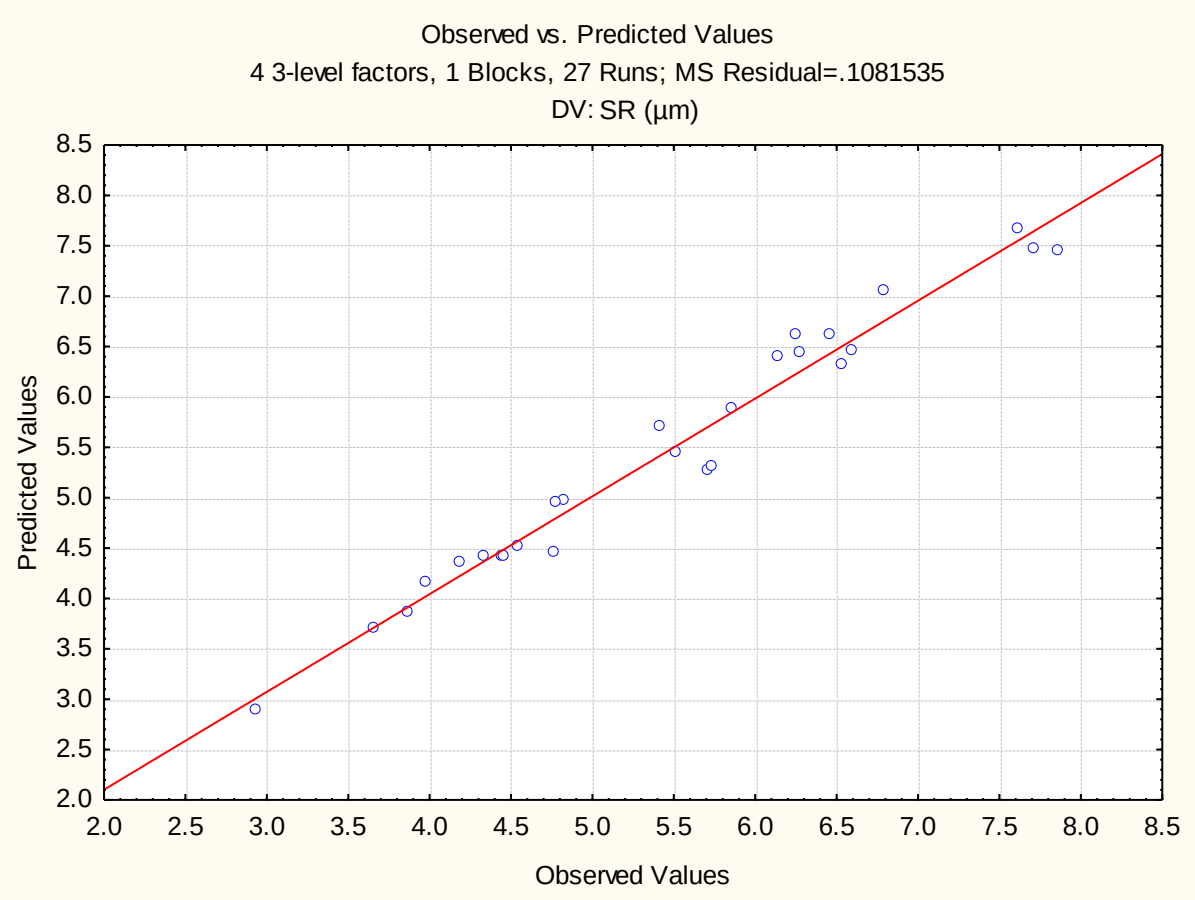

Fig. 22 Plot of observed vs. predicted values of SR

The scatter plot between the observed and the predicted value of plasma cut responses of all 27 runs is shown in Fig. 22. These plots show the comparison between each of the observed values with the predicted value that are calculated from the developed model. Here, the most of the points lie on the normal line of fitted values except the plot of SR, as the uniformity is maintained throughout the region. From this result, it can be concluded that the response model shows in good agreement with experimental data, because linear relation between the actual and predicted SR exists.

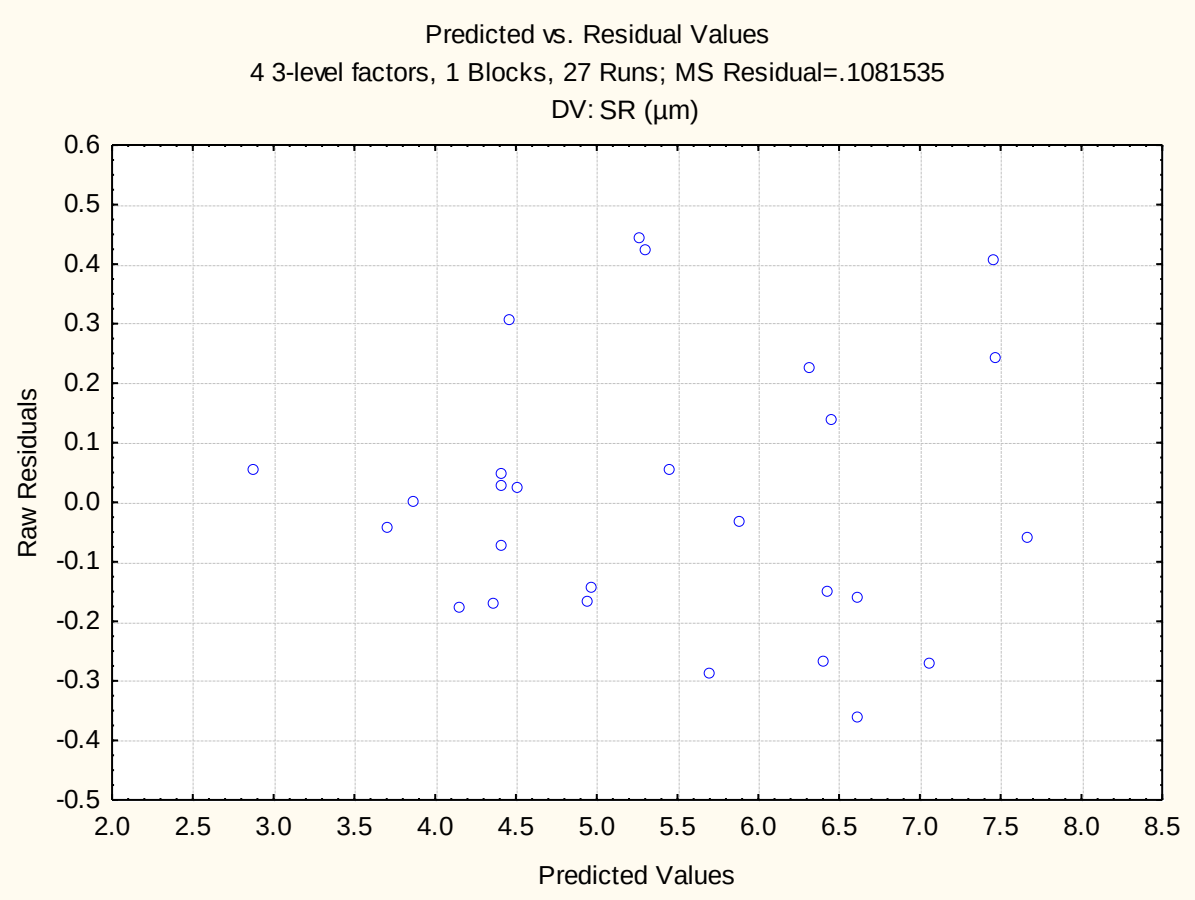

Fig. 23 Plot of predicted vs. residual values of SR

From the Fig. 23, no standard pattern is formed in the plot of predicted vs. residual values which show the adequacy of the fitted model for SR.

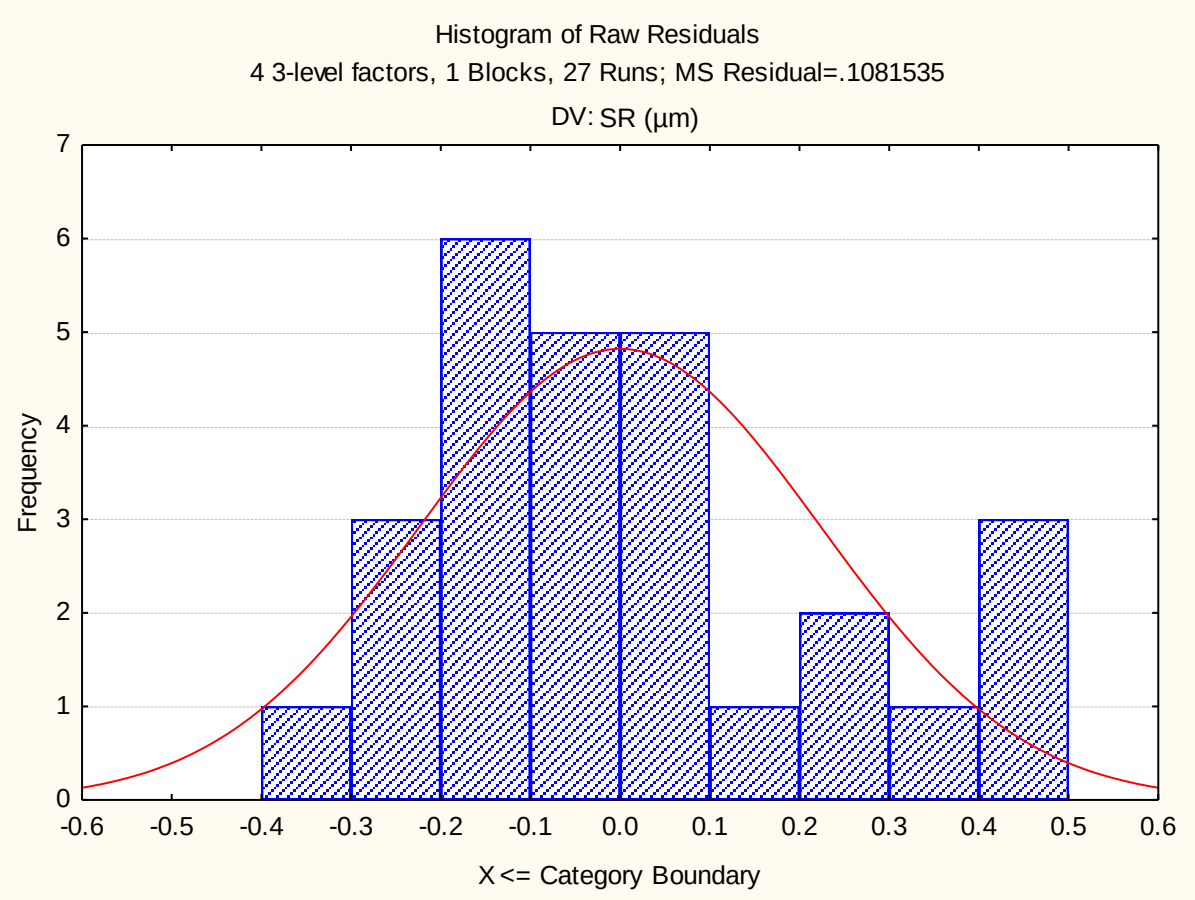

Fig. 24 Histogram plot of predicted values of SR

The perfect normal probability distribution of the histogram plot of residuals for SR response is shown in Fig. 24. From the above graphs, it is seen that the normal probability created in the histogram plot of residual for SR is acceptable.

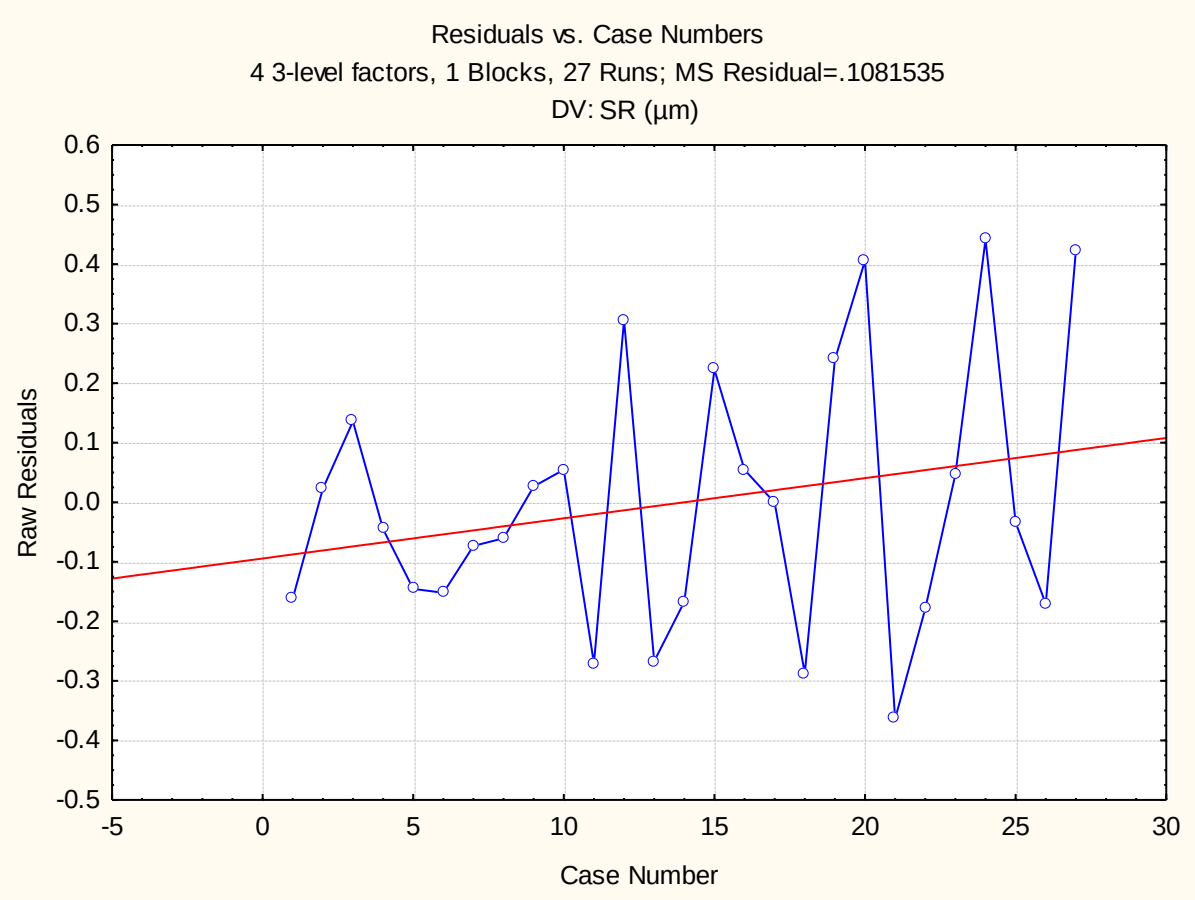

Fig. 25 Plot of residuals vs. case numbers values of SR

From the Fig. 25, it is evident that it is evident that the highest SR value among all experimental runs is by the run number 24. The red line indicates that the value of MRR increases with run order.

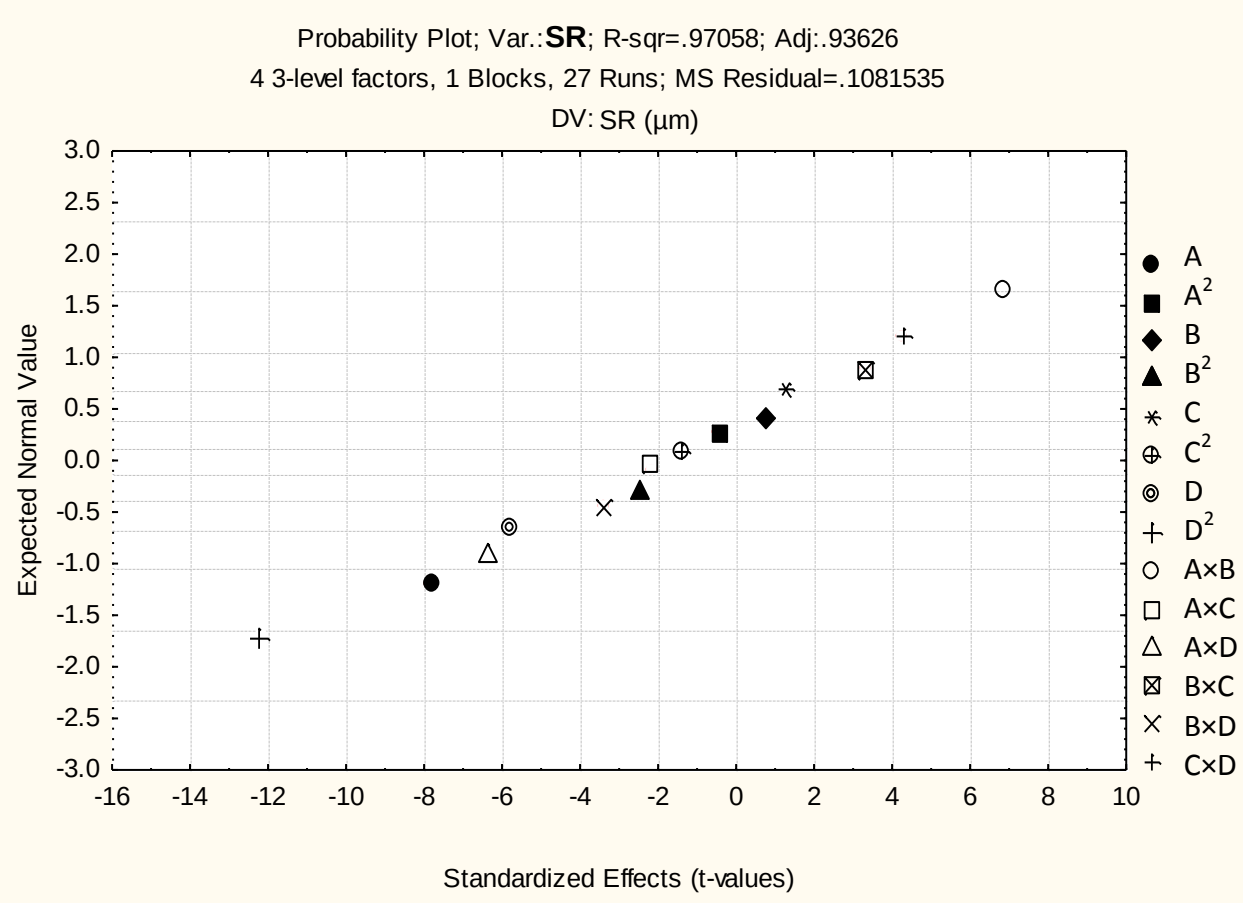

Fig. 26 Probability plot of SR

The normal probability plot of MRR corresponding to each regression terms are figured in Fig. 26. The surface and contour plot of this interaction terms have been considered for further analysis and shown in Fig. 27-29-31-33-35 and Fig. 28-30-32-34-36 respectively.

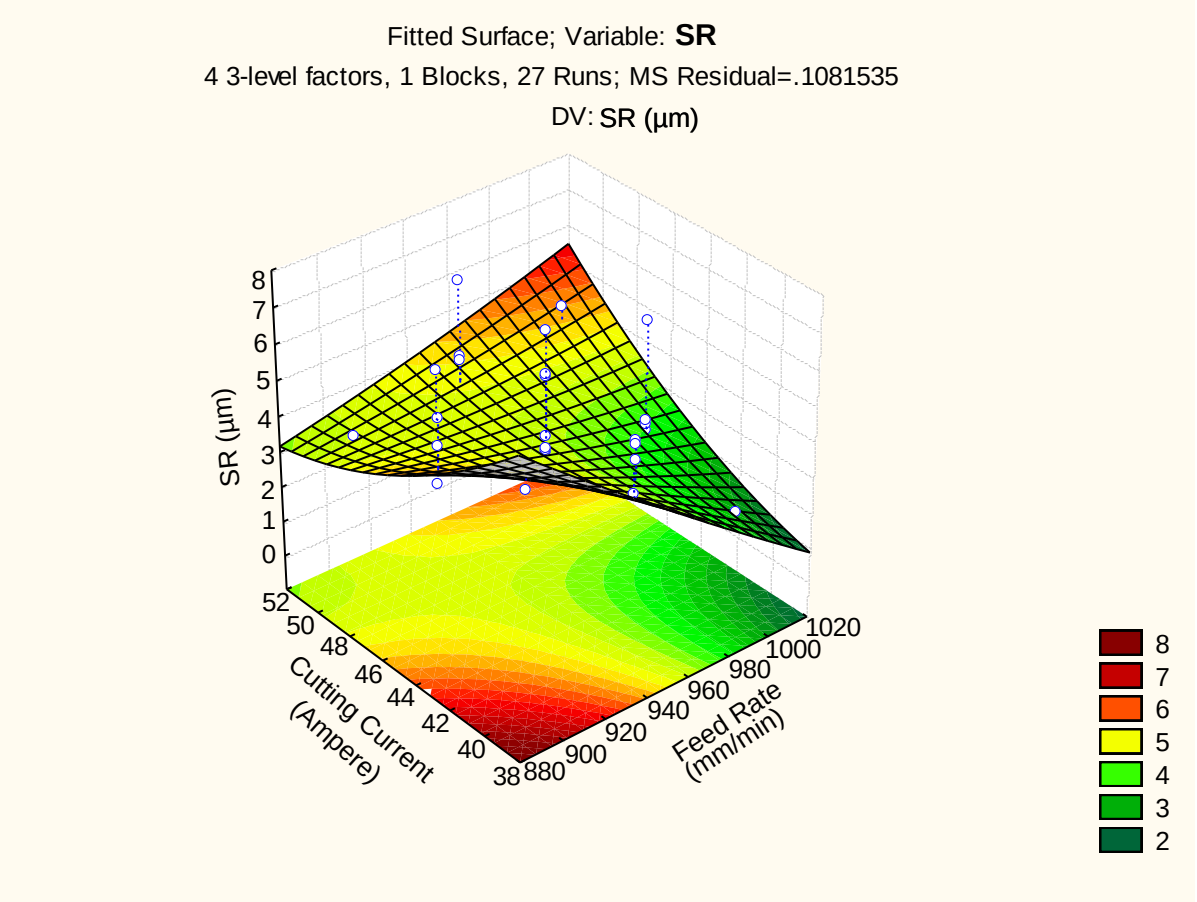

Fig. 27 3D fitted surface plot of SR(1)

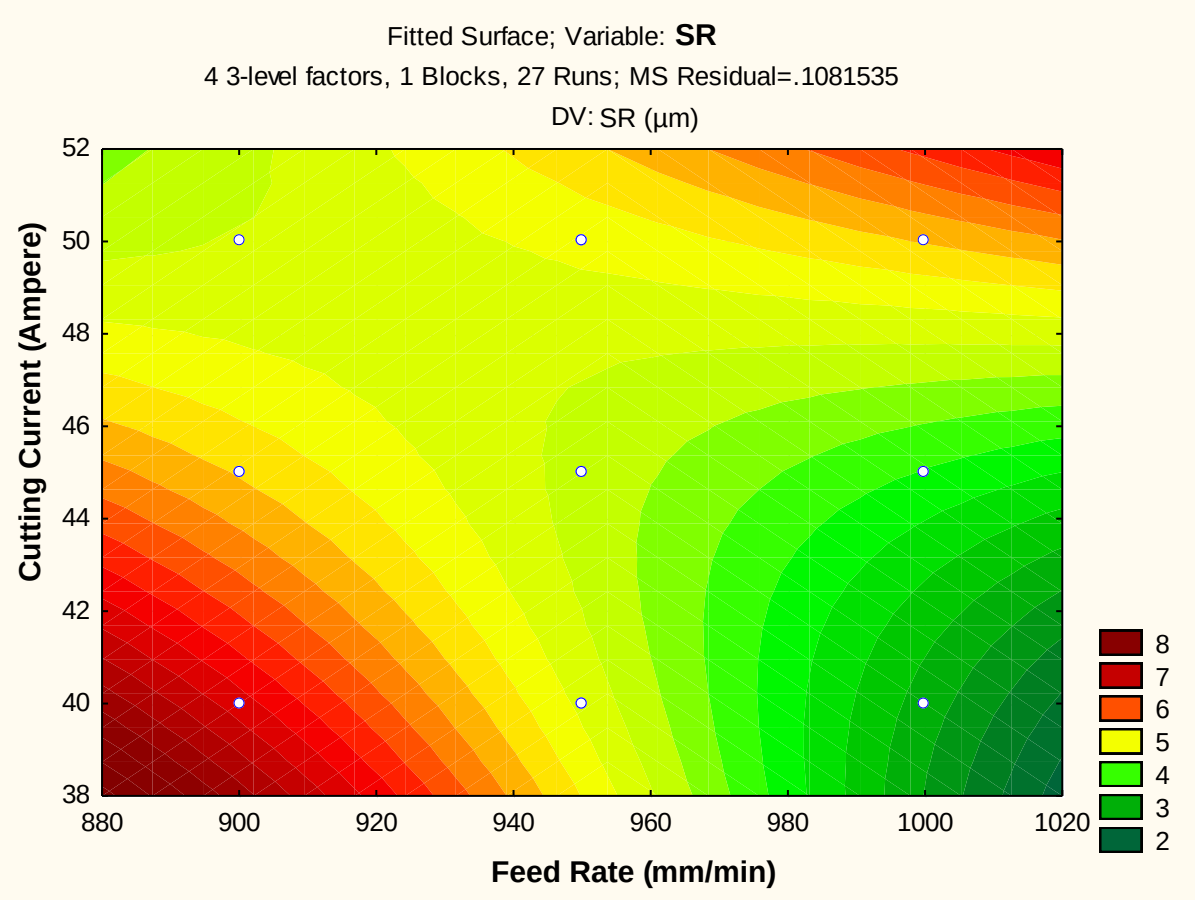

Fig. 28 2D fitted counter plot of SR(1)

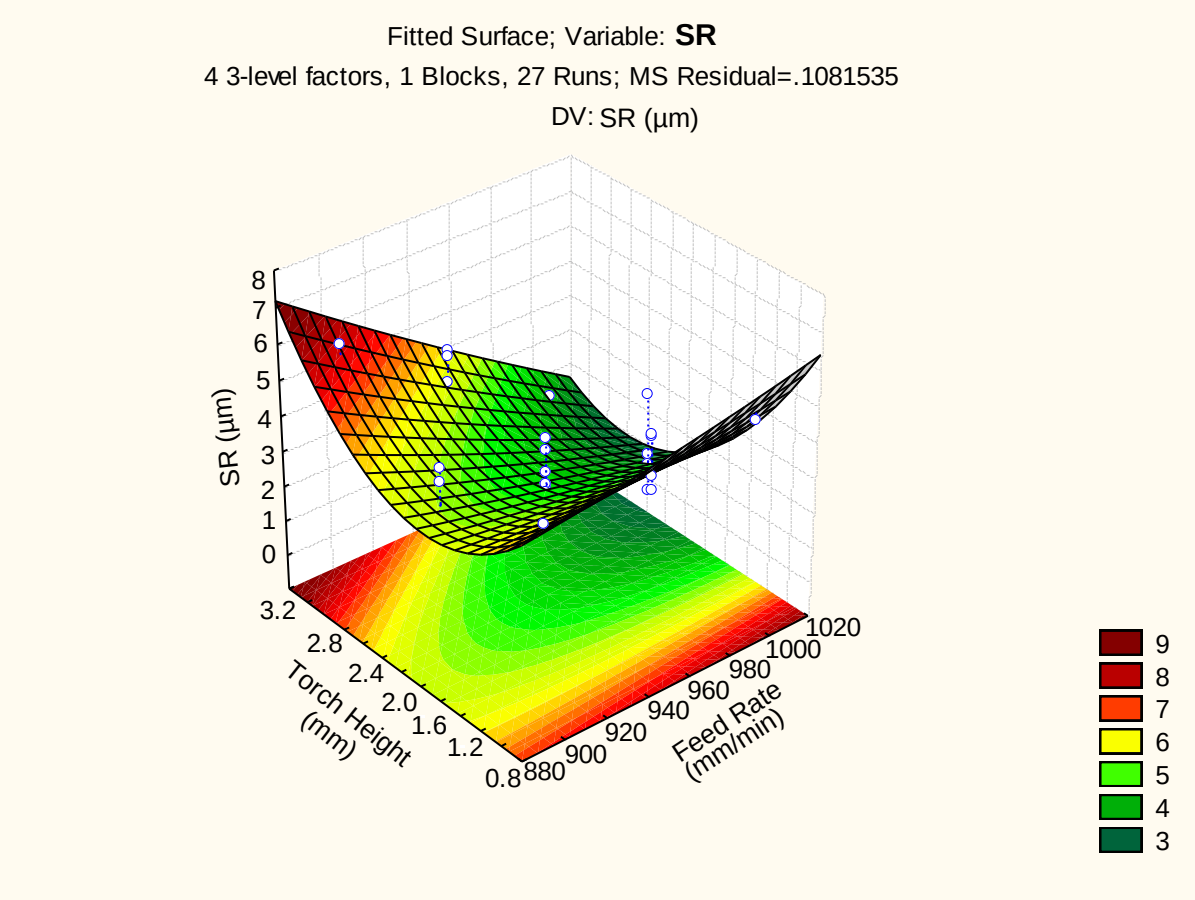

Fig. 29 3D fitted surface plot of SR(2)

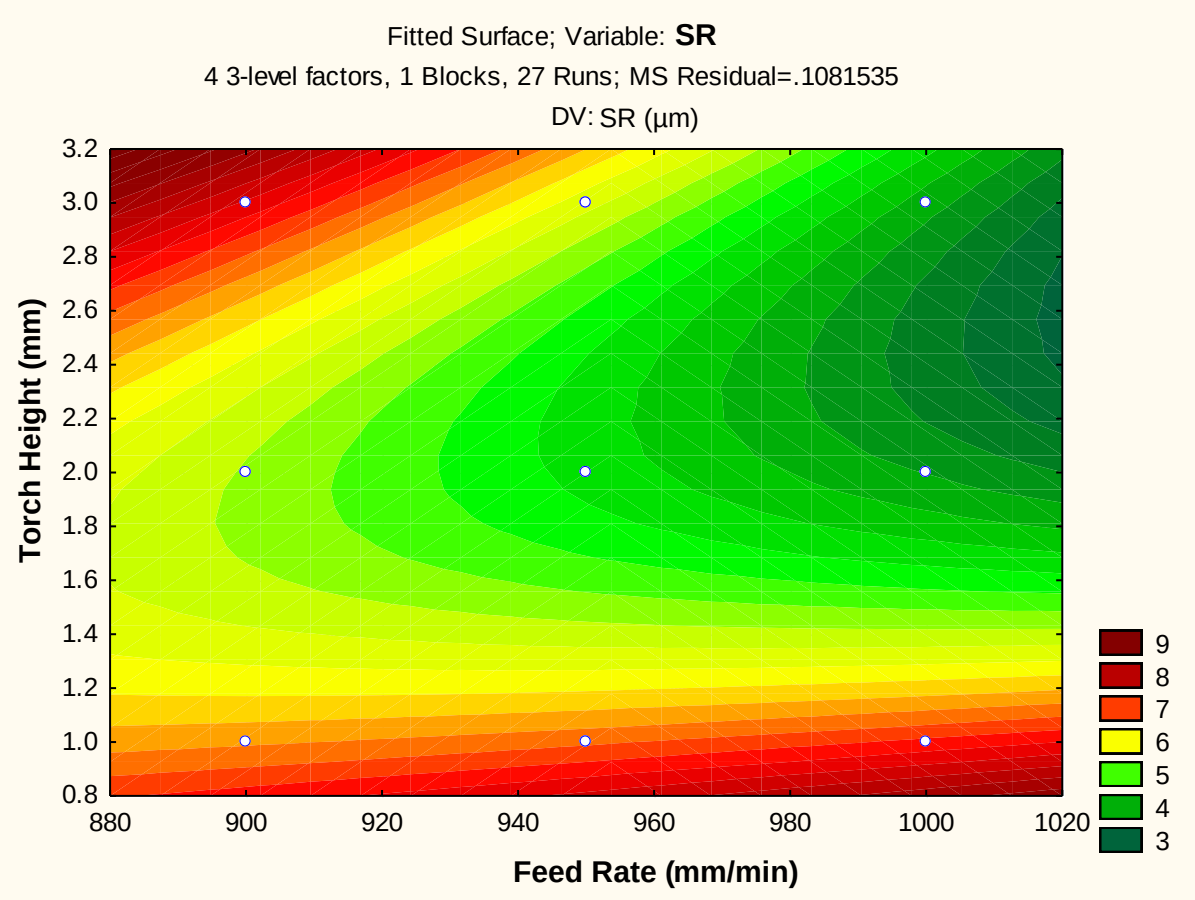

Fig. 30 2D fitted counter plot of SR(2)

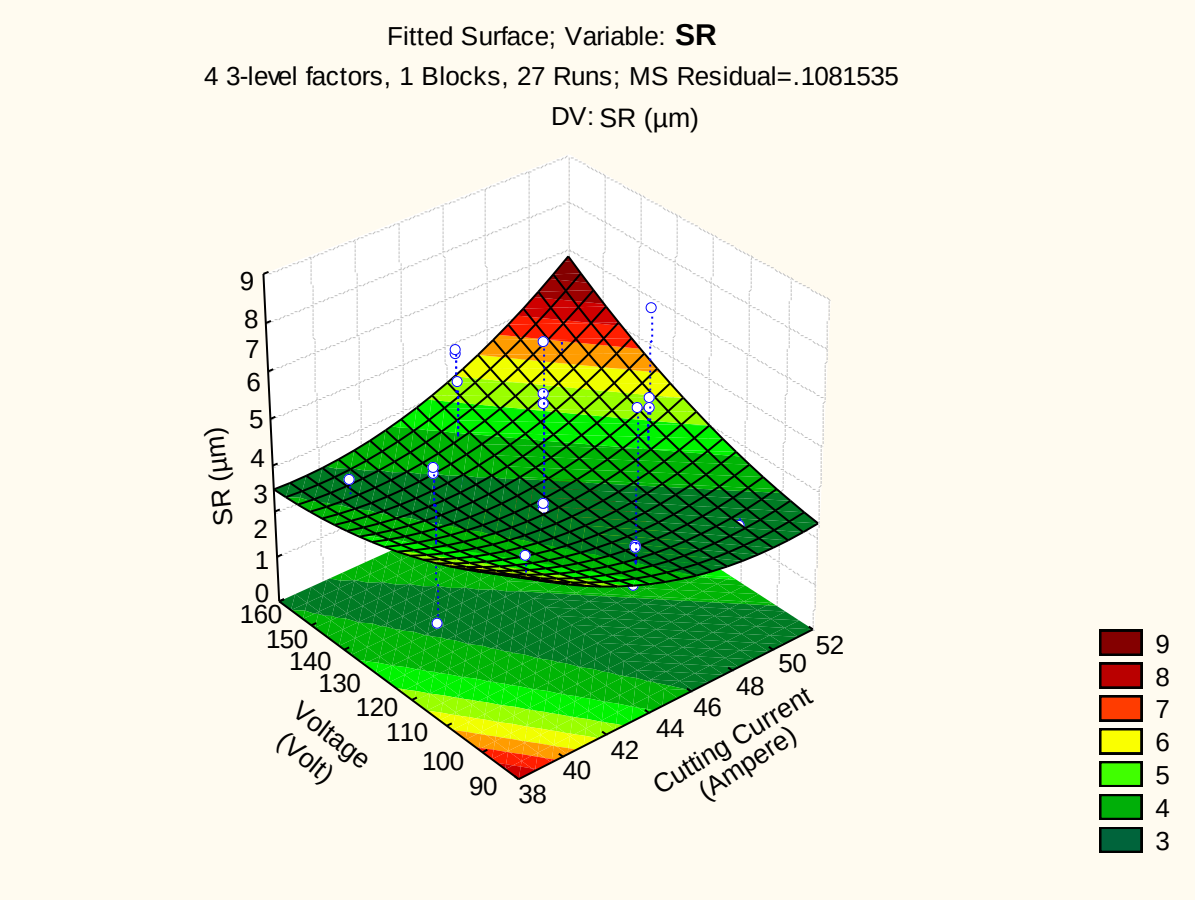

Fig. 31 3D fitted surface plot of SR(3)

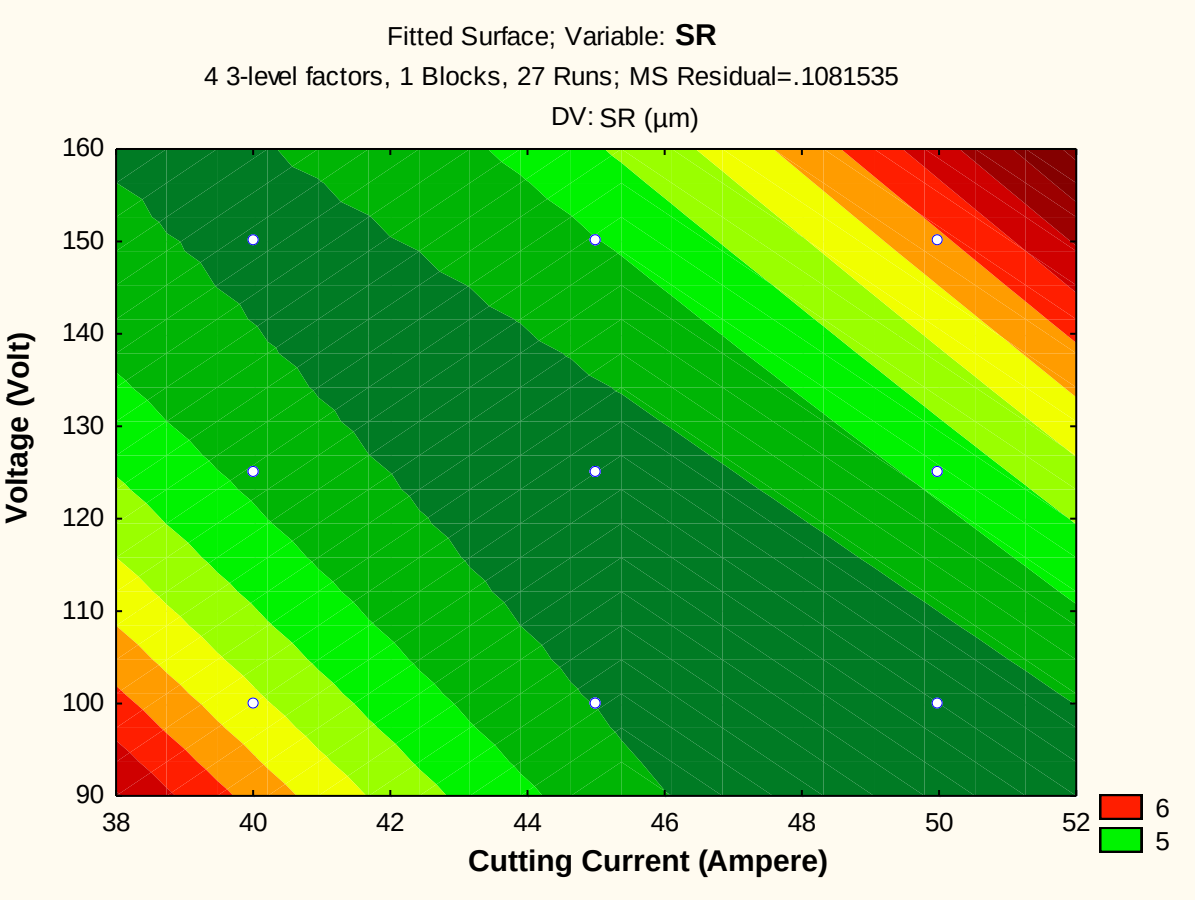

Fig. 32 2D fitted counter plot of SR(3)

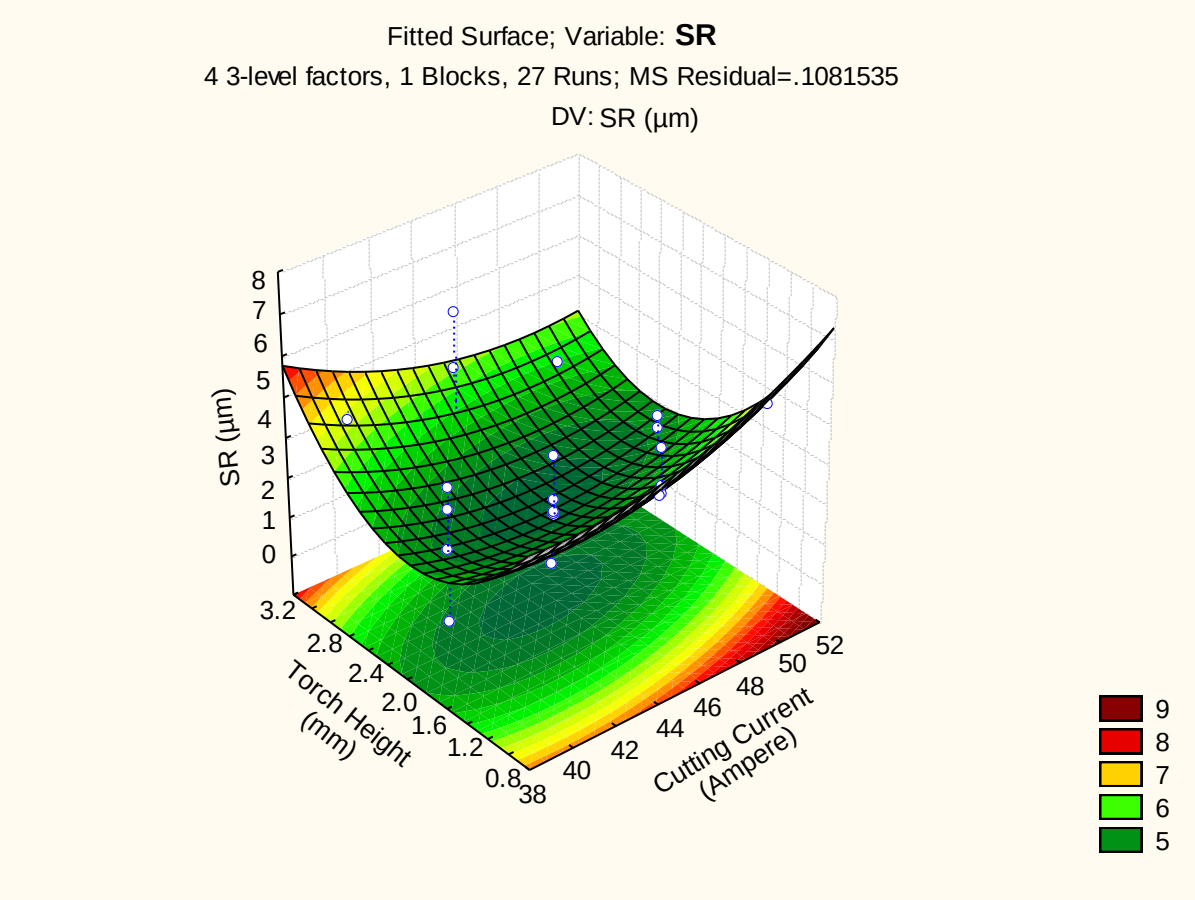

Fig. 33 3D fitted surface plot of SR(4)

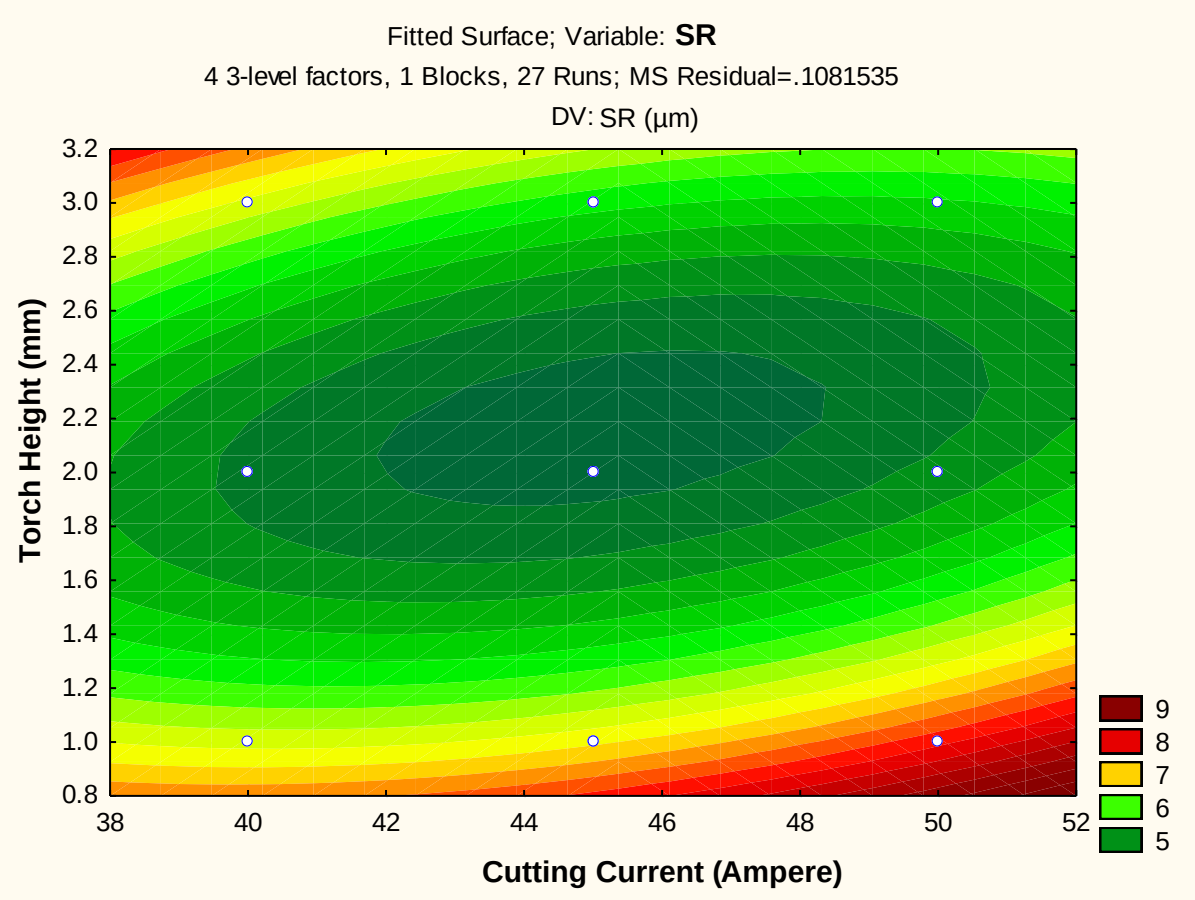

Fig. 34 2D fitted counter plot of SR(4)

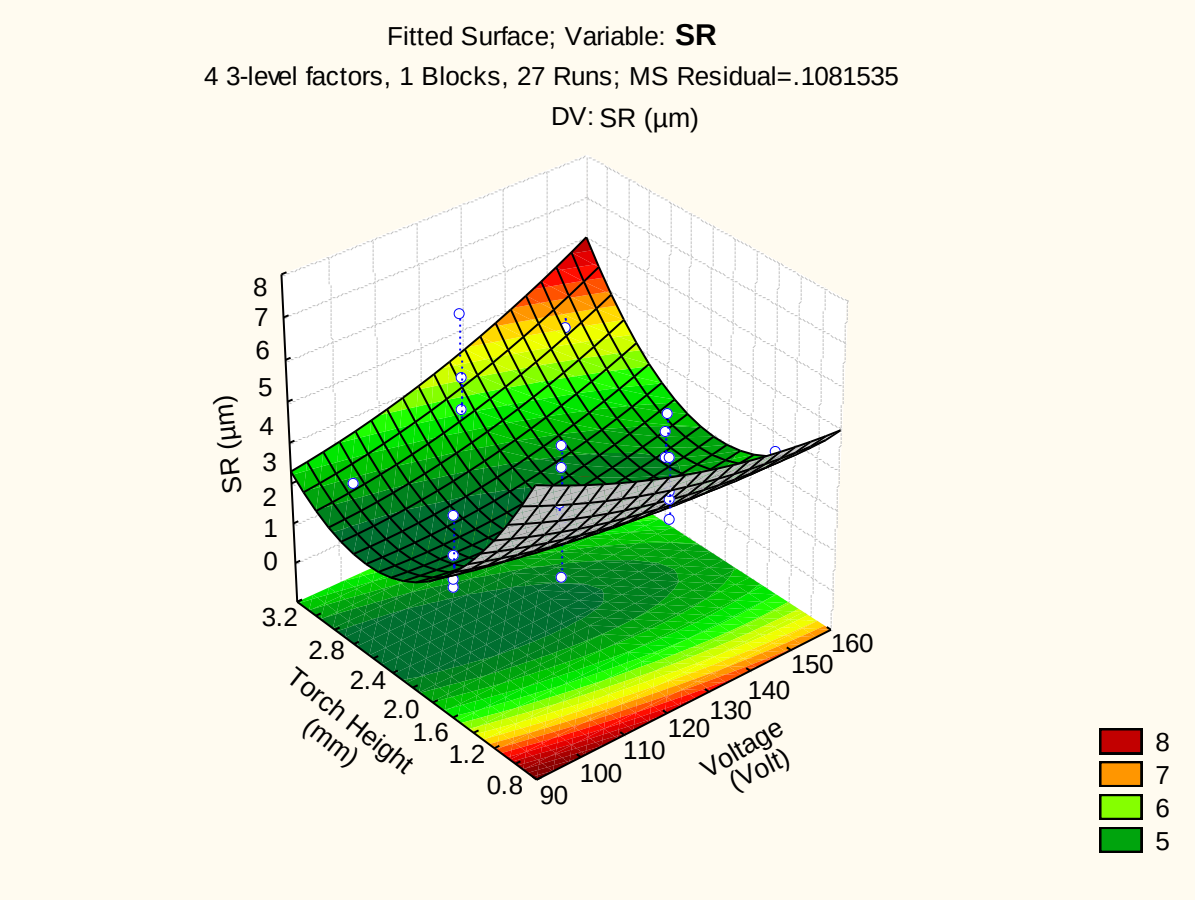

Fig. 35 3D fitted surface plot of SR(5)

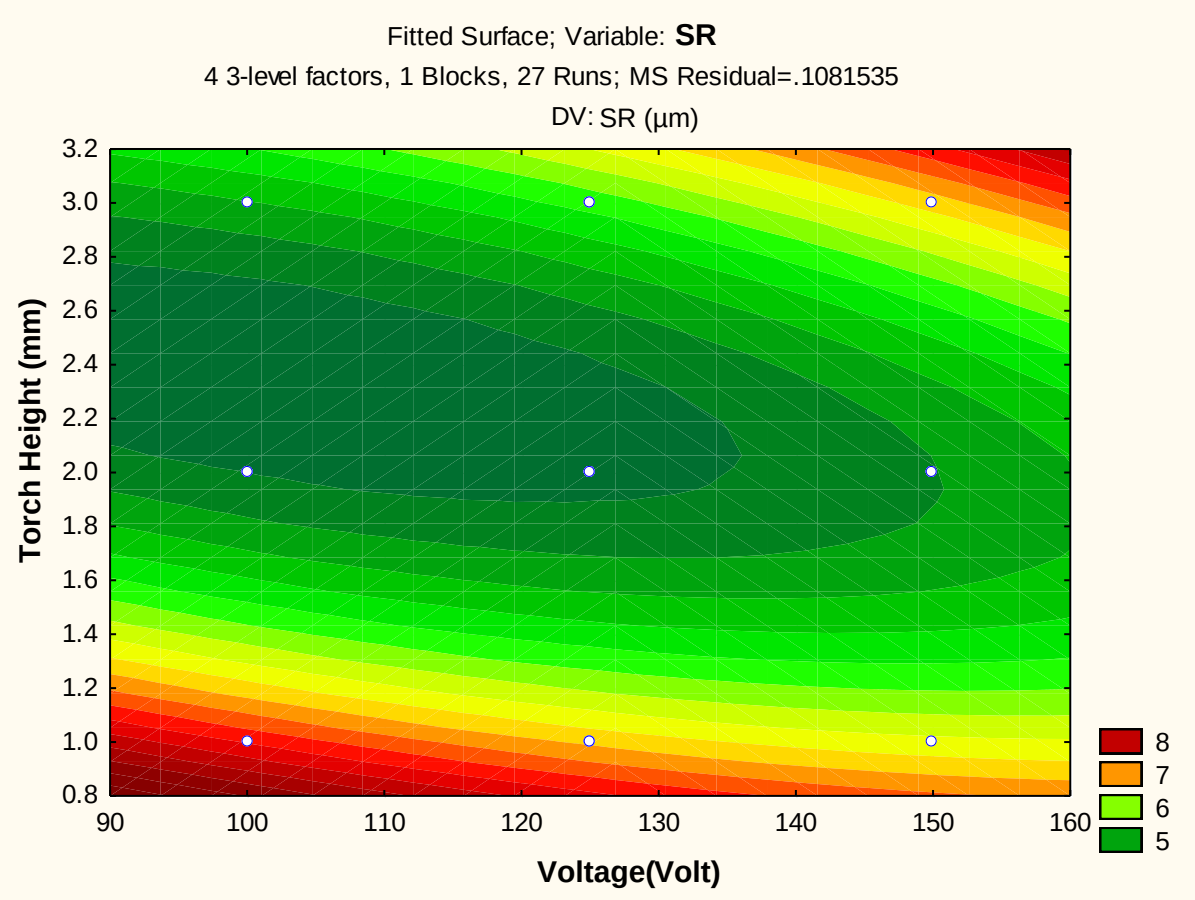

Fig. 36 2D fitted counter plot of SR(5)

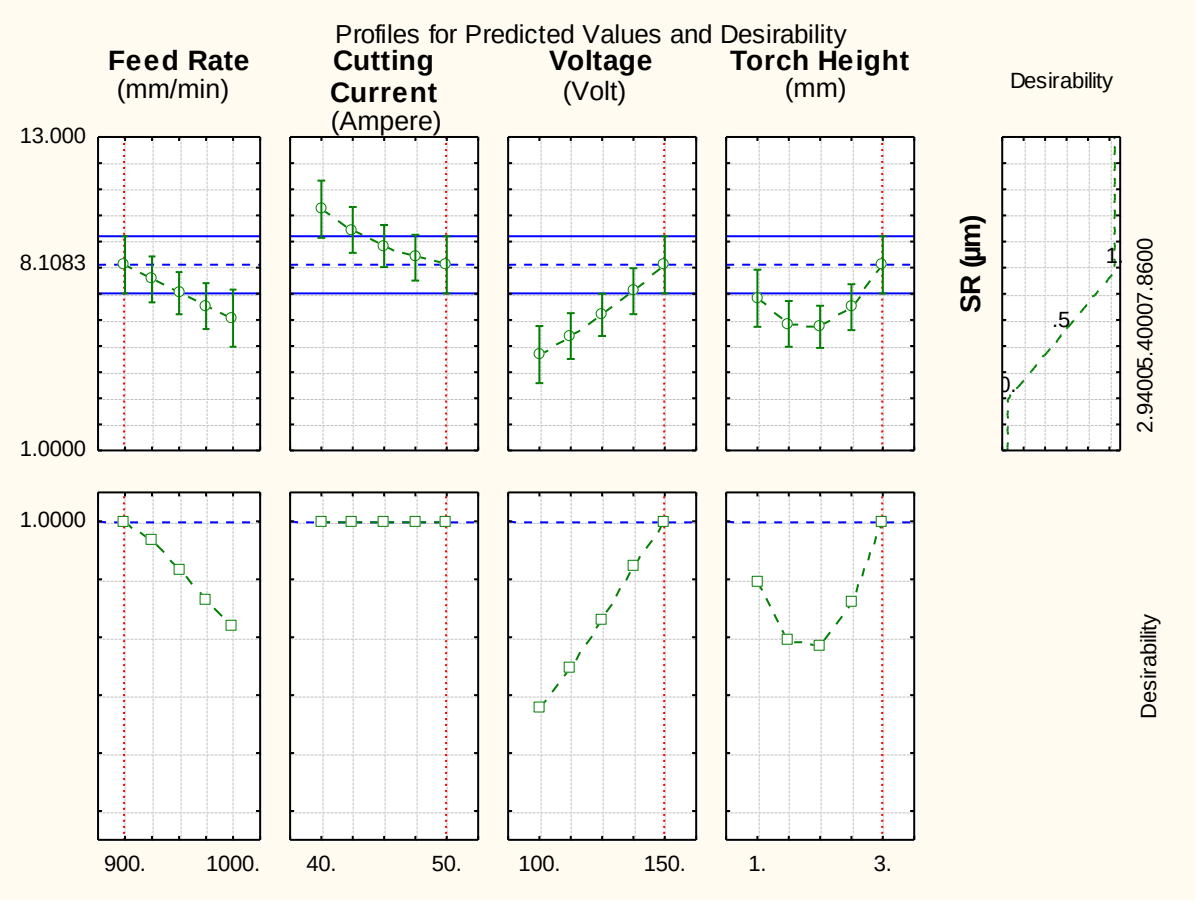

Fig. 37 Profile plot of predicted values and desirability of SR

For finding the optimum value of SR response, the desirability function helped by fitting the quadratic fit model. The level of variable giving the highest desirability i.e. 1.0000 was considered as optimum parametric setting. The optimized levels of variables (A, B, C and D) were determined using the desirability profiles that are shown in Fig. 37 for predicted values of responses and the red dotted line gave the values of desirability function.

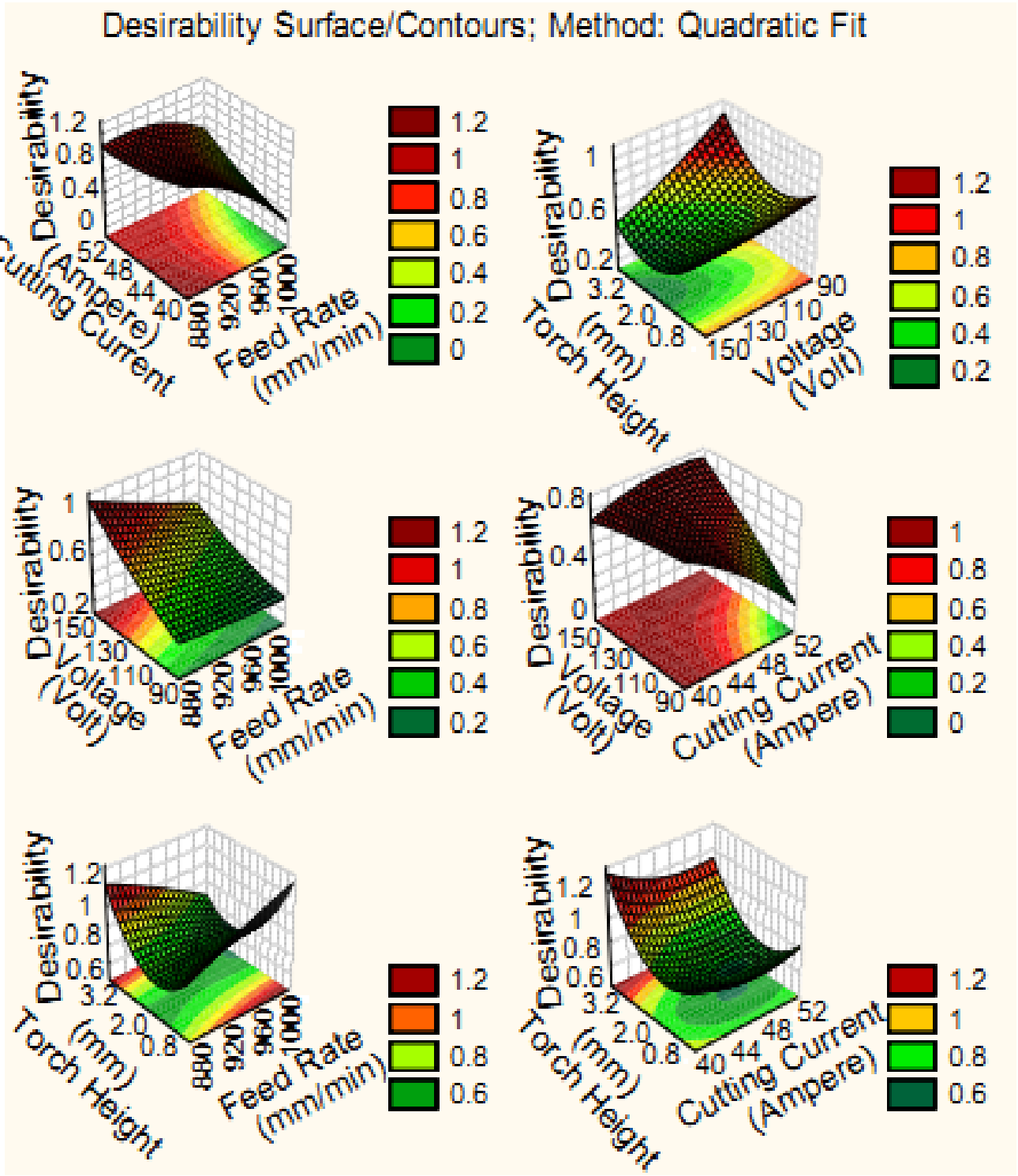

Fig. 38 Desirability 3D surface plot of SR

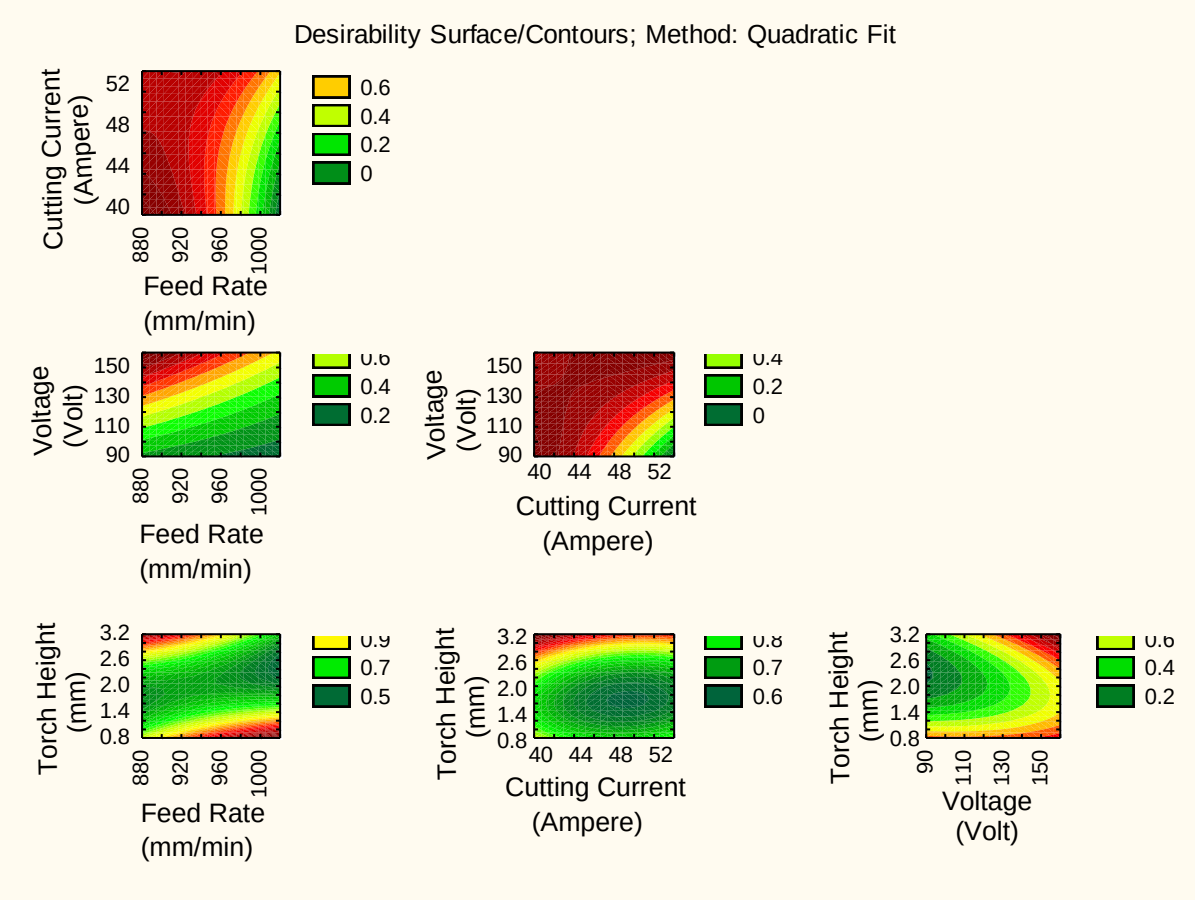

Fig. 39 Desirability 2D counter plot of SR

The 3D and 2D plot of interaction variables were determined using the desirability profiles for SR that is shown in Fig. 38-39 respectively. From these surface plots of interaction terms, it can be predicted that the minimum SR value obtained at the interaction of cutting current and torch height.

5.1.1.3 For right bevel angle:

In Table 10, the effect of estimated values of RBA was computed and recorded. The ANOVA for right bevel angle has been carried out firstly and its results are given in Table 11. Here, the block effect has also been considered because the levels of block are taken as one. Due to this variation in block, there is negligible amount of effect occurred in experiment. This effect is ignored for further calculation of optimization. The total degree

of freedom for all input factors is 26. From the Table 11, it is seen that the most of the terms have P-value less than 0.05 under the confidence interval of 95 %. Hence, these terms show significance within experiment. In case of individual terms, only torch height has shown the most significance among all parameters. Pareto chart of effects of all factors on right bevel angle response are shown in Fig. 40 and the results indicate that the quadratic of torch height is the second most enhancing factor among all considered factors. The scatter plot between the observed and the predicted value of right bevel angle of all 27 runs is shown in Fig. 41. It is concluded that there is a reasonable correlation between the measured and predicted values of right bevel angle response. In Fig. 43, the histogram plot of predicted data of right bevel angle with 95 % confidence interval of normal distribution is displayed. The surface and contour plot of this interaction terms have been considered for further analysis and shown in Fig. 46-47 respectively. In this figure, it is clearly displayed that the value of right bevel angle increases with increase in cutting current and torch height. In Table 12, the model of estimated regression coefficients of the independent variable on the right bevel angle is recorded.

Table 10 Effect of Estimated Values for Right Bevel Angle

Factor	Effect	Std. Err.	T	P
Constant	3.000000	0.083333	36.00000	0.000000
A (mm/min)	0.166667	0.144338	1.15470	0.270690
A^2	0.125000	0.108253	1.15470	0.270690
B (Ampere)	0.333333	0.144338	2.30940	0.039519
B^2	0.750000	0.108253	6.92820	0.000016
C (Volt)	0.333333	0.144338	2.30940	0.039519
C^2	0.000000	0.108253	0.00000	1.000000
D (mm)	0.500000	0.144338	3.46410	0.004682
D^2	0.625000	0.108253	5.77350	0.000088
A×B	0.000000	0.250000	0.00000	1.000000
A×C	0.000000	0.250000	0.00000	1.000000
A×D	0.500000	0.250000	2.00000	0.068655
B×C	0.500000	0.250000	2.00000	0.068655
B×D	1.500000	0.250000	6.00000	0.000062
C×D	0.500000	0.250000	2.00000	0.068655

Table 11 ANOVA Table for Right Bevel Angle

Factors	SS	DoF	MS	F	P
A (mm/min)	0.08333	1	0.083333	1.33333	0.270690
A^2	0.08333	1	0.083333	1.33333	0.270690
B (Ampere)	0.33333	1	0.333333	5.33333	0.039519
B^2	3.00000	1	3.000000	48.00000	0.000016
C (Volt)	0.33333	1	0.333333	5.33333	0.039519
C^2	0.00000	1	0.000000	0.00000	1.000000
D (mm)	0.75000	1	0.750000	12.00000	0.004682
D^2	2.08333	1	2.083333	33.33333	0.000088
A×B	0.00000	1	0.000000	0.00000	1.000000
A×C	0.00000	1	0.000000	0.00000	1.000000
A×D	0.25000	1	0.250000	4.00000	0.068655
B×C	0.25000	1	0.250000	4.00000	0.068655
B×D	2.25000	1	2.250000	36.00000	0.000062
C×D	0.25000	1	0.250000	4.00000	0.068655
Error	0.75000	12	0.062500		
Total SS	10.00000	26			

Table 12 Regression Coefficients of Right Bevel Angle

Factor	Regression Coef.	Std. Err.	T	P
Constant	-72.0417	50.91523	-1.41493	0.182510
A (mm/min)	0.0867	0.08636	1.00353	0.335412
A^2	-0.0001	0.00004	-1.15470	0.270690
B (Ampere)	2.1833	0.62915	3.47027	0.004629
B^2	-0.0300	0.00433	-6.92820	0.000016
C (Volt)	-0.1033	0.11416	-0.90513	0.383208
C^2	-0.0000	0.00017	-0.00000	1.000000
D (mm)	-10.0000	2.73671	-3.65402	0.003302
D^2	-0.6250	0.10825	-5.77350	0.000088
A×B	0.0000	0.00050	0.00000	1.000000
A×C	0.0000	0.00010	0.00000	1.000000
A×D	0.0050	0.00250	2.00000	0.068655
B×C	0.0020	0.00100	2.00000	0.068655
B×D	0.1500	0.02500	6.00000	0.000062
C×D	0.0100	0.00500	2.00000	0.068655

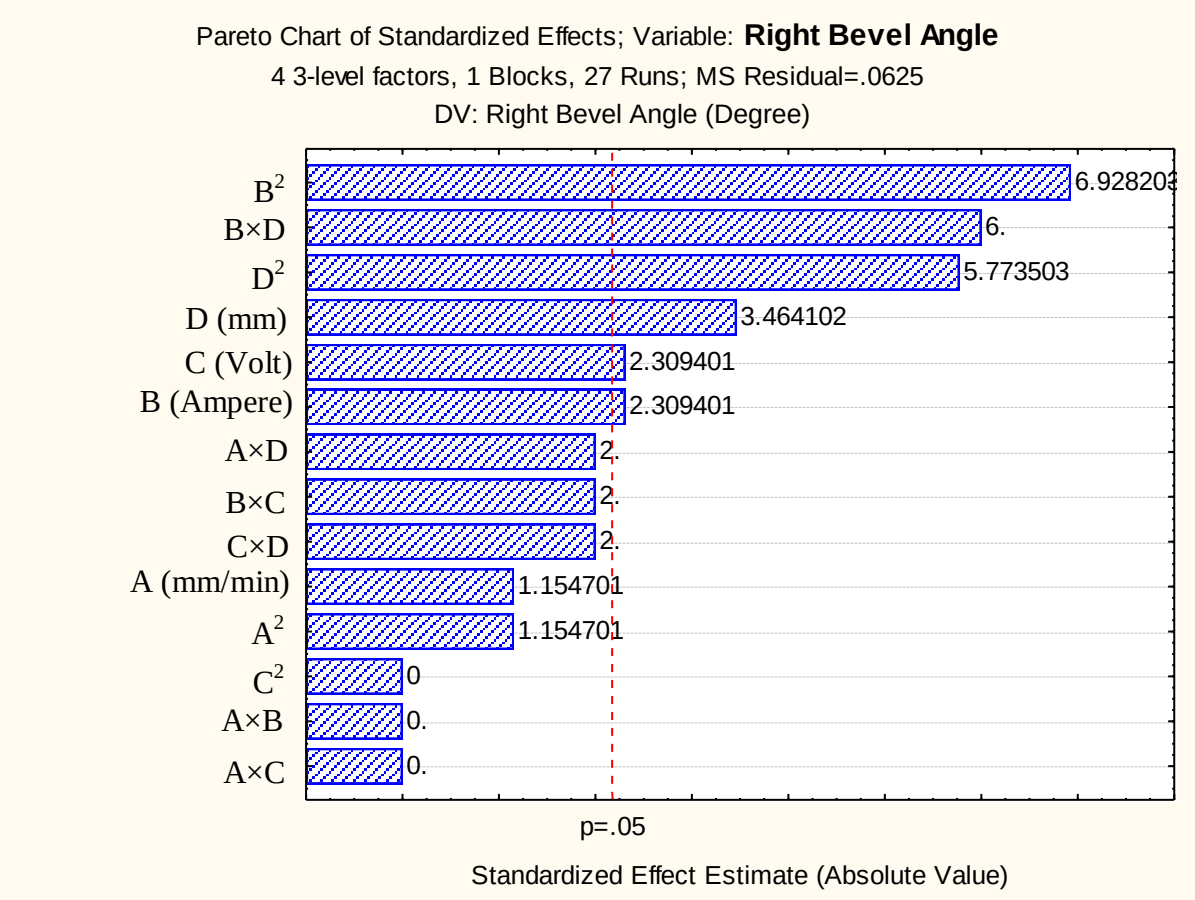

Fig. 40 Pareto chart of standardized effect of factors on right bevel angle

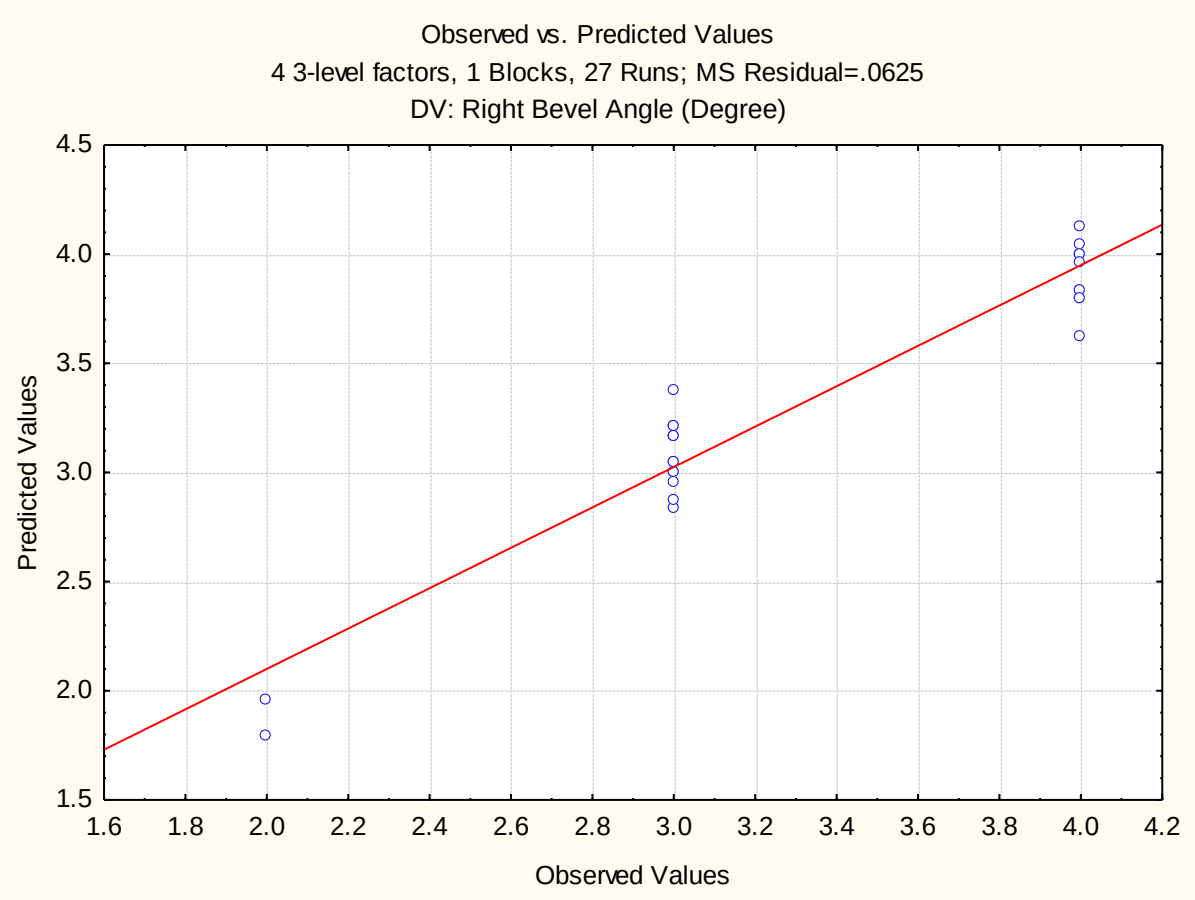

Fig. 41 Plot of observed vs. predicted values of right bevel angle

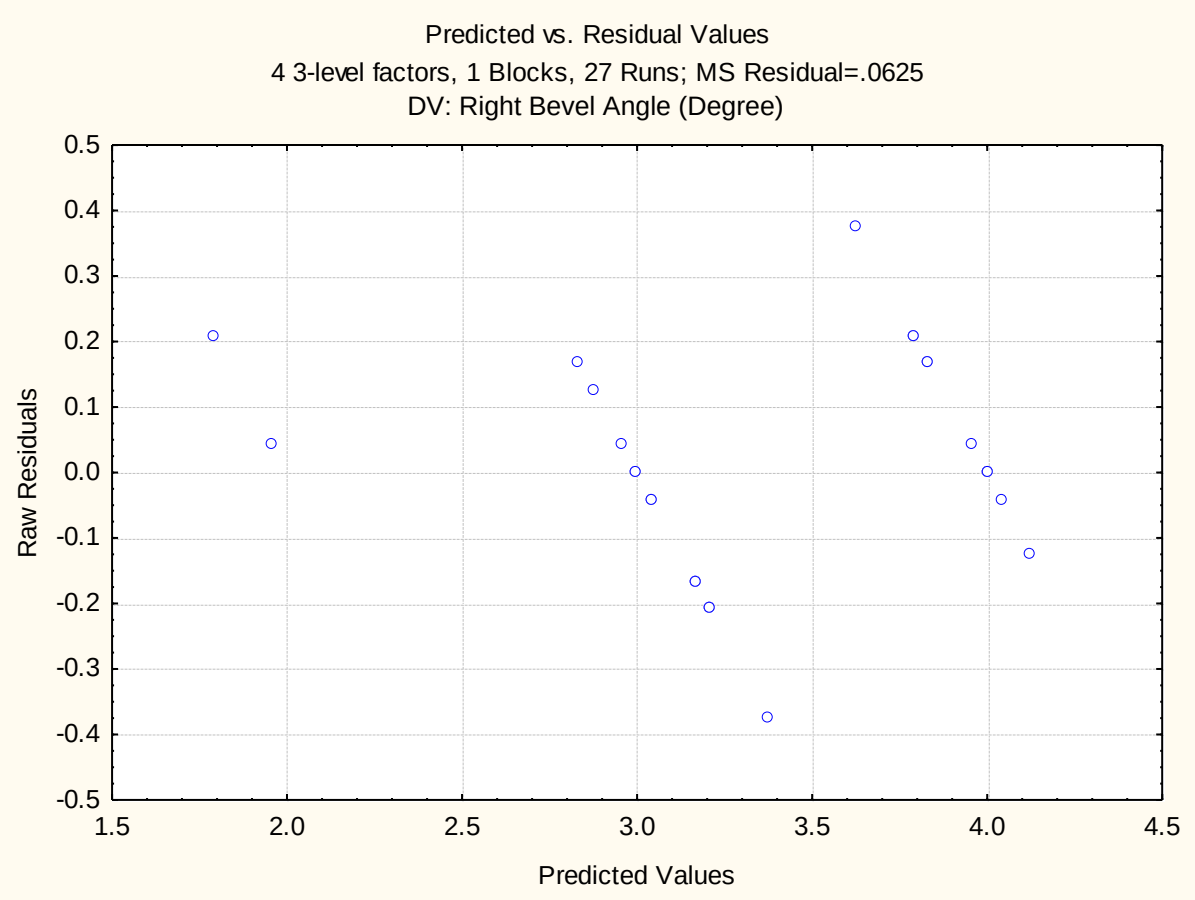

Fig. 42 Plot of predicted vs. residual values of right bevel angle

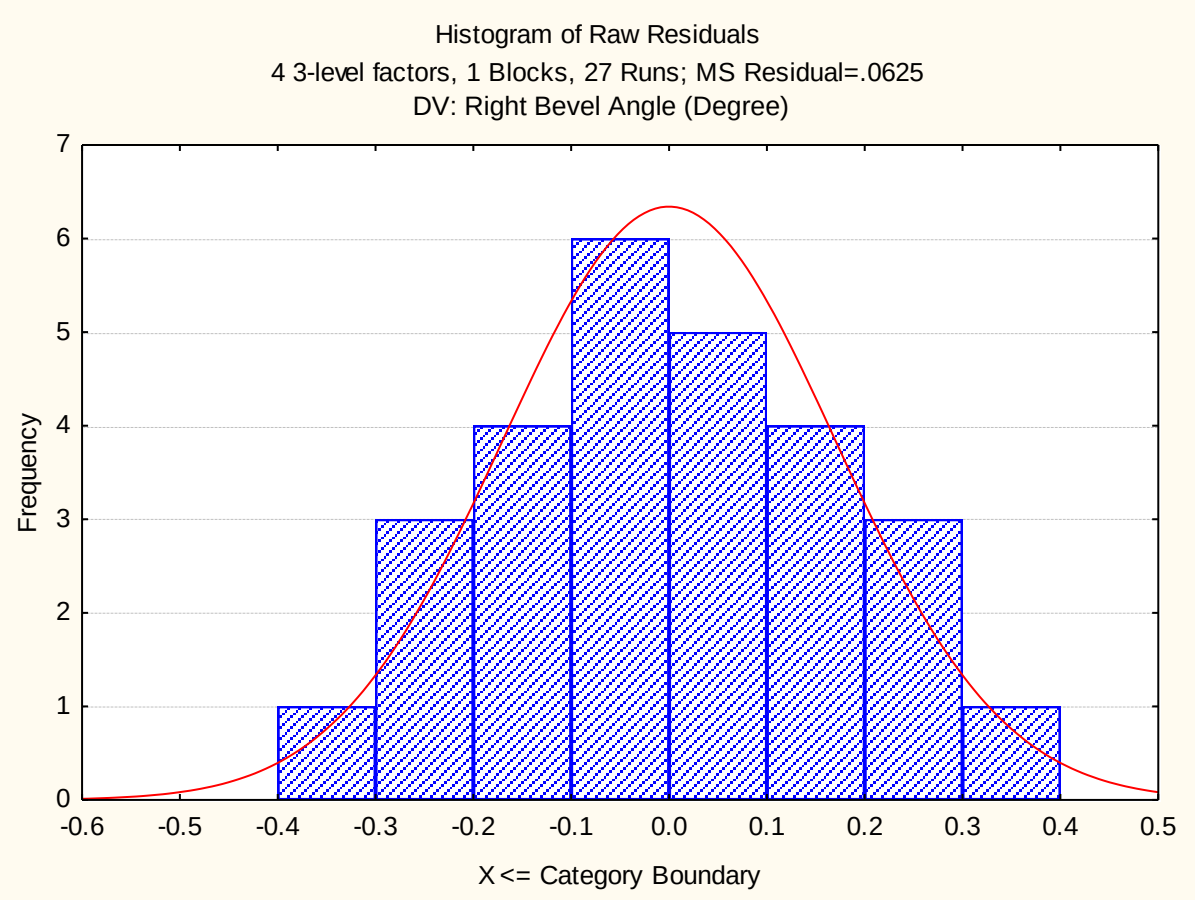

Fig. 43 Histogram plot of predicted values of right bevel angle

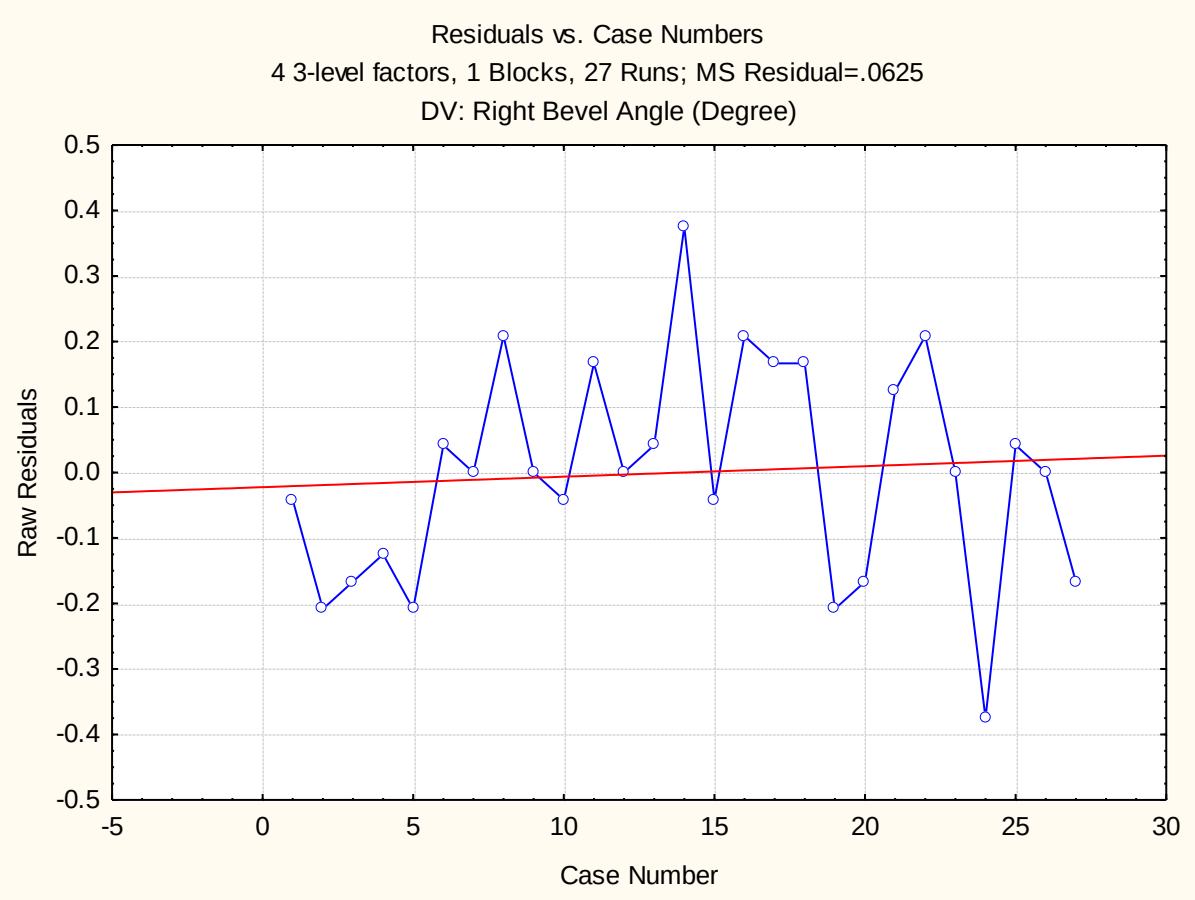

Fig. 44 Plot of residuals vs. case numbers values of right bevel angle

From the Fig. 44, it is evident that the highest right bevel angle value among all experimental runs is by the run number 14. The red line indicates that the value of right bevel angle increases with increase in run order.

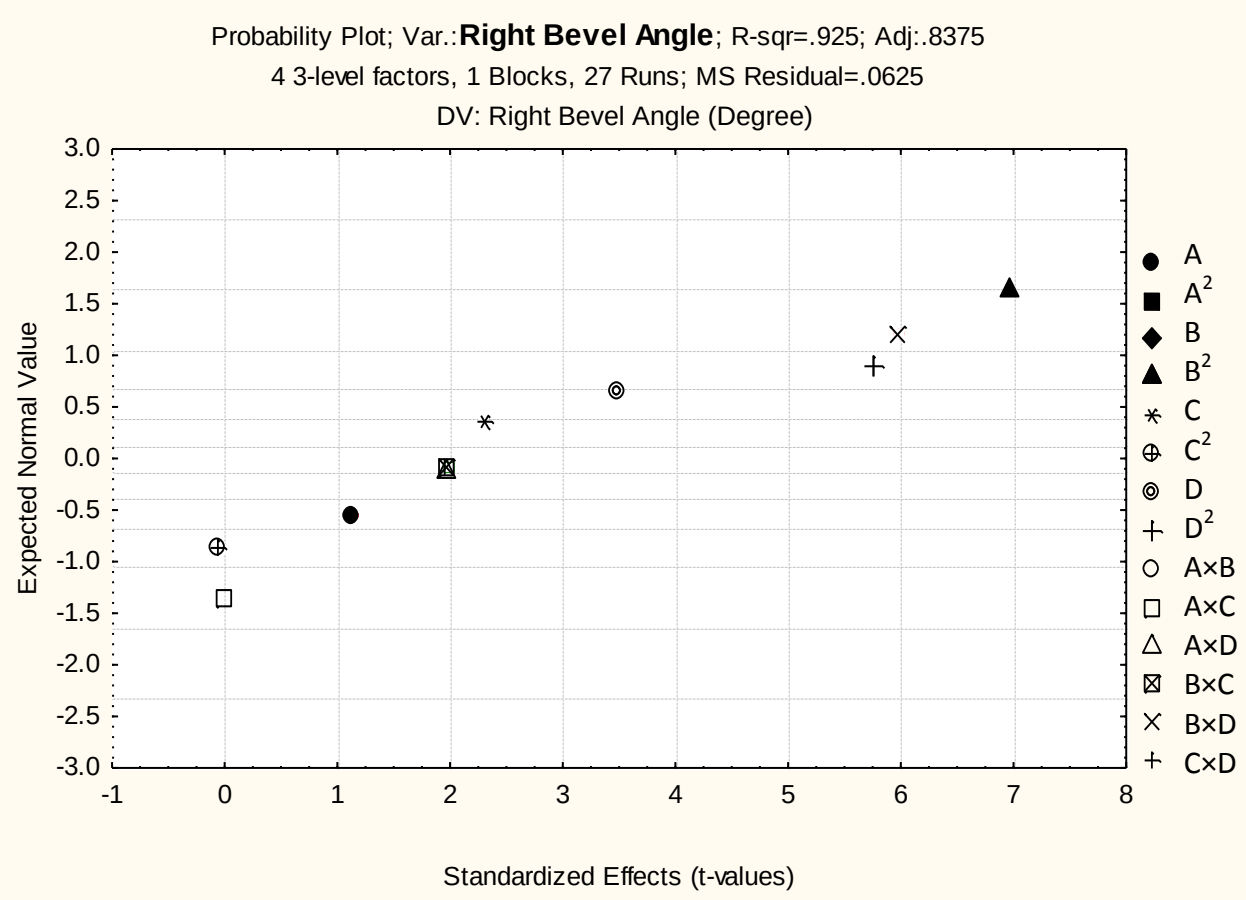

Fig. 45 Probability plot of right bevel angle

The normal probability plot of right bevel angle corresponding to each regression terms is plotted in Fig. 45.

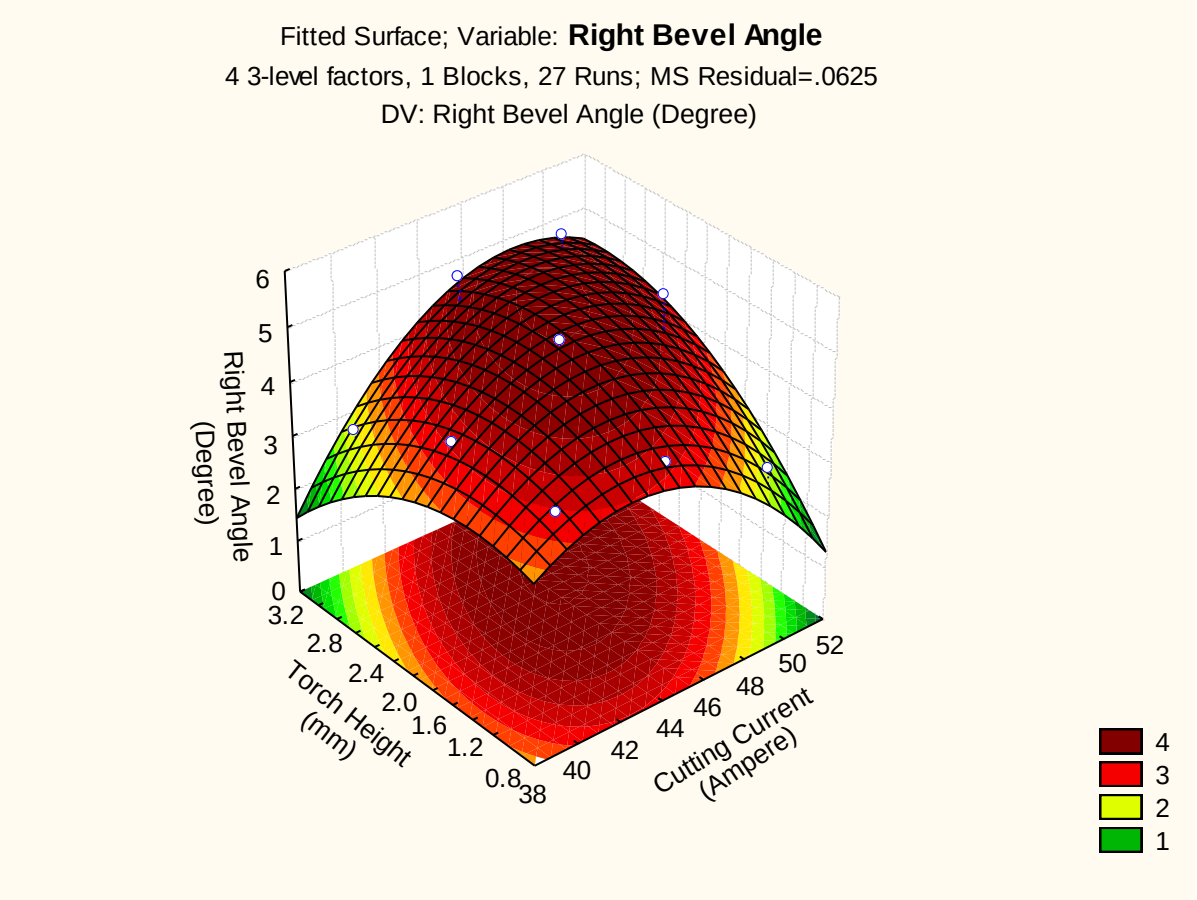

Fig. 46 3D fitted surface plot of right bevel angle

The 3D surface plot of the significant interaction terms can be exerted in Fig. 46. It is to be noted that all other terms are taken into account at their average value. From the figure, it is evident that the interaction of cutting current and torch height is also influenced by the above mentioned output.

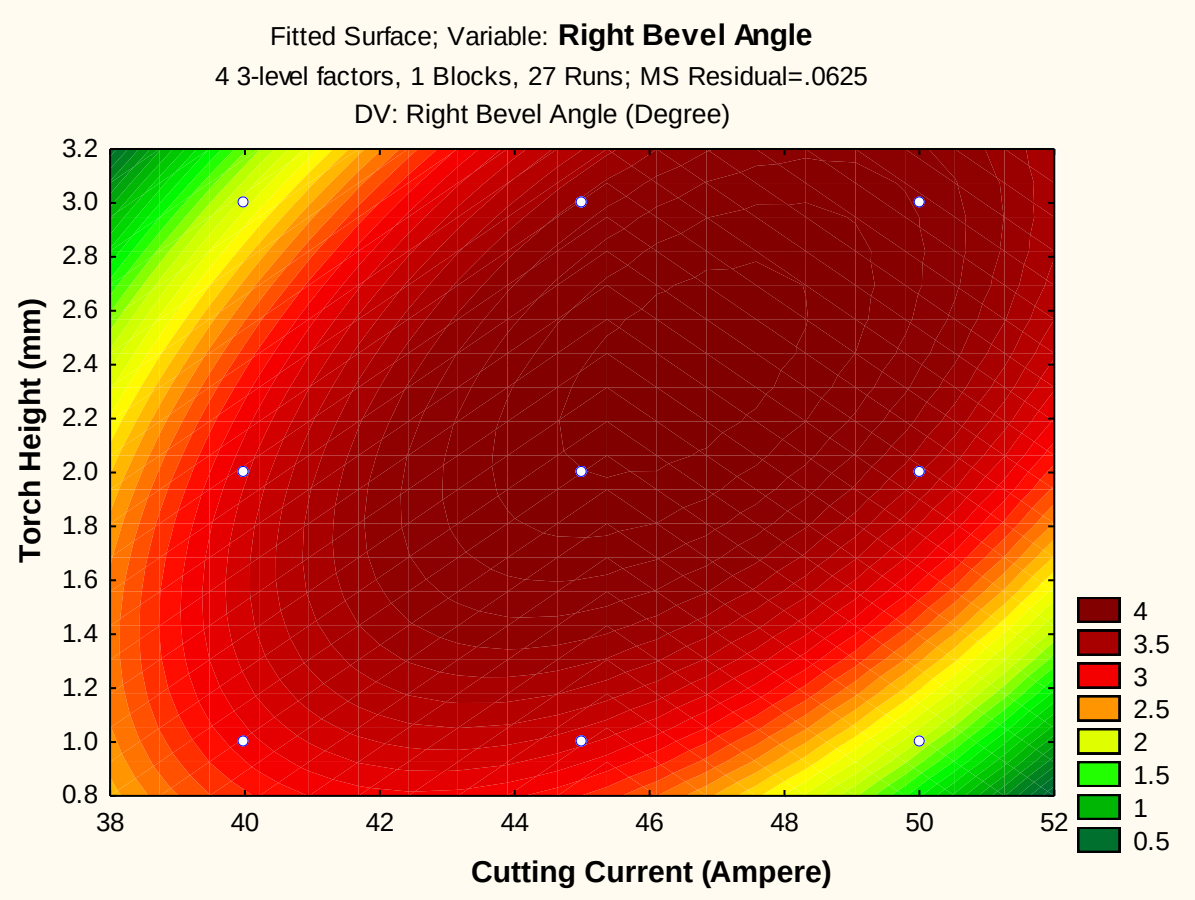

Fig. 47 2D fitted counter plot of right bevel angle

The counter plots of interaction terms at their average level vs. right bevel angle are found in Fig. 47. Mainly the shapes of counter plots might be elliptical, or saddle form which indicates that the combination of each variable are significant except torch height vs. cutting current plot. Because, the lowest value of right bevel angle obtained in the maximum region of current this can be seen in Fig. 47.

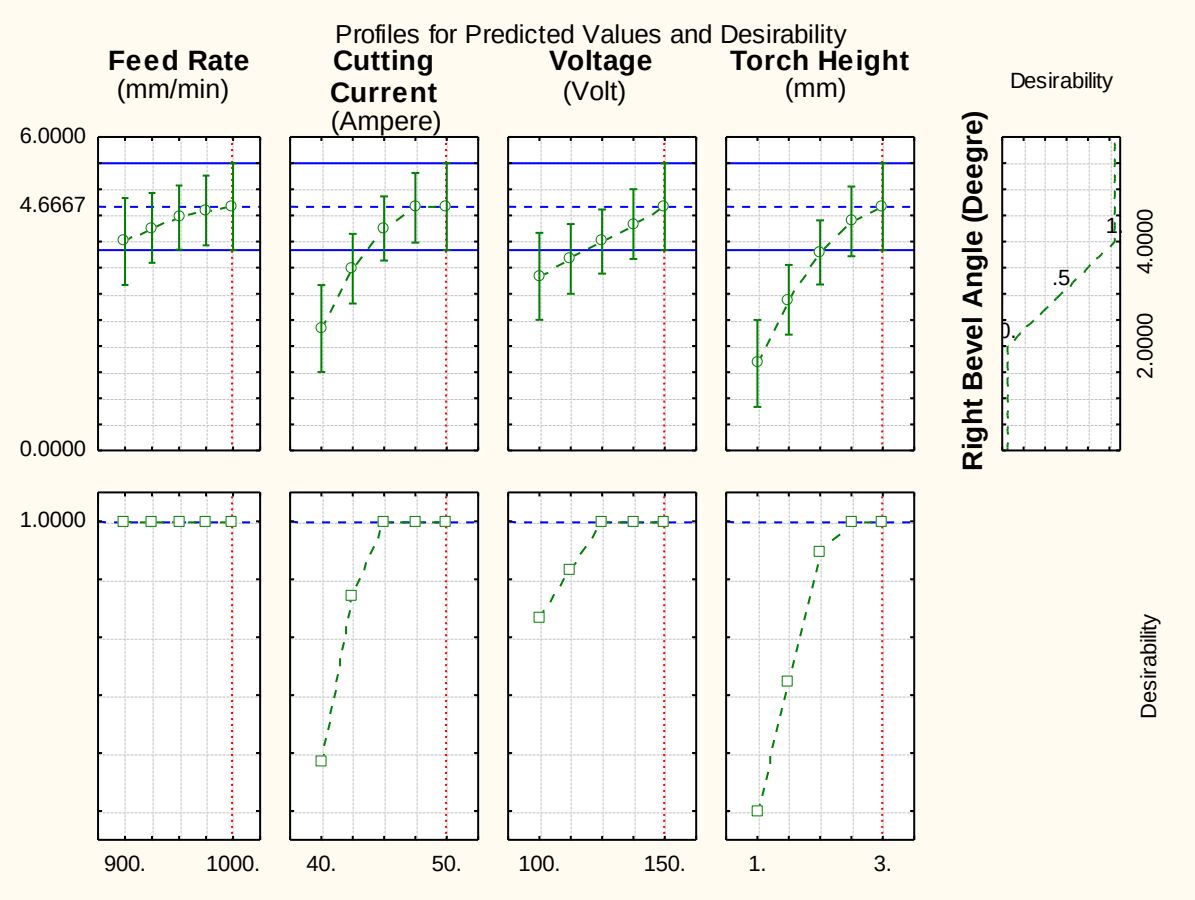

Fig. 48 Profile plot of predicted values and desirability of right bevel angle

In case of right bevel angle, the desirability function helped to get optimum value which was fitted by the quadratic fit model. The level of variable giving the highest desirability i.e., 1.0000 was considered as optimum level. The optimized levels of variables (A, B, C and D) were determined using the desirability profiles that are shown in Fig. 48 for predicted values of responses and desirability function value displayed with dotted line in red color.

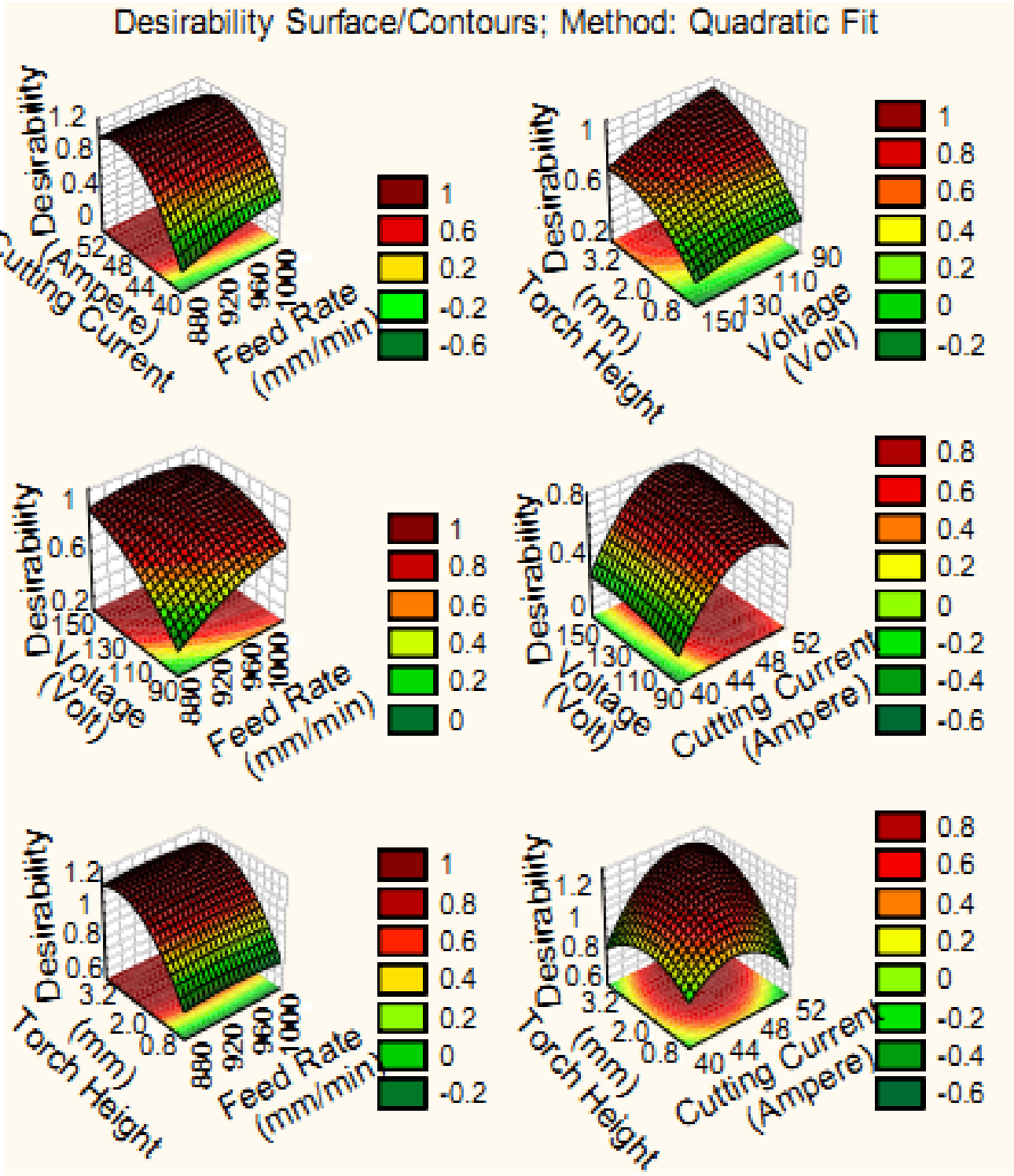

Fig. 49 Desirability 3D surface plot of right bevel angle

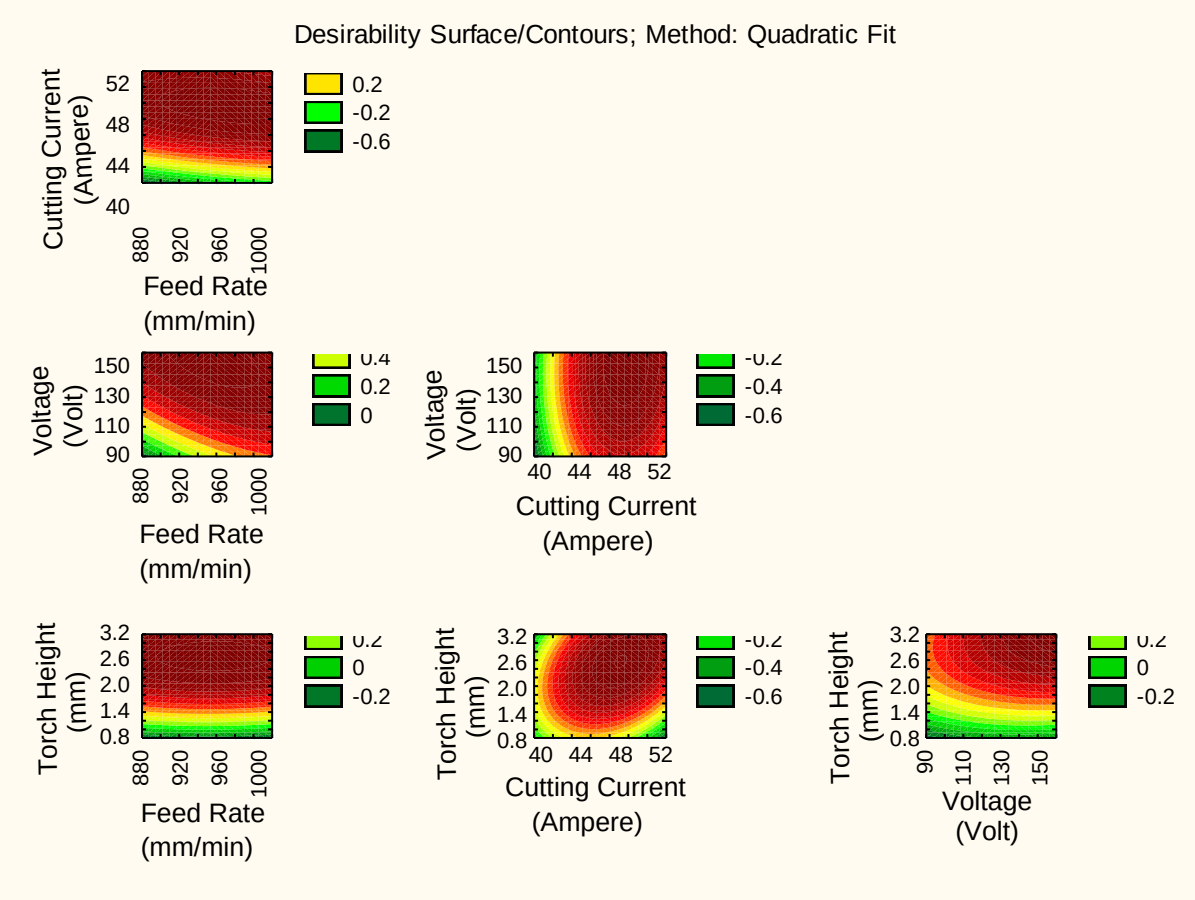

Fig. 50 Desirability 2D counter plot of right bevel angle

The 3D and 2D plot of interaction variables were determined using the desirability profiles that are displayed in Fig. 49-50 respectively. From six interactions of input variables, all are given maximum effect on right bevel angle as the red colored areas are more than green.

5.1.2 Hybrid approach

In this hybrid approach i.e., Grey based principle component (PCA), firstly normalization of all the response values are done between 0 and 1 as per the higher the better and lower the better criteria according to the corresponding problem. The computed normalized value of each response is recorded in Table 13.

Table 13 Normalized Values for Output Responses of PAC

MRR (mm^3/min)	SR (µm)	Right Bevel Angle (Degree)
0.504404	0.284553	0.0
0.103982	0.674797	0.5
0.509809	0.258130	0.5
0.177345	0.853659	0.0
0.463335	0.615854	0.5
0.378471	0.321138	1.0
0.052191	0.715447	0.0
0.149782	0.050813	1.0
0.052191	0.695122	0.0
0.468587	1.000000	0.5
0.517166	0.217480	0.5
0.002626	0.628049	0.5
0.820237	0.349593	0.5
0.057424	0.626016	0.0
0.093069	0.268293	0.5
0.945824	0.477642	0.0
1.000000	0.810976	0.0
0.119577	0.497967	0.0
0.095728	0.030488	0.5
0.805920	0.000000	0.5
0.372220	0.327236	0.5
0.143739	0.788618	0.0
0.052191	0.691057	0.0
0.209053	0.436992	0.5
0.062224	0.406504	0.0
0.155361	0.745935	0.5
0.000000	0.432927	0.5

Then, the value of deviation sequences for normalized outputs are calculated and tabulated in Table 13. The Eigen values and vectors are determined to check the correlation among output responses of PAC operation. The values of Eigen are tabulated in Table 15 and similarly the values of Eigen vectors are recorded in Table 16 for each principal component. The grey relational coefficients are computed for each response. The overall grey relational grade is computed by taking average of grey coefficients in each run order. The grey relational coefficients and overall grey relational grade are tabulated

in Table 17. The ANOVA is carried out for the multi-objective problem of Grey based PCA approach and the obtained results are tabulated in Table 18 and Table 19. The regression coefficients of GRG are recorded in Table 20.

Table 14 Deviation Sequences for Output Responses of PAC

MRR (mm^3/min)	SR (µm)	Right Bevel Angle (Degree)
0.495596	0.715447	1.0
0.896018	0.325203	0.5
0.490191	0.741870	0.5
0.822655	0.146341	1.0
0.536665	0.384146	0.5
0.621529	0.678862	0.0
0.947809	0.284553	1.0
0.850218	0.949187	0.0
0.947809	0.304878	1.0
0.531413	0.000000	0.5
0.482834	0.782520	0.5
0.997374	0.371951	0.5
0.179763	0.650407	0.5
0.942576	0.373984	1.0
0.906931	0.731707	0.5
0.054176	0.522358	1.0
0.000000	0.189024	1.0
0.880423	0.502033	1.0
0.904272	0.969512	0.5
0.194080	1.000000	0.5
0.627780	0.672764	0.5
0.856261	0.211382	1.0
0.947809	0.308943	1.0
0.790947	0.563008	0.5
0.937776	0.593496	1.0
0.844639	0.254065	0.5
1.000000	0.567073	0.5

Table 15 Eigenvalues and Explained Variation for Principal Components

Principal components	Eigen value	Explained variations (%)	Cumulative Eigen value	Cumulative %
First	1.518351	50.61170	1.518351	50.6117
Second	0.984279	32.80929	2.502630	83.4210
Third	0.497370	16.57901	3.000000	100.0000

Table 16 Eigenvectors for Principal Components and Contribution

Variable	Factor 1	Factor 2	Factor 3
MRR (mm^3/min)	0.244846	0.952146	-0.182944
SR (µm)	-0.700998	0.043492	-0.711835
Right Bevel Angle (Degree)	0.669815	-0.302533	-0.678102

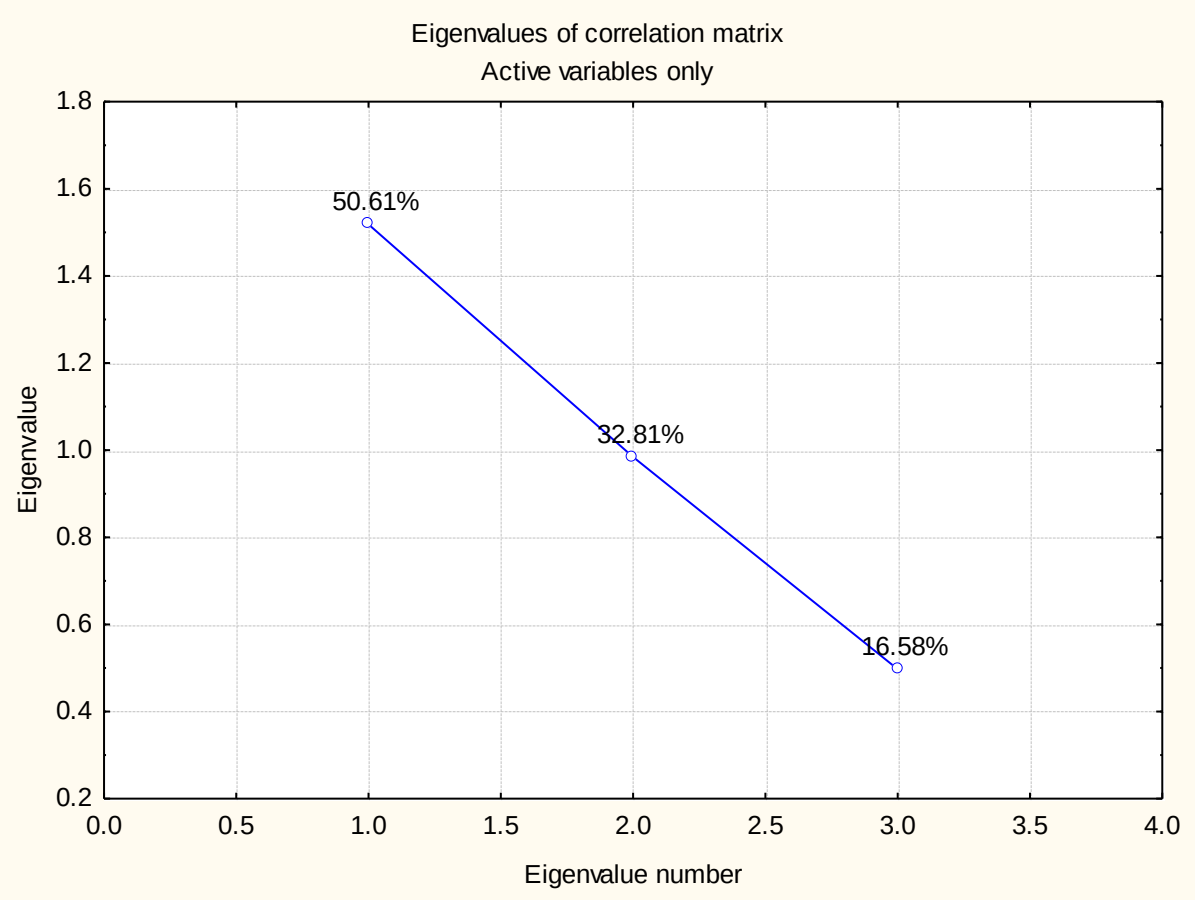

Fig. 51 Plot of Eigen values of correlation matrix for first phase

The Fig. 51 shows the variation in percentage of Eigen values in first phase experimentation.

Table 17 Grey Relational Coefficient and Grade of Output Responses of PAC

Grey relational coefficient 1	Grey relational coefficient 2	Grey relational coefficient 3	Overall grey relational grade
0.502212	0.411371	0.333333	0.415639
0.358162	0.605911	0.500000	0.488024
0.504953	0.402619	0.500000	0.469191
0.378028	0.773585	0.333333	0.494982
0.482316	0.565517	0.500000	0.515944
0.445820	0.424138	1.000000	0.623319
0.345349	0.637306	0.333333	0.438663
0.370311	0.345021	1.000000	0.571777
0.345349	0.621212	0.333333	0.433298
0.484772	1.000000	0.500000	0.661591
0.508733	0.389857	0.500000	0.466197
0.333918	0.573427	0.500000	0.469115
0.735550	0.434629	0.500000	0.556726
0.346602	0.572093	0.333333	0.417343
0.355383	0.405941	0.500000	0.420441
0.902240	0.489066	0.333333	0.574880
1.000000	0.725664	0.333333	0.686332
0.362208	0.498986	0.333333	0.398176
0.356056	0.340249	0.500000	0.398768
0.720378	0.333333	0.500000	0.517904
0.443349	0.426343	0.500000	0.456564
0.368661	0.702857	0.333333	0.468284
0.345349	0.618090	0.333333	0.432258
0.387312	0.470363	0.500000	0.452559
0.347759	0.457249	0.333333	0.379447
0.371847	0.663073	0.500000	0.511640
0.333333	0.468571	0.500000	0.433968

Table 18 Effect of Estimated Values of Responses of PAC

Factor	Effect	Std. Err.	T	P
Constant	0.513354	0.012088	42.46941	0.000000
A (mm/min)	0.083578	0.020936	3.99202	0.001787
A^2	-0.033732	0.015702	-2.14821	0.052811
B (Ampere)	-0.034038	0.020936	-1.62578	0.129952
B^2	-0.063722	0.015702	-4.05814	0.001587
C (Volt)	-0.028025	0.020936	-1.33856	0.205522
C^2	0.045602	0.015702	2.90416	0.013224
D (mm)	0.075153	0.020936	3.58959	0.003716
D^2	-0.066070	0.015702	-4.20764	0.001215
A×B	-0.120246	0.036263	-3.31596	0.006156
A×C	0.032297	0.036263	0.89063	0.390633
A×D	0.085711	0.036263	2.36361	0.035816
B×C	-0.074305	0.036263	-2.04908	0.062974
B×D	-0.031745	0.036263	-0.87542	0.398528
C×D	-0.060989	0.036263	-1.68187	0.118412

Table 19 ANOVA Table for GRG

Factors	SS	DoF	MS	F	P
A (mm/min)	0.020956	1	0.020956	15.93626	0.001787
A^2	0.006068	1	0.006068	4.61482	0.052811
B (Ampere)	0.003476	1	0.003476	2.64317	0.129952
B^2	0.021656	1	0.021656	16.46851	0.001587
C (Volt)	0.002356	1	0.002356	1.79175	0.205522
C^2	0.011091	1	0.011091	8.43412	0.013224
D (mm)	0.016944	1	0.016944	12.88515	0.003716
D^2	0.023281	1	0.023281	17.70427	0.001215
A×B	0.014459	1	0.014459	10.99558	0.006156
A×C	0.001043	1	0.001043	0.79323	0.390633
A×D	0.007346	1	0.007346	5.58664	0.035816
B×C	0.005521	1	0.005521	4.19872	0.062974
B×D	0.001008	1	0.001008	0.76636	0.398528
C×D	0.003720	1	0.003720	2.82868	0.118412
Error	0.015780	12	0.001315		
Total SS	0.167213	26			

Table 20 Regression Coefficients of GRG

Factor	Regression Coef.	Std. Err.	T	P
Constant	6.870780	7.385326	0.93033	0.370539
A (mm/min)	-0.017307	0.012527	-1.38162	0.192272
A^2	0.000013	0.000006	2.14821	0.052811
B (Ampere)	0.039166	0.091260	0.42917	0.675401
B^2	0.002549	0.000628	4.05814	0.001587
C (Volt)	0.021222	0.016560	1.28155	0.224210
C^2	-0.000073	0.000025	-2.90416	0.013224
D (mm)	-0.745630	0.396964	-1.87833	0.084841
D^2	0.066070	0.015702	4.20764	0.001215
A×B	-0.000240	0.000073	-3.31596	0.006156
A×C	0.000013	0.000015	0.89063	0.390633
A×D	0.000857	0.000363	2.36361	0.035816
B×C	-0.000297	0.000145	-2.04908	0.062974
B×D	-0.003175	0.003626	-0.87542	0.398528
C×D	-0.001220	0.000725	-1.68187	0.118412

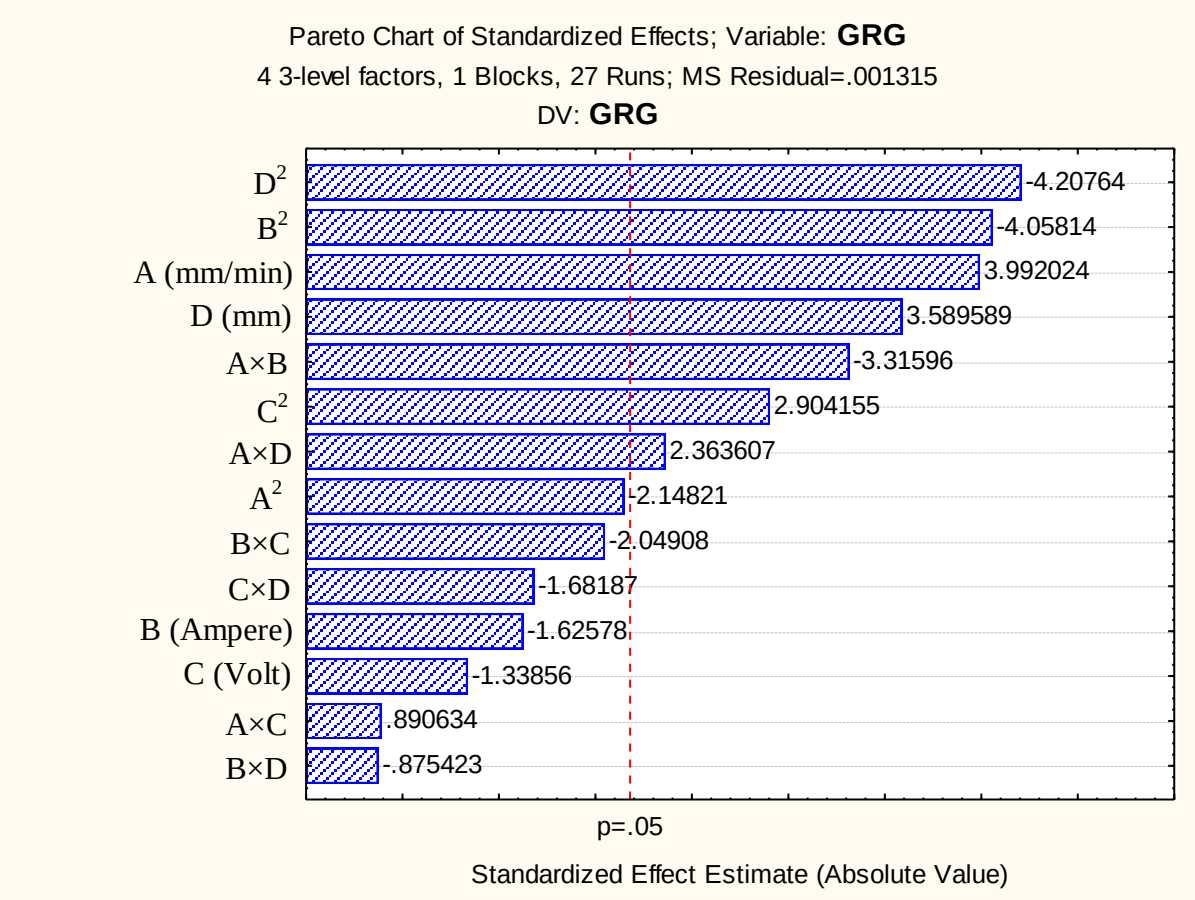

Fig. 52 Pareto chart of standardized effect of factors on GRG

The torch height factor with quadratic form had displayed the most significant influence on the GRG response from Pareto chart in Fig. 52.

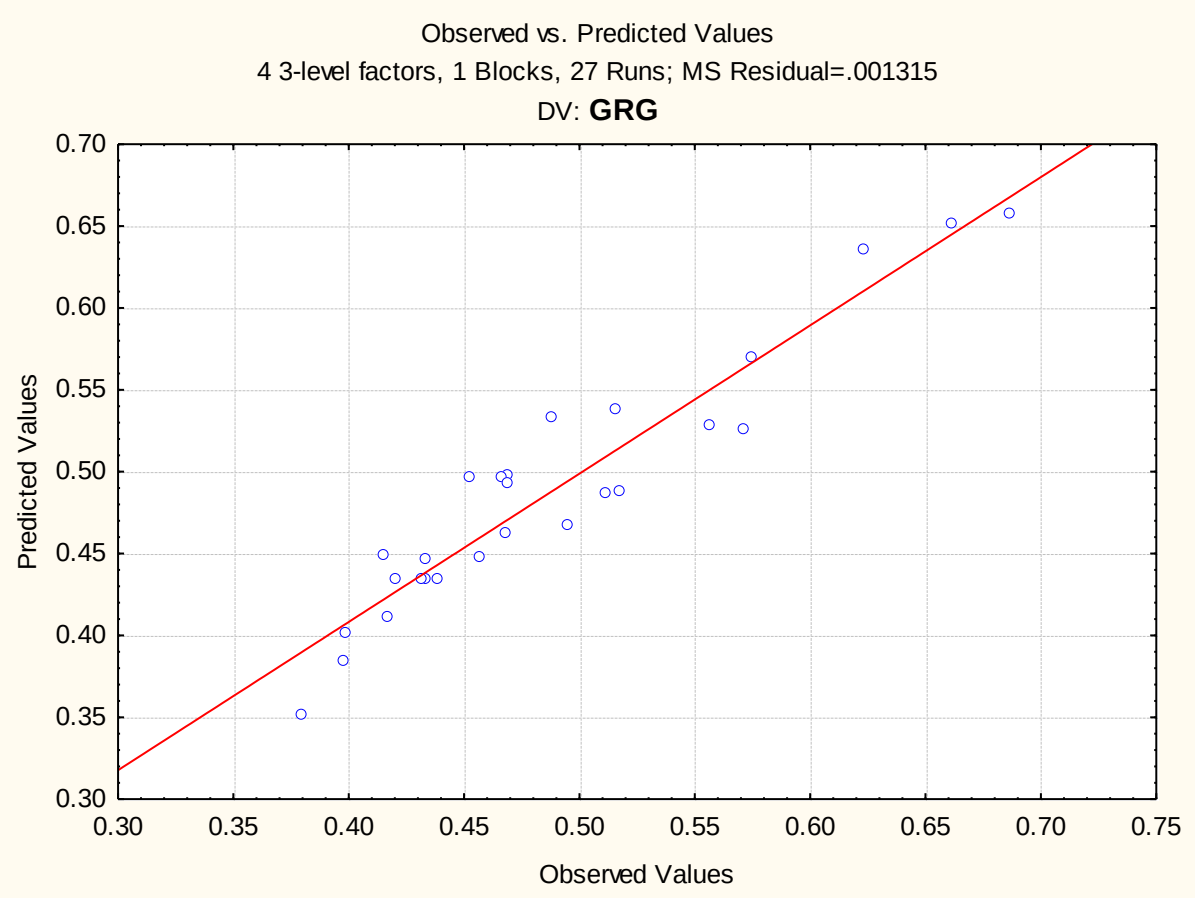

Fig. 53 Plot of observed vs. predicted values of GRG

The scatter plot between the observed and the predicted value of plasma cut responses of all 27 runs is shown in Fig. 53. The comparison between each of the observed values with the predicted value is shown in those plots which are calculated from the developed model. Here, the most of the points lie on the normal line of fitted values except the plot of GRG, because the uniformity lacks in the middle region. From this result it can be revealed that the response model shows good fit to experimental data, because the relationship between the actual and the predicted GRG is linear.

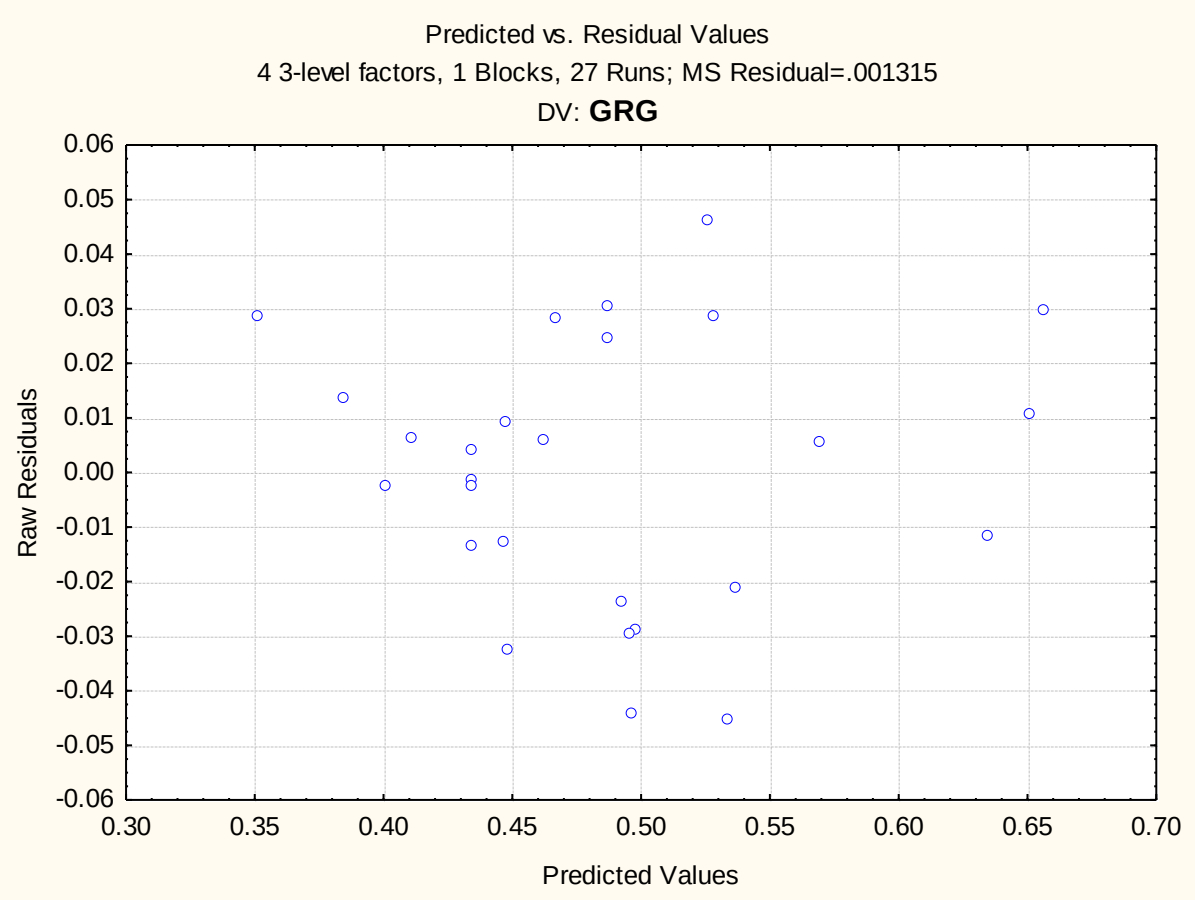

Fig. 54 Plot of predicted vs. residual values of GRG

From the Fig. 54, no standard pattern is formed in the plot of predicted vs. residual values which show the adequacy of the fitted model for GRG.

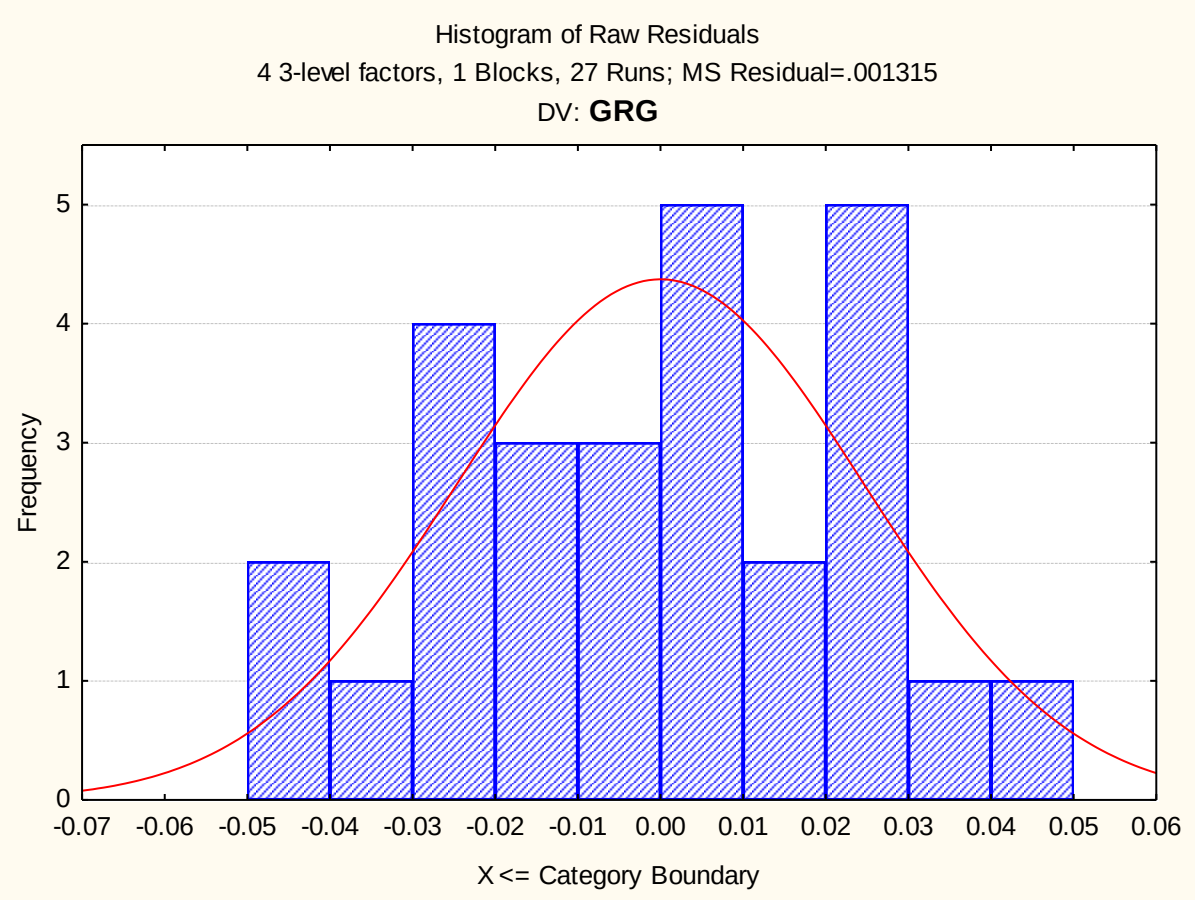

Fig. 55 Histogram plot of predicted values of GRG

The perfect normal probability distribution of the histogram plot of residuals for GRG response is shown in Fig. 55. From the above graphs, it is seen that the normal probability created in the histogram plot of residual for GRG is tolerable.

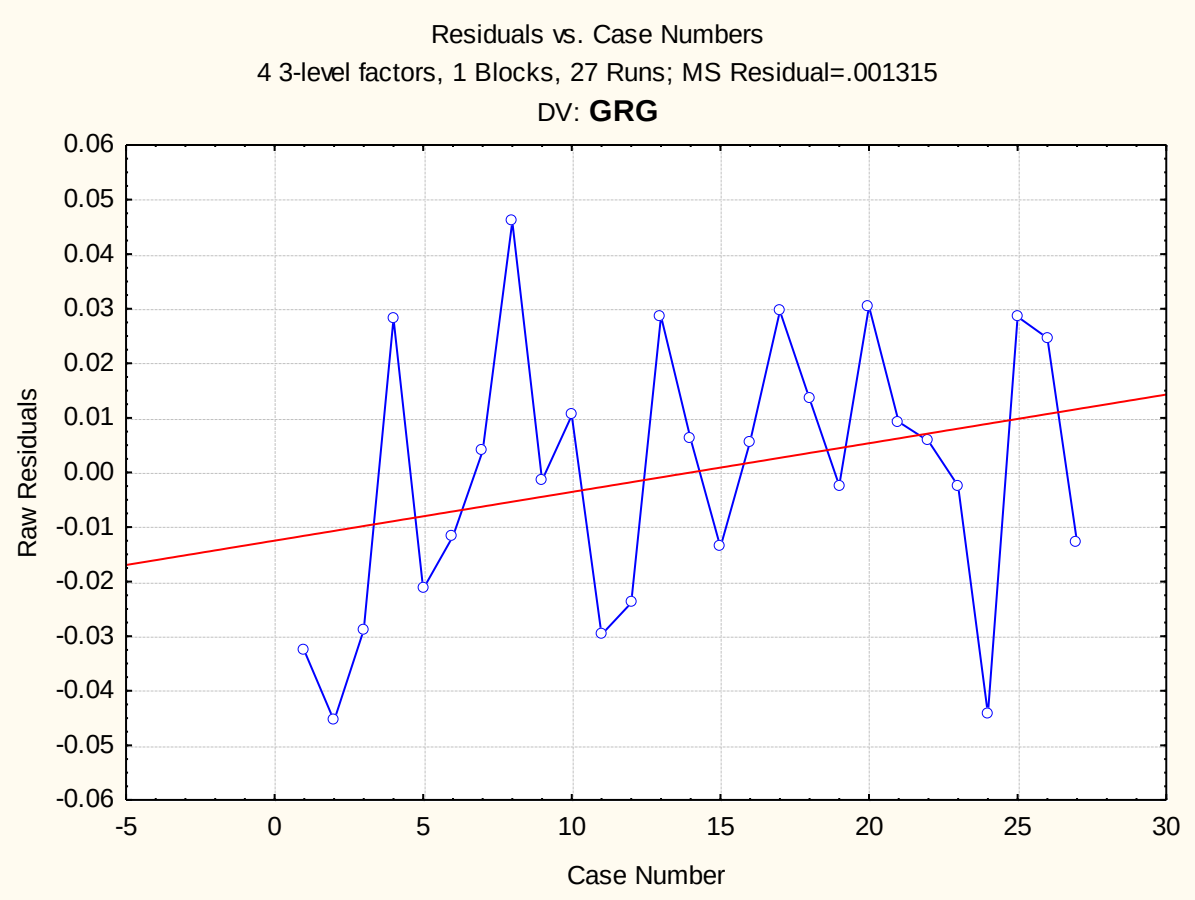

Fig. 56 Plot of residuals vs. case numbers values of GRG

From the Fig. 56, it is evident that the highest GRG value among all experimental runs is by the run number 26. The red line indicates that the value of GRG increases with increase in run order.

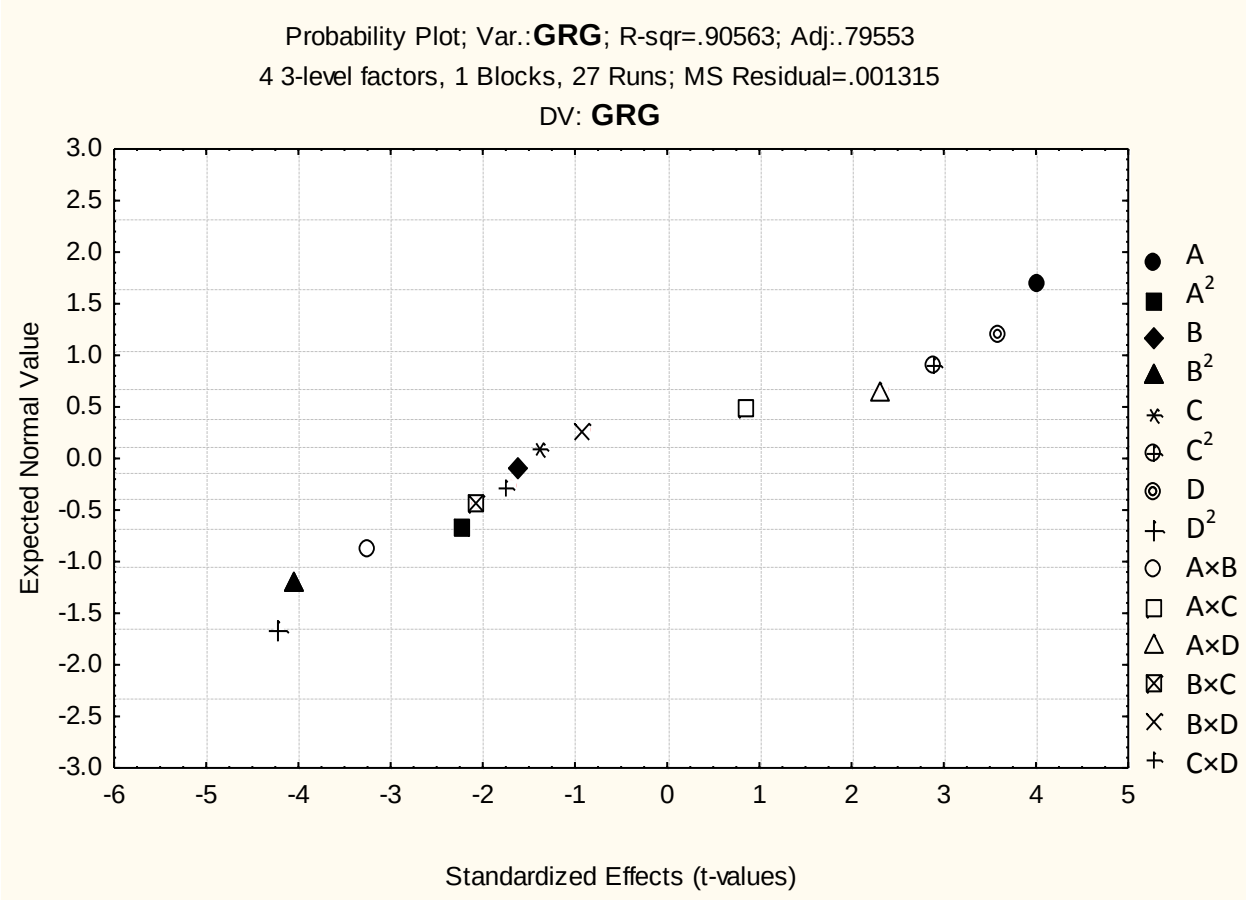

Fig. 57 Probability plot of GRG

The normal probability plot of GRG corresponding to each regression terms is plotted in Fig. 57. The 3D surface plot of the significant interaction terms can be exerted in Fig. 58-60. It is to be noted that all other terms are taken into account at their average value.

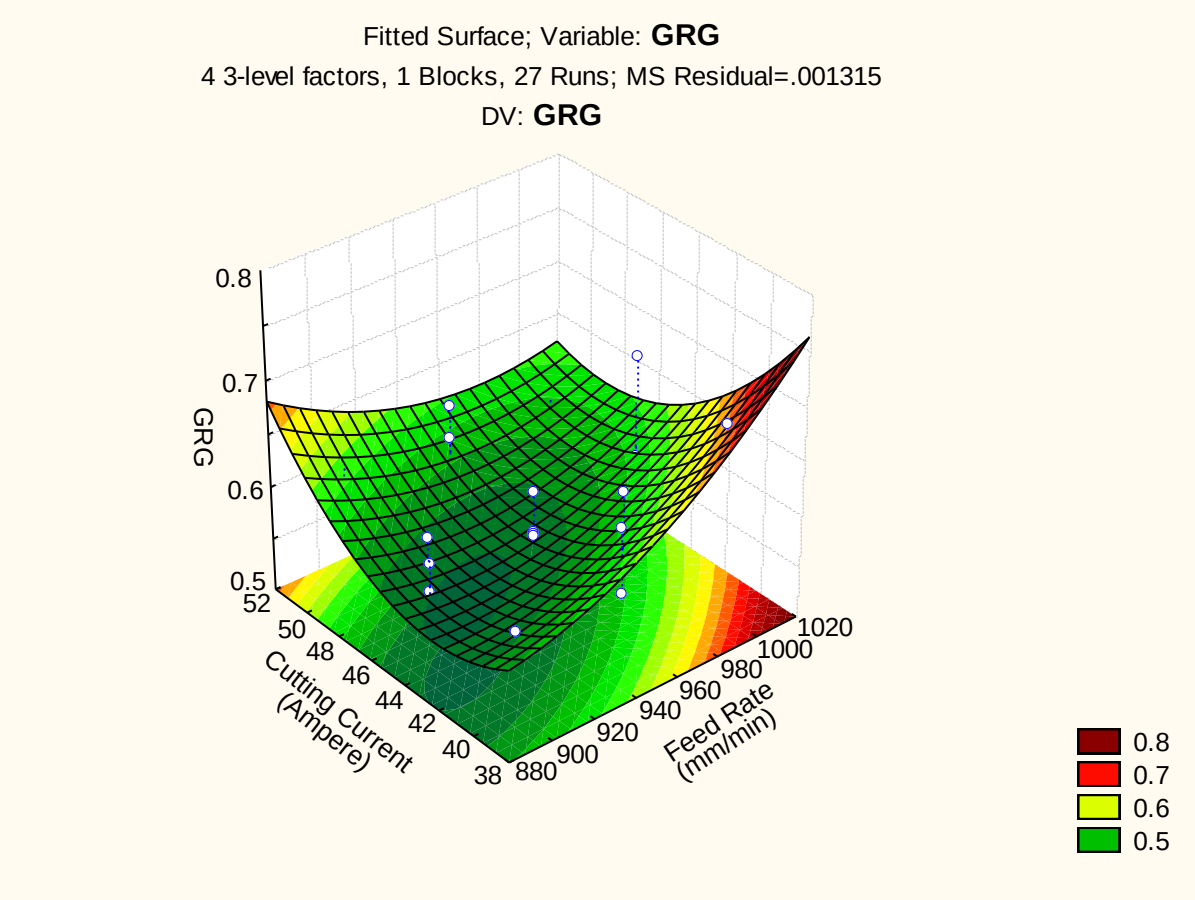

Fig. 58 3D fitted surface plot of GRG(1)

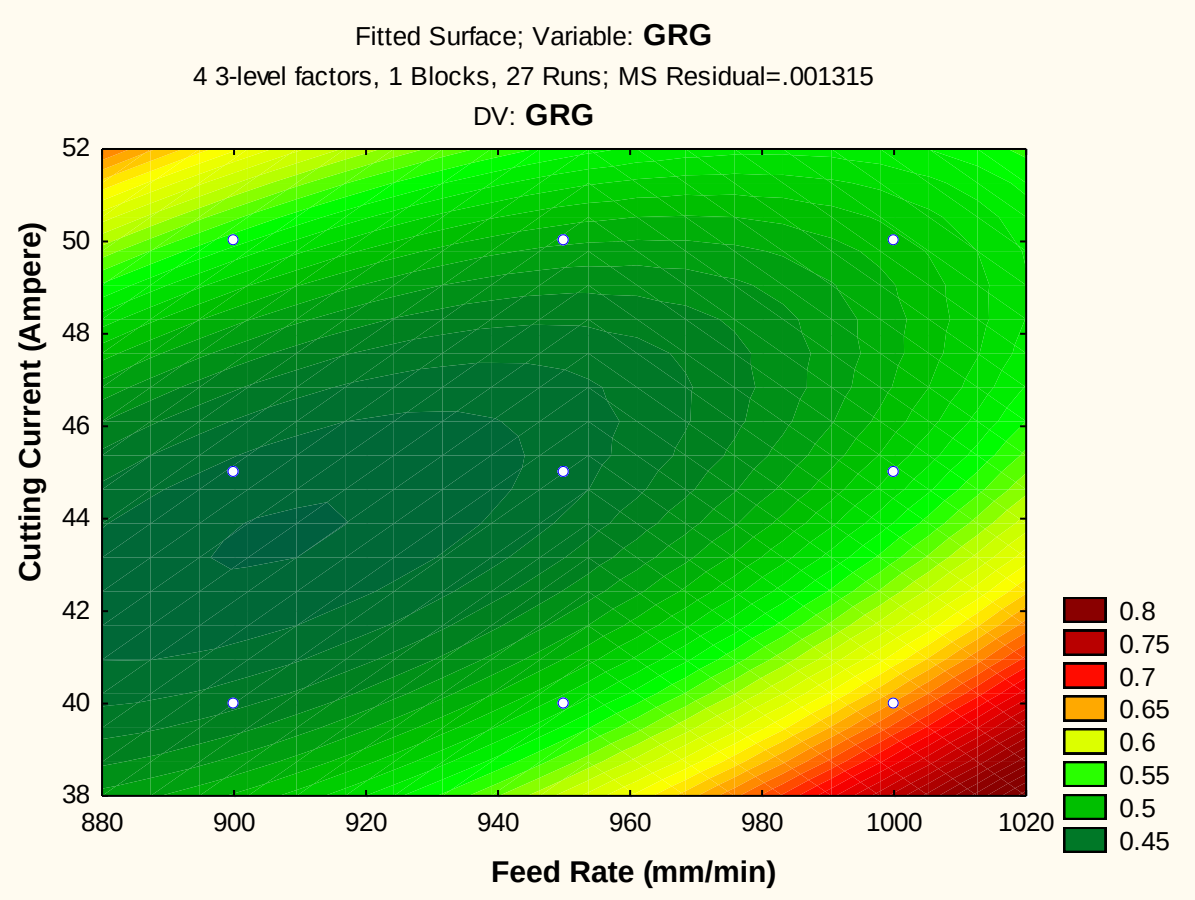

Fig. 59 2D fitted counter plot of GRG (1)

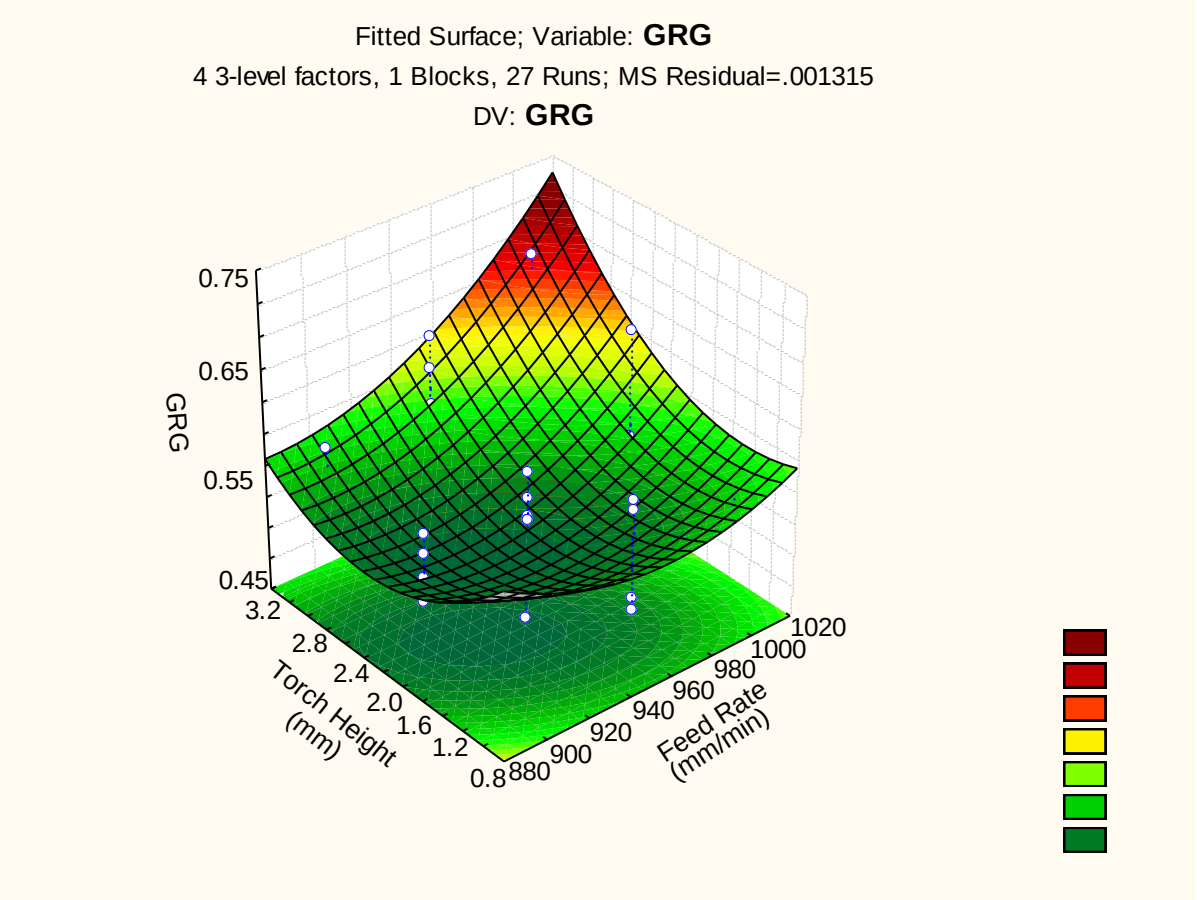

Fig. 60 3D fitted surface plot of GRG(2)

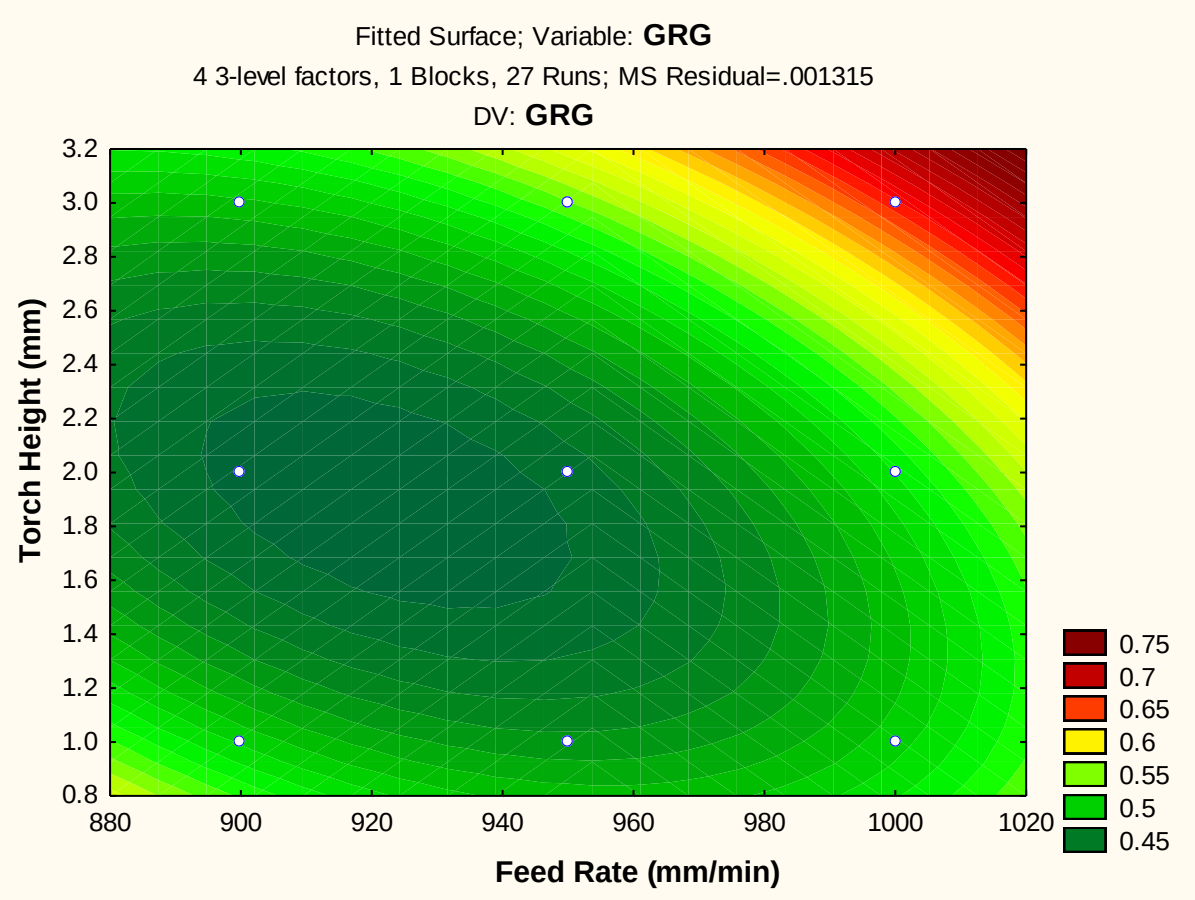

Fig. 61 2D fitted counter plot of GRG (2)

The counter plots of interaction terms at their average level vs. GRG are found in Fig. 59-61.

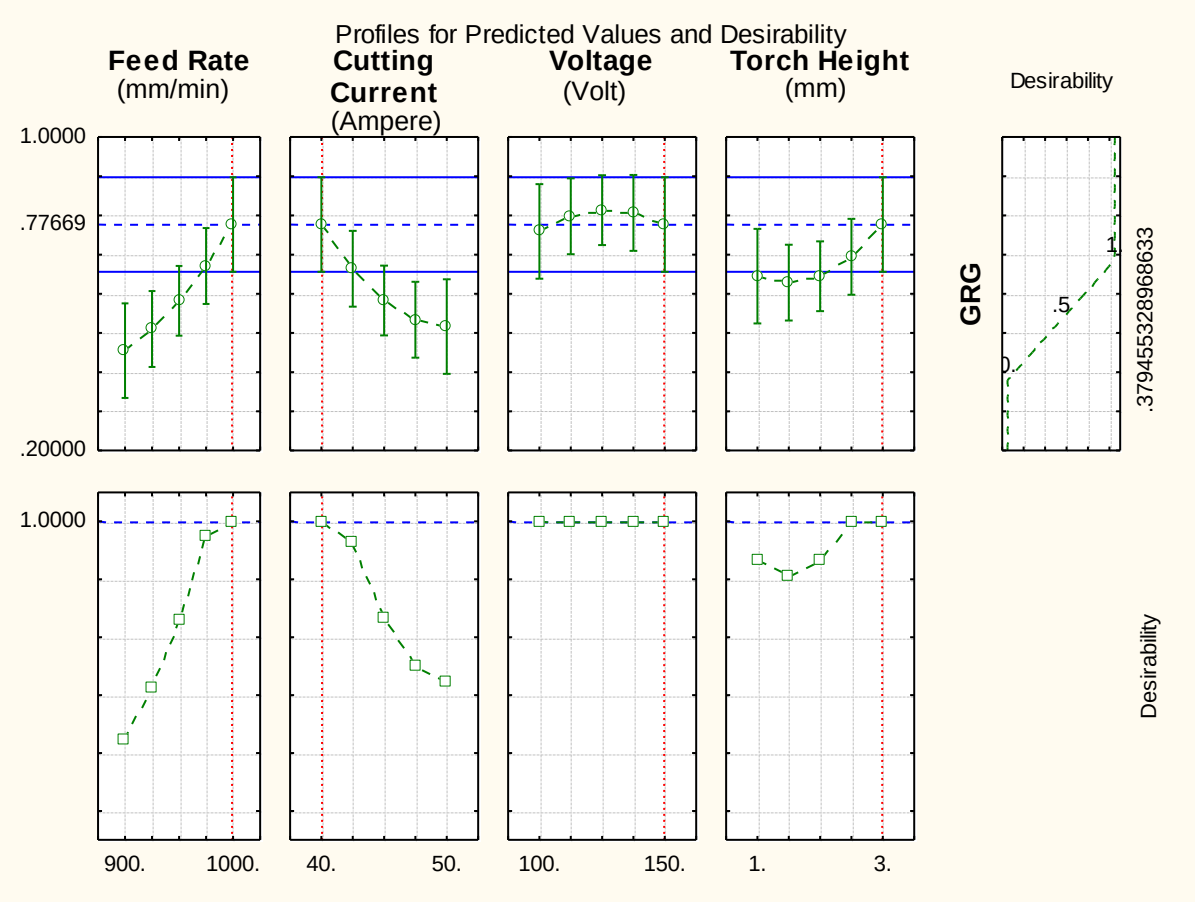

Fig. 62 Profile plot of predicted values and desirability of GRG

By the help of desirability function method, the optimum value of GRG response was discovered which was fitted by the quadratic fit model. The level of variable giving the highest desirability i.e., 1.0000 was considered as optimum level. The optimized levels of variables (A, B, C and D) were determined using the desirability profiles that are shown in Fig. 62 for predicted values of responses and the desirability function value presented with red colored dot lines.

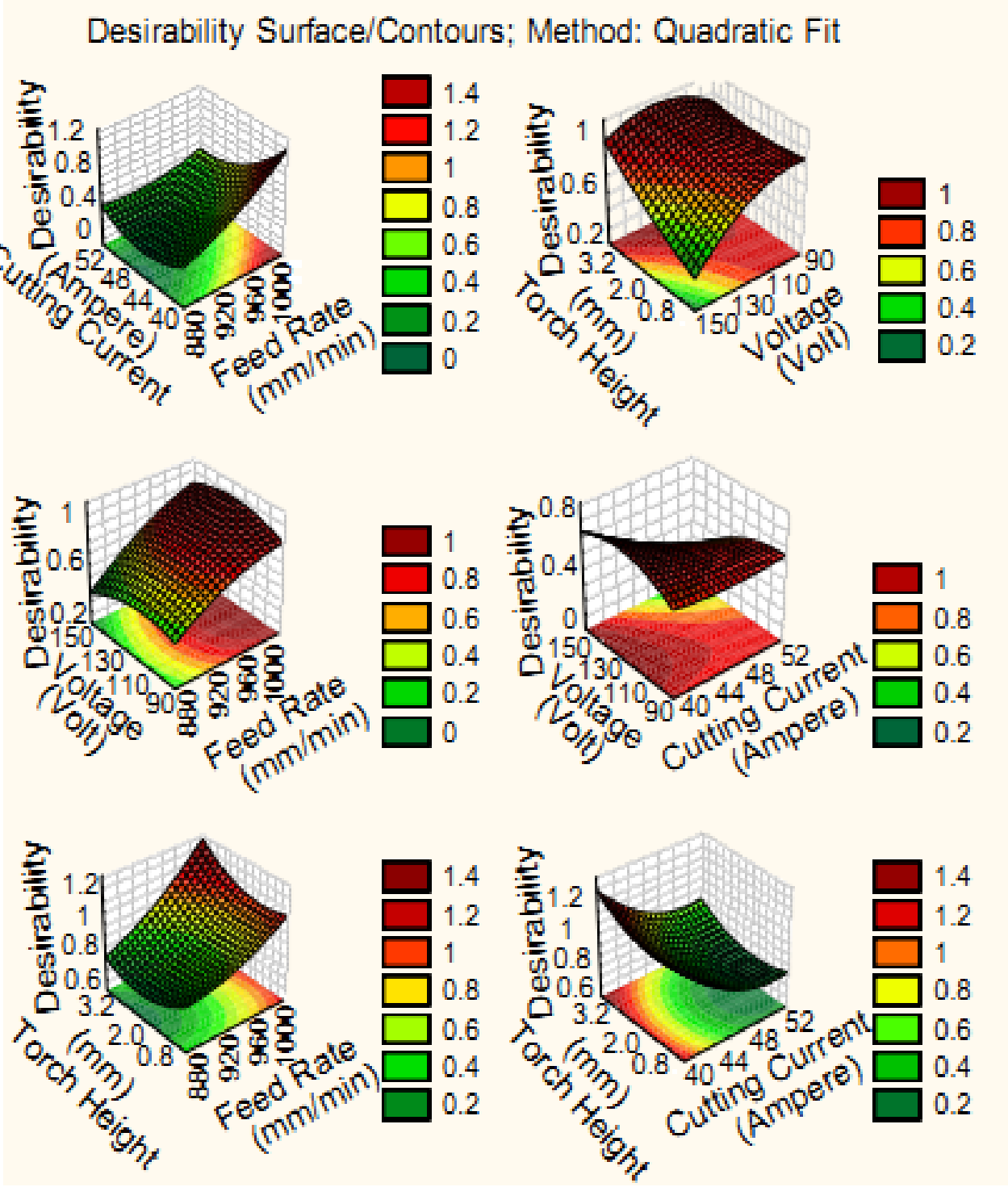

Fig. 63 Desirability 3D surface plot of GRG

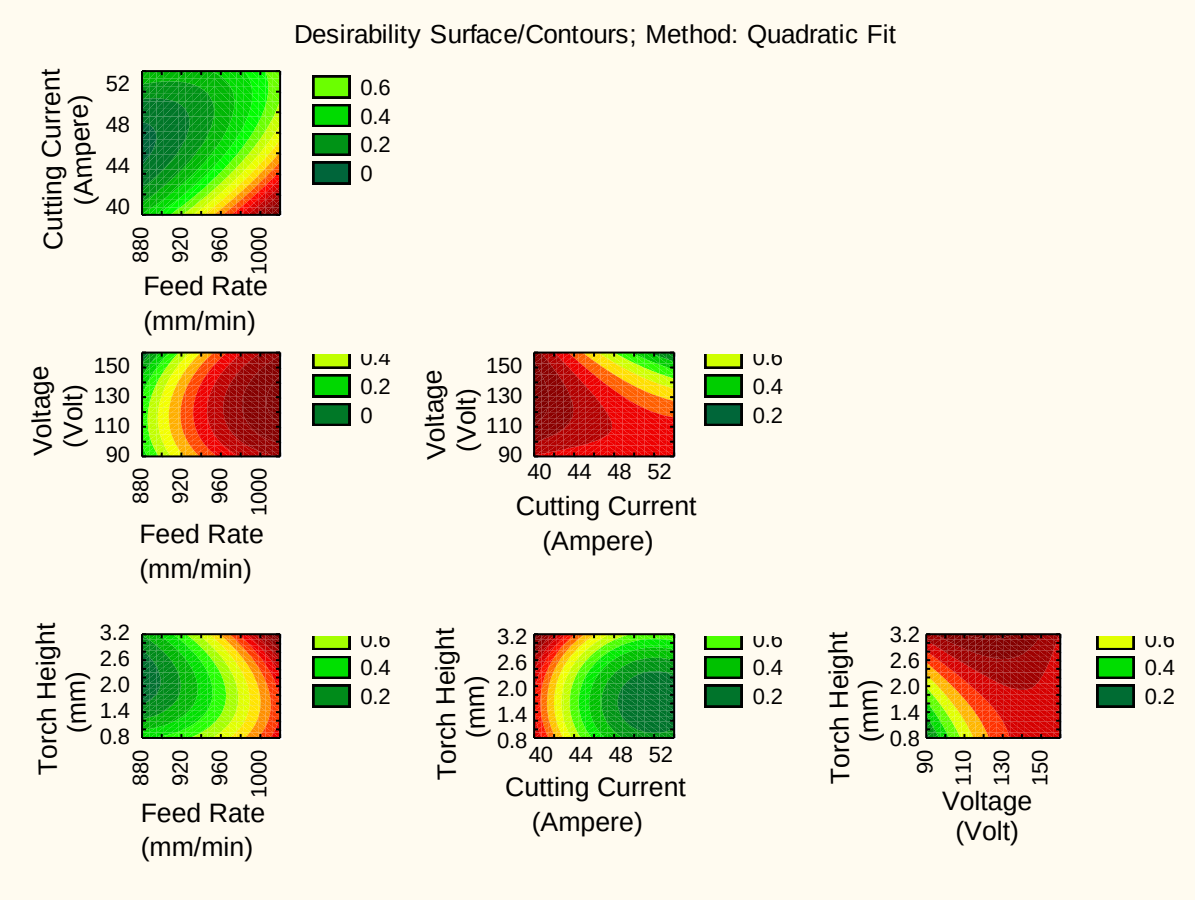

Fig. 64 Desirability 2D counter plot of GRG

The 3D and 2D surface plot of interaction variables were determined using the desirability profiles that are shown in Fig. 63-64 respectively. From all interaction terms, three figures depicted minimum influence of input variables on GRG response.

5.1.3 Genetic algorithm

5.1.3.1 For material removal rate:

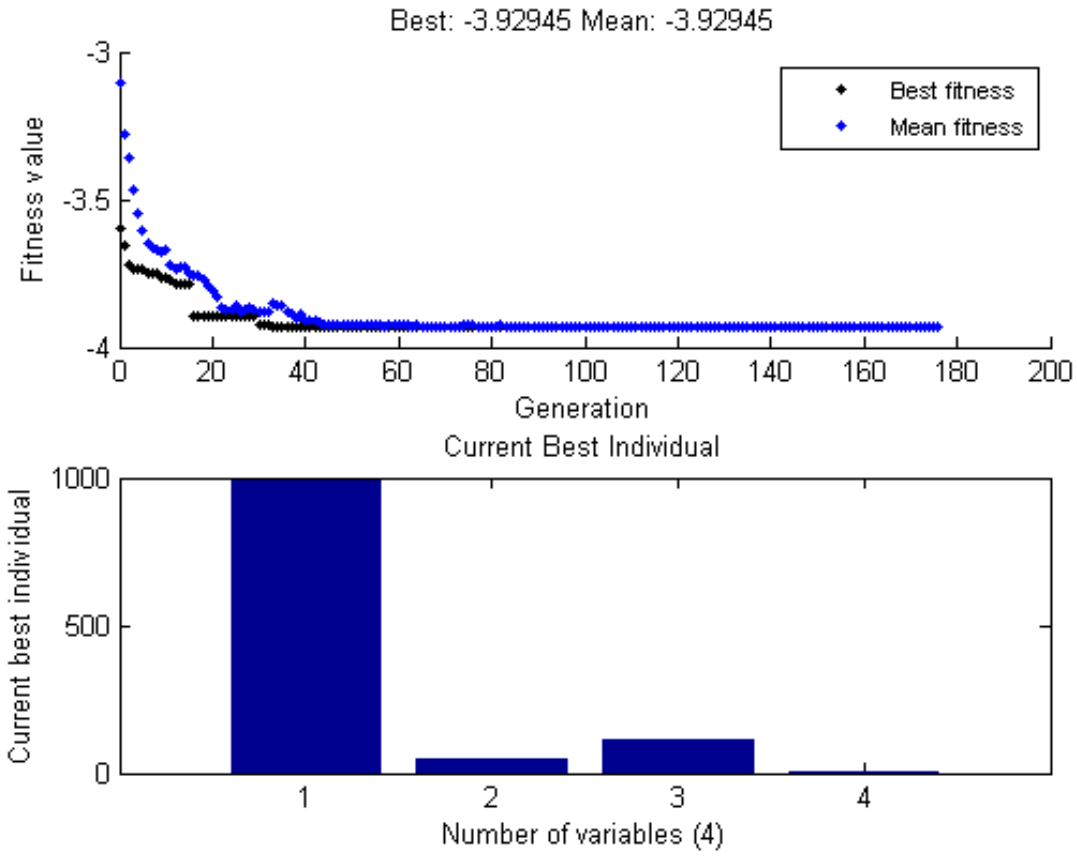

Fig. 65 Results from GA approach for MRR

Best fitness and individual value plot of MRR is shown in Fig. 65 where the best and average value of MRR is obtained as 3.92945 mm^3/min. Here, negative sign is due the application of negativity theory for maximizing problem. Secondly, the best parametric optimal setting is obtained at 1000 mm/min of feed rate, 50 ampere of current, 113.5 volt of voltage and 3 mm of torch height respectively.

5.1.3.2 For surface roughness:

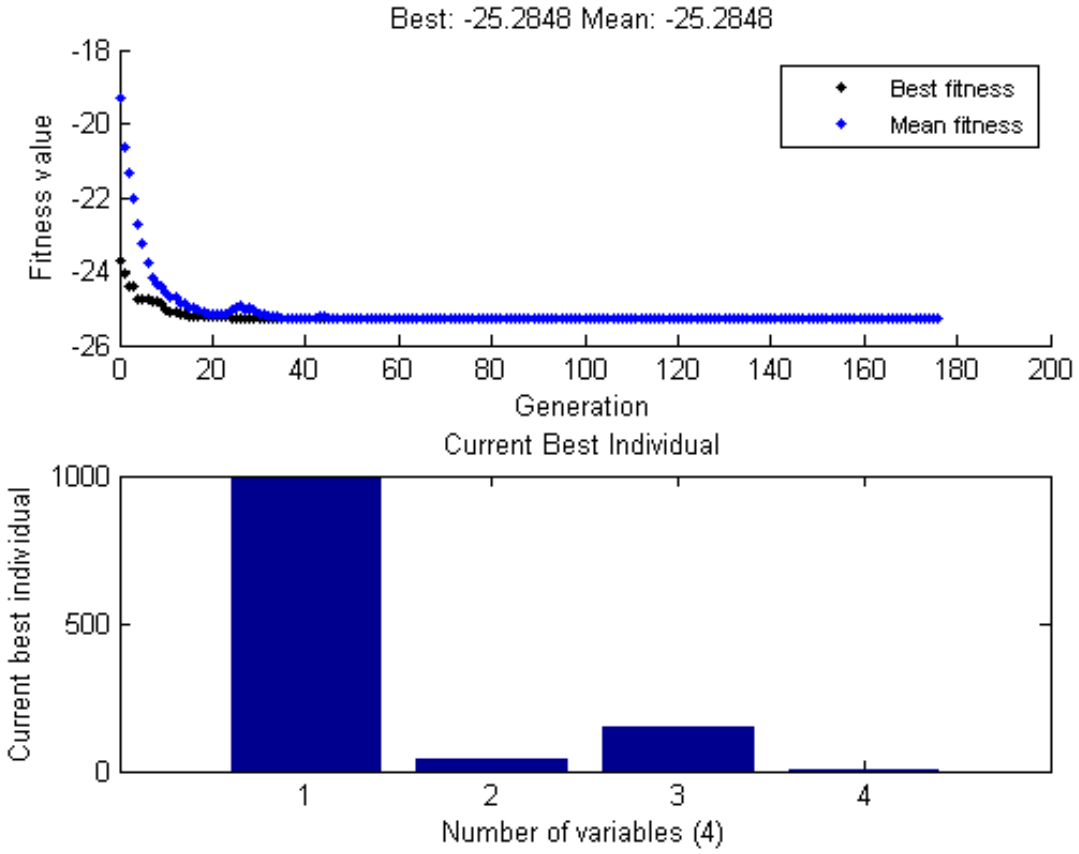

Fig. 66 Results from GA approach for SR

Similarly, for the case of SR the problem is the minimization of the best fitness and individual value plot as given in Fig. 66 where the best and average values of SR are found as 25.28482 µm. The best parametric optimal setting is obtained at 1000 mm/min of feed rate, 40 ampere of current, 150 volt of voltage and 2.082 mm of torch height respectively.

5.1.3.3 For right bevel angle:

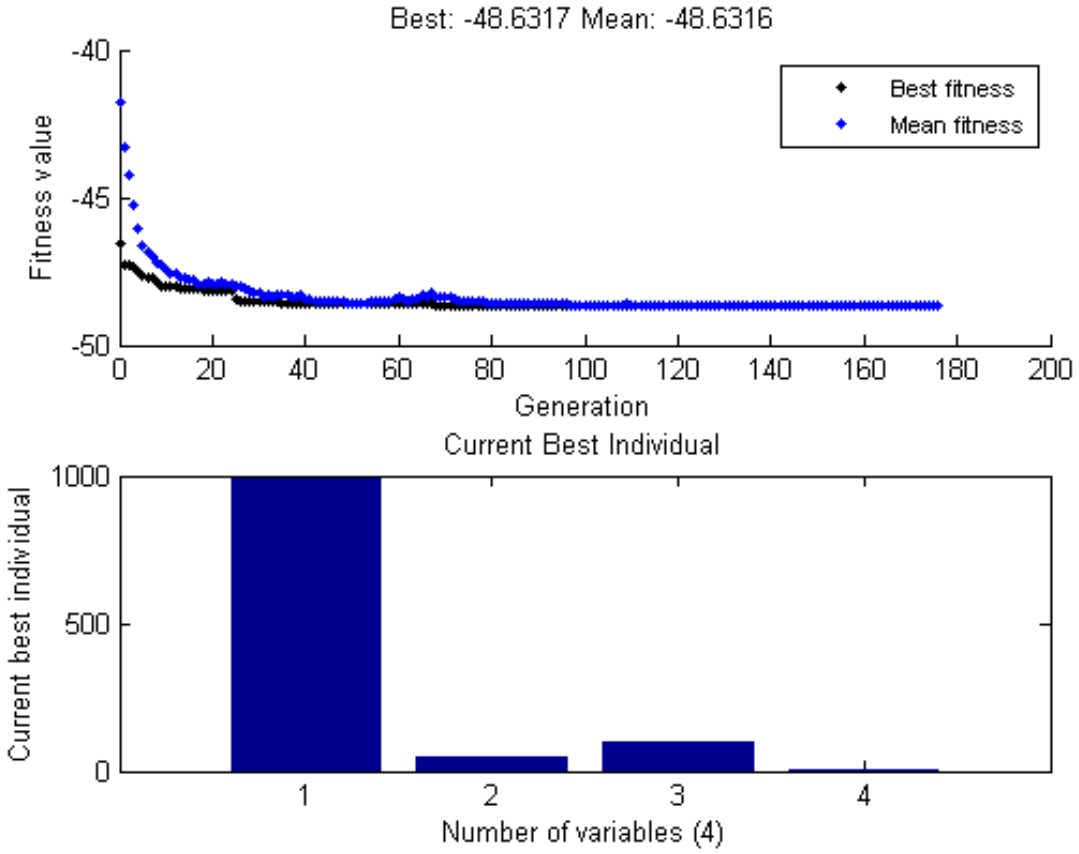

Fig. 67 Results from GA approach for right bevel angle

Similarly, for the case of right bevel angle the problem is the minimization of the best fitness and individual value plot as given in Fig. 67 where the best and average values of right bevel angle are found as 48.6317º and 48.6316º respectively. The best parametric optimal setting is obtained at 1000 mm/min of feed rate, 50 ampere of current, 100 volt of voltage and 1 mm of torch height respectively. Here, the simulation of genetic algorithm toolbox for all output responses stopped at same iteration number i.e., 176.

5.1.4 Particle swarm optimization

5.1.4.1 For material removal rate:

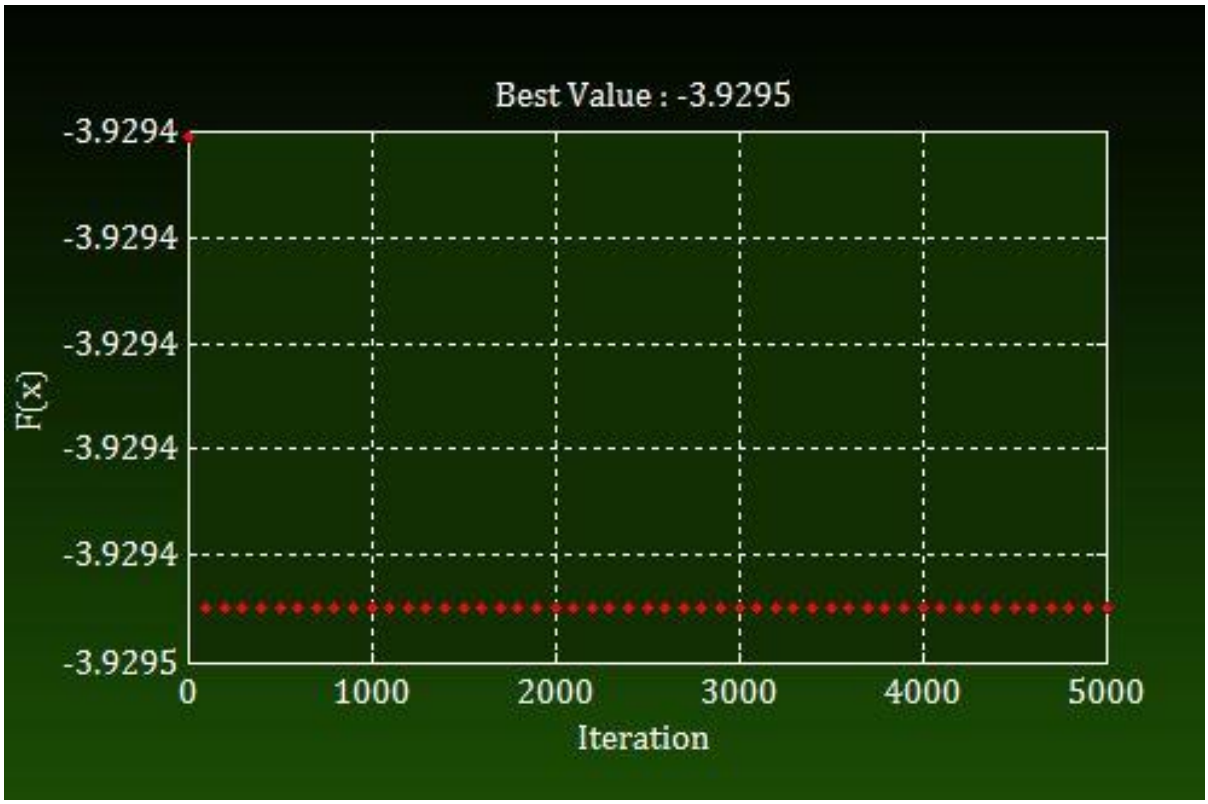

Fig. 68 Results from PSO approach for MRR

The plot of best function value and optimum setting for MRR which was obtained from PSO methodology is shown in Fig. 68. From the graph, it can be seen that the optimum condition for MRR was found as 1000 mm/min of feed rate, 50 ampere of current, 113.499 volt of voltage and 3 mm of torch height respectively. The best value MRR is obtained as 3.92945 mm^3/min.

5.1.4.2 For surface roughness:

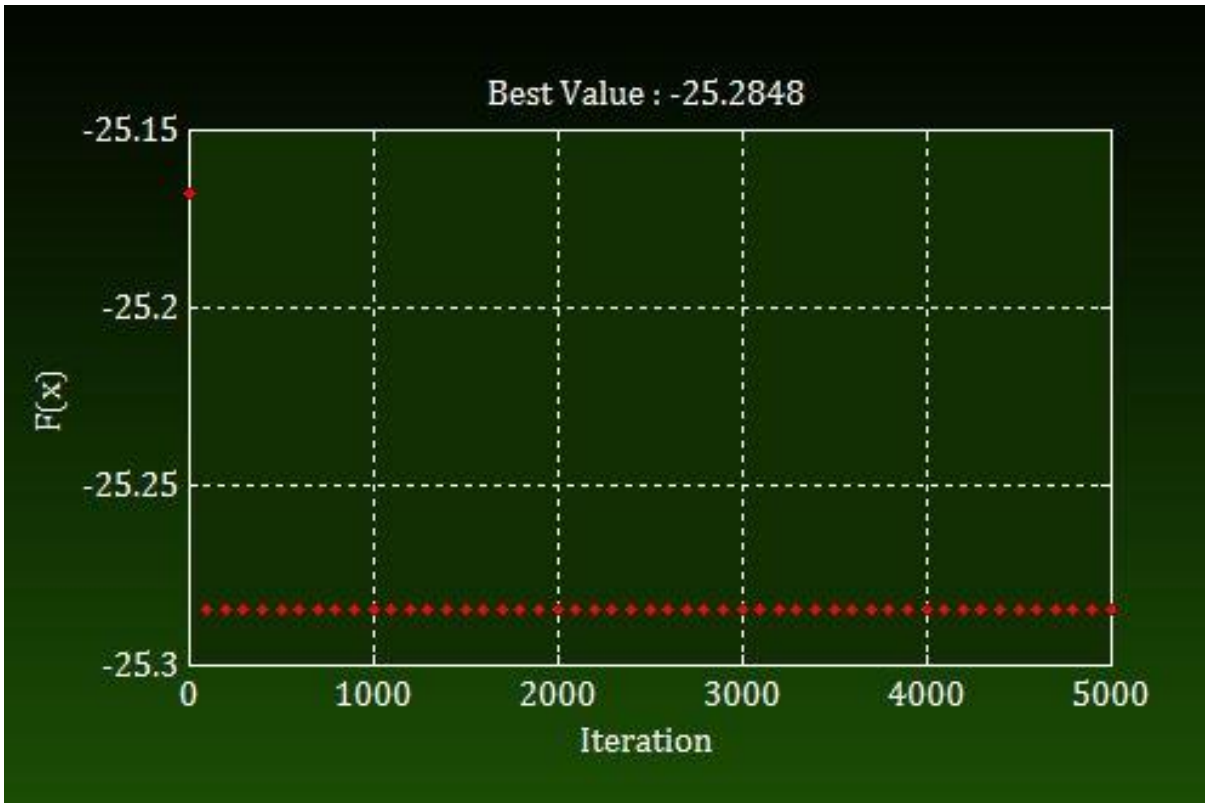

Fig. 69 Results from PSO approach for SR

The plot of best function value and optimum setting for SR which was obtained from PSO methodology is shown in Fig. 69. From the graph, it can be seen that the optimum condition for SR was found as 1000 mm/min of feed rate, 40 ampere of current, 150 volt of voltage and 2.082 mm of torch height respectively. The optimum value of SR is found as 25.28482 µm.

5.1.4.3 For right bevel angle:

Fig. 70 Results from PSO approach for right bevel angle

The plot of best function value and optimum setting for right bevel angle which was obtained from PSO methodology is shown in Fig. 70. From the graph, it can be seen that the optimum condition for MRR was found as 1000 mm/min of feed rate, 50 ampere of current, 100 volt of voltage and 1 mm of torch height respectively. The optimum value of right bevel angle occurred at 48.6317º from this approach.

5.1.5 Simulated annealing

5.1.5.1 For material removal rate:

Nature based novel optimization technique i.e., simulated annealing algorithm is employed to the obtained regression equation of MRR from RSM method. By applying Boltzmann simulated annealing approach to the experimental data, the lowest value of

MRR is found to be 3.2726 mm^3/min at 934.156 mm/min of feed rate, 49.874 ampere of current, 134.595 volt of voltage and 2.976 mm of torch height respectively. In Fig. 71, the best function value and comparative effect of input parameters are shown. Here, the feed rate was the most effective variable than others. The highest number of iteration for simulating the algorithm is 501 where the minimum value of MRR can be found. The best parametric setting of the whole experimentation as per simulated annealing is shown in Fig. 71 with current iteration number.

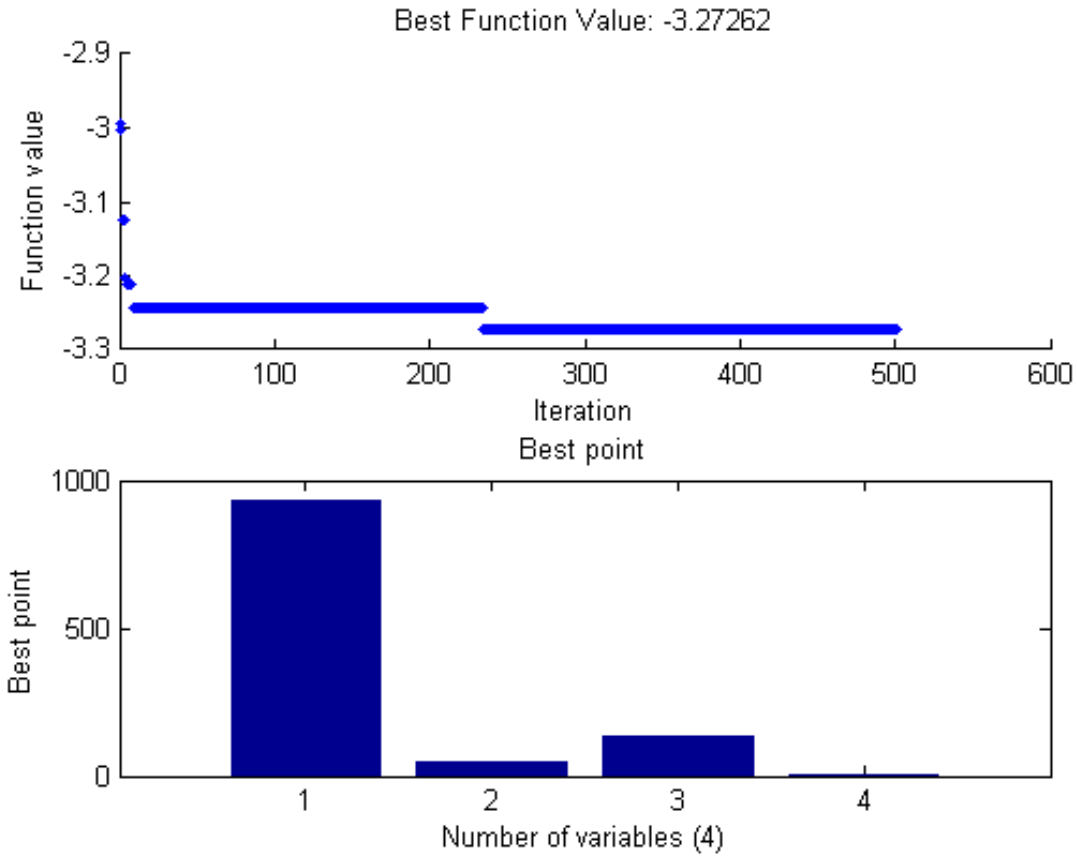

Fig. 71 Results from SA approach for MRR

5.1.5.2 For surface roughness:

Nature based novel optimization technique i.e., simulated annealing algorithm is employed to the obtained regression equation of SR from RSM method. By applying

Boltzmann simulated annealing approach to the experimental data, the lowest value of SR is found as 20.7392 µm at its optimal setting. The optimal condition of surface roughness occurred at 965.496 mm/min of feed rate, 44.99 ampere of current, 111.143 volt of voltage and 2.249 mm of torch height respectively. Fig. 72 represents the best function value and comparative effect of input parameters. Here, the feed rate is found to be the most effective variable. The highest number of iteration for simulating the algorithm is 501 where the minimum value of SR can be found. The best parametric setting of the whole experimentation as per simulated annealing is shown in Fig. 72 with current iteration number.

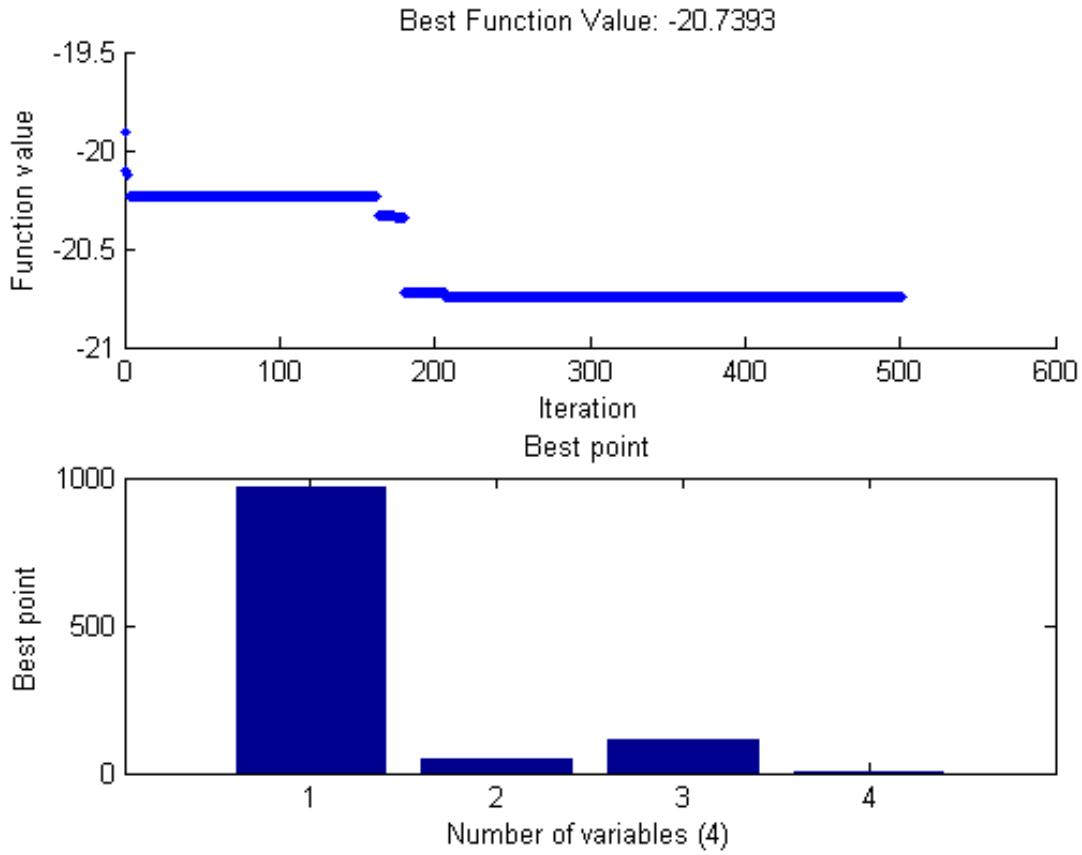

Fig. 72 Results from SA approach for SR

5.1.5.3 For right bevel angle:

Nature based novel optimization technique i.e., simulated annealing algorithm is employed to the obtained regression equation of right bevel angle from RSM method. By applying Boltzmann simulated annealing approach to the experimental data, the lowest value of right bevel angle is found to be 44.9597º at its optimal setting. The optimal condition for right bevel angle occurred at 966.943 mm/min of feed rate, 49.935 ampere of current, 123.613 volt of voltage and 1.007 mm of torch height respectively. Fig. 73 shows the best function value and comparative effect of input parameters. Here also, the feed rate is considered the most effective variable than other parameters. The highest number of iteration for simulating the algorithm is 501 where the minimum value of right bevel angle may be found. The best parametric setting of the whole experimentation as per simulated annealing is shown in Fig. 73 with current iteration number.

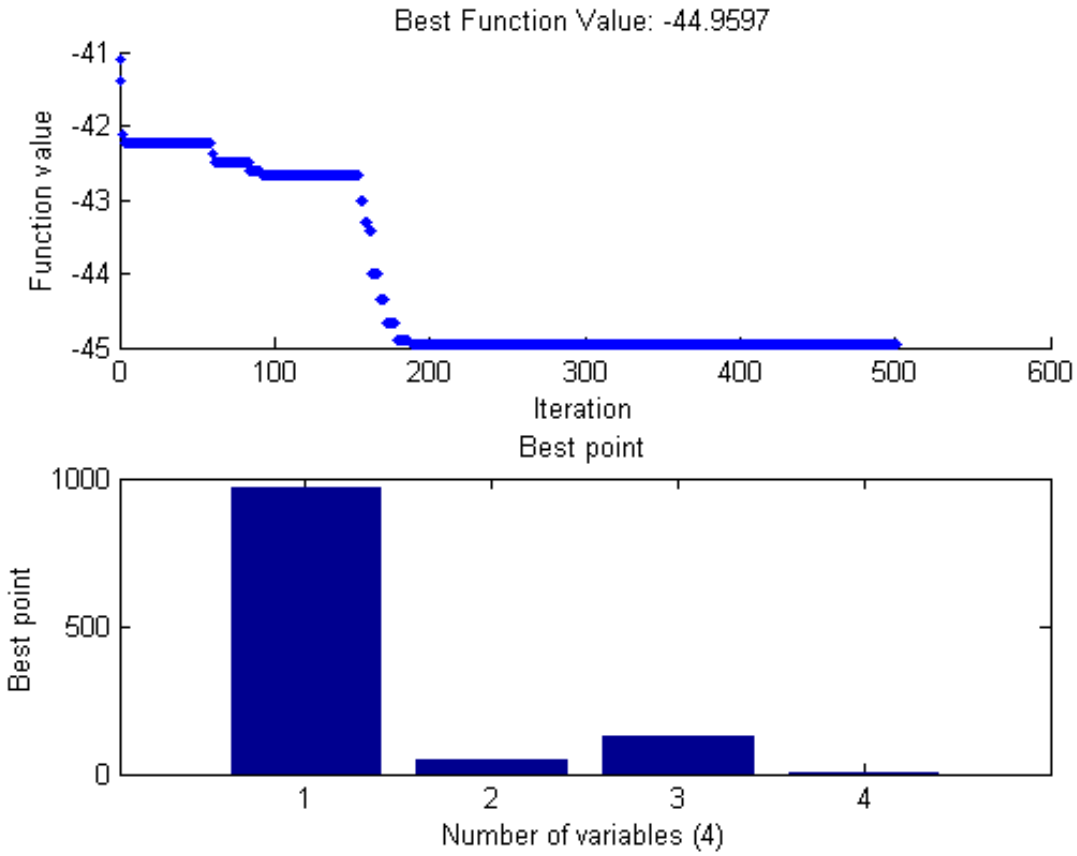

Fig. 73 Results from SA approach for right bevel angle

5.1.6 TLBO results

5.1.6.1 For material removal rate:

The TLBO algorithm is run through Matlab R2012b version software by considering 300 as population size and 500 as number of generations. In each run the maximum number of function evaluations, N is considered as 750000. Only in the case of MRR response, the theory of negativity is applied because the main objective of this is to convert the maximization type to minimization type problem. Fig. 74 depicts plot of the fitness function value for each generation. It can be observed that it converges to the optimum result in very small population size and less number of generations. The optimal condition for material removal rate occurred at 1000.01 mm/min of feed rate, 49.9382

ampere of current, 147.874 volt of voltage and 2.9869 mm of torch height respectively. The best value of objective function using TLBO approach is obtained to be 3.80718 mm^3/min.

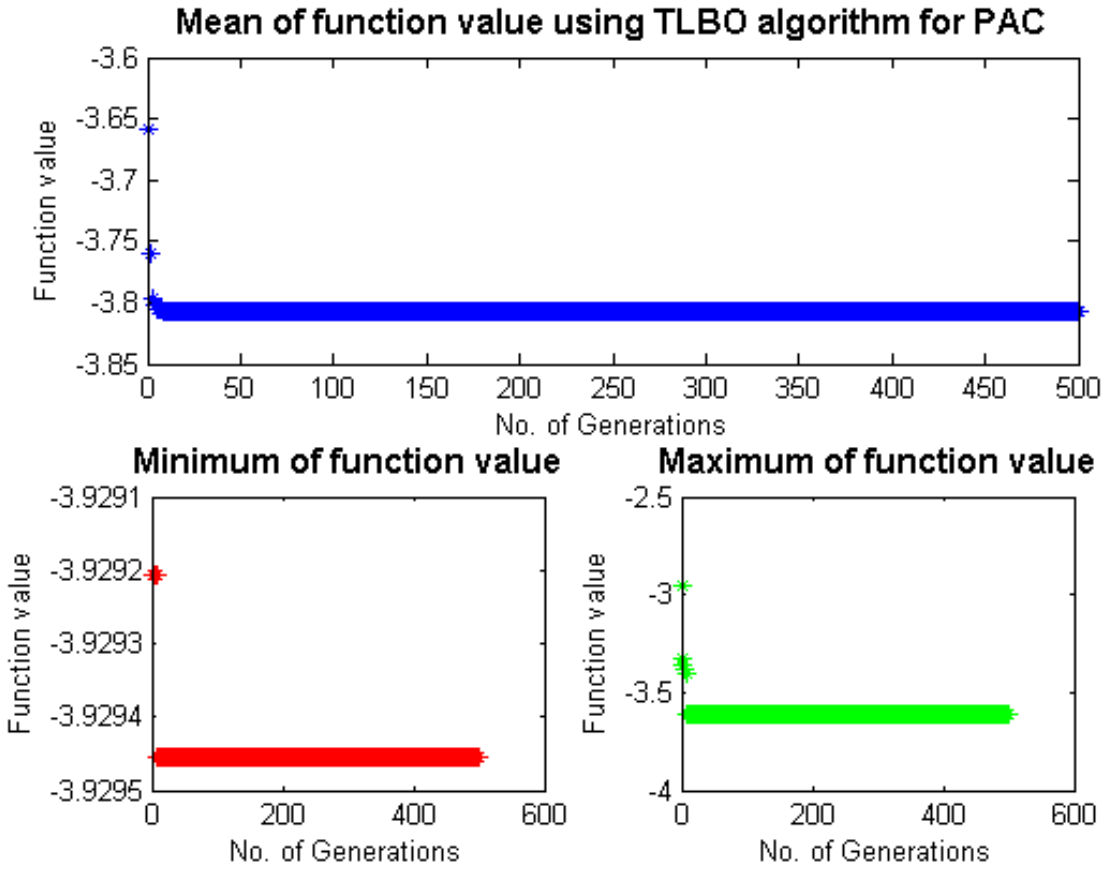

Fig. 74 Obtained plot by TLBO approach for MRR

5.1.6.2 For surface roughness:

For SR response, the optimal condition predicted using novel approach of TLBO is at 1000 mm/min of feed rate, 49.5417 ampere of current, 146.63 volt of voltage and 2.73299 mm of torch height respectively. The best value of the objective function is determined as 21.7302 µm for SR response which is shown in Fig. 75.

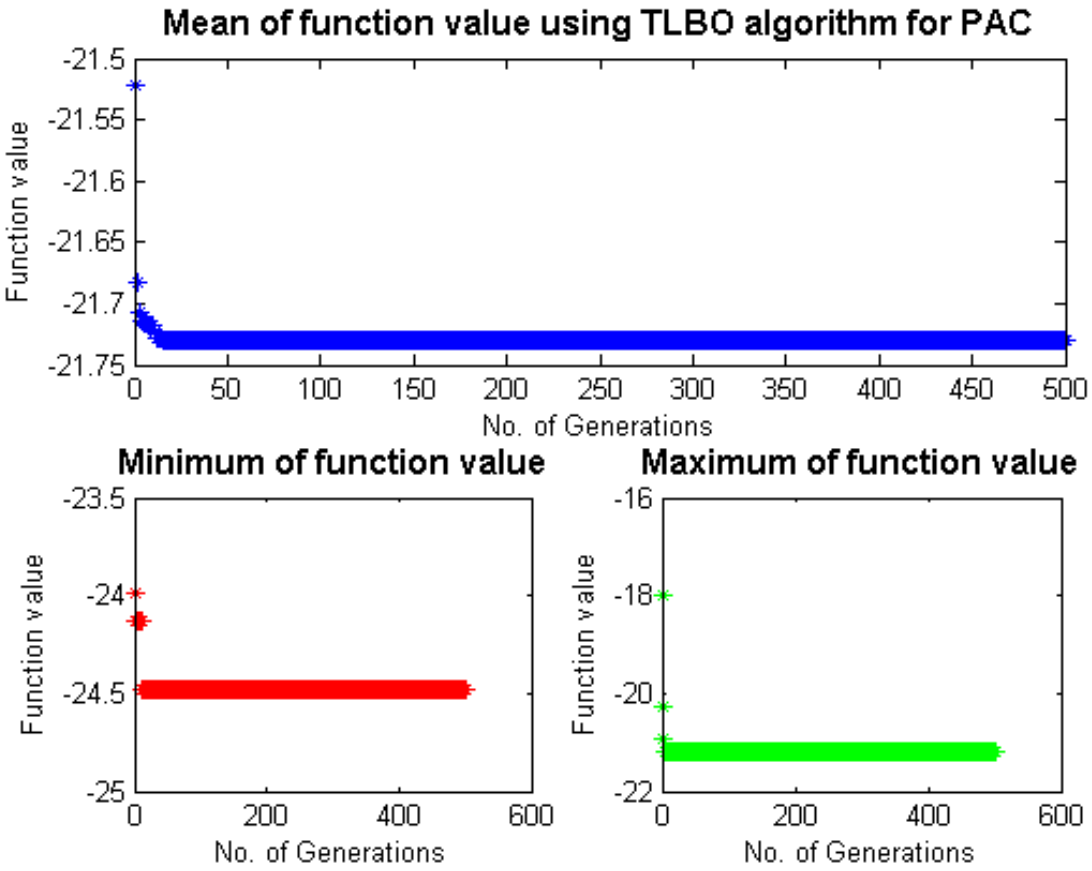

Fig. 75 Obtained plot by TLBO approach for SR

5.1.6.3 For right bevel angle:

In case of right bevel angle response, the optimal condition predicted using novel approach of TLBO is at 1000 mm/min of feed rate, 49.9994 ampere of current, 114.594 volt of voltage and 1 mm of torch height respectively. The best value of the objective function is determined as 48.5337º for right bevel angle response which is depicted in Fig. 76.

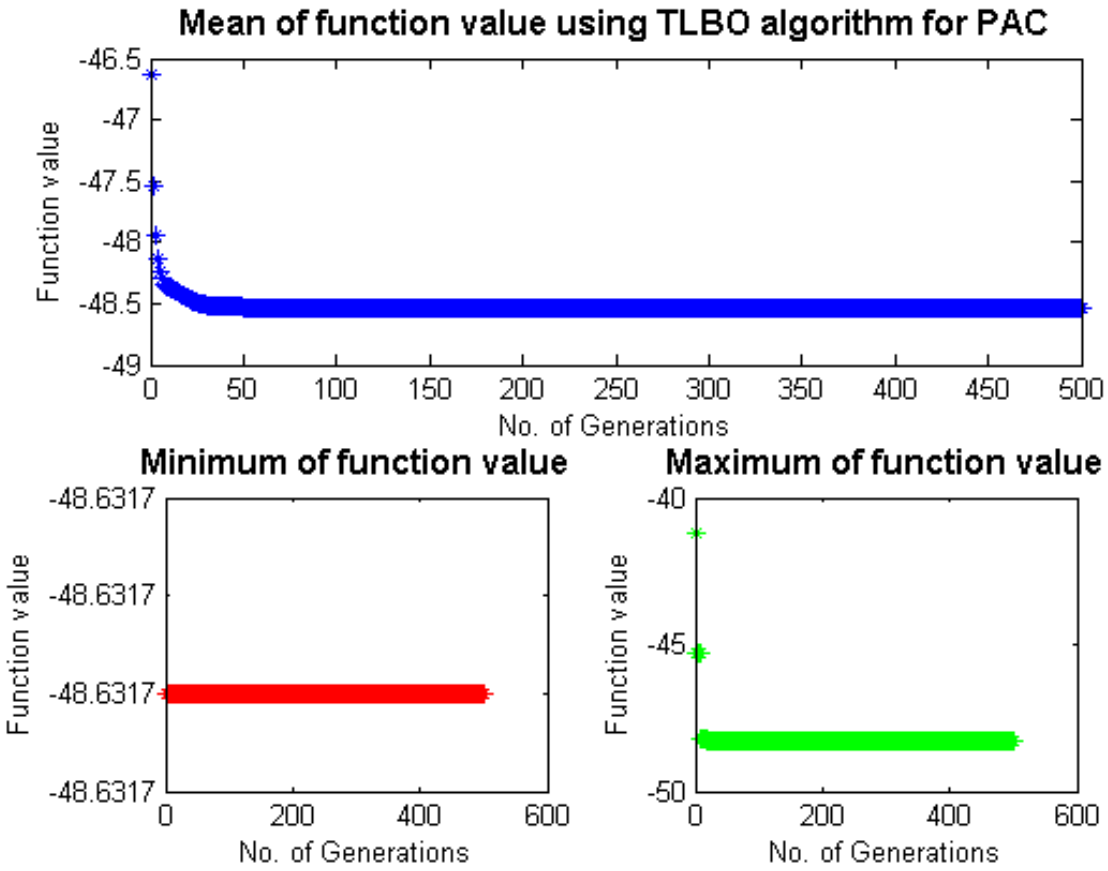

Fig. 76 Obtained plot by TLBO approach for right bevel angle

5.2 Results of Case 2

The Response Surface Methodology was utilized to study the influences of the independent factors Feed Rate (A), cutting current (B), voltage (C) and torch height (C) at three distinct levels in the extraction procedure which is shown in Table 21. The whole experimentation was planned using Statistica software of version 9.1. Three levels are selected for each independent variable such as low (-1), middle (0) and high level (+1) as shown in Table 21. The experimental design consists of thirty cases that run according to single blocked Central Composite Design (CCD). Analysis of variance (ANOVA) and F-test were used as significant criteria for the fitted models. The results obtained were presented as mean values with its standard deviation. After getting the layout of

experimental design of input factors from Statistica software, the cutting operation by plasma arc on the selected work piece have been carried out. According to the DOE, the five output quality characteristics of cut are measured and tabulated in Table 22. The design of experiment consisted of actual level value of input factors with random order of design of experiment and corresponding responses. After simulation of this model using the optimization approach by software, the ANOVA evaluation has been carried out for each response of PAC operation. Then, the estimated coefficients of the model were calculated for every cut quality. The influence of input variables on plasma arc machining for each response is briefly described below:

Table 21 Values of Input Process Parameters

Process parameters	Units	Code	L(1)	L(2)	L(3)
Feed Rate	mm/min	A	920	945	970
Current	Ampere	B	40.0	42.5	45.0
Voltage	Volt	C	100	120	140
Torch Height	mm	D	2.0	2.5	3.0

Table 22 Response Surface Method Design with Input Parameters

Std. Order	Run Order	Feed Rate (mm/min)	Current (Ampere)	Voltage (Volt)	Torch Height (mm)	MRR (mm^3/min)	SR (μm)	Chamfer (mm)	Dross (mm^2)	Kerf (mm)
18	1	945	42.5	120	2.5	4891.10	58.16	1.83	3.63	2.73
7	2	920	45.0	140	2.0	3992.62	46.49	1.01	0.80	3.44
20	3	945	42.5	120	2.5	5541.59	51.81	1.52	9.57	2.64
3	4	920	45.0	100	2.0	4494.18	25.82	1.42	4.26	2.70
9	5	920	40.0	100	3.0	5497.43	71.42	1.88	8.26	3.53
5	6	920	40.0	140	2.0	5082.01	41.88	1.00	7.00	3.30
2	7	970	40.0	100	2.0	3842.59	62.86	1.05	4.29	2.38
11	8	920	45.0	100	3.0	4865.14	69.52	1.64	7.63	3.41
19	9	945	42.5	120	2.5	5345.53	51.13	1.52	8.52	2.61
4	10	970	45.0	100	2.0	5678.41	32.08	1.83	0.45	2.73
17	11	945	42.5	120	2.5	3061.77	37.48	1.24	3.00	3.48
8	12	970	45.0	140	2.0	3929.05	63.29	1.47	1.74	1.93
13	13	920	40.0	140	3.0	3905.86	72.62	1.58	4.56	2.39
16	14	970	45.0	140	3.0	5670.24	52.73	1.05	5.25	2.63
15	15	920	45.0	140	3.0	3489.34	35.60	1.62	2.73	3.73
12	16	970	45.0	100	3.0	4995.12	63.60	1.10	6.34	2.53
14	17	970	40.0	140	3.0	5427.69	34.60	1.53	1.74	3.58
6	18	970	40.0	140	2.0	4223.34	56.61	1.08	6.43	2.65
10	19	970	40.0	100	3.0	4854.34	71.30	1.63	3.83	3.41
1	20	920	40.0	100	2.0	5030.29	54.97	1.38	5.27	2.64
29	21	945	42.5	120	2.5	4072.35	62.76	1.97	8.57	2.34
30	22	945	42.5	120	2.5	5448.16	34.18	1.68	4.56	2.57
25	23	945	42.5	80	2.5	4402.74	43.74	1.47	8.43	2.62
23	24	945	37.5	120	2.5	5470.08	52.35	1.64	9.03	3.73
22	25	995	42.5	120	2.5	4415.95	66.97	1.78	5.89	2.93
26	26	945	42.5	160	2.5	5520.10	26.57	1.93	8.52	2.28
24	27	945	47.5	120	2.5	4649.92	45.13	1.43	3.67	2.04
28	28	945	42.5	120	3.5	3805.88	44.59	1.67	7.27	3.16
27	29	945	42.5	120	1.5	5453.33	63.04	1.24	5.79	2.27
21	30	895	42.5	120	2.5	5538.55	61.25	1.52	8.53	3.07

5.2.1 RSM with desirability function approach

5.2.1.1 For material removal rate:

The influence of estimated values of MRR was computed and recorded in Table 23. The analysis of variance (ANOVA) for MRR has been carried out firstly and its results were given in Table 24. Here, the block effect has also been considered because the levels

of block are taken as one. Due to this variation in block, there is negligible amount of effect occurring in experiment. This effect is ignored for further calculation of optimization. The total degree of freedom for all input factors is 29. From the Table 23, it is seen that the most of the terms have P-value less than 0.05 under the confidence interval of 95 %. Hence, these terms show significance within experiment. In Table 23, no single term has shown the significance in the experiment. Pareto chart of effects of all factors on MRR response are shown in Fig. 77 and the results indicate that the interaction of feed rate and cutting current has given the most influence among all the considered factors. The scatter plot between the observed and the predicted value of MRR for all 30 runs are shown in Fig. 78. It is concluded that there is a reasonable correlation between the measured and predicted values of MRR. In Fig. 80, the histogram plot of predicted data for MRR with 95 % confidence interval of normal distribution is displayed. In Table 24, the model of estimated regression coefficients of the independent variable on the MRR is tabulated.

Table 23 Effect of Estimated Values for MRR

Factor	Effect	Std. Err.	T	P
Constant	4726.750	363.3439	13.00902	0.000000
A (mm/min)	1.559	363.3439	0.00429	0.996633
A^2	51.595	339.8771	0.15180	0.881364
B (Ampere)	-199.148	363.3439	-0.54810	0.591690
B^2	92.970	339.8771	0.27354	0.788169
C (Volt)	-108.552	363.3439	-0.29876	0.769223
C^2	43.680	339.8771	0.12852	0.899448
D (mm)	-71.852	363.3439	-0.19775	0.845893
D^2	-122.228	339.8771	-0.35962	0.724142
A×B	574.896	445.0036	1.29189	0.215946
A×C	412.134	445.0036	0.92614	0.369037
A×D	514.416	445.0036	1.15598	0.265769
B×C	-295.731	445.0036	-0.66456	0.516420
B×D	-72.689	445.0036	-0.16334	0.872428
C×D	12.444	445.0036	0.02796	0.978060

Table 24 ANOVA Table for MRR

Factors	SS	DoF	MS	F	P
A (mm/min)	15	1	15	0.000018	0.996633
A^2	18254	1	18254	0.023045	0.881364
B (Ampere)	237958	1	237958	0.300410	0.591690
B^2	59269	1	59269	0.074824	0.788169
C (Volt)	70702	1	70702	0.089257	0.769223
C^2	13083	1	13083	0.016516	0.899448
D (mm)	30977	1	30977	0.039106	0.845893
D^2	102443	1	102443	0.129329	0.724142
A×B	1322023	1	1322023	1.668983	0.215946
A×C	679417	1	679417	0.857727	0.369037
A×D	1058496	1	1058496	1.336295	0.265769
B×C	349828	1	349828	0.441639	0.516420
B×D	21135	1	21135	0.026681	0.872428
C×D	619	1	619	0.000782	0.978060
Error	11881693	15	792113		
Total SS	15874599	29			

Table 25 Regression Coefficients of MRR

Factor	Regression Coef.	Std. Err.	T	P
Constant	318525.8	302196.6	1.05403	0.308550
A (mm/min)	-374.3	540.2	-0.69291	0.498953
A^2	0.0	0.3	0.15180	0.881364
B (Ampere)	-4590.7	4141.0	-1.10859	0.285067
B^2	7.4	27.2	0.27354	0.788169
C (Volt)	-281.2	475.6	-0.59117	0.563211
C^2	0.1	0.4	0.12852	0.899448
D (mm)	-17133.5	18947.1	-0.90428	0.380142
D^2	-244.5	679.8	-0.35962	0.724142
A×B	4.6	3.6	1.29189	0.215946
A×C	0.4	0.4	0.92614	0.369037
A×D	20.6	17.8	1.15598	0.265769
B×C	-3.0	4.5	-0.66456	0.516420
B×D	-29.1	178.0	-0.16334	0.872428
C×D	0.6	22.3	0.02796	0.978060

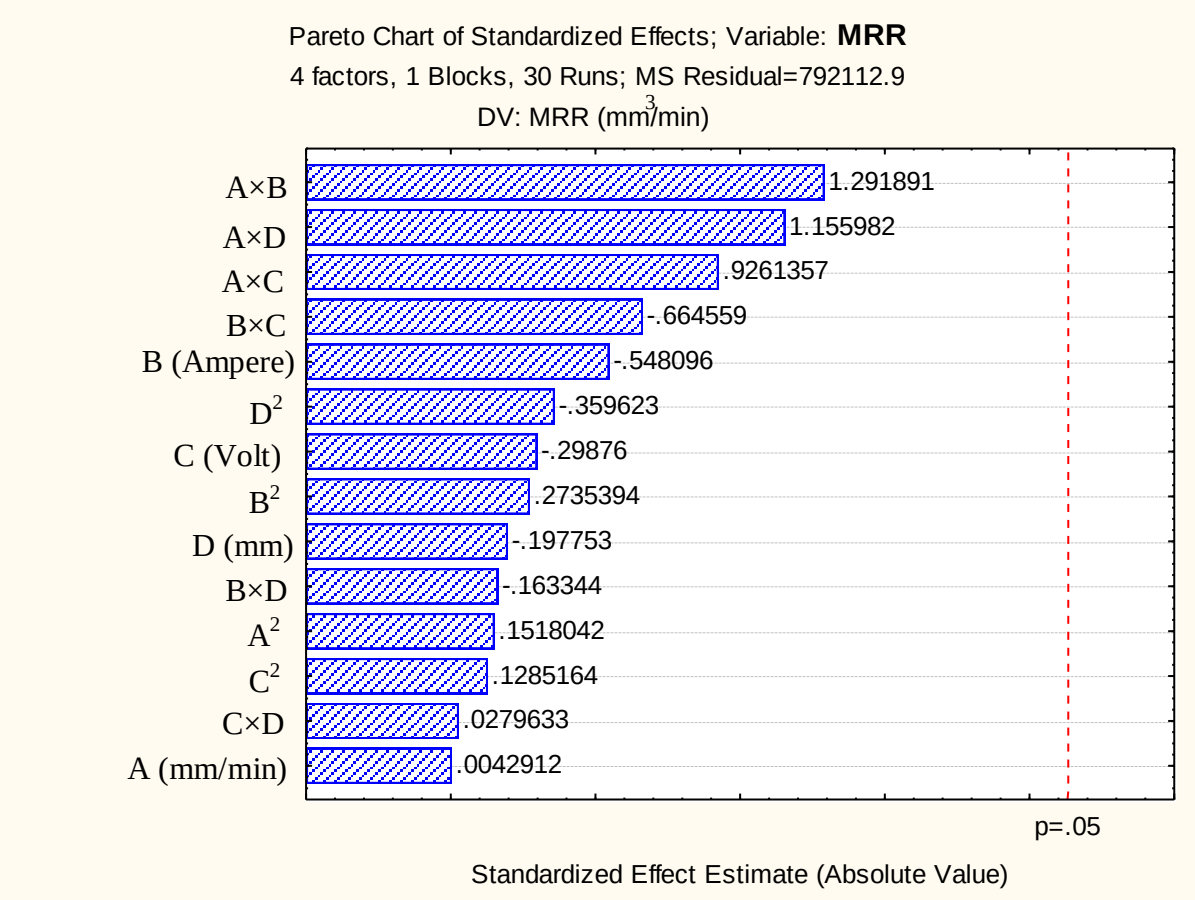

Fig. 77 Pareto chart of standardized effect of factors on MRR

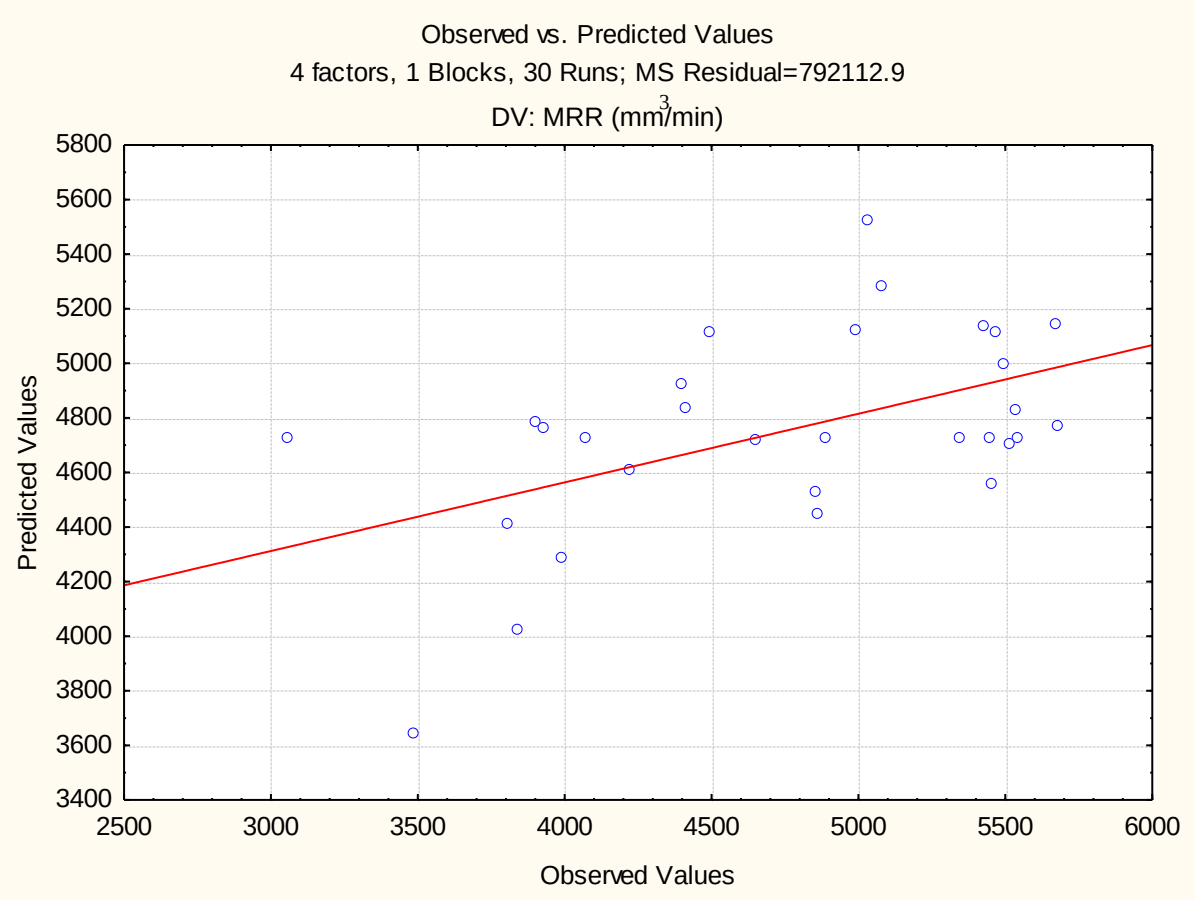

Fig. 78 Plot of observed vs. predicted values of MRR

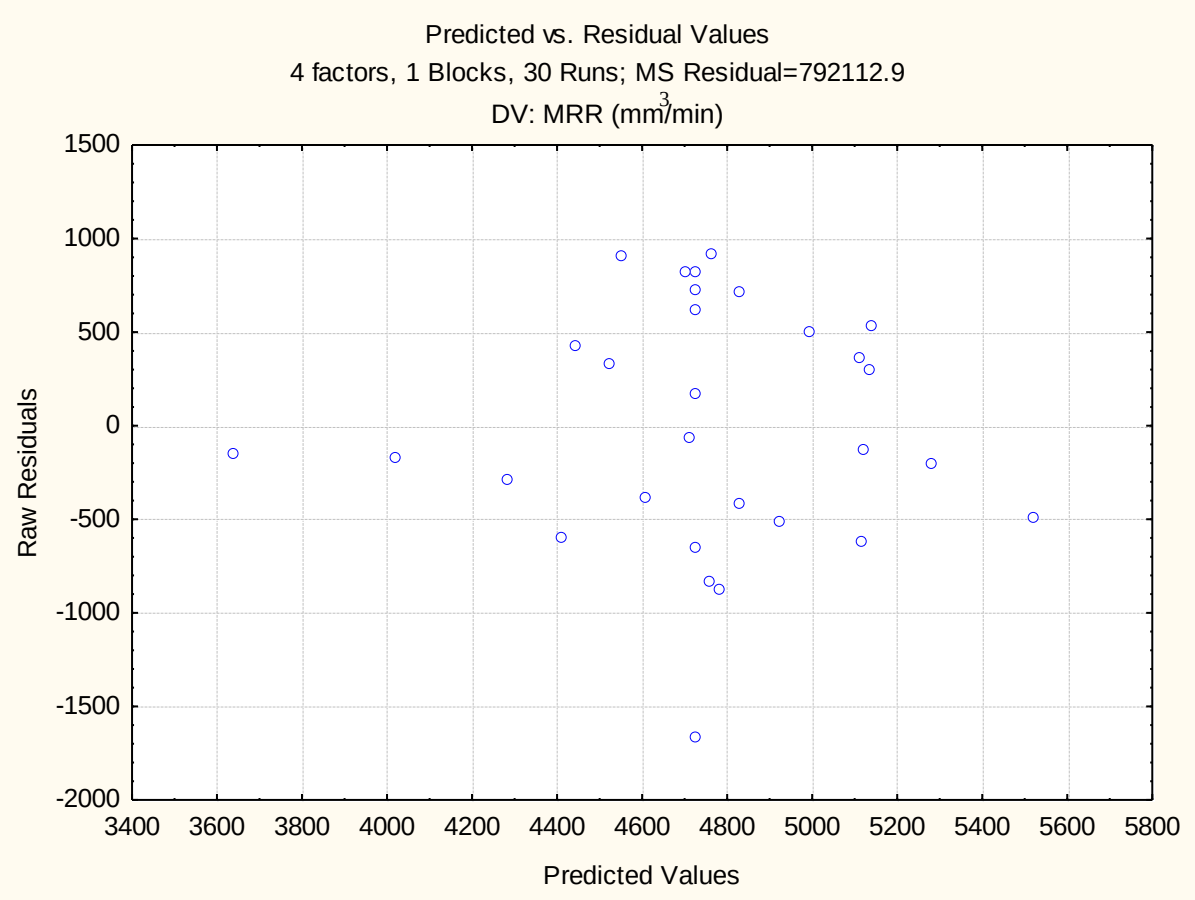

Fig. 79 Plot of predicted vs. residual values of MRR

From the Fig. 79, no standard pattern is formed in the plot of predicted vs. residual values which show the adequacy of the fitted model for MRR.

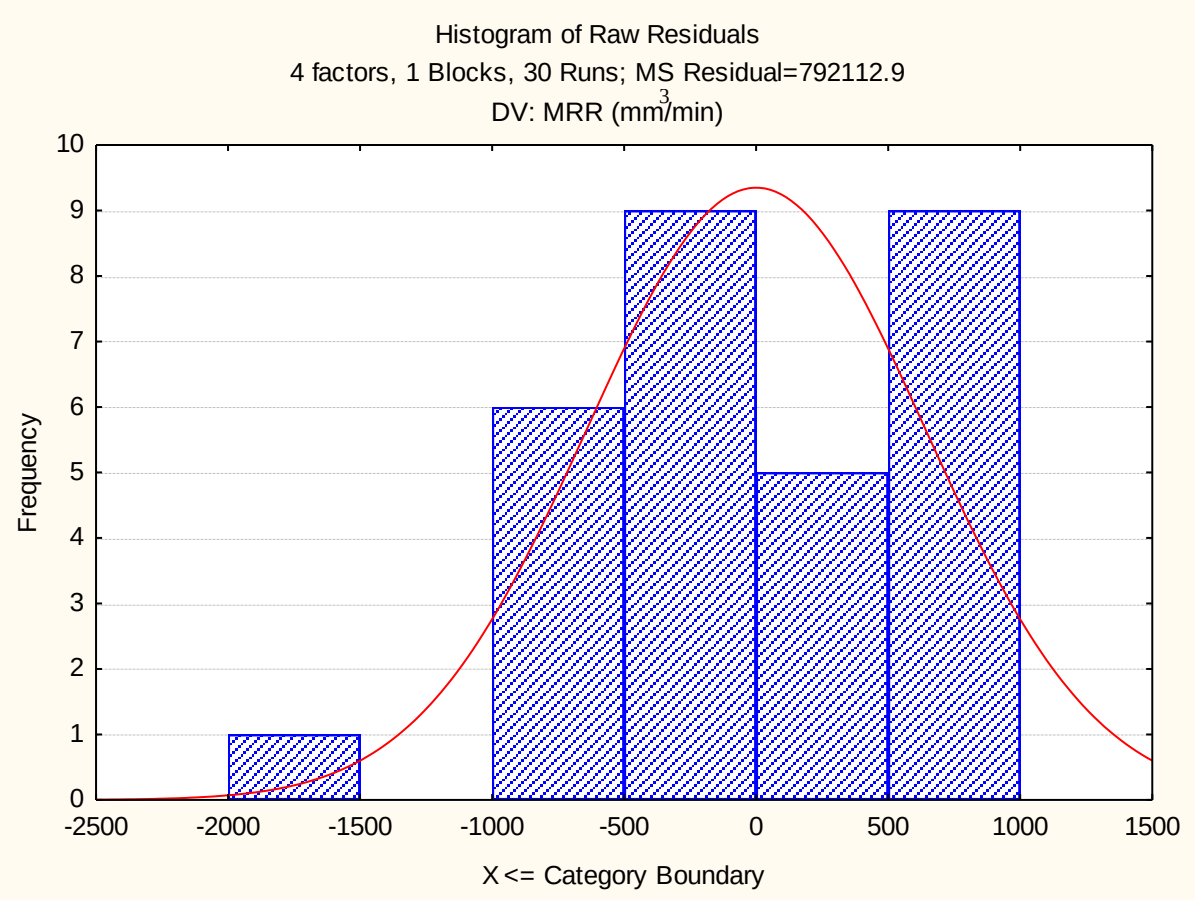

Fig. 80 Histogram plot of predicted values of MRR

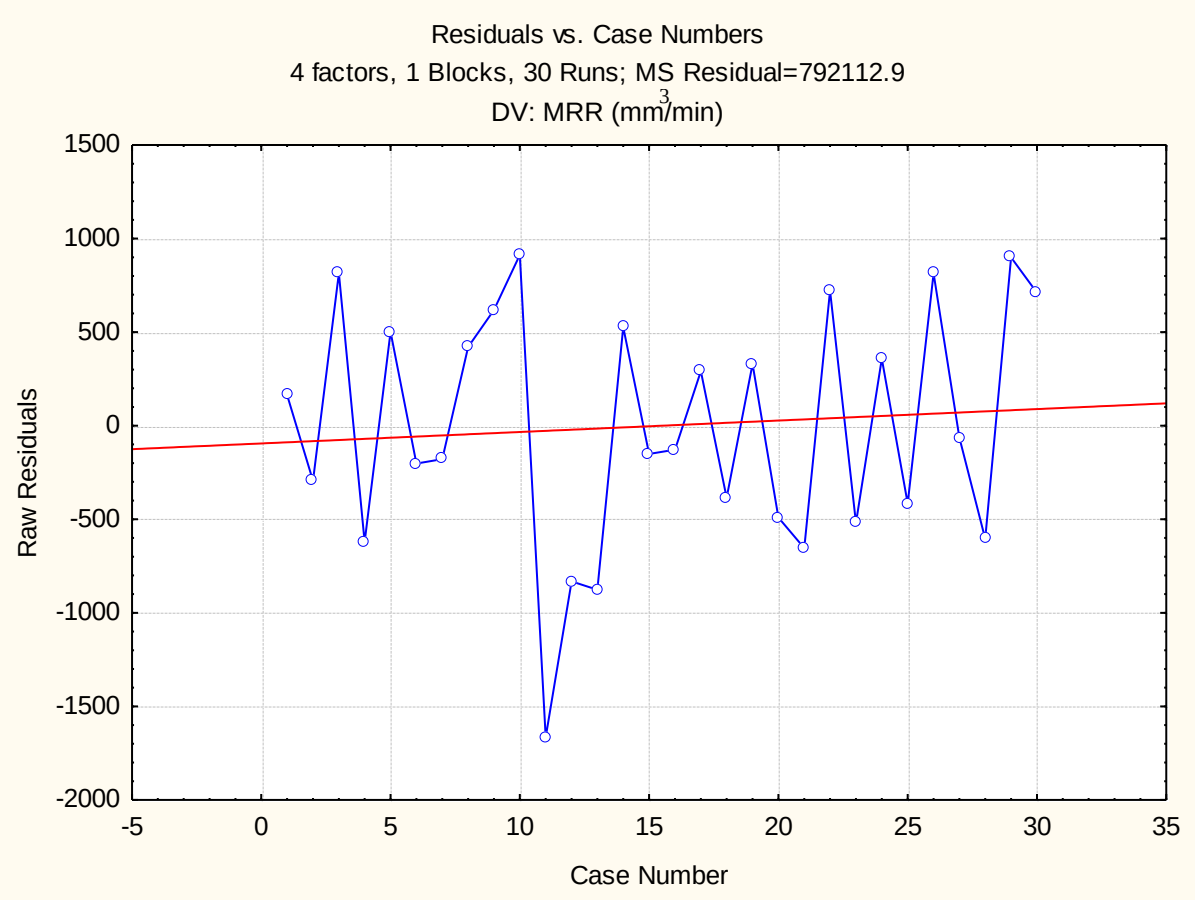

Fig. 81 Plot of residuals vs. case numbers values of MRR

From the Fig. 81, it is evident that the highest MRR value among all experimental runs is by the run number 9. The red line indicates that the value of MRR increases with increase in run order.

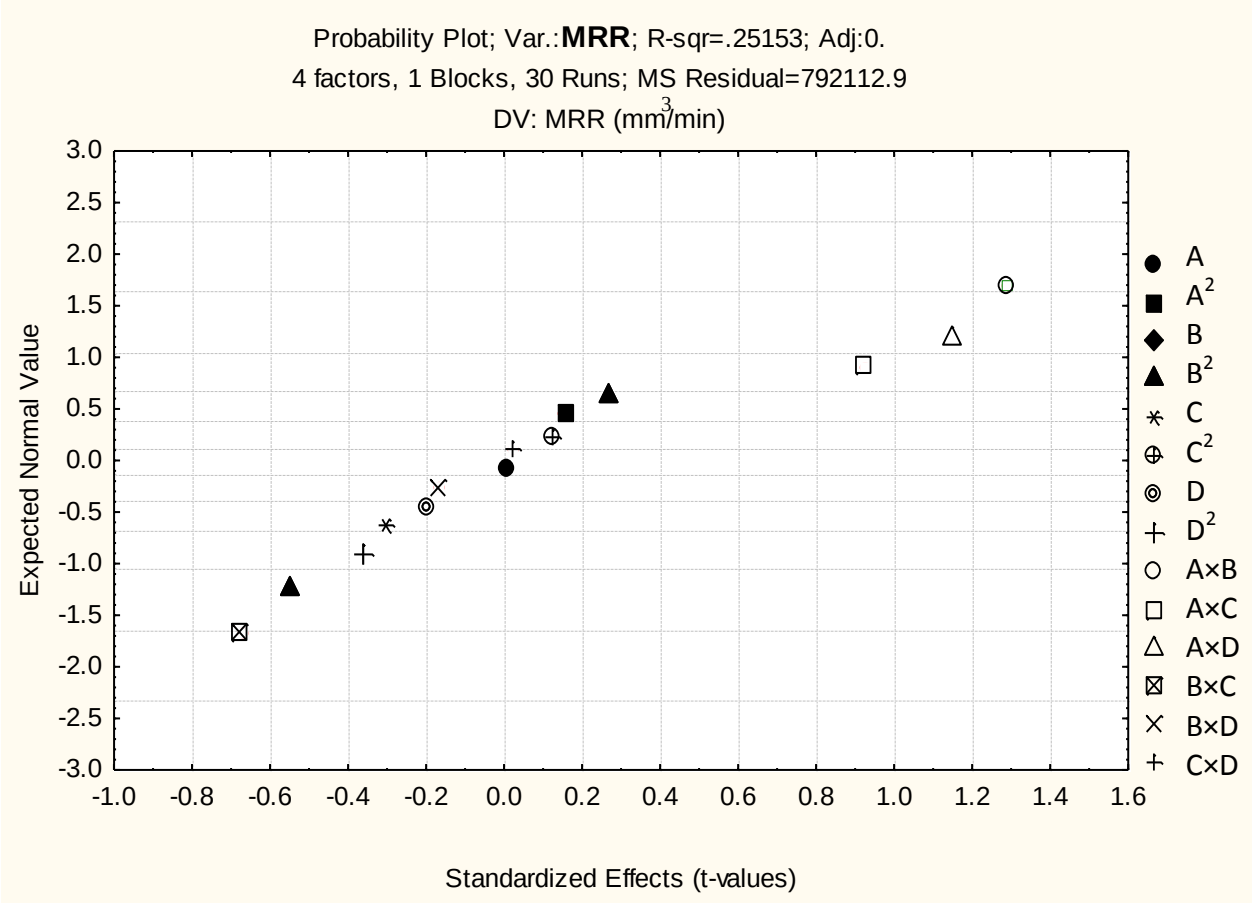

Fig. 82 Probability plot of MRR

The normal probability plot of MRR corresponding to each regression terms is plotted in Fig. 82.

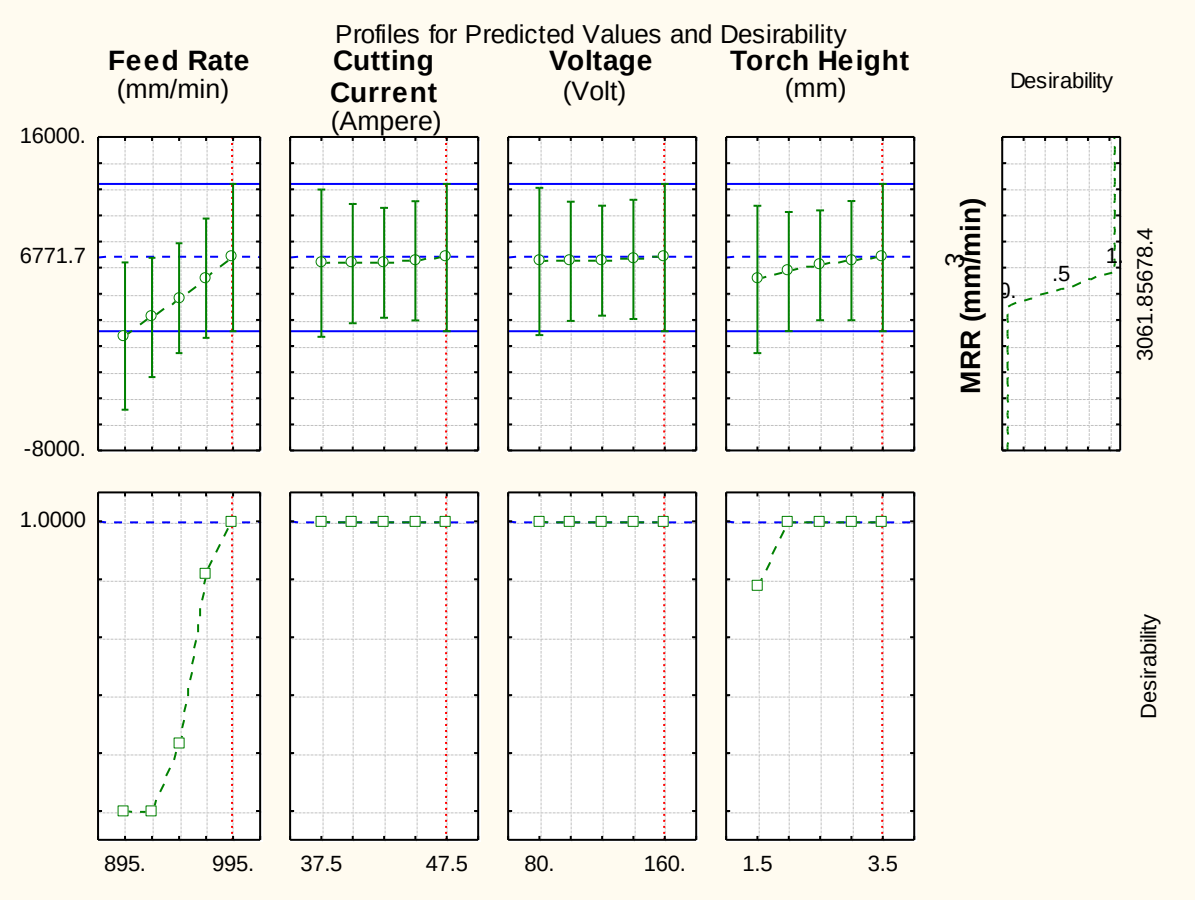

Fig. 83 Profile plot of predicted values and desirability of MRR

In order to get the optimum MRR value, the desirability function helped by fitting the quadratic fit model. The level of variables giving the highest desirability i.e., 1.0000 was considered as optimum level. The optimized levels of variables (A, B, C and D) were determined using the desirability profiles that are shown in Fig. 83 for predicted values of responses. In same figure, the red dotted lines indicated the desirability function values.

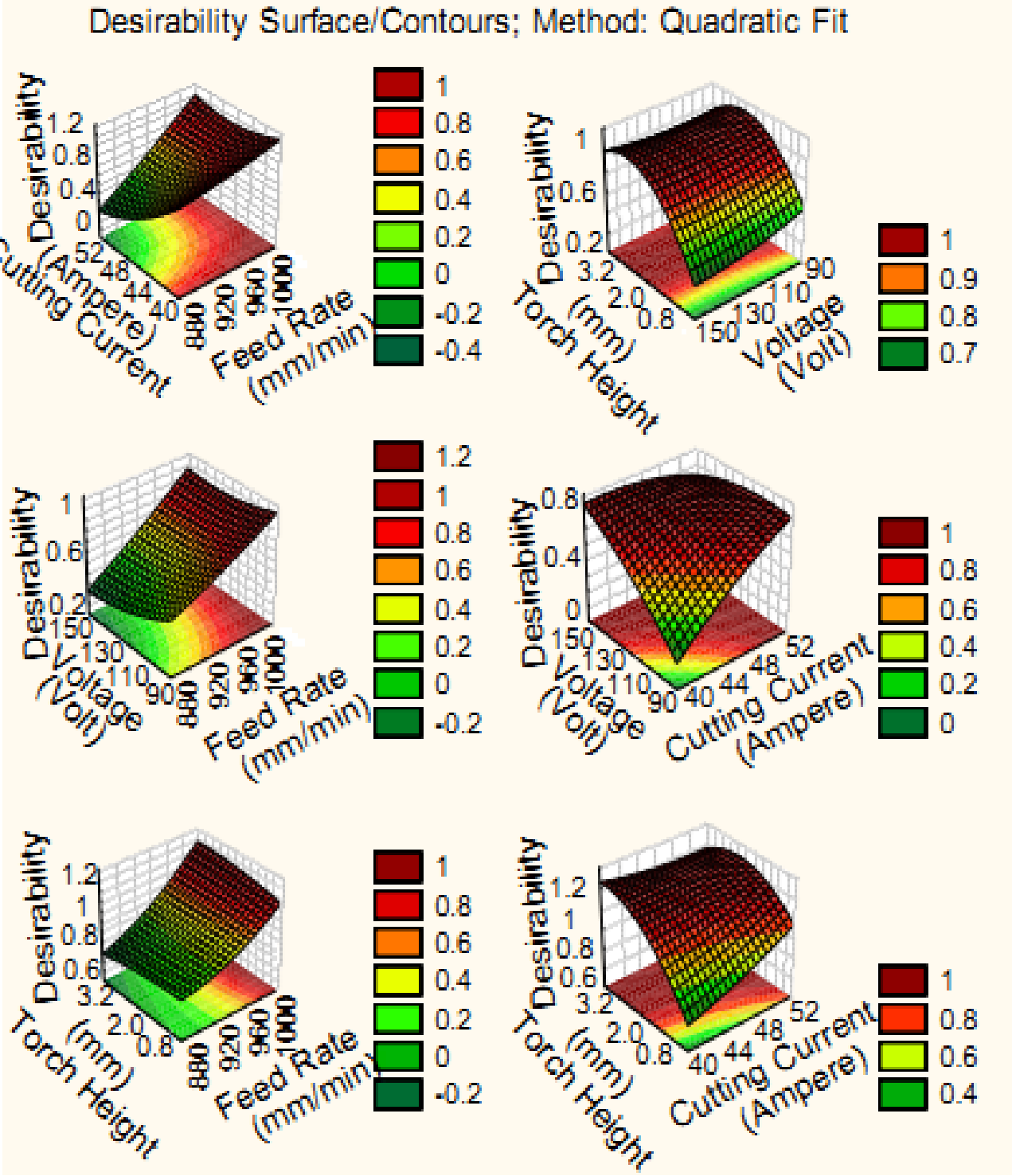

Fig. 84 Desirability 3D surface plot of MRR

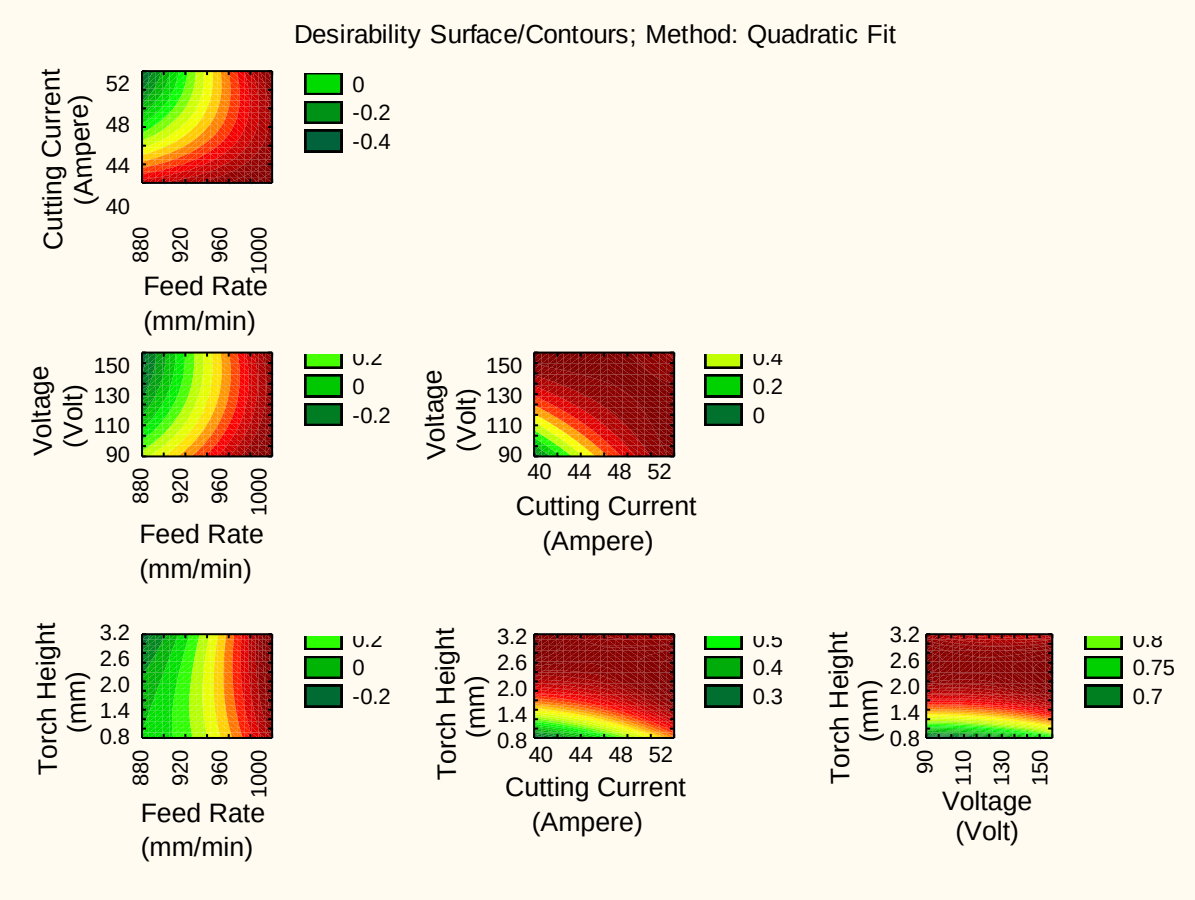

Fig. 85 Desirability 2D counter plot of MRR

The 3D and 2D interaction plot of variables on MRR were determined using the desirability profiles that are shown in Fig. 84-85 respectively. From these figures, it can be concluded that the impact of MRR is enhanced by all input variables with high amount.

5.2.1.2 For surface roughness:

In case of surface roughness response, the effect of estimated values of SR was computed and recorded in Table 26. The ANOVA for SR has been carried out firstly and its results are given in Table 27. Here, the block effect has also been considered because the levels of block are taken as one. Due to this variation in block, there is negligible amount of its effect on the experiment. This effect is ignored for further calculation of optimization. The total degree of freedom for all input factors is 29. From the Table 27, it

is seen that the most of the terms have P-value less than 0.05 under the confidence interval of 95 %. Hence, these terms are significant within experiment. In case of individual terms, only the interaction of voltage and torch height is the most significant among all parameters. Pareto chart for effects of all factors on SR response are shown in Fig. 86 and the results indicate that the quadratic of torch height is the second most enhancing factor among all considered factors. The scatter plot between the observed and the predicted value of SR of all 30 runs is shown in Fig. 87. It is concluded that there is a reasonable correlation between the measured and predicted values of SR response. In Fig. 89, the histogram plot of predicted data of SR with 95 % confidence interval of normal distribution is displayed. The surface and contour plot of this interaction terms have been considered for further analysis and shown in Fig. 92-93 respectively. In this figure, it is clearly displayed that the value of SR increases with increasing cutting current and torch height. In Table 28, the model of estimated regression coefficients of the independent variable on the SR is tabulated.

Table 26 Effect of Estimated Values for SR

Factor	Effect	Std. Err.	T	P
Constant	49.2533	5.132423	9.59651	0.000000
A (mm/min)	2.5158	5.132423	0.49018	0.631096
A^2	8.4306	4.800942	1.75604	0.099474
B (Ampere)	-7.6308	5.132423	-1.48679	0.157787
B^2	0.7456	4.800942	0.15531	0.878649
C (Volt)	-6.8408	5.132423	-1.33287	0.202468
C^2	-6.0469	4.800942	-1.25952	0.227089
D (mm)	4.2075	5.132423	0.81979	0.425172
D^2	3.2831	4.800942	0.68385	0.504498
A×B	6.2237	6.285909	0.99011	0.337823
A×C	0.3162	6.285909	0.05031	0.960538
A×D	-9.0762	6.285909	-1.44390	0.169327
B×C	7.7413	6.285909	1.23152	0.237086
B×D	2.5187	6.285909	0.40070	0.694292
C×D	-14.1038	6.285909	-2.24371	0.040373

Table 27 ANOVA Table for SR

Factors	SS	DoF	MS	F	P
A (mm/min)	37.977	1	37.9765	0.240281	0.631096
A^2	487.374	1	487.3744	3.083661	0.099474
B (Ampere)	349.378	1	349.3777	2.210544	0.157787
B^2	3.812	1	3.8123	0.024121	0.878649
C (Volt)	280.782	1	280.7820	1.776533	0.202468
C^2	250.729	1	250.7294	1.586387	0.227089
D (mm)	106.218	1	106.2183	0.672053	0.425172
D^2	73.913	1	73.9125	0.467651	0.504498
A×B	154.940	1	154.9403	0.980321	0.337823
A×C	0.400	1	0.4001	0.002531	0.960538
A×D	329.513	1	329.5133	2.084859	0.169327
B×C	239.708	1	239.7078	1.516652	0.237086
B×D	25.376	1	25.3764	0.160559	0.694292
C×D	795.663	1	795.6631	5.034230	0.040373
Error	2370.759	15	158.0506		
Total SS	5609.618	29			

Table 28 Regression Coefficients of SR

Factor	Regression Coef.	Std. Err.	T	P
Constant	7607.658	4268.685	1.78220	0.094965
A (mm/min)	-13.943	7.631	-1.82712	0.087645
A^2	0.007	0.004	1.75604	0.099474
B (Ampere)	-65.456	58.494	-1.11903	0.280730
B^2	0.060	0.384	0.15531	0.878649
C (Volt)	-0.183	6.718	-0.02722	0.978641
C^2	-0.008	0.006	-1.25952	0.227089
D (mm)	356.262	267.638	1.33113	0.203024
D^2	6.566	9.602	0.68385	0.504498
A×B	0.050	0.050	0.99011	0.337823
A×C	0.000	0.006	0.05031	0.960538
A×D	-0.363	0.251	-1.44390	0.169327
B×C	0.077	0.063	1.23152	0.237086
B×D	1.007	2.514	0.40070	0.694292
C×D	-0.705	0.314	-2.24371	0.040373

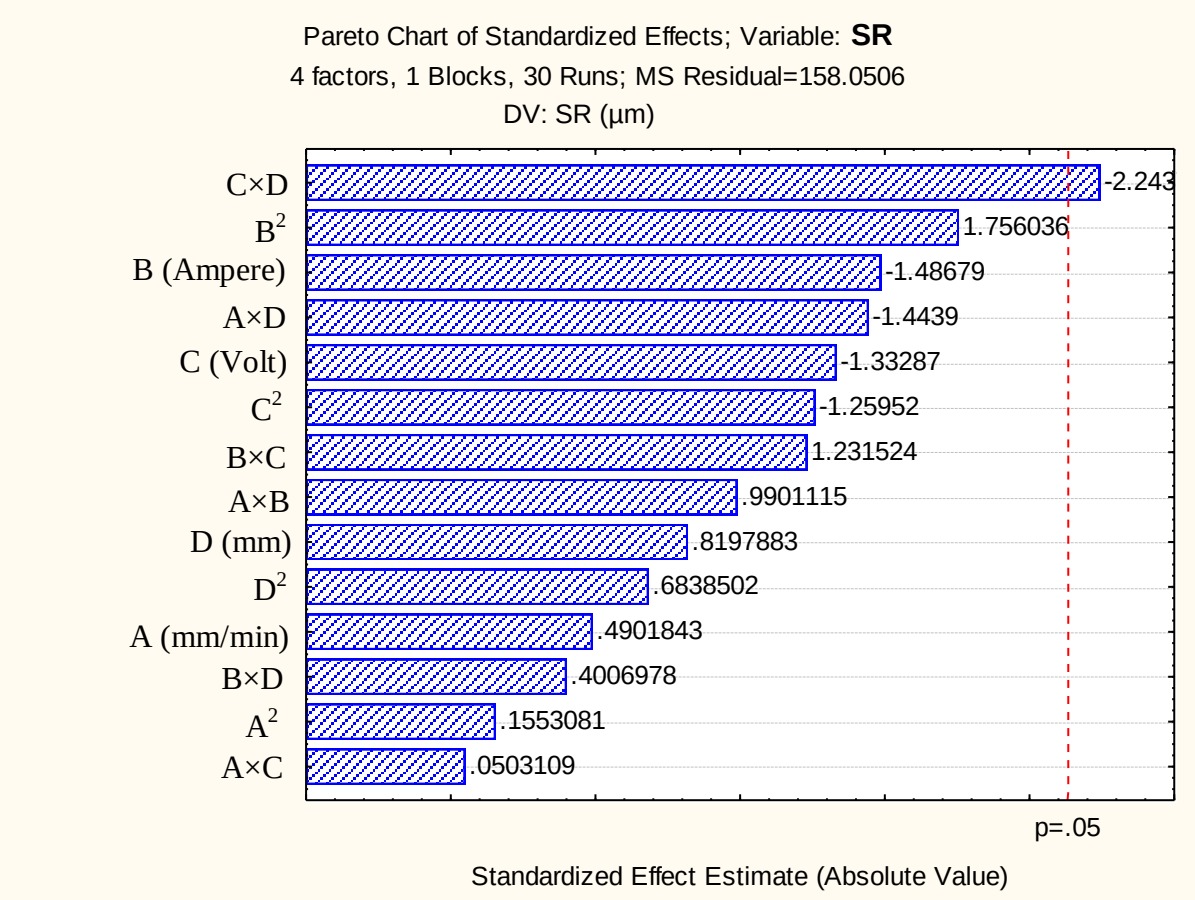

Fig. 86 Pareto chart of standardized effect of factors on SR

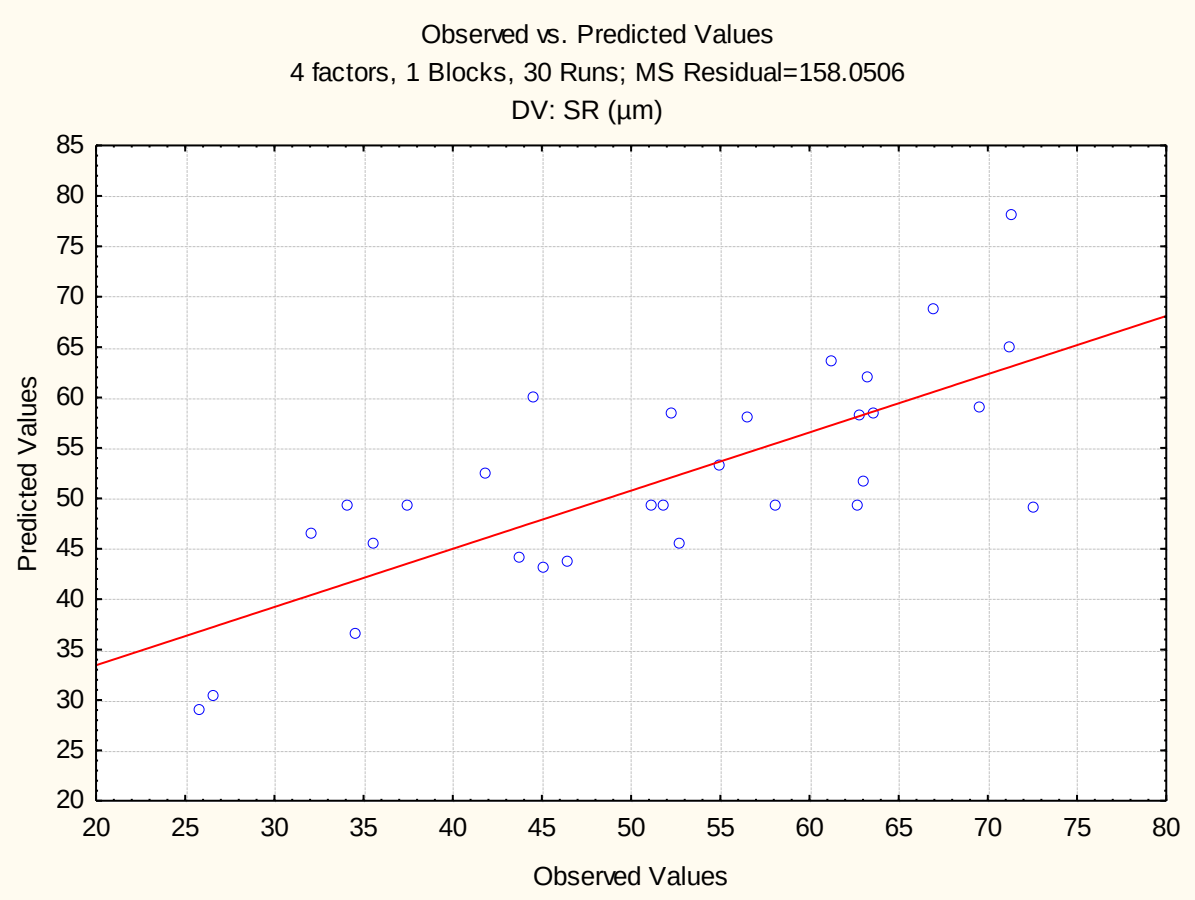

Fig. 87 Plot of observed vs. predicted values of SR

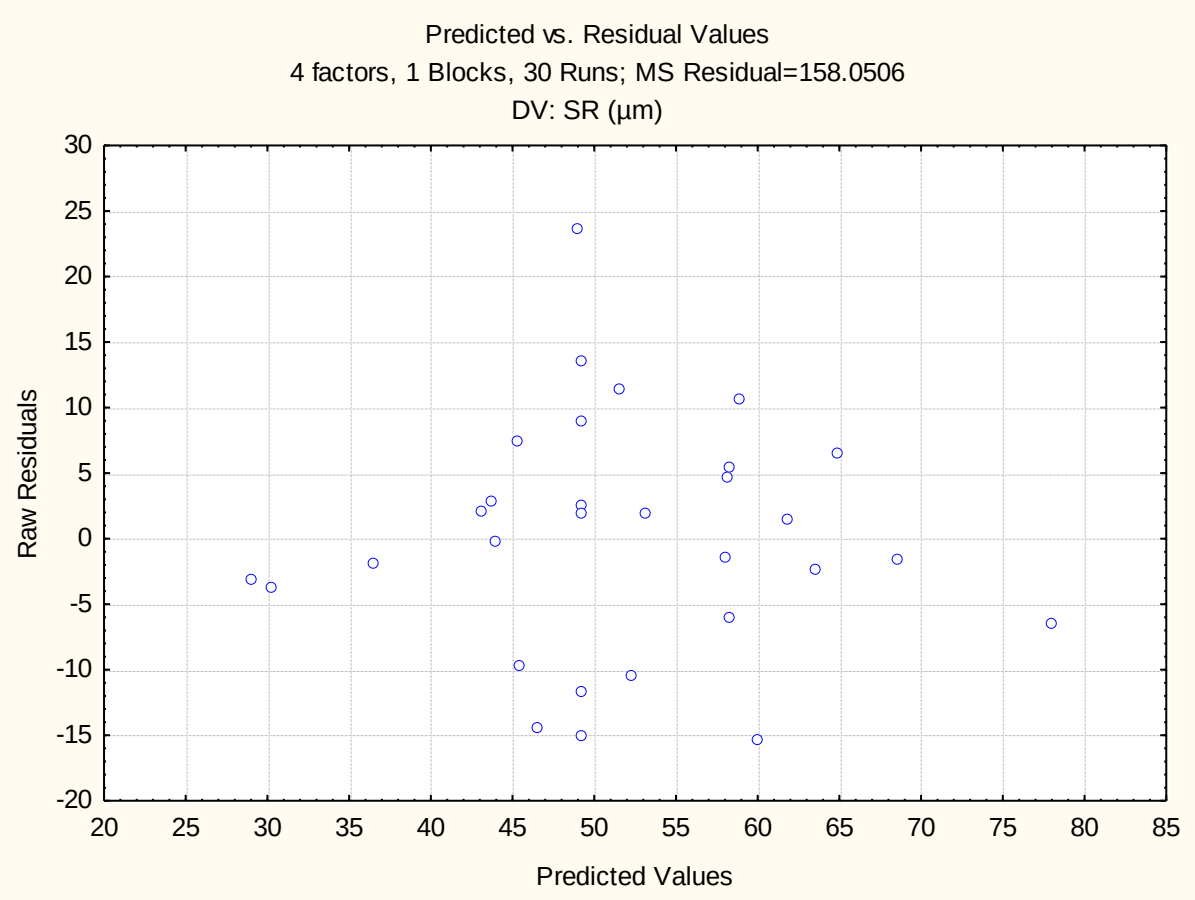

Fig. 88 Plot of predicted vs. residual values of SR

From the Fig. 88, no standard pattern is formed in the plot of predicted vs. residual values which show the adequacy of the fitted model for SR.

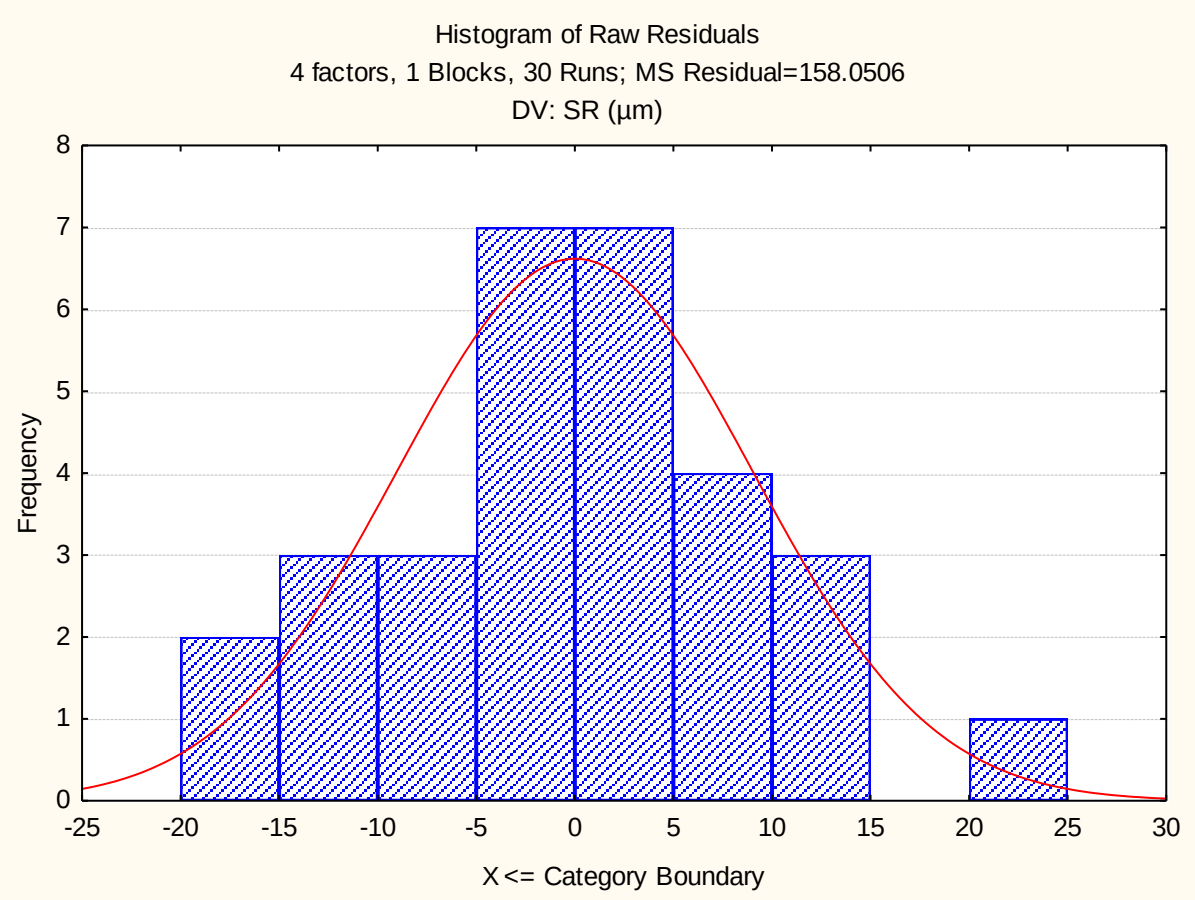

Fig. 89 Histogram plot of predicted values of SR

Fig. 90 Plot of residuals vs. case numbers values of SR

From the Fig. 90, it is evident that the highest SR value among all experimental runs is by the run number 13. The red line indicates that the value of SR decreases with increase in run order.

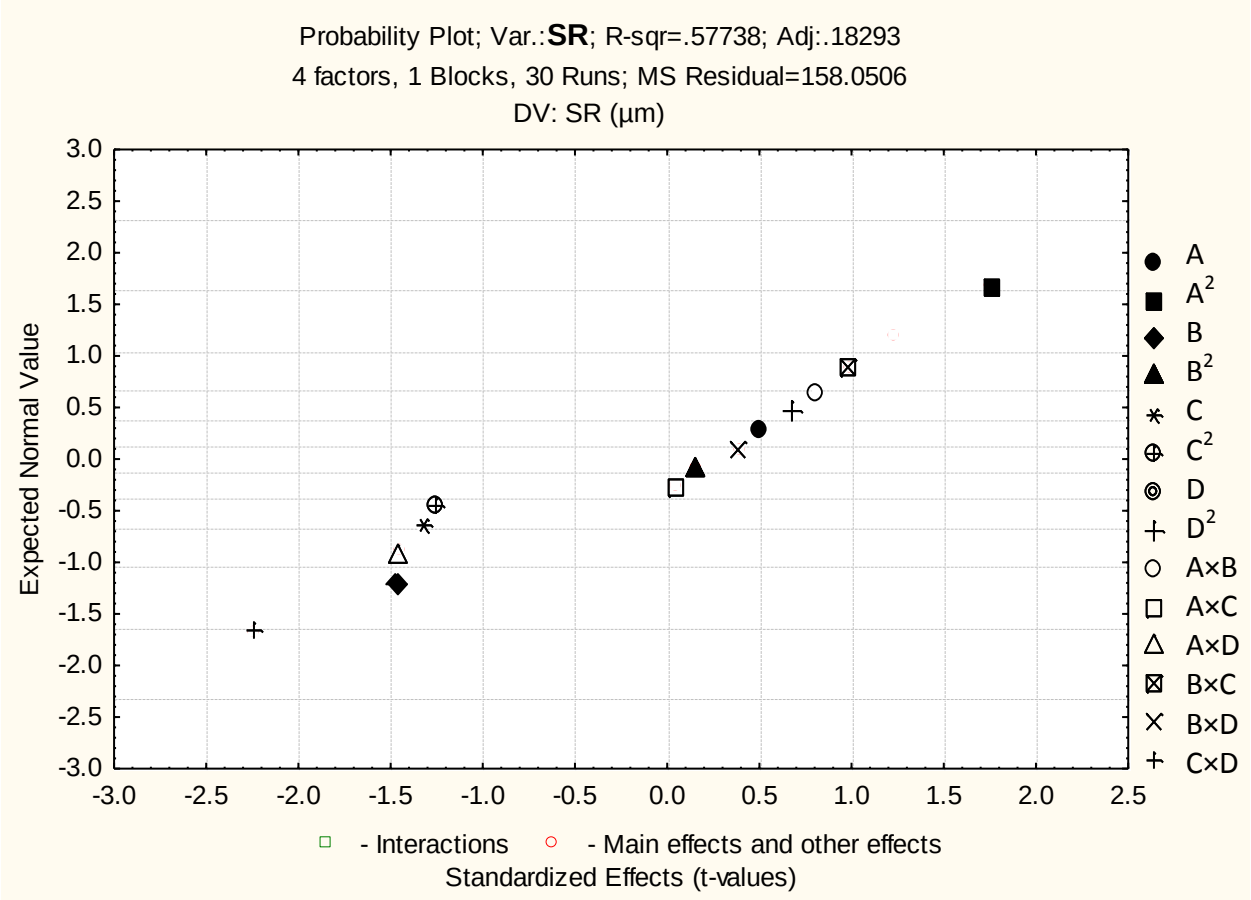

Fig. 91 Probability plot of SR

The normal probability plot of SR corresponding to each regression terms is plotted in Fig. 91.

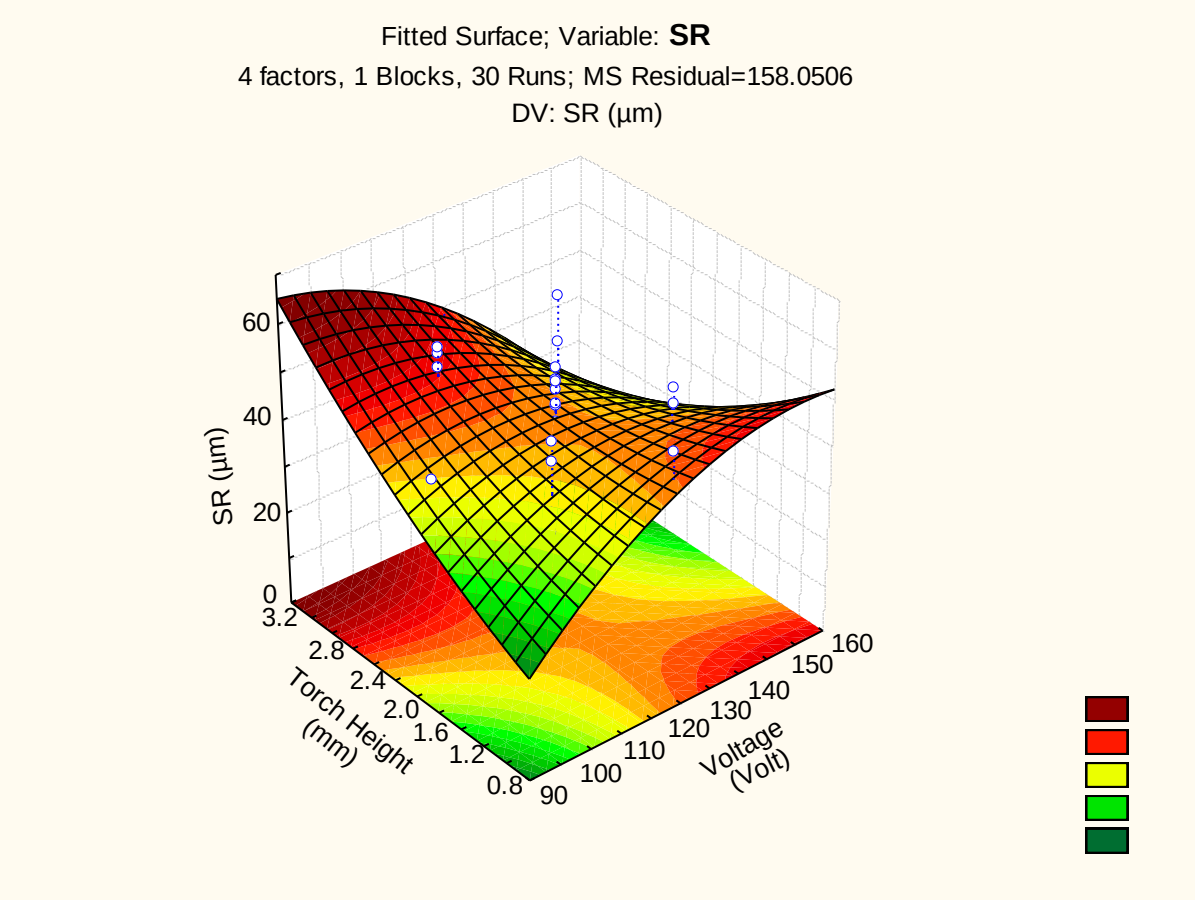

Fig. 92 3D fitted surface plot of SR

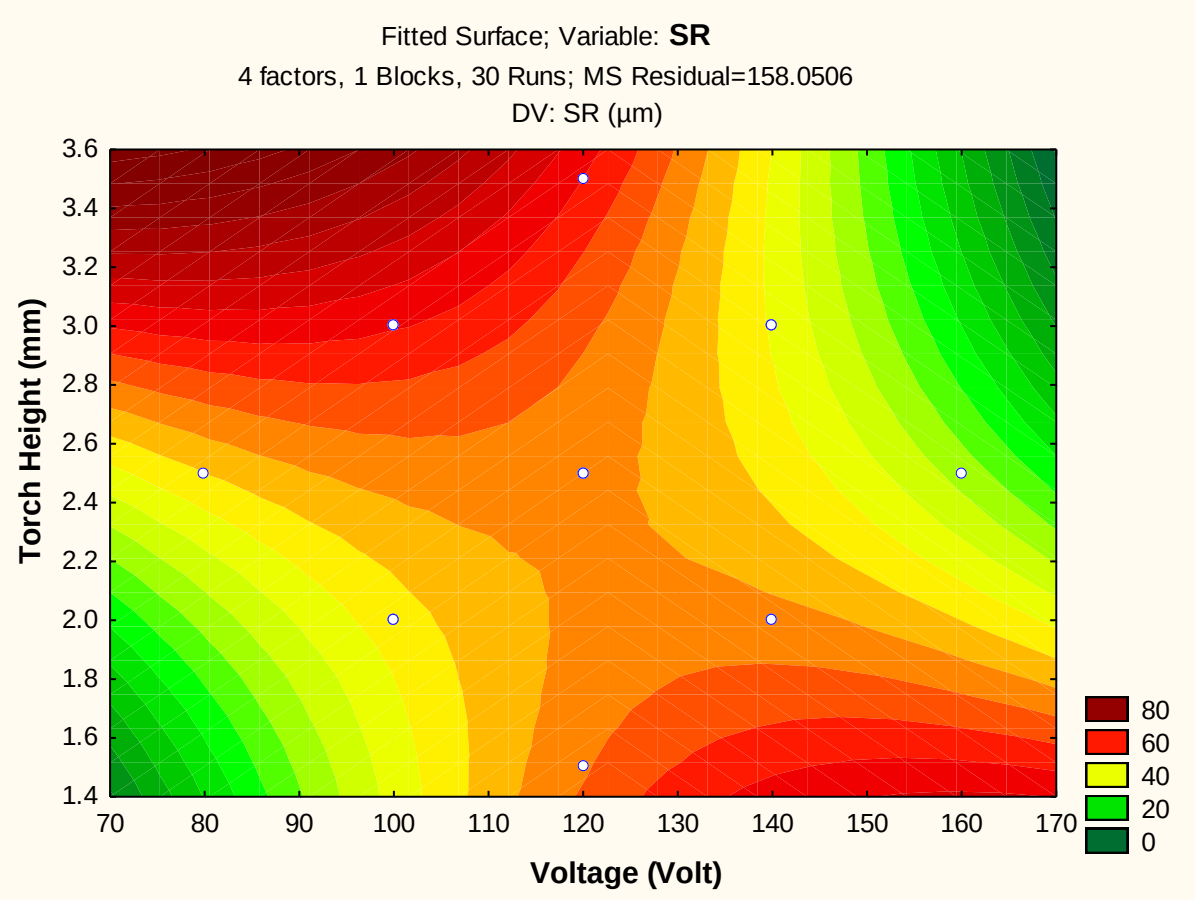

Fig. 93 2D fitted counter plot of SR

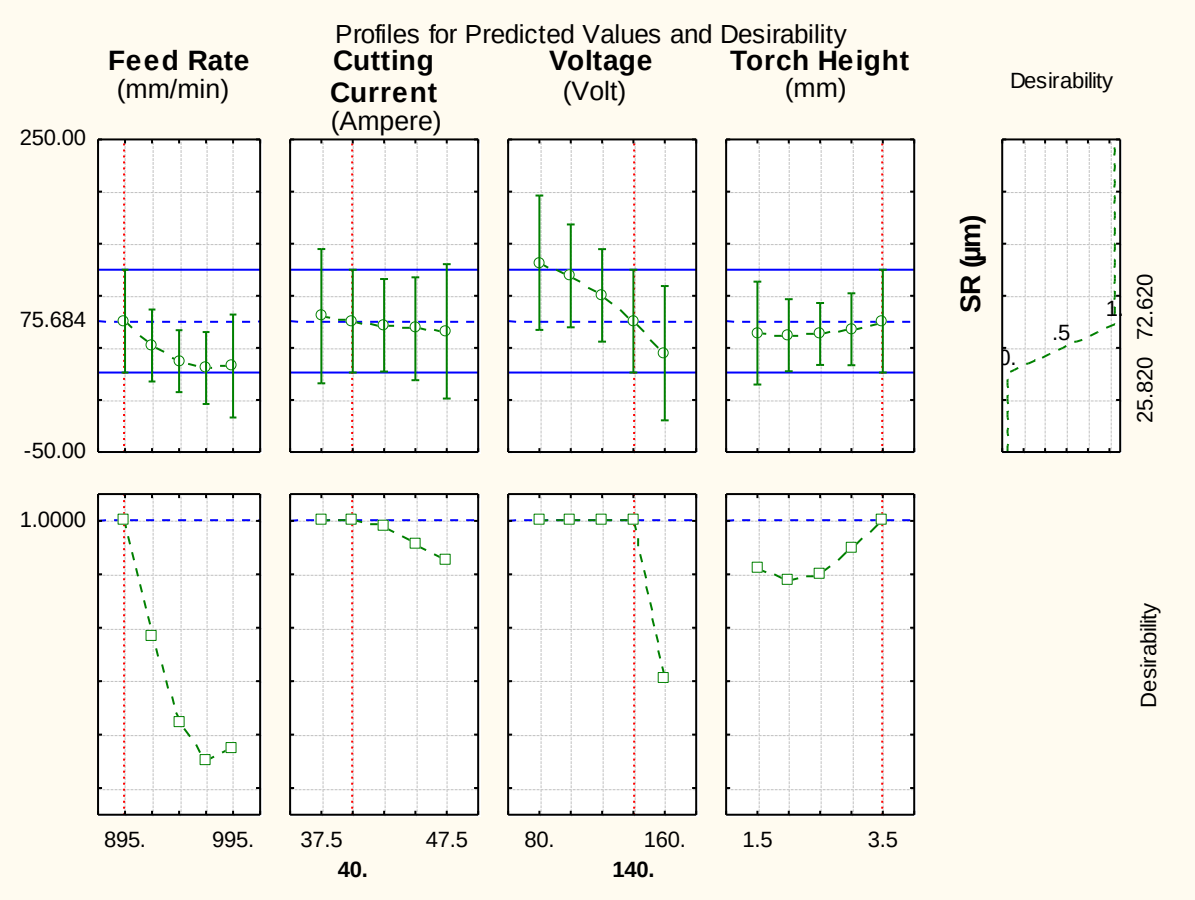

Fig. 94 Profile plot of predicted values and desirability of SR

Similarly in case of surface roughness, the desirability function method helped to get optimum value which was fitted by the quadratic fit model. The level of variable giving the highest desirability i.e., 1.0000 was considered as optimum level. The optimized levels of variables (A, B, C and D) were determined using the desirability profiles that are shown in Fig. 94 for predicted values of responses and desirability function values are plotted by dotted line in red color.

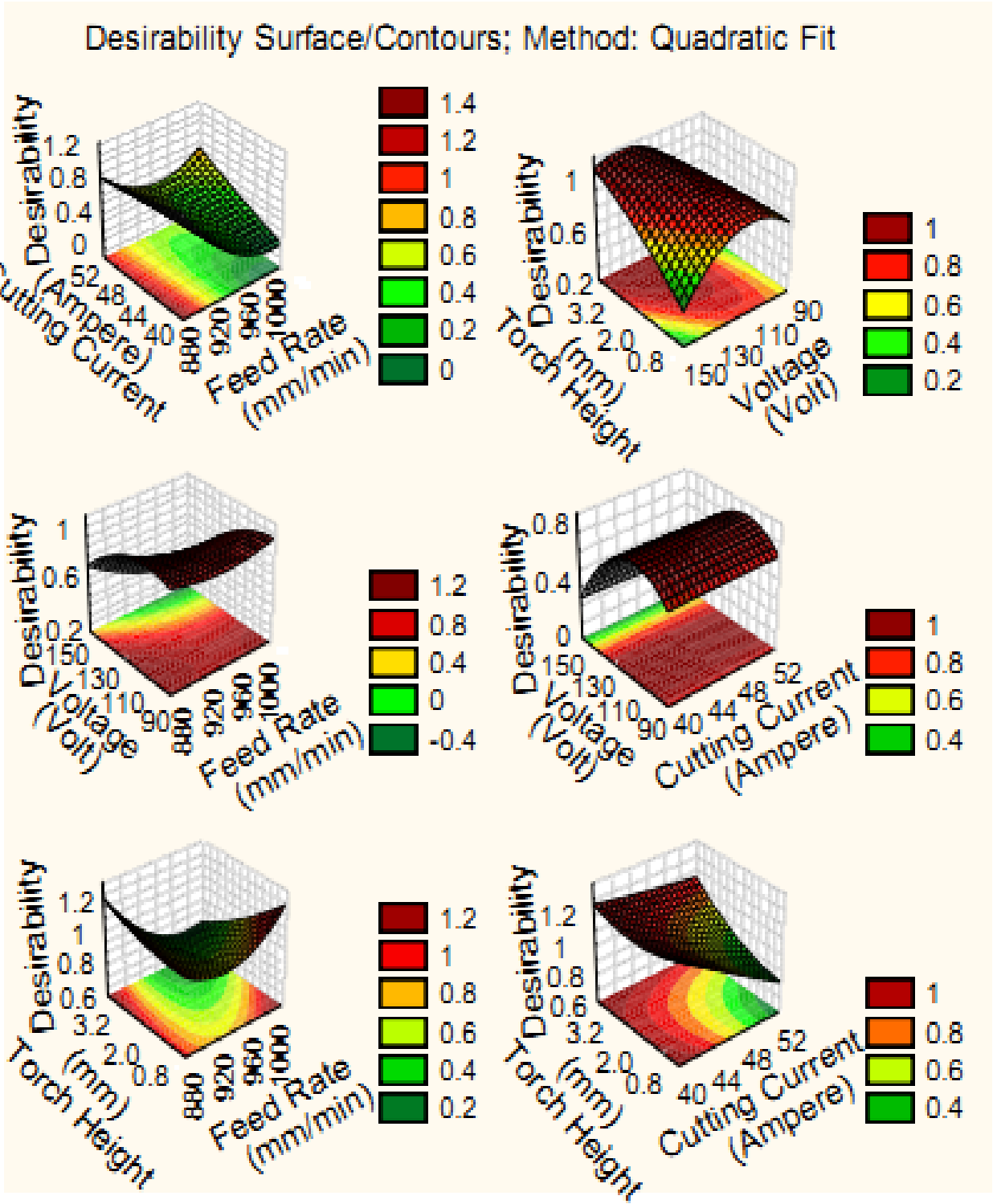

Fig. 95 Desirability 3D surface plot of SR

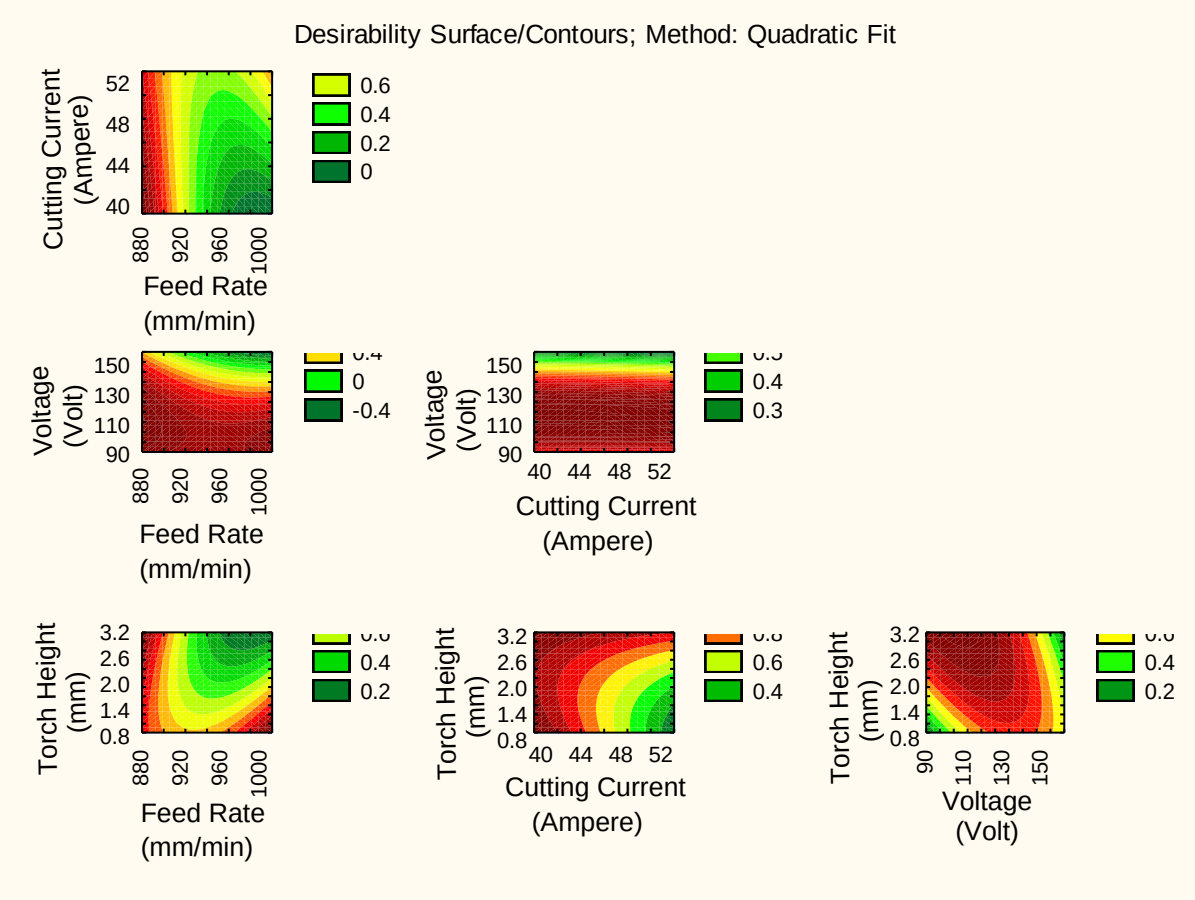

Fig. 96 Desirability 2D counter plot of SR

The 3D and 2D interaction plot of variables on SR response were determined using the desirability profiles that are shown in Fig. 95-96 respectively. From these figures, it can be revealed that the value of SR is rising with decreasing value of voltage. Thus, the high value of voltage is required for minimal surface roughness during machining.

5.2.1.3 For chamfer:

In the same way for chamfer response, the effect of estimated values was computed and recorded in Table 29. The ANOVA for chamfer has been carried out firstly and its results are given in Table 30. Here, the block effect has also been considered because the levels of block are taken as one. Due to this variation in block, there is negligible amount of effect occurred in experiment. This effect is ignored for further calculation of

optimization. The total degree of freedom for all input factors is 29. From the Table 30, it is seen that the most of the terms have P-value less than 0.05 under the confidence interval of 95 %. Hence, these terms show significance within experiment. In case of individual terms, only the interaction of voltage and torch height has shown the most significance among all parameters. Pareto chart of effects of all factors on chamfer response are shown in Fig. 97 and the results indicate that the quadratic of torch height is the second most enhancing factor among all considered factors. The scatter plot between the observed and the predicted value of chamfer of all 30 runs is shown in Fig. 98. It is concluded that there is a reasonable correlation between the measured and predicted values of chamfer response. In Fig. 100, the histogram plot of predicted data of chamfer with 95 % confidence interval of normal distribution is displayed. The surface and contour plot of this interaction terms have been considered for further analysis and shown in Fig. 103-104 respectively. This figure clearly displays that the value of chamfer increases with increase in cutting current and voltage. In Table 31, the model of estimated regression coefficients of the independent variable on the chamfer is computed.

Table 29 Effect of Estimated Values for Chamfer

Factor	Effect	Std. Err.	T	P
Constant	1.626667	0.113495	14.33245	0.000000
A (mm/min)	-0.022500	0.113495	-0.19825	0.845514
A^2	-0.052708	0.106165	-0.49647	0.626756
B (Ampere)	-0.034167	0.113495	-0.30104	0.767517
B^2	-0.110208	0.106165	-1.03808	0.315677
C (Volt)	-0.055833	0.113495	-0.49194	0.629881
C^2	-0.027708	0.106165	-0.26099	0.797647
D (mm)	0.220833	0.113495	1.94575	0.070670
D^2	-0.150208	0.106165	-1.41485	0.177535
A×B	0.038750	0.139003	0.27877	0.784227
A×C	0.078750	0.139003	0.56653	0.579409
A×D	-0.253750	0.139003	-1.82550	0.087899
B×C	-0.011250	0.139003	-0.08093	0.936565
B×D	-0.303750	0.139003	-2.18521	0.045151
C×D	0.081250	0.139003	0.58452	0.567559

Table 30 ANOVA Table for Chamfer

Factors	SS	DoF	MS	F	P
A (mm/min)	0.003038	1	0.003038	0.039301	0.845514
A^2	0.019050	1	0.019050	0.246487	0.626756
B (Ampere)	0.007004	1	0.007004	0.090625	0.767517
B^2	0.083286	1	0.083286	1.077617	0.315677
C (Volt)	0.018704	1	0.018704	0.242009	0.629881
C^2	0.005265	1	0.005265	0.068117	0.797647
D (mm)	0.292604	1	0.292604	3.785932	0.070670
D^2	0.154715	1	0.154715	2.001813	0.177535
A×B	0.006006	1	0.006006	0.077713	0.784227
A×C	0.024806	1	0.024806	0.320962	0.579409
A×D	0.257556	1	0.257556	3.332456	0.087899
B×C	0.000506	1	0.000506	0.006550	0.936565
B×D	0.369056	1	0.369056	4.775126	0.045151
C×D	0.026406	1	0.026406	0.341664	0.567559
Error	1.159308	15	0.077287		
Total SS	2.378097	29			

Table 31 Regression Coefficients of Chamfer

Factor	Regression Coef.	Std. Err.	T	P
Constant	-68.8627	94.39520	-0.72952	0.476925
A (mm/min)	0.0820	0.16875	0.48589	0.634067
A^2	-0.0000	0.00008	-0.49647	0.626756
B (Ampere)	0.7669	1.29350	0.59287	0.562098
B^2	-0.0088	0.00849	-1.03808	0.315677
C (Volt)	-0.0729	0.14856	-0.49057	0.630832
C^2	-0.0000	0.00013	-0.26099	0.797647
D (mm)	15.9909	5.91839	2.70190	0.016396
D^2	-0.3004	0.21233	-1.41485	0.177535
A×B	0.0003	0.00111	0.27877	0.784227
A×C	0.0001	0.00014	0.56653	0.579409
A×D	-0.0102	0.00556	-1.82550	0.087899
B×C	-0.0001	0.00139	-0.08093	0.936565
B×D	-0.1215	0.05560	-2.18521	0.045151
C×D	0.0041	0.00695	0.58452	0.567559

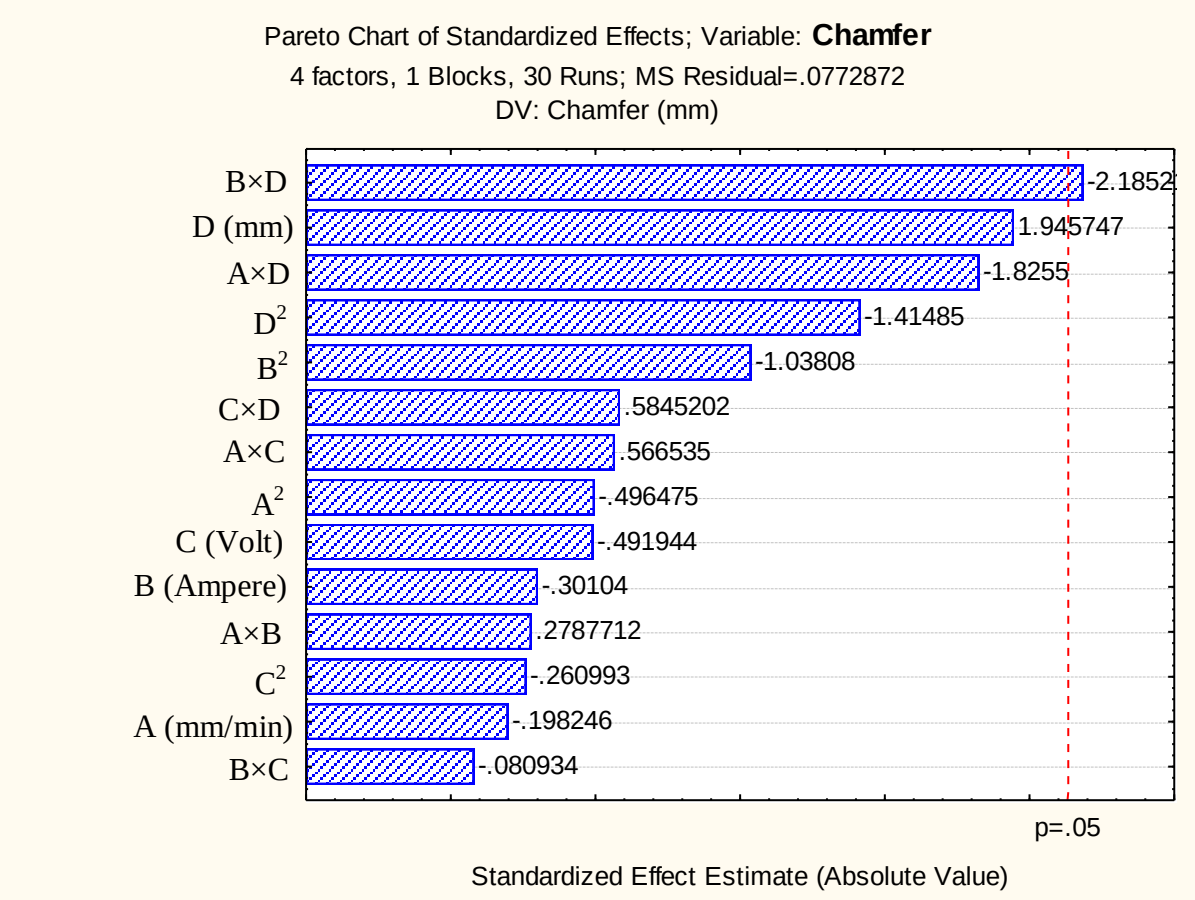

Fig. 97 Pareto chart of standardized effect of factors on chamfer

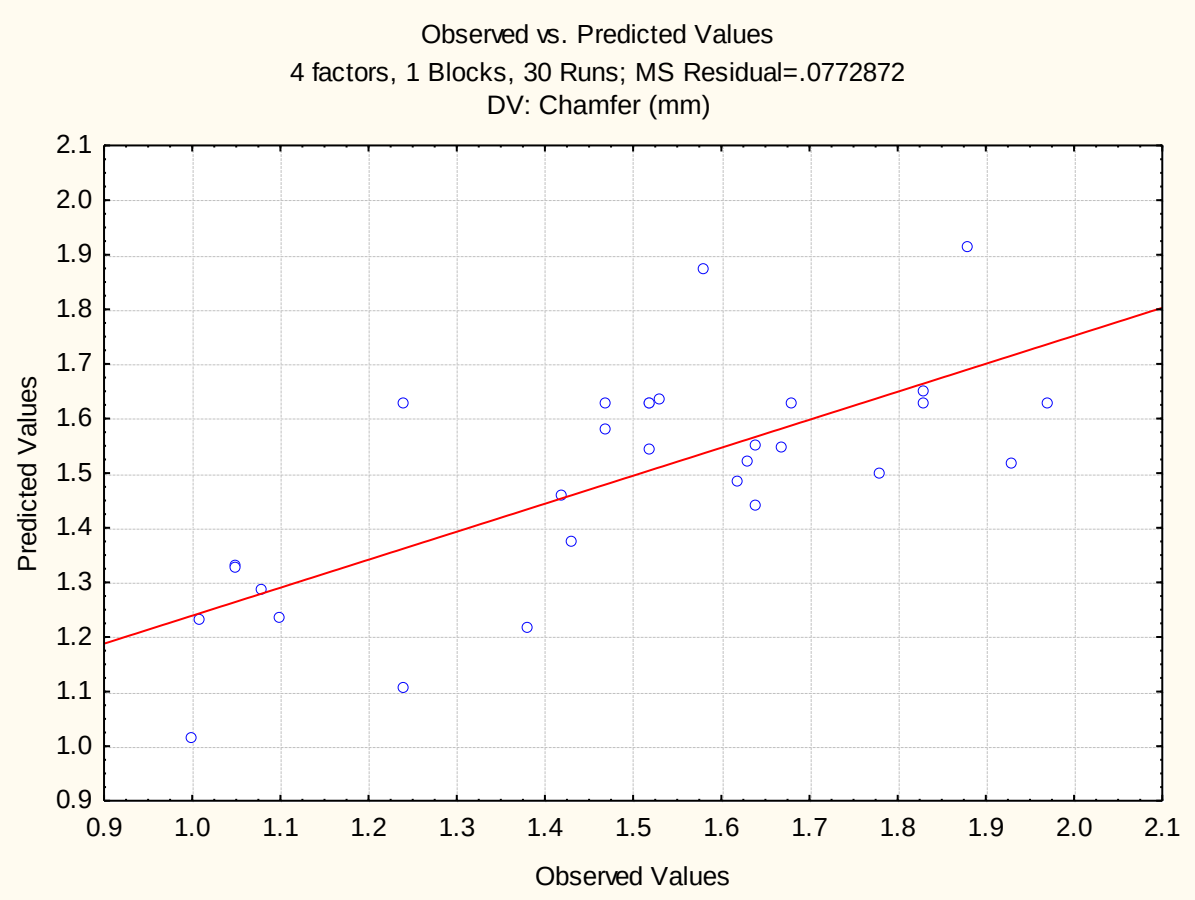

Fig. 98 Plot of observed vs. predicted values of chamfer

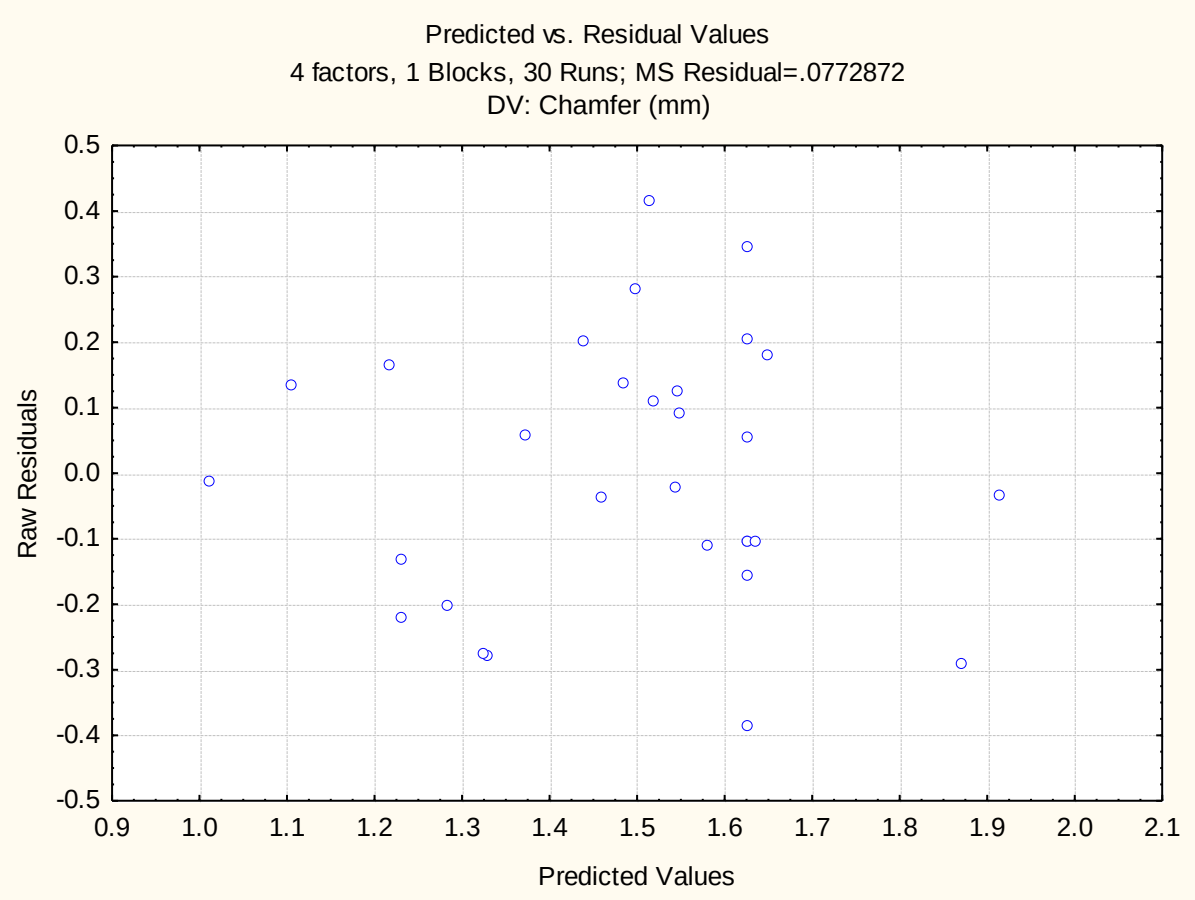

Fig. 99 Plot of predicted vs. residual values of chamfer

From the Fig. 99, no standard pattern is formed in the plot of predicted vs. residual values which show the adequacy of the fitted model for chamfer.

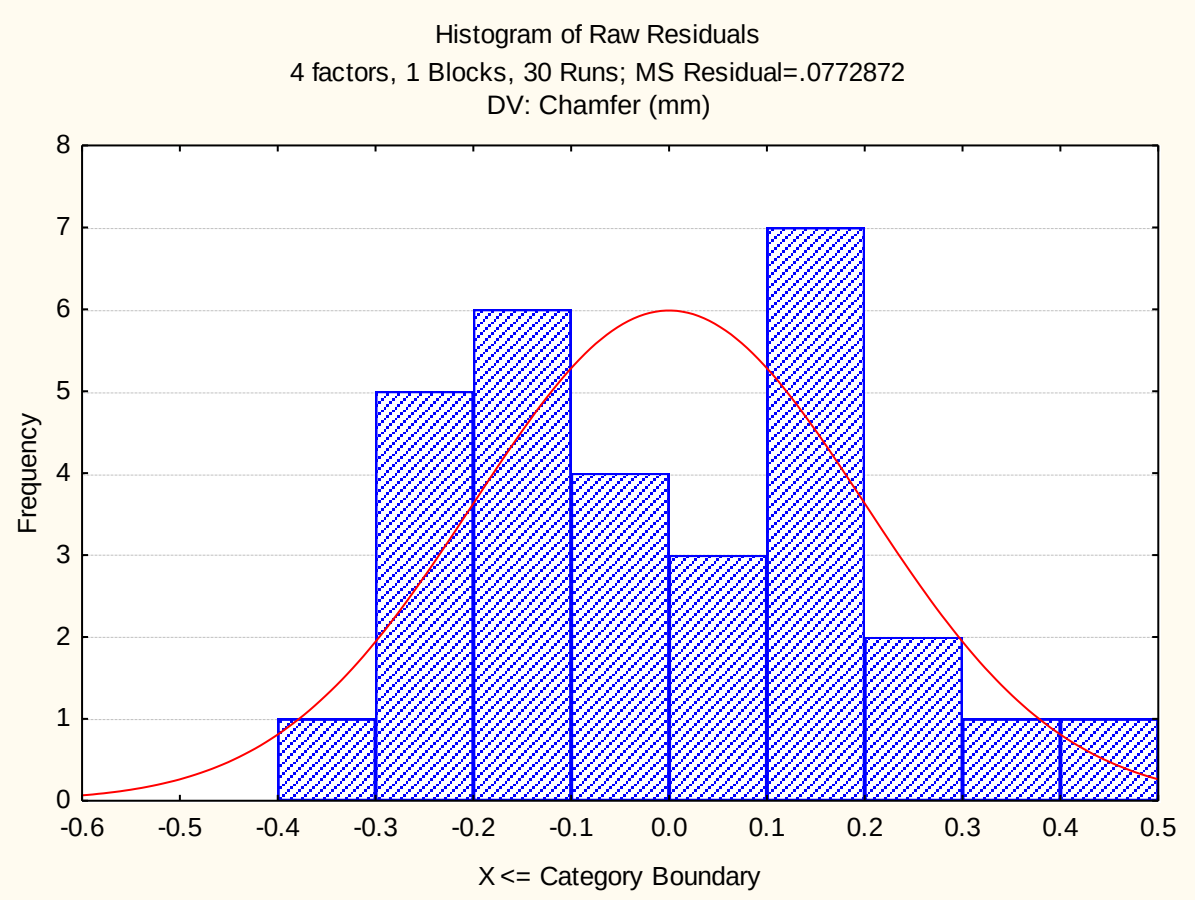

Fig. 100 Histogram plot of predicted values of chamfer

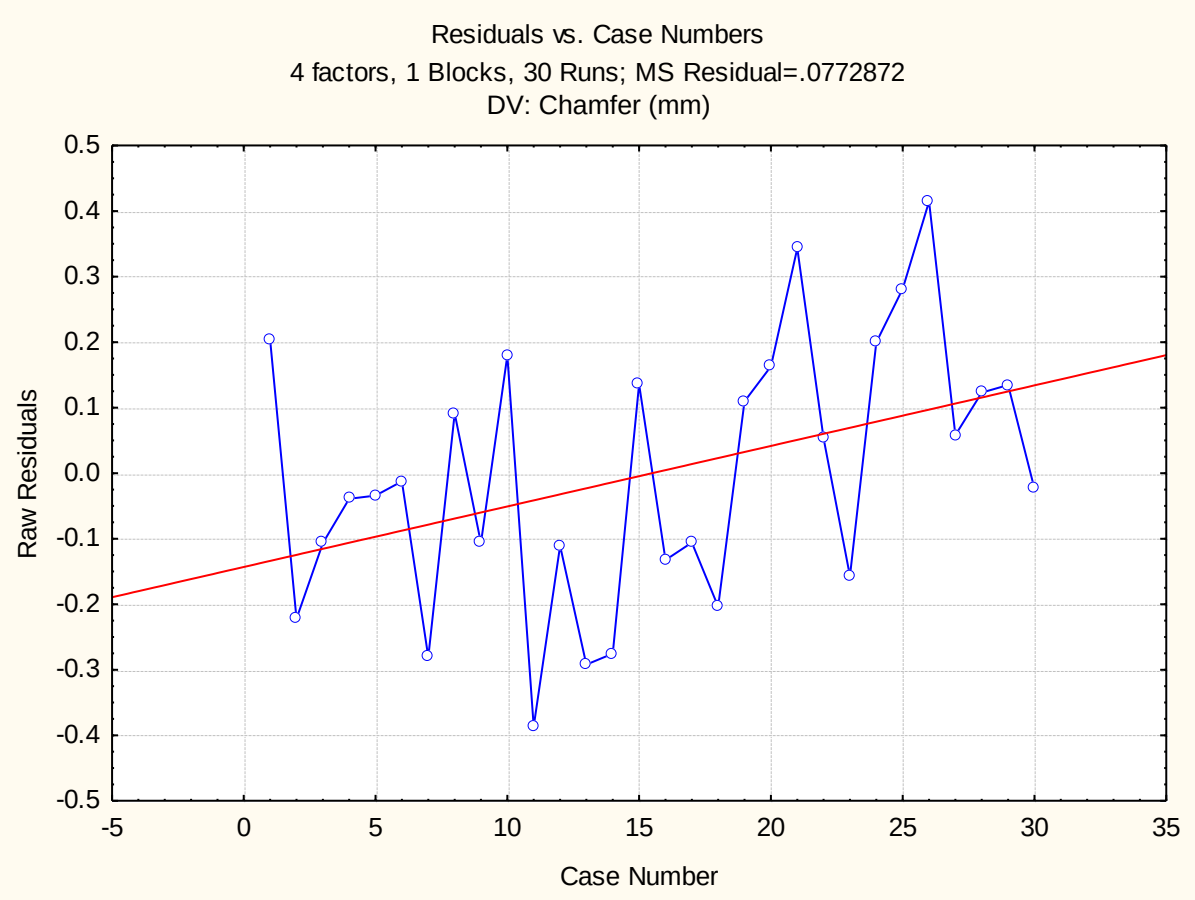

Fig. 101 Plot of residuals vs. case numbers values of chamfer

From the Fig. 101, it is evident that the highest chamfer value among all experimental runs is by the run number 26. The red line indicates that the value of chamfer increases with increase in run order.

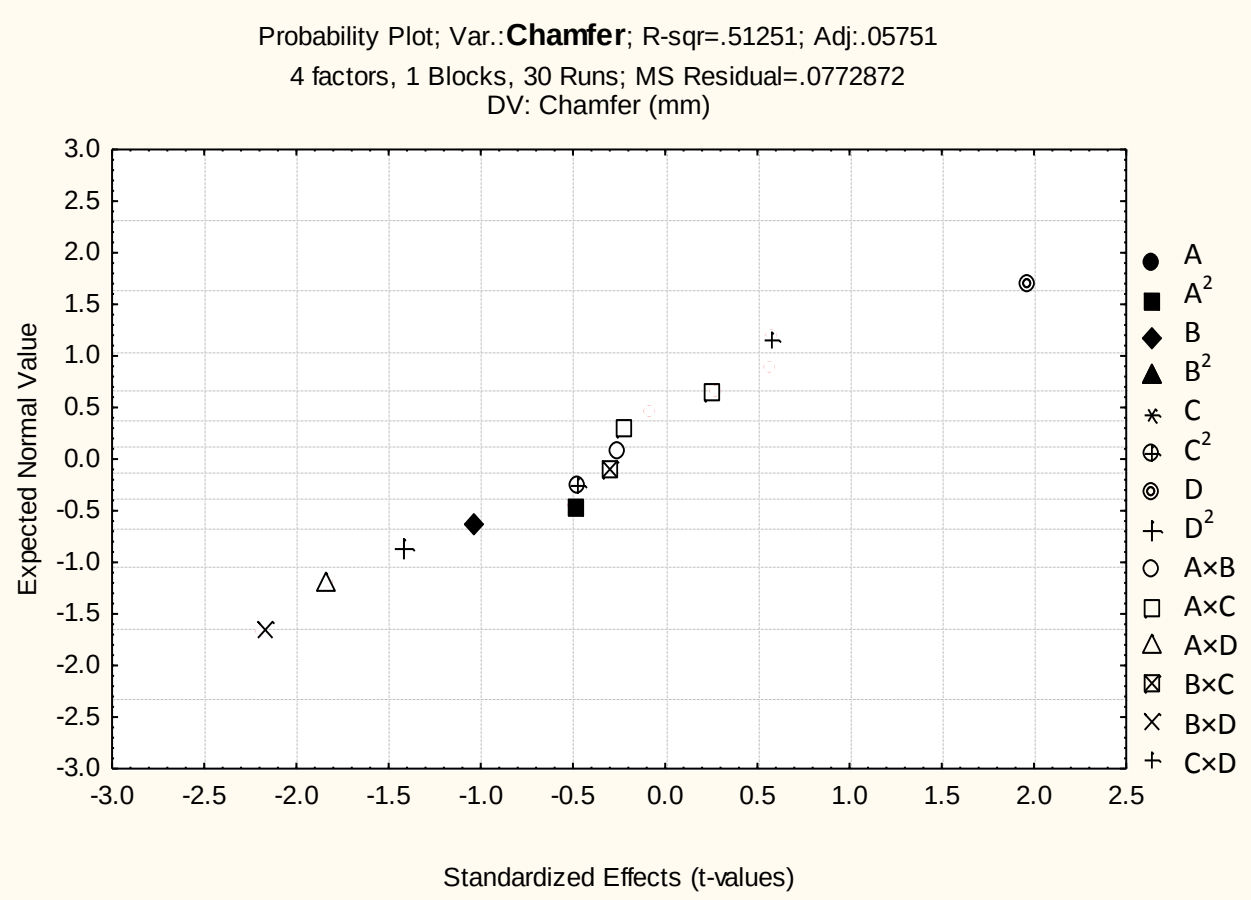

Fig. 102 Probability plot of chamfer

The normal probability plot of chamfer corresponding to each regression terms is plotted in Fig. 102.

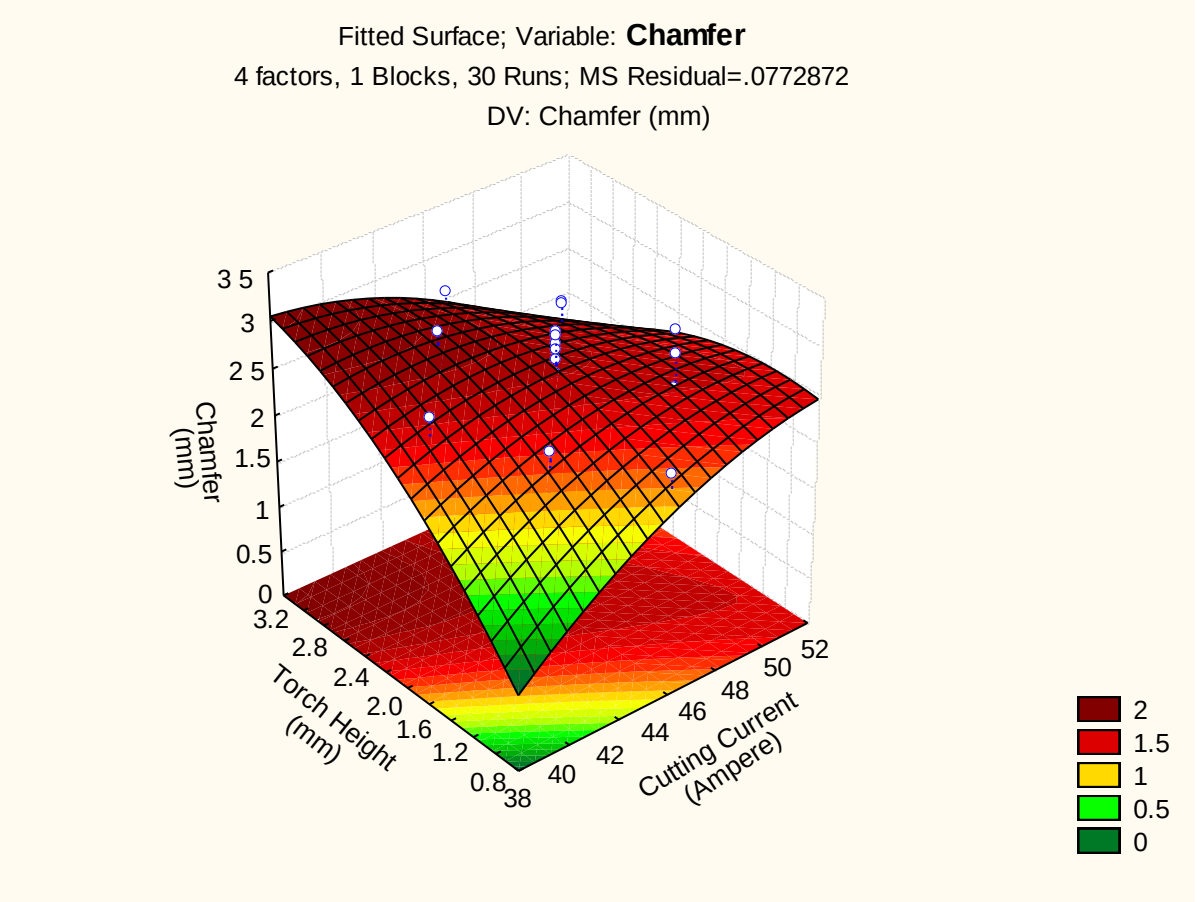

Fig. 103 3D fitted surface plot of chamfer

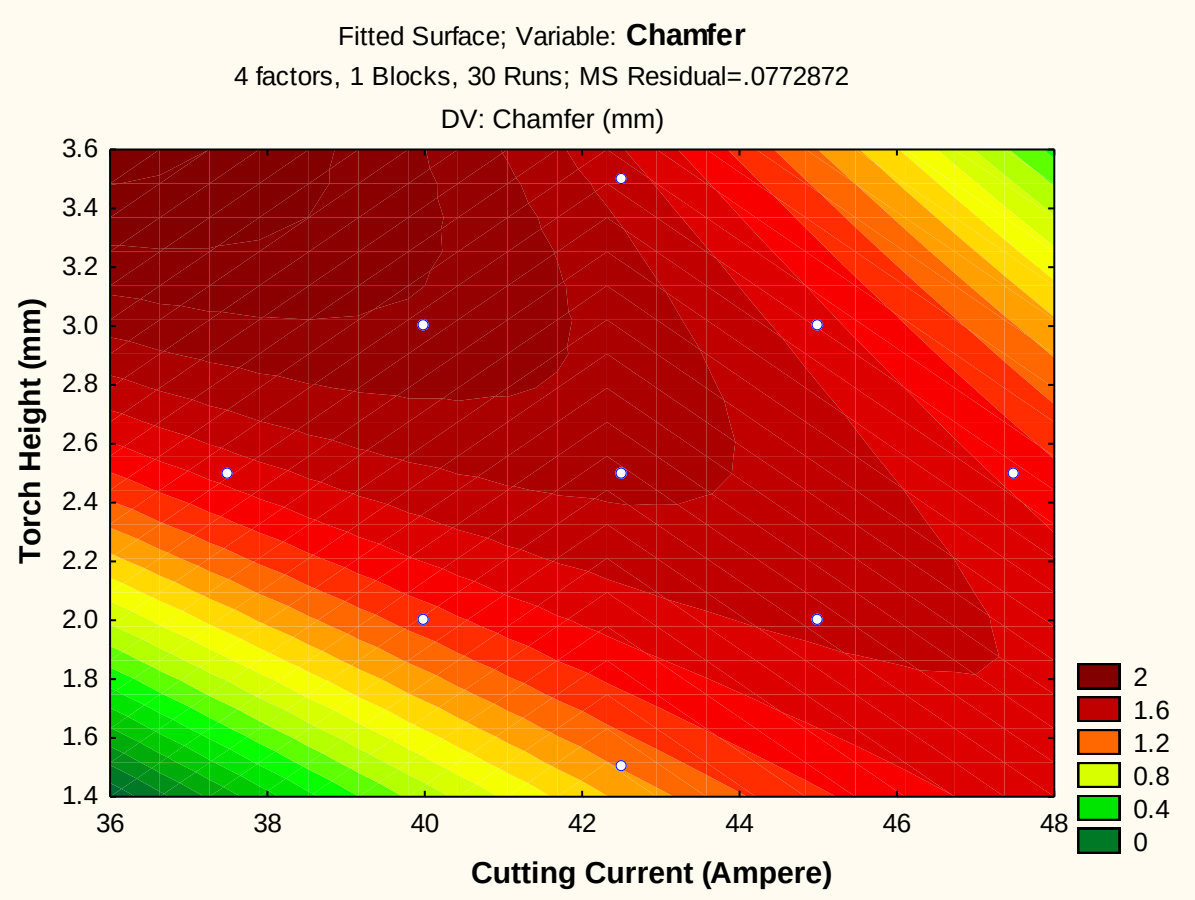

Fig. 104 2D fitted counter plot of chamfer

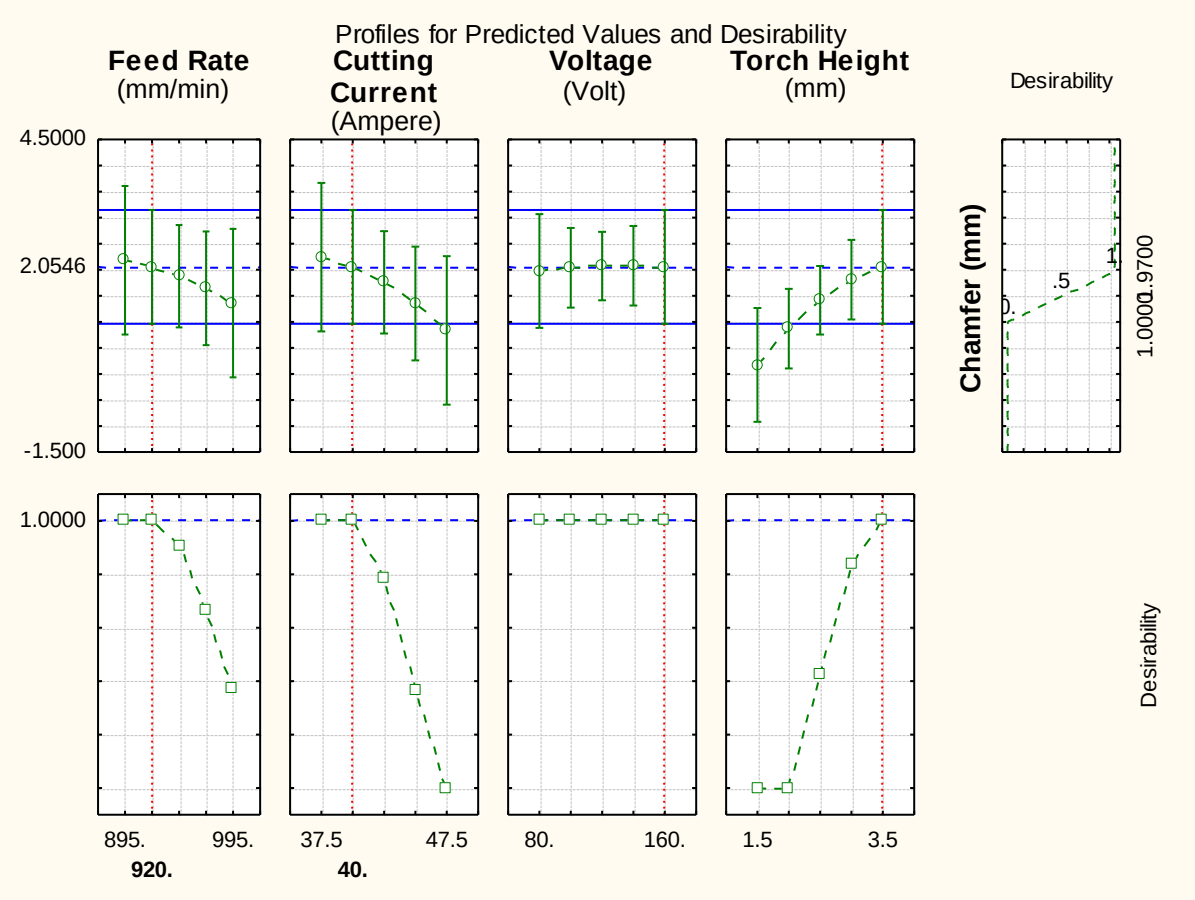

Fig. 105 Profile plot of predicted values and desirability of chamfer

The technique of desirability function helped to get optimum value of chamfer response which was fitted by the quadratic fit model. The level of variable giving the highest desirability i.e., 1.0000 was considered as optimum level. The optimized levels of variables (A, B, C and D) were determined using the desirability profiles that are shown in Fig. 105 for predicted values of responses and red dotted line presented the corresponding values of desirability function.

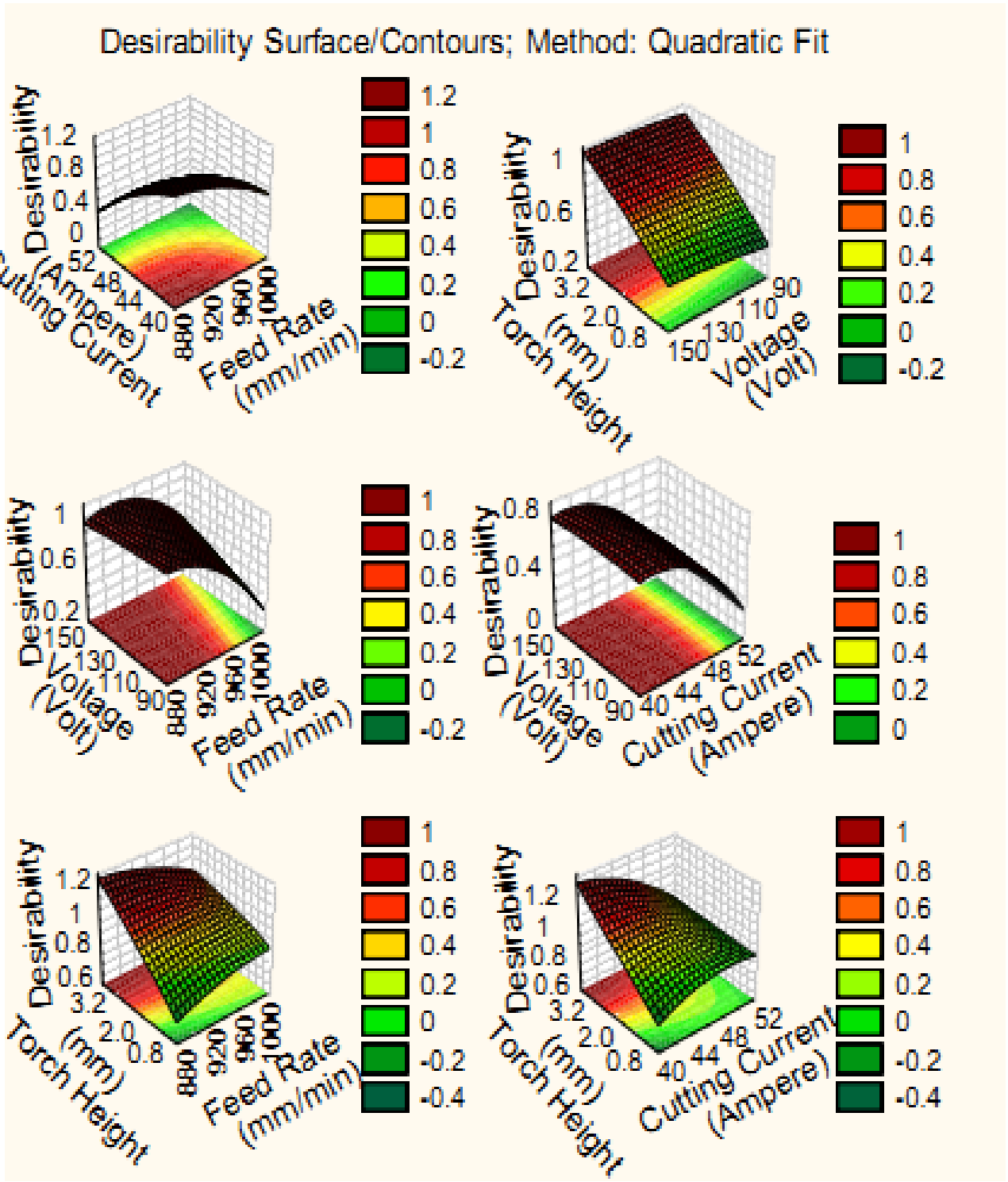

Fig. 106 Desirability 3D surface plot of chamfer

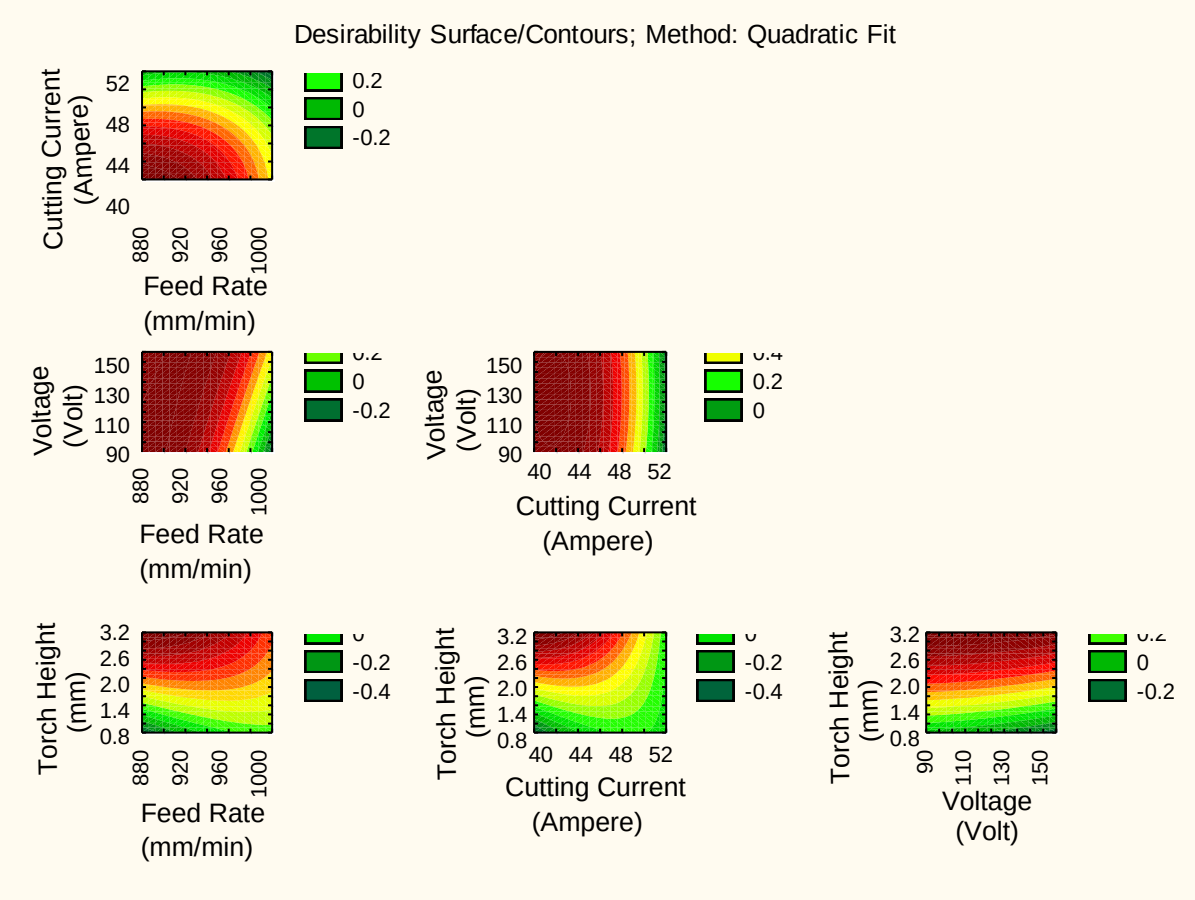

Fig. 107 Desirability 2D counter plot of chamfer

The 3D and 2D interaction plots of input variables on chamfer response were obtained using the desirability profiles that are shown in Fig. 106-107 respectively. From these interaction plots, it can be concluded that the lowest value of torch height is preferred for minimum chamfer during plasma machining.

5.2.1.4 For dross:

Similarly for the case of dross response, the effect of estimated values was computed and recorded in Table 32. The ANOVA for dross has been carried out firstly and its results are given in Table 33. Here, the block effect has also been considered because the levels of block are taken as one. Due to this variation in block, there is negligible amount of effect on experiment. This effect is ignored for further calculation of

optimization. The total degree of freedom for all input factors is 29. From the Table 33, it is seen that the most of the terms have P-value less than 0.05 under the confidence interval of 95 %. Hence, these terms show significance within experiment. In case of individual terms, no single term has shown significance throughout the experiment. Pareto chart of effects of all factors on dross response are shown in Fig. 108 and the results indicate that the quadratic of torch height is the second most enhancing factor among all considered factors. The scatter plot between the observed and the predicted value of dross of all 30 runs is shown in Fig. 109. It is concluded that there is a reasonable correlation between the measured and predicted values of dross response. In Fig. 111, the histogram plot of predicted data of dross with 95 % confidence interval of normal distribution is displayed. In Table 34, the model of estimated regression coefficients of the independent variable on the dross is given.

Table 32 Effect of Estimated Values for Dross

Factor	Effect	Std. Err.	T	P
Constant	6.30833	1.038633	6.07369	0.000021
A (mm/min)	-1.31000	1.038633	-1.26127	0.226474
A^2	-0.45917	0.971552	-0.47261	0.643294
B (Ampere)	-1.90833	1.038633	-1.83735	0.086049
B^2	-0.88917	0.971552	-0.91520	0.374564
C (Volt)	-0.82500	1.038633	-0.79431	0.439400
C^2	0.17333	0.971552	0.17841	0.860789
D (mm)	1.08833	1.038633	1.04785	0.311298
D^2	-0.79917	0.971552	-0.82257	0.423638
A×B	0.89500	1.272061	0.70358	0.492470
A×C	1.32250	1.272061	1.03965	0.314971
A×D	-0.20000	1.272061	-0.15723	0.877164
B×C	-0.78000	1.272061	-0.61318	0.548944
B×D	2.41250	1.272061	1.89653	0.077318
C×D	-1.68500	1.272061	-1.32462	0.205124

Table 33 ANOVA Table for Dross

Factors	SS	DoF	MS	F	P
A (mm/min)	10.2966	1	10.29660	1.590810	0.226474
A^2	1.4457	1	1.44572	0.223362	0.643294
B (Ampere)	21.8504	1	21.85042	3.375858	0.086049
B^2	5.4214	1	5.42138	0.837595	0.374564
C (Volt)	4.0837	1	4.08375	0.630934	0.439400
C^2	0.2060	1	0.20602	0.031830	0.860789
D (mm)	7.1068	1	7.10682	1.097993	0.311298
D^2	4.3794	1	4.37943	0.676616	0.423638
A×B	3.2041	1	3.20410	0.495029	0.492470
A×C	6.9960	1	6.99603	1.080876	0.314971
A×D	0.1600	1	0.16000	0.024720	0.877164
B×C	2.4336	1	2.43360	0.375988	0.548944
B×D	23.2806	1	23.28063	3.596823	0.077318
C×D	11.3569	1	11.35690	1.754625	0.205124
Error	97.0883	15	6.47255		
Total SS	198.1005	29			

Table 34 Regression Coefficients of Dross

Factor	Regression Coef.	Std. Err.	T	P
Constant	39.7616	863.8410	0.04603	0.963895
A (mm/min)	0.2251	1.5443	0.14573	0.886071
A^2	-0.0004	0.0008	-0.47261	0.643294
B (Ampere)	-2.5780	11.8372	-0.21779	0.830528
B^2	-0.0711	0.0777	-0.91520	0.374564
C (Volt)	-0.7803	1.3595	-0.57394	0.574517
C^2	0.0002	0.0012	0.17841	0.860789
D (mm)	-14.2625	54.1611	-0.26333	0.795876
D^2	-1.5983	1.9431	-0.82257	0.423638
A×B	0.0072	0.0102	0.70358	0.492470
A×C	0.0013	0.0013	1.03965	0.314971
A×D	-0.0080	0.0509	-0.15723	0.877164
B×C	-0.0078	0.0127	-0.61318	0.548944
B×D	0.9650	0.5088	1.89653	0.077318
C×D	-0.0843	0.0636	-1.32462	0.205124

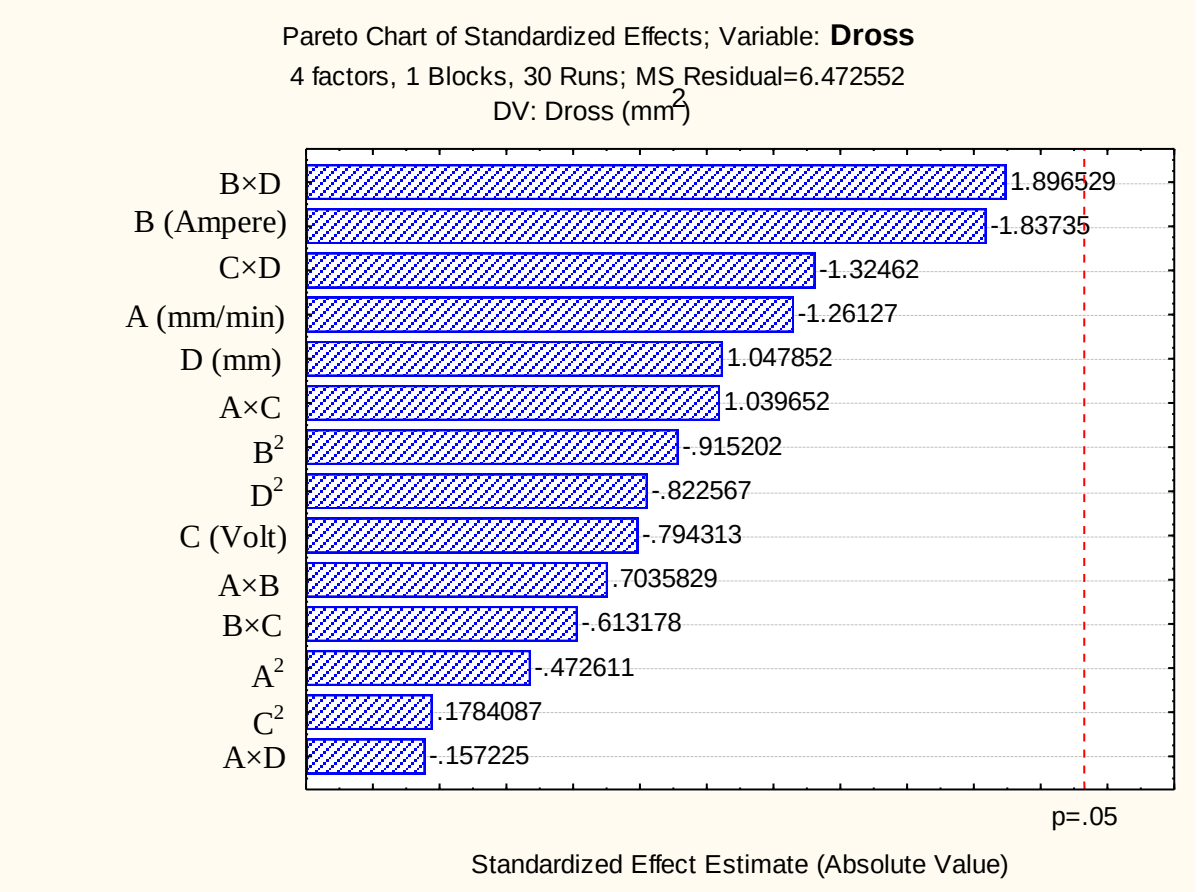

Fig. 108 Pareto chart of standardized effect of factors on dross

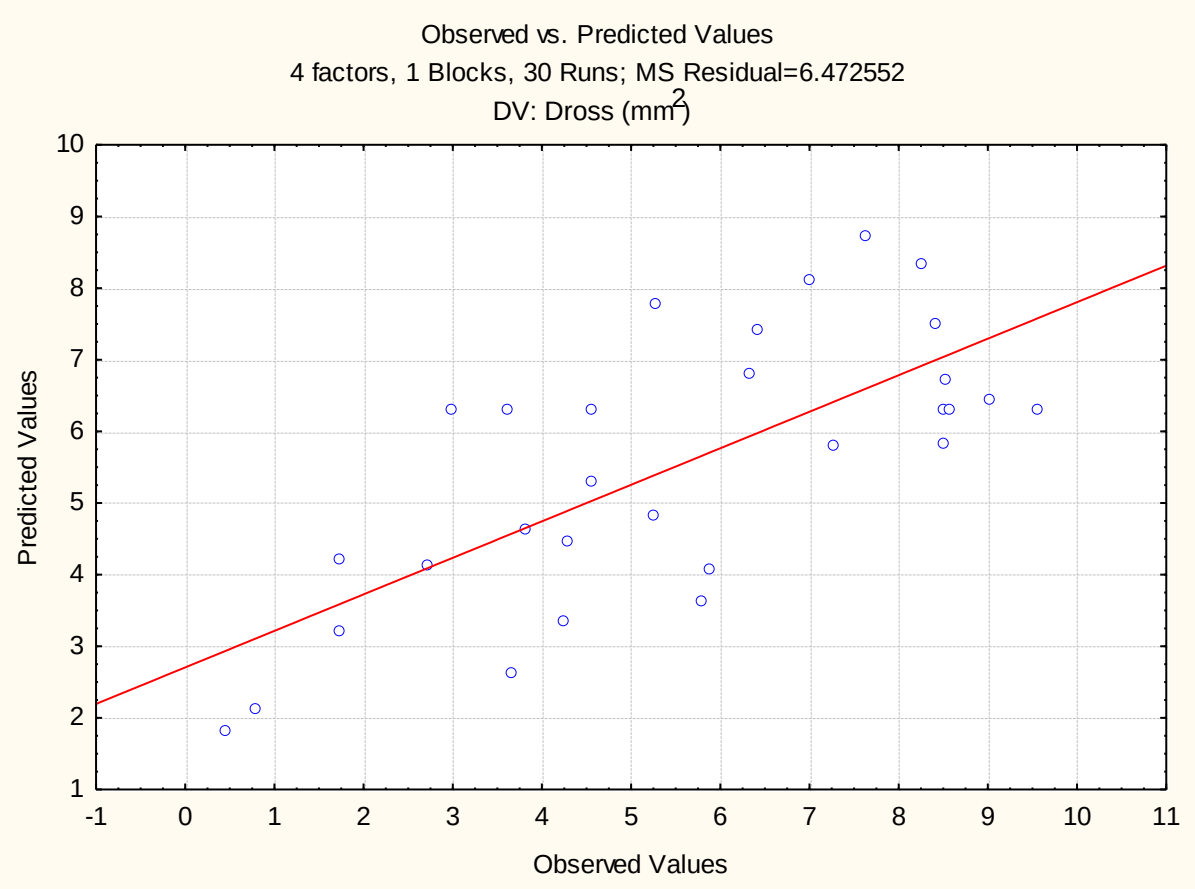

Fig. 109 Plot of observed vs. predicted values of dross

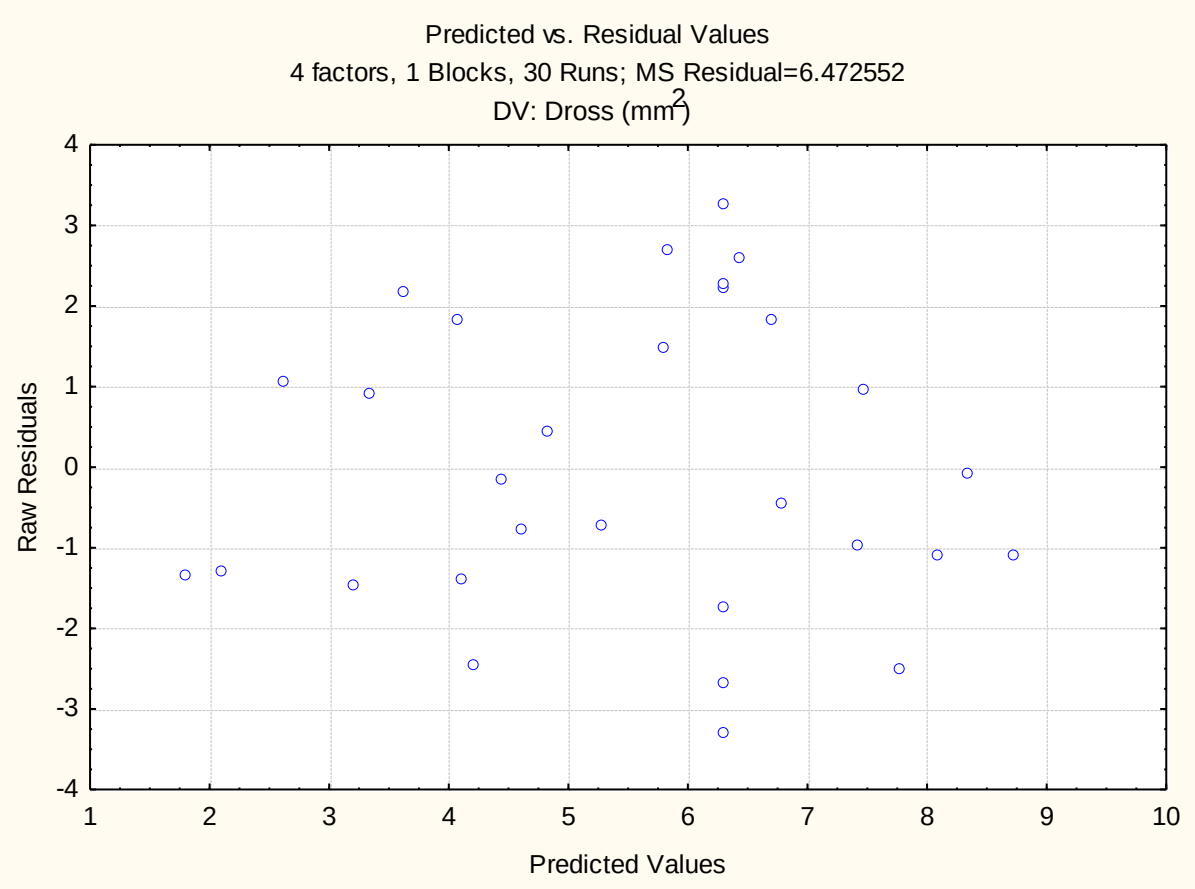

Fig. 110 Plot of predicted vs. residual values of dross

From the Fig. 110, no standard pattern is formed in the plot of predicted vs. residual values which show the adequacy of the fitted model for dross.

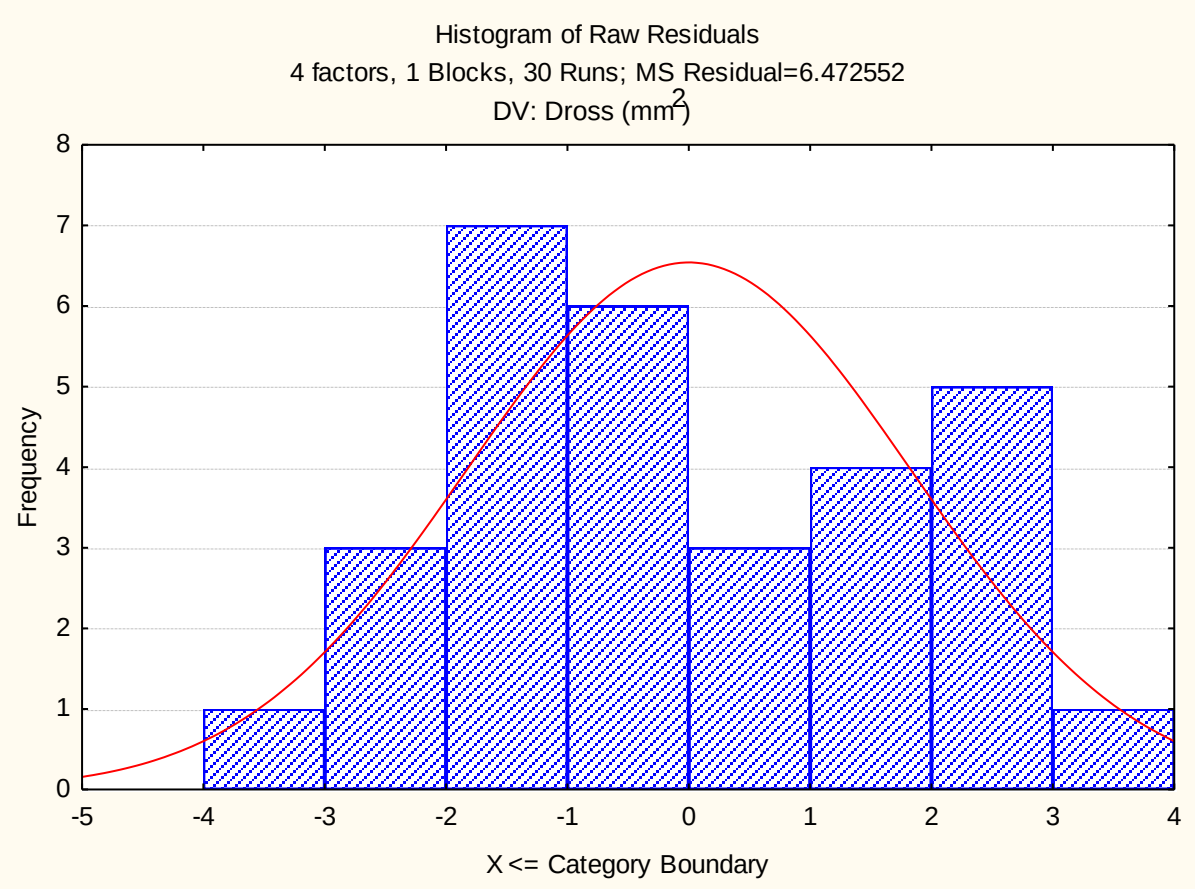

Fig. 111 Histogram plot of predicted values of dross

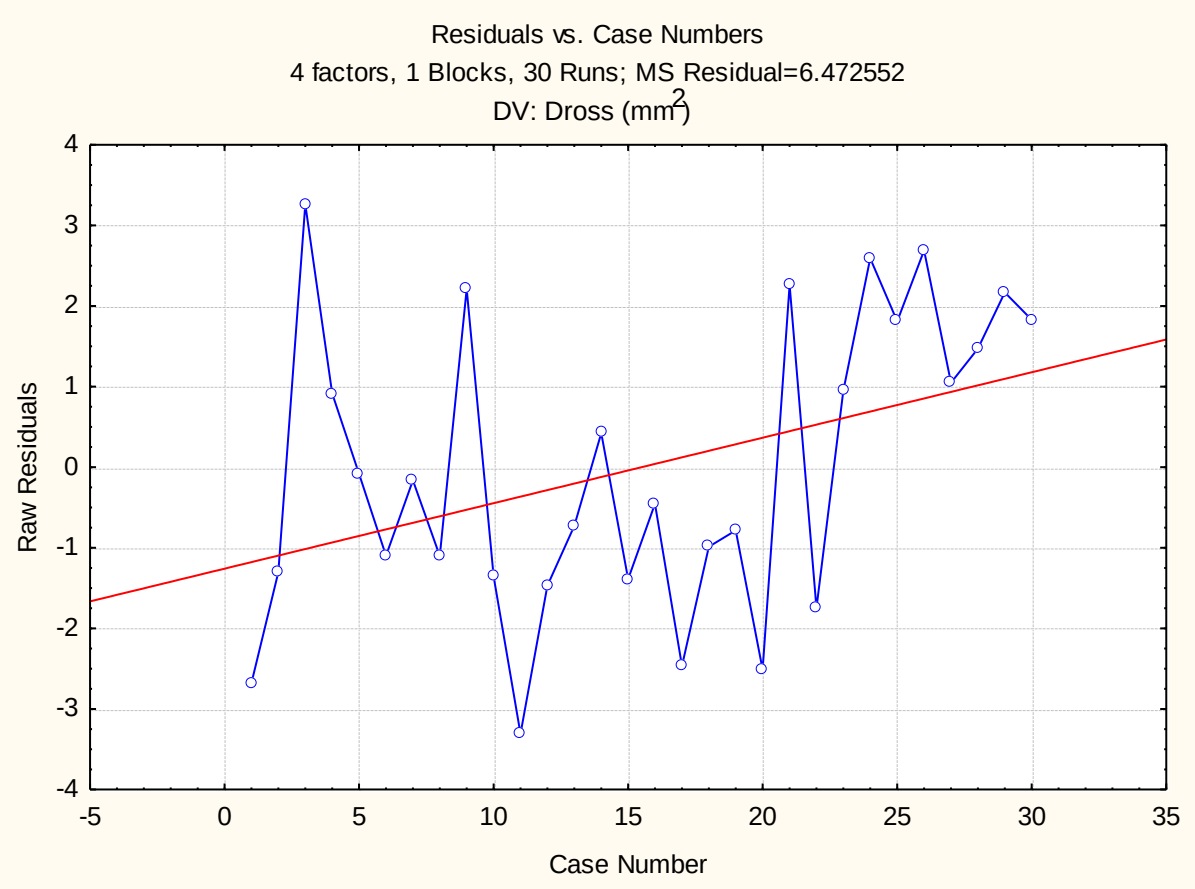

Fig. 112 Plot of residuals vs. case numbers values of dross

From the Fig. 112, it is evident that the highest dross value among all experimental runs is by the run number 3. The red line indicates that the value of dross increases with increase in run order.

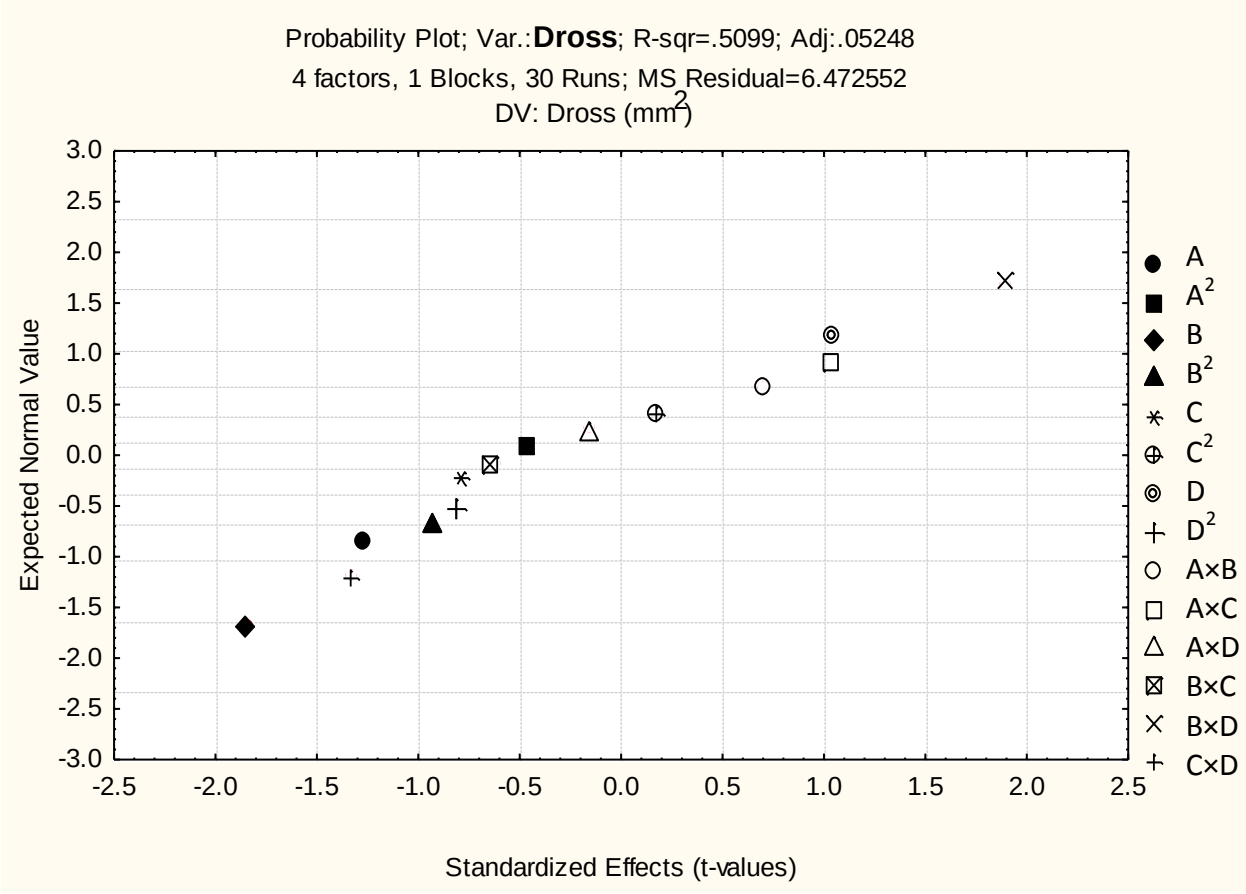

Fig. 113 Probability plot of dross

The normal probability plot of dross corresponding to each regression terms is plotted in Fig. 113.

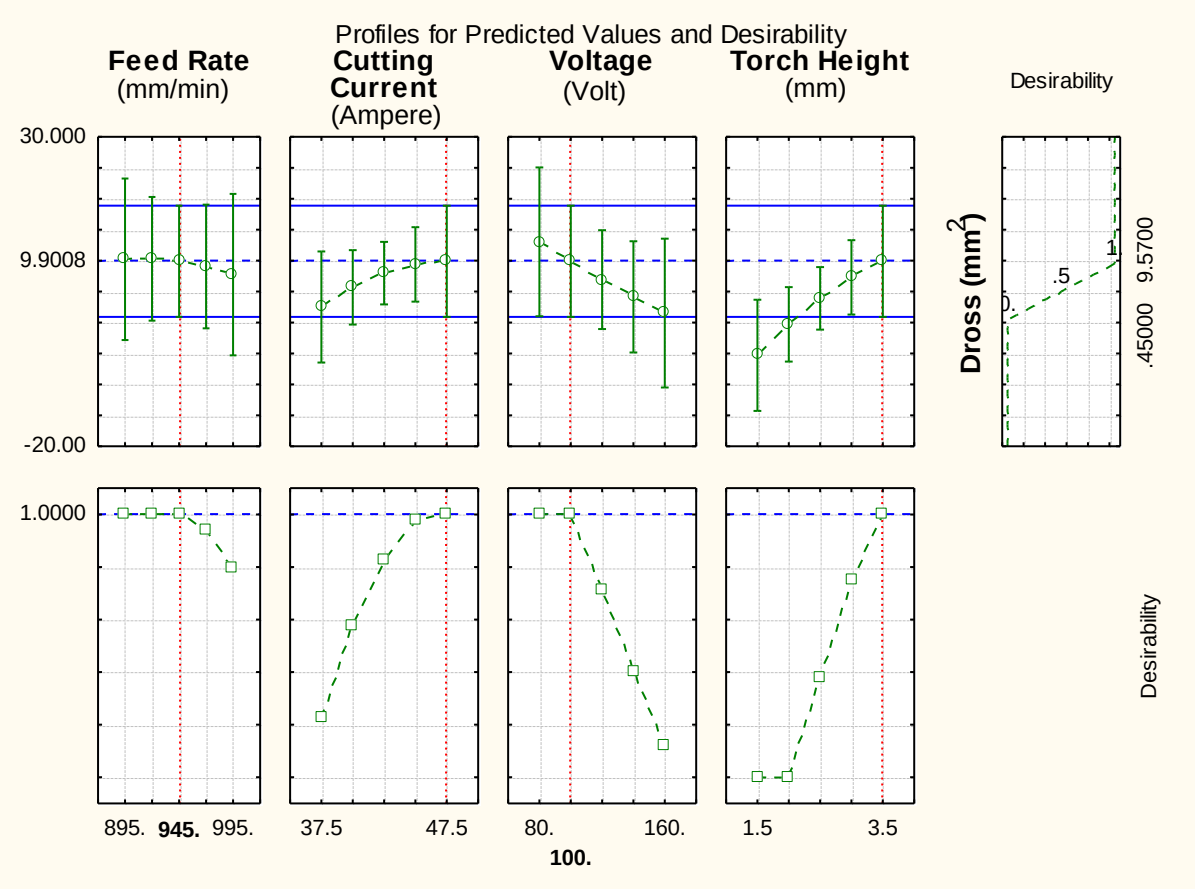

Fig. 114 Profile plot of predicted values and desirability of dross

By the help of desirability function technique, it can be able to find optimum value of dross response with the quadratic fit empirical model. The level of variable giving the highest desirability i.e., 1.0000 was considered as optimum level. The optimized levels of variables (A, B, C and D) were determined using the desirability profiles. The predicted values of responses and desirability function with red dotted lines are displayed in Fig. 114.

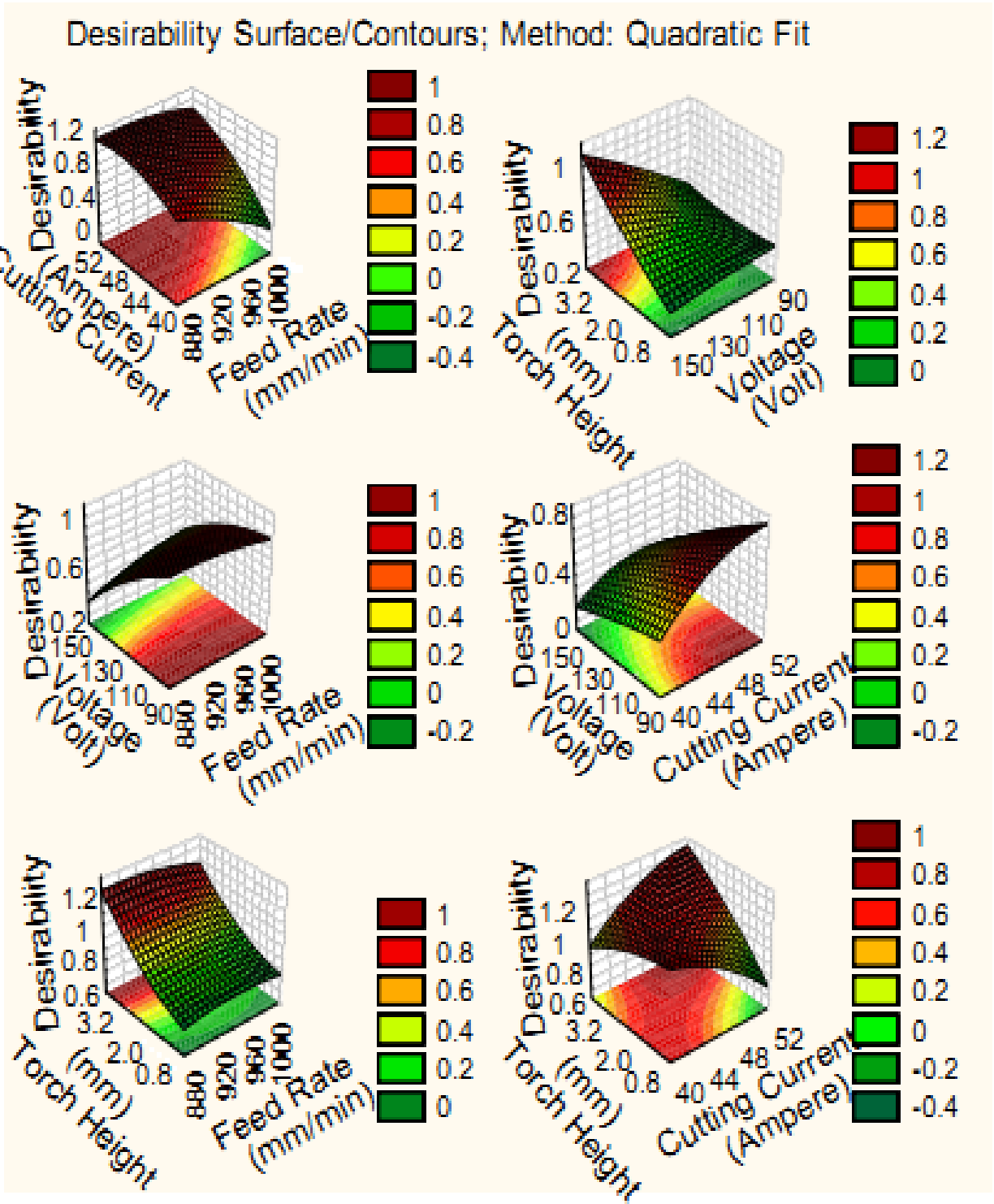

Fig. 115 Desirability 3D surface plot of dross

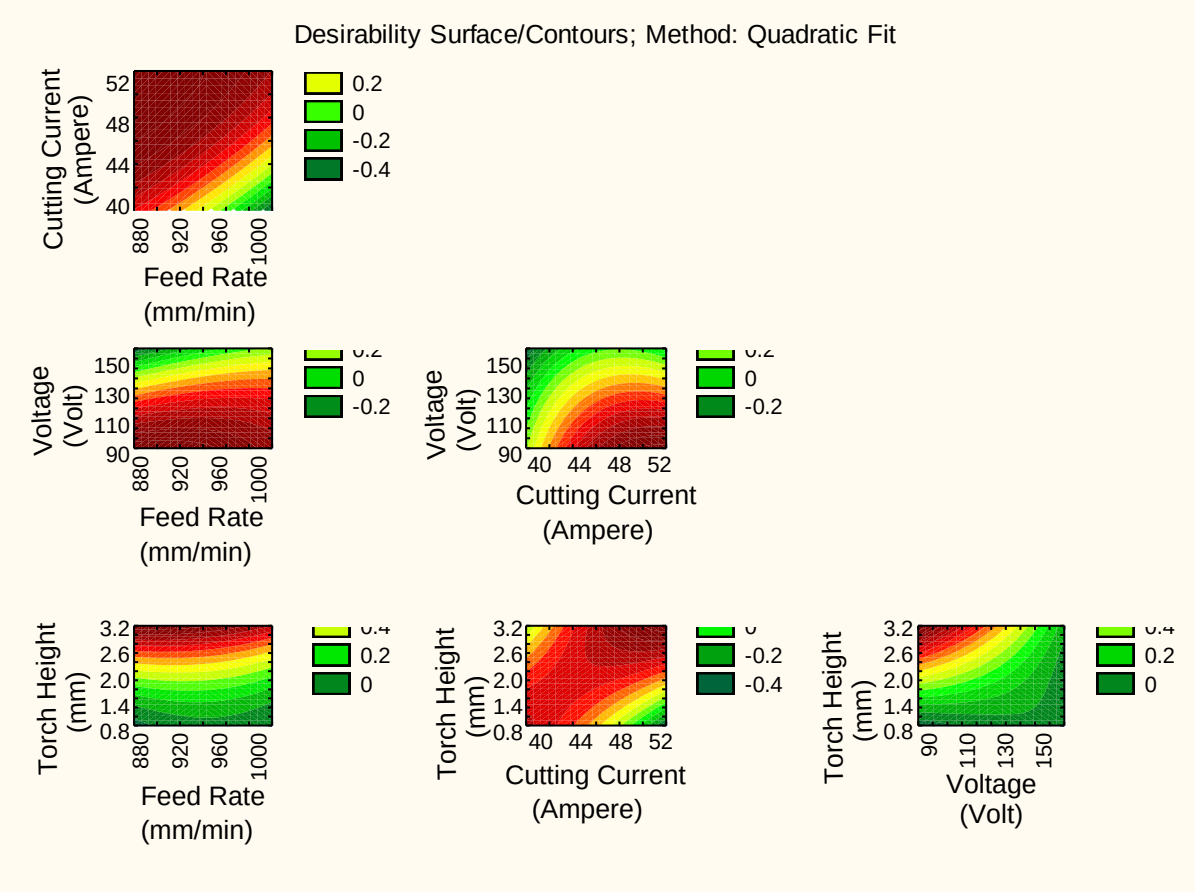

Fig. 116 Desirability 2D counter plot of dross

In Fig. 115-116, the 3D and 2D interaction plots of variables for dross were determined using the desirability profiles. Here, highest value of feed rate and voltage along with torch height gave minimum influence on dross whereas cutting current is opposite during cutting process by plasma arc.

5.2.1.5 For kerf:

In Table 35, the effect of estimated values of kerf was computed and tabulated. The ANOVA for kerf has been carried out firstly and its results are given in Table 36. Here, the block effect has also been considered because the levels of block are taken as one. Due to this variation in block, there is negligible amount of effect occurred in experiment. This effect is ignored for further calculation of optimization. The total degree of freedom for all

input factors is 29. From the Table 36, it is seen that the most of the terms have P-value less than 0.05 under the confidence interval of 95 %. Hence, these terms show significance within the experiment. In case of individual terms, only torch height has shown significance within the experiment. Pareto chart of effects of all factors on kerf response are shown in Fig. 117 and the results indicate that the linear form of torch height is the second most enhancing factor among all considered factors. The scatter plot between the observed and the predicted value of kerf of all 30 runs is shown in Fig. 118. It is concluded that there is a reasonable correlation between the measured and predicted values of kerf output. In Fig. 120, the histogram plot of predicted data of kerf with 95 % confidence interval of normal distribution is displayed. In Table 37, the model of estimated regression coefficients of the independent variable on the kerf is shown.

Table 35 Effect of Estimated Values for kerf

Factor	Effect	Std. Err.	T	P
Constant	2.728333	0.201400	13.54683	0.000000
A (mm/min)	-0.298333	0.201400	-1.48130	0.159227
A^2	0.193750	0.188393	1.02844	0.320043
B (Ampere)	-0.346667	0.201400	-1.72128	0.105752
B^2	0.136250	0.188393	0.72322	0.480669
C (Volt)	-0.030000	0.201400	-0.14896	0.883572
C^2	-0.081250	0.188393	-0.43128	0.672399
D (mm)	0.435000	0.201400	2.15988	0.047379
D^2	0.051250	0.188393	0.27204	0.789301
A×B	-0.452500	0.246664	-1.83448	0.086494
A×C	-0.105000	0.246664	-0.42568	0.676385
A×D	0.185000	0.246664	0.75001	0.464852
B×C	0.050000	0.246664	0.20271	0.842089
B×D	-0.055000	0.246664	-0.22298	0.826562
C×D	-0.177500	0.246664	-0.71960	0.482832

Table 36 ANOVA Table for Kerf

Factors	SS	DoF	MS	F	P
A (mm/min)	0.534017	1	0.534017	2.194238	0.159227
A^2	0.257411	1	0.257411	1.057683	0.320043
B (Ampere)	0.721067	1	0.721067	2.962814	0.105752
B^2	0.127296	1	0.127296	0.523052	0.480669
C (Volt)	0.005400	1	0.005400	0.022188	0.883572
C^2	0.045268	1	0.045268	0.186003	0.672399
D (mm)	1.135350	1	1.135350	4.665076	0.047379
D^2	0.018011	1	0.018011	0.074005	0.789301
A×B	0.819025	1	0.819025	3.365318	0.086494
A×C	0.044100	1	0.044100	0.181204	0.676385
A×D	0.136900	1	0.136900	0.562513	0.464852
B×C	0.010000	1	0.010000	0.041089	0.842089
B×D	0.012100	1	0.012100	0.049718	0.826562
C×D	0.126025	1	0.126025	0.517828	0.482832
Error	3.650583	15	0.243372		
Total SS	7.645217	29			

Table 37 Regression Coefficients of Kerf

Factor	Regression Coef.	Std. Err.	T	P
Constant	25.33838	167.5065	0.15127	0.881780
A (mm/min)	-0.15097	0.2995	-0.50414	0.621489
A^2	0.00015	0.0002	1.02844	0.320043
B (Ampere)	2.42007	2.2953	1.05434	0.308417
B^2	0.01090	0.0151	0.72322	0.480669
C (Volt)	0.12379	0.2636	0.46957	0.645414
C^2	-0.00010	0.0002	-0.43128	0.672399
D (mm)	-5.07050	10.5023	-0.48280	0.636210
D^2	0.10250	0.3768	0.27204	0.789301
A×B	-0.00362	0.0020	-1.83448	0.086494
A×C	-0.00011	0.0002	-0.42568	0.676385
A×D	0.00740	0.0099	0.75001	0.464852
B×C	0.00050	0.0025	0.20271	0.842089
B×D	-0.02200	0.0987	-0.22298	0.826562
C×D	-0.00887	0.0123	-0.71960	0.482832

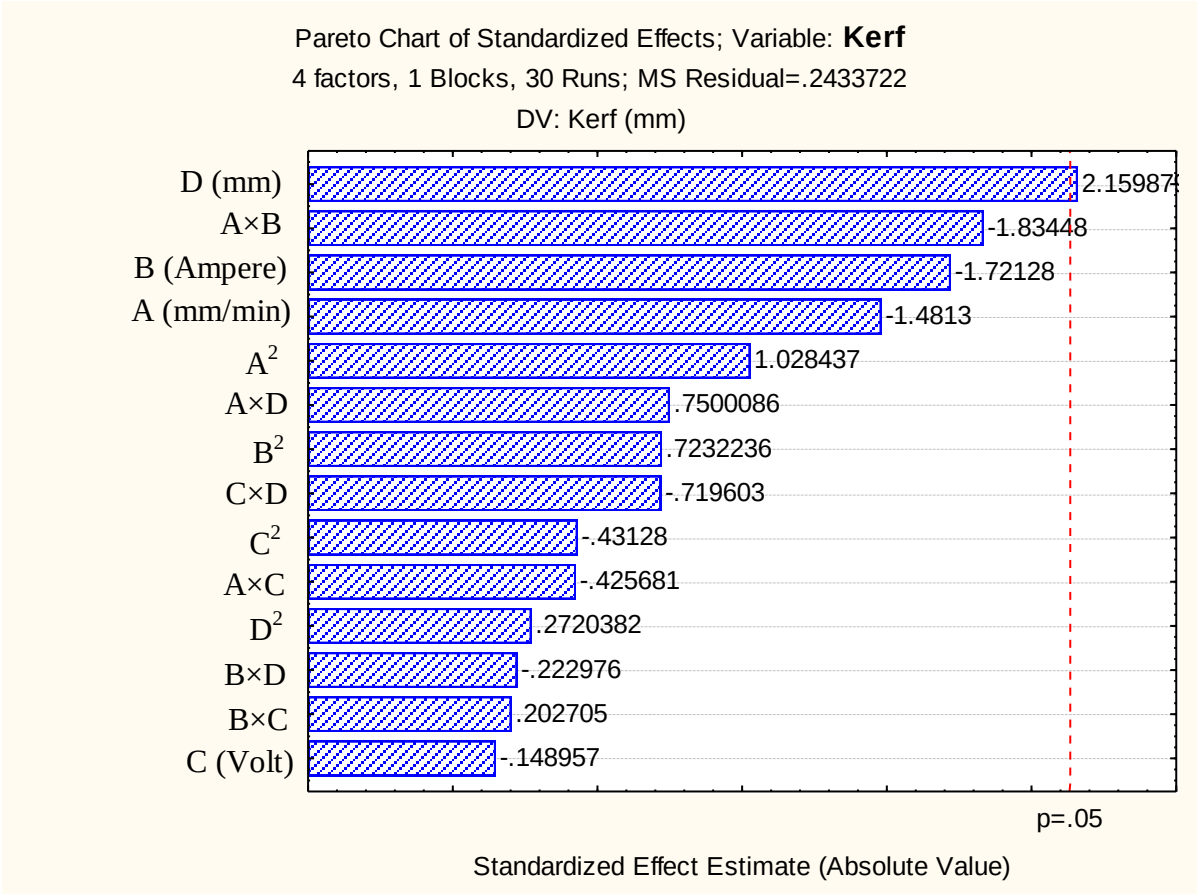

Fig. 117 Pareto chart of standardized effect of factors on kerf

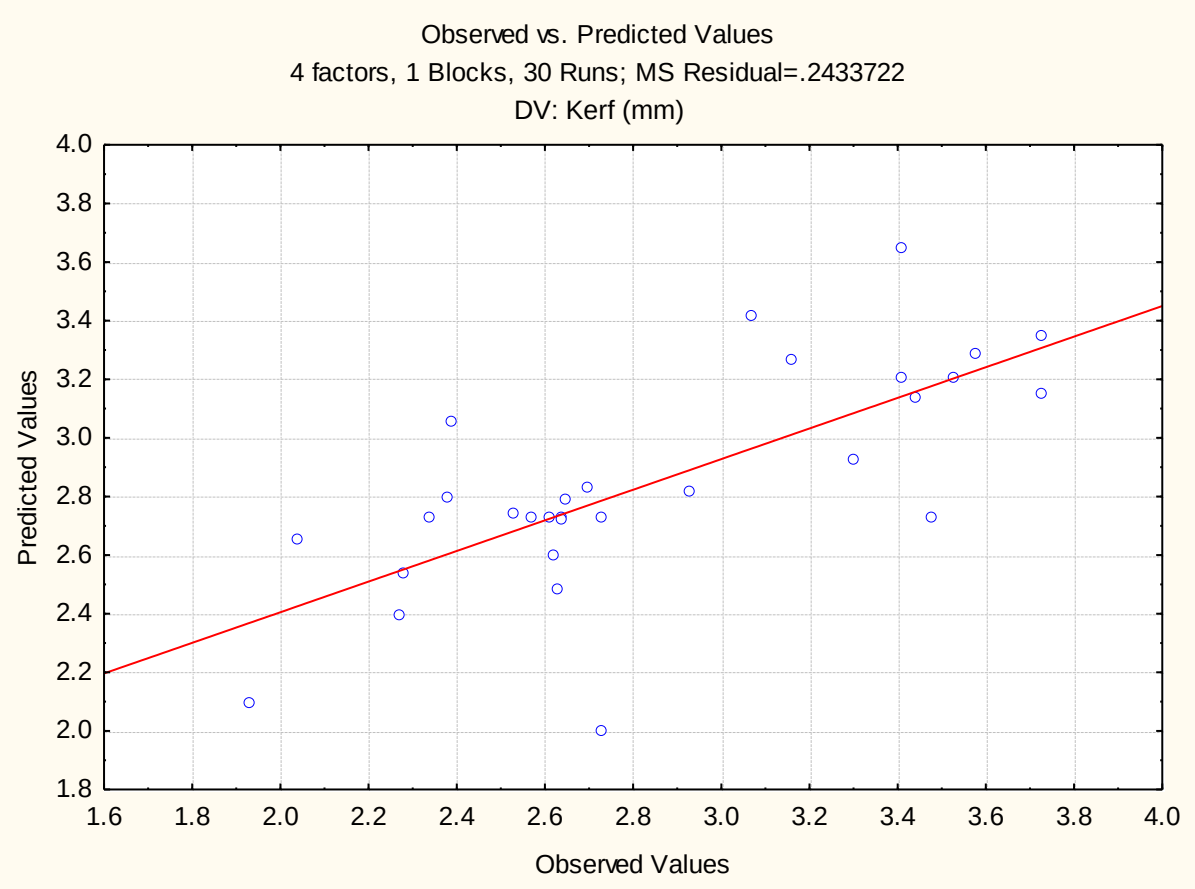

Fig. 118 Plot of observed vs. predicted values of kerf

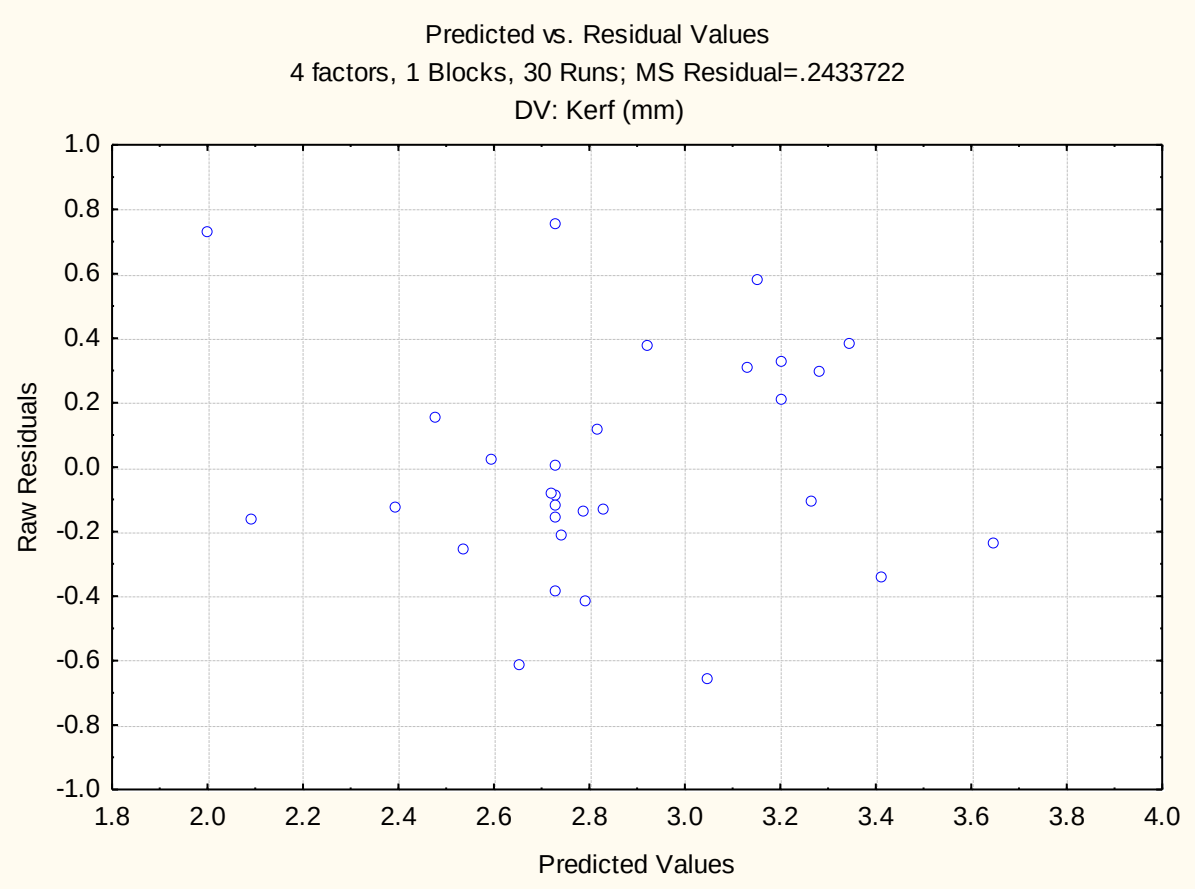

Fig. 119 Plot of predicted vs. residual values of kerf

From the Fig. 119, no standard pattern is formed in the plot of predicted vs. residual values which show the adequacy of the fitted model for kerf.

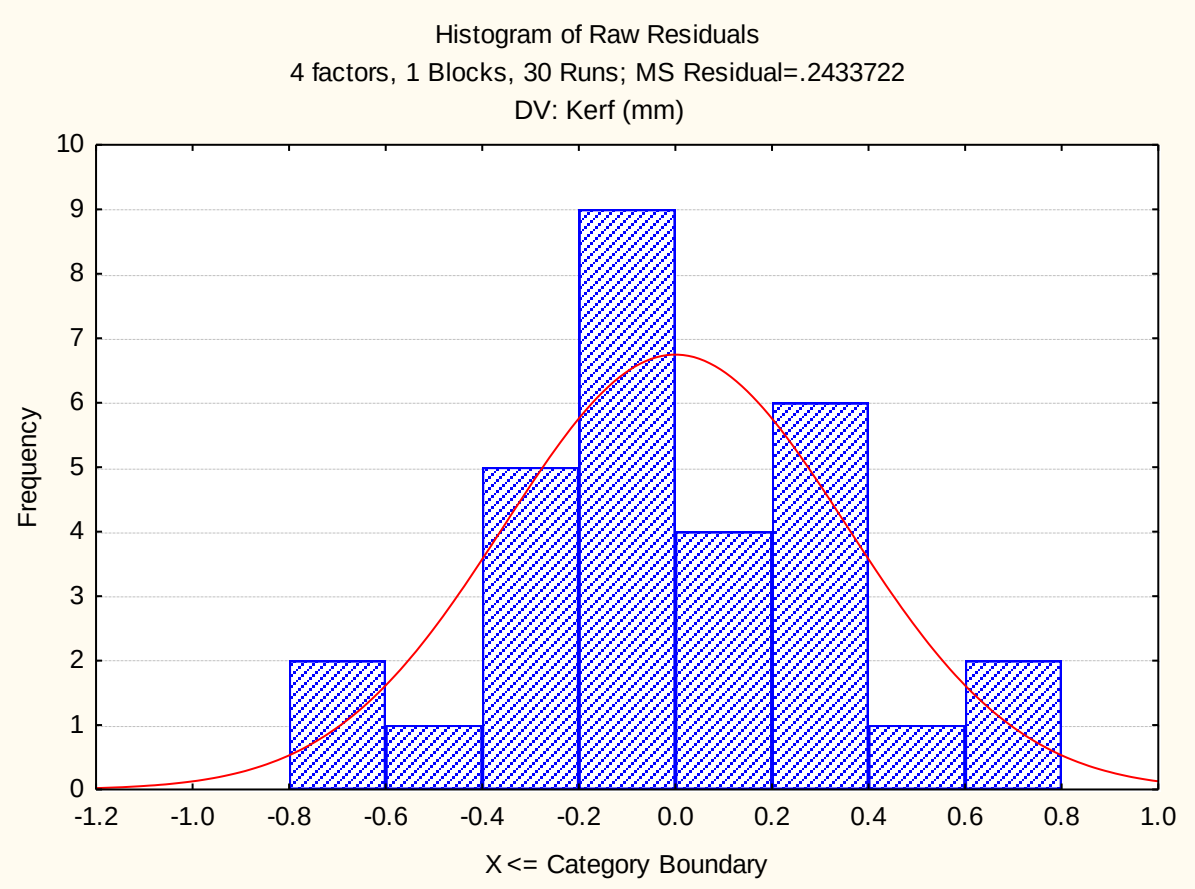

Fig. 120 Histogram plot of predicted values of kerf

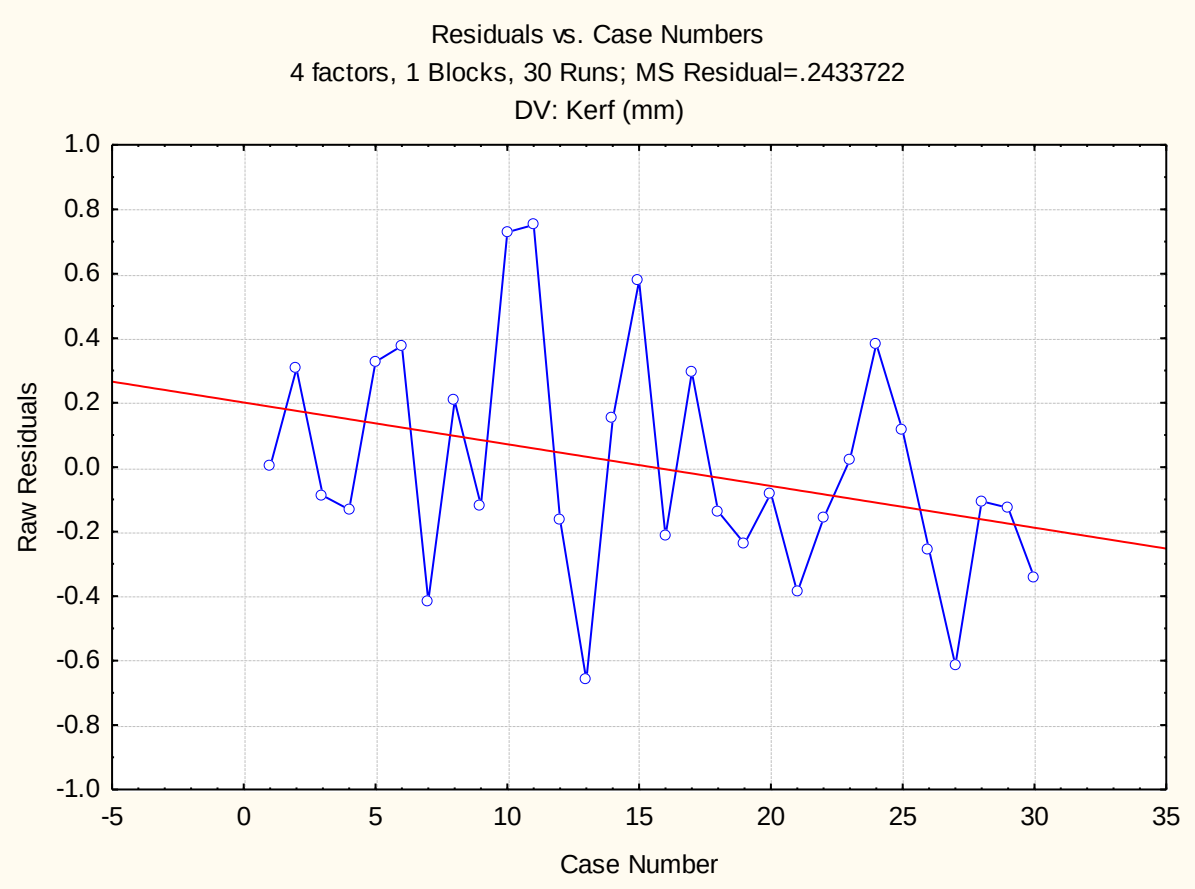

Fig. 121 Plot of residuals vs. case numbers values of kerf

From the Fig. 121, it is evident that the highest kerf value among all experimental runs is by the run number 11. The red line indicates that the value of kerf decreases with increase in run order.

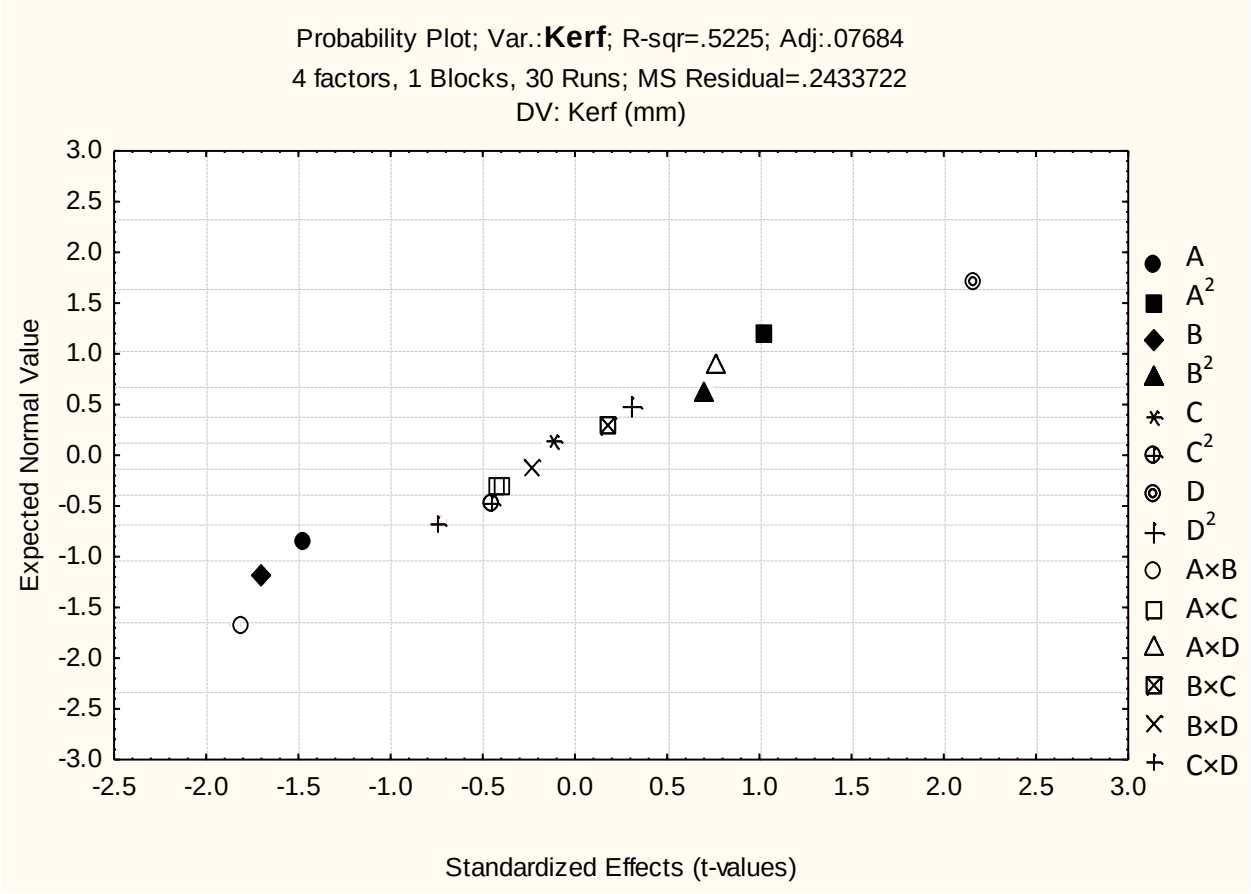

Fig. 122 Probability plot of kerf

The normal probability plot of kerf corresponding to each regression terms is plotted in Fig. 122.

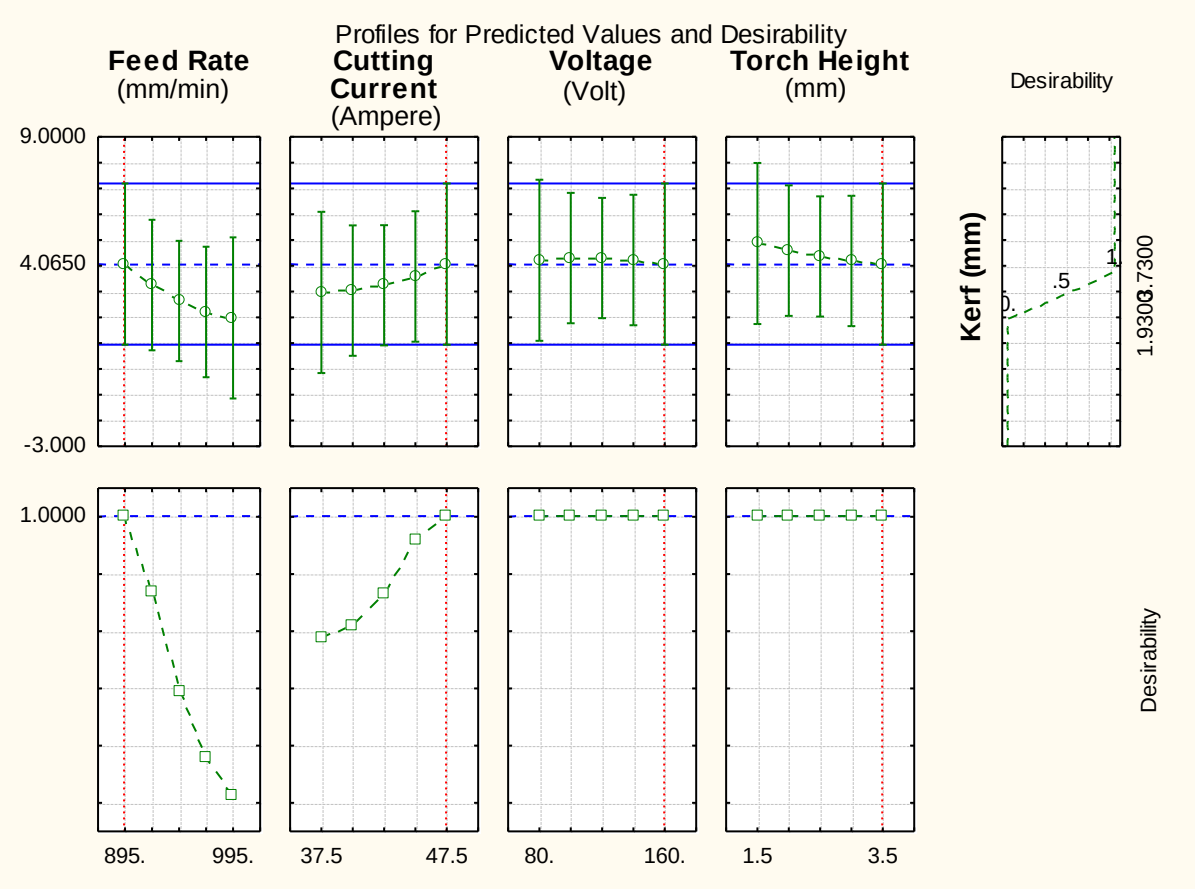

Fig. 123 Profile plot of predicted values and desirability of kerf

The method of desirability function helped to get optimum value of kerf response which was fitted by the quadratic fit model. The level of variable giving the highest desirability i.e., 1.0000 was considered as optimum level. In Fig. 123, the optimized levels of variables (A, B, C and D) were determined using the desirability profiles. The predicted values of responses and desirability function with red dotted lines are displayed in the same figure i.e. Fig. 123.

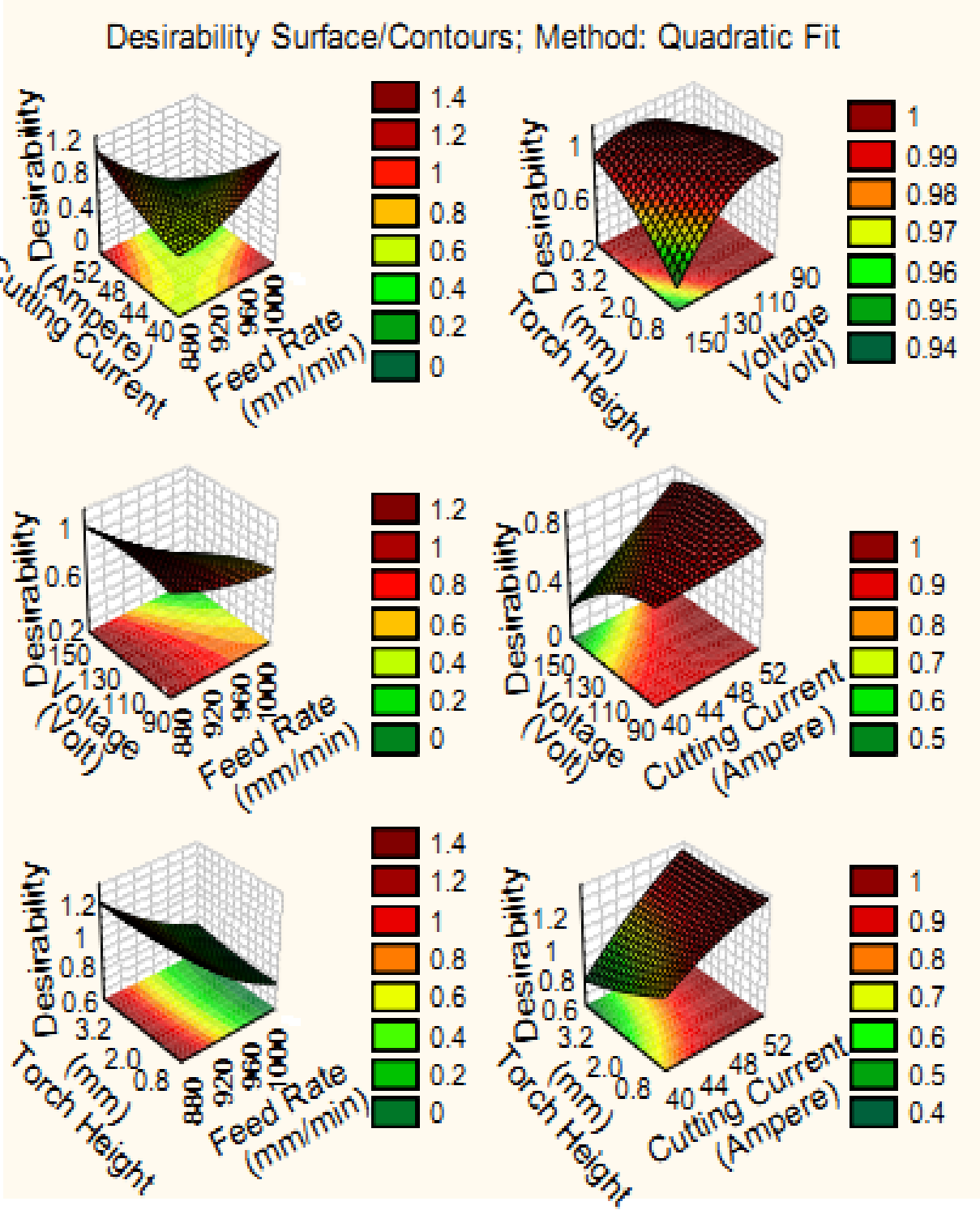

Fig. 124 Desirability 3D surface plot of kerf

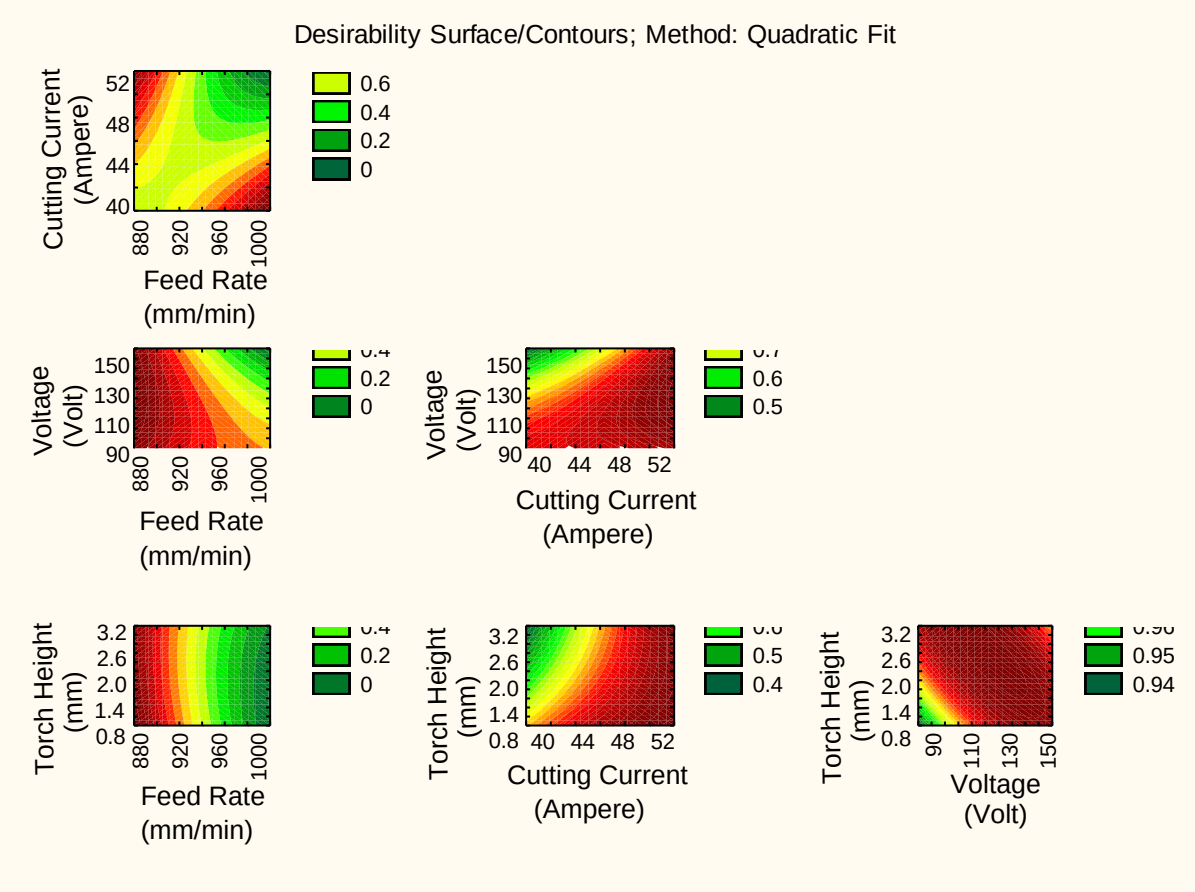

Fig. 125 Desirability 2D counter plot of kerf

The interaction plots in 3D and 2D version of input variables on kerf response were found out using the desirability profiles that are shown in Fig. 124-125 respectively. Here, only voltage parameter gave red area with raising its value that means the voltage should be minimized for required minimum kerf width.

5.2.2 Hybrid approach

In this hybrid approach i.e., Grey PCA, all values of responses are normalized in between 0 and 1 as per the higher the better and lower the better criteria according to the corresponding problem. The computed normalized value of each response is recorded in Table 38. Then, the value of deviation sequences for corresponding outputs are calculated and tabulated in Table 39. The Eigen values and vectors are determined to check the

correlation among output responses of PAC operation. The values of Eigen are tabulated in Table 40 and similarly the values of Eigen vectors are recorded in Table 41 for each principal component. The grey relational coefficients are computed for each response and lastly computed the overall grey relational grade by averaging the grey coefficients for each run order. The grey relational coefficients and overall grey relational grade are tabulated in Table 42. The ANOVA is carried out for the multi-objective problem of Grey based PCA approach and the obtained results are tabulated Table 43 in and Table 44. The regression coefficients of GRG are recorded in Table 45.

Table 38 Normalized Values for Output Response

MRR (mm^3/min)	SR (µm)	Chamfer (mm)	Dross (mm^2)	Kerf (mm)
0.699113	0.308974	0.144330	0.651316	0.555556
0.355736	0.558333	0.989691	0.961623	0.161111
0.947715	0.444658	0.463918	0.000000	0.605556
0.547420	1.000000	0.567010	0.582237	0.572222
0.930838	0.025641	0.092784	0.143640	0.111111
0.772074	0.656838	1.000000	0.281798	0.238889
0.298399	0.208547	0.948454	0.578947	0.750000
0.689192	0.066239	0.340206	0.212719	0.177778
0.872785	0.459188	0.463918	0.115132	0.622222
1.000004	0.866239	0.144330	1.000000	0.555556
-1.1E-05	0.750855	0.752577	0.720395	0.138889
0.331442	0.199359	0.515464	0.858553	1.000000
0.322579	0.000000	0.402062	0.549342	0.744444
0.996881	0.425000	0.948454	0.473684	0.611111
0.163395	0.791026	0.360825	0.750000	0.000000
0.738867	0.192735	0.896907	0.354167	0.666667
0.904185	0.812393	0.453608	0.858553	0.083333
0.443912	0.342094	0.917526	0.344298	0.600000
0.685065	0.028205	0.350515	0.629386	0.177778
0.752308	0.377137	0.608247	0.471491	0.605556
0.386207	0.210684	0.000000	0.109649	0.772222
0.912008	0.821368	0.298969	0.549342	0.644444
0.512474	0.617094	0.515464	0.125000	0.616667
0.920385	0.433120	0.340206	0.059211	0.000000
0.517523	0.120726	0.195876	0.403509	0.444444
0.939502	0.983974	0.041237	0.115132	0.805556
0.606940	0.587393	0.556701	0.646930	0.938889
0.284369	0.598932	0.309278	0.252193	0.316667
0.913984	0.204701	0.752577	0.414474	0.811111
0.946553	0.242949	0.463918	0.114035	0.366667

Table 39 Deviation Sequences for Output Responses of PAC

MRR (mm^3/min)	SR (µm)	Chamfer (mm)	Dross (mm^2)	Kerf (mm)
0.300887	0.691026	0.855670	0.348684	0.444444
0.644264	0.441667	0.010309	0.038377	0.838889
0.052285	0.555342	0.536082	1.000000	0.394444
0.452580	0.000000	0.432990	0.417763	0.427778
0.069162	0.974359	0.907216	0.856360	0.888889
0.227926	0.343162	0.000000	0.718202	0.761111
0.701601	0.791453	0.051546	0.421053	0.250000
0.310808	0.933761	0.659794	0.787281	0.822222
0.127215	0.540812	0.536082	0.884868	0.377778
-3.8E-06	0.133761	0.855670	0.000000	0.444444
1.000011	0.249145	0.247423	0.279605	0.861111
0.668558	0.800641	0.484536	0.141447	0.000000
0.677421	1.000000	0.597938	0.450658	0.255556
0.003119	0.575000	0.051546	0.526316	0.388889
0.836605	0.208974	0.639175	0.250000	1.000000
0.261133	0.807265	0.103093	0.645833	0.333333
0.095815	0.187607	0.546392	0.141447	0.916667
0.556088	0.657906	0.082474	0.655702	0.400000
0.314935	0.971795	0.649485	0.370614	0.822222
0.247692	0.622863	0.391753	0.528509	0.394444
0.613793	0.789316	1.000000	0.890351	0.227778
0.087992	0.178632	0.701031	0.450658	0.355556
0.487526	0.382906	0.484536	0.875000	0.383333
0.079615	0.566880	0.659794	0.940789	1.000000
0.482477	0.879274	0.804124	0.596491	0.555556
0.060498	0.016026	0.958763	0.884868	0.194444
0.393060	0.412607	0.443299	0.353070	0.061111
0.715631	0.401068	0.690722	0.747807	0.683333
0.086016	0.795299	0.247423	0.585526	0.188889
0.053447	0.757051	0.536082	0.885965	0.633333

Table 40 Eigenvalues and Explained Variation for Principal Components

Principal components	Eigen value	Explained variations (%)	Cumulative Eigen value	Cumulative %
First	1.517185	30.34369	1.517185	30.3437
Second	1.131617	22.63233	2.648801	52.9760
Third	0.963514	19.27028	3.612315	72.2463
Fourth	0.822231	16.44462	4.434546	88.6909
Fifth	0.565454	11.30908	5.000000	100.0000

Table 41 Eigenvectors for Principal Components and Contribution

Variable	Factor 1	Factor 2	Factor 3	Factor 4	Factor 5
MRR (mm^3/min)	0.545948	-0.275111	0.380823	0.442568	-0.534193
SR (µm)	-0.283886	-0.677908	0.492808	0.062001	0.461677
Chamfer (mm)	-0.433712	0.392407	0.104119	0.799239	0.091031
Dross (mm^2)	-0.651759	-0.119488	0.142578	-0.234208	-0.696958
Kerf (mm)	0.091940	0.544513	0.762197	-0.326579	0.086339

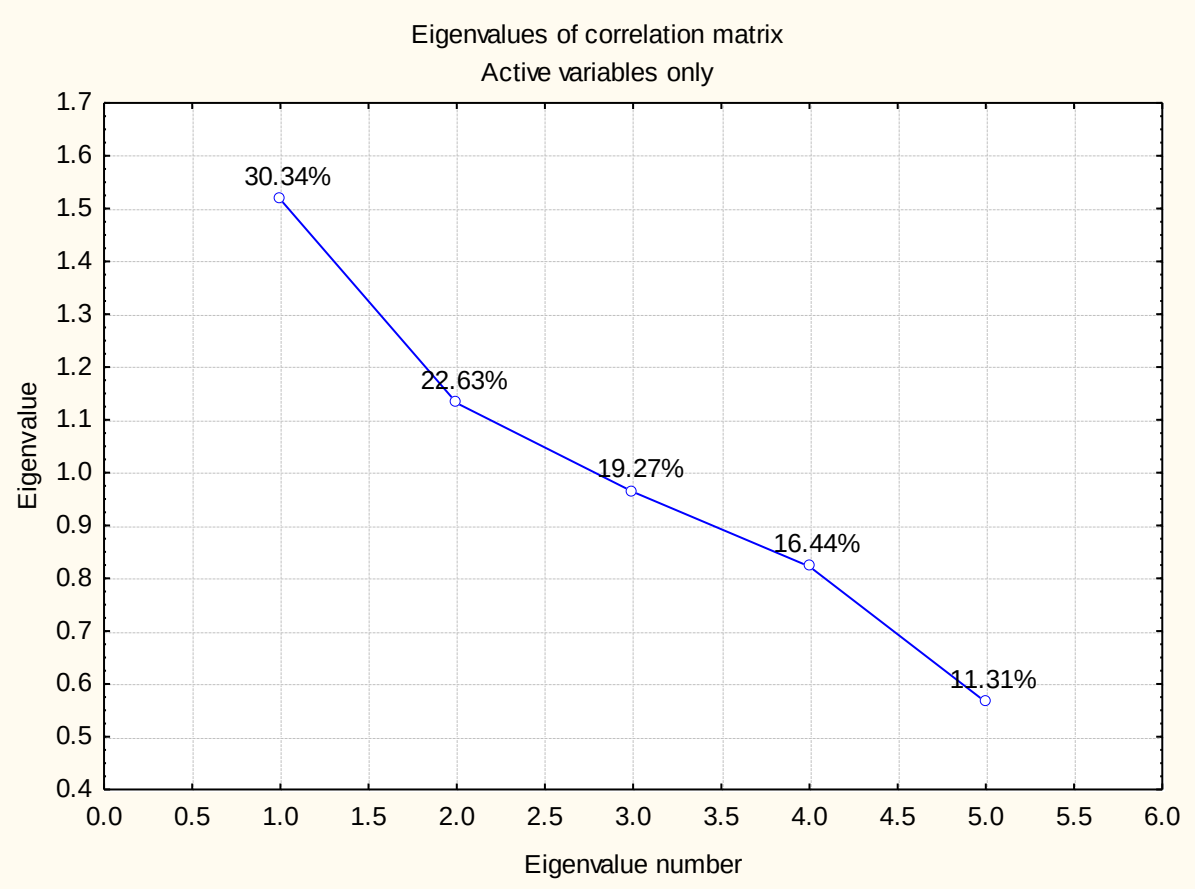

Fig. 126 Plot of Eigen values of correlation matrix for second phase

The Fig. 126 shows the variation in percentage of Eigen values in first phase experimentation.

Table 42 Grey Relational Coefficient and Grade of Output Responses of PAC

Grey relational coefficient 1	Grey relational coefficient 2	Grey relational coefficient 3	Grey relational coefficient 4	Grey relational coefficient 5	Overall grey relational grade
0.624308	0.419806	0.368821	0.589147	0.529412	0.506299
0.436962	0.530973	0.979798	0.928717	0.373444	0.649979
0.905329	0.473780	0.482587	0.333333	0.559006	0.550807
0.524890	1.000000	0.535912	0.544803	0.538922	0.628905
0.878484	0.339130	0.355311	0.368634	0.360000	0.460312
0.686883	0.593006	1.000000	0.410441	0.396476	0.617361
0.416111	0.387161	0.906542	0.542857	0.666667	0.583868
0.616669	0.348733	0.431111	0.388416	0.378151	0.432616
0.797175	0.480394	0.482587	0.361045	0.569620	0.538164
1.000008	0.788941	0.368821	1.000000	0.529412	0.737436
0.333331	0.667427	0.668966	0.641350	0.367347	0.535684
0.427878	0.384426	0.507853	0.779487	1.000000	0.619929
0.424657	0.333333	0.455399	0.525952	0.661765	0.480221
0.993802	0.465116	0.906542	0.487179	0.562500	0.683028
0.374082	0.705244	0.438914	0.666667	0.333333	0.503648
0.656916	0.382478	0.829060	0.436364	0.600000	0.580963
0.839186	0.727160	0.477833	0.779487	0.352941	0.635321
0.473445	0.431814	0.858407	0.432638	0.555556	0.550372
0.613546	0.339721	0.434978	0.574307	0.378151	0.468141
0.668725	0.445290	0.560694	0.486141	0.559006	0.543971
0.448917	0.387802	0.333333	0.359621	0.687023	0.443339
0.850352	0.736776	0.416309	0.525952	0.584416	0.622761
0.506316	0.566312	0.507853	0.363636	0.566038	0.502031
0.862642	0.468656	0.431111	0.347032	0.333333	0.488555
0.508918	0.362510	0.383399	0.456000	0.473684	0.436902
0.892063	0.968944	0.342756	0.361045	0.720000	0.656962
0.559873	0.547881	0.530055	0.586118	0.891089	0.623003
0.411309	0.554897	0.419913	0.400703	0.422535	0.441871
0.853219	0.386011	0.668966	0.460606	0.725806	0.618922
0.903429	0.397756	0.482587	0.360759	0.441176	0.517142

Table 43 Effect of Estimated Values of Responses of Pac

Factor	Effect	Std. Err.	T	P
Constant	0.532842	0.025084	21.24266	0.000000
A (mm/min)	0.031797	0.025084	1.26765	0.224250
A^2	-0.015300	0.023464	-0.65207	0.524221
B (Ampere)	0.063820	0.025084	2.54427	0.022451
B^2	0.024079	0.023464	1.02621	0.321056
C (Volt)	0.051126	0.025084	2.03821	0.059563
C^2	0.035937	0.023464	1.53162	0.146432
D (mm)	-0.086806	0.025084	-3.46067	0.003495
D^2	0.011387	0.023464	0.48532	0.634459
A×B	0.033796	0.030721	1.10011	0.288627
A×C	-0.008395	0.030721	-0.27328	0.788367
A×D	0.054909	0.030721	1.78733	0.094103
B×C	-0.018790	0.030721	-0.61164	0.549934
B×D	-0.023052	0.030721	-0.75037	0.464639
C×D	0.052091	0.030721	1.69561	0.110611

Table 44 ANOVA Table for GRG

Factors	SS	DoF	MS	F	P
A (mm/min)	0.006066	1	0.006066	1.60693	0.224250
A^2	0.001605	1	0.001605	0.42520	0.524221
B (Ampere)	0.024438	1	0.024438	6.47333	0.022451
B^2	0.003976	1	0.003976	1.05312	0.321056
C (Volt)	0.015683	1	0.015683	4.15431	0.059563
C^2	0.008856	1	0.008856	2.34587	0.146432
D (mm)	0.045212	1	0.045212	11.97620	0.003495
D^2	0.000889	1	0.000889	0.23554	0.634459
A×B	0.004569	1	0.004569	1.21024	0.288627
A×C	0.000282	1	0.000282	0.07468	0.788367
A×D	0.012060	1	0.012060	3.19454	0.094103
B×C	0.001412	1	0.001412	0.37411	0.549934
B×D	0.002126	1	0.002126	0.56306	0.464639
C×D	0.010854	1	0.010854	2.87509	0.110611
Error	0.056627	15	0.003775		
Total SS	0.194690	29			

Table 45 Regression Coefficients of GRG

Factor	Regression Coef.	Std. Err.	T	P
Constant	6.73001	20.86227	0.32259	0.751457
A (mm/min)	0.00780	0.03730	0.20901	0.837252
A^2	-0.00001	0.00002	-0.65207	0.524221
B (Ampere)	-0.36087	0.28588	-1.26234	0.226102
B^2	0.00193	0.00188	1.02621	0.321056
C (Volt)	-0.00009	0.03283	-0.00289	0.997731
C^2	0.00004	0.00003	1.53162	0.146432
D (mm)	-2.19688	1.30802	-1.67954	0.113749
D^2	0.02277	0.04693	0.48532	0.634459
A×B	0.00027	0.00025	1.10011	0.288627
A×C	-0.00001	0.00003	-0.27328	0.788367
A×D	0.00220	0.00123	1.78733	0.094103
B×C	-0.00019	0.00031	-0.61164	0.549934
B×D	-0.00922	0.01229	-0.75037	0.464639
C×D	0.00260	0.00154	1.69561	0.110611

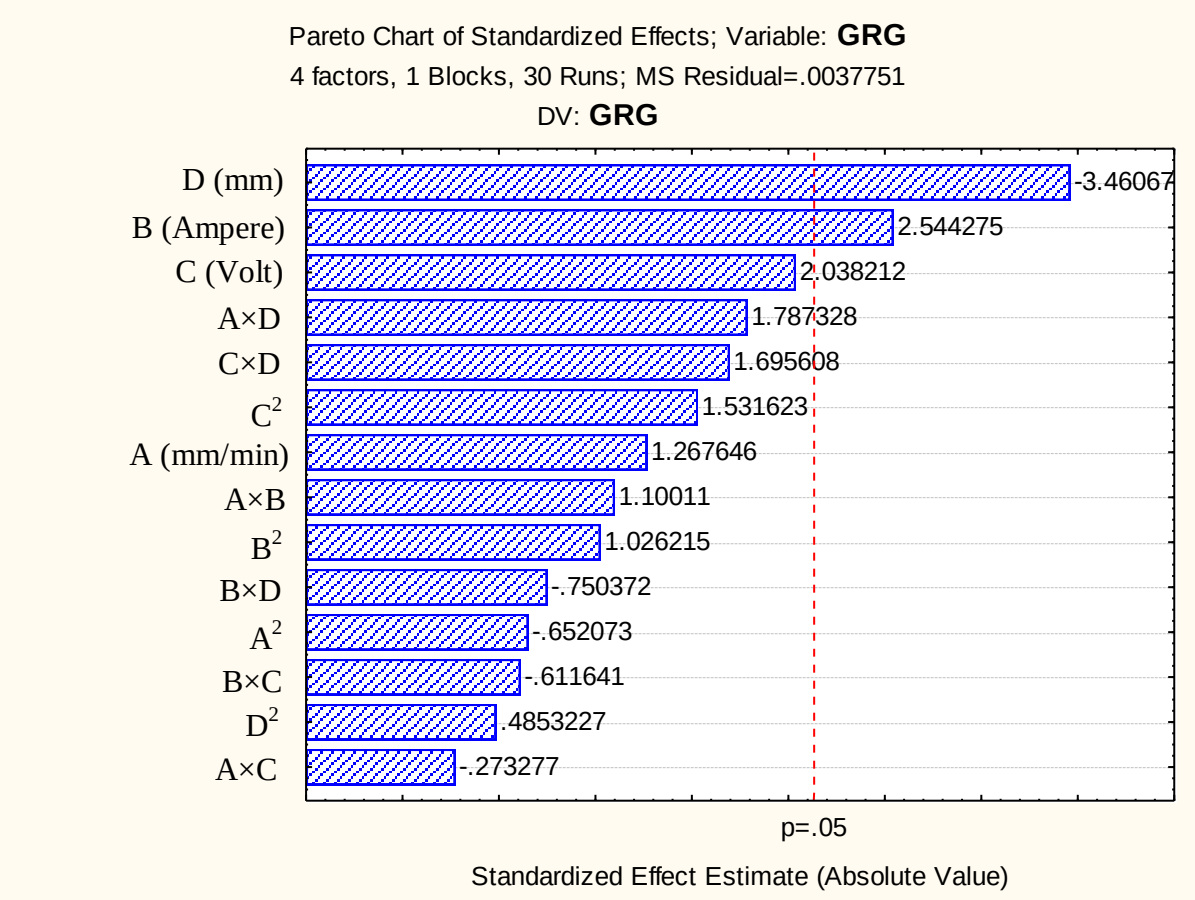

Fig. 127 Pareto chart of standardized effect of factors on GRG

According to Pareto chart of GRG response i.e. in Fig. 127, the torch height factor with linear form had the most significant influence on the response of plasma arc cutting procedure.

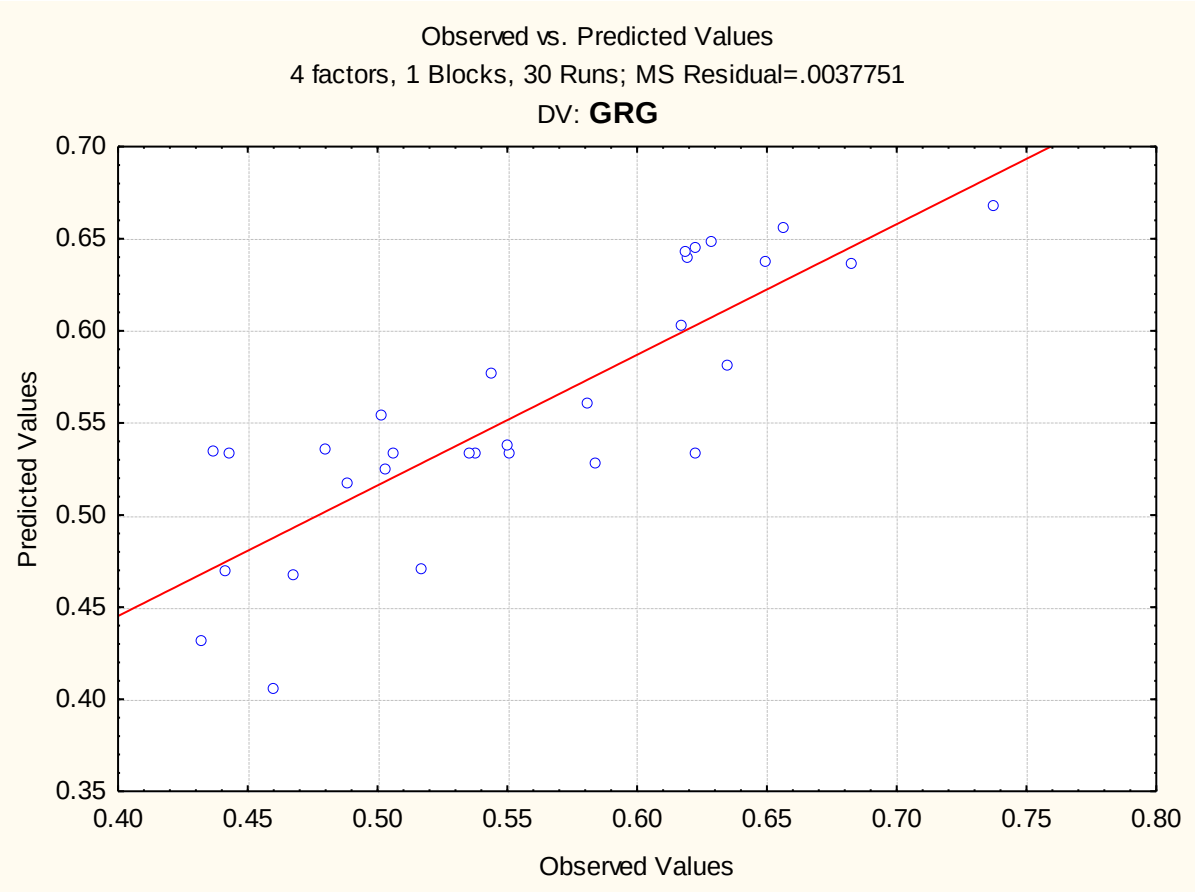

Fig. 128 Plot of observed vs. predicted values of GRG

The scatter plot between the observed and the predicted value of plasma cut responses of all 27 runs is shown in Fig. 128. The comparison between each of the observed values with the predicted value is shown in those plots which are calculated from the developed model. Here, the most of the points lie on the normal line of fitted values except the plot of GRG, because the uniformity lacks in the middle region. From this result it can be revealed that the response model shows good fit to experimental data, because the relationship between the actual and the predicted GRG is linear.

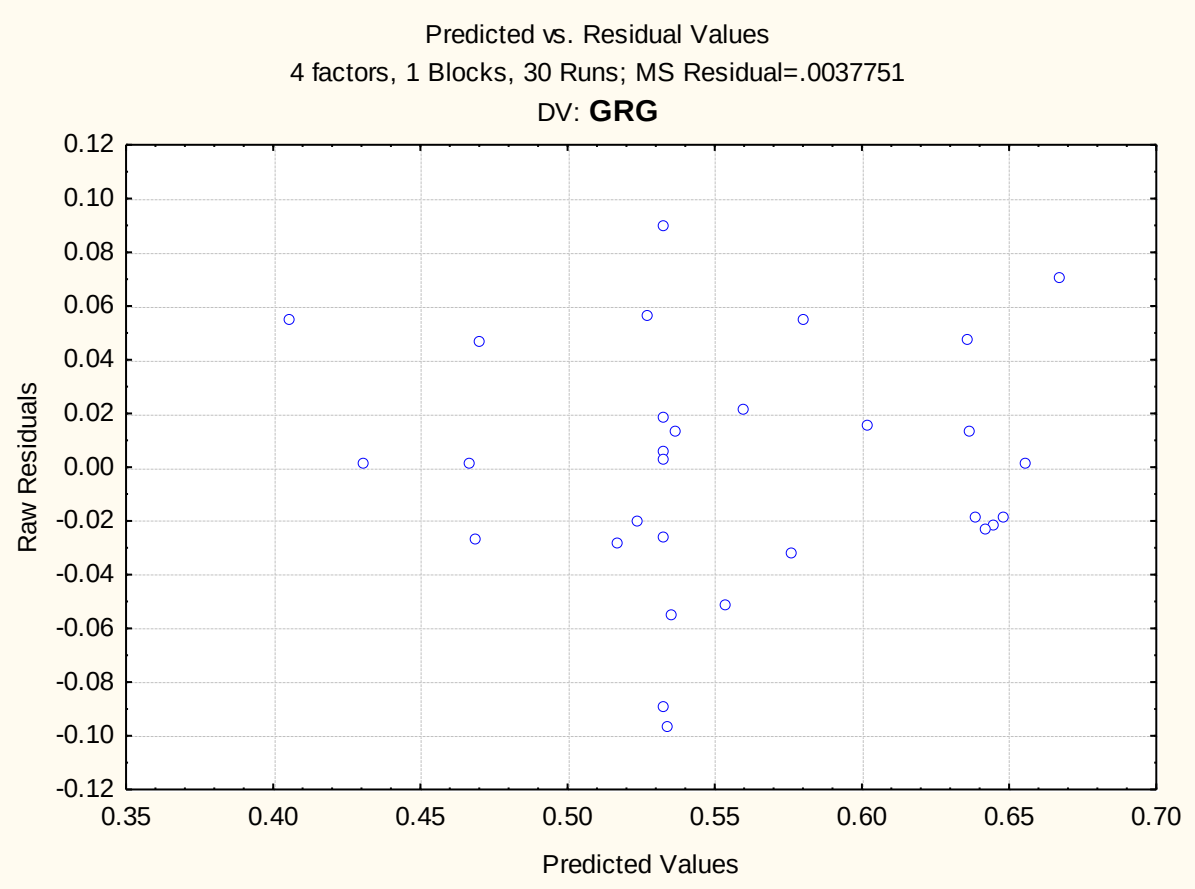

Fig. 129 Plot of predicted vs. residual values of GRG

From the Fig. 129, no standard pattern is formed in the plot of predicted vs. residual values which show the adequacy of the fitted model for GRG.

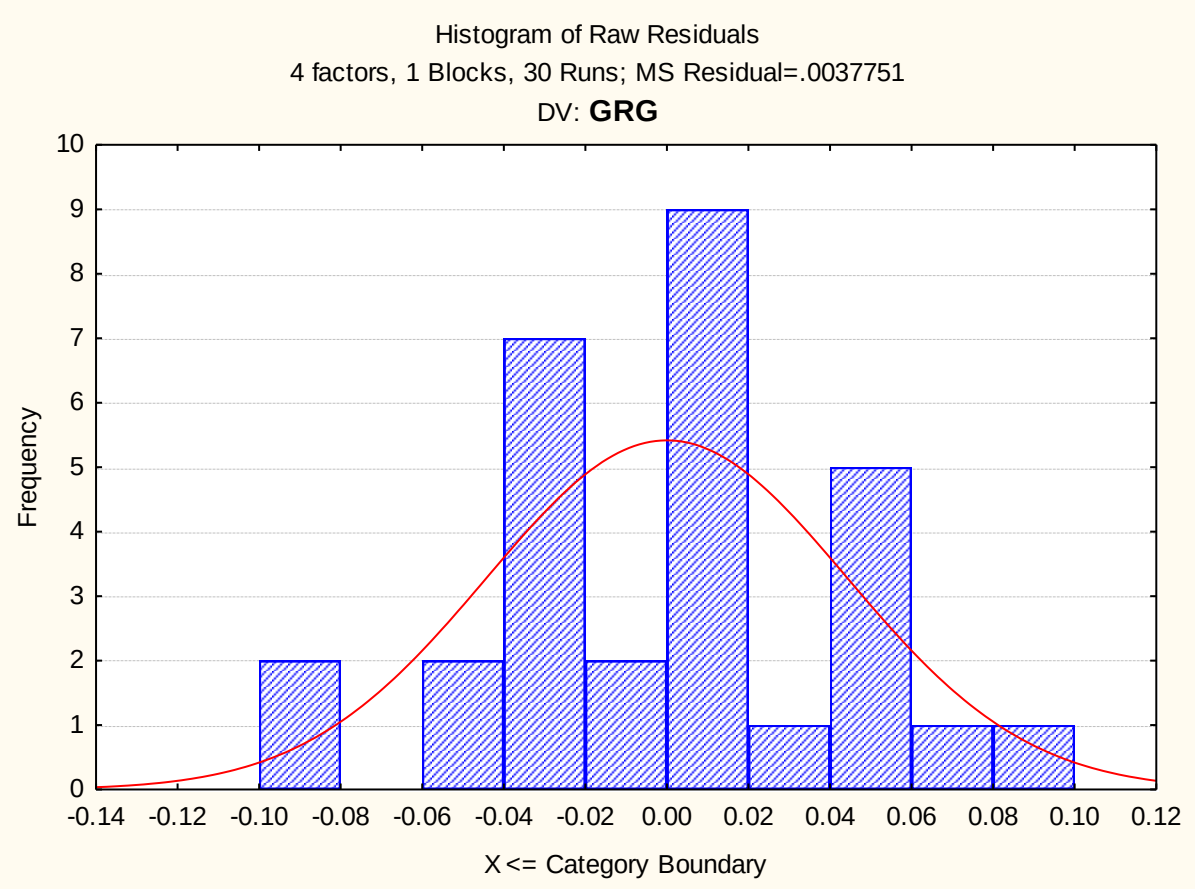

Fig. 130 Histogram plot of predicted values of GRG

The perfect normal probability distribution of the histogram plot of residuals for GRG response is shown in Fig. 130. From the above graphs, it is seen that the normal probability created in the histogram plot of residual for GRG is tolerable.

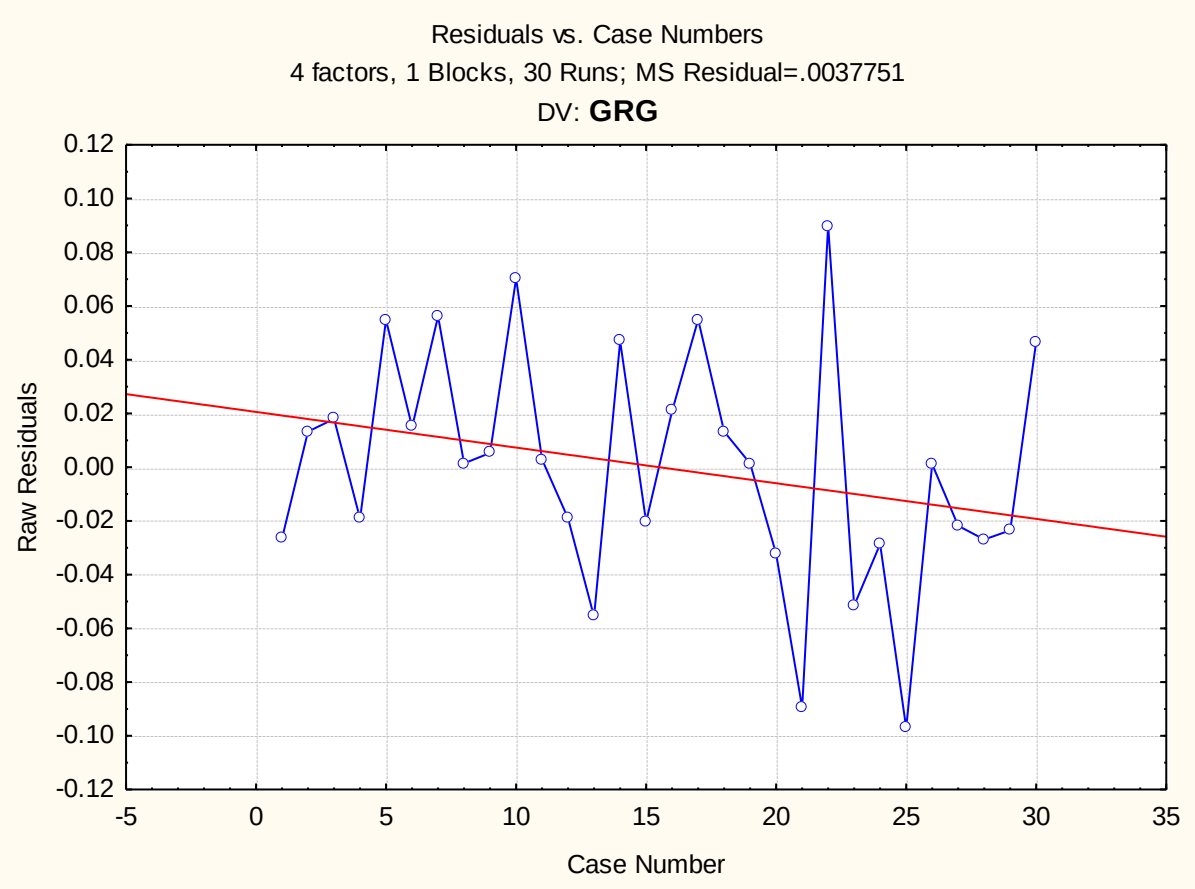

Fig. 131 Plot of residuals vs. case numbers values of GRG

From the Fig. 131, it is evident that the highest GRG value among all experimental runs is by the run number 22. The red line indicates that the value of GRG increases with increase in run order.

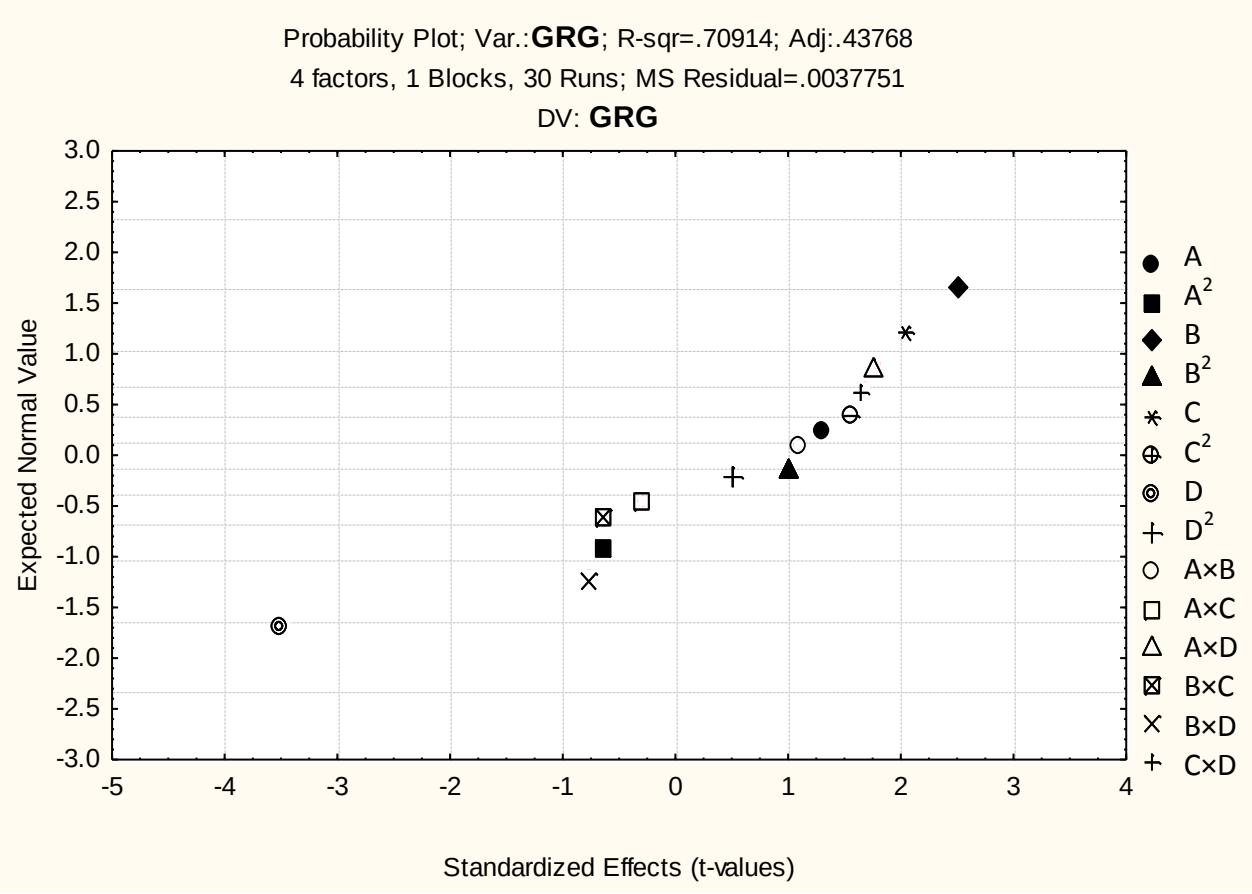

Fig. 132 Probability plot of GRG

The normal probability plot of GRG corresponding to each regression terms is plotted in Fig. 132.

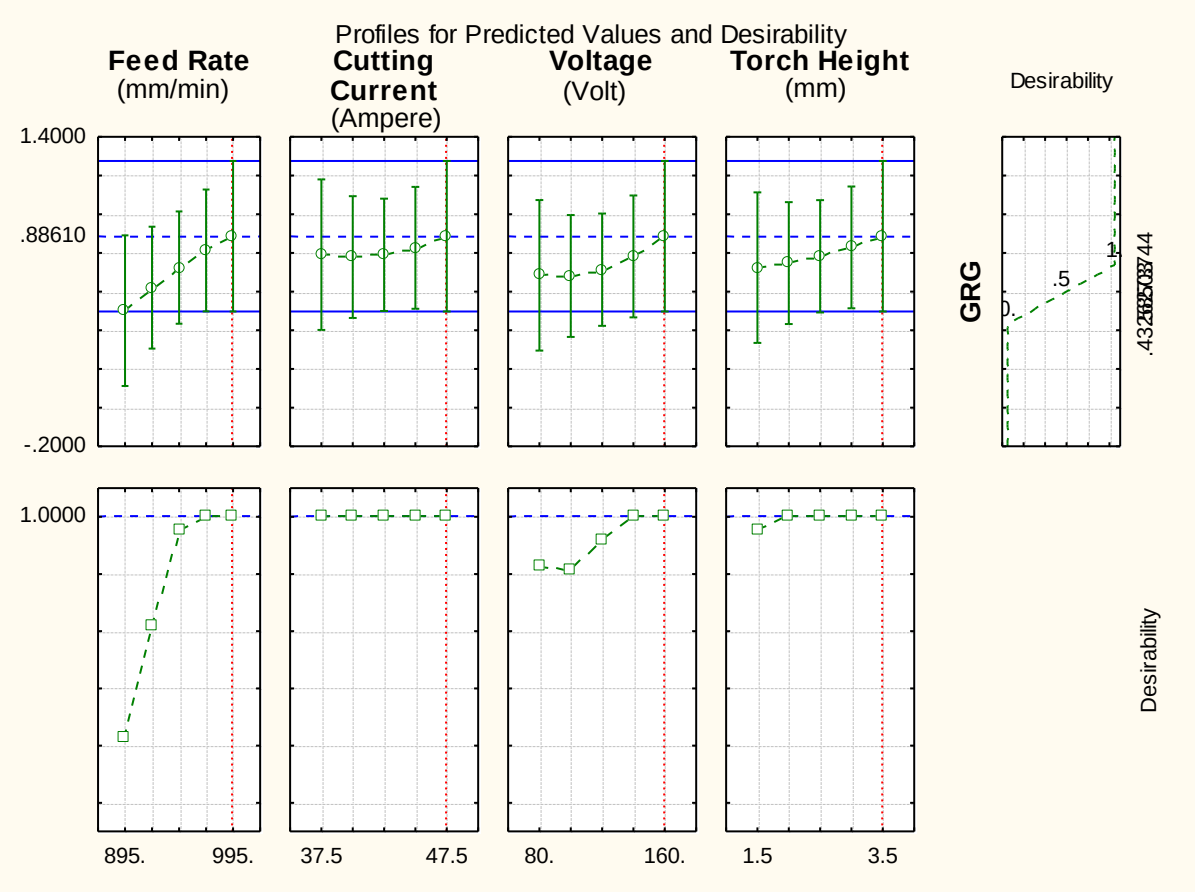

Fig. 133 Profile plot of predicted values and desirability of GRG

The methodology of desirability function facilitated to determine optimum GRG response which was fitted by the quadratic fit model. The level of variable giving the highest desirability i.e., 1.0000 was considered as optimum level. The optimized levels of variables (A, B, C and D) were determined using the desirability profiles. The predicted values of responses and desirability function with red dotted lines that are demonstrated in Fig. 133.

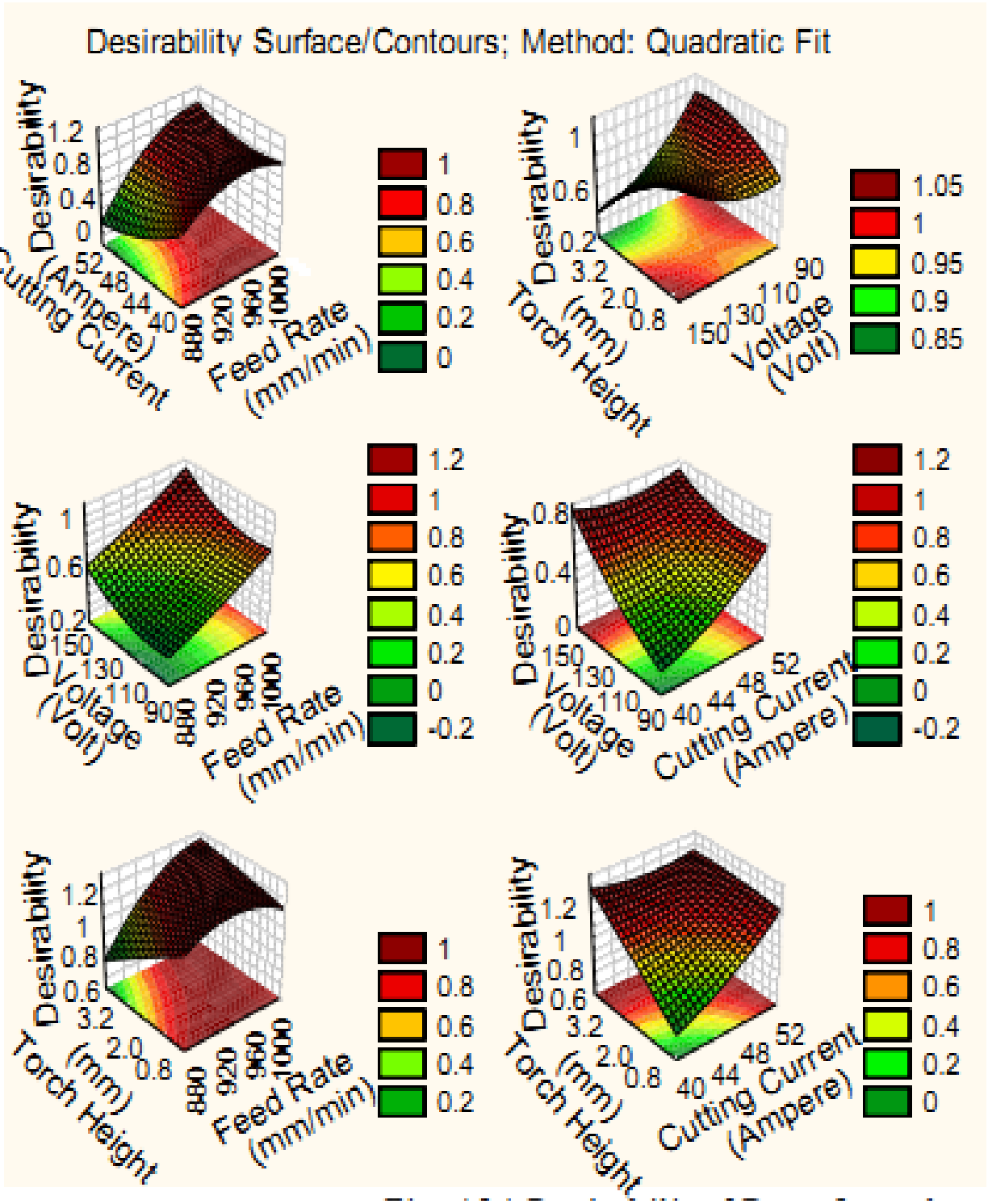

Fig. 134 Desirability 3D surface plot of GRG

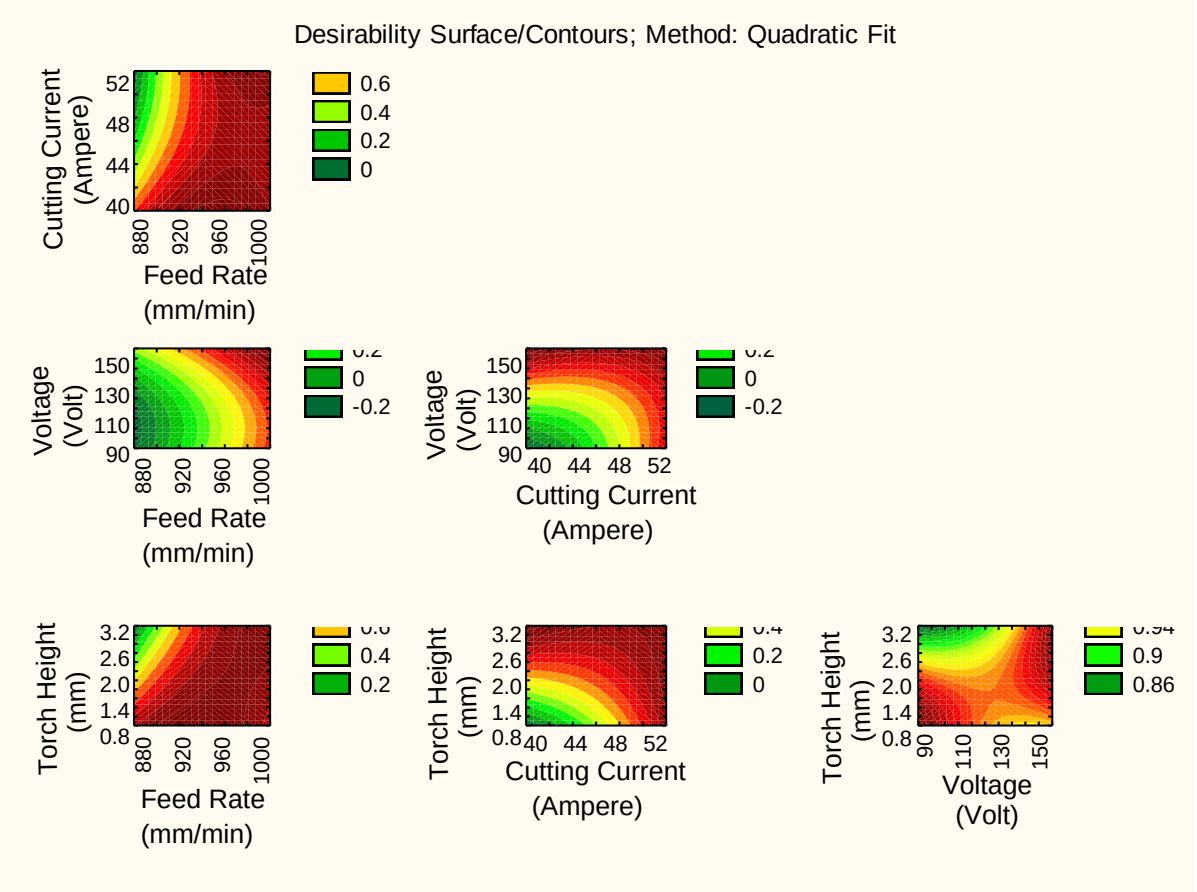

Fig. 135 Desirability 2D counter plot of GRG

The surface interaction plot in 3D and 2D were found using the desirability profiles that are displayed in Fig. 134-135 respectively. In this case, the influential value of GRG is increased with maximum value in feed rate only.

5.2.3 Genetic algorithm

5.2.3.1 For material removal rate:

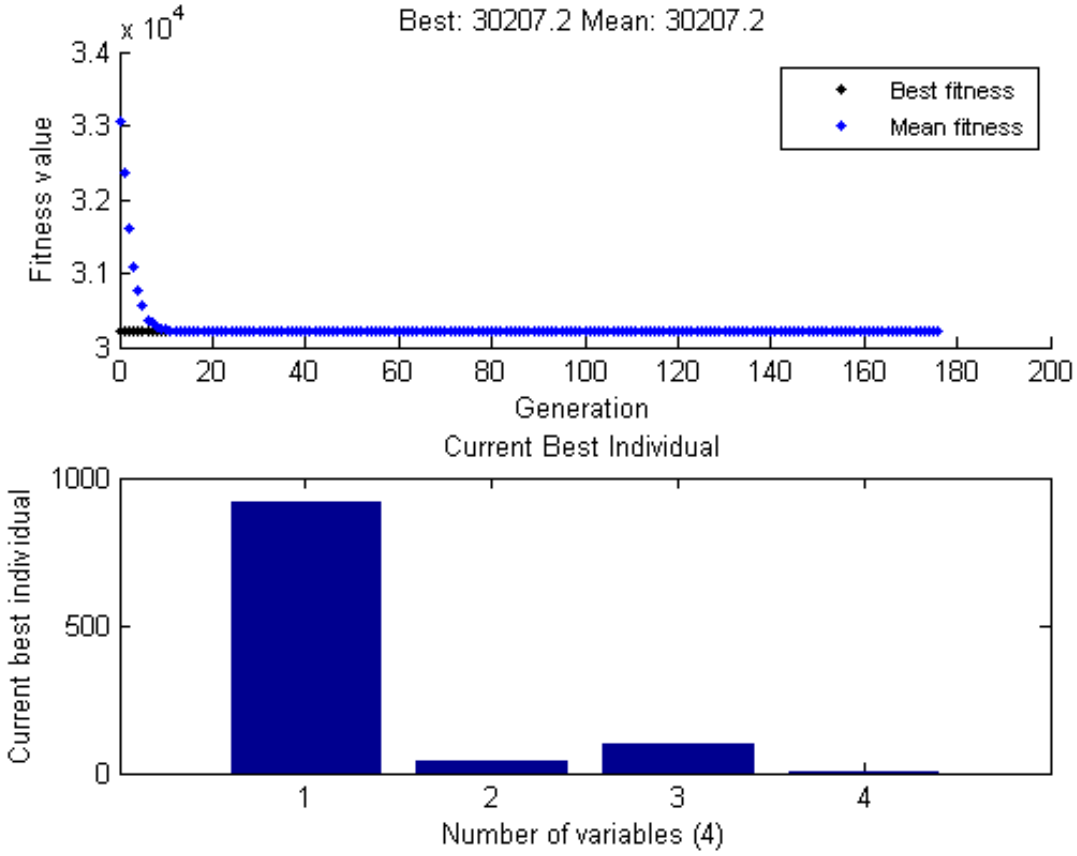

Fig. 136 Results from GA approach for MRR

The best fitness and individual value plot of MRR is shown in Fig. 136 where the best and average value of MRR is obtained as 30207.2 mm^3/min. Here, negative sign is due the application of negativity theory for maximizing problem. Secondly, the best parametric optimal setting is obtained at 920 mm/min of feed rate, 40 ampere of current, 100 volt of voltage and 2 mm of torch height respectively.

5.2.3.2 For surface roughness:

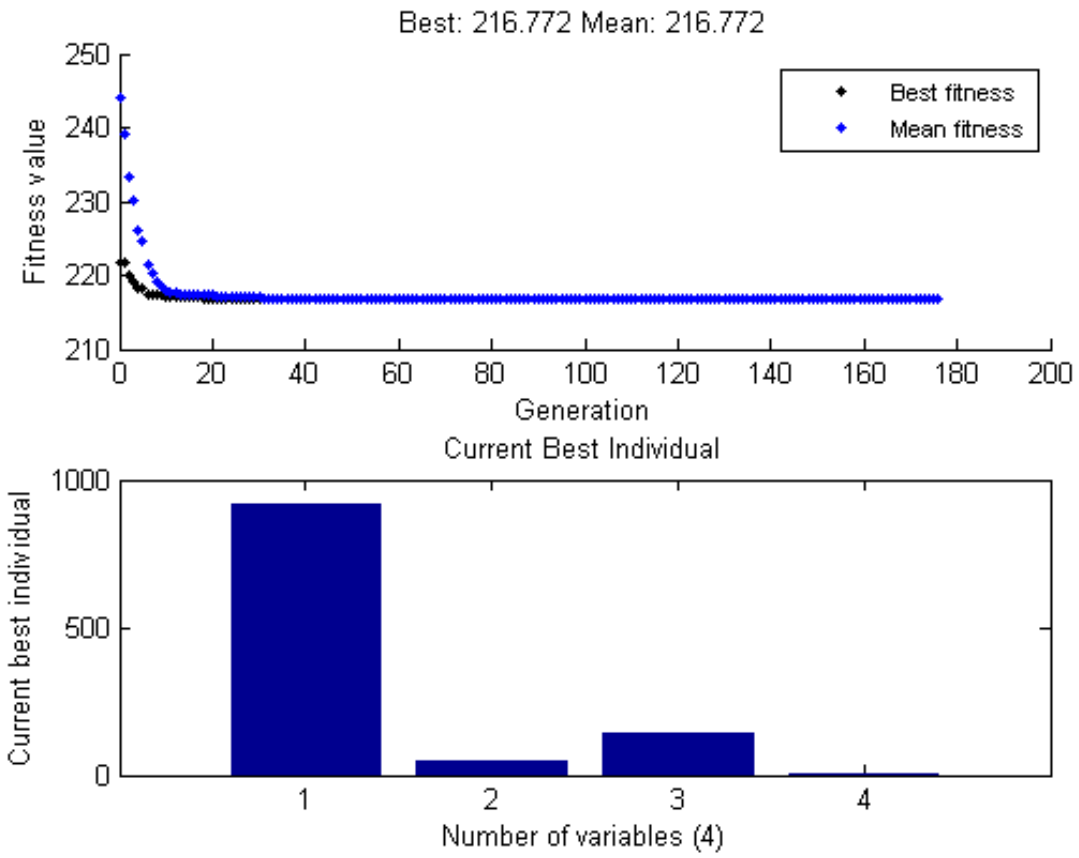

Fig. 137 Results from GA approach for SR

Similarly, for the case of SR the problem is the minimization of the best fitness and individual value plot as given in Fig. 137 where the best and average values of SR are found as 216.77179 µm. The best parametric optimal setting is obtained at 920 mm/min of feed rate, 45 ampere of current, 140 volt of voltage and 2.367 mm of torch height respectively.

5.2.3.3 For chamfer:

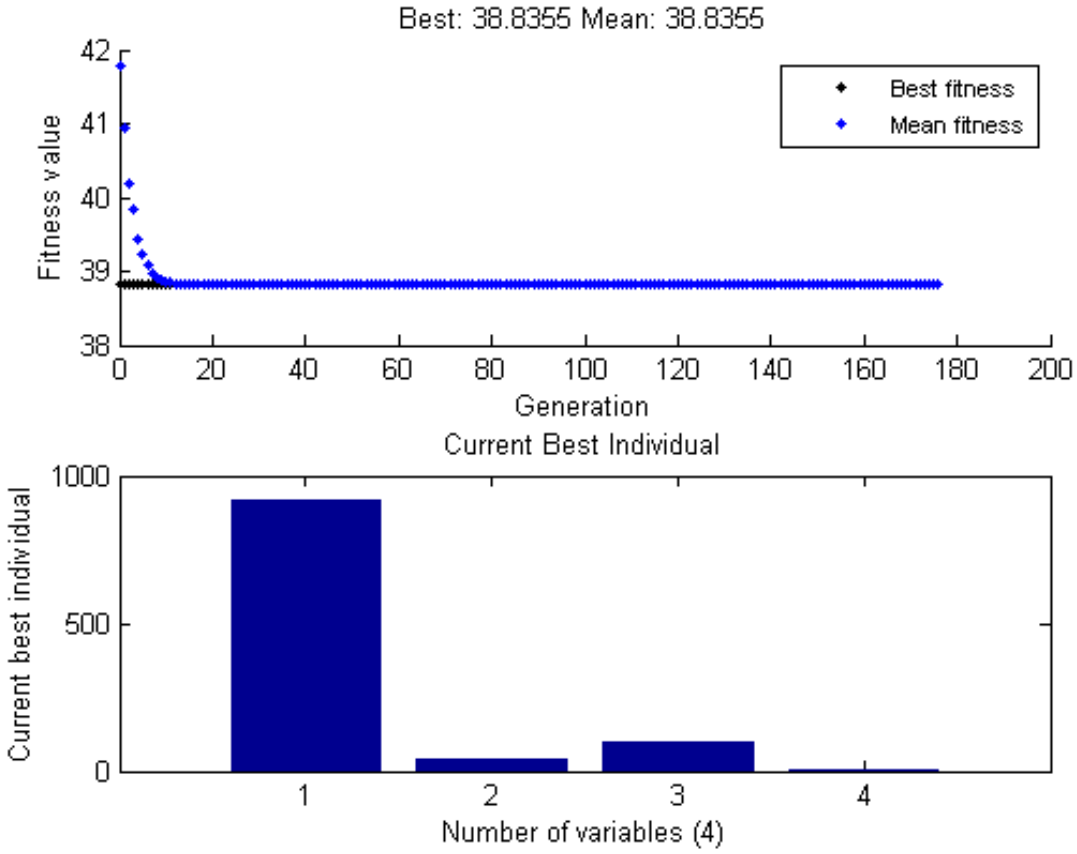

Fig. 138 Results from GA approach for chamfer

Similarly, for the case of chamfer the problem is the minimization of the best fitness and individual value plot as given in Fig. 138 where the best and average values of chamfer are found as 38.8355 mm. The best parametric optimal setting is obtained at 920 mm/min of feed rate, 40 ampere of current, 100 volt of voltage and 2 mm of torch height respectively. Here, the simulation of genetic algorithm toolbox for all output responses stopped at same iteration number i.e., 176.

5.2.3.4 For dross:

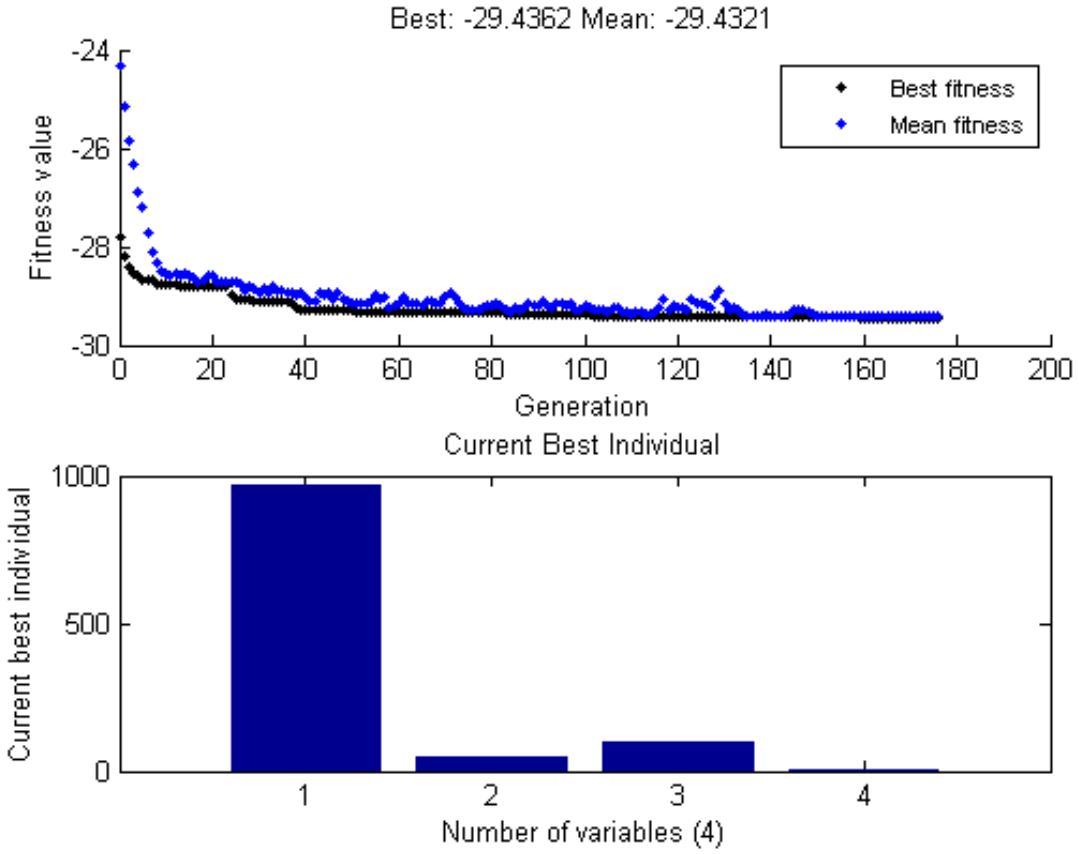

Fig. 139 Results from GA approach for dross

In the case of dross, the best fitness and individual value plot as given in Fig. 139 where the best and average values of dross are found as 29.4362 mm^2 and 29.4321 mm^2 respectively. The best parametric optimal setting is obtained at 970 mm/min of feed rate, 45 ampere of current, 100.003 volt of voltage and 2 mm of torch height respectively. Here, the simulation of genetic algorithm toolbox for all output responses stopped at same iteration number i.e., 176.

5.2.3.5 For kerf:

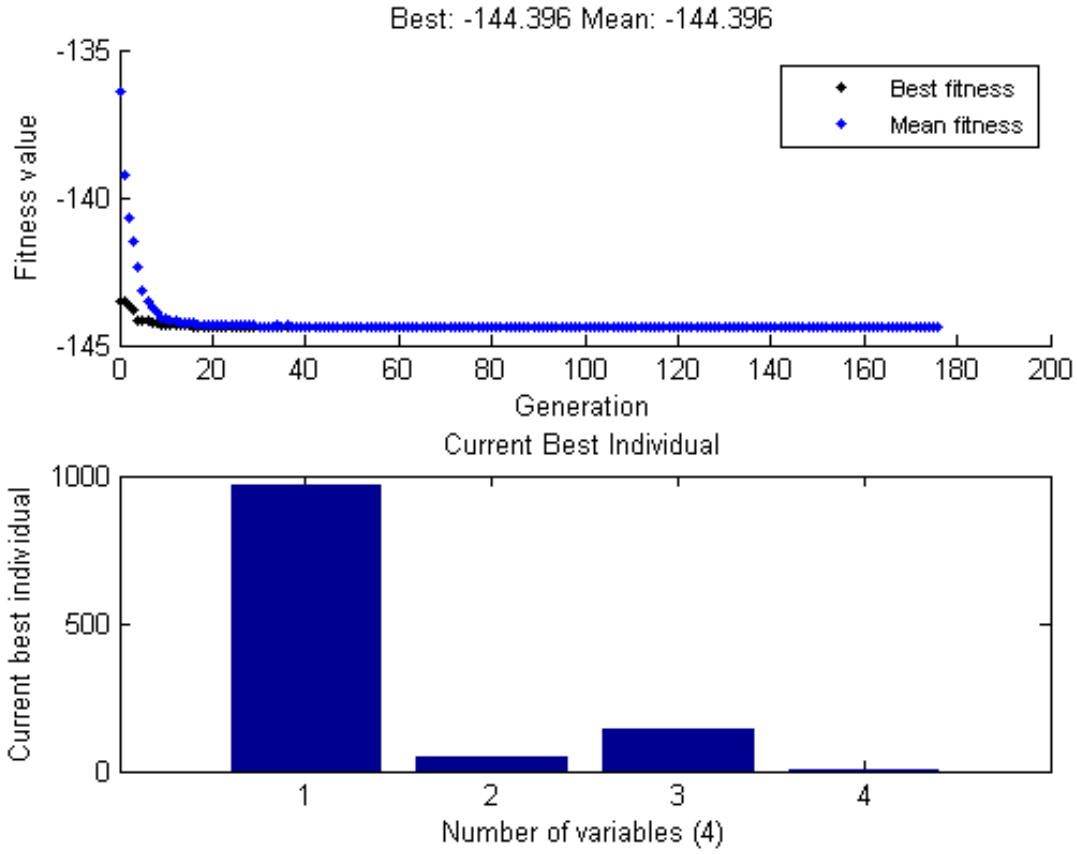

Fig. 140 Results from GA approach for kerf

In the case of kerf, the best fitness and individual value plot as given in Fig. 140 where the best and average values of kerf are found as 144.3957 mm. The best parametric optimal setting is obtained at 970 mm/min of feed rate, 45 ampere of current, 140 volt of voltage and 2 mm of torch height respectively. Here, the simulation of genetic algorithm toolbox for all output responses stopped at same iteration number i.e., 176.

5.2.4 Particle swarm optimization

5.2.4.1 For material removal rate:

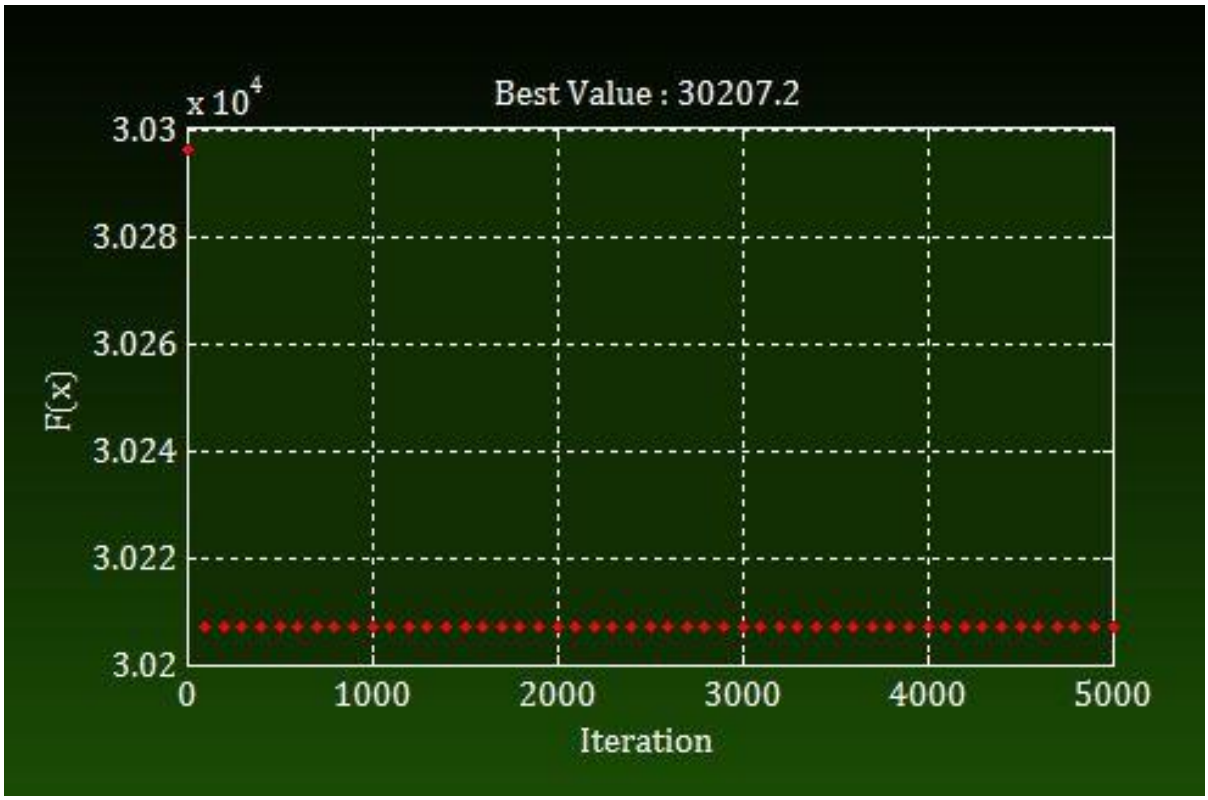

Fig. 141 Results from PSO approach for MRR

The plot of best function value and optimum setting for MRR which was obtained from PSO methodology is shown in Fig. 141. From the graph, it can be seen that the optimum condition for MRR was found as 920 mm/min of feed rate, 40 ampere of current, 100 volt of voltage and 2 mm of torch height respectively. The optimal value of MRR is determined using PSO technique as 3020.72 mm^3/min.

5.2.4.2 Mean surface roughness:

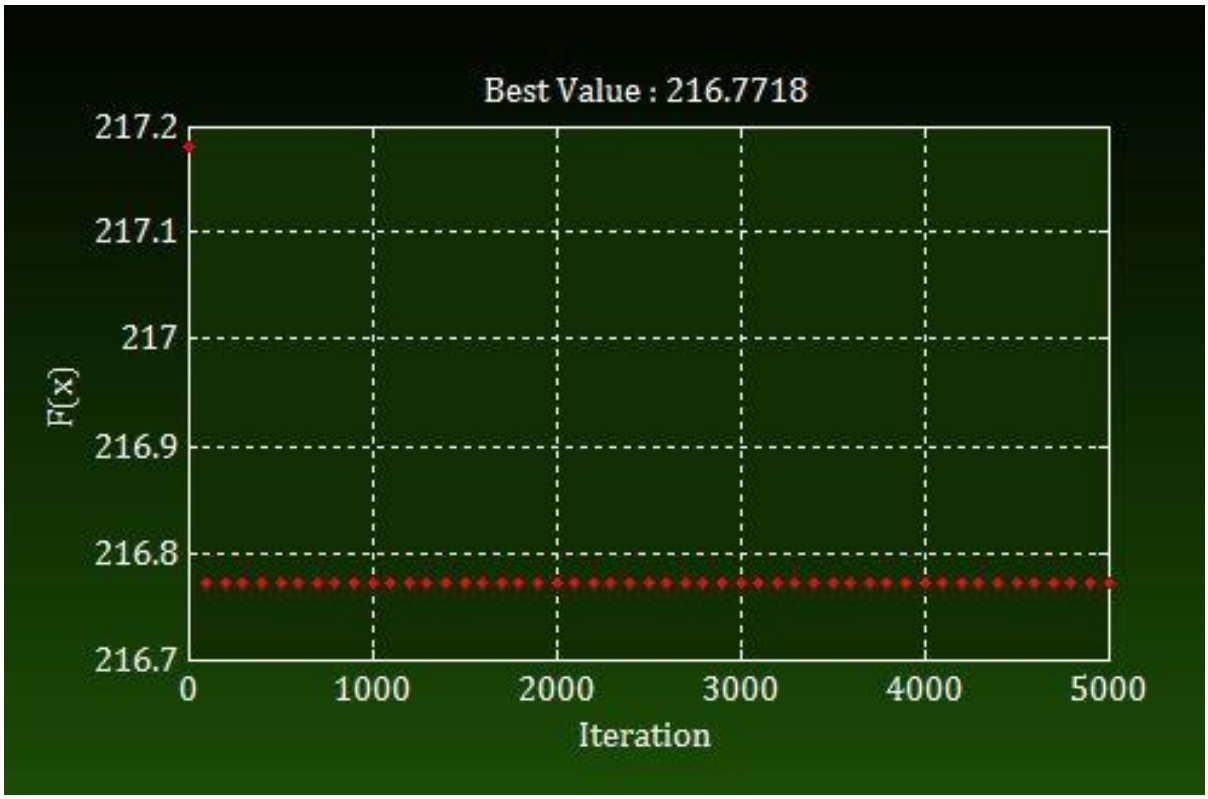

Fig. 142 Results from PSO approach for SR

The plot of best function value and optimum setting for SR which was obtained from PSO methodology is shown in Fig. 142. From the graph, it can be seen that the optimum condition for SR was found as 920 mm/min of feed rate, 45 ampere of current, 140 volt of voltage and 2.3669 mm of torch height respectively. The optimum value of SR is obtained as 216.7718 µm by PSO approach.

5.2.4.3 For chamfer:

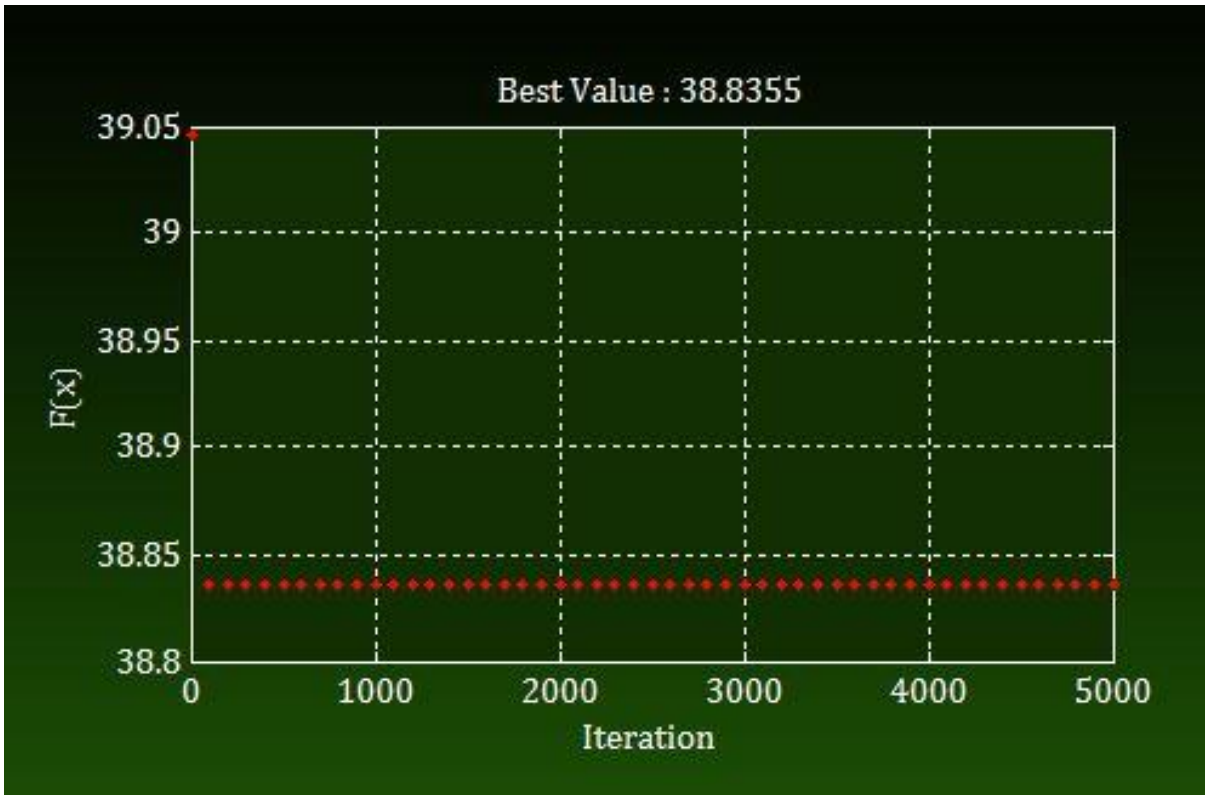

Fig. 143 Results from PSO approach for chamfer

The plot of best function value and optimum setting for chamfer which was obtained from PSO methodology is shown in Fig. 143. From the graph, it can be seen that the optimum condition for chamfer was found as 920 mm/min of feed rate, 40 ampere of current, 100 volt of voltage and 2 mm of torch height respectively. The best value of chamfer utilizing PSO technique is determined as 38.8355 mm.

5.2.4.4 For dross:

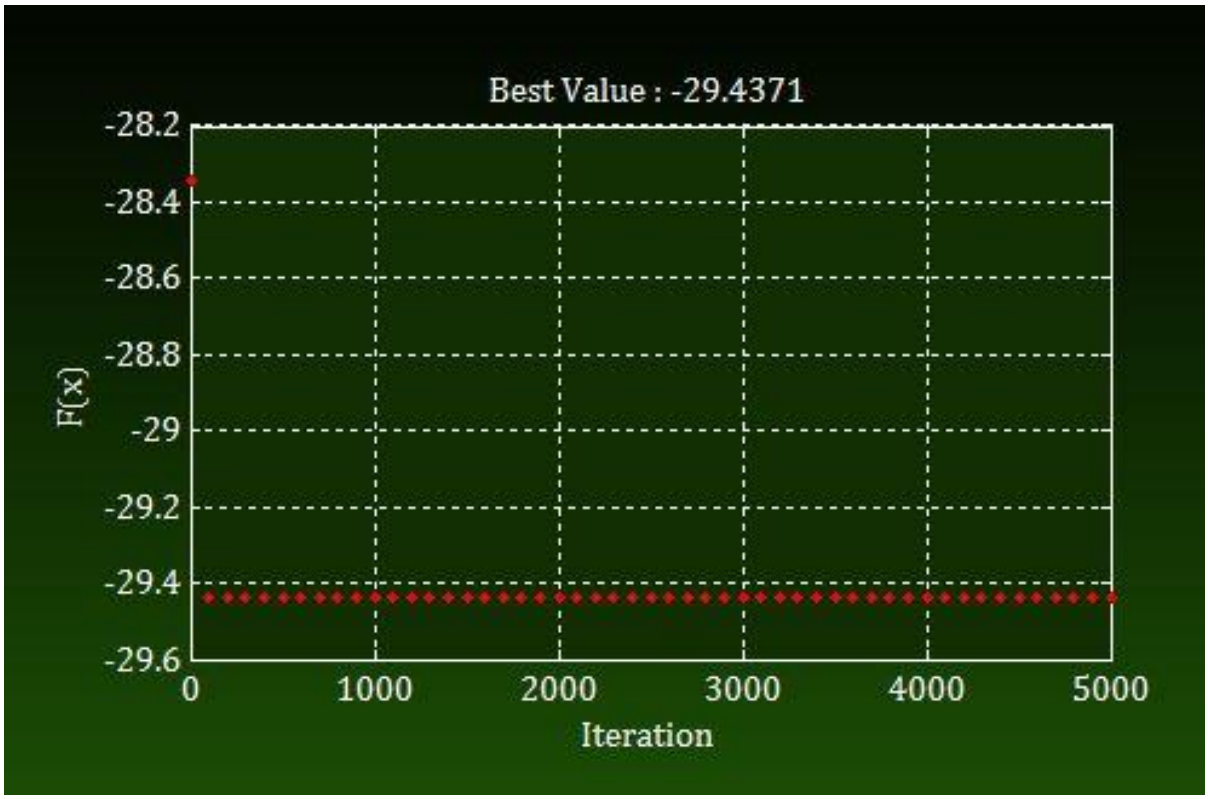

Fig. 144 Results from PSO approach for dross

The plot of best function value and optimum setting for dross which was obtained from PSO methodology is shown in Fig. 144. From the graph, it can be seen that the optimum condition for dross was found as 970 mm/min of feed rate, 45 ampere of current, 100 volt of voltage and 2 mm of torch height respectively. The optimal worth of dross response using novel approach of PSO technique is evaluated as 29.4371 mm^2.

5.2.4.5 For kerf:

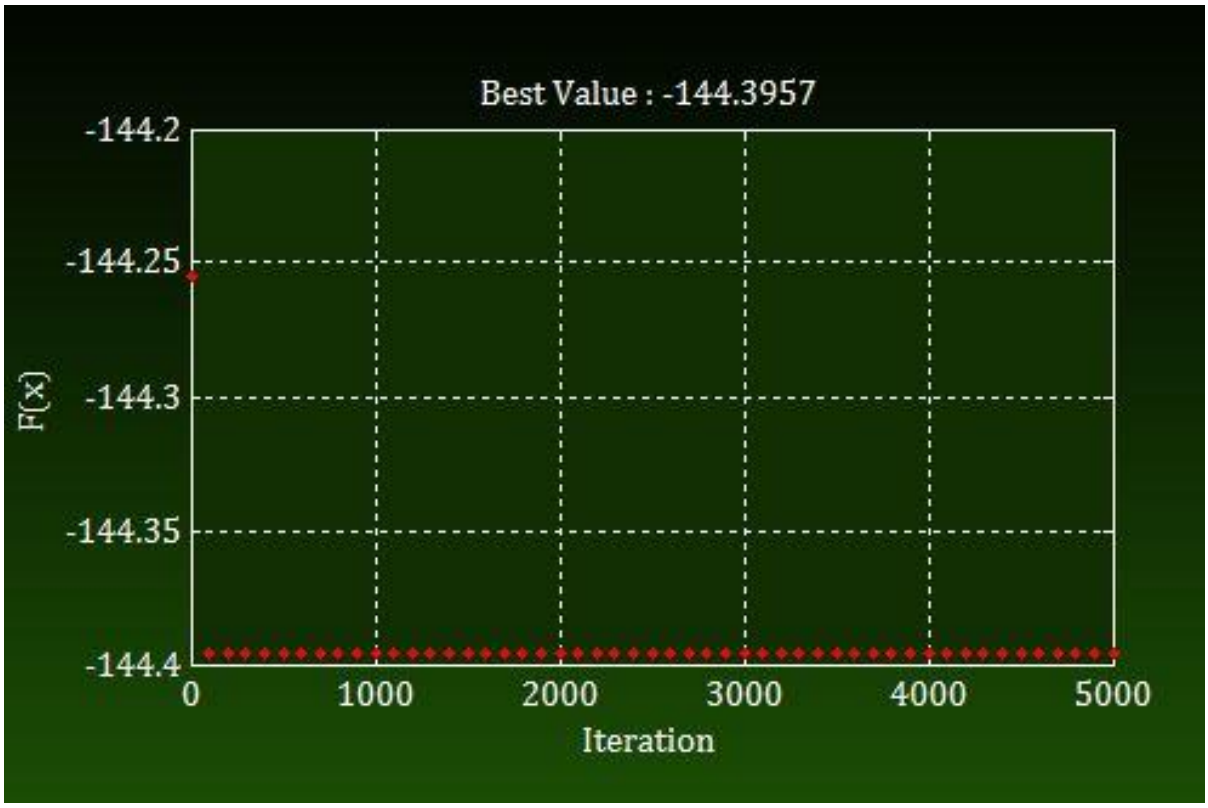

Fig. 145 Results from PSO approach for kerf

The plot of best function value and optimum setting for kerf which was obtained from PSO methodology is shown in Fig. 145. From the graph, it can be seen that the optimum condition for kerf was found as 970 mm/min of feed rate, 45 ampere of current, 140 volt of voltage and 2 mm of torch height respectively. The best function value of kerf using PSO methodology is obtained as 144.3957 mm.

5.2.5 Simulated annealing

5.2.5.1 For material removal rate:

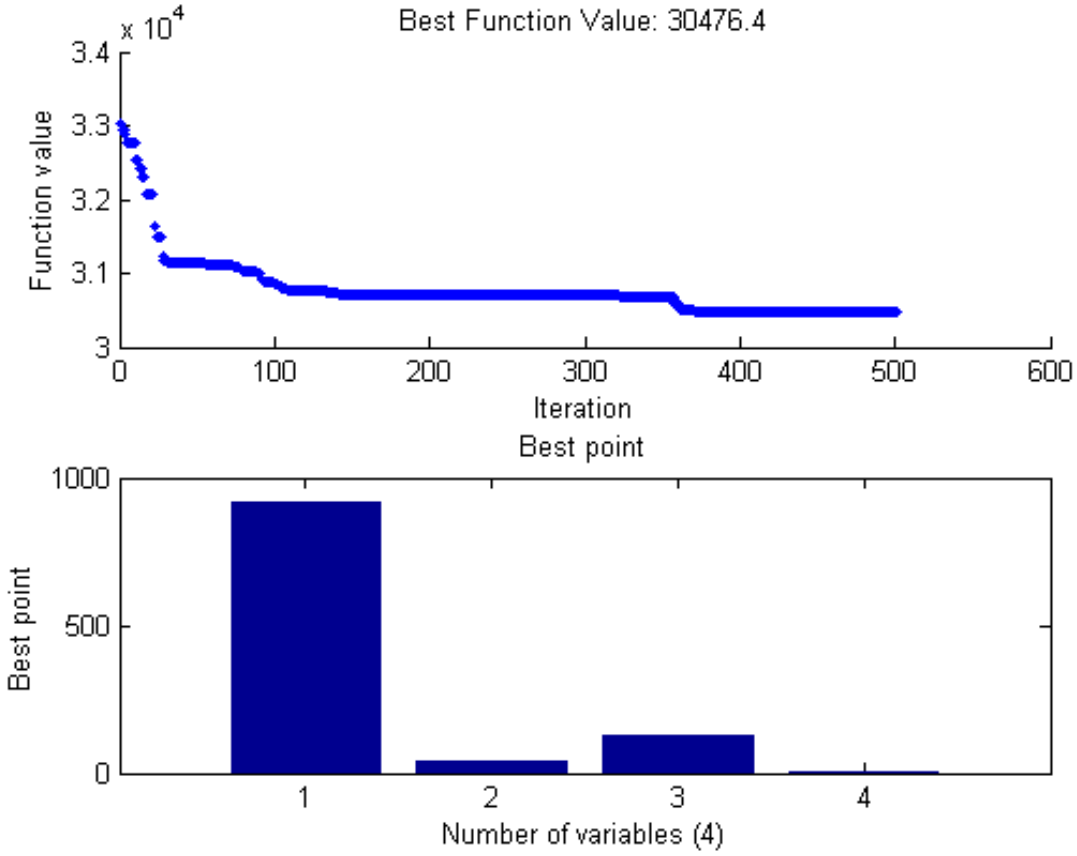

Fig. 146 Results from SA approach for MRR

Nature based novel optimization technique i.e., simulated annealing algorithm is employed to the obtained regression equation of surface roughness from RSM method. By applying Boltzmann annealing approach to the experimental data, the lowest value of MRR is found as 30476.41078 mm^3/min at 920 mm/min of feed rate, 40 ampere of current, 129.869 volt of voltage and 2 mm of torch height respectively. From the Fig. 146, the best function value and comparative effect of input parameters are shown. Here, the feed rate gave the most effective variable than other two parameters. The highest number of iteration for simulating the algorithm is 501 where the minimum value of MRR found.

The best parametric setting of the whole experimentation as per simulated annealing is shown in Fig. 146 with current iteration number.

5.2.5.2 For surface roughness:

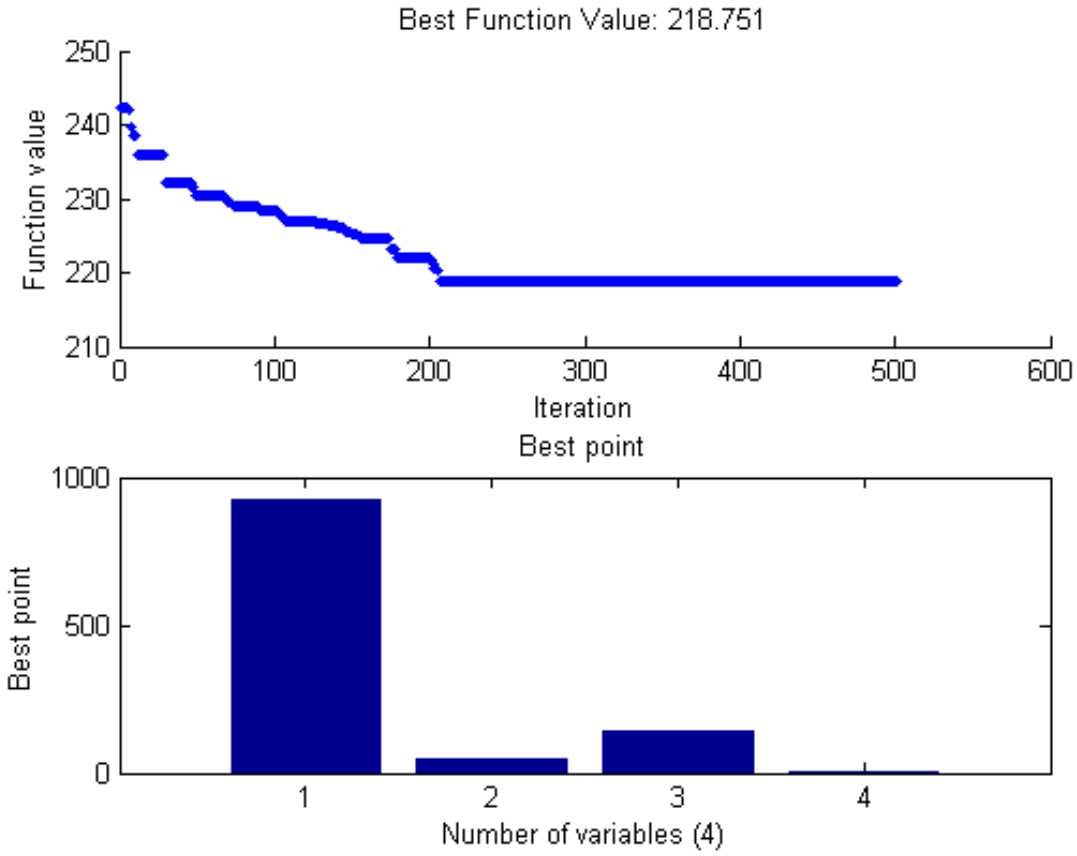

Fig. 147 Results from SA approach for SR

Nature based novel optimization technique i.e., simulated annealing algorithm is employed to the obtained regression equation of surface roughness from RSM method. By applying Boltzmann annealing approach to the experimental data, the lowest value of SR is found as 218.75136 µm at 922.97 mm/min of feed rate, 44.149 ampere of current, 139.545 volt of voltage and 2.399 mm of torch height respectively. From the Fig. 147, the best function value and comparative effect of input parameters are shown. Here, the feed rate gave the most effective variable than other two parameters. The highest number of

iteration for simulating the algorithm is 501 where the minimum value of SR obtained. The best parametric setting of the whole experimentation as per simulated annealing is shown in Fig. 147 with current iteration number.

5.2.5.3 For chamfer:

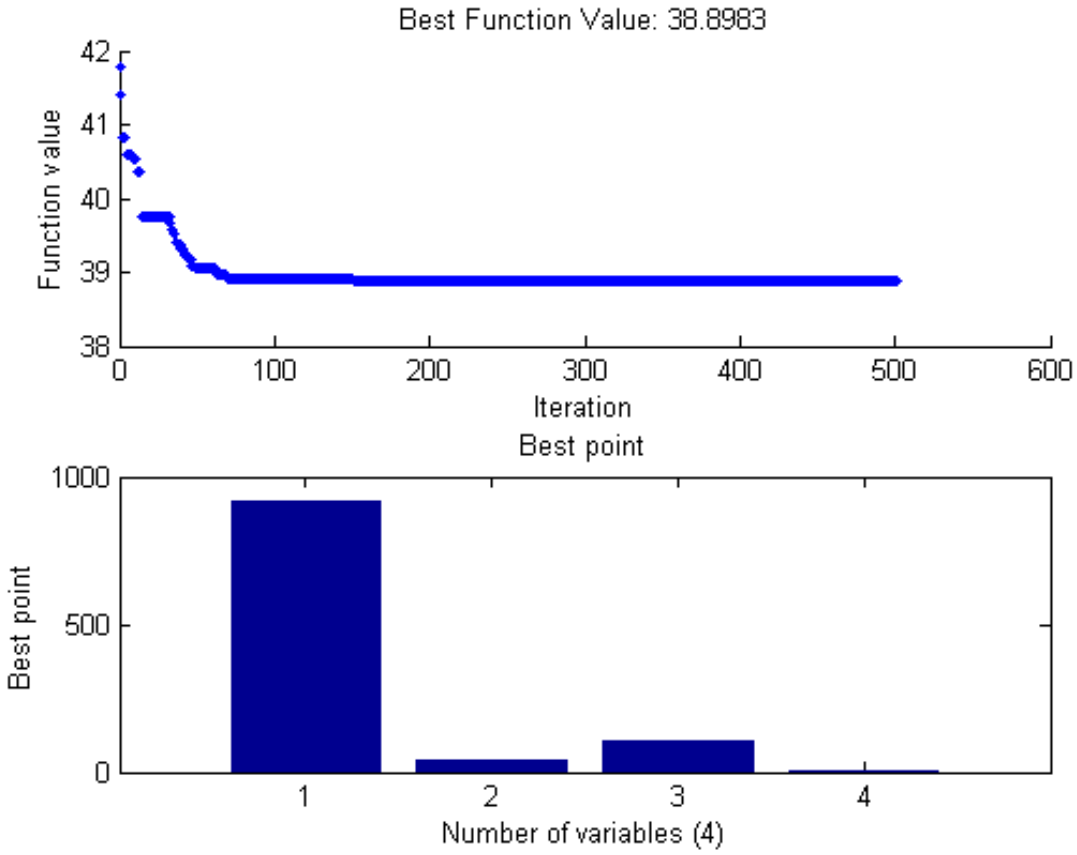

Fig. 148 Results from SA approach for chamfer

Nature based novel optimization technique i.e., simulated annealing algorithm is employed to the obtained regression equation of surface roughness from RSM method. By applying Boltzmann annealing approach to the experimental data, the lowest value of chamfer is found as 38.8983 mm at 920.011 mm/min of feed rate, 40.211 ampere of current, 101.854 volt of voltage and 2.001 mm of torch height respectively. From the Fig. 148, the best function value and comparative effect of input parameters are shown. Here,

the feed rate gave the most effective variable than other two parameters. The highest number of iteration for simulating the algorithm is 501 where the minimum value of chamfer observed. The best parametric setting of the whole experimentation as per simulated annealing is shown in Fig. 148 with current iteration number.

5.2.5.4 For dross:

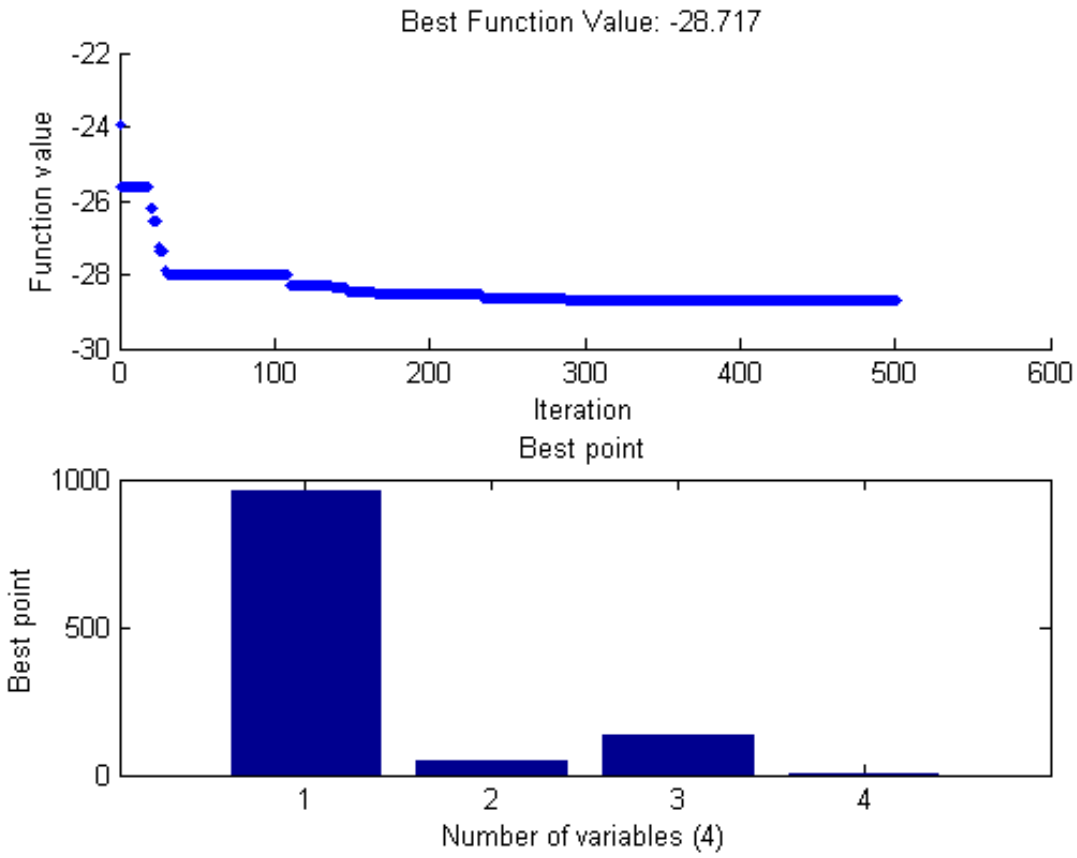

Fig. 149 Results from SA approach for dross

Nature based novel optimization technique i.e., simulated annealing algorithm is employed to the obtained regression equation of dross from RSM method. By applying Boltzmann annealing approach to the experimental data, the lowest value of dross is found as 28.717 mm^2 at 963.512 mm/min of feed rate, 45 ampere of current, 137.263 volt of voltage and 2 mm of torch height respectively. From the Fig. 149, the best function

value and comparative effect of input parameters are shown. Here, the feed rate gave the most effective variable than other two parameters. The highest number of iteration for simulating the algorithm is 501 where the minimum value of dross found. The best parametric setting of the whole experimentation as per simulated annealing is shown in Fig. 149 with current iteration number.

5.2.5.5 For kerf:

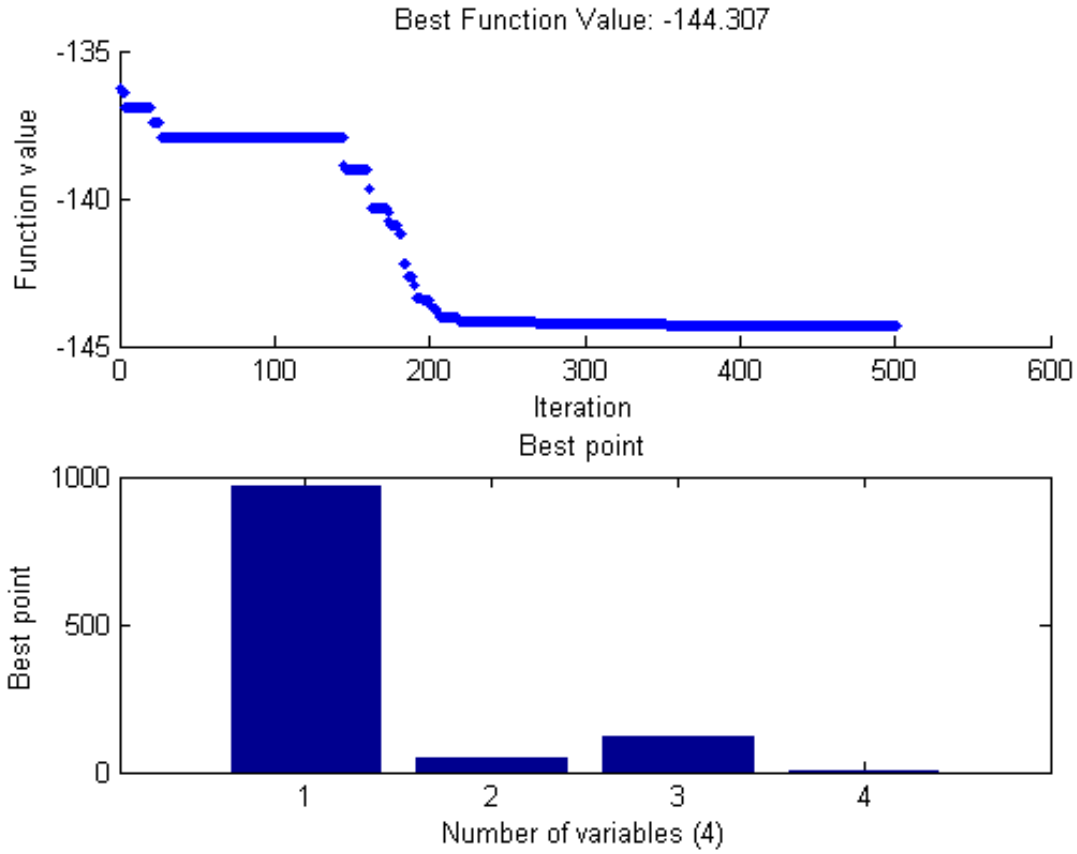

Fig. 150 Results from SA approach for kerf

Nature based novel optimization technique i.e., simulated annealing algorithm is employed to the obtained regression equation of kerf from RSM method. By applying Boltzmann annealing approach to the experimental data, the lowest value of kerf is found as 144.30718 mm at 969.99 mm/min of feed rate, 44.997 ampere of current, 117.413 volt

of voltage and 2 mm of torch height respectively. From the Fig. 150, the best function value and comparative effect of input parameters are shown. Here, the feed rate gave the most effective variable than other two parameters. The highest number of iteration for simulating the algorithm is 501 where the minimum value of kerf found. The best parametric setting of the whole experimentation as per simulated annealing is shown in Fig. 150 with current iteration number.

5.2.6 TLBO results

5.2.6.1 For material removal rate:

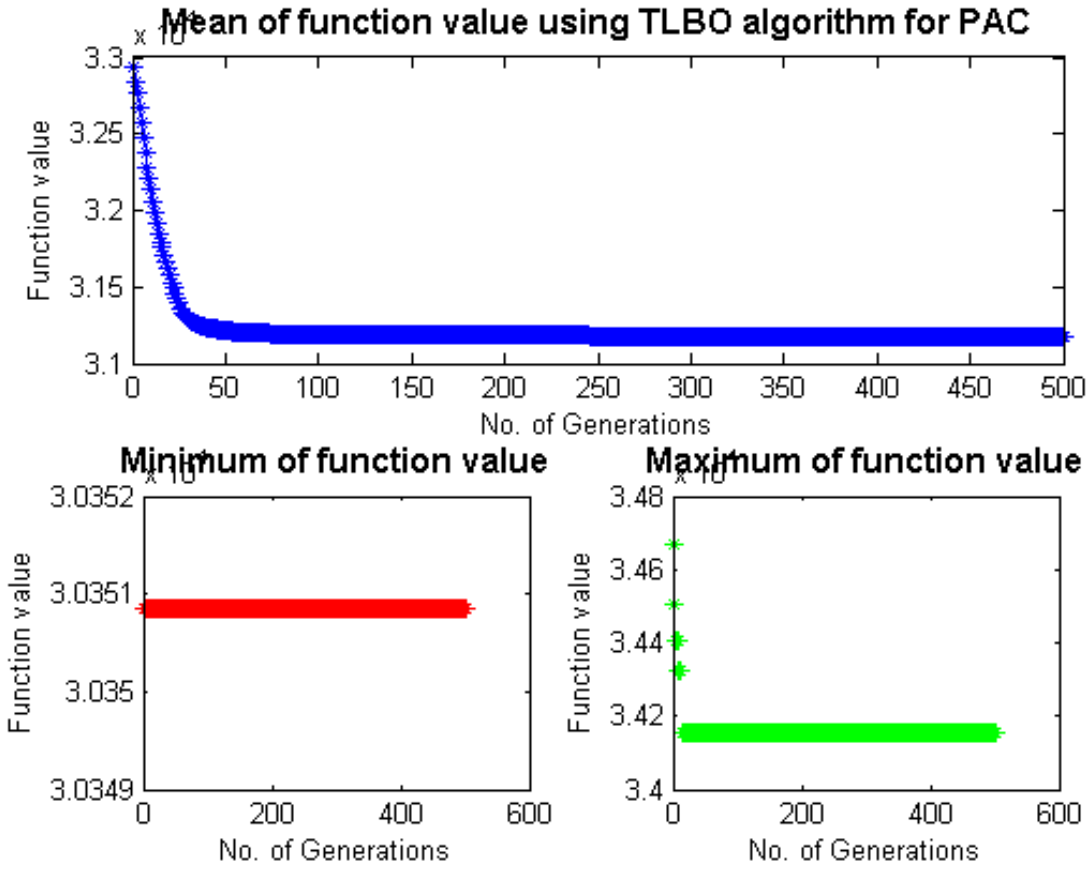

Fig. 151 Obtained plot by TLBO approach for MRR

The TLBO algorithm is run through Matlab R2012b version software by considering 300 as population size and 500 as number of generations. In each run the

maximum number of function evaluations N is considered as 750000. Only in the case of MRR response, the theory of negativity is applied because the main objective of this is to convert the maximization type to minimization type problem. Fig. 151 depicts plot of the fitness function value for each generation. It can be observed that it converges to the optimum result in very small population size and less number of generations. From Fig. 151, the optimal condition for MRR occurred at 924.226 mm/min of feed rate, 40.6128 ampere of current, 105.911 volt of voltage and 2.97552 mm of torch height respectively. The best objective function value of MRR is found as 31180.1 mm^3/min.

5.2.6.2 For surface roughness:

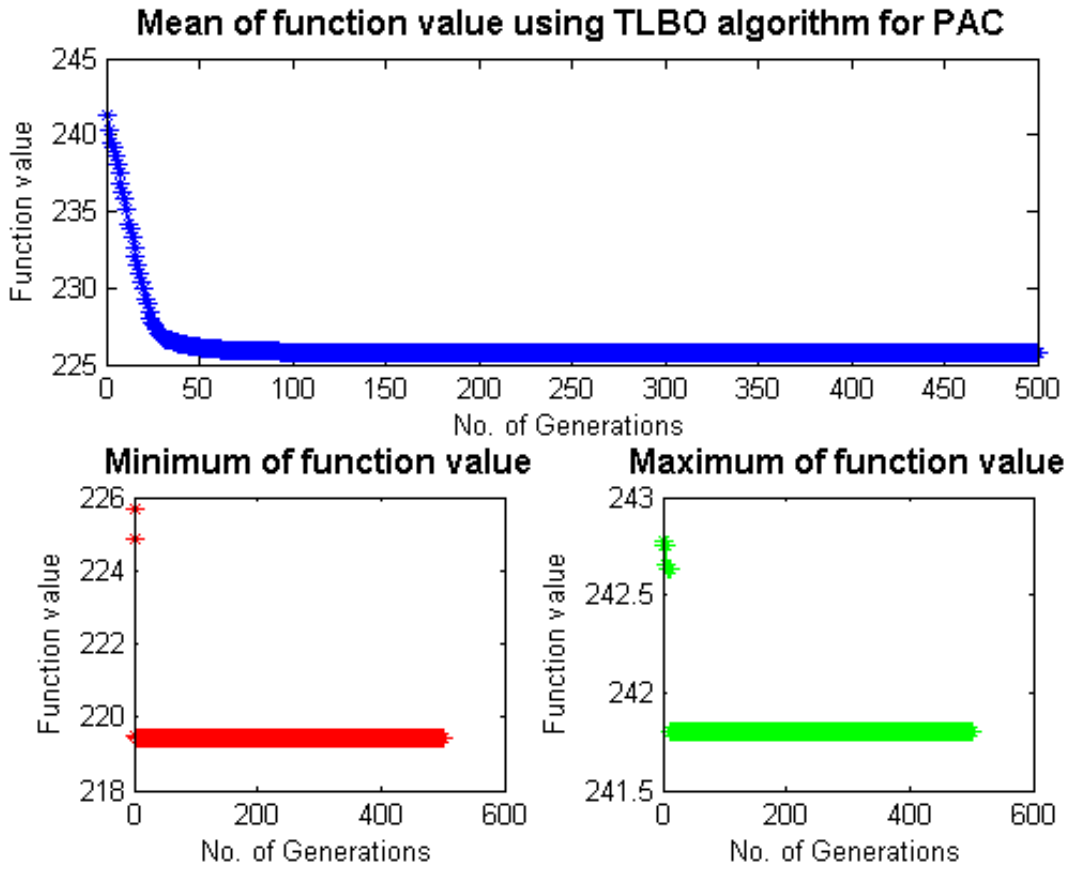

Fig. 152 Obtained plot by TLBO approach for SR

The TLBO algorithm is run by considering 300 as population size and 500 as number of generations. In each run the maximum number of function evaluations N is considered as 750000. Fig. 152 depicts plot of the fitness function value for each generation. It can be observed that it converges to the optimum result in very small population size and less number of generations. From Fig. 152, the optimal condition for SR occurred at 938.349 mm/min of feed rate, 43.8974 ampere of current, 139.636 volt of voltage and 3 mm of torch height respectively. The best objective function value of SR is found as 225.793 µm.

5.2.6.3 For chamfer:

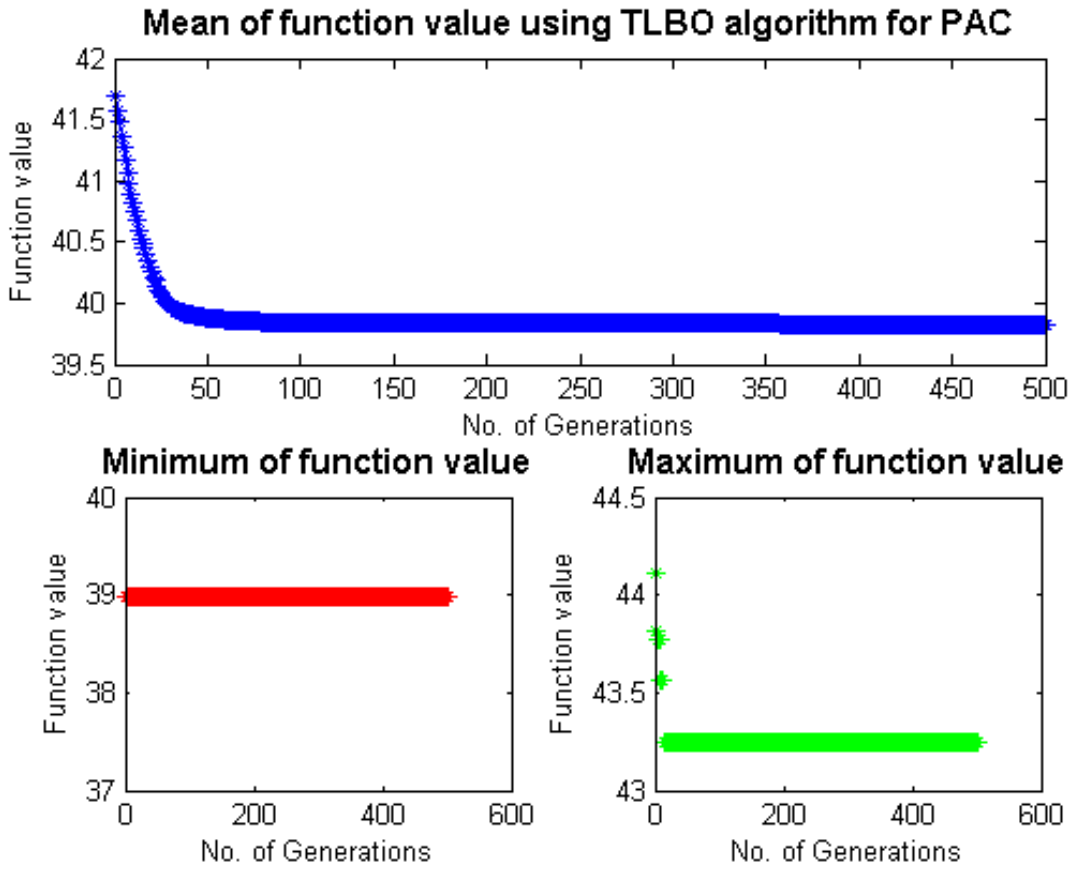

Fig. 153 Obtained plot by TLBO approach for chamfer

The TLBO algorithm is run by considering 300 as population size and 500 as number of generations. In each run the maximum number of function evaluations N is considered as 750000. Fig. 153 depicts plot of the fitness function value for each generation. It can be observed that it converges to the optimum result in very small population size and less number of generations. From Fig. 153, the optimal condition for chamfer occurred at 924.454 mm/min of feed rate, 41.8109 ampere of current, 105.083 volt of voltage and 2.97086 mm of torch height respectively. The best objective function value of chamfer is found as 39.8281 mm.

5.2.6.4 For dross:

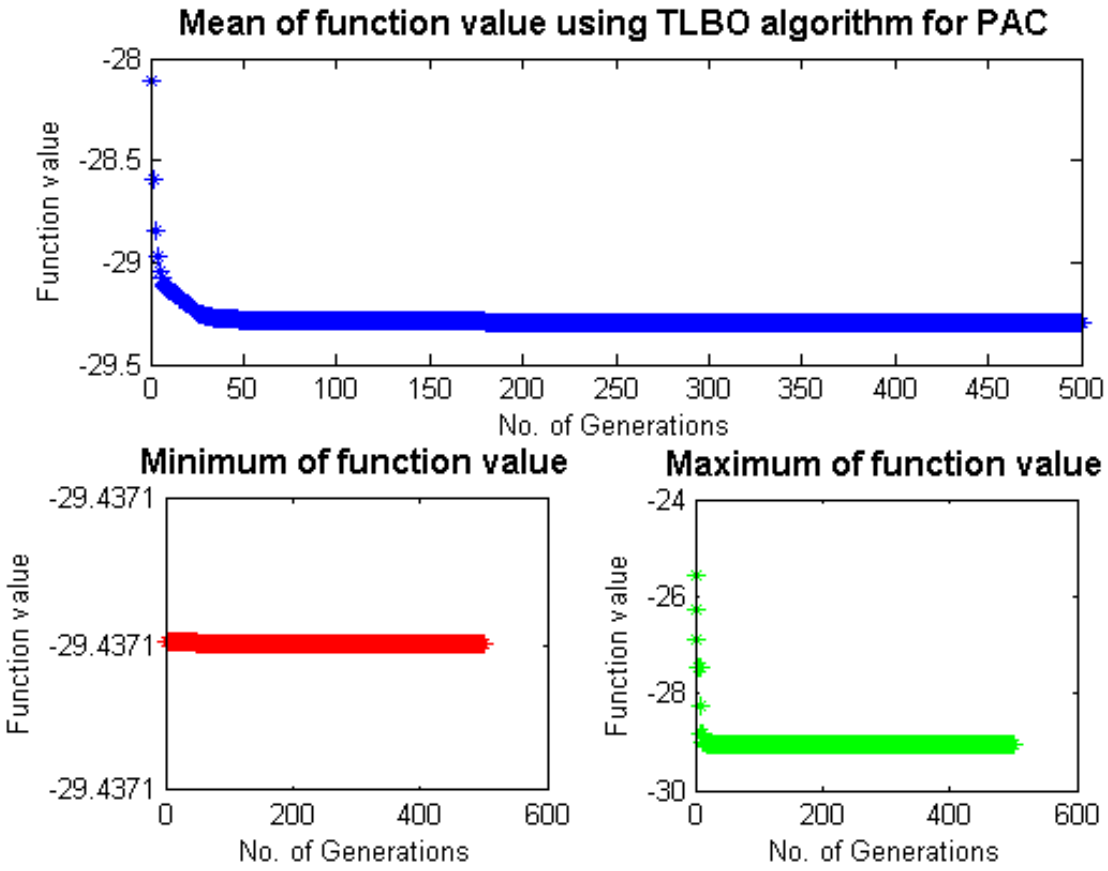

Fig. 154 Obtained plot by TLBO approach for dross

The TLBO algorithm is run by considering 300 as population size and 500 as number of generations. In each run the maximum number of function evaluations N is considered as 750000. Fig. 154 depicts plot of the fitness function value for each generation. It can be observed that it converges to the optimum result in very small population size and less number of generations. From Fig. 154, the optimal condition for dross occurred at 969.999 mm/min of feed rate, 44.9999 ampere of current, 117.292 volt of voltage and 2 mm of torch height respectively. The best objective function value of dross is found as 29.2925 mm^2.

5.2.6.5 For kerf:

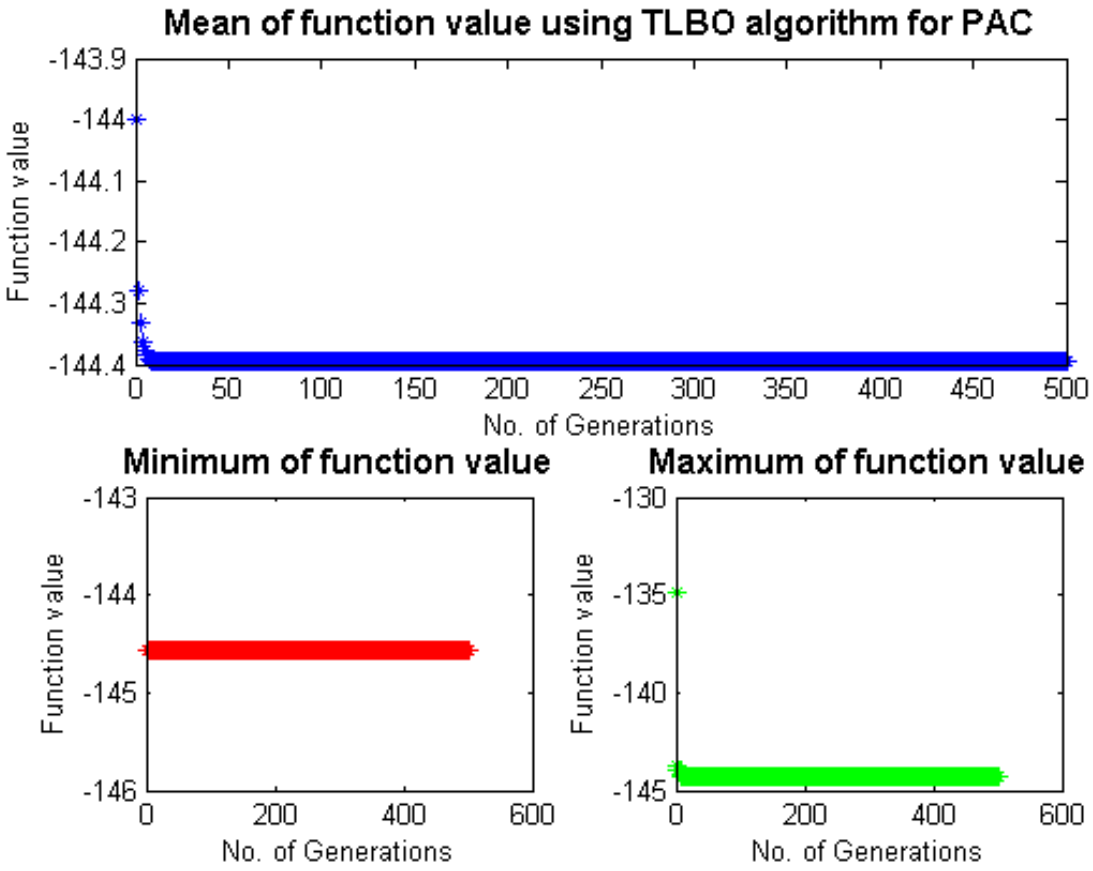

Fig. 155 Obtained plot by TLBO approach for kerf

The TLBO algorithm is run by considering 300 as population size and 500 as number of generations. In each run the maximum number of function evaluations N is considered as 750000. Fig. 155 depicts plot of the fitness function value for each generation. It can be observed that it converges to the optimum result in very small population size and less number of generations. From Fig. 155, the optimal condition for kerf occurred at 970.006 mm/min of feed rate, 45.0006 ampere of current, 139.898volt of voltage and 2.00345 mm of torch height respectively. The best objective function value of kerf is found as 144.396 mm.

5.3 Results of Case 3

The Response Surface Methodology was utilized to study the influences of the independent factors cutting current (A), cutting speed (B), gas pressure (C) and stand-off gap (D) at three variation levels in the extraction procedure which is shown in Table 46. The whole experimentations were planned using Statistica software version 9.1 (Statsoft company made). Three levels are selected for each independent variable such as low (-1), middle (0) and high level (+1) which is shown in Table 46. The experimental design consisted of twenty seven cases or runs according to 3 blocked Box-Behnken Design (BBD). Analysis of variance (ANOVA) and F-test were used as significant criteria for the fitted models. The results obtained were presented as mean values with standard deviation. After getting the layout of experimental design of input factors from Statistica software, the cutting operation by plasma arc on the selected work piece have been carried out. According to the DOE, the seven output quality characteristics of cut are measured and tabulated in Table 47. The design of experiment consisted of actual level value of input factors with standard order of BBD and correspondingly the output responses. After

simulating the optimization approach by software to this model, the ANOVA evaluation has been carried out to each response. Similarly, the estimated coefficients of the model were calculated for each cut quality. The influences of input variables in plasma arc machining for each response is briefly described below:

Table 46 Values of Input Process Parameters

Process parameters	Units	Code	L(1)	L(2)	L(3)
Cutting Current	Ampere	A	100	150	200
Cutting Speed	mm/s	B	2	3	4
Gas Pressure	L/min	C	12	15	18
Stand-off Gap	mm	D	2.0	2.5	3.0

Table 47 Cut Quality Responses with L_{27} Orthogonal Array

Run	Cutting Current (Ampere)	Cutting Speed (mm/s)	Gas Pressure (L/min)	Stand-off Gap (mm)	MRR (mm^3/min)	SR (μm)	Chamfer (mm)	Dross (mm^2)	Right Bevel Angle (Degree)	Kerf (mm)	HAZ (mm)
1	100	2	15	2.5	1087.08	23.00	0.28	1.43	3	2.90	1.36
2	200	2	15	2.5	375.16	14.91	0.15	0.91	3	2.61	2.77
3	100	4	15	2.5	1531.83	29.60	0.43	1.67	3	3.02	1.33
4	200	4	15	2.5	983.91	21.94	0.25	1.35	3	2.79	1.71
5	150	3	12	2.0	1104.75	22.92	0.27	1.45	4	2.80	1.68
6	150	3	18	2.0	1321.83	26.07	0.35	1.54	4	2.96	1.49
7	150	3	12	3.0	952.66	20.84	0.22	1.33	4	2.86	1.91
8	150	3	18	3.0	879.75	20.22	0.21	1.28	3	2.74	1.90
9	150	3	15	2.5	994.54	21.47	0.24	1.36	3	2.71	1.61
10	100	3	15	2.0	1442.68	27.58	0.38	1.62	4	2.91	1.33
11	200	3	15	2.0	679.26	17.98	0.19	1.08	3	2.57	2.49
12	100	3	15	3.0	1012.59	21.88	0.25	1.38	3	2.76	1.91
13	200	3	15	3.0	617.18	15.76	0.13	1.03	4	2.57	2.25
14	150	2	12	2.5	596.76	15.16	0.13	1.10	3	2.59	2.38
15	150	4	12	2.5	1325.51	21.41	0.26	1.42	4	2.72	1.82
16	150	2	18	2.5	671.34	15.84	0.17	1.12	4	2.59	2.27
17	150	4	18	2.5	1195.09	23.25	0.29	1.48	3	2.72	1.74
18	150	3	15	2.5	870.09	18.69	0.20	1.26	3	2.61	1.90
19	100	3	12	2.5	1172.25	23.76	0.27	1.49	3	2.80	1.64
20	200	3	12	2.5	530.55	14.50	0.13	1.05	3	2.53	2.67
21	100	3	18	2.5	1233.08	23.73	0.29	1.51	3	2.80	1.68
22	200	3	18	2.5	615.91	17.19	0.15	1.11	3	2.56	2.44
23	150	2	15	2.0	667.95	16.65	0.14	1.12	3	2.65	2.22
24	150	4	15	2.0	1358.50	24.82	0.34	1.56	4	2.73	1.79
25	150	2	15	3.0	585.16	14.04	0.12	1.15	4	2.55	2.45
26	150	4	15	3.0	895.16	19.81	0.16	1.29	3	2.72	2.00
27	150	3	15	2.5	840.37	18.29	0.18	1.26	3	2.40	1.93

5.3.1 RSM with desirability function approach

5.3.1.1 For material removal rate:

In the 3rd step, the effect of estimated values of MRR was computed and recorded in Table 48. The ANOVA for MRR has been carried out firstly and its results are given in Table 49. Here, the block effect has also been considered because the levels of block are taken as one. Due to this variation in block, there is negligible amount of effect occurred in experiment. This effect is ignored for further calculation of optimization. The total degree of freedom for all input factors is 26. From the Table 49, it is seen that the most of the terms have P-value less than 0.05 under the confidence interval of 95 %. Hence, these terms show significance within experiment. In case of individual terms, cutting current, cutting speed and gas pressure have shown the most significance among all parameters. Pareto chart of effects of all factors on MRR response are shown in Fig. 156 and the results indicate that the linear form of cutting current is the second most enhancing factor among all considered factors. The scatter plot between the observed and the predicted value of MRR of all 27 runs is shown in Fig. 157. It is concluded that there is a reasonable correlation between the measured and predicted values of MRR response. In Fig. 159, the histogram plot of predicted data of MRR with 95 % confidence interval of normal distribution is displayed. In Table 50, the model of estimated regression coefficients of the independent variable on the MRR is represented.

Table 48 Effect of Estimated Values for MRR

Factor	Effect	Std. Err.	T	P
Constant	968.108	33.28832	29.0825	0.000000
A (Ampere)	-612.923	57.65707	-10.6305	0.000000
A^2	-7.854	43.24280	-0.1816	0.858905
B (mm/s)	551.092	57.65707	9.5581	0.000001
B^2	-6.850	43.24280	-0.1584	0.876763
C (L/min)	39.087	57.65707	0.6779	0.510685
C^2	-47.604	43.24280	-1.1009	0.292551
D (mm)	-272.078	57.65707	-4.7189	0.000498
D^2	-37.353	43.24280	-0.8638	0.404636
A×B	82.000	99.86497	0.8211	0.427596
A×C	12.265	99.86497	0.1228	0.904286
A×D	184.005	99.86497	1.8425	0.090228
B×C	-102.500	99.86497	-1.0264	0.324955
B×D	-190.275	99.86497	-1.9053	0.080975
C×D	-144.995	99.86497	-1.4519	0.172166

Table 49 ANOVA Table for MRR

Factors	SS	DoF	MS	F	P
A (Ampere)	1127025	1	1127025	113.0075	0.000000
A^2	329	1	329	0.0330	0.858905
B (mm/s)	911106	1	911106	91.3572	0.000001
B^2	250	1	250	0.0251	0.876763
C (L/min)	4583	1	4583	0.4596	0.510685
C^2	12086	1	12086	1.2119	0.292551
D (mm)	222080	1	222080	22.2681	0.000498
D^2	7441	1	7441	0.7461	0.404636
A×B	6724	1	6724	0.6742	0.427596
A×C	150	1	150	0.0151	0.904286
A×D	33858	1	33858	3.3949	0.090228
B×C	10506	1	10506	1.0535	0.324955
B×D	36205	1	36205	3.6303	0.080975
C×D	21024	1	21024	2.1080	0.172166
Error	119676	12	9973		
Total SS	2509854	26			

Table 50 Regression Coefficients of MRR

Factor	Regression Coef.	Std. Err.	T	P
Constant	1665.937	2912.110	0.57207	0.577833
A (Ampere)	-19.345	9.279	-2.08483	0.059114
A^2	0.003	0.017	0.18163	0.858905
B (mm/s)	843.381	463.951	1.81782	0.094127
B^2	6.850	43.243	0.15842	0.876763
C (L/min)	13.781	181.057	0.07611	0.940584
C^2	5.289	4.805	1.10086	0.292551
D (mm)	-275.352	1086.342	-0.25347	0.804198
D^2	149.412	172.971	0.86380	0.404636
A×B	0.820	0.999	0.82111	0.427596
A×C	0.041	0.333	0.12282	0.904286
A×D	3.680	1.997	1.84254	0.090228
B×C	-17.083	16.644	-1.02639	0.324955
B×D	-190.275	99.865	-1.90532	0.080975
C×D	-48.332	33.288	-1.45191	0.172166

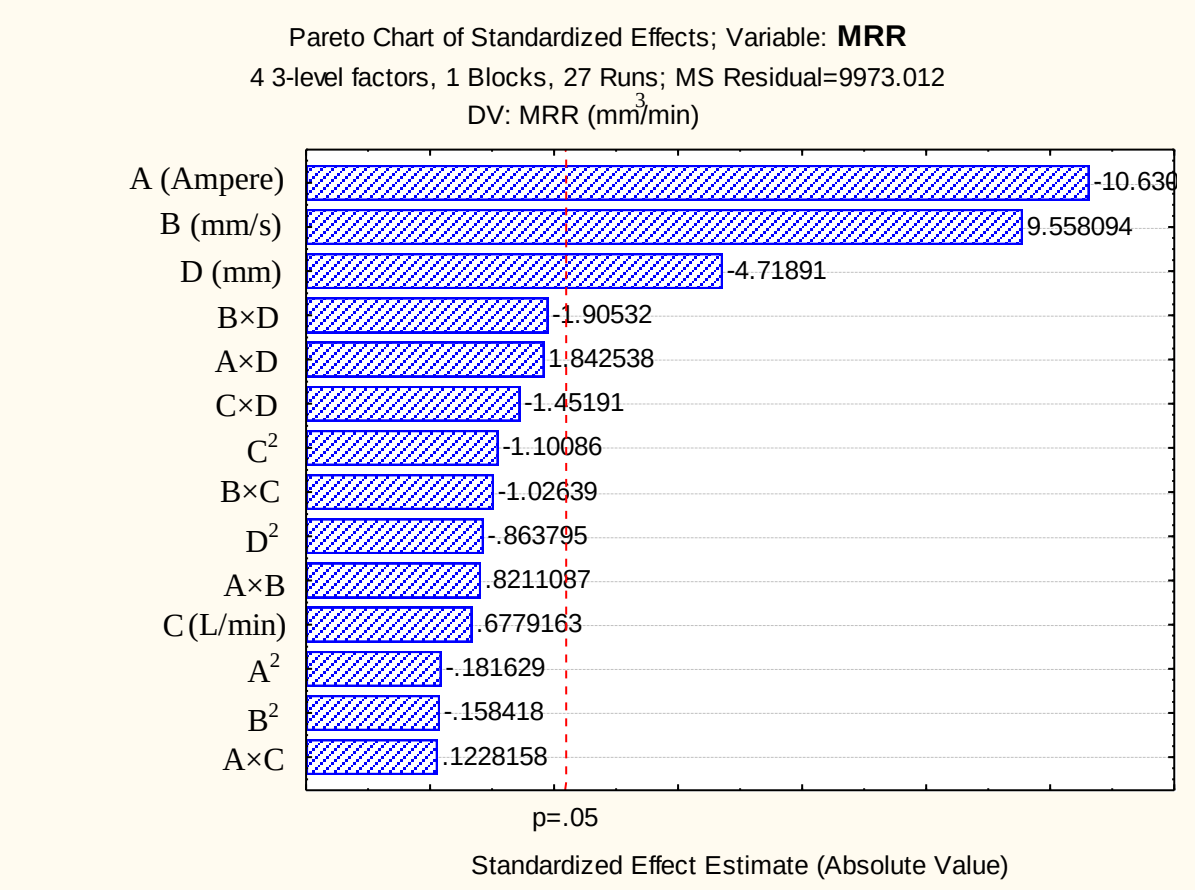

Fig. 156 Pareto chart of standardized effect of factors on MRR

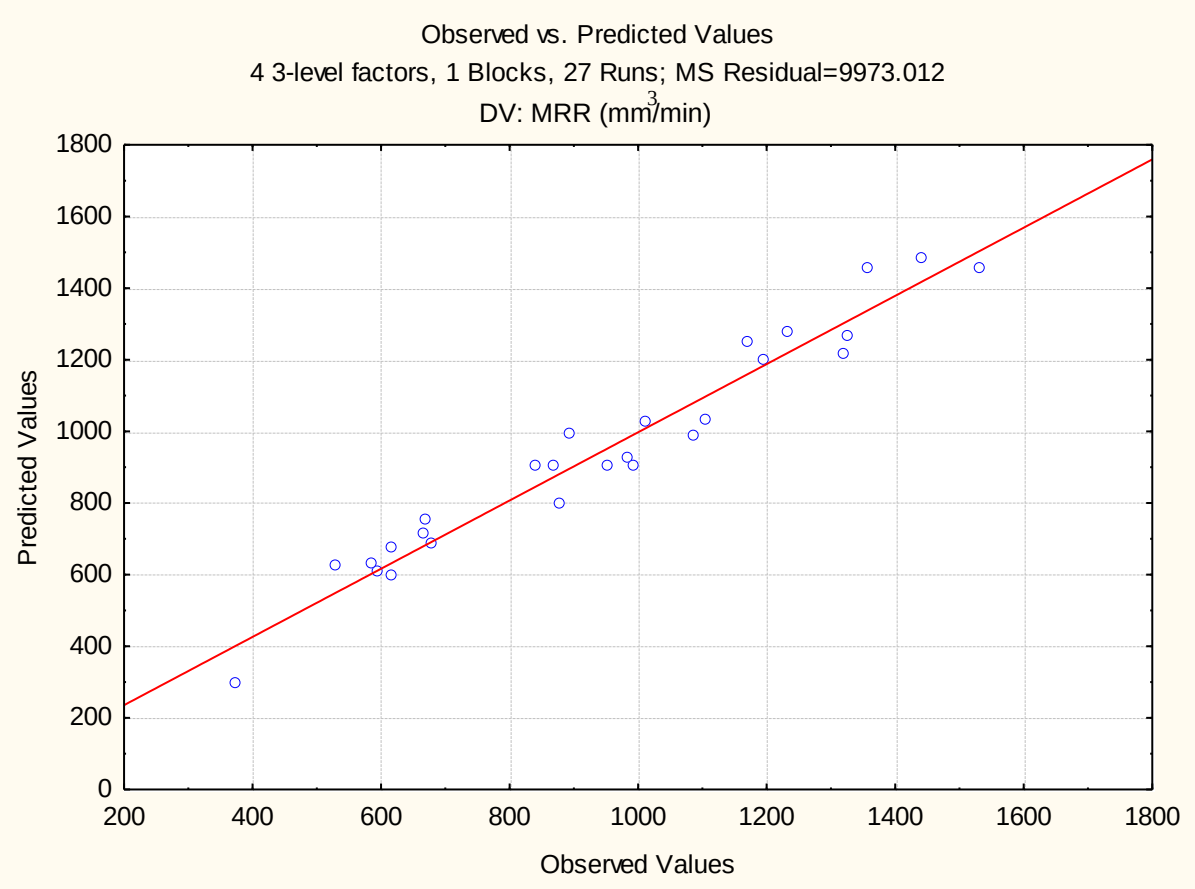

Fig. 157 Plot of observed vs. predicted values of MRR

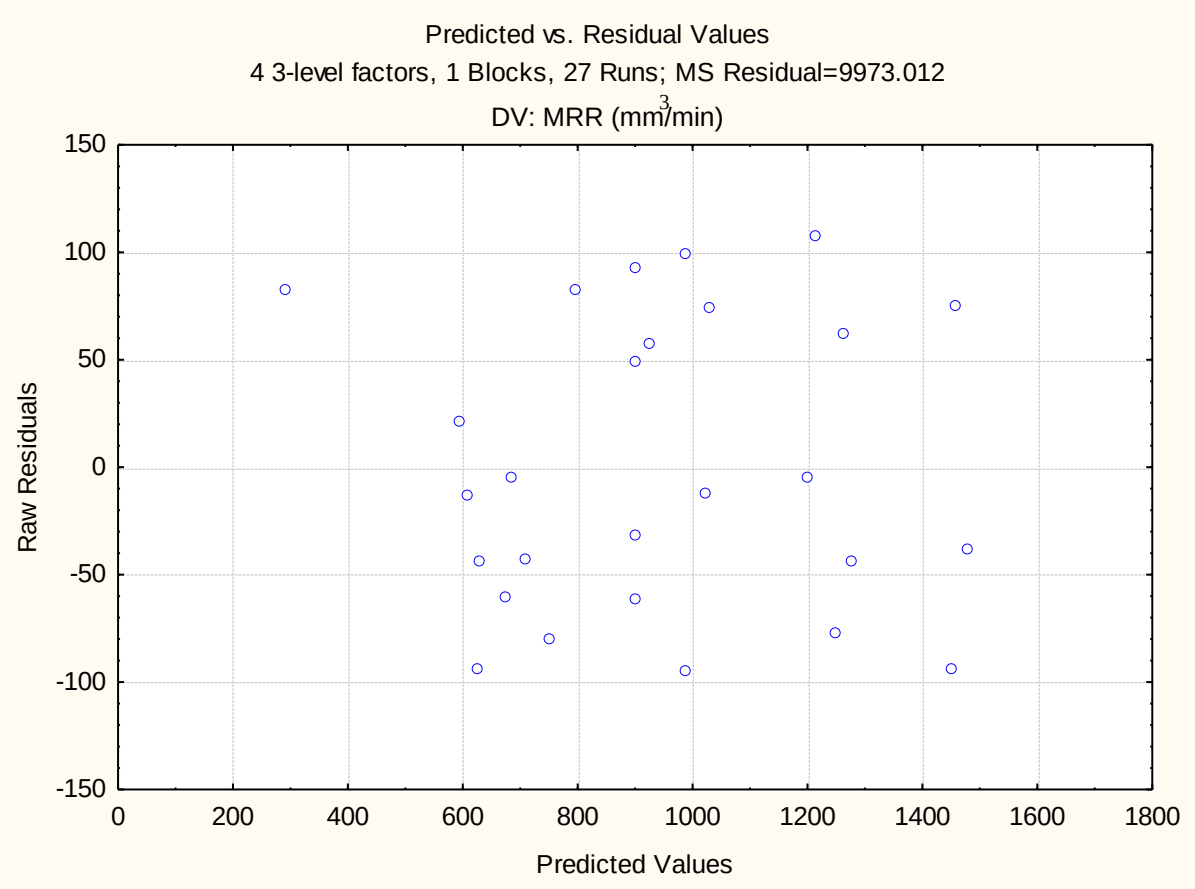

Fig. 158 Plot of predicted vs. residual values of MRR

From the Fig. 158, no standard pattern is formed in the plot of predicted vs. residual values which show the adequacy of the fitted model for MRR.

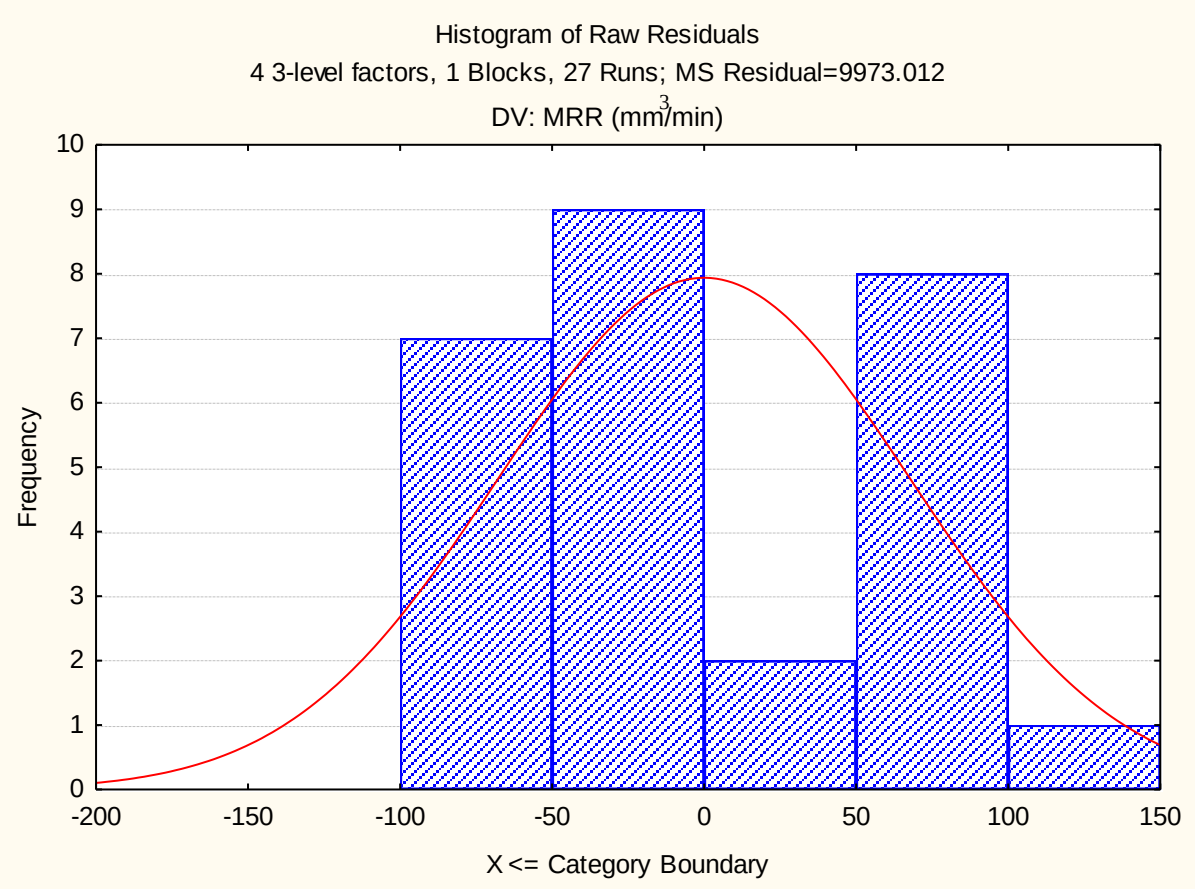

Fig. 159 Histogram plot of predicted values of MRR

Fig. 160 Plot of residuals vs. case numbers values of MRR

From the Fig. 160, it is evident that the highest MRR value among all experimental runs is by the run number 6. The red line indicates that the value of MRR decreases with increase in run order.

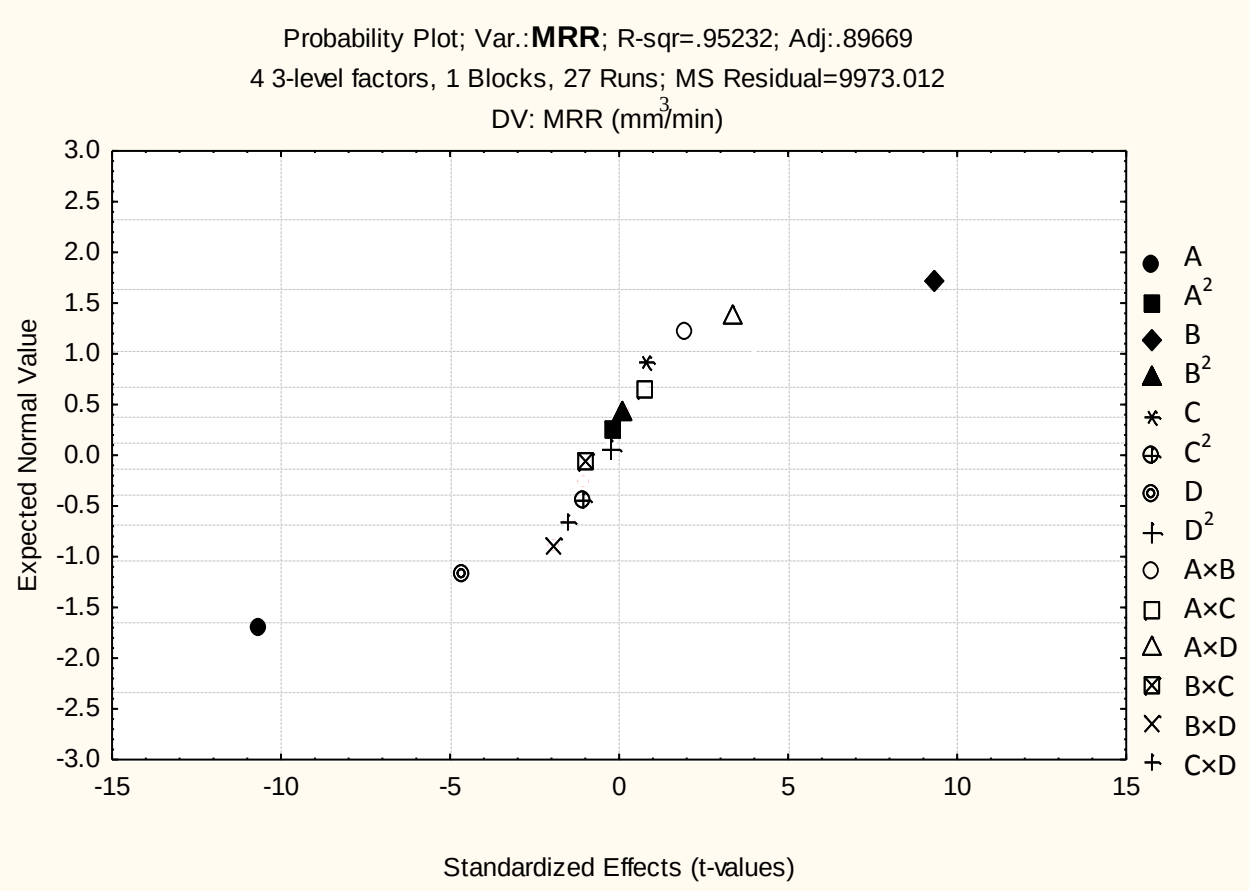

Fig. 161 Probability plot of MRR

The normal probability plot of MRR corresponding to each regression terms is plotted in Fig. 161.

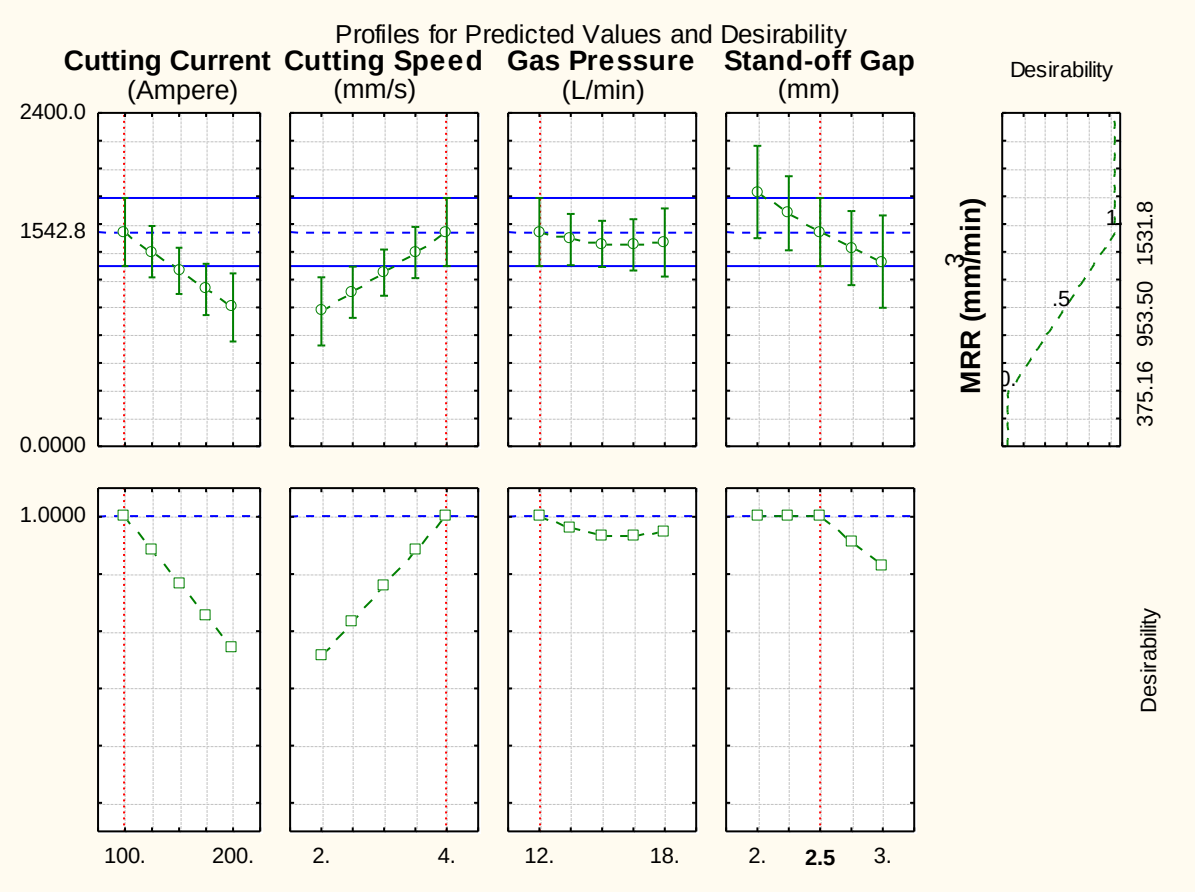

Fig. 162 Profile plot of predicted values and desirability of MRR

By the assistance of the desirability function, the optimum value of MRR response is obtained from the quadratic fit empirical model. The level of variable giving the highest desirability i.e., 1.0000 was considered as optimum level. The optimized levels of variables (A, B, C and D) were determined using the desirability profiles that are depicted in Fig. 162. The predicted values of responses and desirability function with red dotted lines are recorded in Fig. 162.

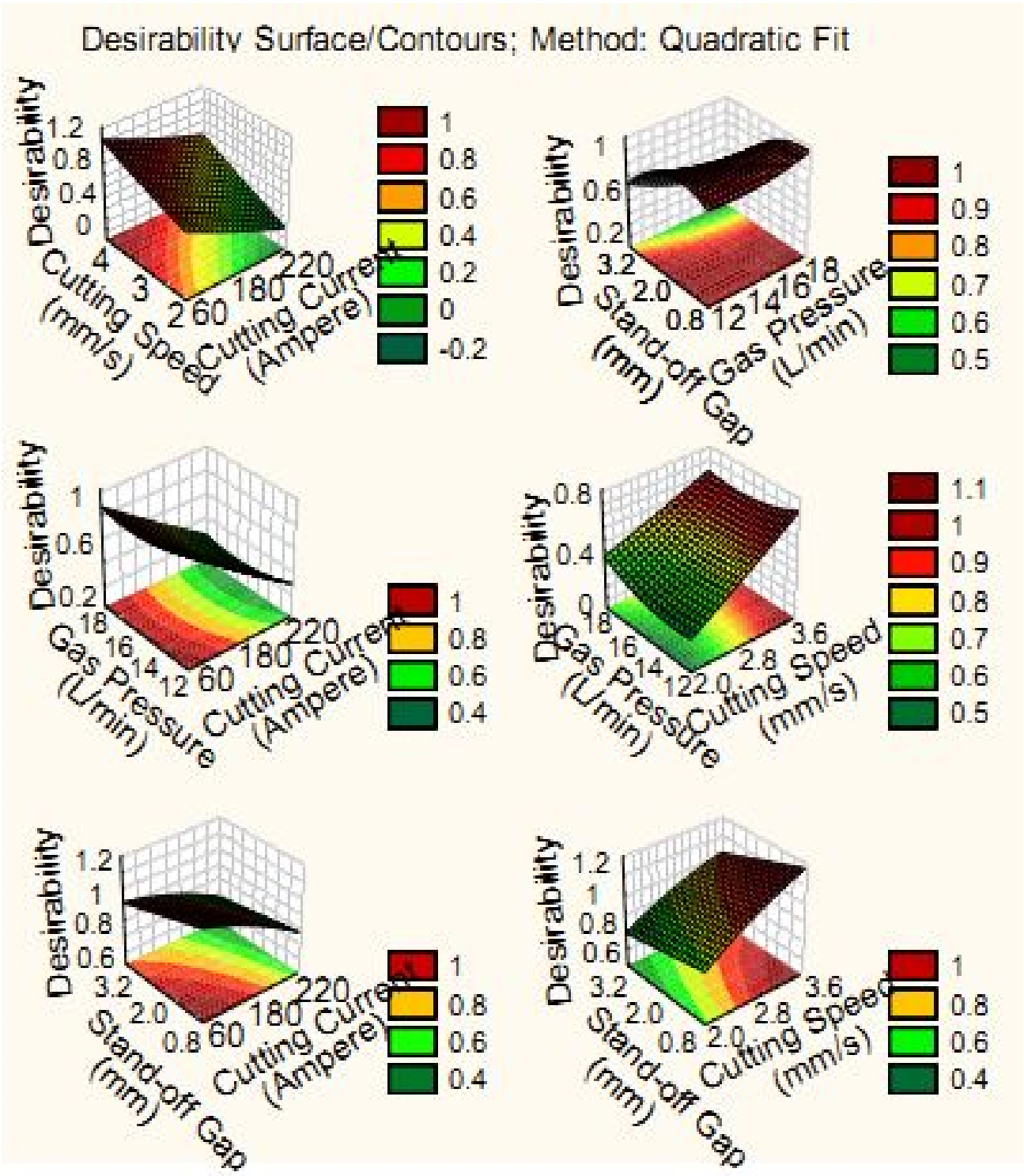

Fig. 163 Desirability 3D surface plot of MRR

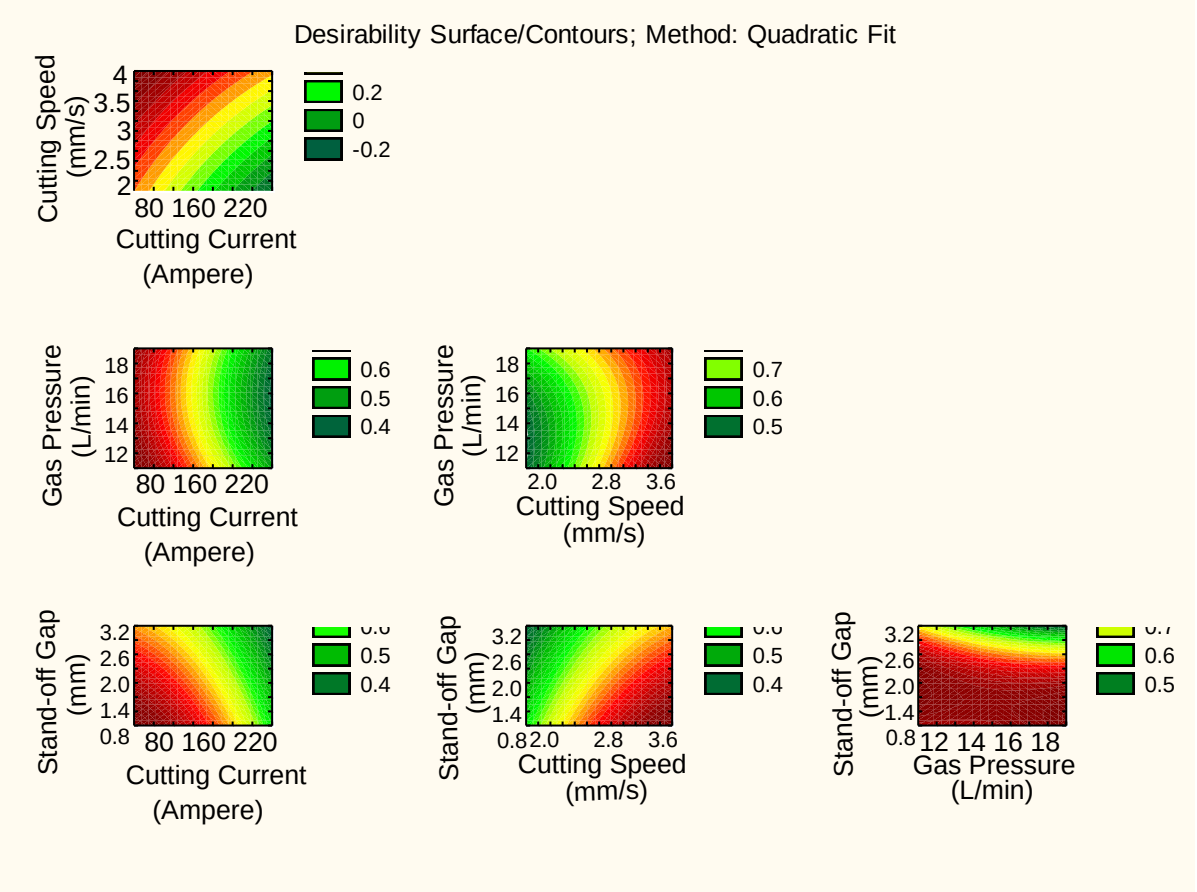

Fig. 164 Desirability 2D counter plot of MRR

The 3D and 2D surface plot of interaction terms on material removal rate output response were determined using the desirability profiles that are figured in Fig. 163-164 respectively. The highest amount MRR can be achieved by low and high value of stand-off gap and cutting speed respectively.

5.3.1.2 For surface roughness:

In the same way, the effect of estimated values for surface roughness was computed and recorded in Table 51. The ANOVA for SR has been carried out firstly and its results are given in Table 52. Here, the block effect has also been considered because the levels of block are taken as one. Due to this variation in block, there is negligible amount of effect occurred in experiment. This effect is ignored for further calculation of

optimization. The total degree of freedom for all input factors is 26. From the Table 52, it is seen that the most of the terms have P-value less than 0.05 under the confidence interval of 95 %. Hence, these terms show significance within experiment. In case of individual terms, cutting current, cutting speed and stand-off gap have shown the most significance among all parameters. Pareto chart of effects of all factors on SR response are shown in Fig. 165 and the results indicate that the linear form of cutting current is the second most enhancing factor among all considered factors. The scatter plot between the observed and the predicted value of MRR of all 27 runs is shown in Fig. 166. It is concluded that there is a reasonable correlation between the measured and predicted values of SR response. In Fig. 168, the histogram plot of predicted data of SR with 95 % confidence interval of normal distribution is displayed. In Table 53, the model of estimated regression coefficients of the independent variable on the SR is displayed.

Table 51 Effect of Estimated Values for SR

Factor	Effect	Std. Err.	T	P
Constant	20.88667	0.684609	30.50892	0.000000
A (Ampere)	-7.87833	1.185777	-6.64403	0.000024
A^2	-1.20125	0.889333	-1.35073	0.201702
B (mm/s)	6.87167	1.185777	5.79508	0.000085
B^2	0.22375	0.889333	0.25159	0.805613
C (L/min)	1.28500	1.185777	1.08368	0.299801
C^2	-0.33375	0.889333	-0.37528	0.714000
D (mm)	-3.91167	1.185777	-3.29882	0.006355
D^2	-0.79375	0.889333	-0.89252	0.389660
A×B	0.21500	2.053826	0.10468	0.918357
A×C	1.36000	2.053826	0.66218	0.520371
A×D	1.74000	2.053826	0.84720	0.413462
B×C	0.58000	2.053826	0.28240	0.782449
B×D	-1.20000	2.053826	-0.58428	0.569856
C×D	-1.88500	2.053826	-0.91780	0.376802

Table 52 ANOVA Table for SR

Factors	SS	DoF	MS	F	P
A (Ampere)	186.2044	1	186.2044	44.14310	0.000024
A^2	7.6960	1	7.6960	1.82448	0.201702
B (mm/s)	141.6594	1	141.6594	33.58290	0.000085
B^2	0.2670	1	0.2670	0.06330	0.805613
C (L/min)	4.9537	1	4.9537	1.17436	0.299801
C^2	0.5941	1	0.5941	0.14084	0.714000
D (mm)	45.9034	1	45.9034	10.88223	0.006355
D^2	3.3602	1	3.3602	0.79660	0.389660
A×B	0.0462	1	0.0462	0.01096	0.918357
A×C	1.8496	1	1.8496	0.43848	0.520371
A×D	3.0276	1	3.0276	0.71775	0.413462
B×C	0.3364	1	0.3364	0.07975	0.782449
B×D	1.4400	1	1.4400	0.34138	0.569856
C×D	3.5532	1	3.5532	0.84236	0.376802
Error	50.6184	12	4.2182		
Total SS	451.5603	26			

Table 53 Regression Coefficients of SR

Factor	Regression Coef.	Std. Err.	T	P
Constant	60.5500	59.89053	1.01101	0.331963
A (Ampere)	-0.3844	0.19083	-2.01424	0.066959
A^2	0.0005	0.00036	1.35073	0.201702
B (mm/s)	6.0058	9.54164	0.62943	0.540863
B^2	-0.2237	0.88933	-0.25159	0.805613
C (L/min)	-0.2975	3.72362	-0.07990	0.937638
C^2	0.0371	0.09881	0.37528	0.714000
D (mm)	-11.9817	22.34175	-0.53629	0.601558
D^2	3.1750	3.55733	0.89252	0.389660
A×B	0.0022	0.02054	0.10468	0.918357
A×C	0.0045	0.00685	0.66218	0.520371
A×D	0.0348	0.04108	0.84720	0.413462
B×C	0.0967	0.34230	0.28240	0.782449
B×D	-1.2000	2.05383	-0.58428	0.569856
C×D	-0.6283	0.68461	-0.91780	0.376802

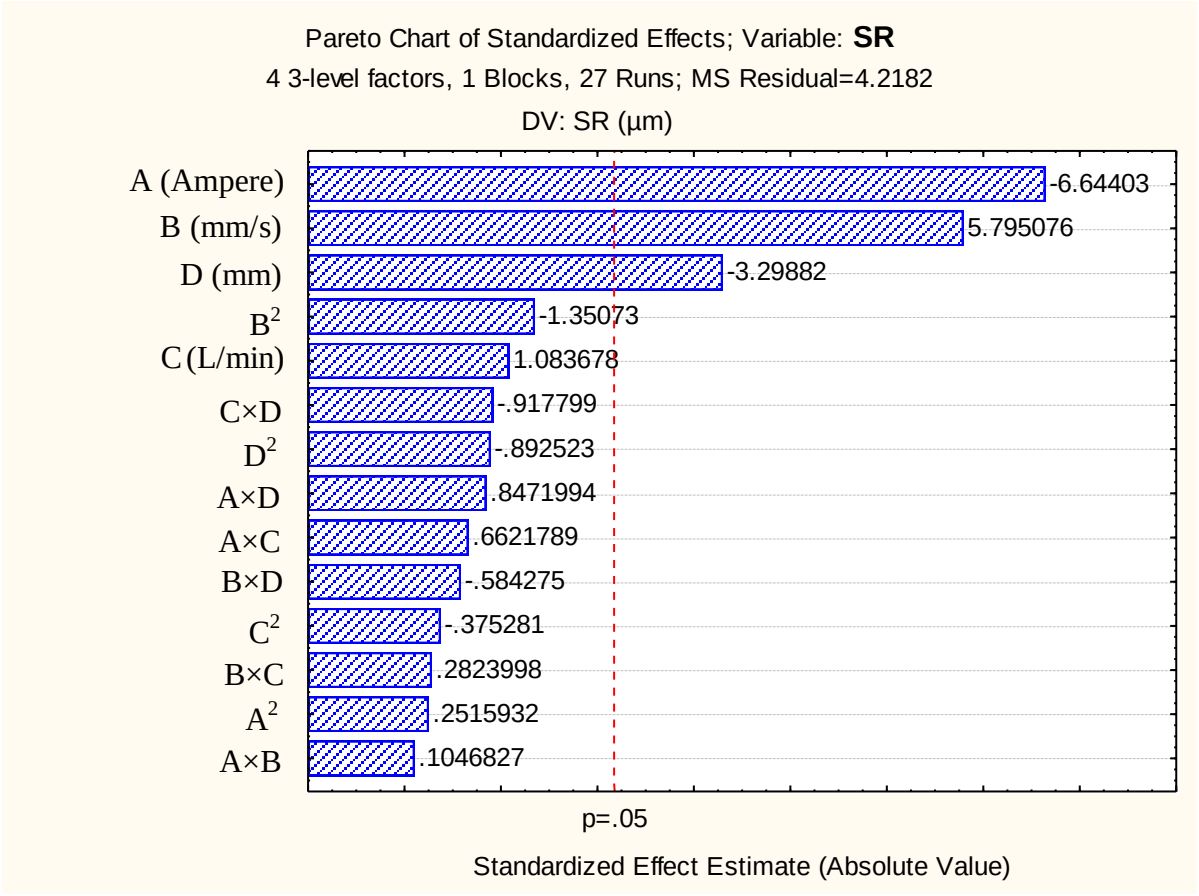

Fig. 165 Pareto chart of standardized effect of factors on SR

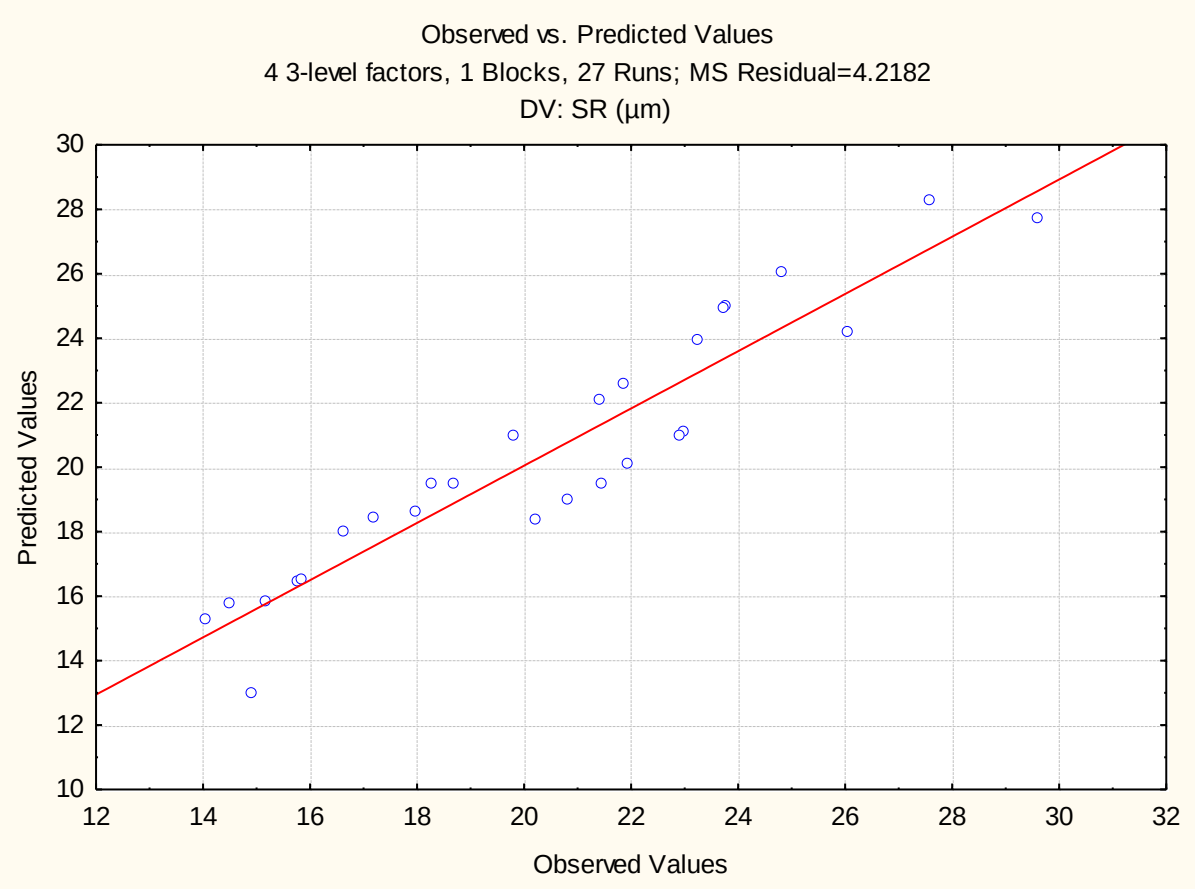

Fig. 166 Plot of observed vs. predicted values of SR

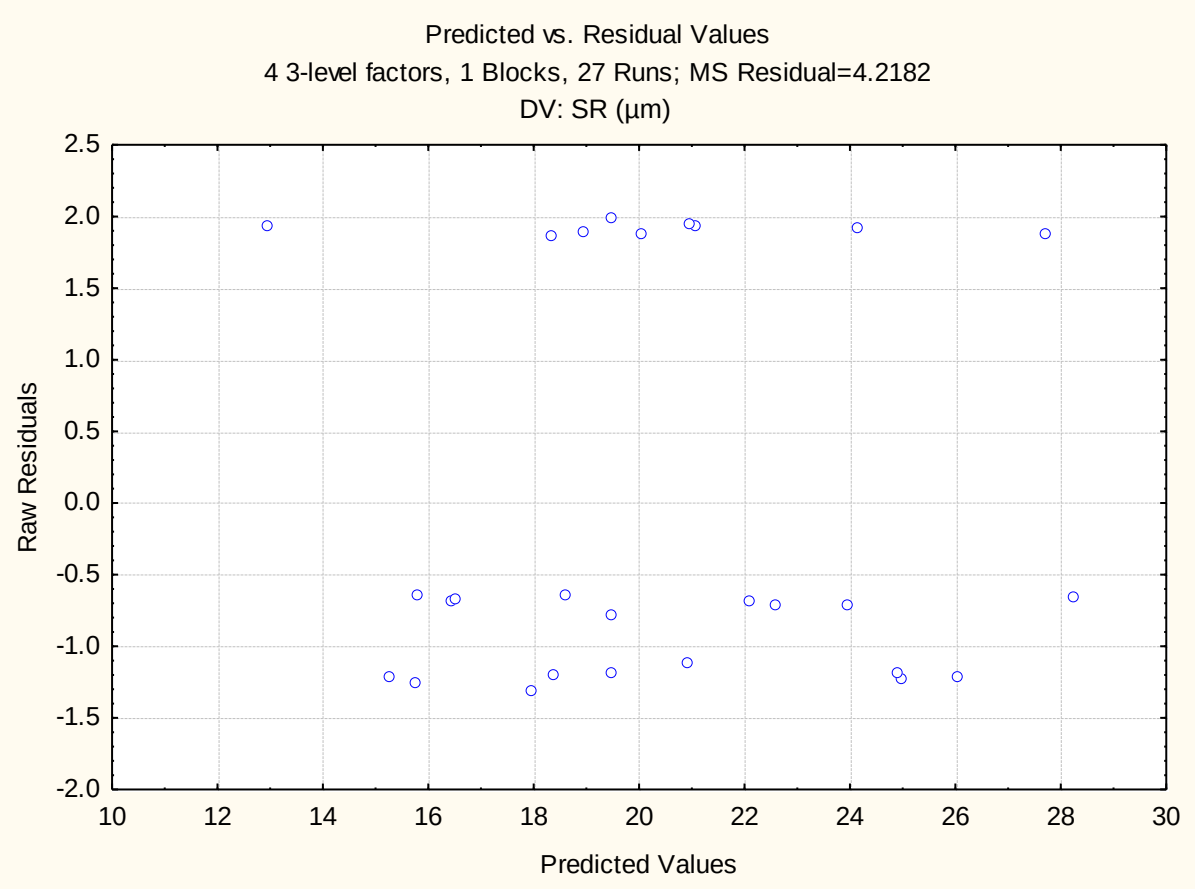

Fig. 167 Plot of predicted vs. residual values of SR

From the Fig. 167, no standard pattern is formed in the plot of predicted vs. residual values which show the adequacy of the fitted model for SR.

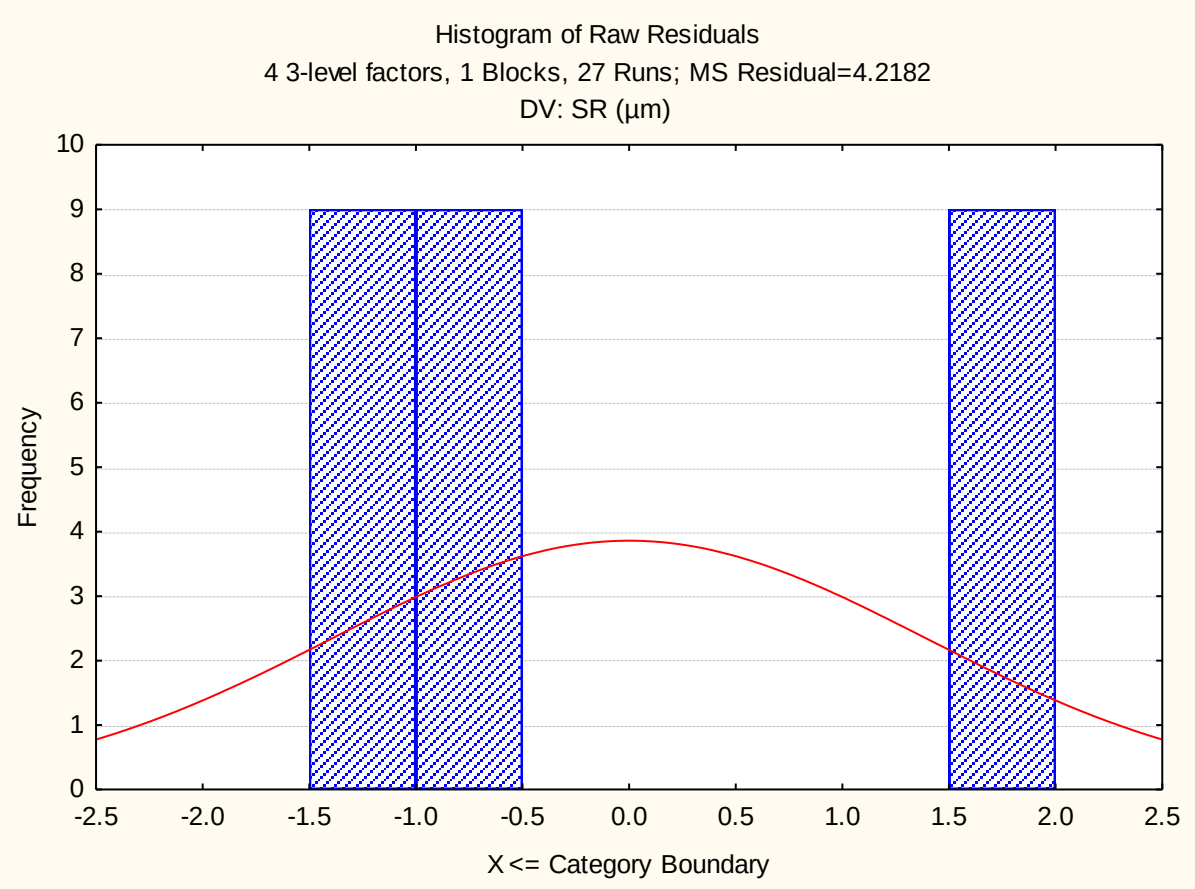

Fig. 168 Histogram plot of predicted values of SR

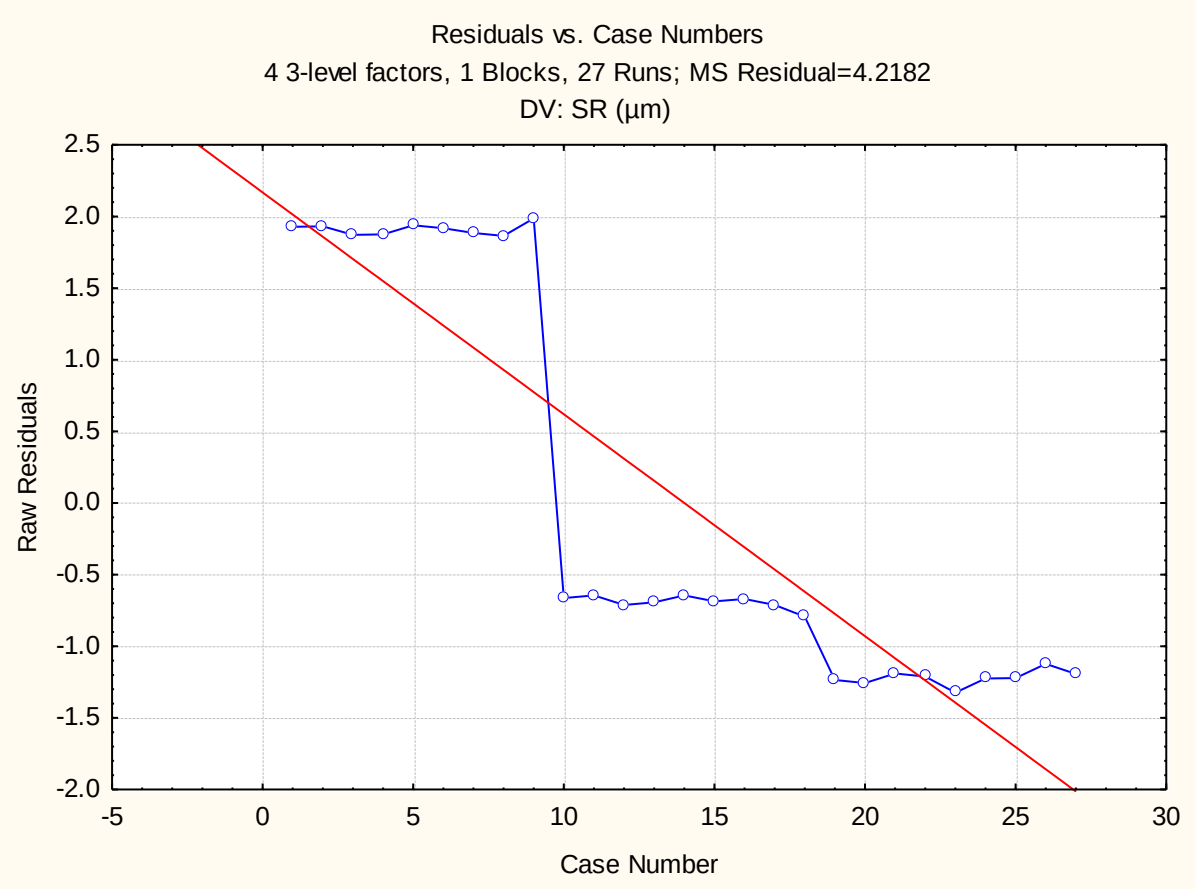

Fig. 169 Plot of residuals vs. case numbers values of SR

From the Fig. 169, it is evident that the highest SR value among all experimental runs is by the run number 9. The red line indicates that the value of SR decreases with increase in run order.

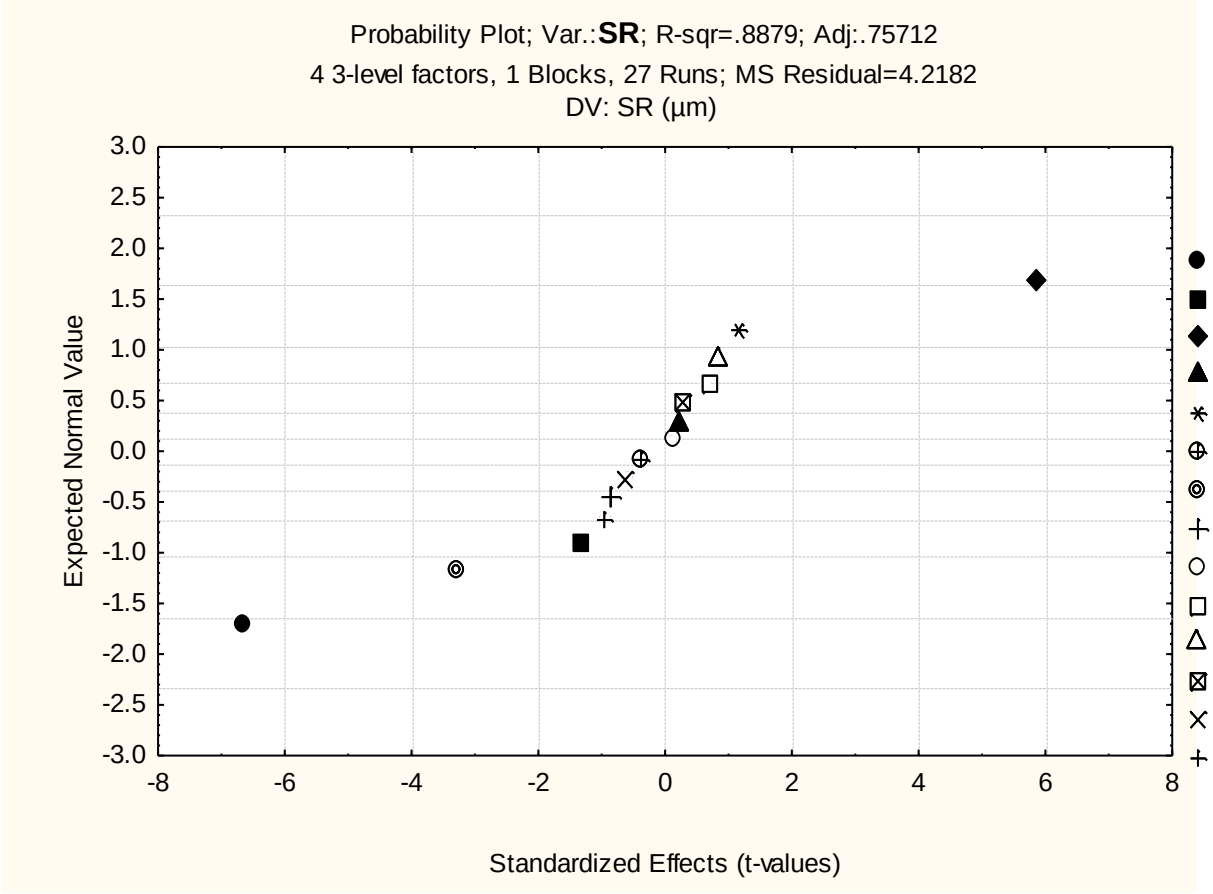

Fig. 170 Probability plot of SR

The normal probability plot of SR corresponding to each regression terms is plotted in Fig. 170.

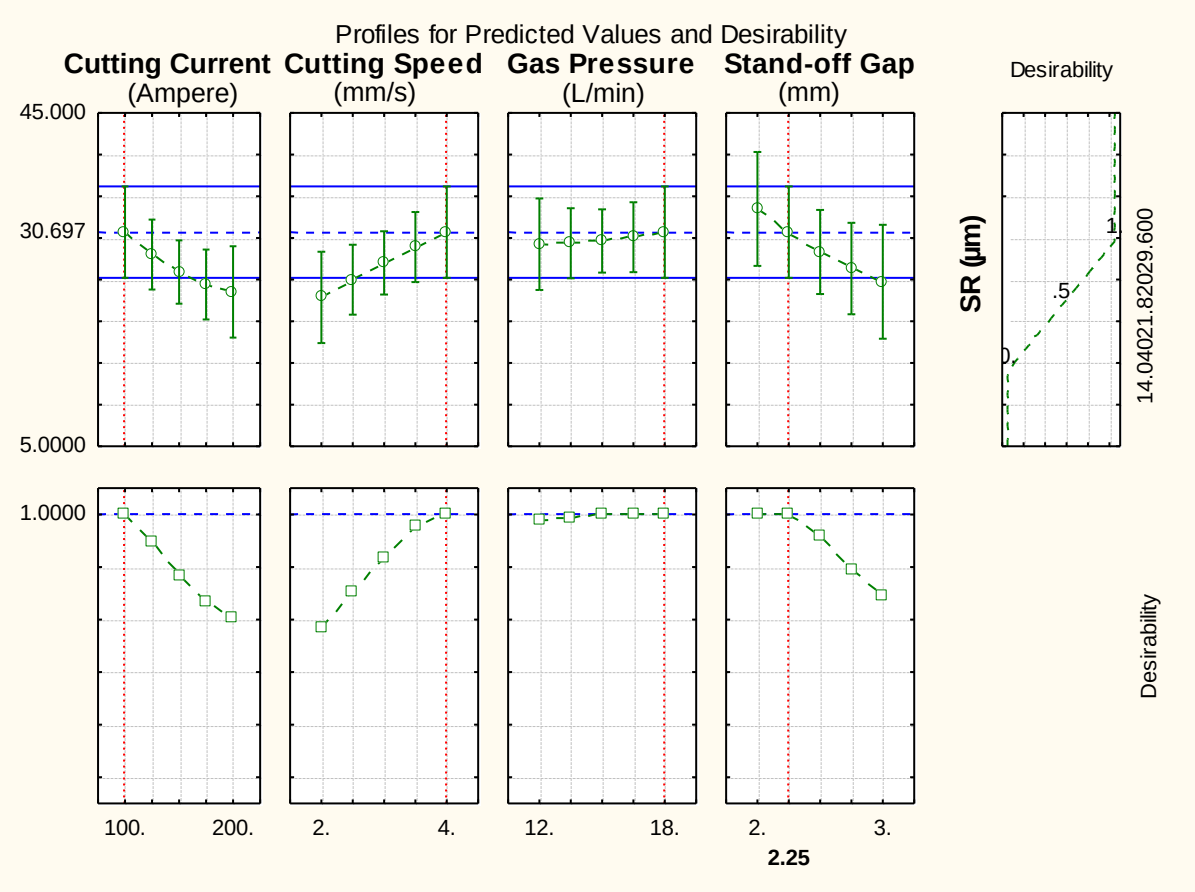

Fig. 171 Profile plot of predicted values and desirability of SR

The methodology of desirability function aided to obtain optimum SR response value which was fitted by the quadratic fit model. The level of variable giving the highest desirability i.e., 1.0000 was considered as optimum level. The optimized levels of variables (A, B, C and D) were determined using the desirability profiles that are shown in Fig. 171. And, the predicted values of responses and desirability function with red dotted lines are presented in same figure i.e. Fig. 171.

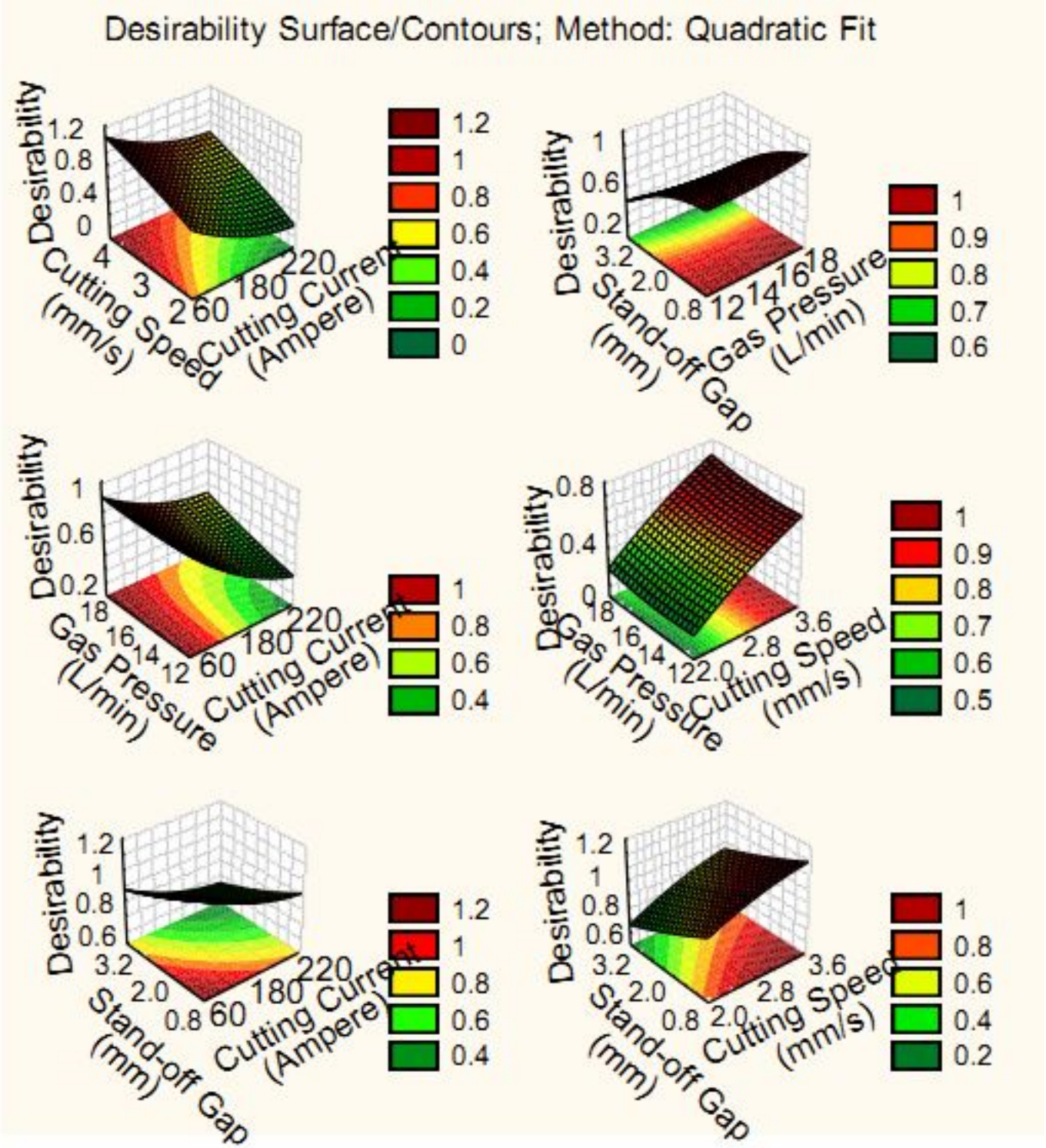

Fig. 172 Desirability 3D surface plot of SR

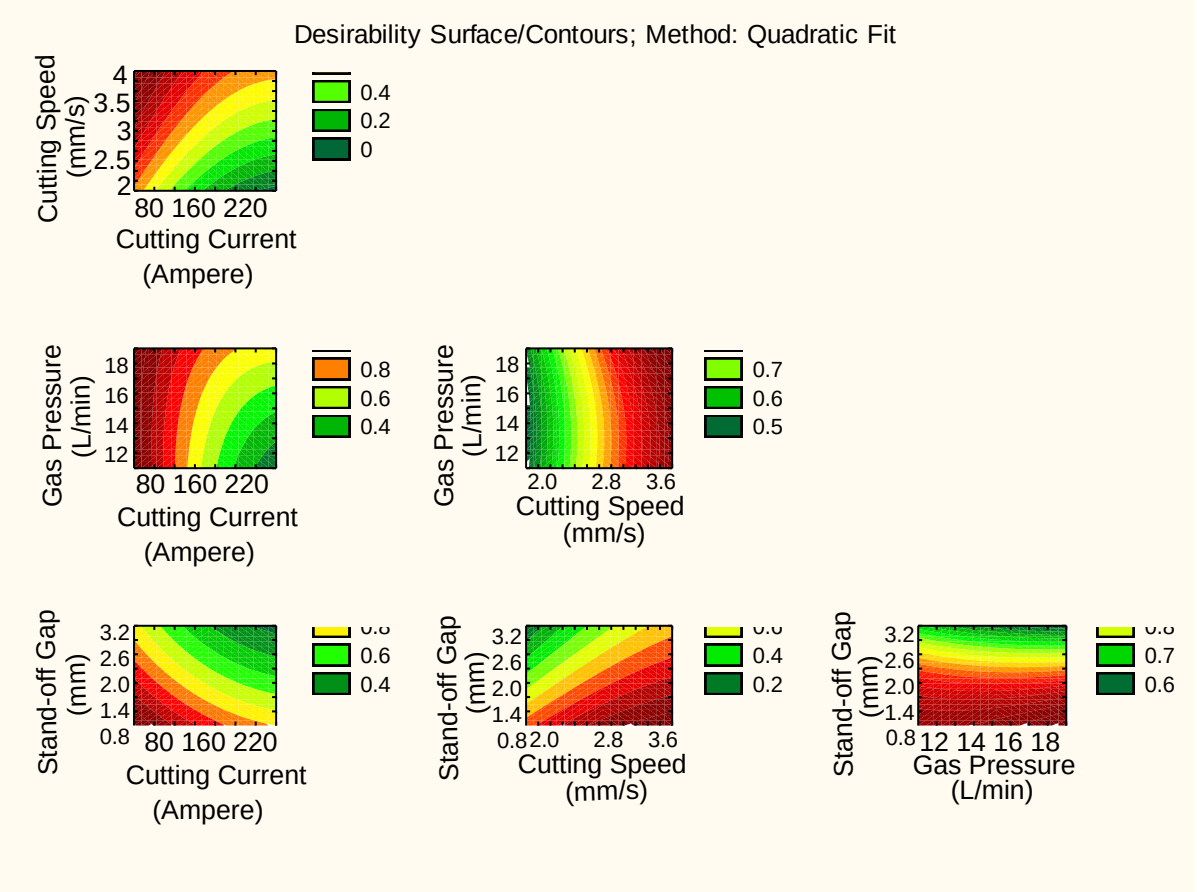

Fig. 173 Desirability 2D counter plot of SR

The 3D and 2D surface plot of interaction variables on surface roughness were determined using the desirability profiles that are presented in Fig. 172-173 respectively. The minimum value of SR response was occurred with highest amount of cutting current and lowest amount of cutting speed.

5.3.1.3 For chamfer:

In case of chamfer, the ANOVA has been done in Table 55. It is evident that the cutting current has shown very significance than other individual terms as its F-value got the highest considering all terms with P-value less than 0.05. Fig. 174 shows the Pareto chart of effects of all factors on chamfer response and the results reveal that the linear form cutting current is the second most enhancing factor among all chosen factors. The

scatter plot between the observed and the predicted value of chamfer of all 27 runs is shown in Fig. 175. From this result it can be revealed that the response model shows good fit to experimental data. In Fig. 177, the histogram plot of predicted data of chamfer with 95 % confidence interval of normal distribution is shown. The model of estimated coefficient by multiple regressions for chamfer is calculated in Table 54 from the institute licensed software of Statistica 9.1. Similarly, the regression model of chamfer is recorded in Table 56.

Table 54 Effect of Estimated Values for Chamfer

Factor	Effect	Std. Err.	T	P
Constant	0.240000	0.014380	16.68962	0.000000
A (Ampere)	-0.150000	0.024907	-6.02235	0.000060
A^2	-0.027500	0.018680	-1.47213	0.166722
B (mm/s)	0.123333	0.024907	4.95171	0.000335
B^2	-0.005000	0.018680	-0.26766	0.793506
C (L/min)	0.030000	0.024907	1.20447	0.251627
C^2	-0.007500	0.018680	-0.40149	0.695117
D (mm)	-0.096667	0.024907	-3.88107	0.002184
D^2	-0.010000	0.018680	-0.53532	0.602209
A×B	-0.025000	0.043141	-0.57950	0.572970
A×C	0.000000	0.043141	0.00000	1.000000
A×D	0.035000	0.043141	0.81130	0.432991
B×C	-0.005000	0.043141	-0.11590	0.909649
B×D	-0.080000	0.043141	-1.85440	0.088409
C×D	-0.045000	0.043141	-1.04310	0.317461

Table 55 ANOVA Table for Chamfer

Factors	SS	DoF	MS	F	P
A (Ampere)	0.067500	1	0.067500	36.26866	0.000060
A^2	0.004033	1	0.004033	2.16716	0.166722
B (mm/s)	0.045633	1	0.045633	24.51940	0.000335
B^2	0.000133	1	0.000133	0.07164	0.793506
C (L/min)	0.002700	1	0.002700	1.45075	0.251627
C^2	0.000300	1	0.000300	0.16119	0.695117
D (mm)	0.028033	1	0.028033	15.06269	0.002184
D^2	0.000533	1	0.000533	0.28657	0.602209
A×B	0.000625	1	0.000625	0.33582	0.572970
A×C	0.000000	1	0.000000	0.00000	1.000000
A×D	0.001225	1	0.001225	0.65821	0.432991
B×C	0.000025	1	0.000025	0.01343	0.909649
B×D	0.006400	1	0.006400	3.43881	0.088409
C×D	0.002025	1	0.002025	1.08806	0.317461
Error	0.022333	12	0.001861		
Total SS	0.180667	26			

Table 56 Regression Coefficients of Chamfer

Factor	Regression Coef.	Std. Err.	T	P
Constant	0.093333	1.258000	0.07419	0.942080
A (Ampere)	-0.005800	0.004008	-1.44695	0.173525
A^2	0.000011	0.000007	1.47213	0.166722
B (mm/s)	0.281667	0.200422	1.40537	0.185269
B^2	0.005000	0.018680	0.26766	0.793506
C (L/min)	0.020000	0.078215	0.25571	0.802508
C^2	0.000833	0.002076	0.40149	0.695117
D (mm)	0.063333	0.469288	0.13496	0.894884
D^2	0.040000	0.074722	0.53532	0.602209
A×B	-0.000250	0.000431	-0.57950	0.572970
A×C	-0.000000	0.000144	-0.00000	1.000000
A×D	0.000700	0.000863	0.81130	0.432991
B×C	-0.000833	0.007190	-0.11590	0.909649
B×D	-0.080000	0.043141	-1.85440	0.088409
C×D	-0.015000	0.014380	-1.04310	0.317461

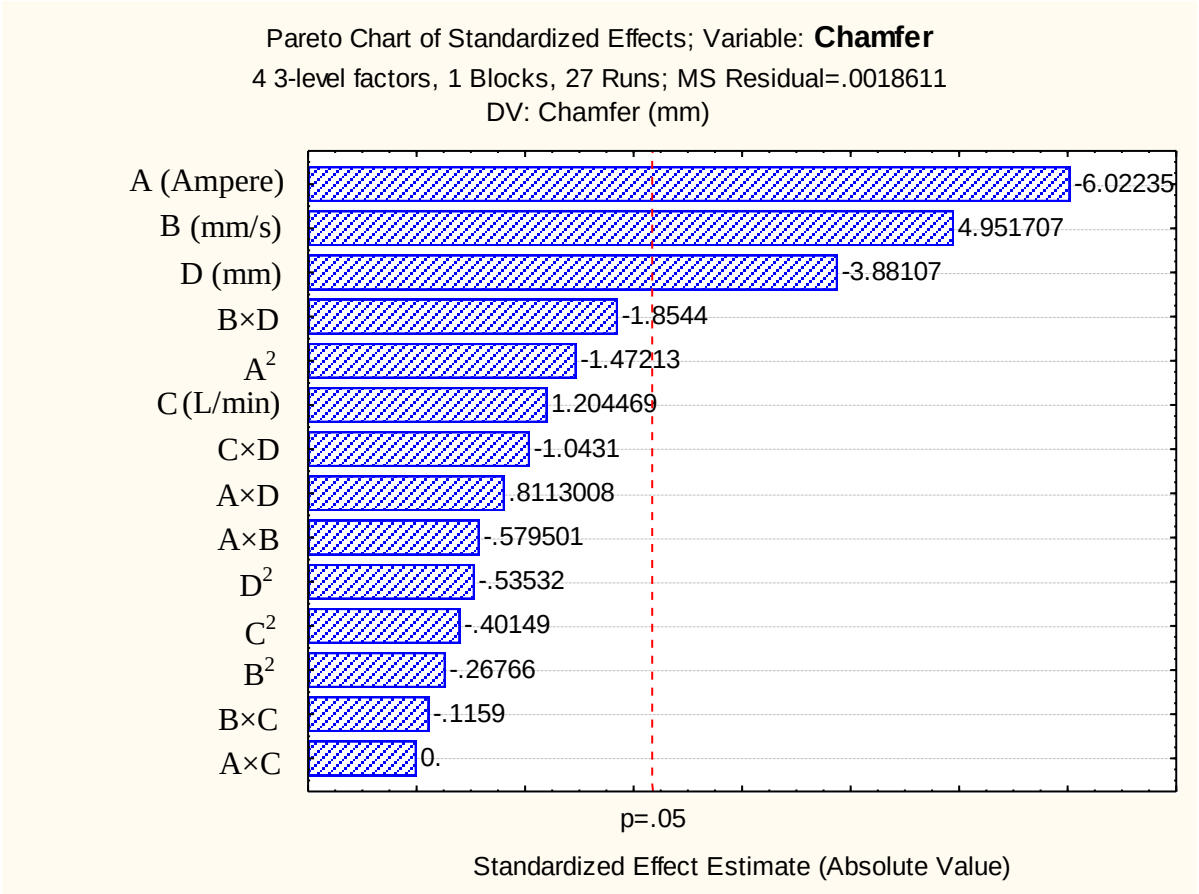

Fig. 174 Pareto chart of standardized effect of factors on chamfer

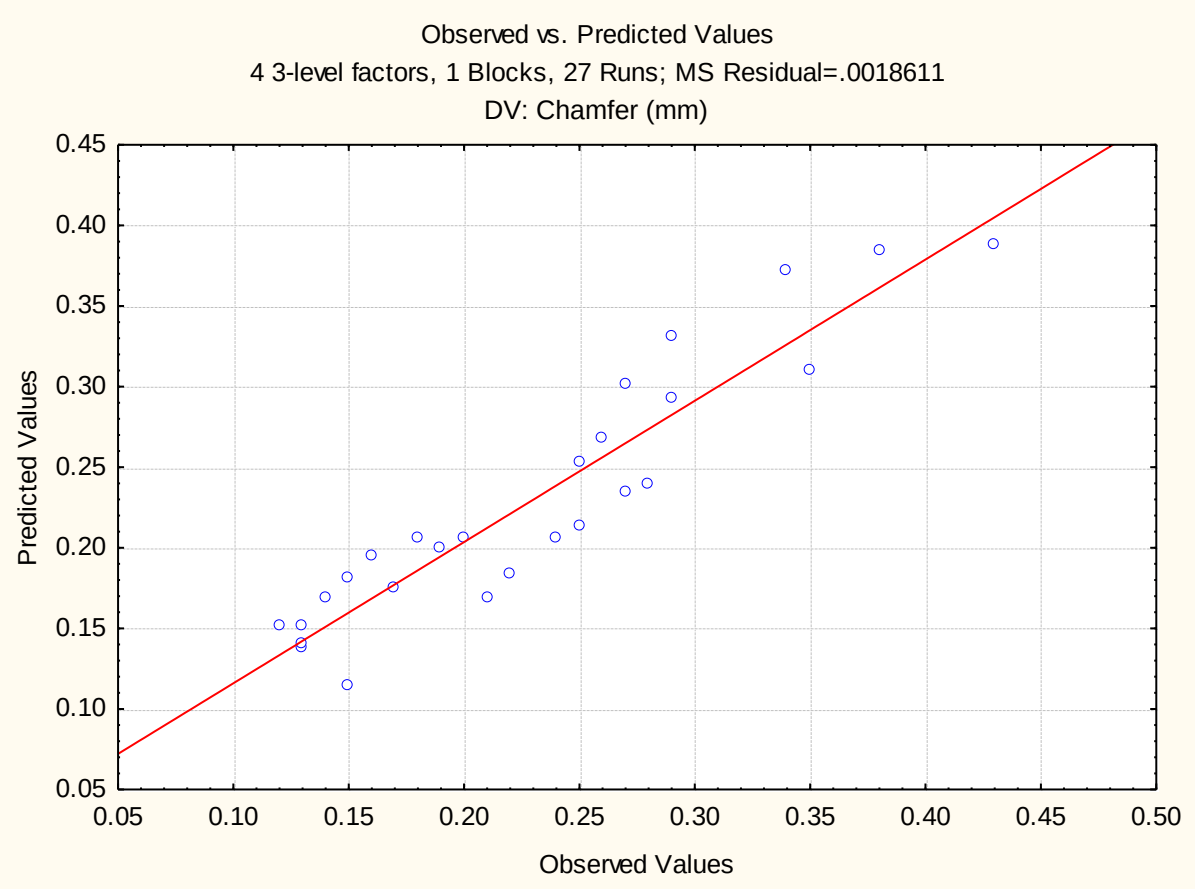

Fig. 175 Plot of observed vs. predicted values of chamfer

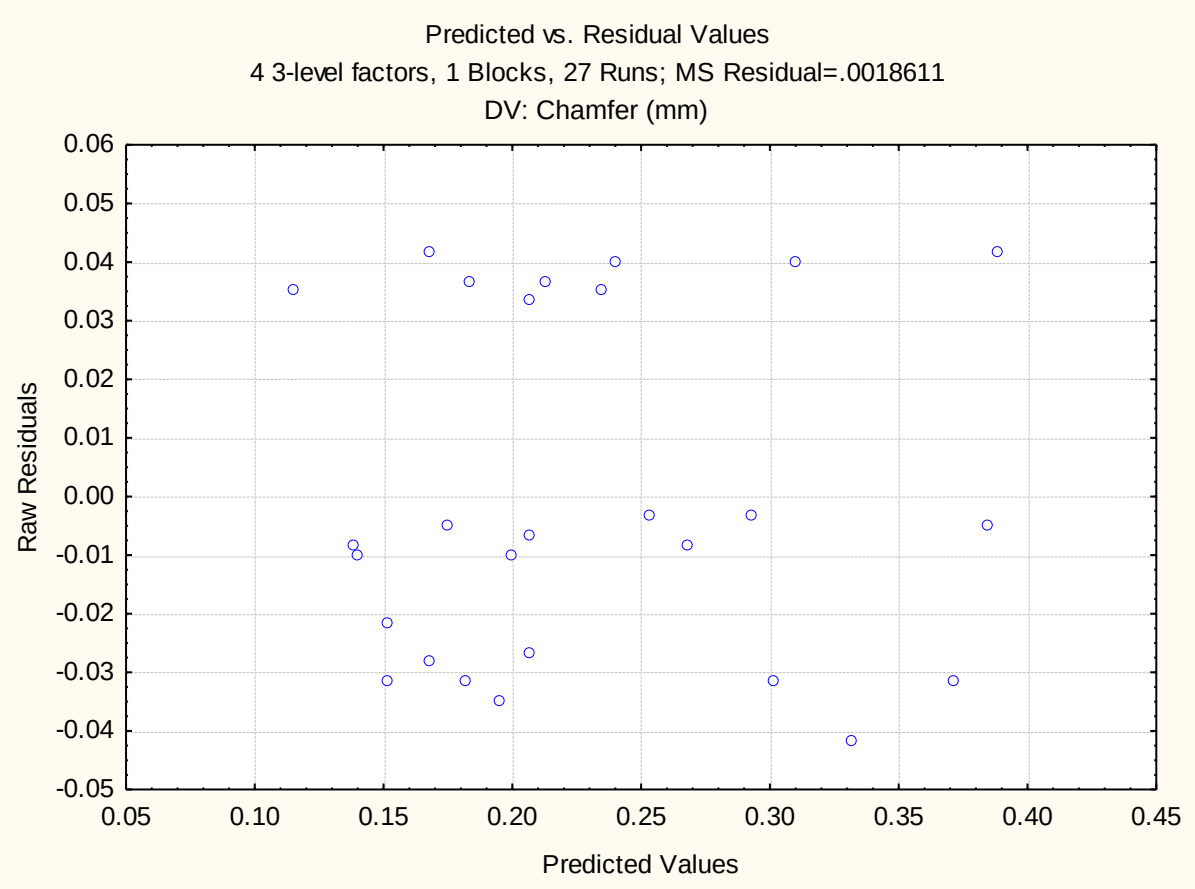

Fig. 176 Plot of predicted vs. residual values of chamfer

From the Fig. 176, no standard pattern is formed in the plot of predicted vs. residual values which show the adequacy of the fitted model for chamfer.

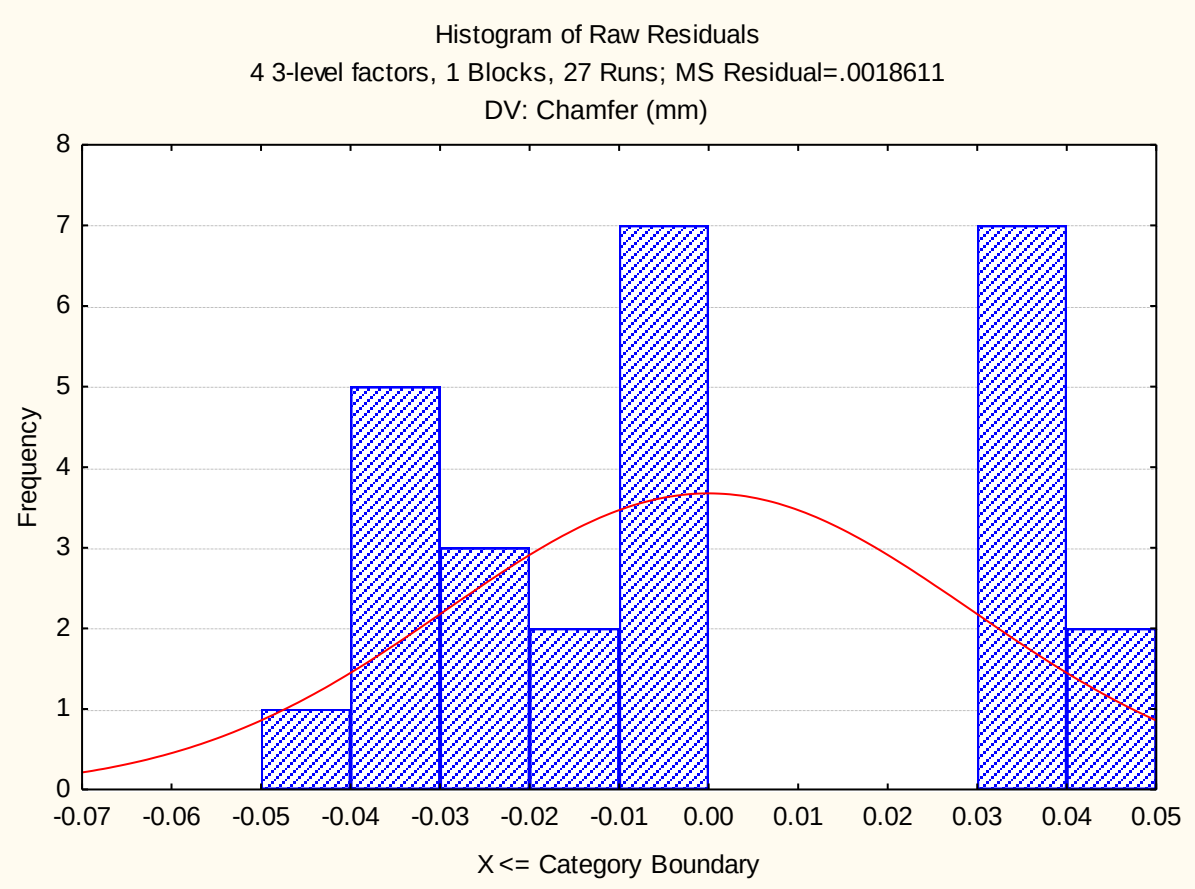

Fig. 177 Histogram plot of predicted values of chamfer

Fig. 178 Plot of residuals vs. case numbers values of chamfer

From the Fig. 178, it is evident that the highest chamfer value among all experimental runs is by the run number 8. The red line indicates that the value of chamfer increases with increase in run order.

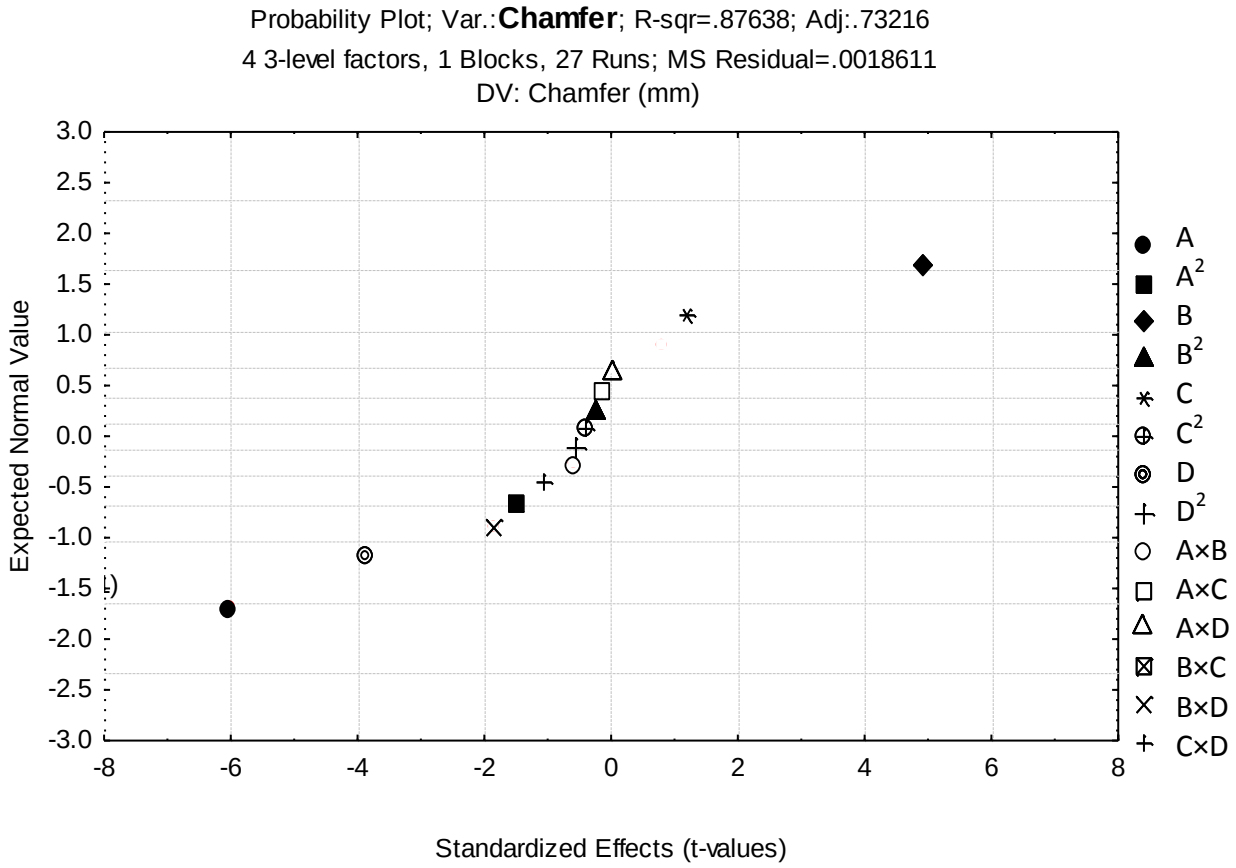

Fig. 179 Probability plot of chamfer

The normal probability plot of chamfer corresponding to each regression terms is plotted in Fig. 179.

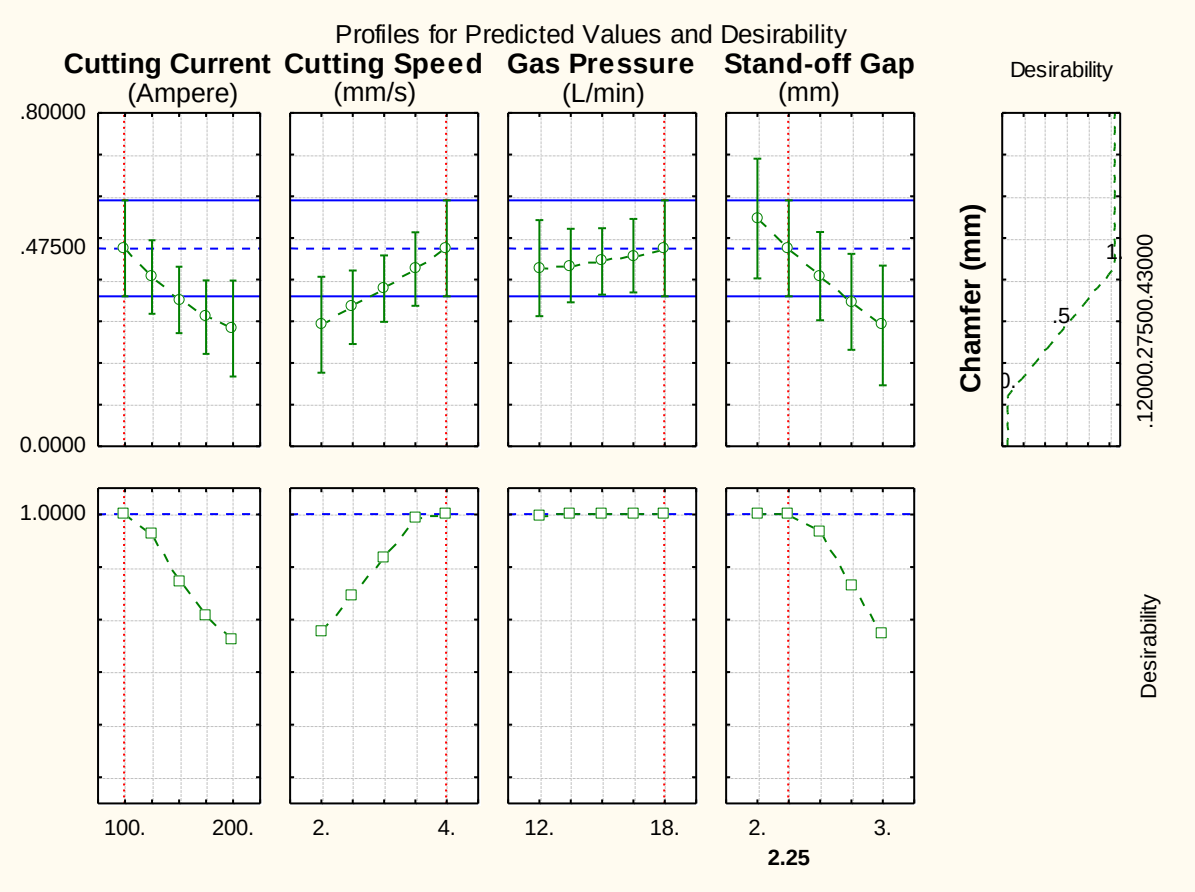

Fig. 180 Profile plot of predicted values and desirability of chamfer

The noble technique of desirability function used to get optimum value of chamfer response by the help of quadratic fit model. The level of variable giving the highest desirability i.e., 1.0000 was considered as optimum level. The optimized levels of variables (A, B, C and D) were determined using the desirability profiles that are shown in Fig. 180. The predicted values of responses and desirability function with red dotted lines are figured in Fig. 180.

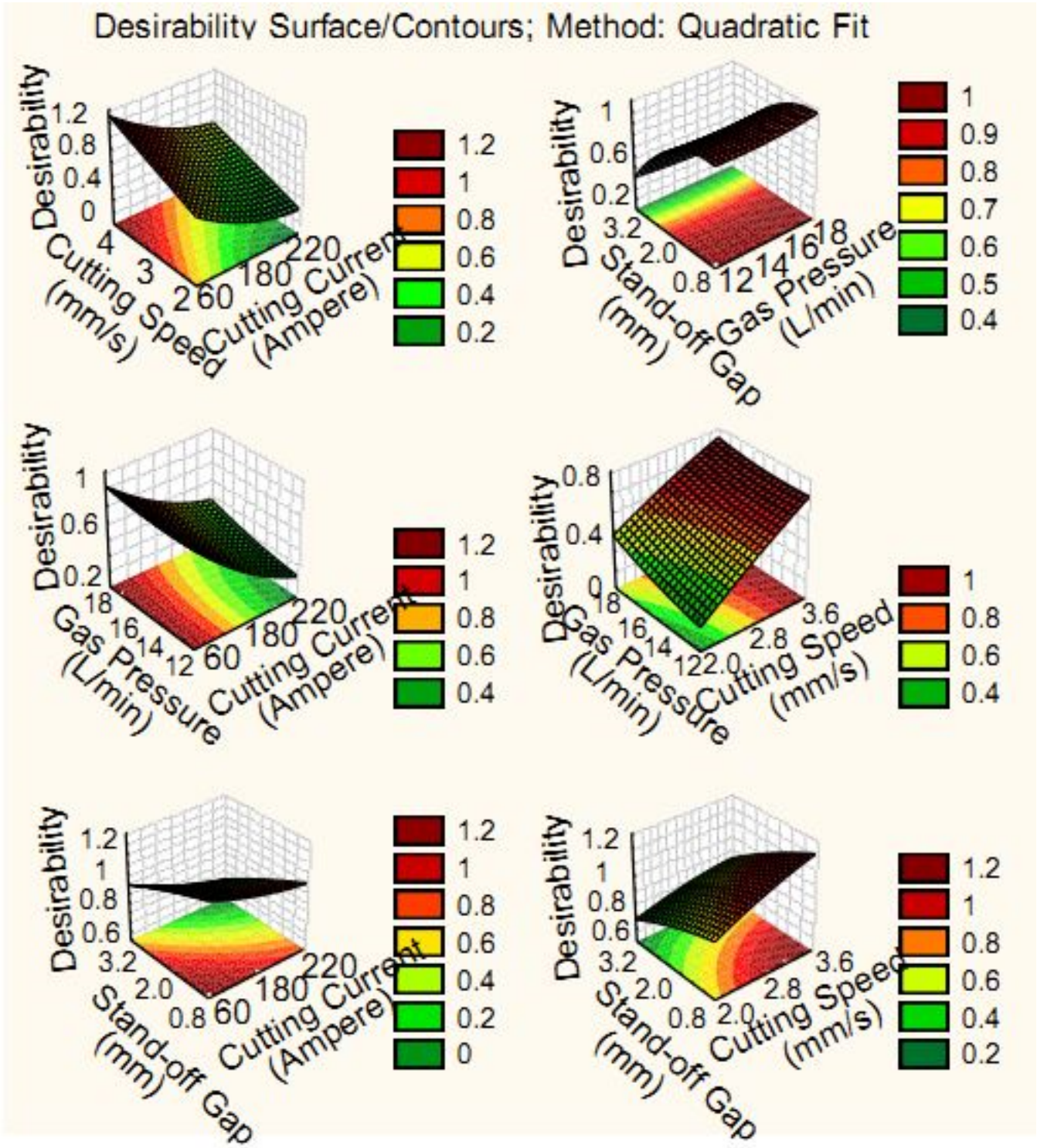

Fig. 181 Desirability 3D surface plot of chamfer

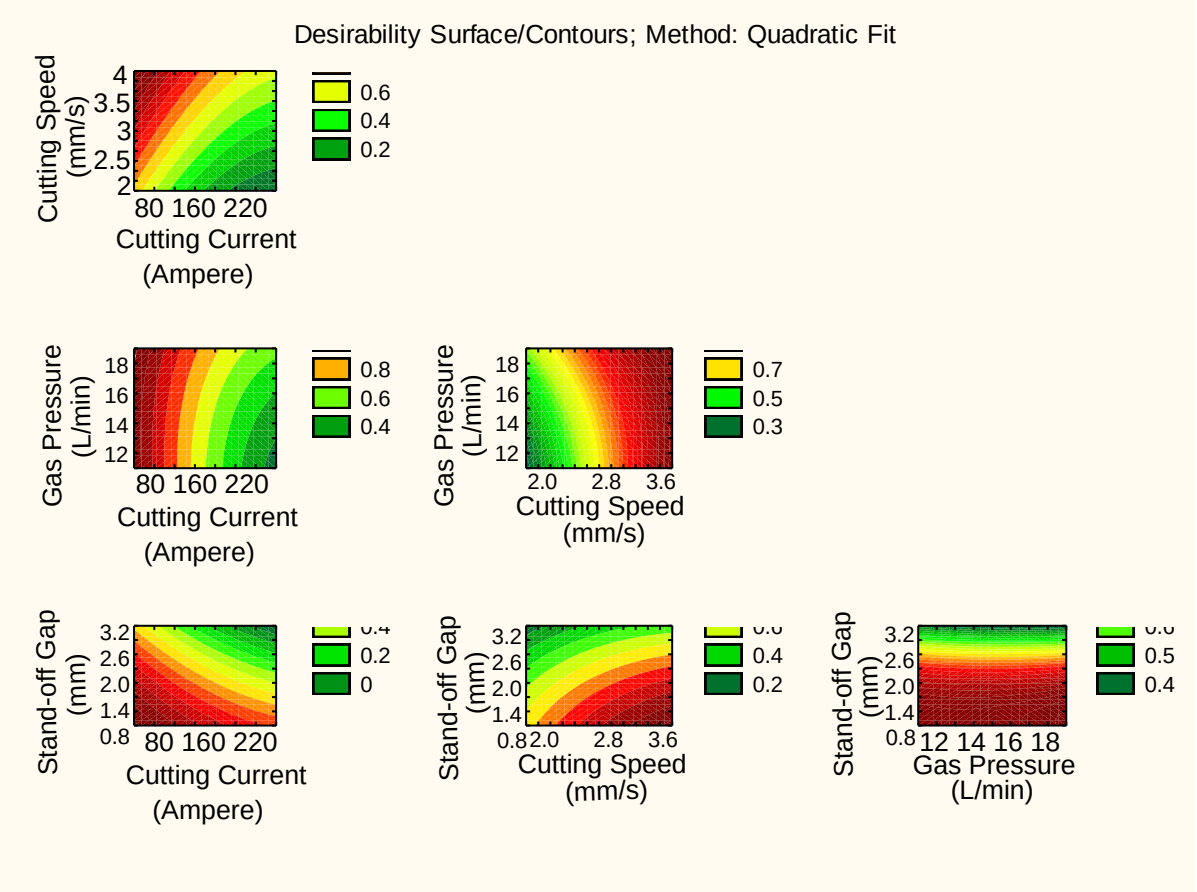

Fig. 182 Desirability 2D counter plot of chamfer

The 3D and 2D plot of interaction variables were determined using the desirability profiles that are shown in Fig. 181-182 respectively. From these figures, it can be concluded that with the highest value of cutting speed and lowest value of cutting current, maximum chamfer value can be achieved. But in plasma cutting process, only minimum chamfer required so, minimum and maximum value of cutting speed and current respectively should be given to the machine.

5.3.1.4 For dross:

From the analysis of ANOVA table of dross i.e., Table 58, it is concluded that cutting current and the interaction term of cutting speed and stand-off gap have shown significance according to F-test. The Pareto chart of effects of all factors on dross

response is shown in Fig. 183 and the results show that the linear form of cutting current is the second most influencing factor among all considered factors. In Fig. 184, the scatter plot between the observed and the predicted value of dross of all 27 runs is displayed. Referring to the figure it is concluded that the relationship between the actual and the predicted dross is linear. The histogram plot of predicted data of dross with 95 % confidence interval of normal distribution is displayed in Fig. 186. Then, the surface and contour graph for the interaction term is displayed in Fig. 189-190 respectively. This figure demonstrates that with increasing speed of cutting and decreasing stand-off gap simultaneously improve the value of dross. The model of estimated coefficient by multiple regressions for dross is given in Table 57. Similarly, the regression model of chamfer is recorded in Table 59.

Table 57 Effect of Estimated Values for Dross

Factor	Effect	Std. Err.	T	P
Constant	1.317222	0.022175	59.4004	0.000000
A (Ampere)	-0.428333	0.038409	-11.1520	0.000000
A^2	0.004167	0.028807	0.1446	0.887394
B (mm/s)	0.323333	0.038409	8.4182	0.000002
B^2	0.007917	0.028807	0.2748	0.788128
C (L/min)	0.033333	0.038409	0.8679	0.402494
C^2	-0.027083	0.028807	-0.9402	0.365666
D (mm)	-0.151667	0.038409	-3.9488	0.001932
D^2	-0.020833	0.028807	-0.7232	0.483407
A×B	0.100000	0.066526	1.5032	0.158648
A×C	0.020000	0.066526	0.3006	0.768838
A×D	0.095000	0.066526	1.4280	0.178793
B×C	0.020000	0.066526	0.3006	0.768838
B×D	-0.150000	0.066526	-2.2548	0.043621
C×D	-0.070000	0.066526	-1.0522	0.313425

Table 58 ANOVA Table for Dross

Factors	SS	DoF	MS	F	P
A (Ampere)	0.550408	1	0.550408	124.3665	0.000000
A^2	0.000093	1	0.000093	0.0209	0.887394
B (mm/s)	0.313633	1	0.313633	70.8665	0.000002
B^2	0.000334	1	0.000334	0.0755	0.788128
C (L/min)	0.003333	1	0.003333	0.7532	0.402494
C^2	0.003912	1	0.003912	0.8839	0.365666
D (mm)	0.069008	1	0.069008	15.5927	0.001932
D^2	0.002315	1	0.002315	0.5230	0.483407
A×B	0.010000	1	0.010000	2.2595	0.158648
A×C	0.000400	1	0.000400	0.0904	0.768838
A×D	0.009025	1	0.009025	2.0392	0.178793
B×C	0.000400	1	0.000400	0.0904	0.768838
B×D	0.022500	1	0.022500	5.0839	0.043621
C×D	0.004900	1	0.004900	1.1072	0.313425
Error	0.053108	12	0.004426		
Total SS	1.044985	26			

Table 59 Regression Coefficients of Dross

Factor	Regression Coef.	Std. Err.	T	P
Constant	2.298333	1.939927	1.18475	0.259049
A (Ampere)	-0.012533	0.006181	-2.02762	0.065402
A^2	-0.000002	0.000012	-0.14464	0.887394
B (mm/s)	0.384167	0.309065	1.24300	0.237608
B^2	-0.007917	0.028807	-0.27482	0.788128
C (L/min)	-0.046389	0.120613	-0.38461	0.707255
C^2	0.003009	0.003201	0.94018	0.365666
D (mm)	-0.053333	0.723676	-0.07370	0.942465
D^2	0.083333	0.115226	0.72321	0.483407
A×B	0.001000	0.000665	1.50317	0.158648
A×C	0.000067	0.000222	0.30063	0.768838
A×D	0.001900	0.001331	1.42802	0.178793
B×C	0.003333	0.011088	0.30063	0.768838
B×D	-0.150000	0.066526	-2.25476	0.043621
C×D	-0.023333	0.022175	-1.05222	0.313425

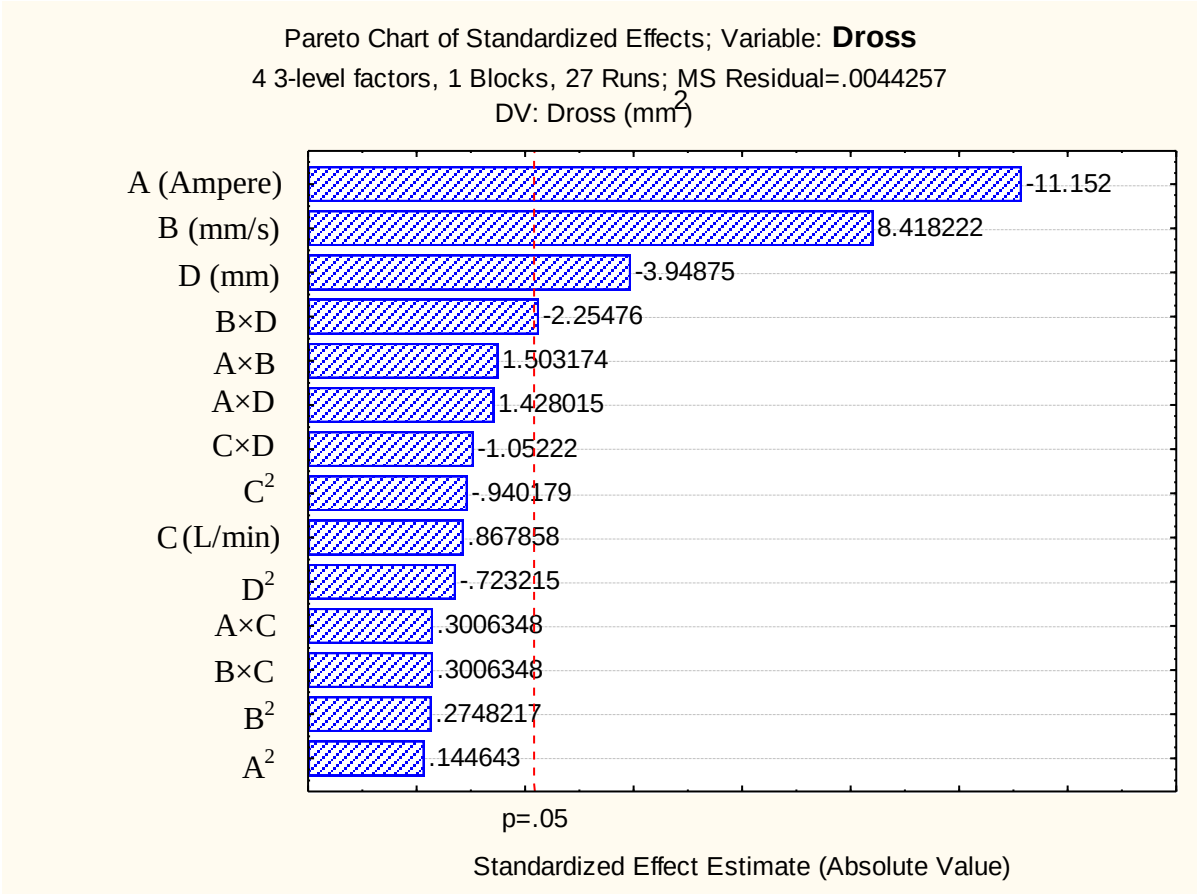

Fig. 183 Pareto chart of standardized effect of factors on dross

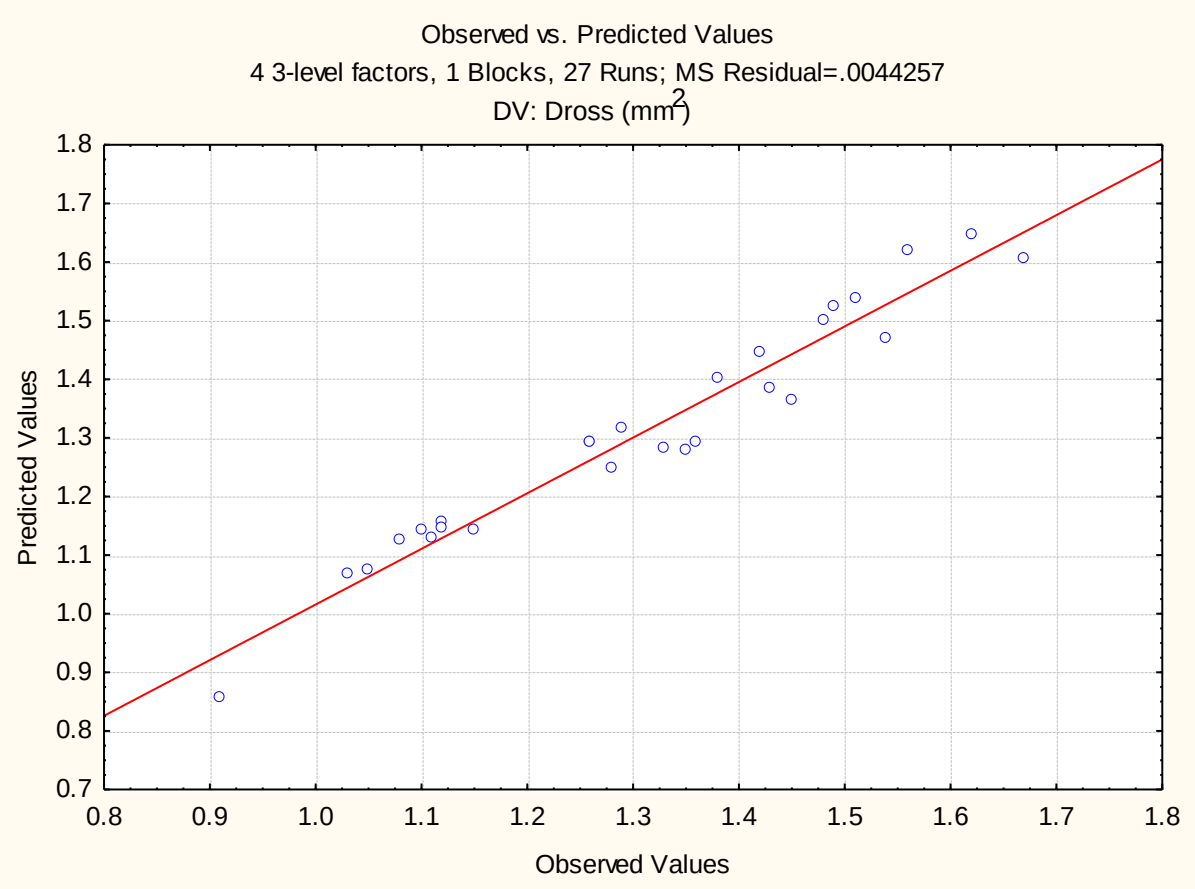

Fig. 184 Plot of observed vs. predicted values of dross

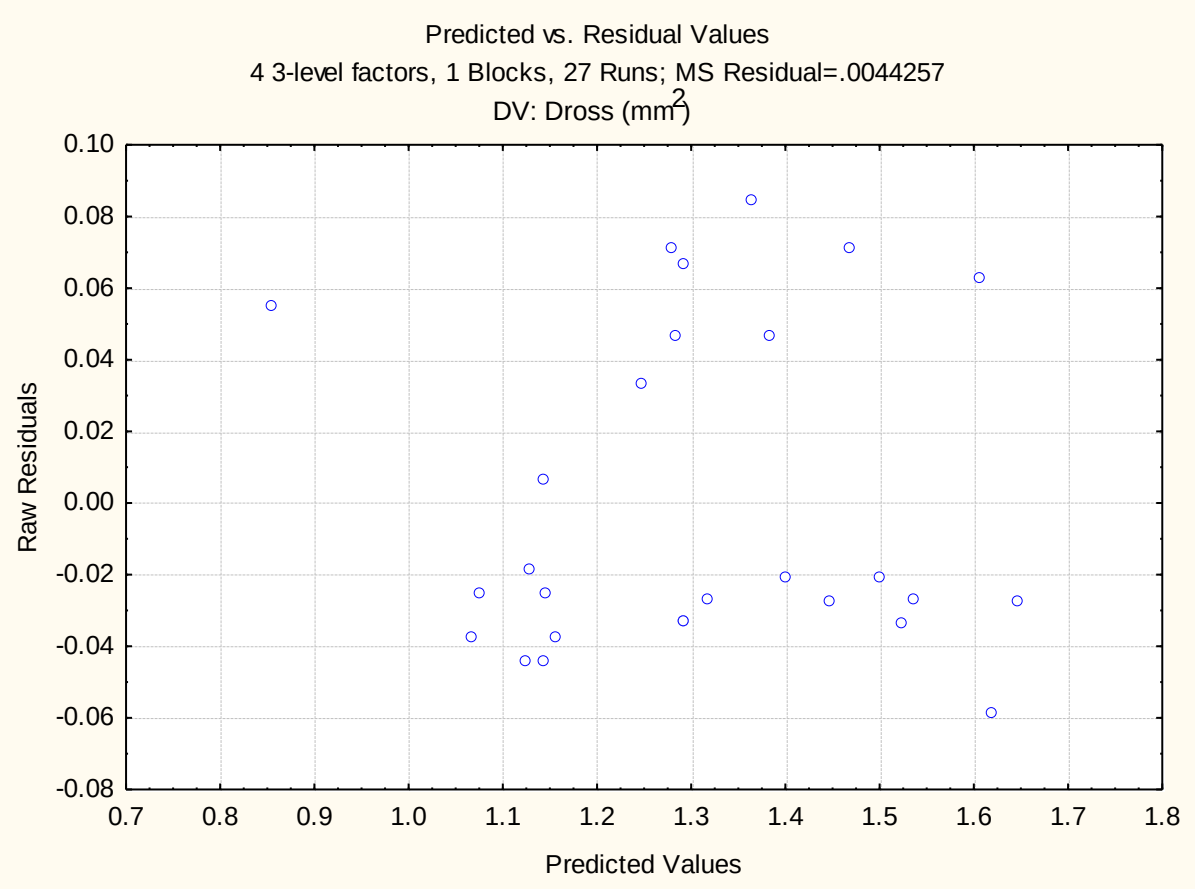

Fig. 185 Plot of predicted vs. residual values of dross

From the Fig. 185, no standard pattern is formed in the plot of predicted vs. residual values which show the adequacy of the fitted model for dross.

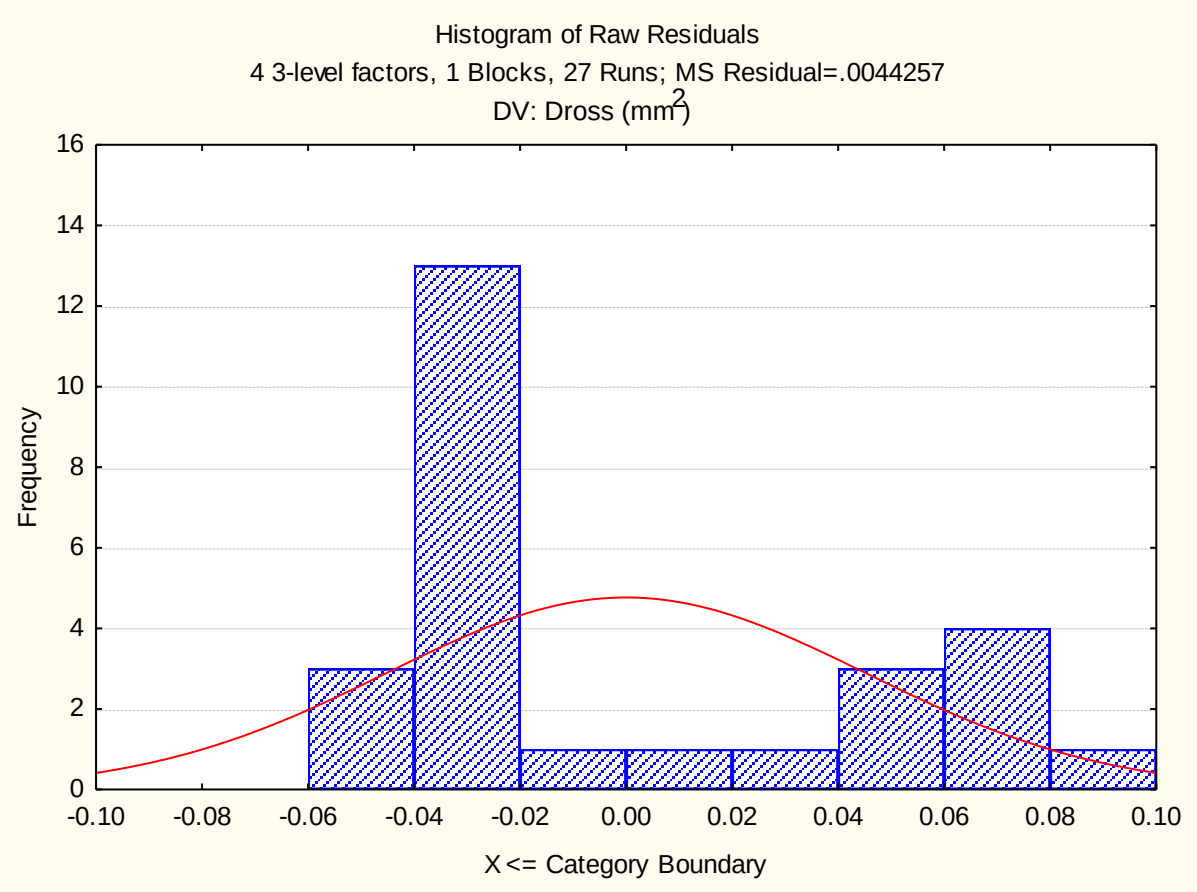

Fig. 186 Histogram plot of predicted values of dross

Fig. 187 Plot of residuals vs. case numbers values of dross

From the Fig. 187, it is evident that the highest dross value among all experimental runs is by the run number 5. The red line indicates that the value of dross decreases with increase in run order.

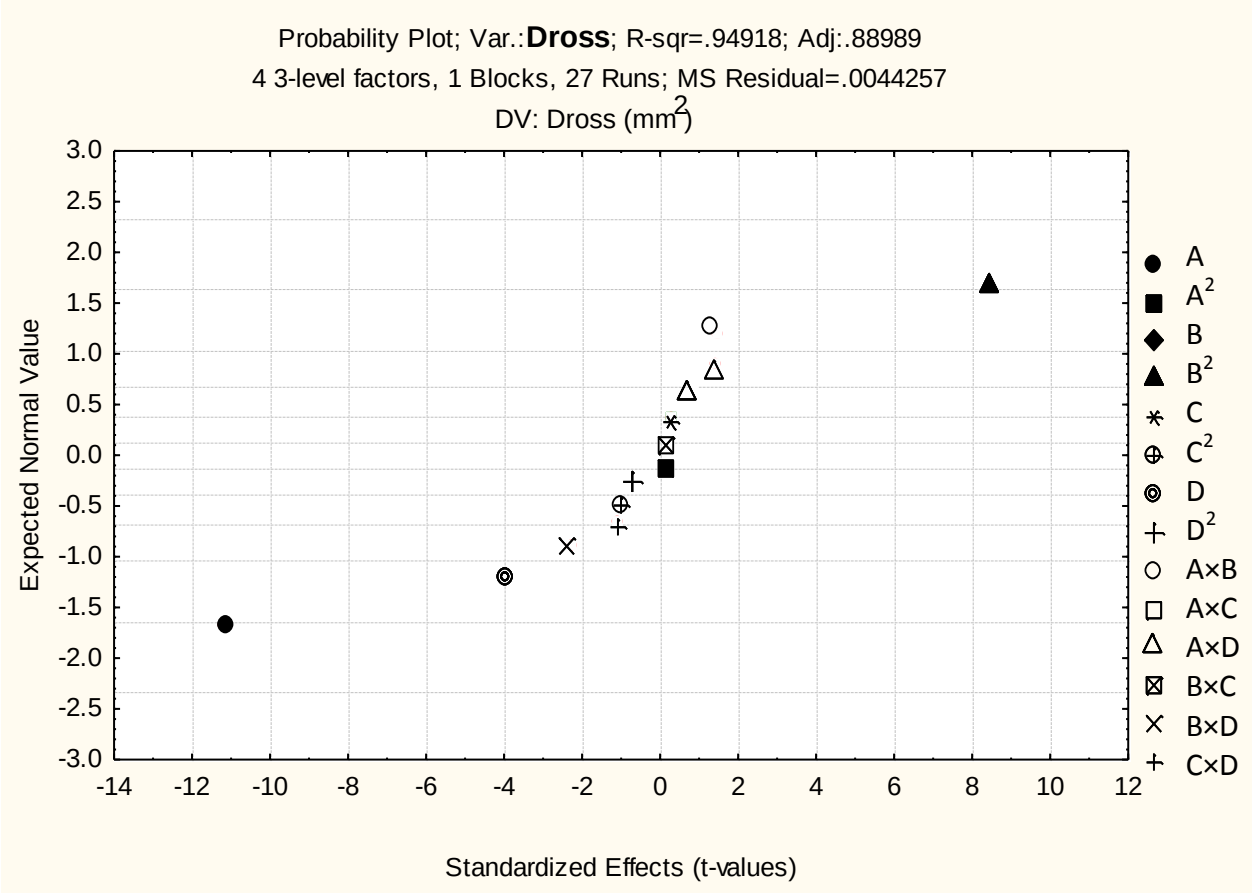

Fig. 188 Probability plot of dross

The normal probability plot of dross corresponding to each regression terms is plotted in Fig. 188.

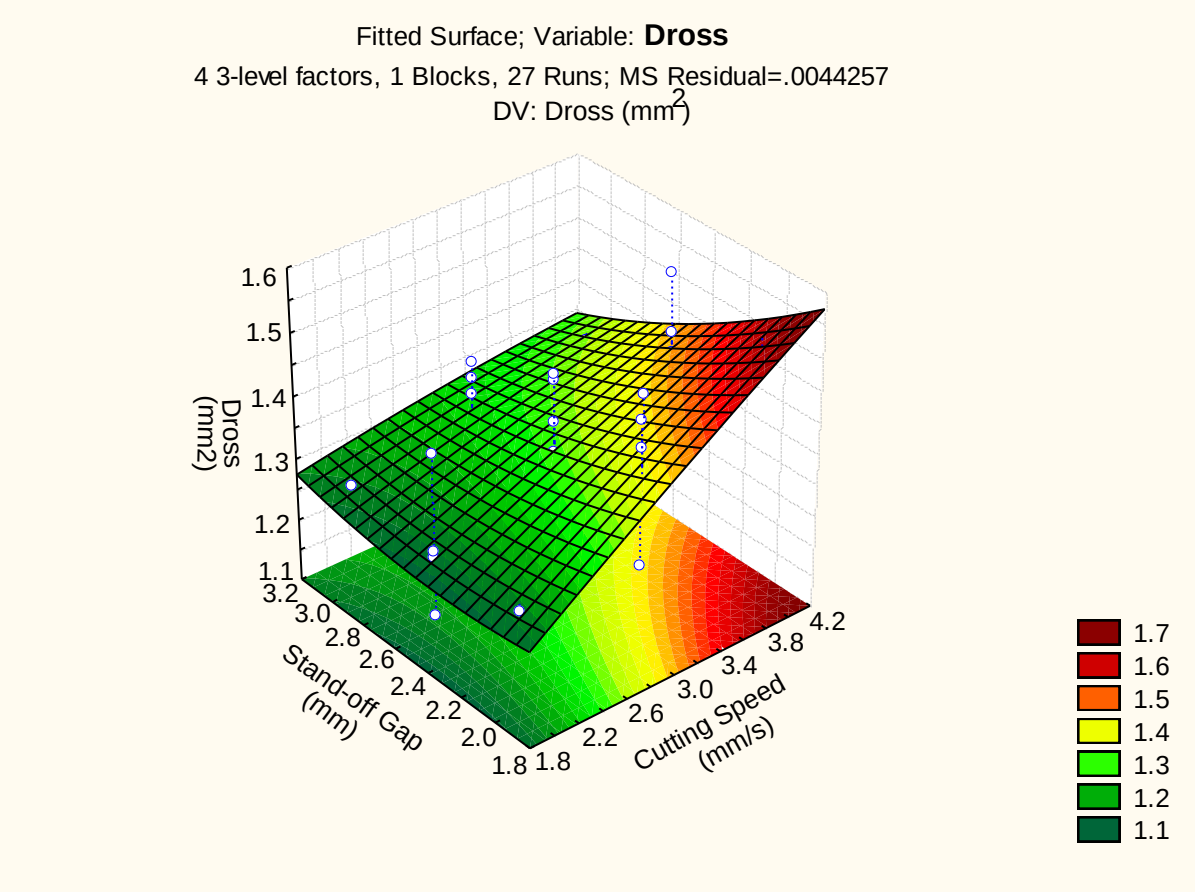

Fig. 189 3D fitted surface plot of dross

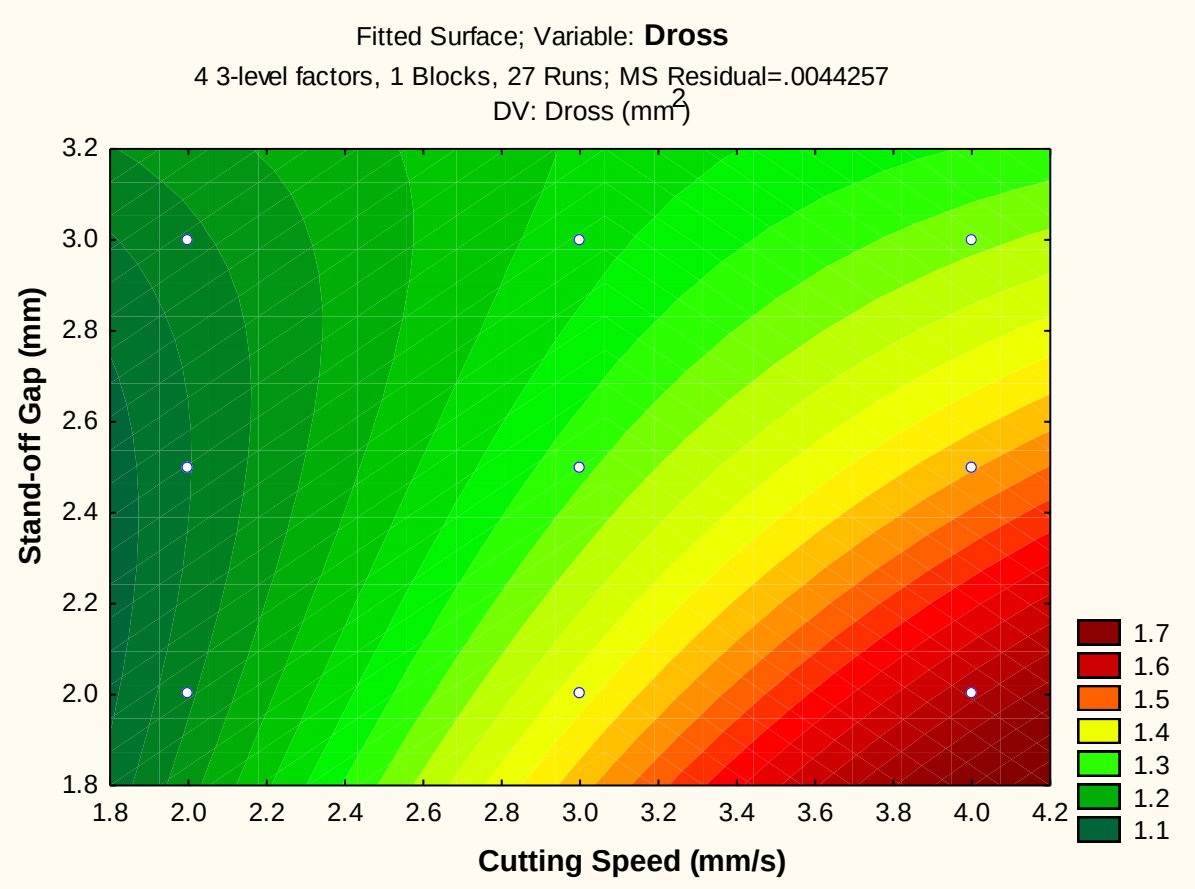

Fig. 190 2D fitted counter plot of dross

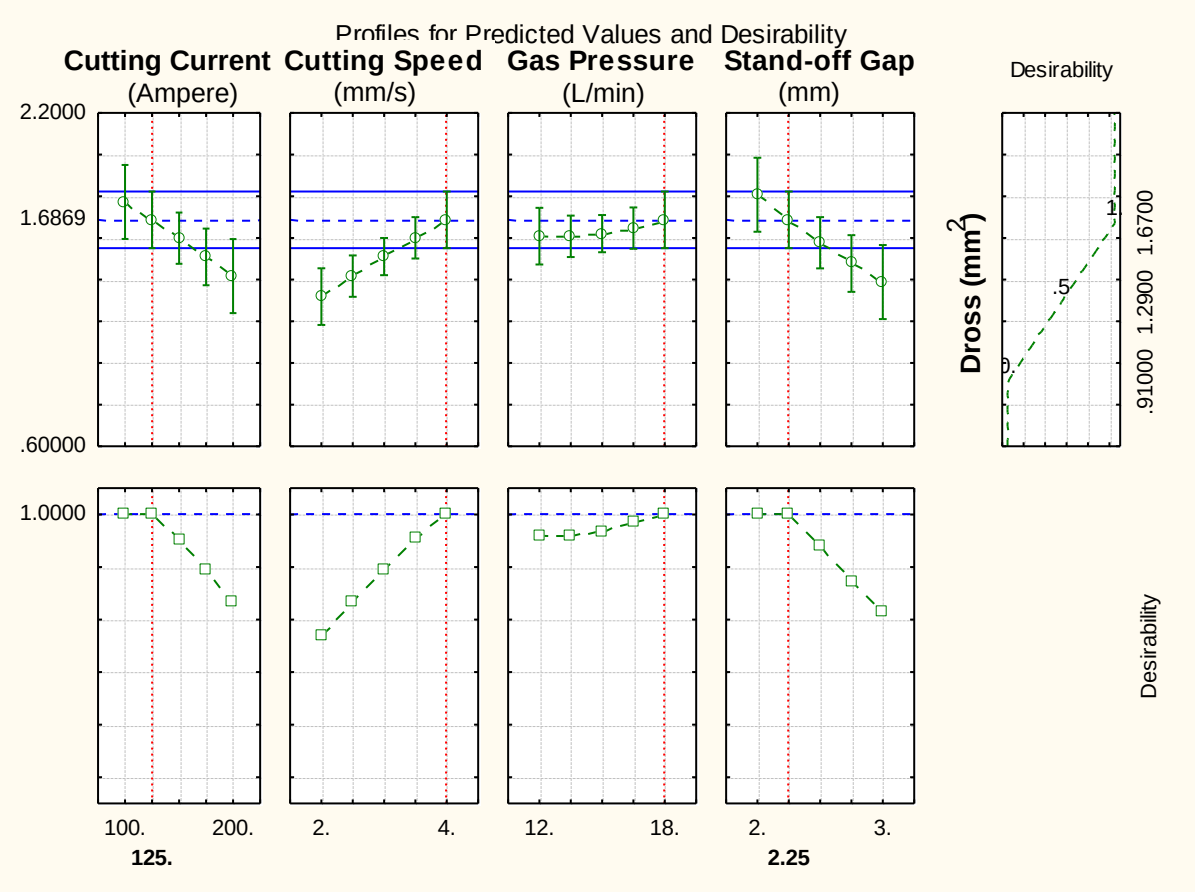

Fig. 191 Profile plot of predicted values and desirability of dross

The desirability function method helped to find the value of optimum dross response which was fitted by the quadratic fit model. The level of variable giving the highest desirability i.e., 1.0000 was considered as optimum level. The optimized levels of variables (A, B, C and D) were determined using the desirability profiles that are shown in Fig. 191. The desirability function with red dotted lines and predicted values of responses are also shown in same figure (i.e. Fig. 191).

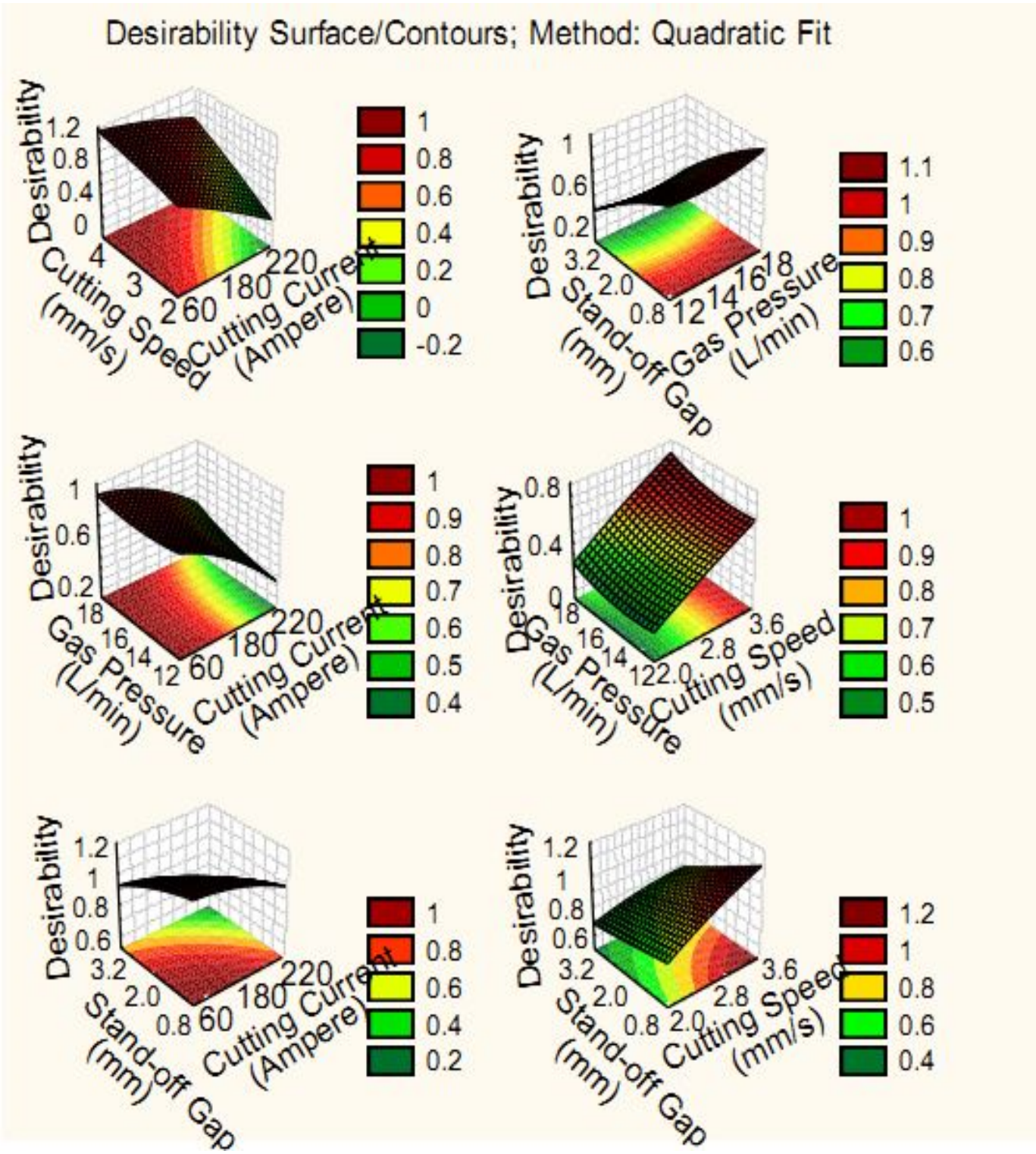

Fig. 192 Desirability 3D surface plot of dross

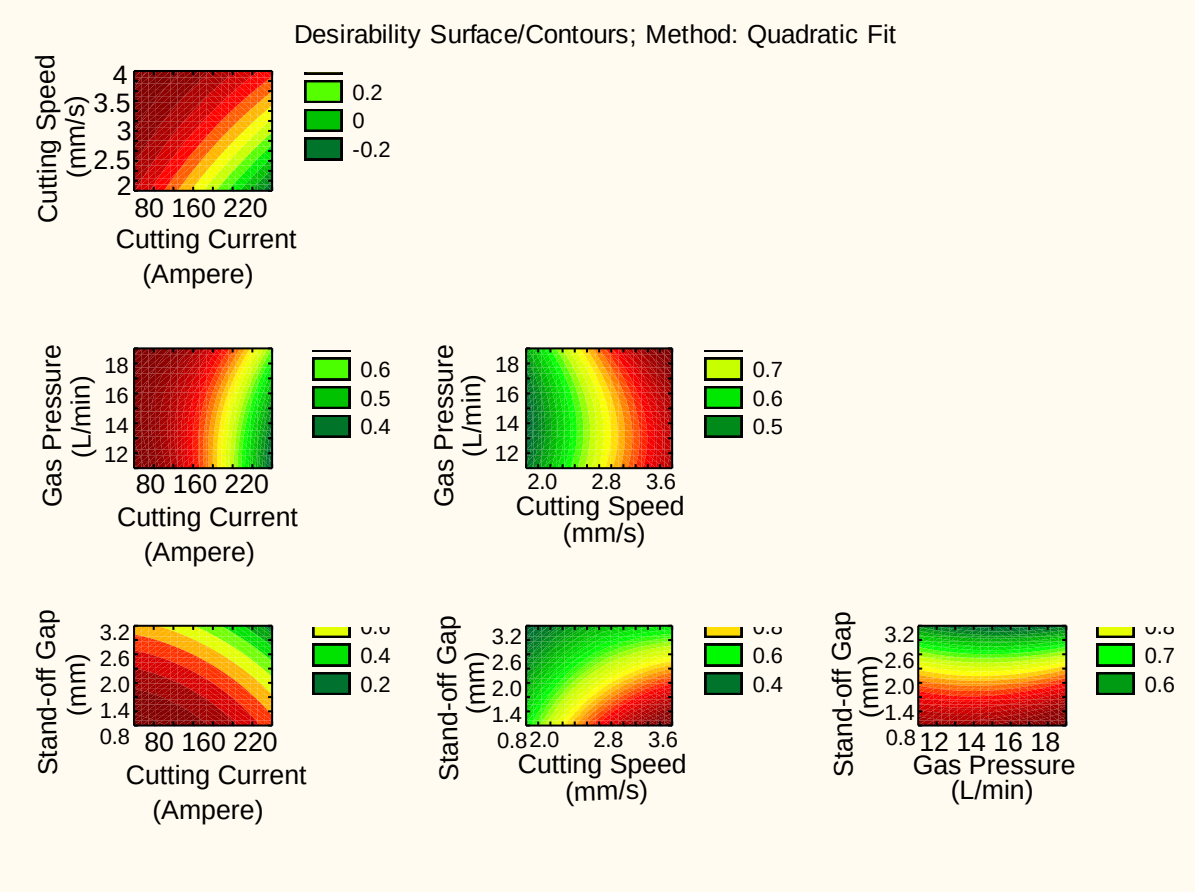

Fig. 193 Desirability 2D counter plot of dross

The 3D and 2D counter plot of interaction variables were determined using the desirability profiles that are shown in Fig. 192-193 respectively. Here, only minimum value of cutting speed is needed to get better minimal dross during plasma arc cutting operation.

5.3.1.5 For right bevel angle:

From the ANOVA of right bevel angle, it is revealed that only the square term of gas pressure and stand-off gap gave a tremendous effect on experimental results as its P-value is lowest than others which are shown in Table 61. Here, the interaction terms i.e., A×D, B×C, B×D and C×D are taken into account as significant terms due to the lowest value in P in ANOVA table. This type of results mainly occurred due to the equality of

values in the measurement of right bevel angle. The present analysis is compatible with the results of Kechagias et al. [9; 105] as they concluded that the cutting current is the main enhancing factor on the right bevel angle. The Pareto chart of effects of all factors on right bevel angle response is shown in Fig. 194 and the results indicate that the interaction of cutting current and stand-off distance is the second most improving factor among all considered factors. The scatter plot between the observed and the predicted value of right bevel angle of all 27 runs is shown in Fig. 195. It is concluded that the relationship between the actual and the predicted MRR was not in linear. So, it can be revealed that the response model showed bad fit to the experimental data set. In Fig. 197, the histogram plot of predicted data of right bevel angle with 95 % confidence interval of normal distribution is plotted. Furthermore, the surface and contour plot of above said interaction terms are shown in Fig. 200-202-204-206-201-203-205-207 respectively. Then, the model of estimated coefficient by multiple regressions for right bevel angle is tabulated in Table 60. Similarly, the regression model of chamfer is recorded in Table 62.

Table 60 Effect of Estimated Values for Right Bevel Angle

Factor	Effect	Std. Err.	T	P
Constant	3.50000	0.073493	47.62352	0.000000
A (Ampere)	0.00000	0.127294	0.00000	1.000000
A^2	0.12500	0.095470	1.30931	0.214946
B (mm/s)	0.00000	0.127294	0.00000	1.000000
B^2	-0.12500	0.095470	-1.30931	0.214946
C (L/min)	-0.16667	0.127294	-1.30931	0.214946
C^2	-0.25000	0.095470	-2.61861	0.022442
D (mm)	-0.16667	0.127294	-1.30931	0.214946
D^2	-0.50000	0.095470	-5.23723	0.000209
A×B	0.00000	0.220479	0.00000	1.000000
A×C	0.00000	0.220479	0.00000	1.000000
A×D	1.00000	0.220479	4.53557	0.000683
B×C	-1.00000	0.220479	-4.53557	0.000683
B×D	-1.00000	0.220479	-4.53557	0.000683
C×D	-0.50000	0.220479	-2.26779	0.042608

Table 61 ANOVA Table for Right Bevel Angle

Factors	SS	DoF	MS	F	P
A (Ampere)	0.000000	1	0.000000	0.00000	1.000000
A^2	0.083333	1	0.083333	1.71429	0.214946
B (mm/s)	0.000000	1	0.000000	0.00000	1.000000
B^2	0.083333	1	0.083333	1.71429	0.214946
C (L/min)	0.083333	1	0.083333	1.71429	0.214946
C^2	0.333333	1	0.333333	6.85714	0.022442
D (mm)	0.083333	1	0.083333	1.71429	0.214946
D^2	1.333333	1	1.333333	27.42857	0.000209
A×B	0.000000	1	0.000000	0.00000	1.000000
A×C	0.000000	1	0.000000	0.00000	1.000000
A×D	1.000000	1	1.000000	20.57143	0.000683
B×C	1.000000	1	1.000000	20.57143	0.000683
B×D	1.000000	1	1.000000	20.57143	0.000683
C×D	0.250000	1	0.250000	5.14286	0.042608
Error	0.583333	12	0.048611		
Total SS	6.000000	26			

Table 62 Regression Coefficients of Right Bevel Angle

Factor	Regression Coef.	Std. Err.	T	P
Constant	8.83333	6.429281	1.37392	0.194586
A (Ampere)	-0.03500	0.020486	-1.70848	0.113259
A^2	-0.00005	0.000038	-1.30931	0.214946
B (mm/s)	4.25000	1.024300	4.14918	0.001349
B^2	0.12500	0.095470	1.30931	0.214946
C (L/min)	0.05556	0.399733	0.13898	0.891770
C^2	0.02778	0.010608	2.61861	0.022442
D (mm)	-7.66667	2.398398	-3.19658	0.007681
D^2	2.00000	0.381881	5.23723	0.000209
A×B	0.00000	0.002205	0.00000	1.000000
A×C	0.00000	0.000735	0.00000	1.000000
A×D	0.02000	0.004410	4.53557	0.000683
B×C	-0.16667	0.036747	-4.53557	0.000683
B×D	-1.00000	0.220479	-4.53557	0.000683
C×D	-0.16667	0.073493	-2.26779	0.042608

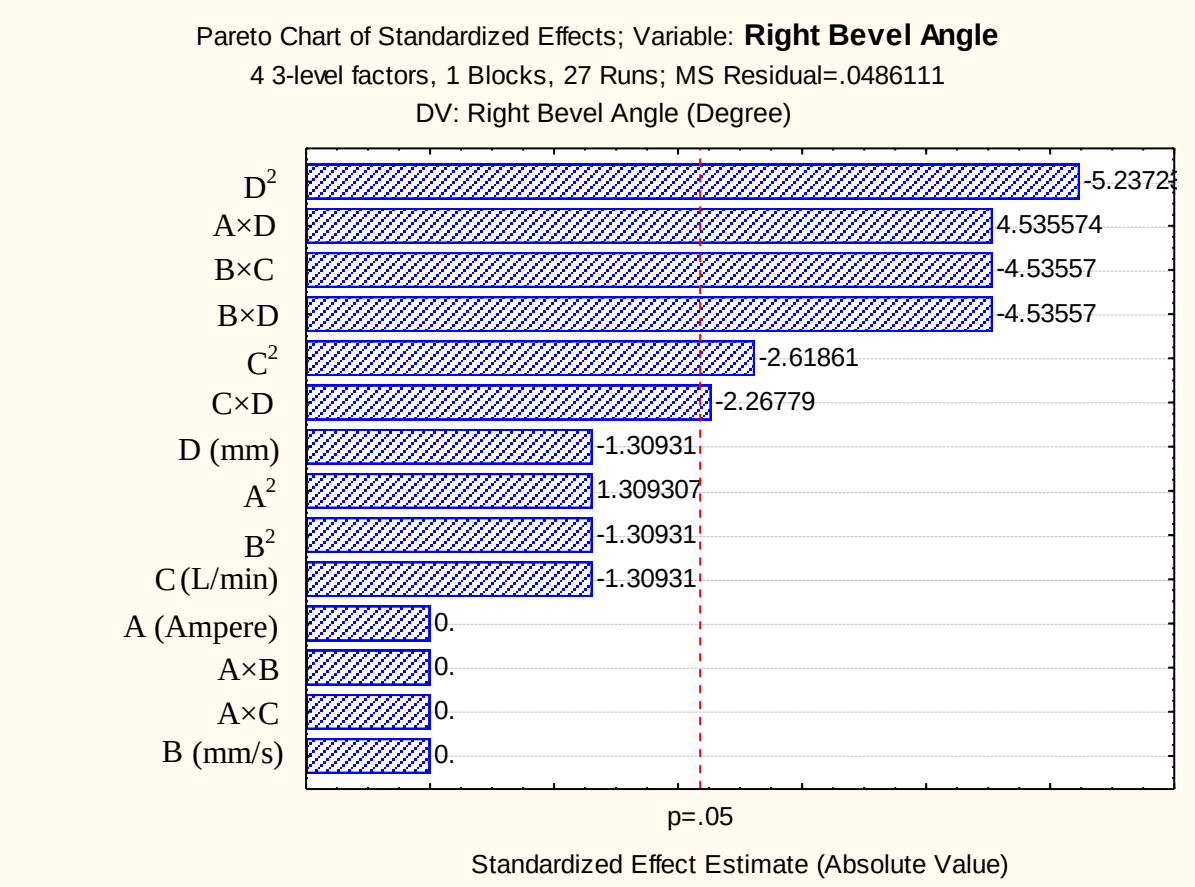

Fig. 194 Pareto chart of standardized effect of factors on right bevel angle

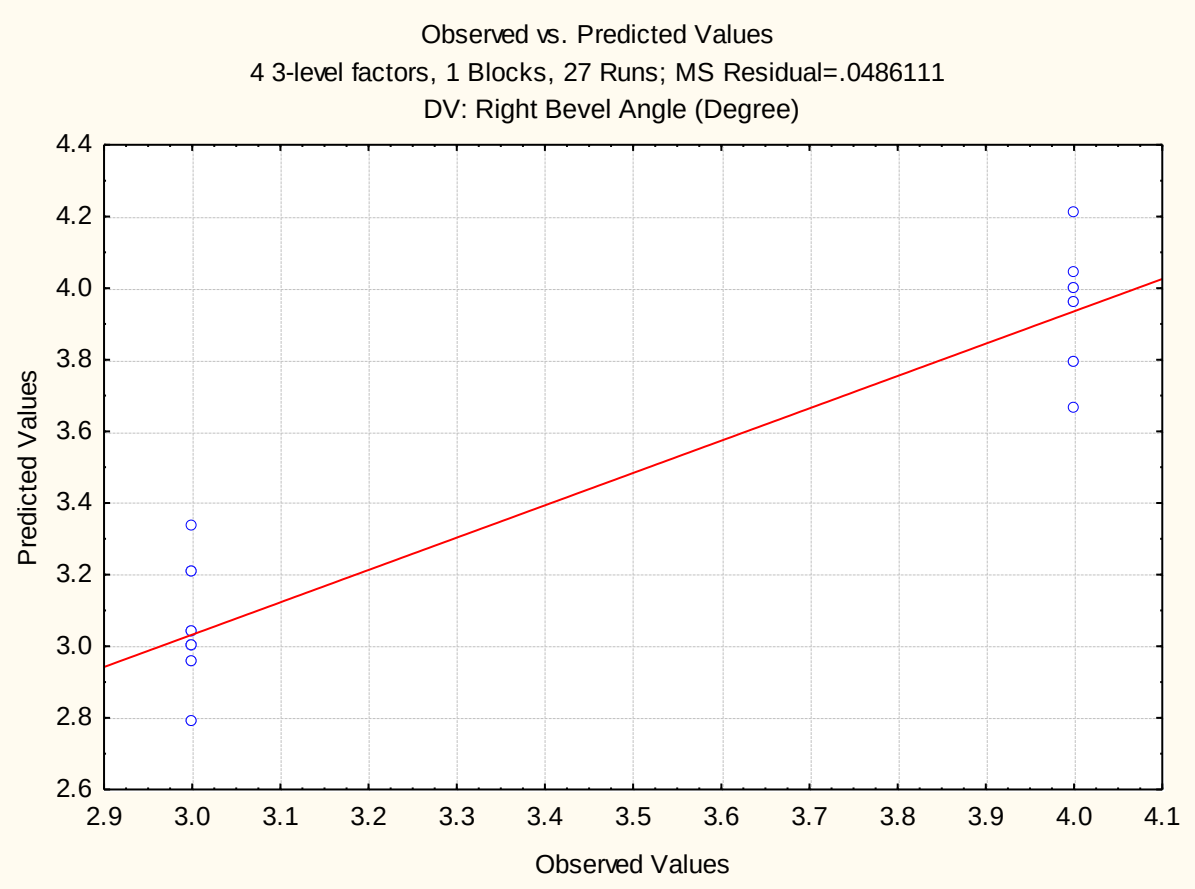

Fig. 195 Plot of observed vs. predicted values of right bevel angle

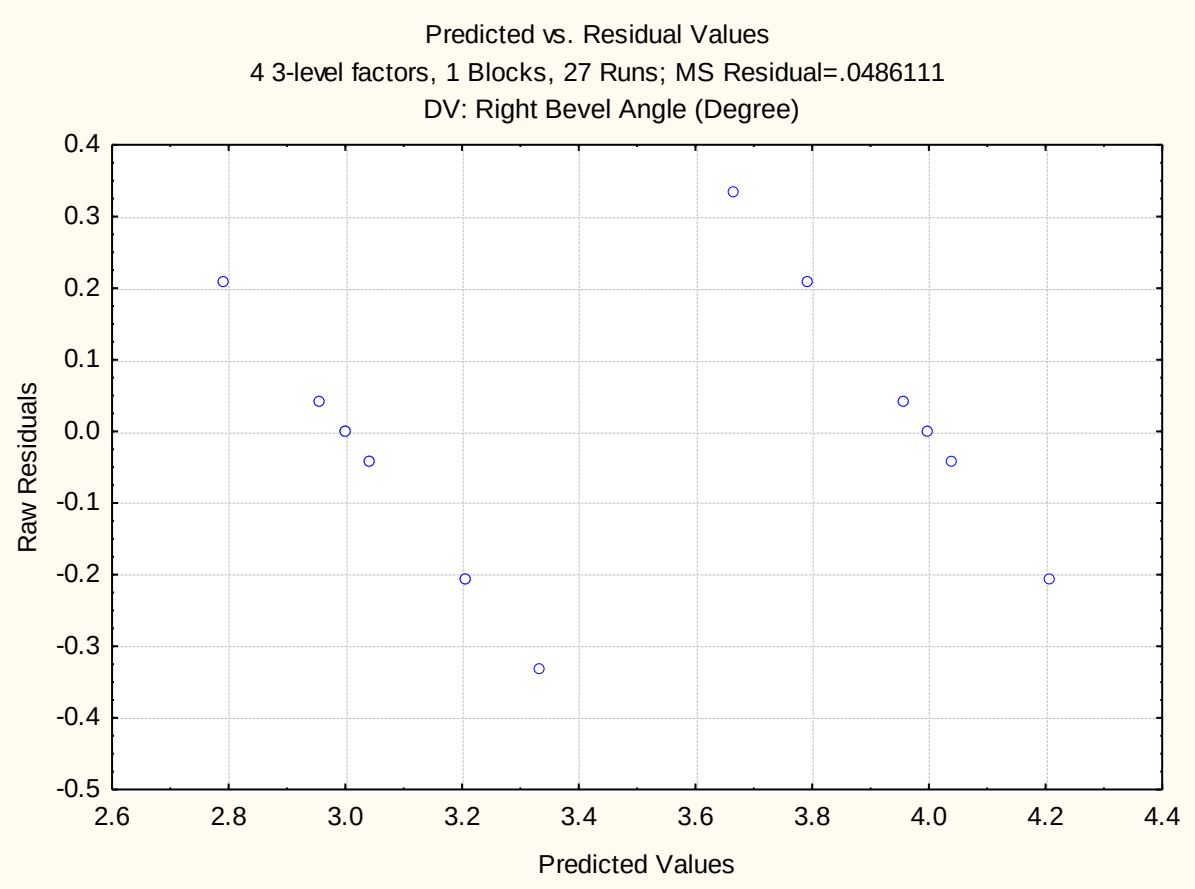

Fig. 196 Plot of predicted vs. residual values of right bevel angle

From the Fig. 196, no standard pattern is formed in the plot of predicted vs. residual values which show the adequacy of the fitted model for right bevel angle.

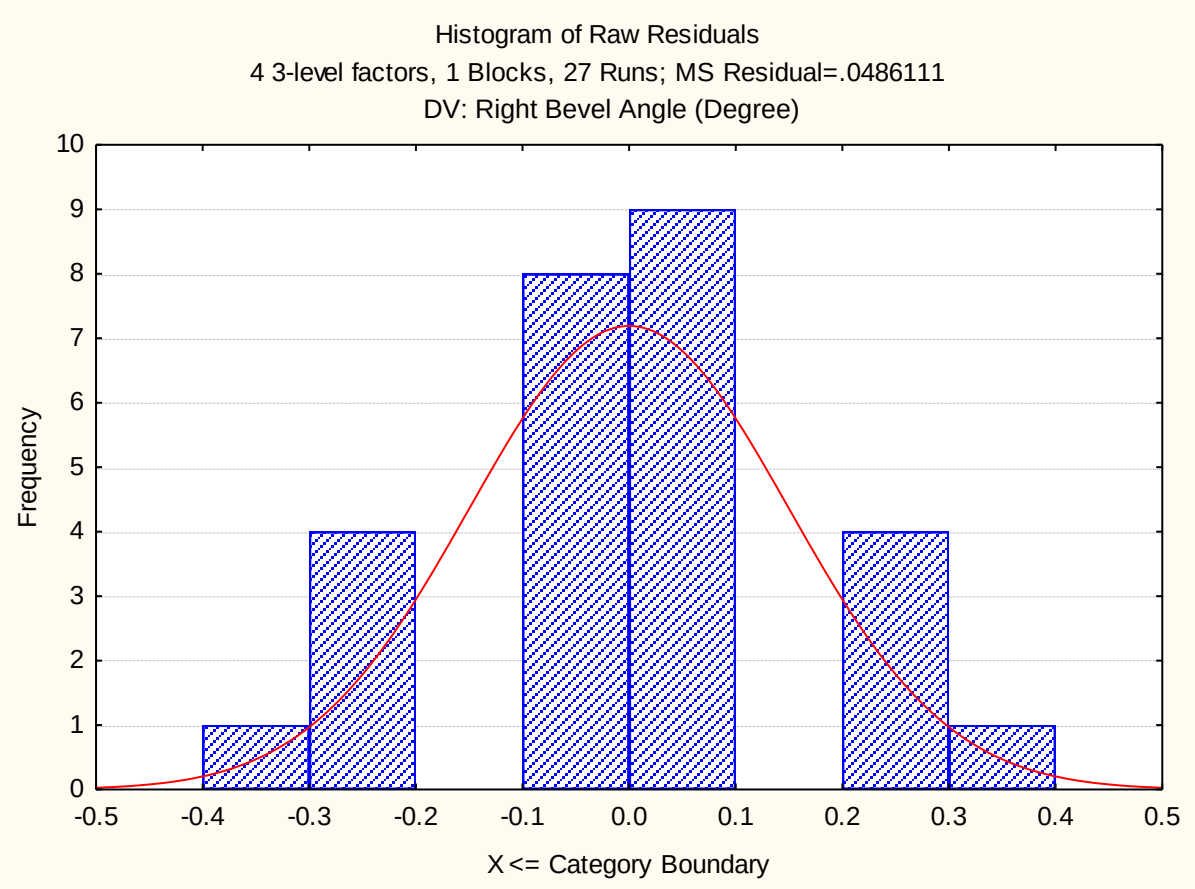

Fig. 197 Histogram plot of predicted values of right bevel angle

Fig. 198 Plot of residuals vs. case numbers values of right bevel angle

From the Fig. 198, it is evident that the highest right bevel angle value among all experimental runs is by the run number 5. The red line indicates that the value of right bevel angle increases with increase in run order.

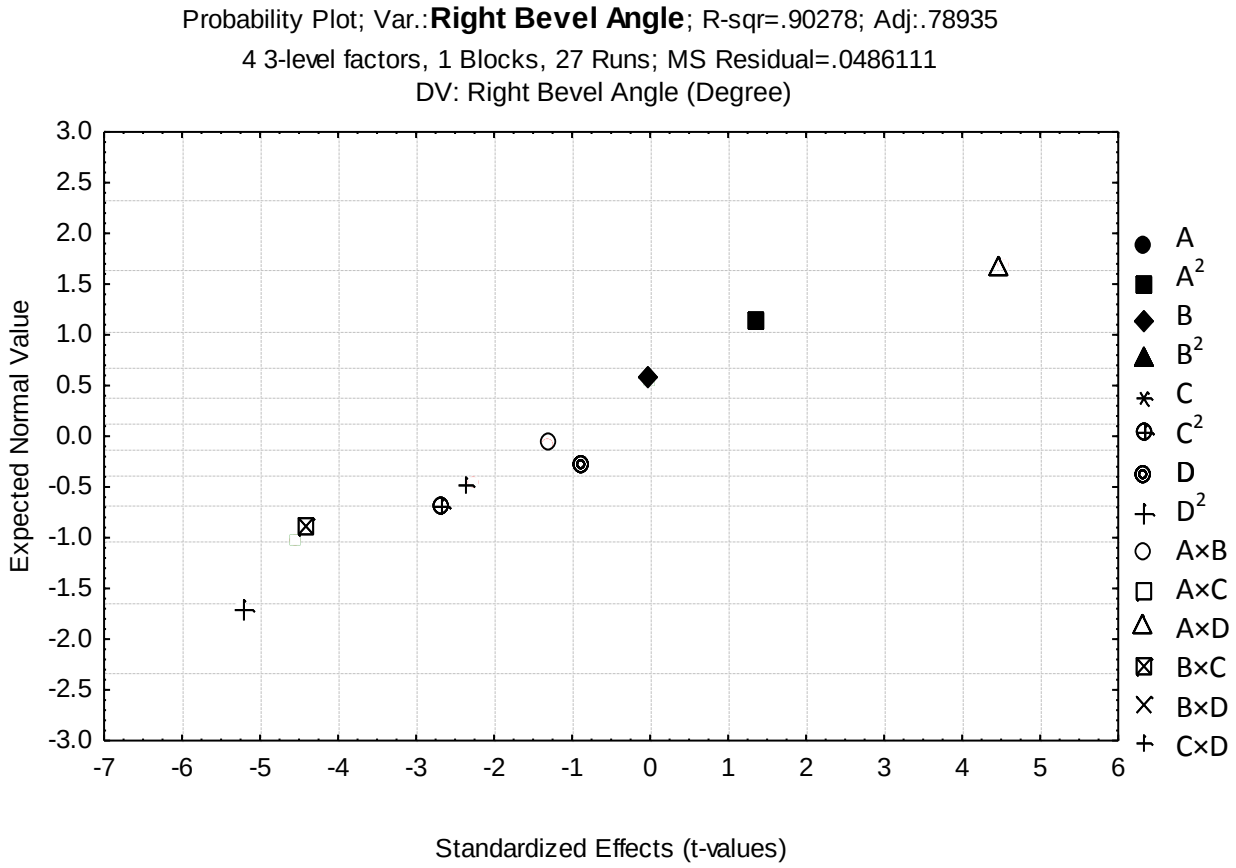

Fig. 199 Probability plot of right bevel angle

The normal probability plot of right bevel angle corresponding to each regression terms is plotted in Fig. 199.

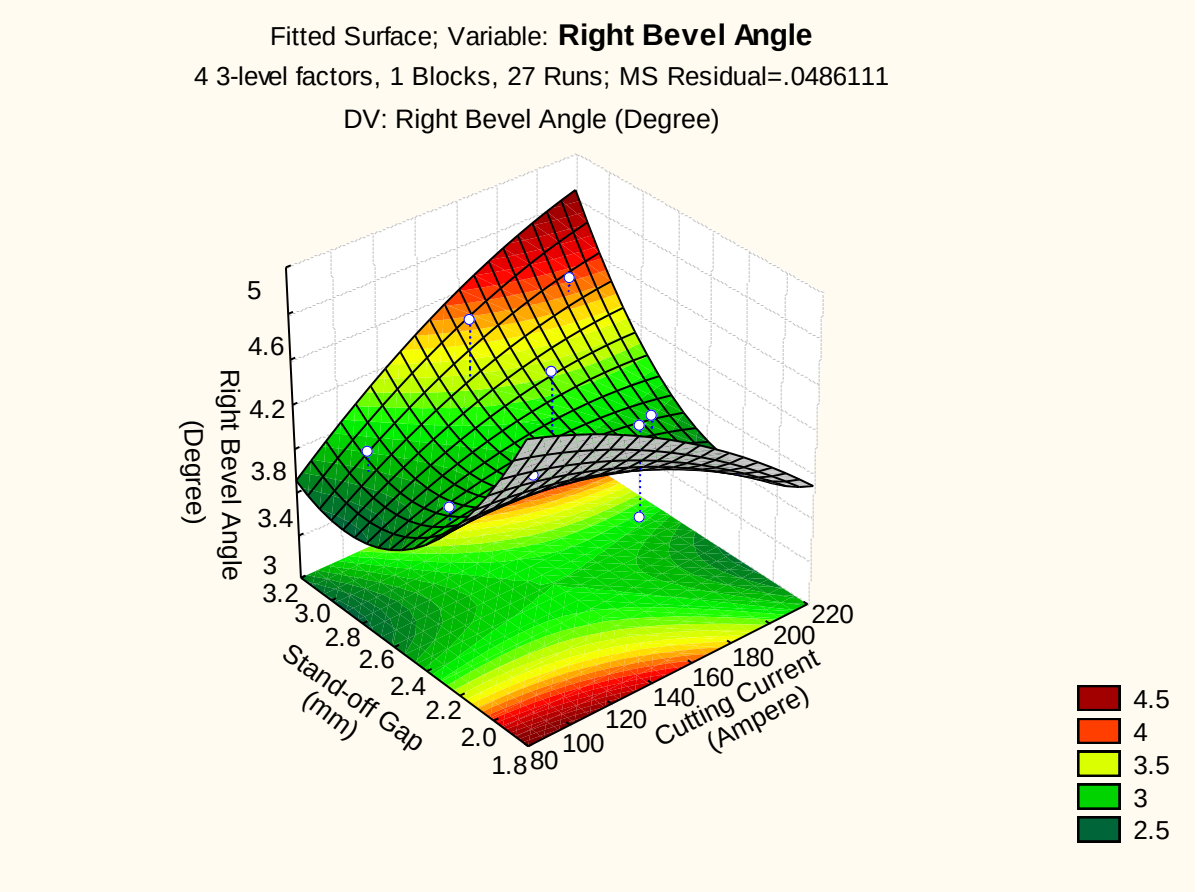

Fig. 200 3D fitted surface plot of right bevel angle (1)

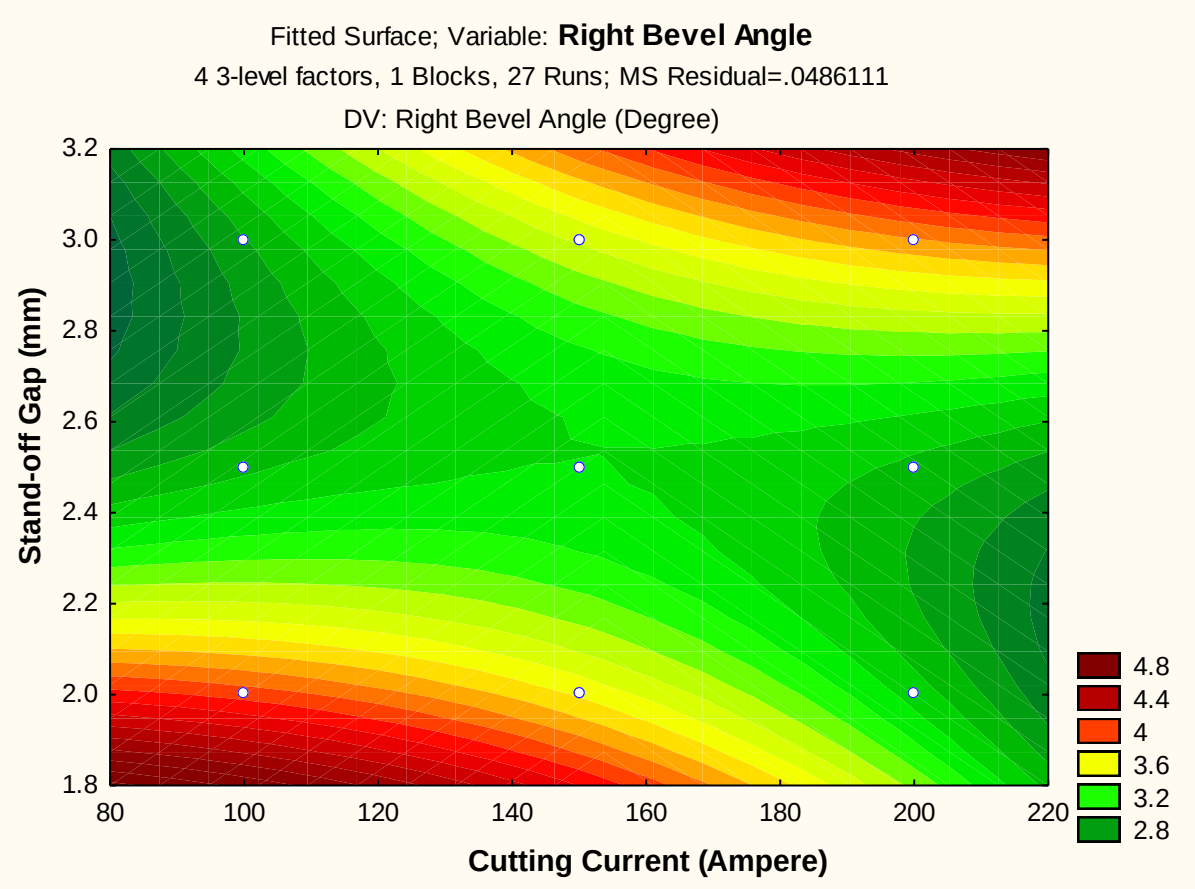

Fig. 201 2D fitted counter plot of right bevel angle (1)

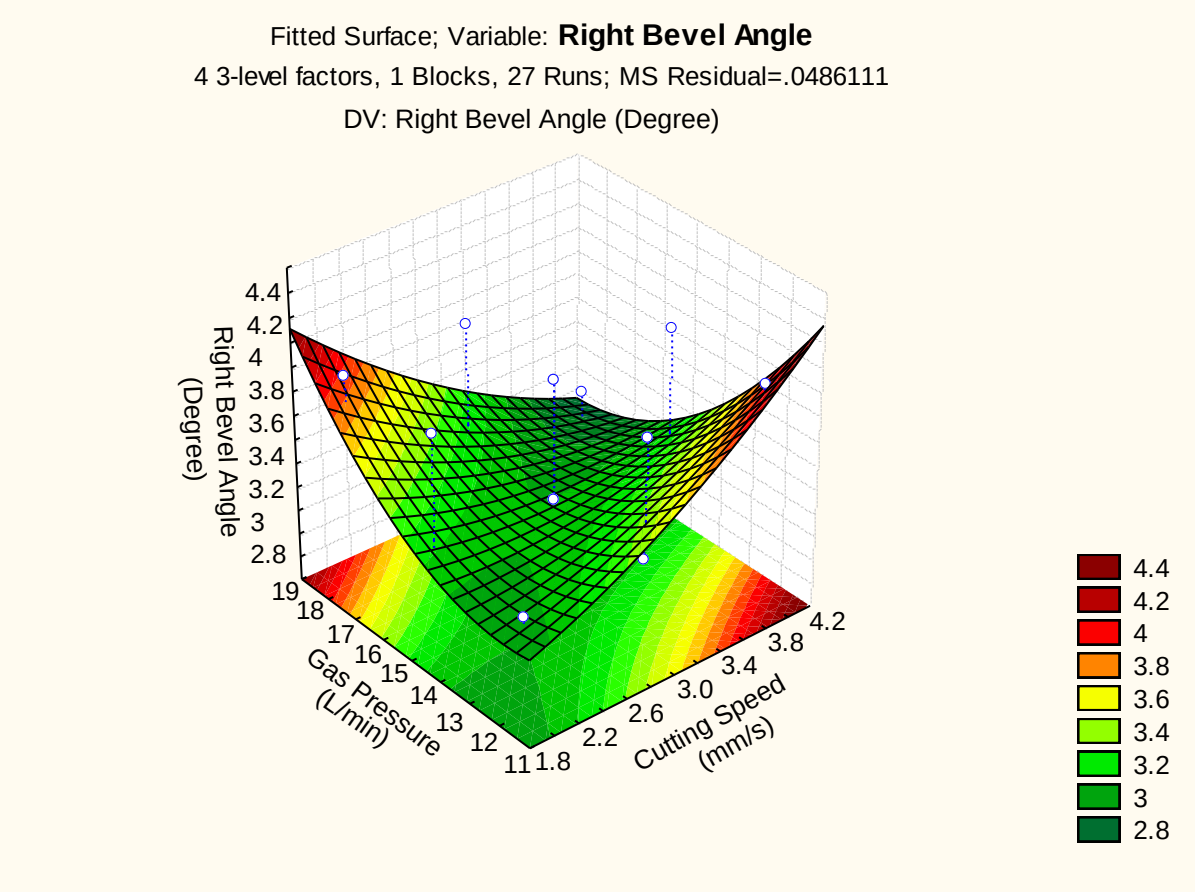

Fig. 202 3D fitted surface plot of right bevel angle (2)

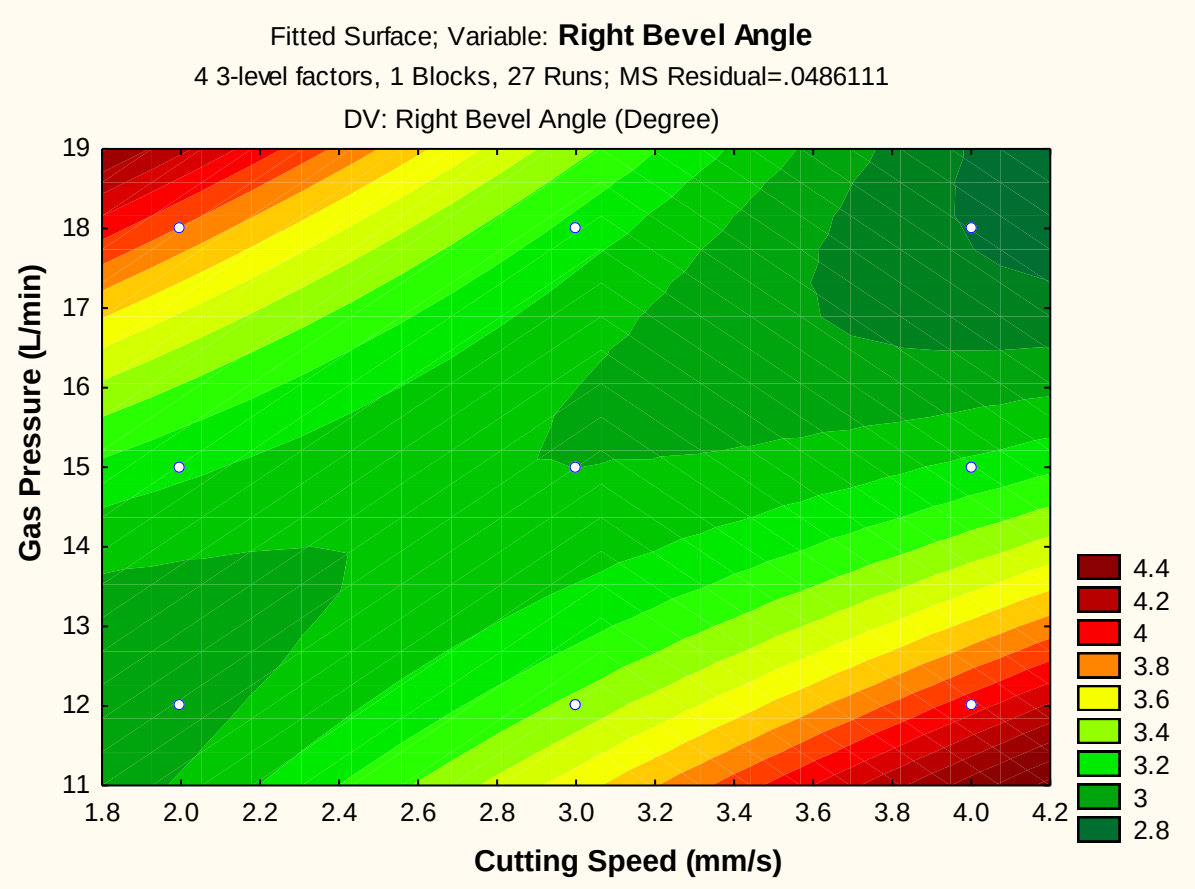

Fig. 203 2D fitted counter plot of right bevel angle (2)

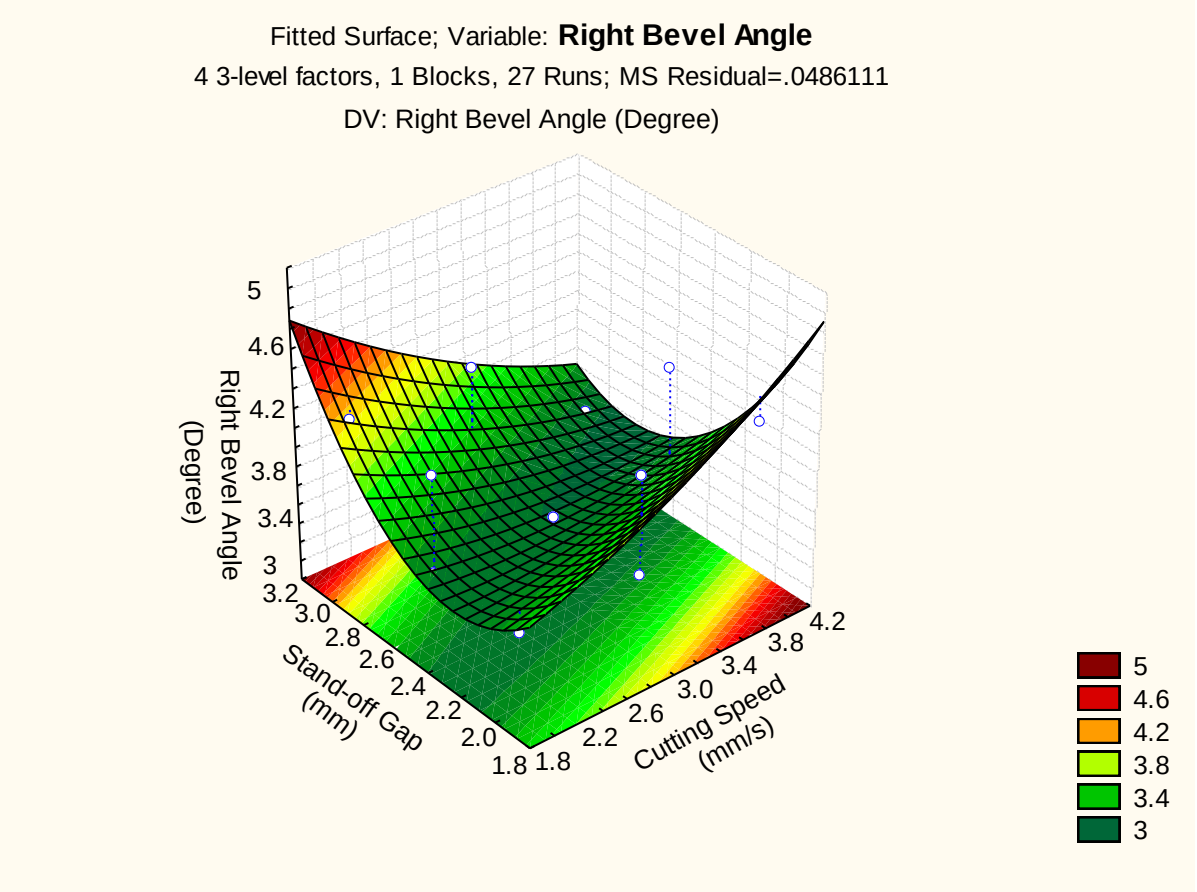

Fig. 204 3D fitted surface plot of right bevel angle (3)

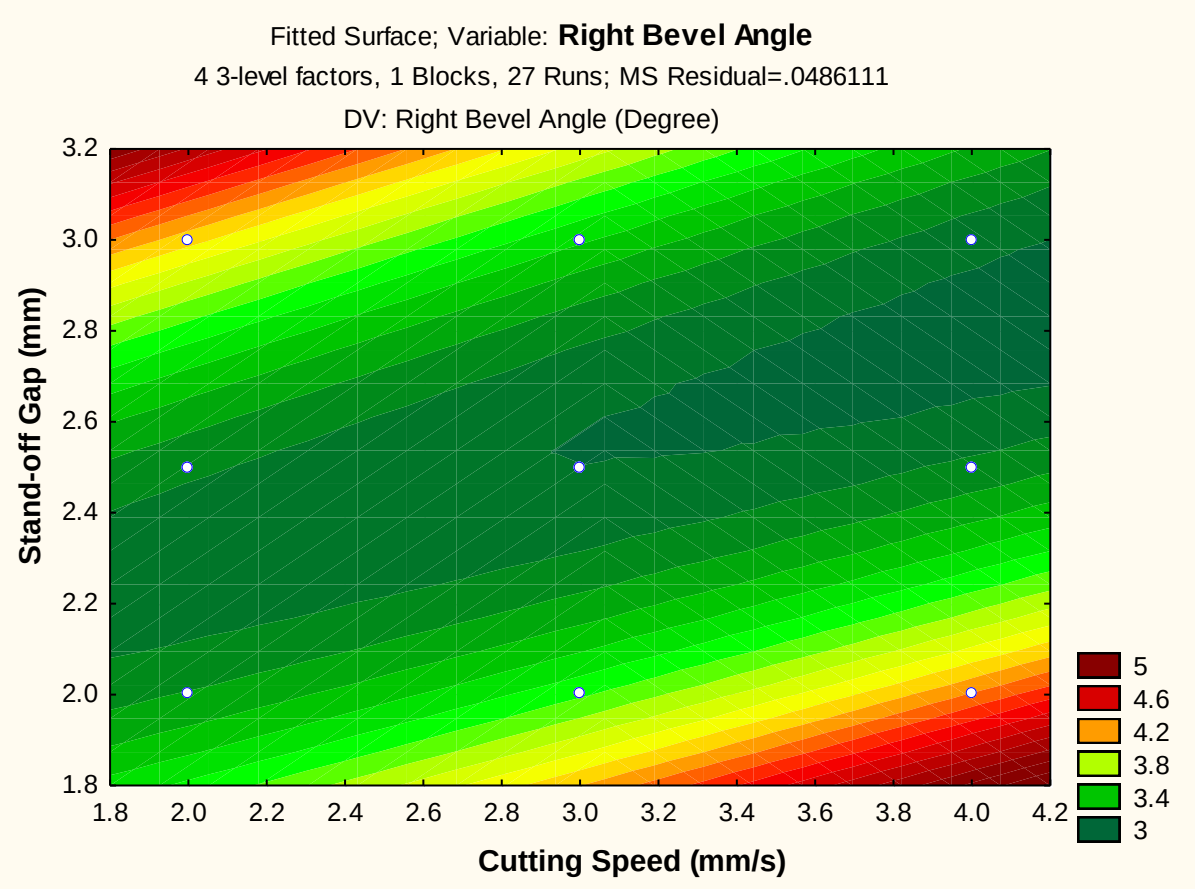

Fig. 205 2D fitted counter plot of right bevel angle (3)

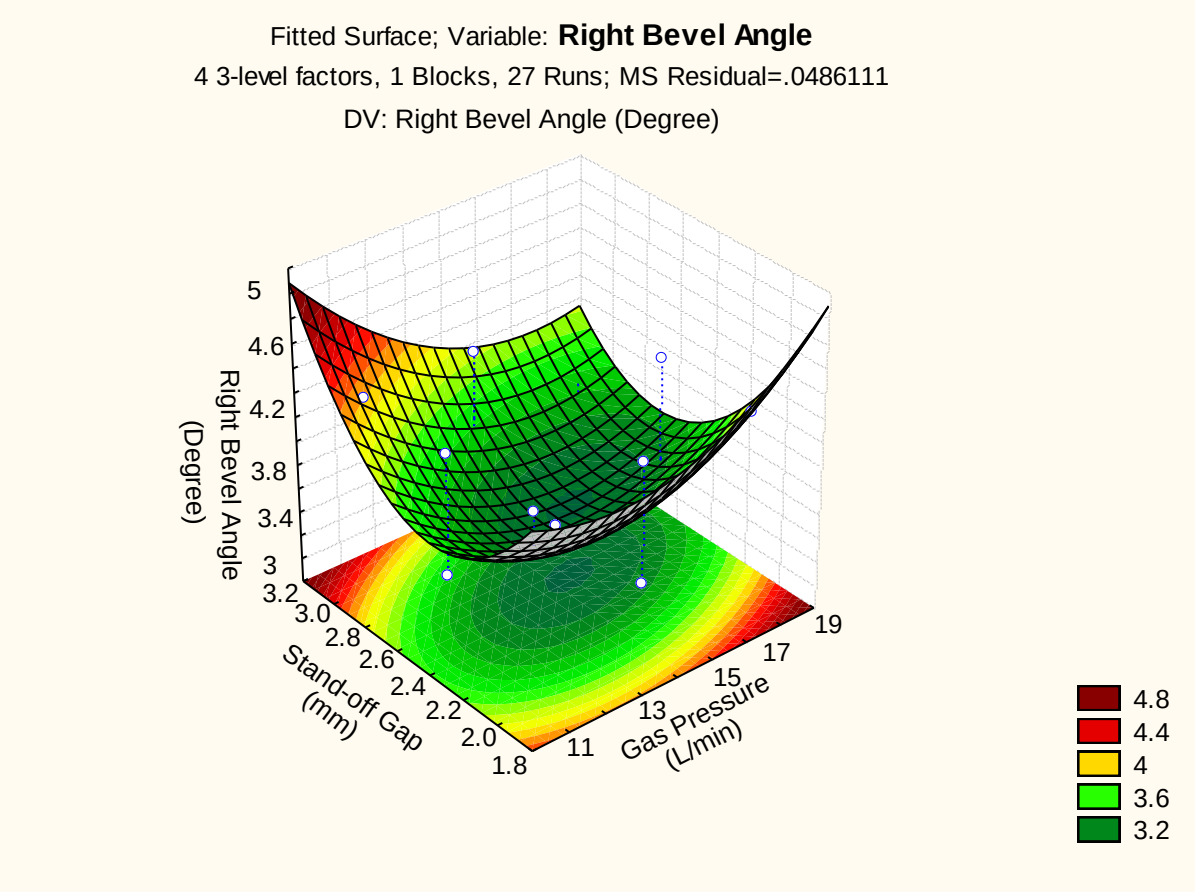

Fig. 206 3D fitted surface plot of right bevel angle (4)

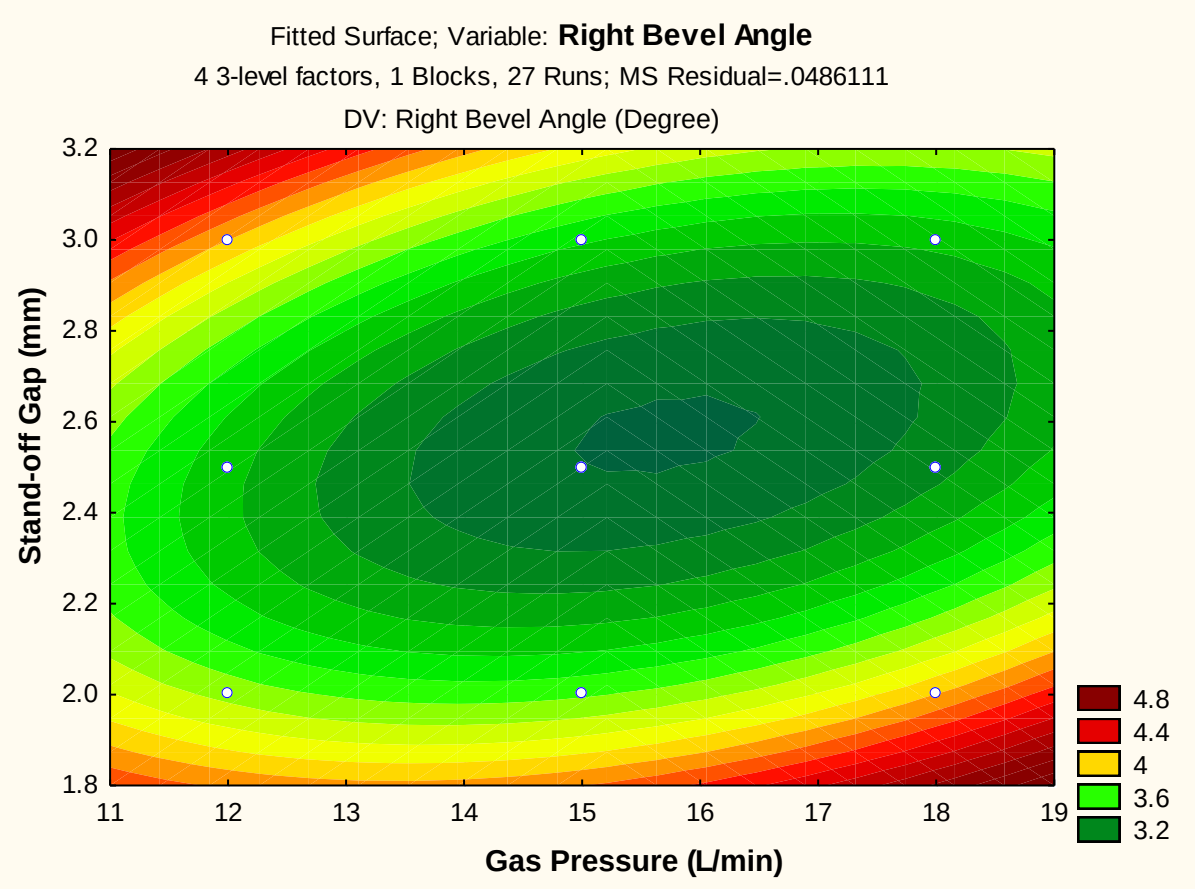

Fig. 207 2D fitted counter plot of right bevel angle (4)

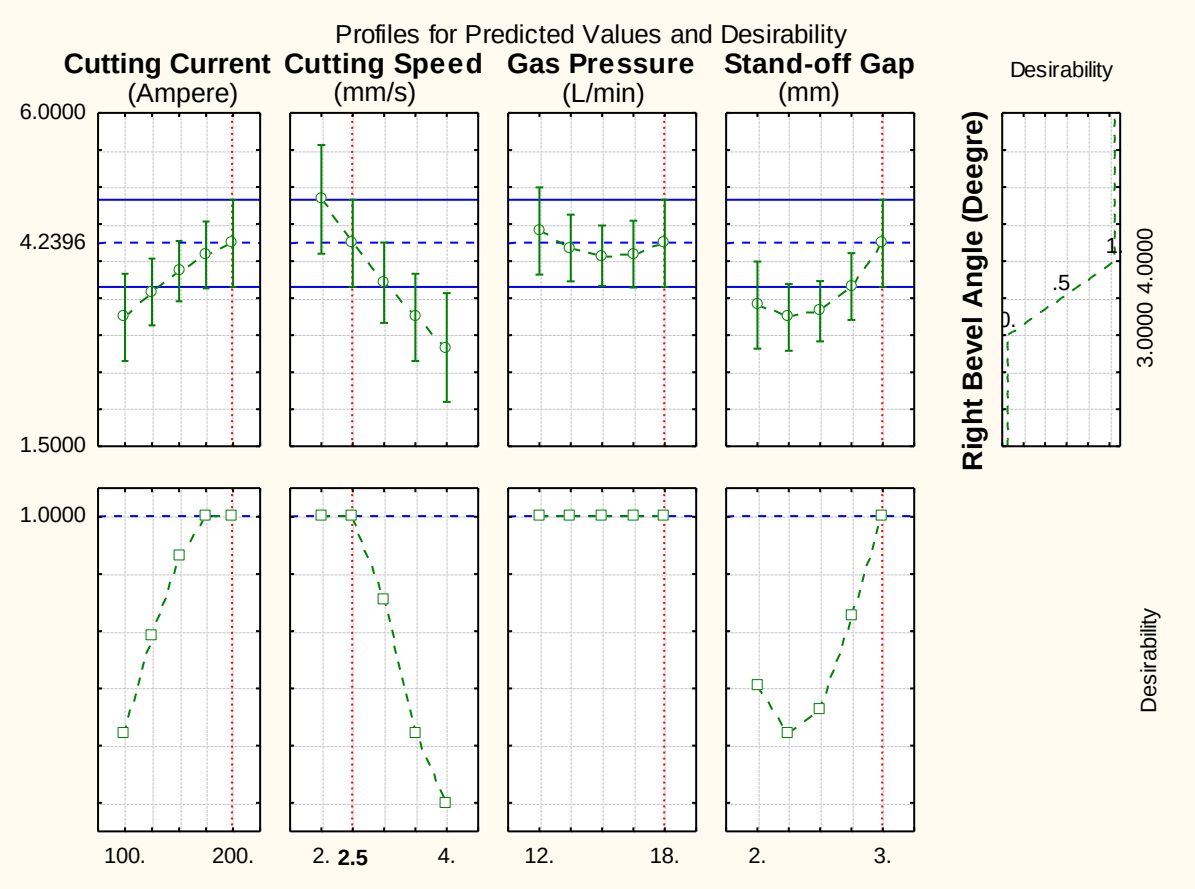

Fig. 208 Profile plot of predicted values and desirability of right bevel angle

Here, the technique of desirability function adopted to get optimum value of right bevel angle response from its quadratic fit empirical model. The level of variable giving the highest desirability i.e., 1.0000 was considered as optimum level. The optimized levels of variables (A, B, C and D) were determined using the desirability profiles that are shown in Fig. 208. The predicted values of responses and desirability function with red dotted lines are depicted in Fig. 208.

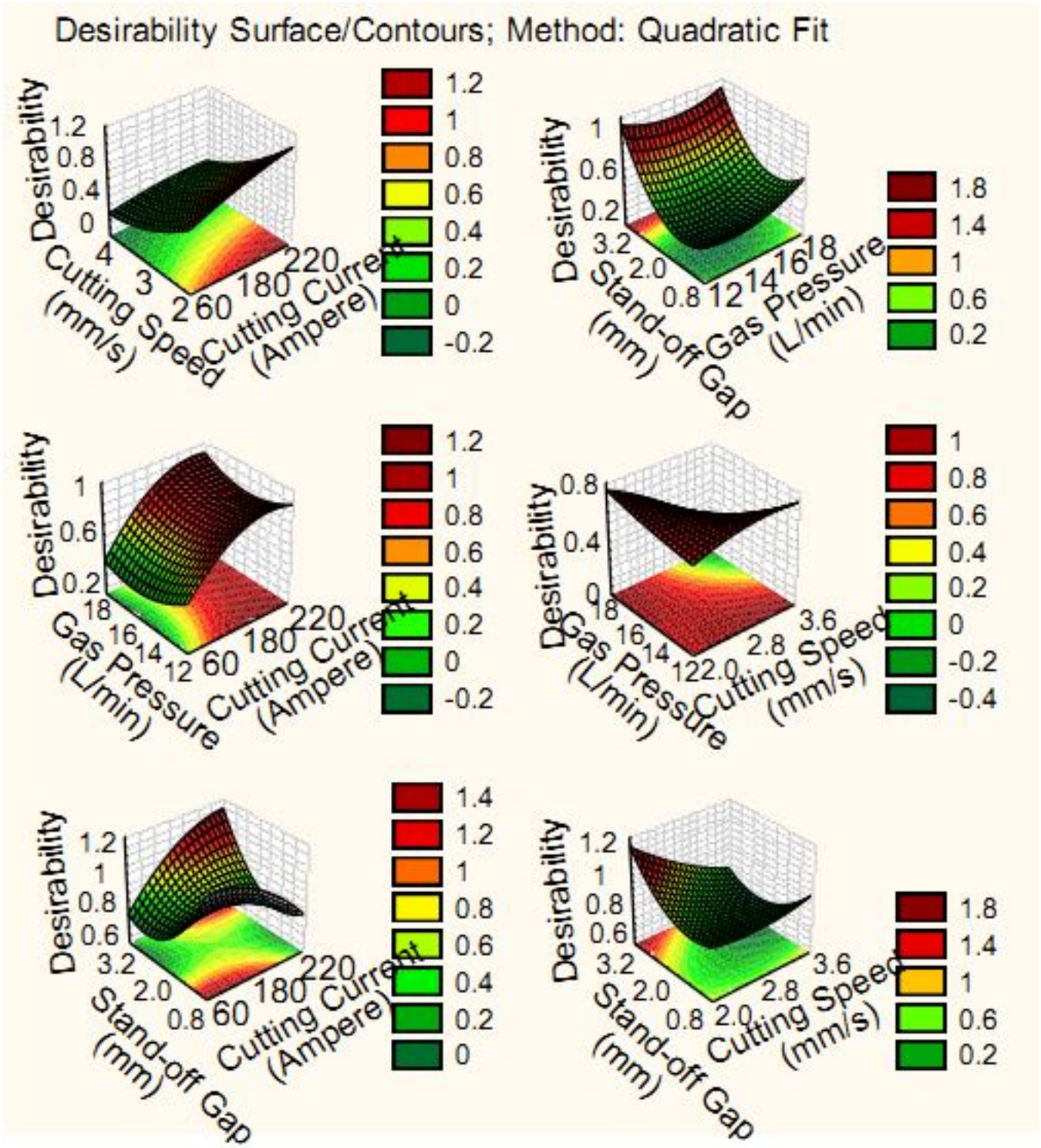

Fig. 209 Desirability 3D surface plot of right bevel angle

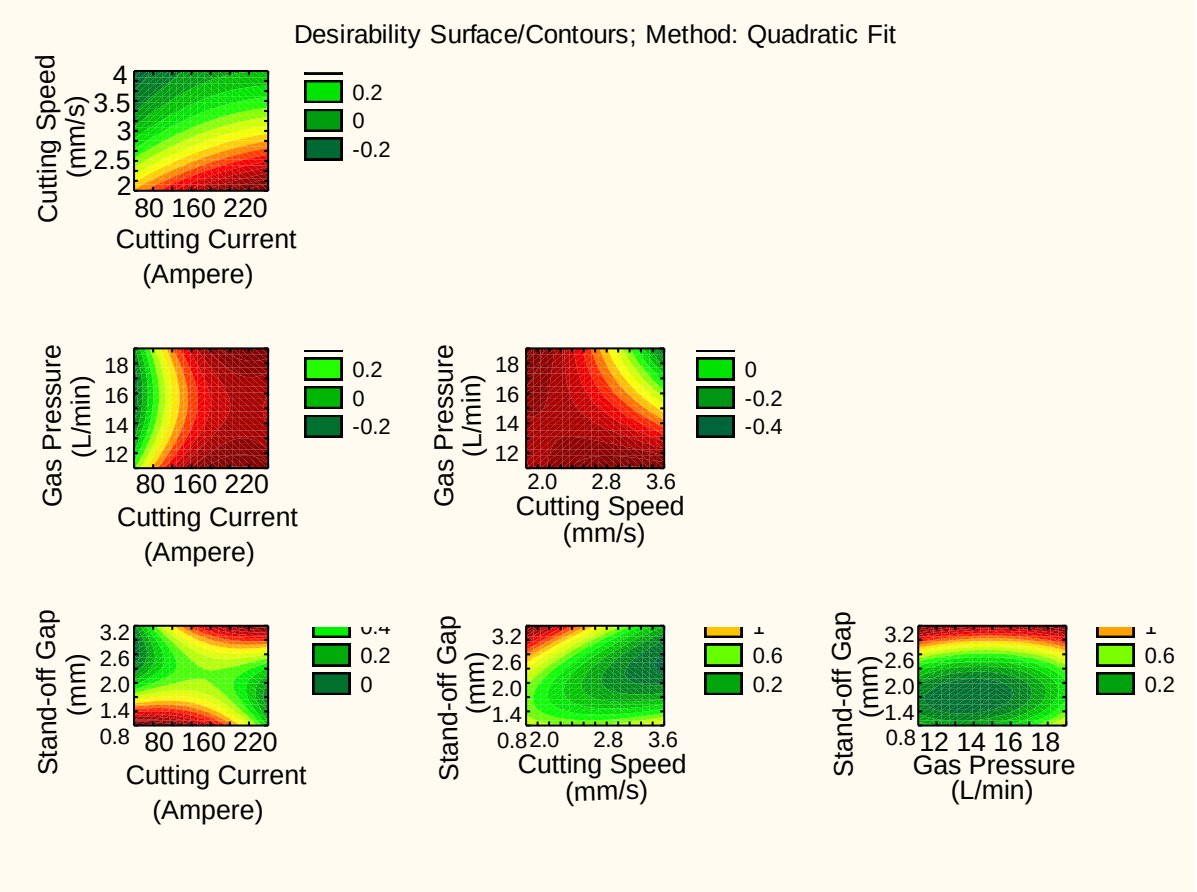

Fig. 210 Desirability 2D counter plot of right bevel angle

The 3D and 2D plot of interaction variables were determined using the desirability profiles that are shown in Fig. 209-210 respectively. For the requirement of minimum right bevel angle, only maximum cutting speed is needed during machining.

5.3.1.6 For kerf:

The cutting current has shown the highest significance than other individual factors in the ANOVA. It is shown in Table 64. The Pareto chart of effects of all factors on kerf width response is shown in Fig. 211 and the results indicate that block effect is the second most enhancing factor among all considered factors. The plot of scatter between the observed and the predicted value of kerf width of all 27 runs is shown in Fig. 212. It is concluded that the response model of kerf width presented good fit to experimental data.

In Fig. 214, the histogram plot of predicted data of kerf width with 95 % confidence interval of normal distribution is presented. Furthermore, the estimated coefficient model using multiple regressions for kerf width is resulted in Table 63. Similarly, the regression model of chamfer is recorded in Table 65.

Table 63 Effect of Estimated Values for Kerf

Factor	Effect	Std. Err.	T	P
Constant	2.778333	0.042086	66.01585	0.000000
A (Ampere)	-0.260000	0.072895	-3.56678	0.003875
A^2	-0.088750	0.054671	-1.62334	0.130476
B (mm/s)	0.135000	0.072895	1.85198	0.088777
B^2	-0.060000	0.054671	-1.09747	0.293969
C (L/min)	0.011667	0.072895	0.16005	0.875506
C^2	-0.070000	0.054671	-1.28038	0.224606
D (mm)	-0.070000	0.072895	-0.96029	0.355861
D^2	-0.088750	0.054671	-1.62334	0.130476
A×B	0.030000	0.126258	0.23761	0.816192
A×C	0.015000	0.126258	0.11880	0.907396
A×D	0.075000	0.126258	0.59402	0.563527
B×C	0.000000	0.126258	0.00000	1.000000
B×D	0.045000	0.126258	0.35641	0.727718
C×D	-0.140000	0.126258	-1.10884	0.289226

Table 64 ANOVA Table for Kerf

Factors	SS	DoF	MS	F	P
A (Ampere)	0.202800	1	0.202800	12.72193	0.003875
A^2	0.042008	1	0.042008	2.63524	0.130476
B (mm/s)	0.054675	1	0.054675	3.42984	0.088777
B^2	0.019200	1	0.019200	1.20444	0.293969
C (L/min)	0.000408	1	0.000408	0.02562	0.875506
C^2	0.026133	1	0.026133	1.63938	0.224606
D (mm)	0.014700	1	0.014700	0.92215	0.355861
D^2	0.042008	1	0.042008	2.63524	0.130476
A×B	0.000900	1	0.000900	0.05646	0.816192
A×C	0.000225	1	0.000225	0.01411	0.907396
A×D	0.005625	1	0.005625	0.35286	0.563527
B×C	0.000000	1	0.000000	0.00000	1.000000
B×D	0.002025	1	0.002025	0.12703	0.727718
C×D	0.019600	1	0.019600	1.22954	0.289226
Error	0.191292	12	0.015941		
Total SS	0.560200	26			

Table 65 Regression Coefficients of Kerf

Factor	Regression Coef.	Std. Err.	T	P
Constant	7.61167	3.681731	2.06742	0.060966
A (Ampere)	-0.01865	0.011731	-1.58976	0.137874
A^2	0.00004	0.000022	1.62334	0.130476
B (mm/s)	-0.45000	0.586566	-0.76718	0.457805
B^2	0.06000	0.054671	1.09747	0.293969
C (L/min)	-0.12222	0.228907	-0.53394	0.603135
C^2	0.00778	0.006075	1.28038	0.224606
D (mm)	-1.50500	1.373444	-1.09579	0.294678
D^2	0.35500	0.218685	1.62334	0.130476
A×B	0.00030	0.001263	0.23761	0.816192
A×C	0.00005	0.000421	0.11880	0.907396
A×D	0.00150	0.002525	0.59402	0.563527
B×C	-0.00000	0.021043	-0.00000	1.000000
B×D	0.04500	0.126258	0.35641	0.727718
C×D	-0.04667	0.042086	-1.10884	0.289226

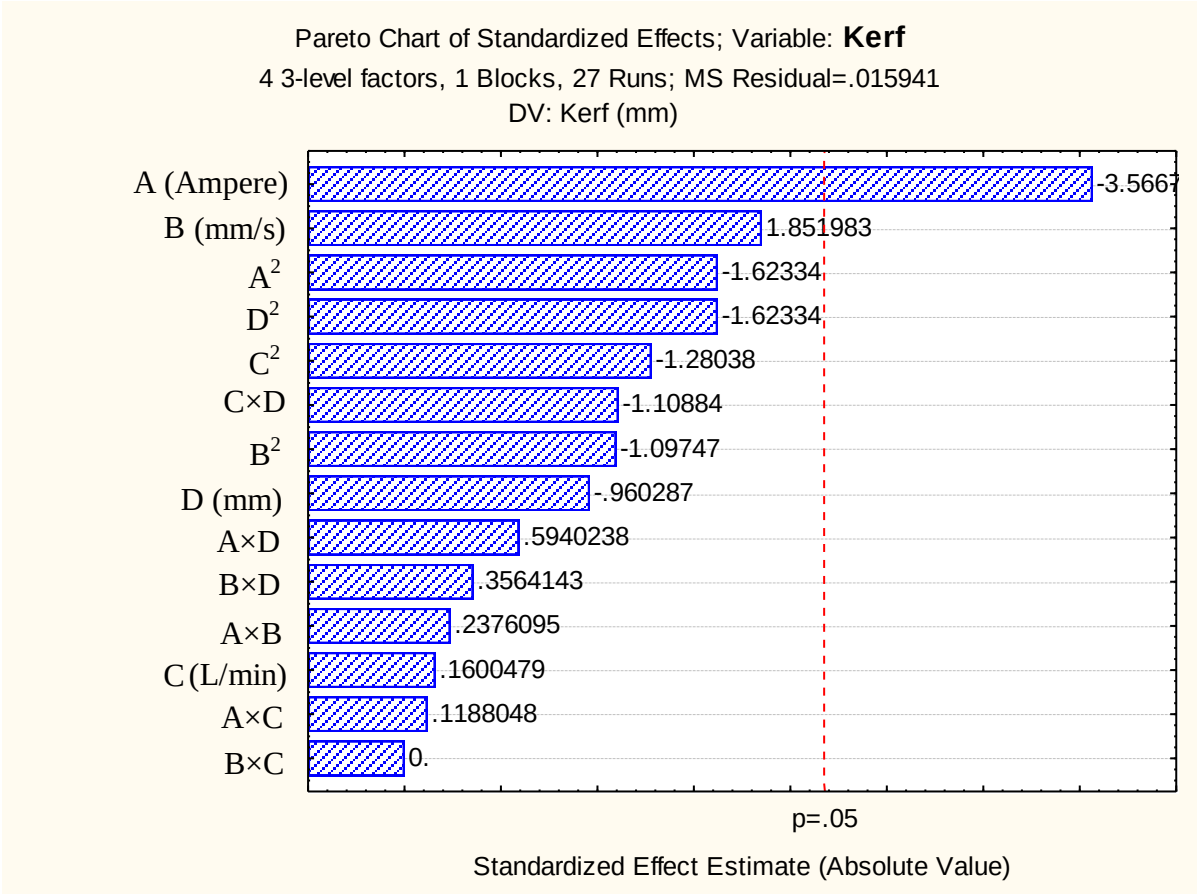

Fig. 211 Pareto chart of standardized effect of factors on kerf

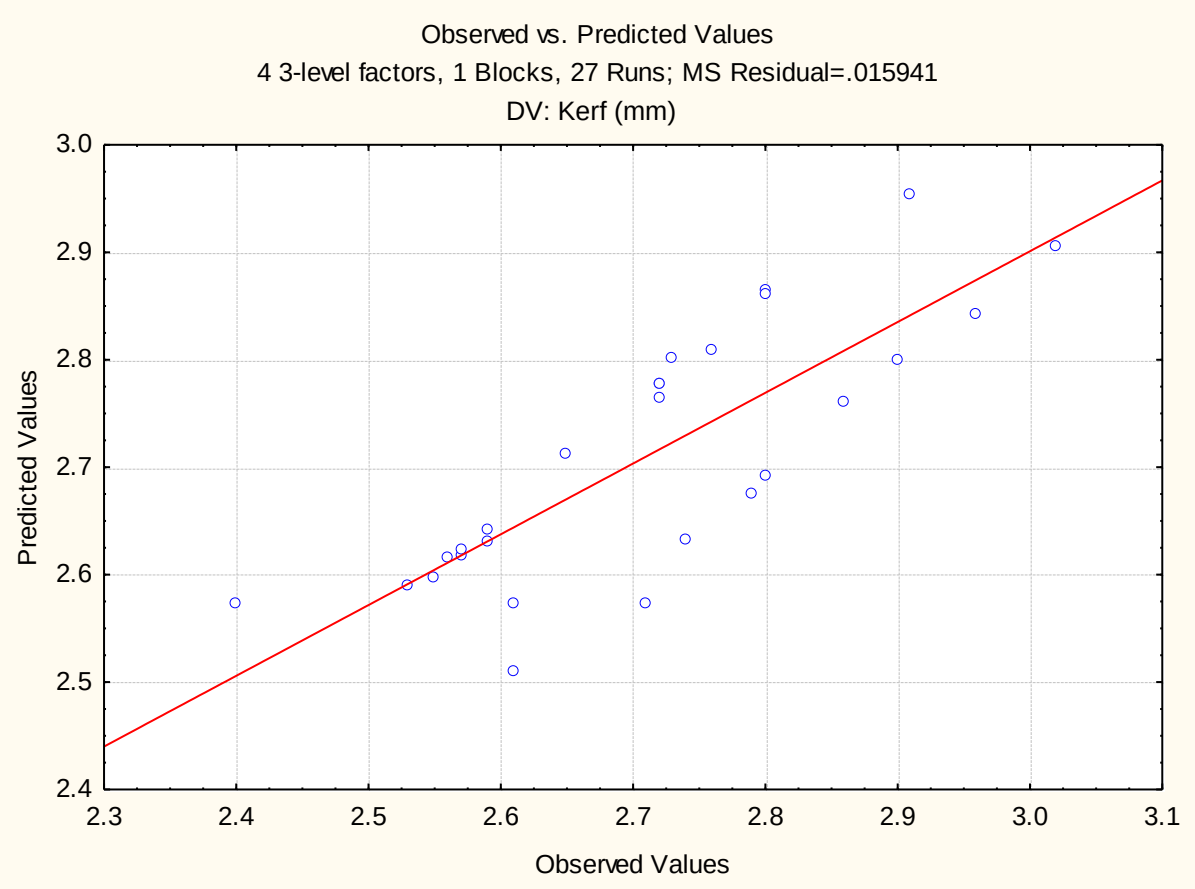

Fig. 212 Plot of observed vs. predicted values of kerf

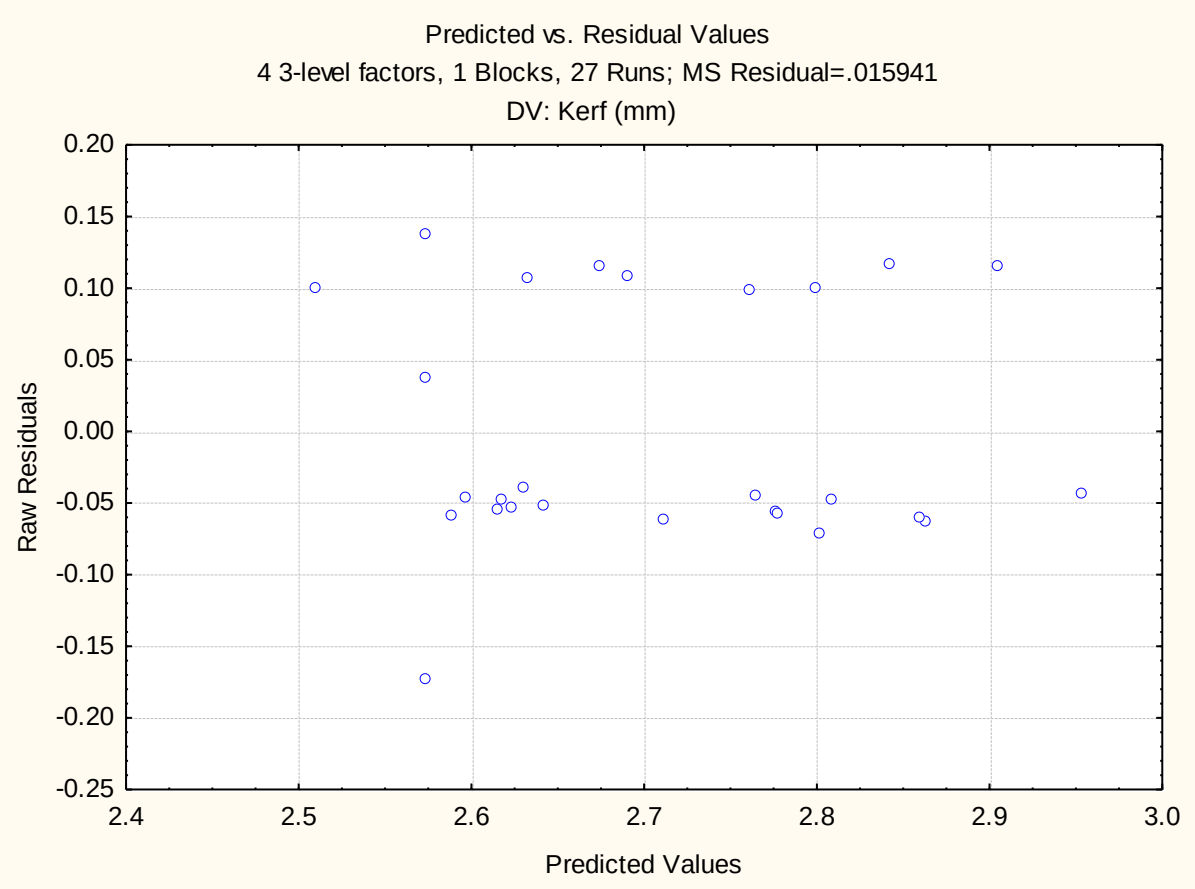

Fig. 213 Plot of predicted vs. residual values of kerf

From the Fig. 213, no standard pattern is formed in the plot of predicted vs. residual values which show the adequacy of the fitted model for kerf.

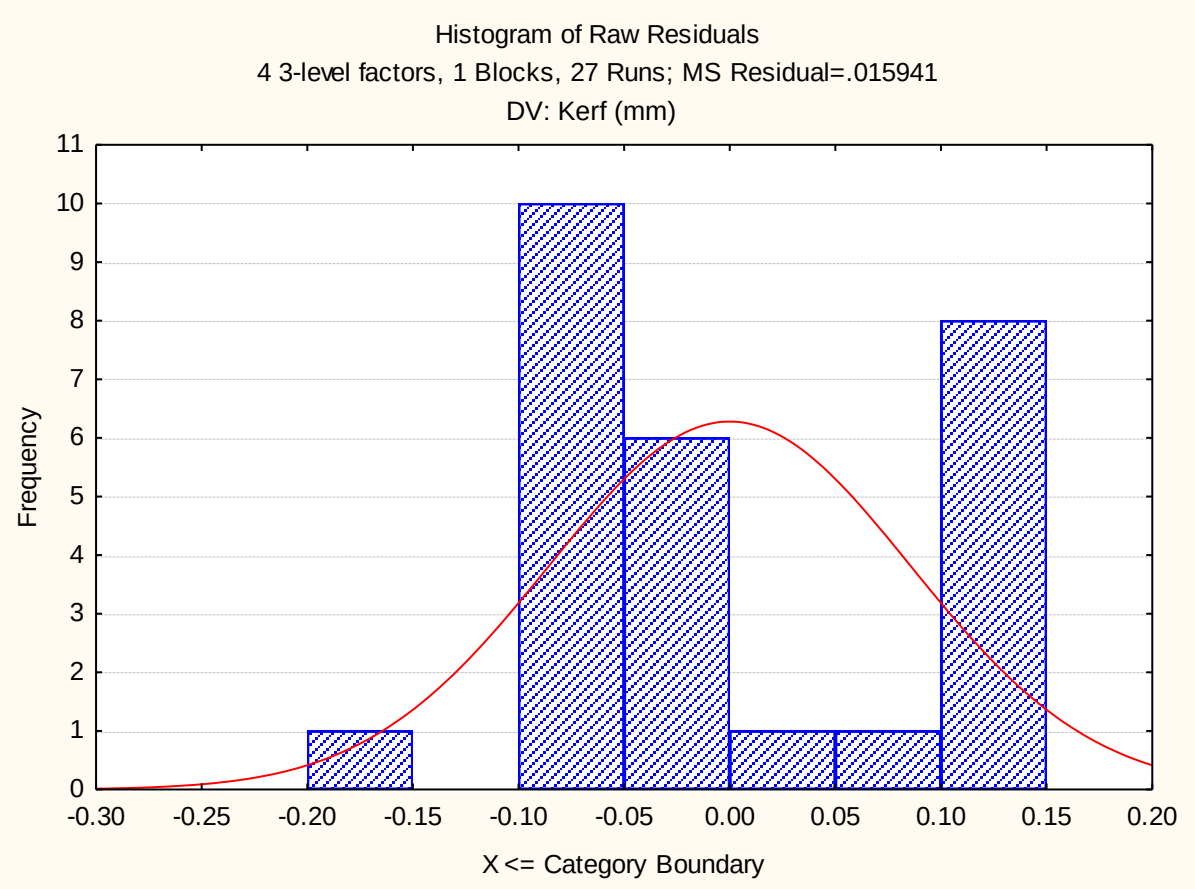

Fig. 214 Histogram plot of predicted values of kerf

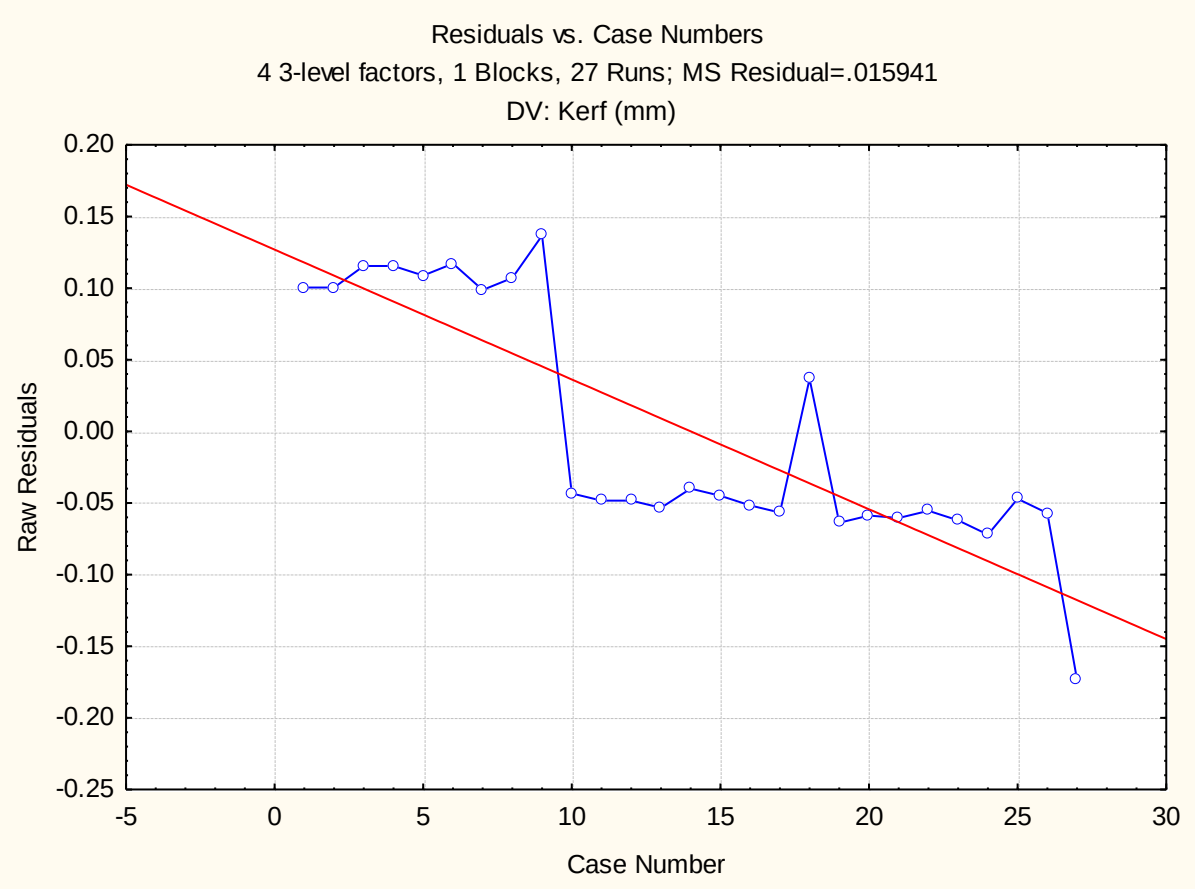

Fig. 215 Plot of residuals vs. case numbers values of kerf

From the Fig. 215, it is evident that the highest kerf value among all experimental runs is by the run number 9. The red line indicates that the value of kerf decreases with increase in run order.

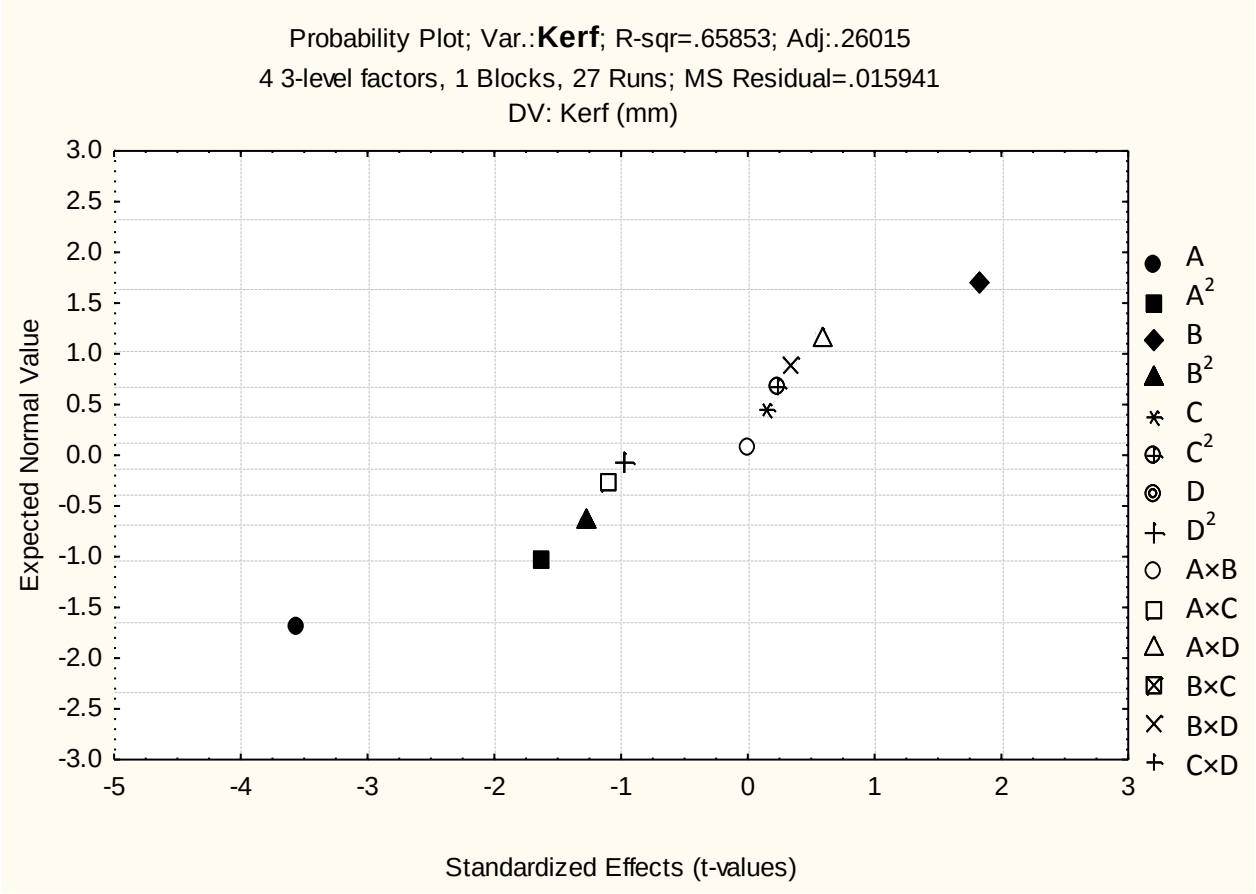

Fig. 216 Probability plot of kerf

The normal probability plot of kerf corresponding to each regression terms is plotted in Fig. 216.

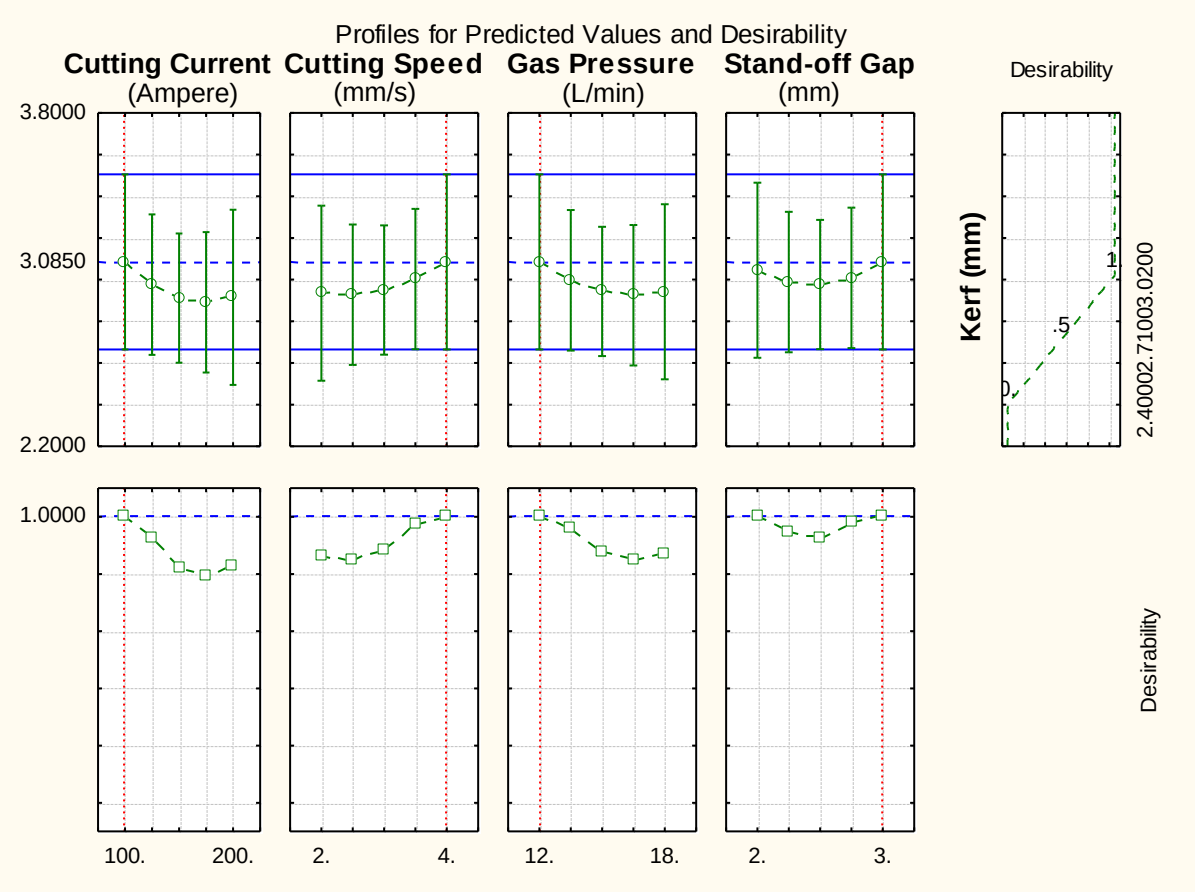

Fig. 217 Profile plot of predicted values and desirability of kerf

The methodology of desirability function was taken to determine the value of optimum kerf response from its quadratic fit model. The level of variable giving the highest desirability i.e., 1.0000 was considered as optimum level. The optimized levels of variables (A, B, C and D) were determined using the desirability profiles that are shown in Fig. 217. The predicted values of responses and desirability function with red dotted lines are presented in Fig. 217 simultaneously.

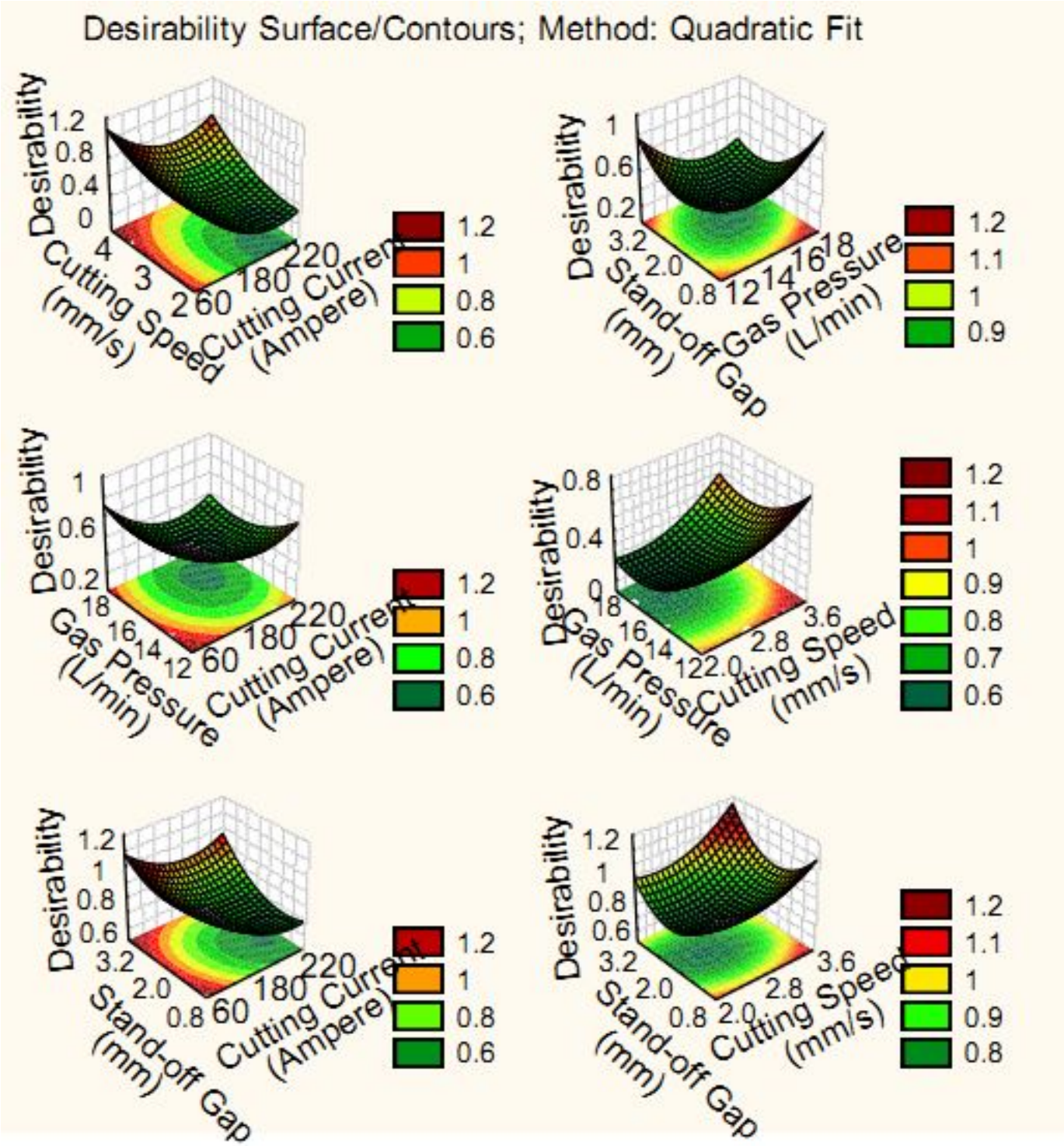

Fig. 218 Desirability 3D surface plot of kerf

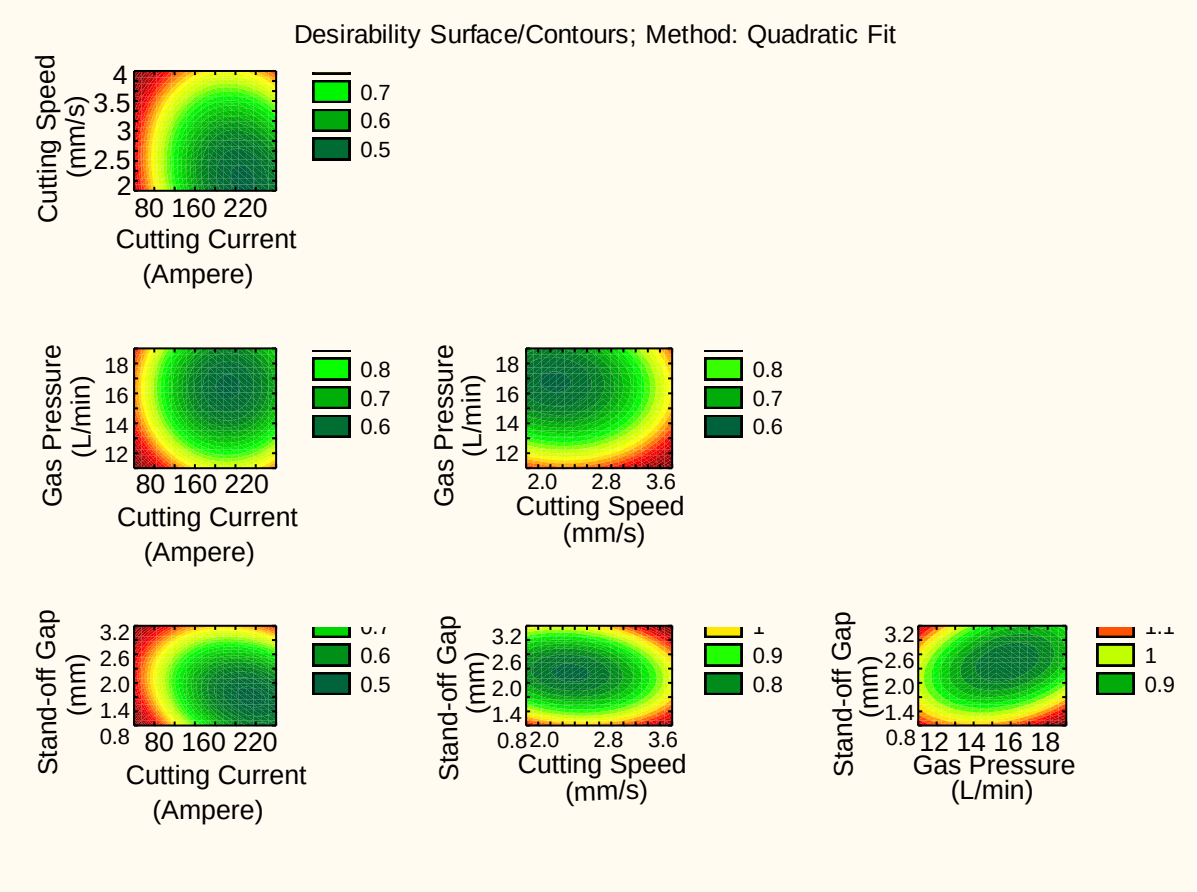

Fig. 219 Desirability 2D counter plot of kerf

The 3D and 2D plot of interaction variables on kerf width were obtained utilizing the desirability profiles that are shown in Fig. 218-219 respectively. In these figures, green circular section in middle occurred in every surface plot that means all interaction terms are suitable for minimizing kerf width.

5.3.1.7 For heat affected zone:

Table 67 presents the ANOVA for heat affected zone with respect to all individual and interaction terms. From this analysis it is determined that the cutting current has very influencing characteristics than other factors as its F-value is the highest. This type of claim satisfies the findings of Kadirgamma et al. [106] and Salonitis and Vatousianos [107] i.e., the cutting current has major role in controlling the HAZ response. The Pareto

chart of effects of all factors on heat affected zone is shown in Fig. 220 and these results concluded that cutting current is the most enhancing factor among all considered factors. Again for interactions, only the combination between cutting current and speed has shown the noticeable effect due to its lowest P-value. In Fig. 221, the scatter plot of the observed vs. the predicted value of heat affected zone of all 27 runs is presented. It was determined that the relationship between the actual and the predicted HAZ was linear and the model could be considered relevant for predictions and optimization in RSM. The histogram plot of predicted data of heat affected zone with 95 % confidence interval of normal distribution is shown in Fig. 223. Moreover, the surface and contour graph of the interaction between cutting current and speed is displayed in Fig. 226-227 respectively. It is concluded that at lower value of cutting current and speed, the minimum value of HAZ is achieved due less temperature generated in this type of condition in plasma arc machining. For HAZ, the model of estimated coefficient is collected in Table 66. Further, the estimated regression model of HAZ is given in Table 68.

Table 66 Effect of Estimated Values for HAZ

Factor	Effect	Std. Err.	T	P
Constant	2.019444	0.074669	27.04528	0.000000
A (Ampere)	0.846667	0.129331	6.54653	0.000027
A^2	-0.072917	0.096998	-0.75173	0.466699
B (mm/s)	-0.510000	0.129331	-3.94338	0.001951
B^2	-0.105417	0.096998	-1.08679	0.298477
C (L/min)	-0.096667	0.129331	-0.74744	0.469193
C^2	-0.077917	0.096998	-0.80328	0.437434
D (mm)	0.236667	0.129331	1.82994	0.092198
D^2	-0.052917	0.096998	-0.54554	0.595375
A×B	-0.515000	0.224007	-2.29903	0.040268
A×C	-0.135000	0.224007	-0.60266	0.557953
A×D	-0.410000	0.224007	-1.83030	0.092140
B×C	0.015000	0.224007	0.06696	0.947715
B×D	-0.010000	0.224007	-0.04464	0.965127
C×D	0.090000	0.224007	0.40177	0.694915

Table 67 ANOVA Table for HAZ

Factors	SS	DoF	MS	F	P
A (Ampere)	2.150533	1	2.150533	42.85710	0.000027
A^2	0.028356	1	0.028356	0.56510	0.466699
B (mm/s)	0.780300	1	0.780300	15.55028	0.001951
B^2	0.059268	1	0.059268	1.18112	0.298477
C (L/min)	0.028033	1	0.028033	0.55866	0.469193
C^2	0.032379	1	0.032379	0.64526	0.437434
D (mm)	0.168033	1	0.168033	3.34867	0.092198
D^2	0.014934	1	0.014934	0.29762	0.595375
A×B	0.265225	1	0.265225	5.28556	0.040268
A×C	0.018225	1	0.018225	0.36320	0.557953
A×D	0.168100	1	0.168100	3.35000	0.092140
B×C	0.000225	1	0.000225	0.00448	0.947715
B×D	0.000100	1	0.000100	0.00199	0.965127
C×D	0.008100	1	0.008100	0.16142	0.694915
Error	0.602150	12	0.050179		
Total SS	4.263985	26			

Table 68 Regression Coefficients of HAZ

Factor	Regression Coef.	Std. Err.	T	P
Constant	0.591667	6.532153	0.09058	0.929323
A (Ampere)	0.042417	0.020814	2.03791	0.064227
A^2	0.000029	0.000039	0.75173	0.466699
B (mm/s)	-0.127500	1.040689	-0.12251	0.904519
B^2	0.105417	0.096998	1.08679	0.298477
C (L/min)	-0.290833	0.406129	-0.71611	0.487625
C^2	0.008657	0.010778	0.80328	0.437434
D (mm)	-0.011667	2.436774	-0.00479	0.996259
D^2	0.211667	0.387992	0.54554	0.595375
A×B	-0.005150	0.002240	-2.29903	0.040268
A×C	-0.000450	0.000747	-0.60266	0.557953
A×D	-0.008200	0.004480	-1.83030	0.092140
B×C	0.002500	0.037335	0.06696	0.947715
B×D	-0.010000	0.224007	-0.04464	0.965127
C×D	0.030000	0.074669	0.40177	0.694915

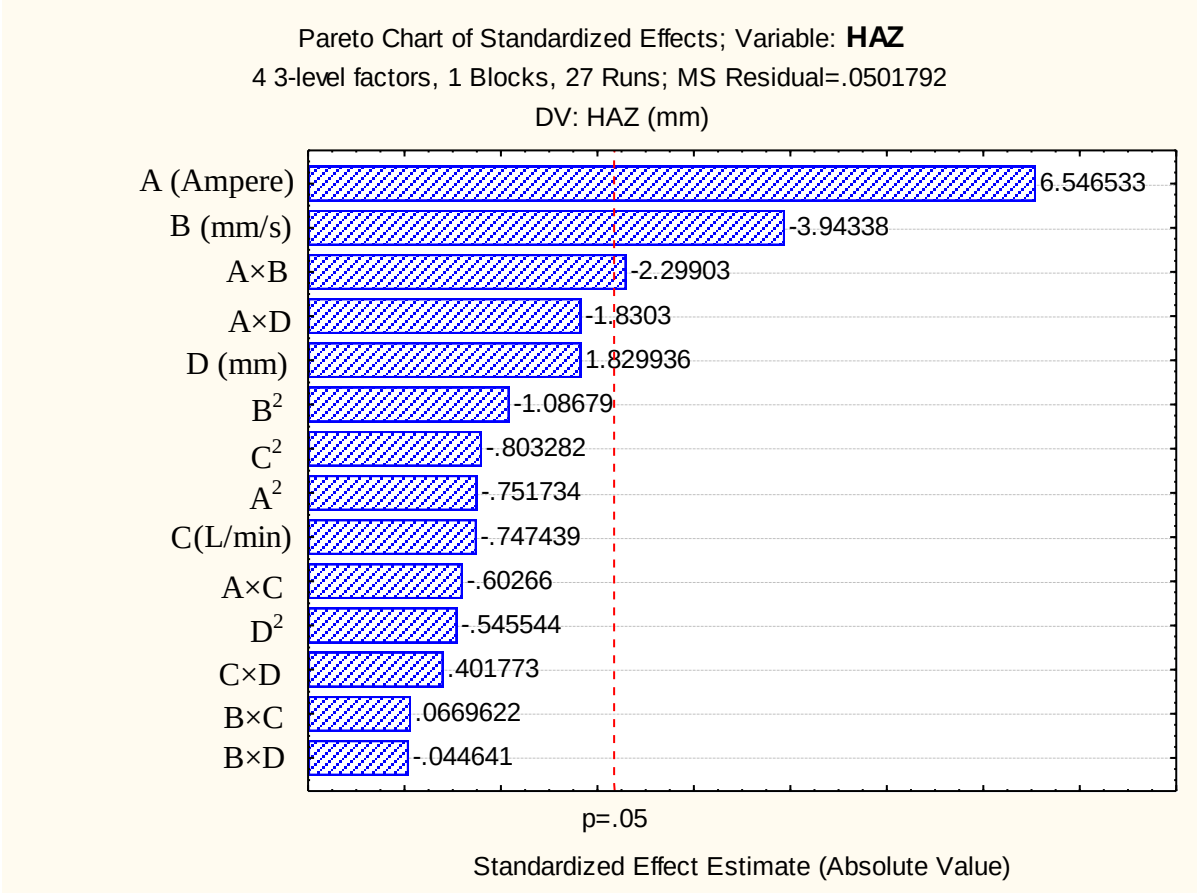

Fig. 220 Pareto chart of standardized effect of factors on MRR

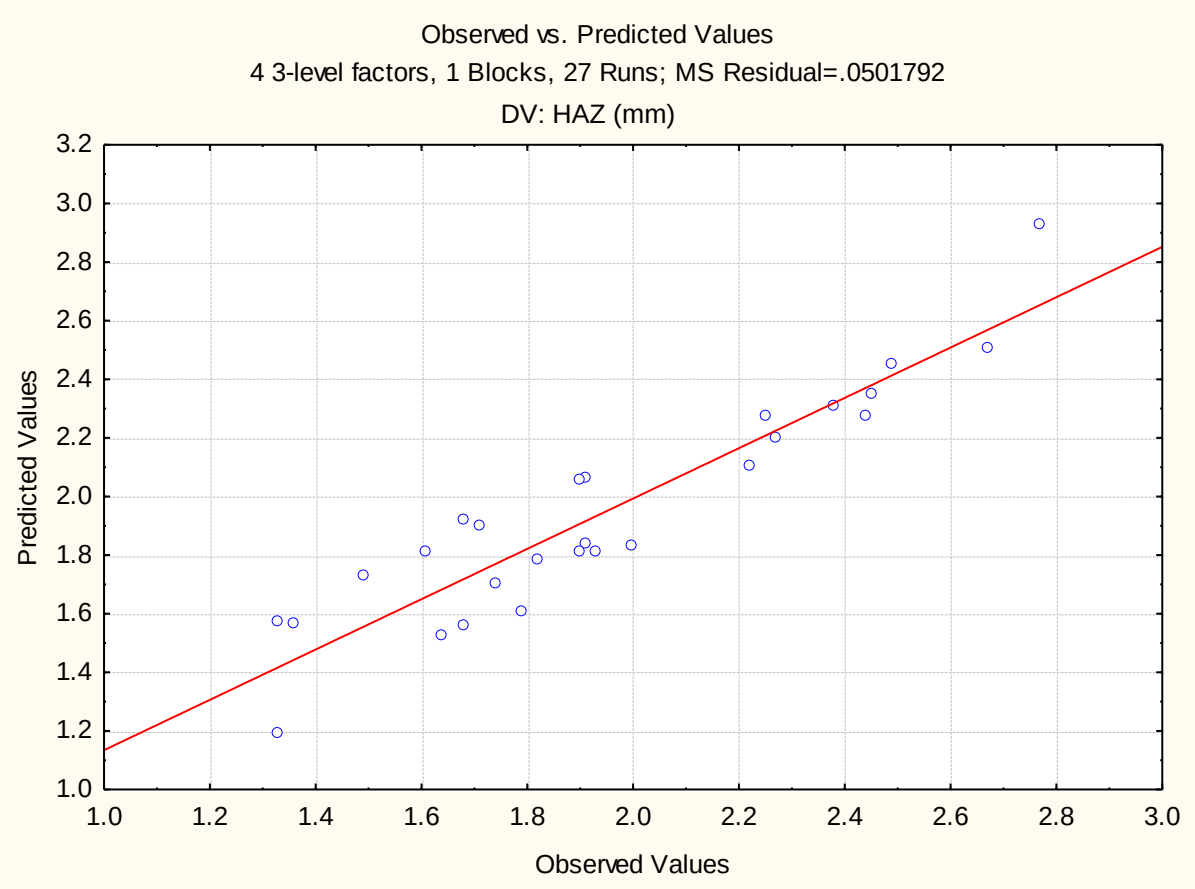

Fig. 221 Plot of observed vs. predicted values of HAZ

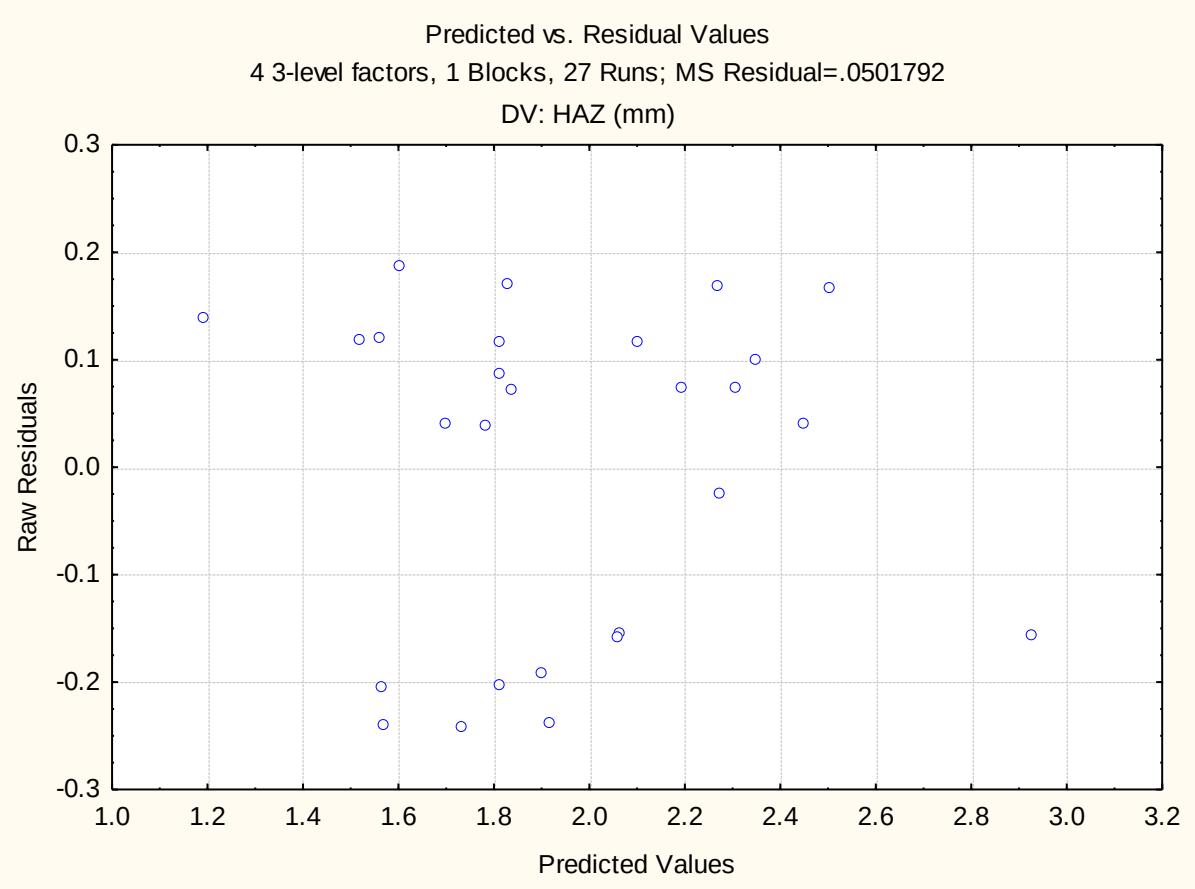

Fig. 222 Plot of predicted vs. residual values of HAZ

From the Fig. 222, no standard pattern is formed in the plot of predicted vs. residual values which show the adequacy of the fitted model for HAZ.

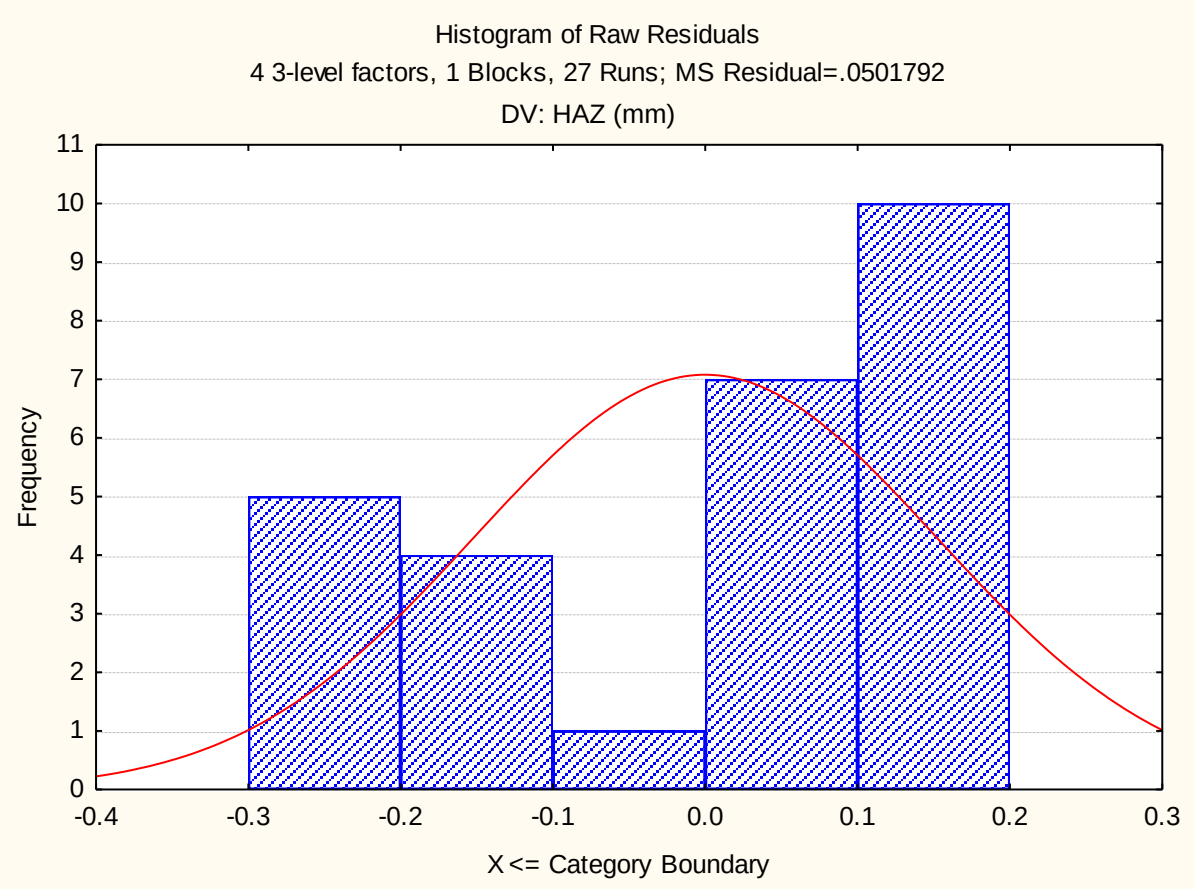

Fig. 223 Histogram plot of predicted values of HAZ

Fig. 224 Plot of residuals vs. case numbers values of HAZ

From the Fig. 224, it is evident that the highest HAZ value among all experimental runs is by the run number 26. The red line indicates that the value of HAZ increases with increase in run order.

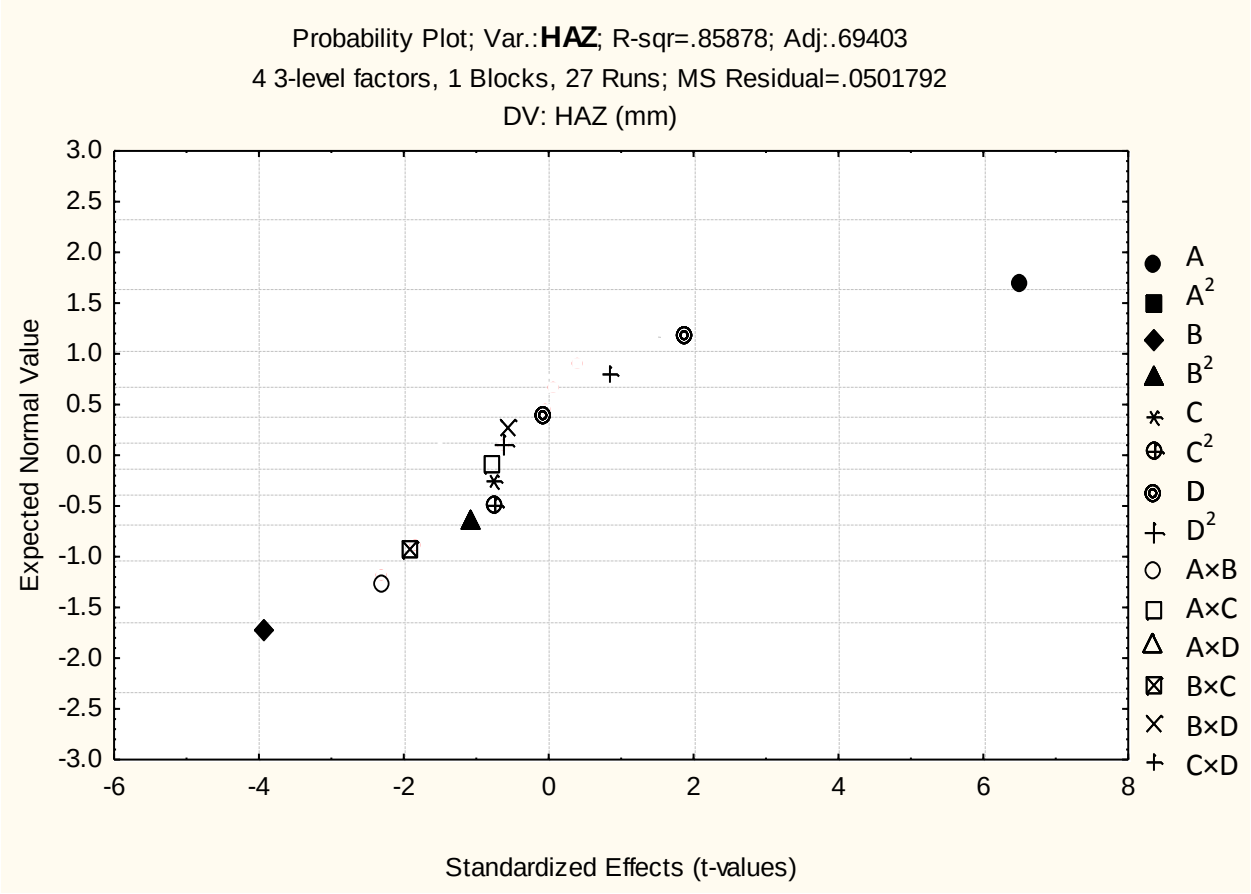

Fig. 225 Probability plot of HAZ

The normal probability plot of HAZ corresponding to each regression terms is plotted in Fig. 225.

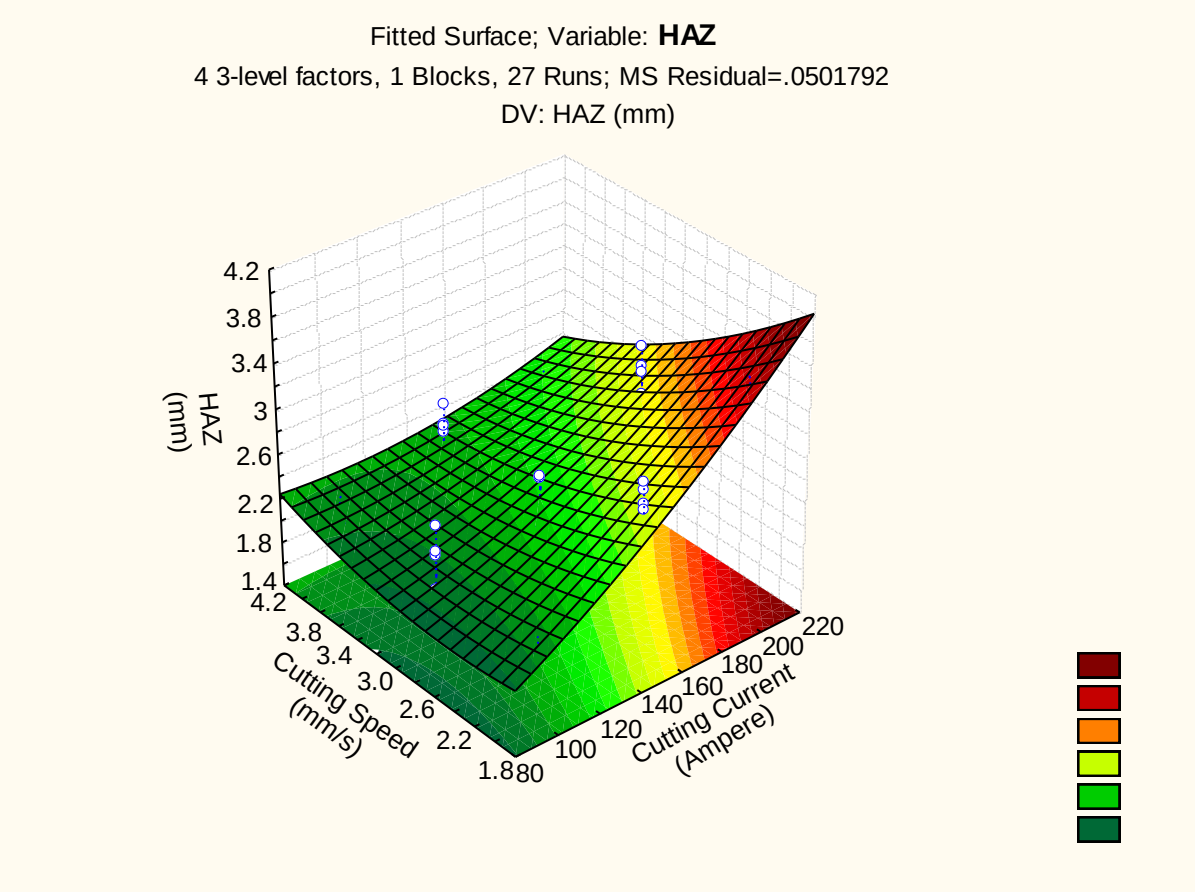

Fig. 226 3D fitted surface plot of HAZ

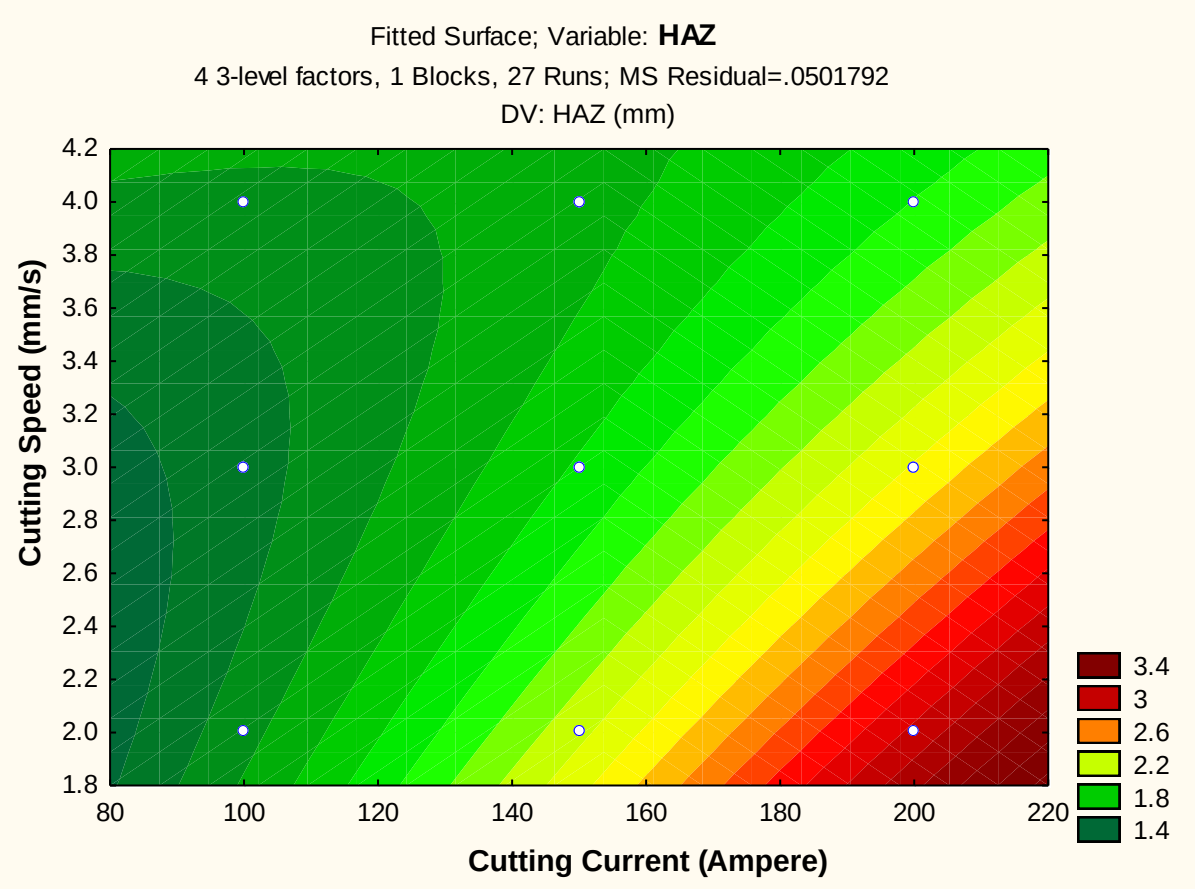

Fig. 227 2D fitted counter plot of HAZ

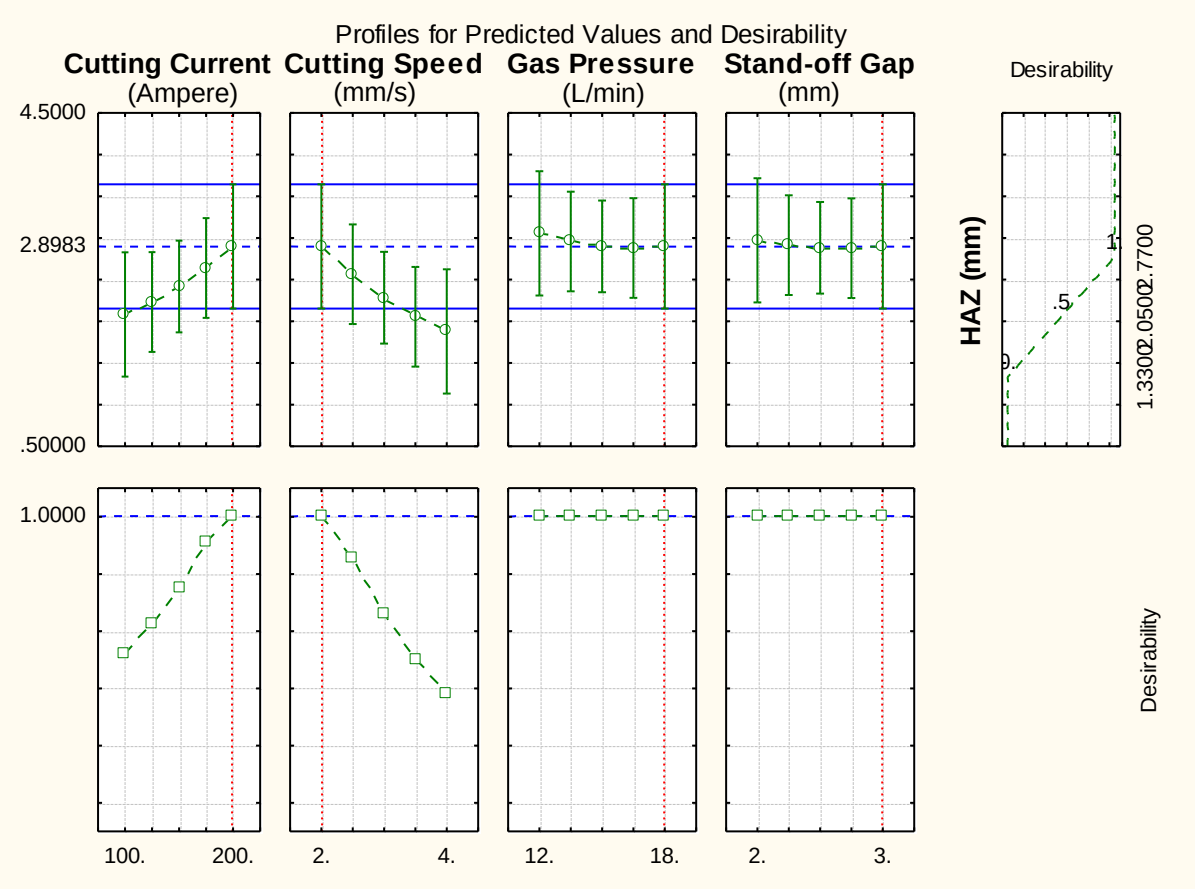

Fig. 228 Profile plot of predicted values and desirability of HAZ

Similarly, the desirability function helped to find optimum value of heat affected zone (HAZ) response which was fitted by the quadratic fit model. The level of variable giving the highest desirability i.e., 1.0000 was considered as optimum level. The optimized levels of variables (A, B, C and D) were determined using the desirability profiles that are shown in Fig. 228. The predicted values of responses and desirability function with red dotted lines are shown in Fig. 228 concurrently.

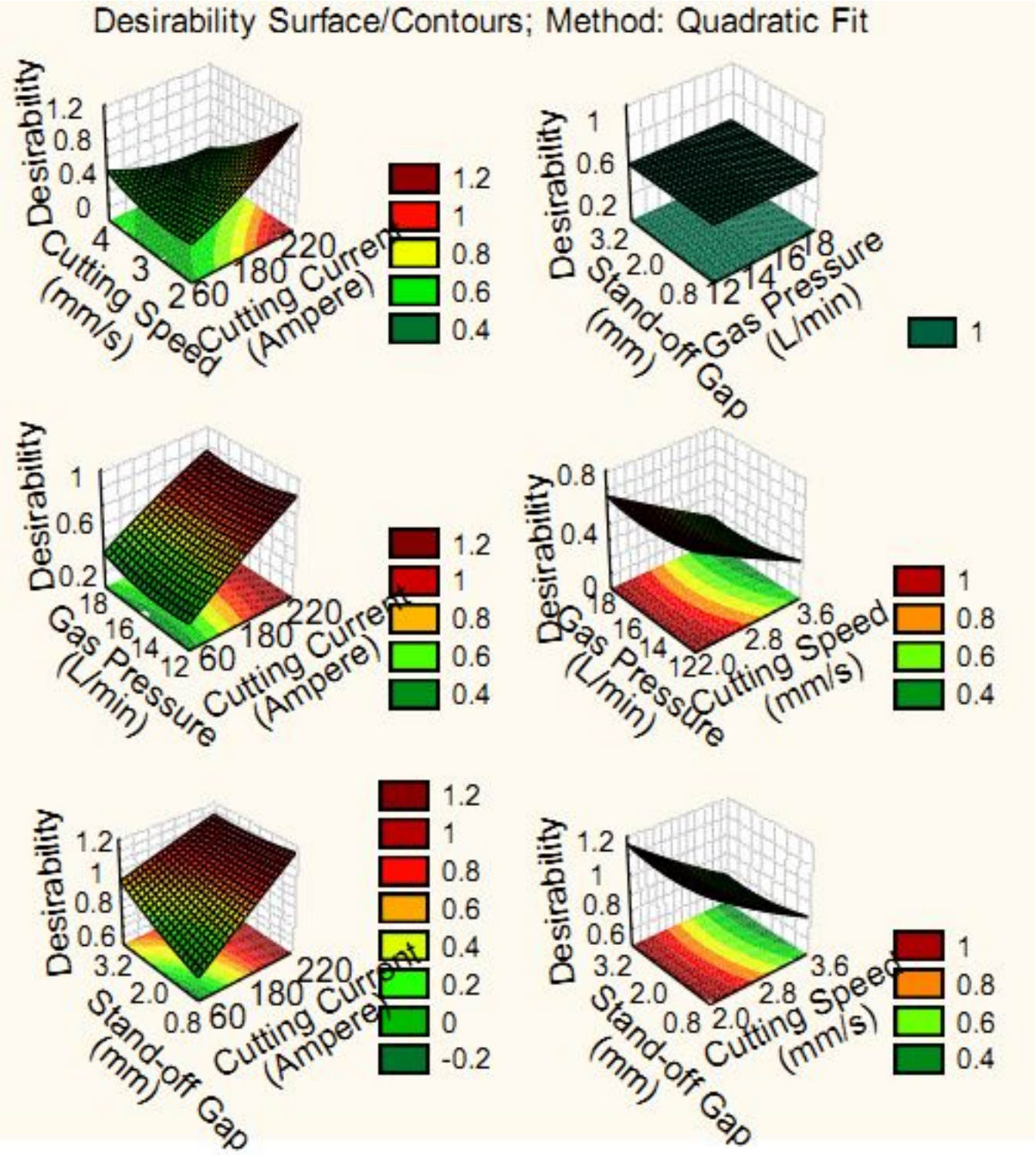

Fig. 229 Desirability 3D surface plot of HAZ

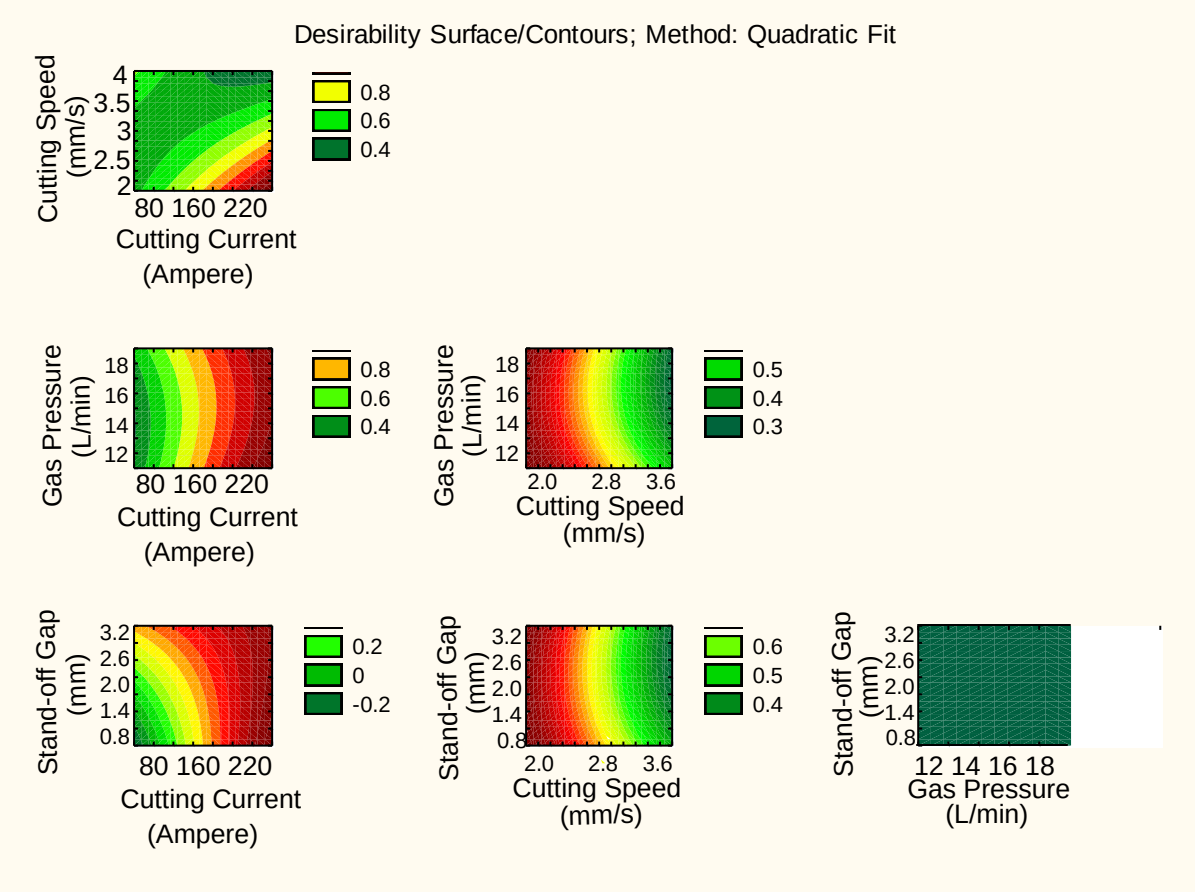

Fig. 230 Desirability 2D counter plot of HAZ

The 3D and 2D surface interaction plots of variables on heat affected zone were determined using the desirability profiles that are shown in Fig. 229-230 respectively. The interaction term of stand-off gap and gas pressure gave no effect on HAZ which showed no influential characteristics occurred on HAZ response throughout plasma machining.

5.3.2 Hybrid approach

In this hybrid approach i.e., Grey PCA, all values of responses are normalized in between 0 and 1 as per the higher the better and lower the better criteria according to the corresponding problem. The computed normalized value of each response is recorded in Table 69. Then, the value of deviation sequences for corresponding outputs are calculated and tabulated in Table 70. The Eigen values and vectors are determined to check the

correlation among output responses of PAC operation. The values of Eigen are tabulated in Table 71 and similarly the values of Eigen vectors are recorded in Table 72 for each principal component. The grey relational coefficients are computed for each response and the overall grey relational grade is calculated by averaging the grey coefficients in each run order. The grey relational coefficients and overall grey relational grade are tabulated in Table 73. ANOVA is carried out for the multi-objective problem of Grey based PCA approach and the obtained results are tabulated in Table 74 and Table 75. The regression coefficients for GRG are recorded in Table 76.

Table 69 Normalized Values for Output Response

MRR (mm^3/min)	SR (µm)	Chamfer (mm)	Dross (mm^2)	Right Bevel Angle (Degree)	Kerf (mm)	HAZ (mm)
0.615491	0.424165	0.483871	0.315789	1	0.193548	0.979167
0.000000	0.944087	0.903226	1.000000	1	0.661290	0.000000
1.000000	0.000000	0.000000	0.000000	1	0.000000	1.000000
0.526295	0.492288	0.580645	0.421053	1	0.370968	0.736111
0.630768	0.429306	0.516129	0.289474	0	0.354839	0.756944
0.818444	0.226864	0.258065	0.171053	0	0.096774	0.888889
0.499278	0.562982	0.677419	0.447368	0	0.258065	0.597222
0.436244	0.602828	0.709677	0.513158	1	0.451613	0.604167
0.535485	0.522494	0.612903	0.407895	1	0.500000	0.805556
0.922925	0.129820	0.161290	0.065789	0	0.177419	1.000000
0.262910	0.746787	0.774194	0.776316	1	0.725806	0.194444
0.551091	0.496144	0.580645	0.381579	1	0.419355	0.597222
0.209239	0.889460	0.967742	0.842105	0	0.725806	0.361111
0.191584	0.928021	0.967742	0.750000	1	0.693548	0.270833
0.821626	0.526350	0.548387	0.328947	0	0.483871	0.659722
0.256063	0.884319	0.838710	0.723684	0	0.693548	0.347222
0.708871	0.408098	0.451613	0.250000	1	0.483871	0.715278
0.427892	0.701157	0.741935	0.539474	1	0.661290	0.604167
0.689125	0.375321	0.516129	0.236842	1	0.354839	0.784722
0.134343	0.970437	0.967742	0.815789	1	0.790323	0.069444
0.741715	0.377249	0.451613	0.210526	1	0.354839	0.756944
0.208141	0.797558	0.903226	0.736842	1	0.741935	0.229167
0.253132	0.832262	0.935484	0.723684	1	0.596774	0.381944
0.850147	0.307198	0.290323	0.144737	0	0.467742	0.680556
0.181556	1.000000	1.000000	0.684211	0	0.758065	0.222222
0.449566	0.629177	0.870968	0.500000	1	0.483871	0.534722
0.402198	0.726864	0.806452	0.539474	1	1.000000	0.583333

Table 70 Deviation Sequences for Output Responses of PAC

MRR (mm^3/min)	SR (µm)	Chamfer (mm)	Dross (mm^2)	Right Bevel Angle (Degree)	Kerf (mm)	HAZ (mm)
0.384509	0.575835	0.516129	0.684211	0	0.806452	0.020833
1.000000	0.055913	0.096774	0.000000	0	0.338710	1.000000
0.000000	1.000000	1.000000	1.000000	0	1.000000	0.000000
0.473705	0.507712	0.419355	0.578947	0	0.629032	0.263889
0.369232	0.570694	0.483871	0.710526	1	0.645161	0.243056
0.181556	0.773136	0.741935	0.828947	1	0.903226	0.111111
0.500722	0.437018	0.322581	0.552632	1	0.741935	0.402778
0.563756	0.397172	0.290323	0.486842	0	0.548387	0.395833
0.464515	0.477506	0.387097	0.592105	0	0.500000	0.194444
0.077075	0.870180	0.838710	0.934211	1	0.822581	0.000000
0.737090	0.253213	0.225806	0.223684	0	0.274194	0.805556
0.448909	0.503856	0.419355	0.618421	0	0.580645	0.402778
0.790761	0.110540	0.032258	0.157895	1	0.274194	0.638889
0.808416	0.071979	0.032258	0.250000	0	0.306452	0.729167
0.178374	0.473650	0.451613	0.671053	1	0.516129	0.340278
0.743937	0.115681	0.161290	0.276316	1	0.306452	0.652778
0.291129	0.591902	0.548387	0.750000	0	0.516129	0.284722
0.572108	0.298843	0.258065	0.460526	0	0.338710	0.395833
0.310875	0.624679	0.483871	0.763158	0	0.645161	0.215278
0.865657	0.029563	0.032258	0.184211	0	0.209677	0.930556
0.258285	0.622751	0.548387	0.789474	0	0.645161	0.243056
0.791859	0.202442	0.096774	0.263158	0	0.258065	0.770833
0.746868	0.167738	0.064516	0.276316	0	0.403226	0.618056
0.149853	0.692802	0.709677	0.855263	1	0.532258	0.319444
0.818444	0.000000	0.000000	0.315789	1	0.241935	0.777778
0.550434	0.370823	0.129032	0.500000	0	0.516129	0.465278
0.597802	0.273136	0.193548	0.460526	0	0.000000	0.416667

Table 71 Eigenvalues and Explained Variation for Principal Components

Principal components	Eigen value	Explained variations (%)	Cumulative Eigen value	Cumulative (%)
First	5.520784	78.86834	5.520784	78.8683
Second	0.977063	13.95804	6.497847	92.8264
Third	0.274189	3.91698	6.772036	96.7434
Fourth	0.150522	2.15032	6.922558	98.8937
Fifth	0.049129	0.70185	6.971687	99.5955
Sixth	0.015563	0.22233	6.987250	99.8179
Seventh	0.012750	0.18214	7.000000	100.0000

Table 72 Eigenvectors for Principal Components and Contribution

Variable	Factor 1	Factor 2	Factor 3	Factor 4	Factor 5	Factor 6	Factor 7
MRR (mm^3/min)	0.415699	0.029965	0.310553	0.120791	-0.401154	0.726812	-0.161501
SR (µm)	-0.419695	0.095500	-0.008270	-0.229302	-0.164886	-0.003745	-0.857256
Chamfer (mm)	-0.411630	0.020350	-0.025145	-0.557169	-0.539364	0.141607	0.456192
Dross (mm^2)	-0.415884	0.021975	-0.291246	0.048264	0.533776	0.668072	0.090370
Right Bevel Angle (Degree)	-0.085649	-0.990710	-0.000673	0.040253	-0.061612	0.034426	-0.067495
Kerf (mm)	-0.375778	0.014236	0.887638	0.108014	0.214203	-0.040862	0.107082
HAZ (mm)	0.400134	-0.085881	0.173580	-0.778958	0.431716	0.050026	-0.082036

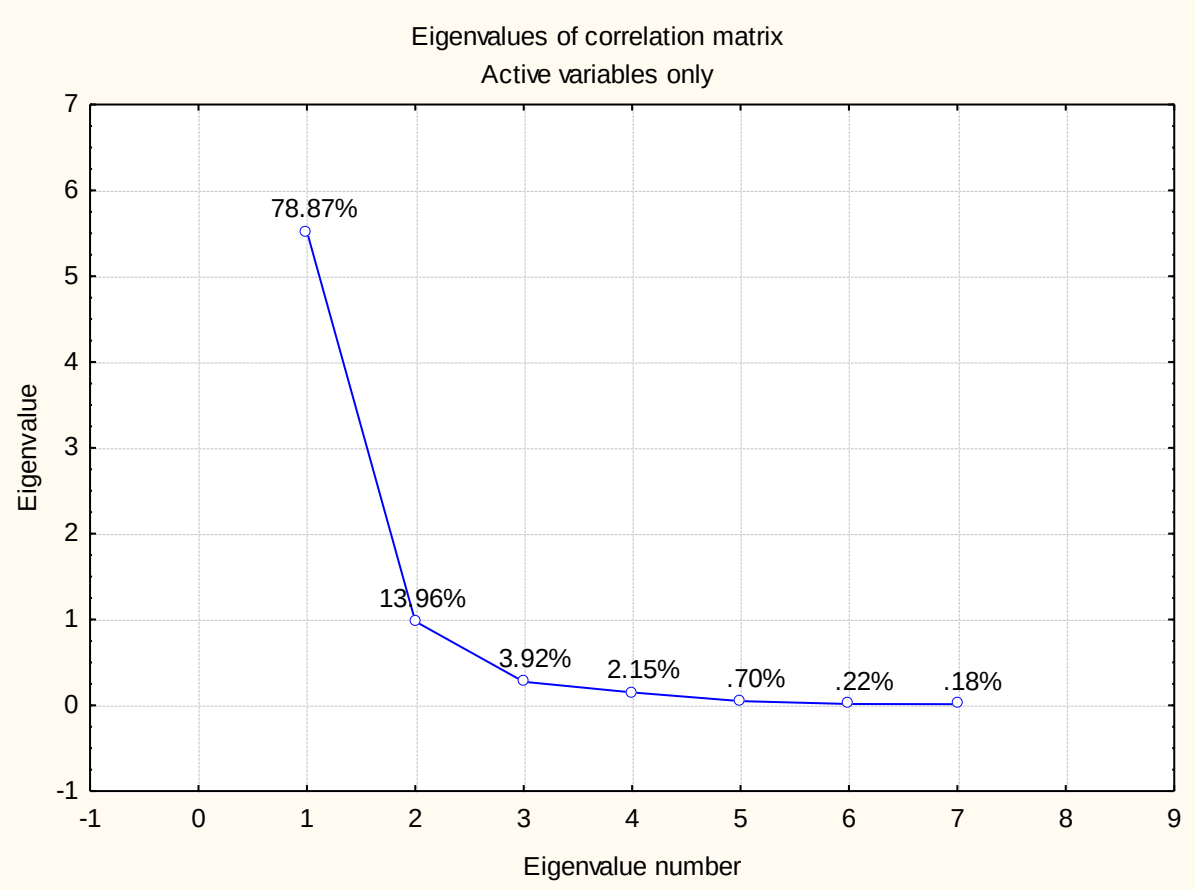

Fig. 231 Plot of Eigen values of correlation matrix for third phase

The Fig. 231 shows the variation in percentage of Eigen values in first phase experimentation.

Table 73 Grey Relational Coefficient and Grade of Output Responses of PAC

Grey relational coefficient 1	Grey relational coefficient 2	Grey relational coefficient 3	Grey relational coefficient 4	Grey relational coefficient 5	Grey relational coefficient 6	Grey relational coefficient 7	Overall grey relational grade
0.565285	0.464755	0.492063	0.422222	1.000000	0.382716	0.960000	0.612435
0.333333	0.899422	0.837838	1.000000	1.000000	0.596154	0.333333	0.714297
1.000000	0.333333	0.333333	0.333333	1.000000	0.333333	1.000000	0.619048
0.513503	0.496173	0.543860	0.463415	1.000000	0.442857	0.654545	0.587765
0.575220	0.466987	0.508197	0.413043	0.333333	0.436620	0.672897	0.486614
0.733616	0.392731	0.402597	0.376238	0.333333	0.356322	0.818182	0.487574
0.499639	0.533608	0.607843	0.475000	0.333333	0.402597	0.553846	0.486552
0.470032	0.557307	0.632653	0.506667	1.000000	0.476923	0.558140	0.600246
0.518396	0.511506	0.563636	0.457831	1.000000	0.500000	0.720000	0.610196
0.866439	0.364916	0.373494	0.348624	0.333333	0.378049	1.000000	0.523551
0.404174	0.663823	0.688889	0.690909	1.000000	0.645833	0.382979	0.639515
0.526921	0.498079	0.543860	0.447059	1.000000	0.462687	0.553846	0.576064
0.387368	0.818947	0.939394	0.760000	0.333333	0.645833	0.439024	0.617700
0.382142	0.874157	0.939394	0.666667	1.000000	0.620000	0.406780	0.698448
0.737056	0.513531	0.525424	0.426966	0.333333	0.492063	0.595041	0.517631
0.401950	0.812109	0.756098	0.644068	0.333333	0.620000	0.433735	0.571613
0.632008	0.457916	0.476923	0.400000	1.000000	0.492063	0.637168	0.585154
0.466371	0.625905	0.659574	0.520548	1.000000	0.596154	0.558140	0.632385
0.616618	0.444571	0.508197	0.395833	1.000000	0.436620	0.699029	0.585838
0.366124	0.944175	0.939394	0.730769	1.000000	0.704545	0.349515	0.719217
0.659383	0.445335	0.476923	0.387755	1.000000	0.436620	0.672897	0.582702
0.387039	0.711802	0.837838	0.655172	1.000000	0.659574	0.393443	0.663553
0.401005	0.748797	0.885714	0.644068	1.000000	0.553571	0.447205	0.668623
0.769405	0.419181	0.413333	0.368932	0.333333	0.484375	0.610169	0.485533
0.379235	1.000000	1.000000	0.612903	0.333333	0.673913	0.391304	0.627241
0.475994	0.574170	0.794872	0.500000	1.000000	0.492063	0.517986	0.622155
0.455455	0.646717	0.720930	0.520548	1.000000	1.000000	0.545455	0.698444

Table 74 Effect of Estimated Values of Responses of PAC

Factor	Effect	Std. Err.	T	P
Constant	0.577612	0.014171	40.75991	0.000000
A (Ampere)	0.073735	0.024545	3.00407	0.010983
A^2	-0.011745	0.018409	-0.63803	0.535438
B (mm/s)	-0.079229	0.024545	-3.22789	0.007248
B^2	0.004722	0.018409	0.25653	0.801889
C (L/min)	-0.000577	0.024545	-0.02349	0.981645
C^2	0.045322	0.018409	2.46199	0.029929
D (mm)	0.039758	0.024545	1.61981	0.131238
D^2	0.065794	0.018409	3.57406	0.003824
A×B	-0.066573	0.042513	-1.56593	0.143343
A×C	-0.026264	0.042513	-0.61779	0.548261
A×D	-0.037165	0.042513	-0.87419	0.399175
B×C	0.097179	0.042513	2.28586	0.041239
B×D	0.089002	0.042513	2.09351	0.058212
C×D	0.056367	0.042513	1.32586	0.209571

Table 75 ANOVA Table for GRG

Factors	SS	DoF	MS	F	P
A (Ampere)	0.016311	1	0.016311	9.02442	0.010983
A^2	0.000736	1	0.000736	0.40709	0.535438
B (mm/s)	0.018832	1	0.018832	10.41928	0.007248
B^2	0.000119	1	0.000119	0.06581	0.801889
C (L/min)	0.000001	1	0.000001	0.00055	0.981645
C^2	0.010955	1	0.010955	6.06140	0.029929
D (mm)	0.004742	1	0.004742	2.62378	0.131238
D^2	0.023087	1	0.023087	12.77390	0.003824
A×B	0.004432	1	0.004432	2.45213	0.143343
A×C	0.000690	1	0.000690	0.38166	0.548261
A×D	0.001381	1	0.001381	0.76420	0.399175
B×C	0.009444	1	0.009444	5.22515	0.041239
B×D	0.007921	1	0.007921	4.38278	0.058212
C×D	0.003177	1	0.003177	1.75790	0.209571
Error	0.021689	12	0.001807		
Total SS	0.126518	26			

Table 76 Regression Coefficients of GRG

Factor	Regression Coef.	Std. Err.	T	P
Constant	-0.831757	1.239707	-0.67093	0.514972
A (Ampere)	0.004497	0.003950	1.13831	0.277206
A^2	0.000005	0.000007	0.63803	0.535438
B (mm/s)	-0.376874	0.197508	-1.90815	0.080579
B^2	-0.004722	0.018409	-0.25653	0.801889
C (L/min)	0.068548	0.077077	0.88934	0.391298
C^2	-0.005036	0.002045	-2.46199	0.029929
D (mm)	0.918295	0.462464	1.98566	0.070403
D^2	-0.263176	0.073635	-3.57406	0.003824
A×B	-0.000666	0.000425	-1.56593	0.143343
A×C	-0.000088	0.000142	-0.61779	0.548261
A×D	-0.000743	0.000850	-0.87419	0.399175
B×C	0.016197	0.007086	2.28586	0.041239
B×D	0.089002	0.042513	2.09351	0.058212
C×D	0.018789	0.014171	1.32586	0.209571

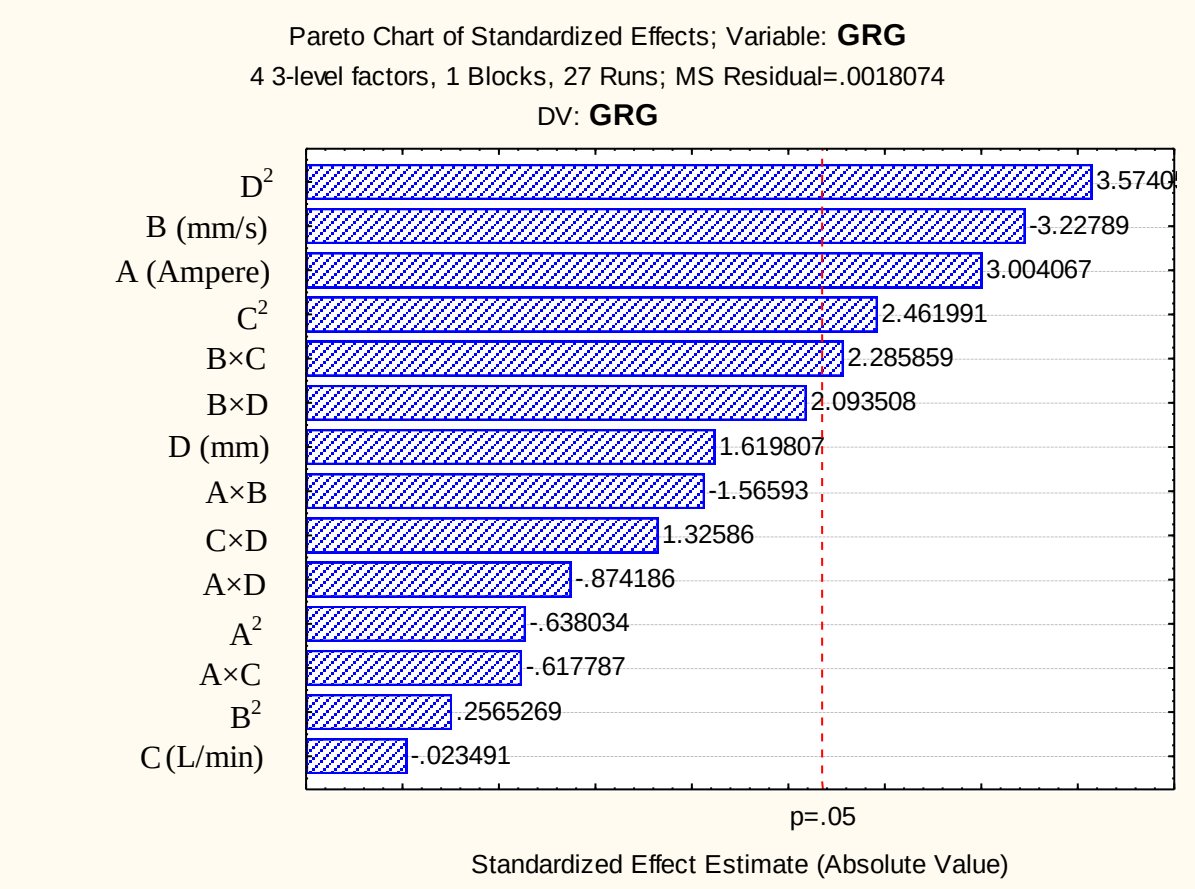

Fig. 232 Pareto chart of standardized effect of factors on GRG

The stand-off gap factor with quadratic form had the most significant influence on the GRG response of PAC operation as shown in Fig. 232.

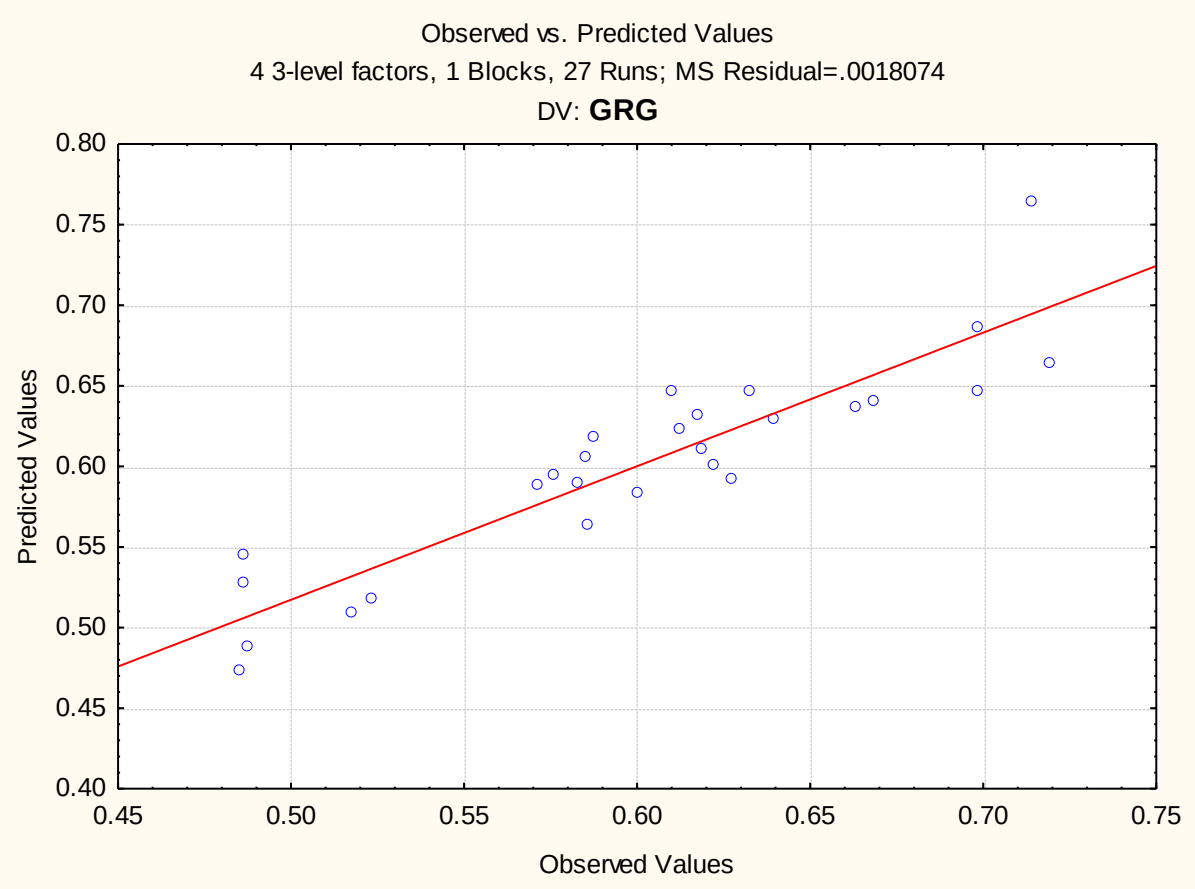

Fig. 233 Plot of observed vs. predicted values of GRG

The scatter plot between the observed and the predicted value of plasma cut responses of all 27 runs is shown in Fig. 233. The comparison between each of the observed values with the predicted value is shown in those plots which are calculated from the developed model. Here, the most of the points lie on the normal line of fitted values except the plot of GRG, because the uniformity lacks in the middle region. From this result it can be revealed that the response model shows good fit to experimental data, because the relationship between the actual and the predicted GRG is linear.

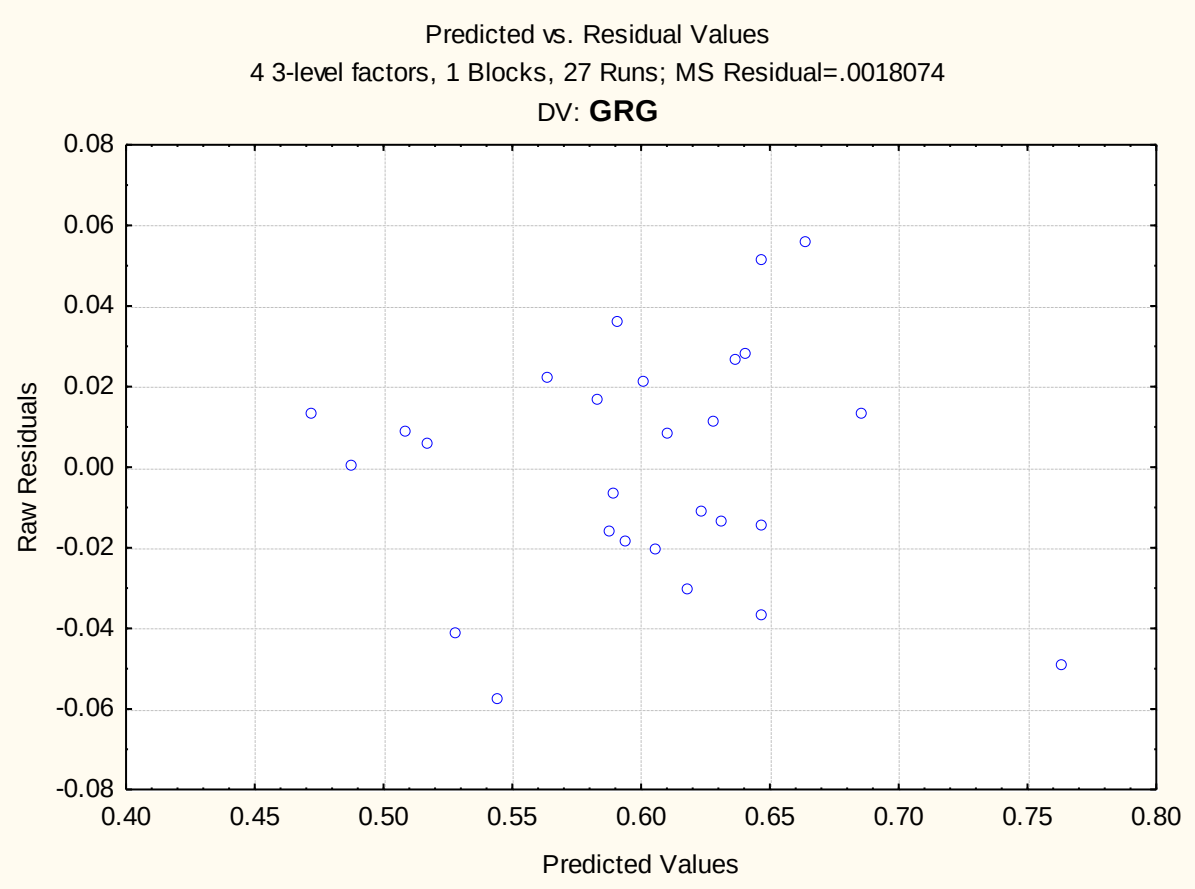

Fig. 234 Plot of predicted vs. residual values of GRG

From the Fig. 234, no standard pattern is formed in the plot of predicted vs. residual values which show the adequacy of the fitted model for GRG.

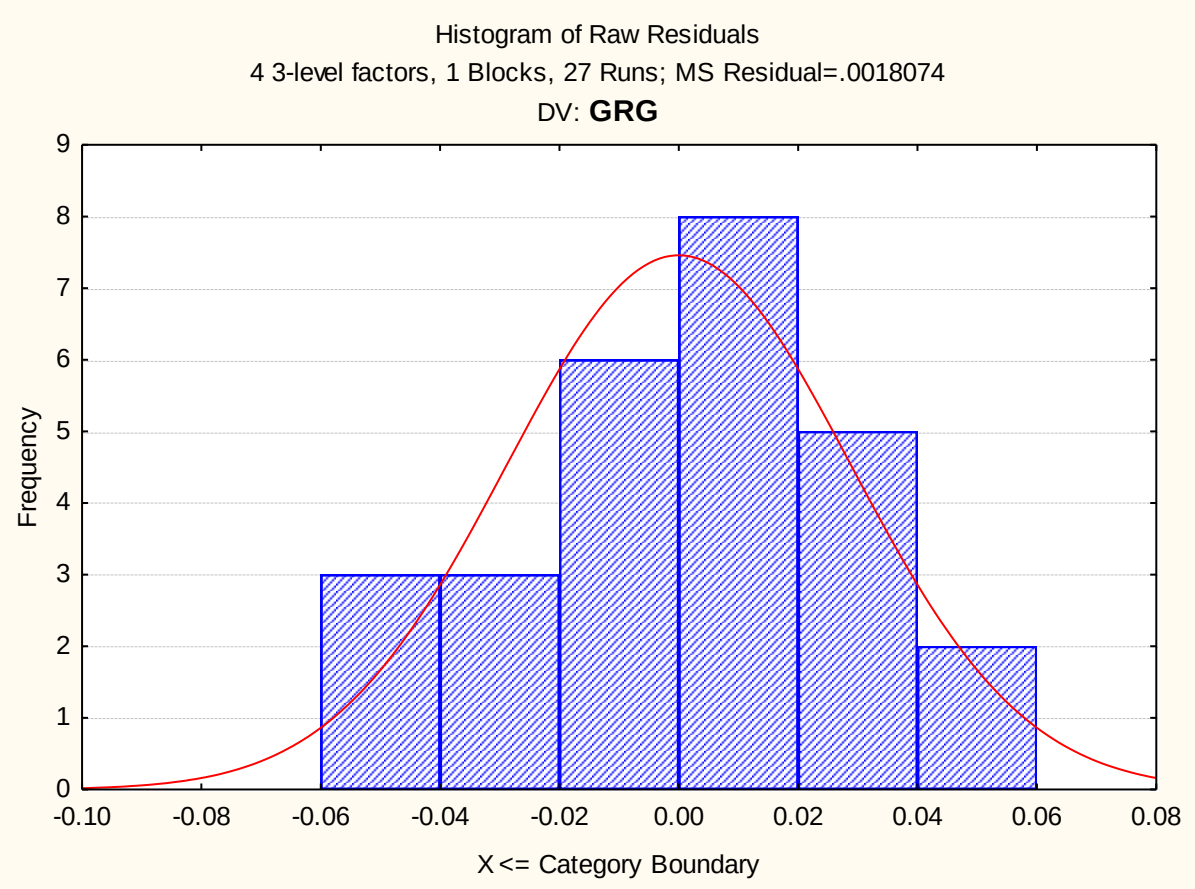

Fig. 235 Histogram plot of predicted values of GRG

The perfect normal probability distribution of the histogram plot of residuals for GRG response is shown in Fig. 235. From the above graphs, it is seen that the normal probability created in the histogram plot of residual for GRG is tolerable.

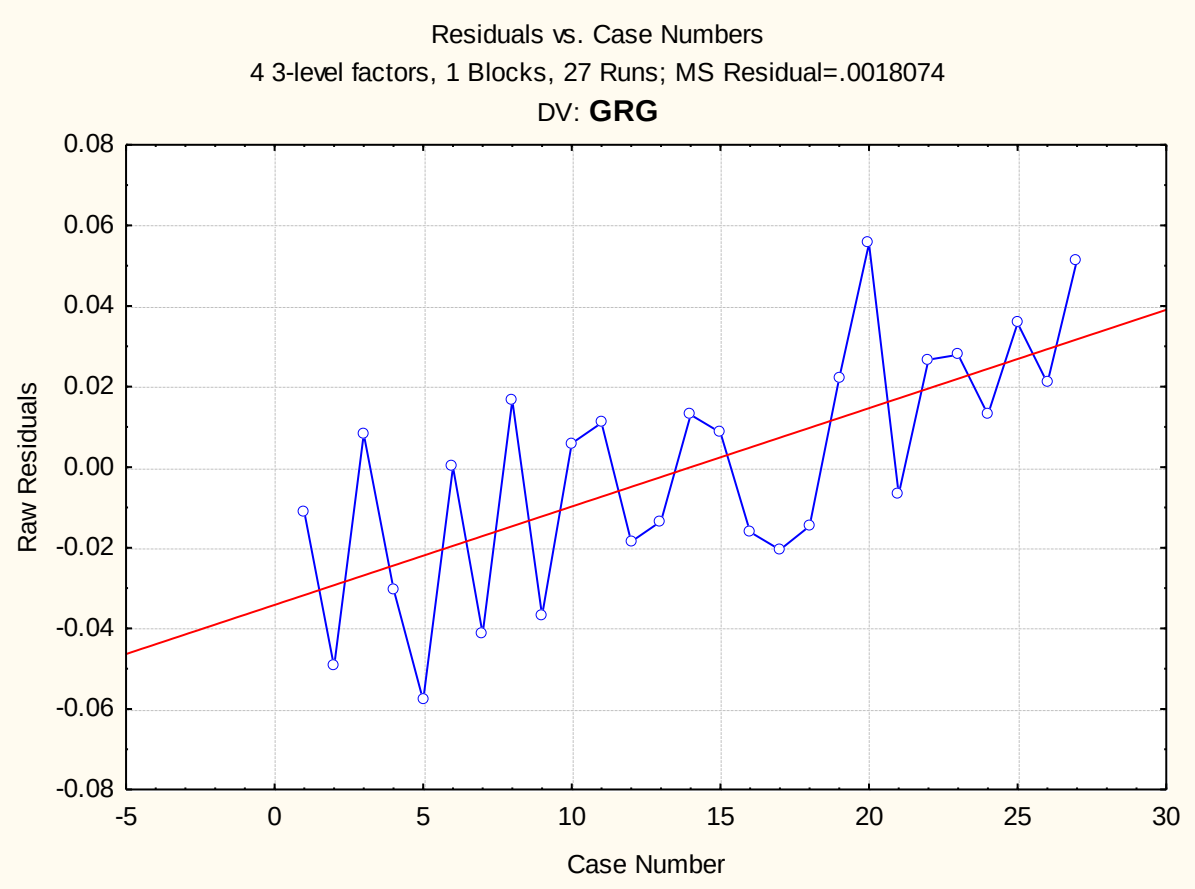

Fig. 236 Plot of residuals vs. case numbers values of GRG

From the Fig. 236, it is evident that the highest GRG value among all experimental runs is by the run number 20. The red line indicates that the value of GRG increases with increase in run order.

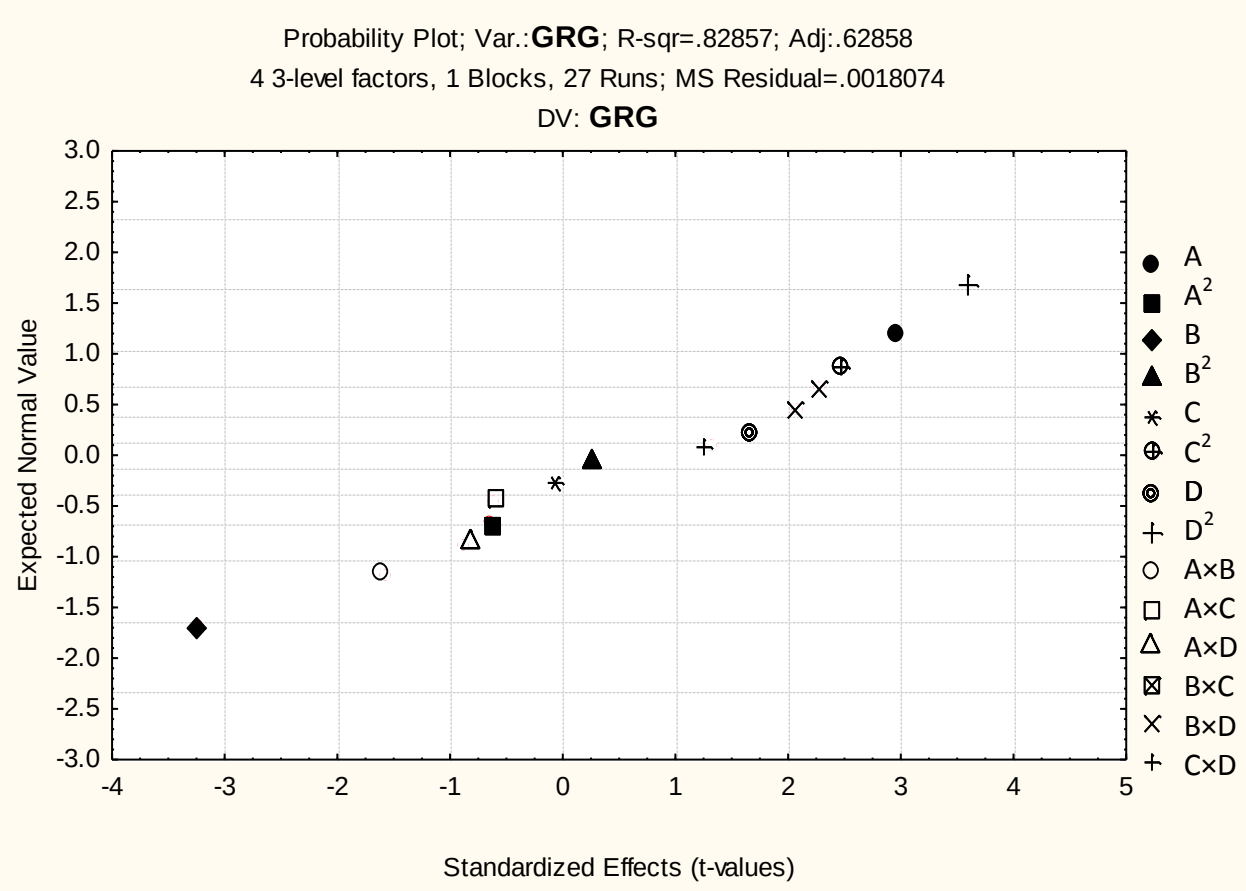

Fig. 237 Probability plot of GRG

The normal probability plot of GRG corresponding to each regression terms is plotted in Fig. 237.

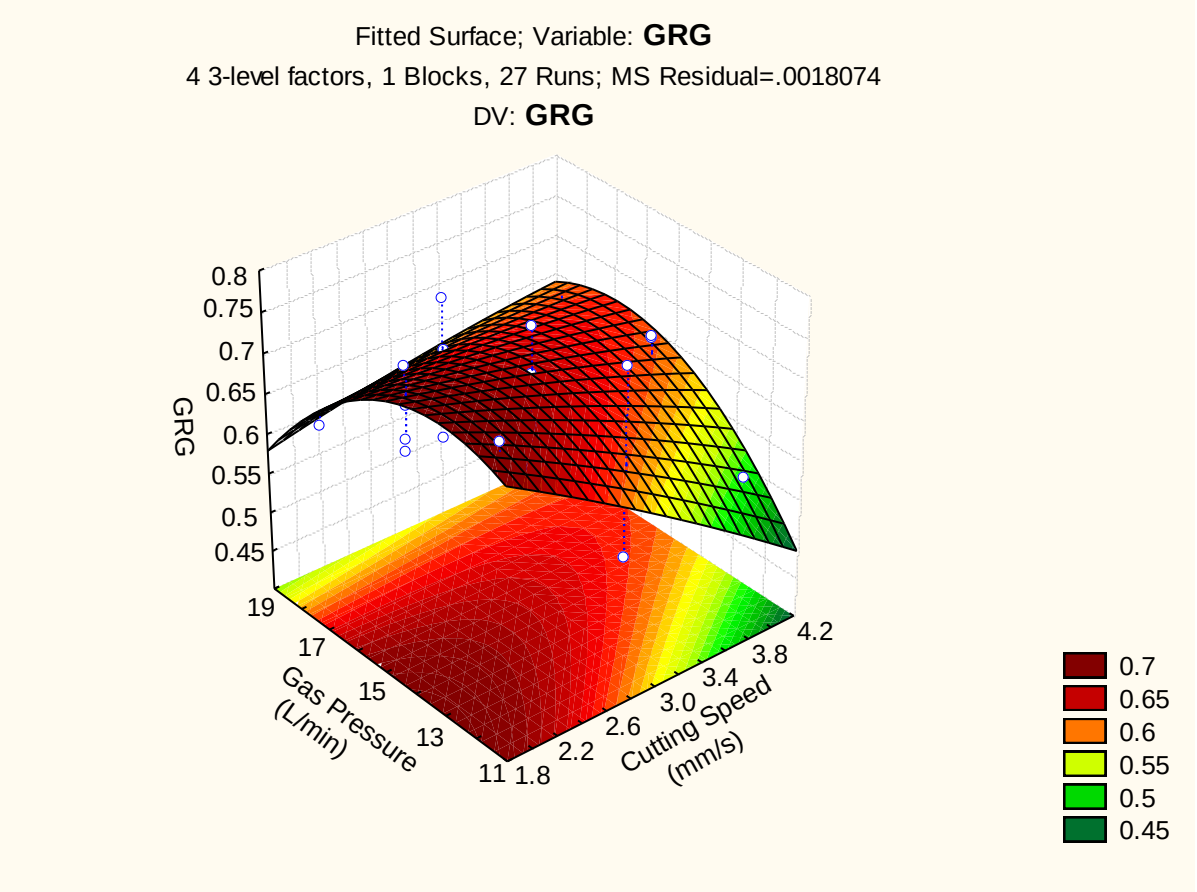

Fig. 238 3D fitted surface plot of GRG

The 3D surface plot of the significant interaction terms is shown in Fig. 238. It is to be noted that all other terms are taken into account at their average values. The figure evidenced that the interaction of gas pressure and cutting speed is also influenced by the above mentioned output.

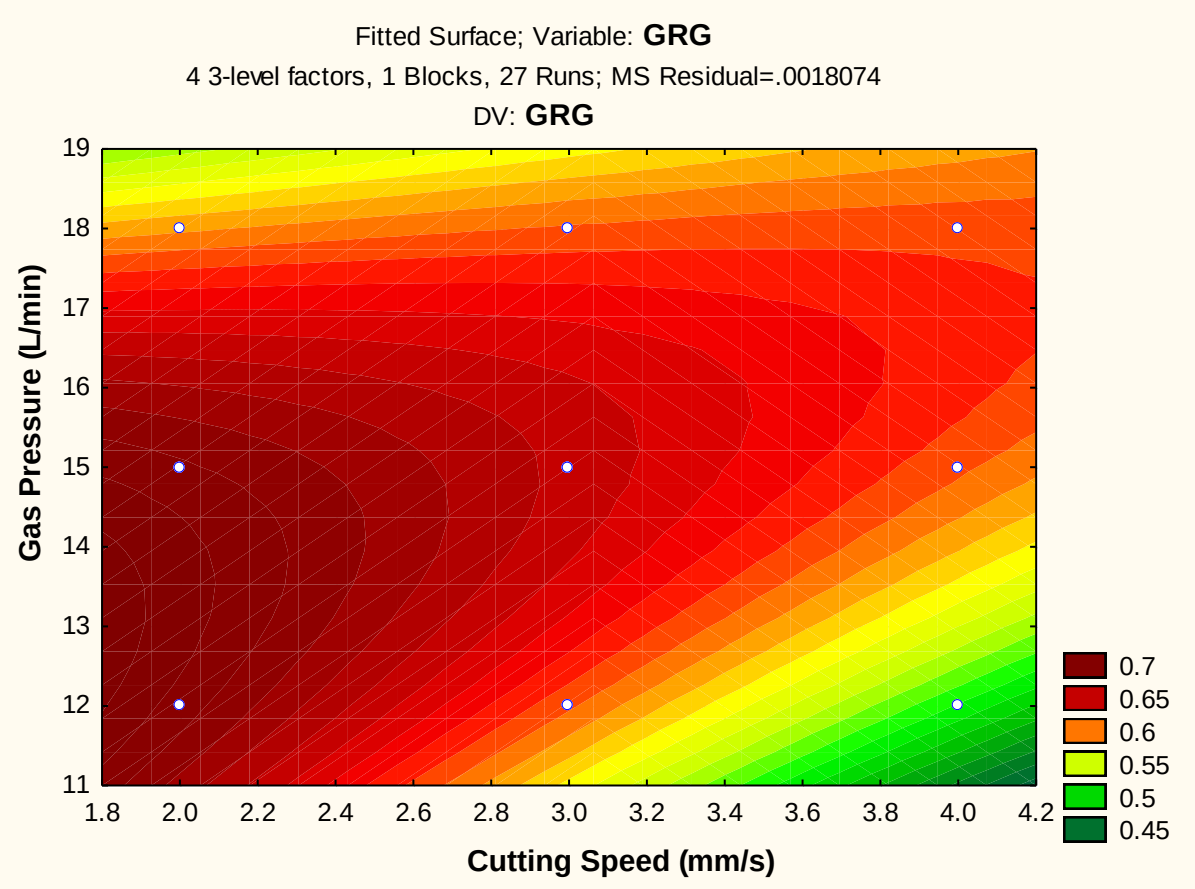

Fig. 239 2D fitted counter plot of GRG

The counter plots of interaction terms at their average level vs. GRG are found in Fig. 239. Mainly the shapes of counter plots might be elliptical or saddle form which indicates that the combination of each variable are significant except gas pressure vs. cutting speed plot. The lowest value of GRG obtained in the maximum region of current this can be seen in Fig. 239.

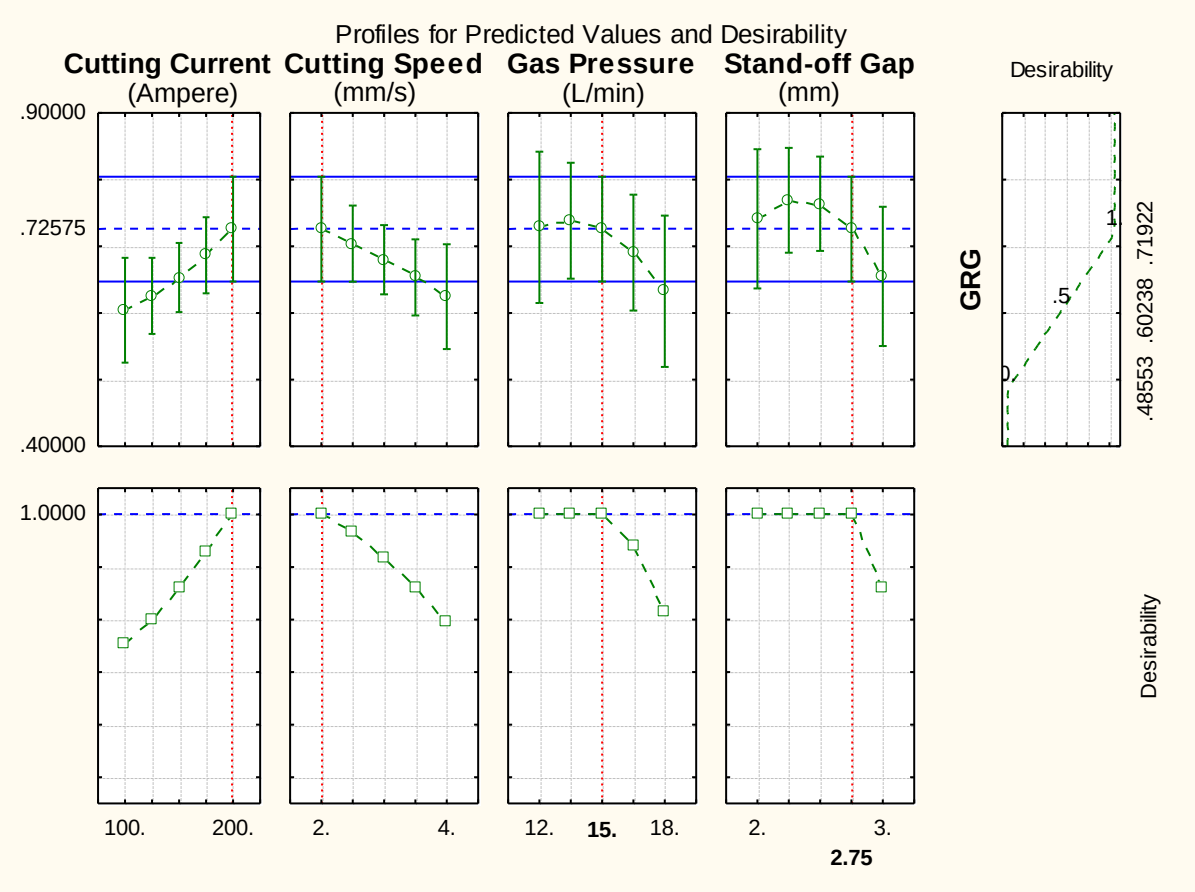

Fig. 240 Profile plot of predicted values and desirability of GRG

In case of GRG response, the desirability function method also adopted to specify the optimum value from its quadratic fit empirical model. The level of variable giving the highest desirability i.e., 1.0000 was considered as optimum level. The optimized levels of variables (A, B, C and D) were determined using the desirability profiles that are shown in Fig. 240. And, this figure displayed the predicted values of responses and desirability function with red dotted lines at the same time.

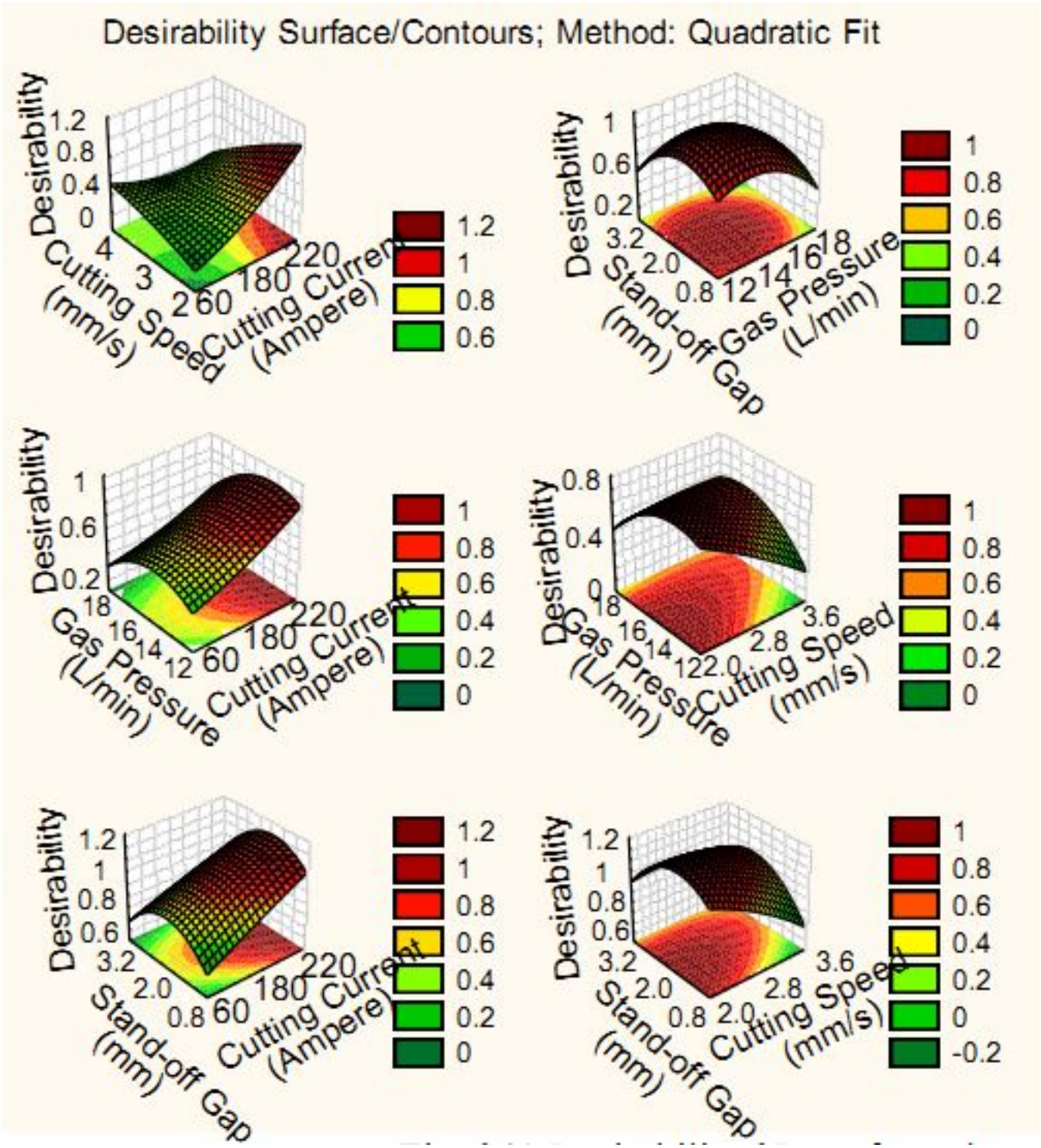

Fig. 241 Desirability 3D surface plot of GRG

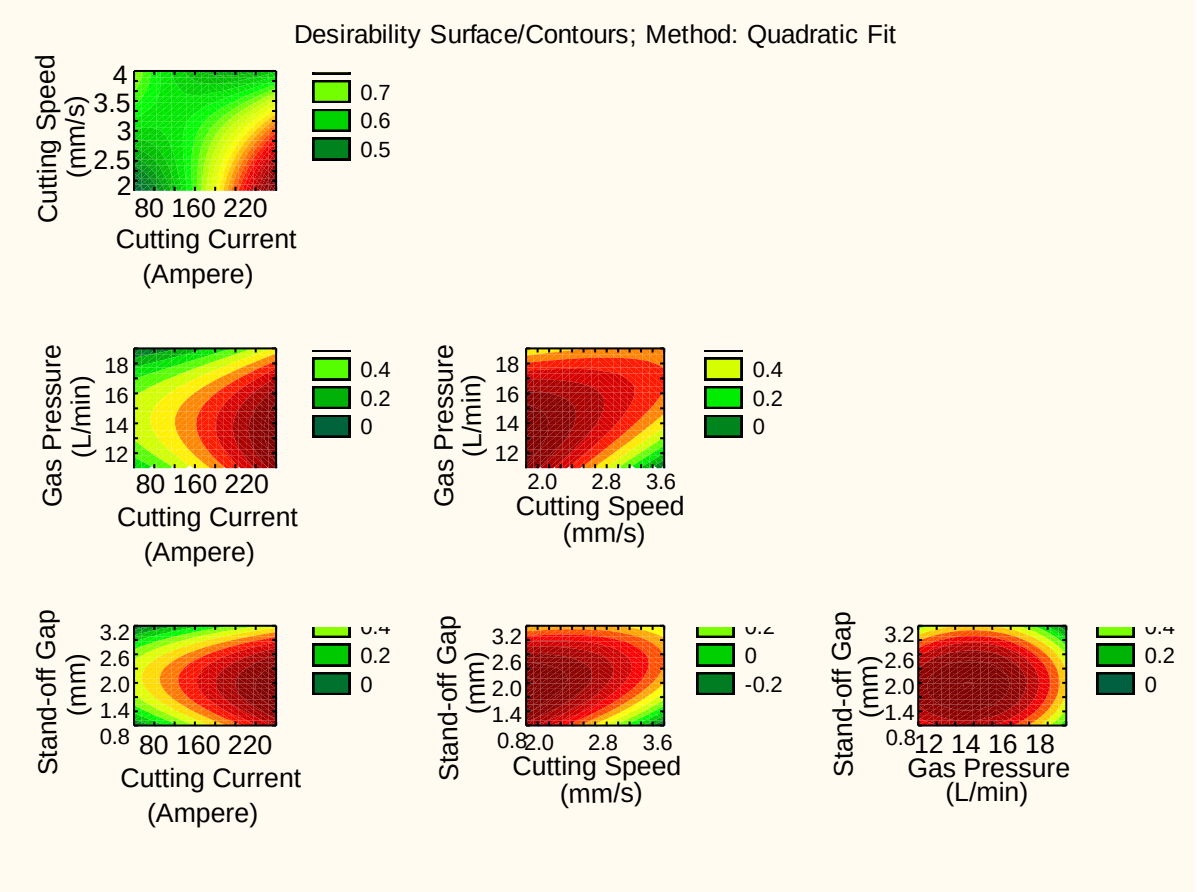

Fig. 242 Desirability 2D counter plot of GRG

The 3D and 2D plot of interaction variables on GRG output were determined using the desirability profiles that are shown in Fig. 241-242 respectively. The interaction of cutting speed and current gave minimum value of GRG whereas interaction of gas pressure and stand-off gap gave maximum value of GRG in the third case experimentation of plasma arc cutting process.

5.3.3 Genetic algorithm

5.3.3.1 For material removal rate:

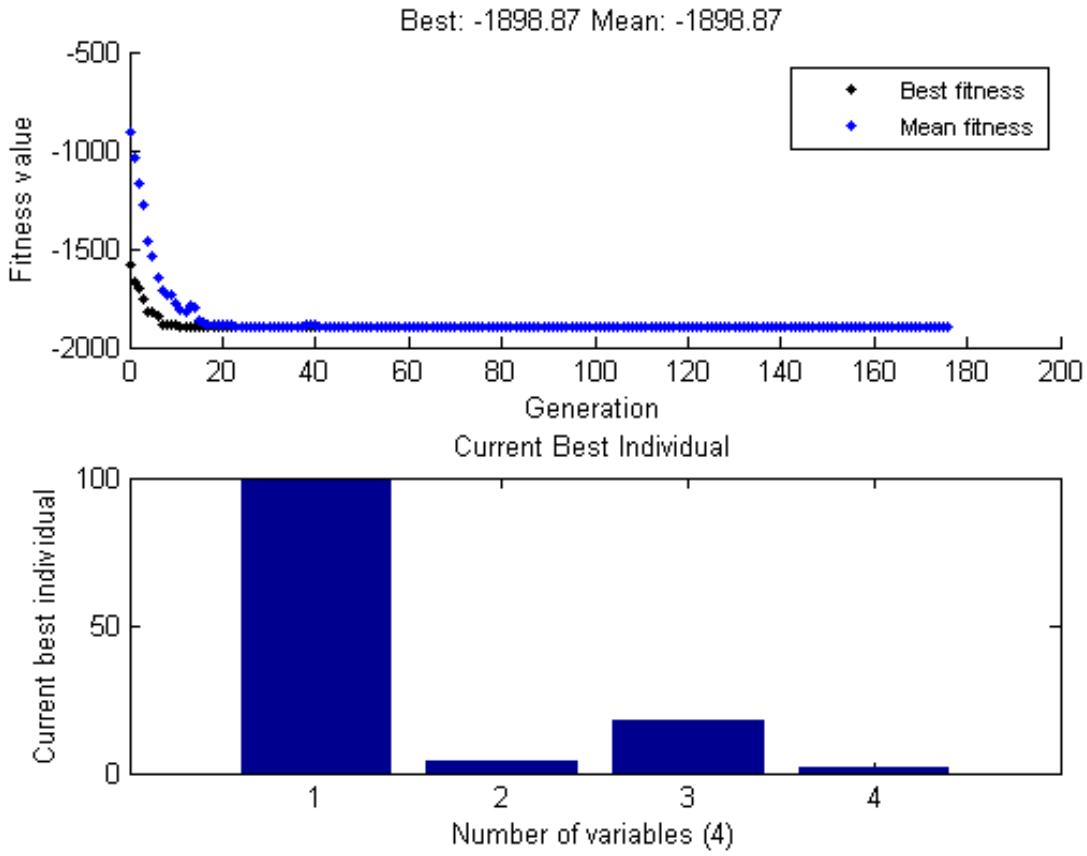

Fig. 243 Results from GA approach for MRR

Best fitness and individual value plot of MRR is shown in Fig. 243, where the best and average value of MRR is obtained as 1898.87099 mm^3/min. Here, negative sign is due the application of negativity theory for maximizing problem. Secondly, the best parametric optimal setting is obtained at 100 ampere of cutting current, 4 mm/s of cutting speed, 18 L/min of gas pressure and 2 mm of stand-off gap.

5.3.3.2 For surface roughness:

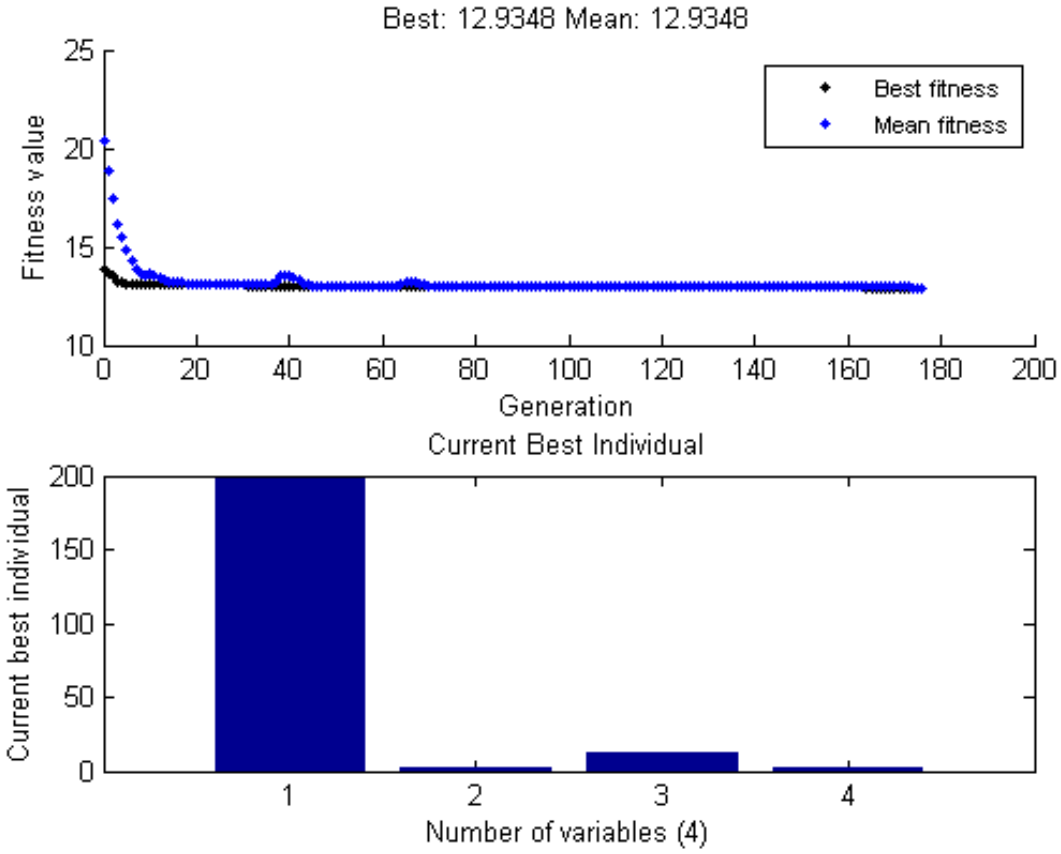

Fig. 244 Results from GA approach for SR

Similarly, for the case of SR the problem is the minimization and the best fitness and individual value plot as given in Fig. 244, where the best and average value of SR is found as 12.93477 µm. The best parametric optimal setting is obtained at 200 ampere of cutting current, 2 mm/s of cutting speed, 12 L/min of gas pressure and 2.356 mm of stand-off gap.

5.3.3.3 For chamfer:

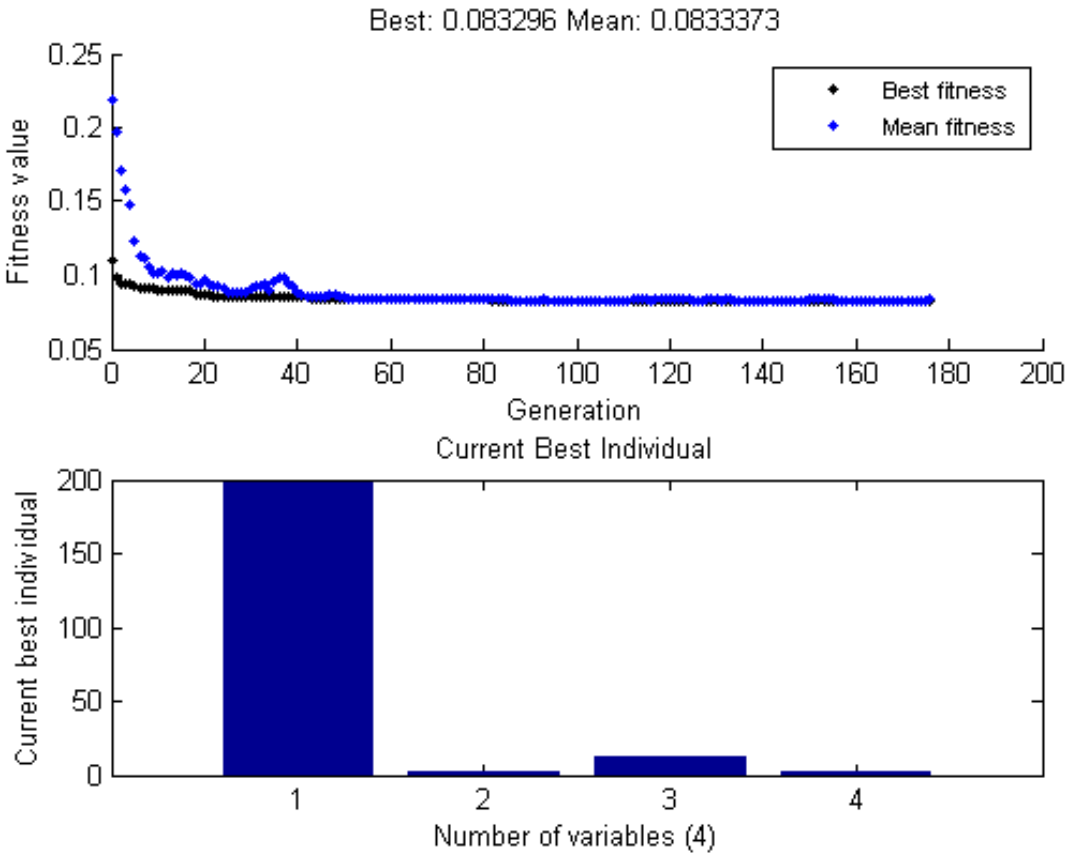

Fig. 245 Results from GA approach for chamfer

Similarly, for the case of chamfer the problem is the minimization, and the best fitness and individual value plot as given in Fig. 245 where the best and average values of chamfer are found as 0.083296 mm. The best parametric optimal setting is obtained at 200 ampere of cutting current, 2 mm/s of cutting speed, 12 L/min of gas pressure and 2 mm of stand-off gap.

5.3.3.4 For dross:

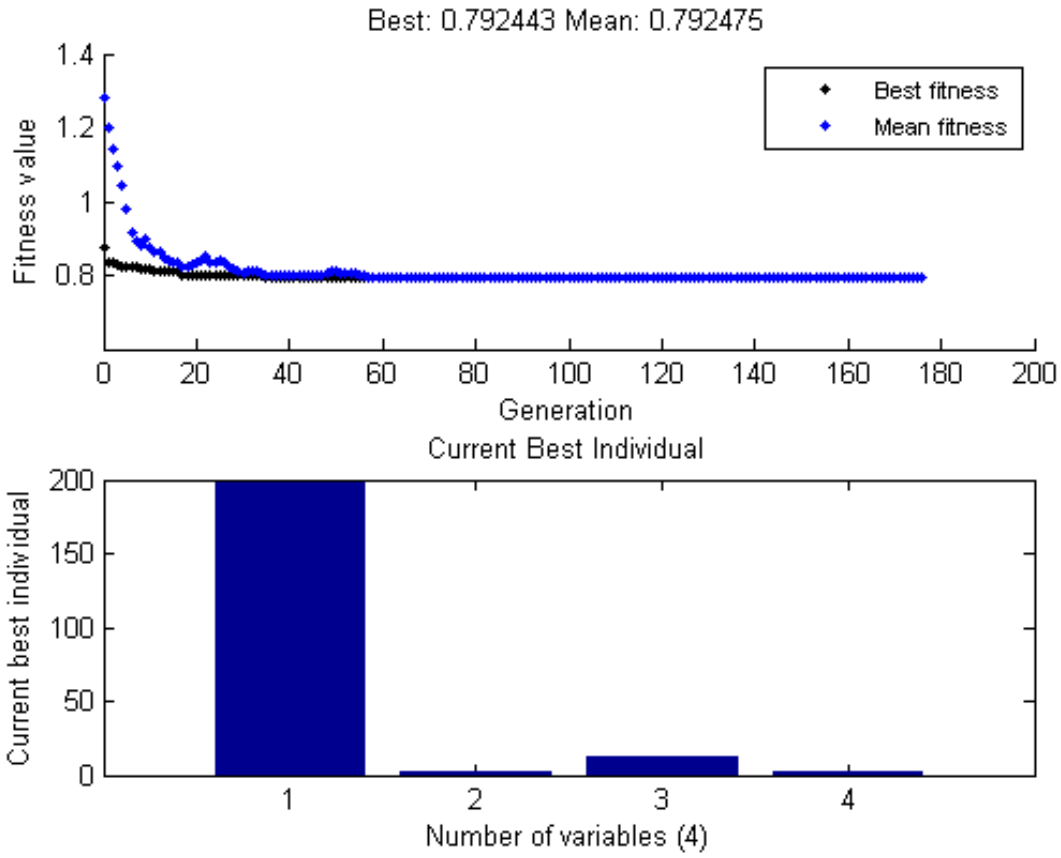

Fig. 246 Results from GA approach for dross

Similarly, for the case of dross the problem is the minimization and the best fitness and individual value plot as given in Fig. 246, where the best and average value of dross is found to be 0.79244 mm^2. The best parametric optimal setting is obtained at 200 ampere of cutting current, 2 mm/s of cutting speed, 12.128 L/min of gas pressure and 2 mm of stand-off gap.

5.3.3.5 For right bevel angle:

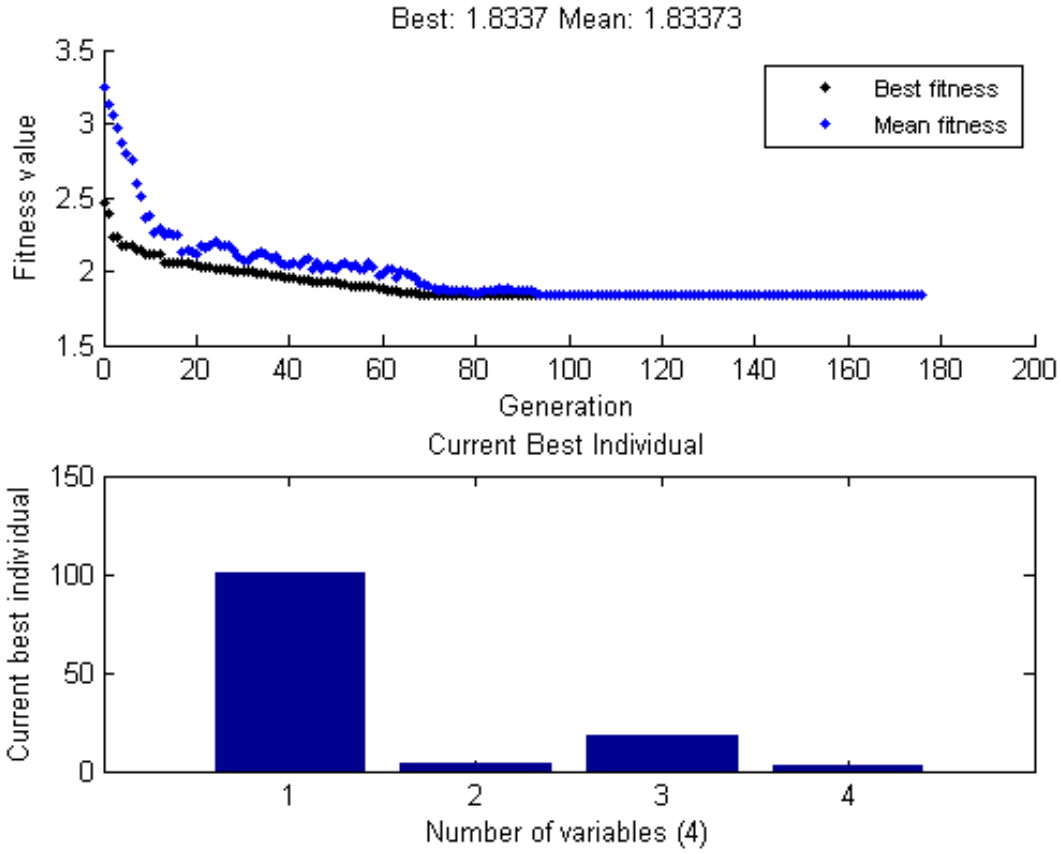

Fig. 247 Results from GA approach for right bevel angle

Similarly, for the case of right bevel angle the problem is the minimization and the best fitness and individual value plot as given in Fig. 247, where the best and average values of right bevel angle is found to be 1.8337º. The parametric optimal setting is obtained at 100 ampere of cutting current, 4 mm/s of cutting speed, 18 L/min of gas pressure and 3 mm of stand-off gap. Here, the simulation of genetic algorithm toolbox for all output responses stopped at same iteration number i.e., 176.

5.3.3.6 For kerf:

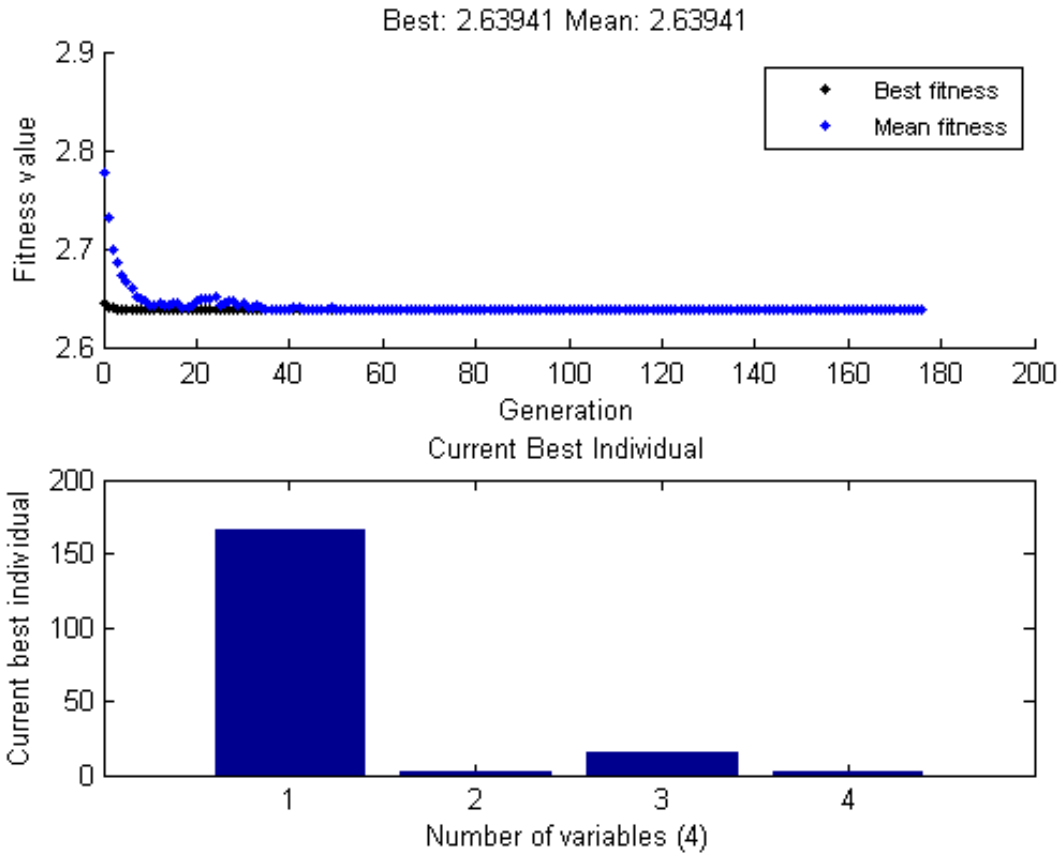

Fig. 248 Results from GA approach for kerf

Similarly, for the case of kerf the objective is minimization and the best fitness and individual value plot as given in Fig. 248, where the best and average value of kerf is found as 2.6394 mm. The parametric optimal setting is obtained at 165.73 ampere of cutting current, 2.354 mm/s of cutting speed, 15.174 L/min of gas pressure and 2.618 mm of stand-off gap. Here, the simulation of genetic algorithm toolbox for all responses stopped at same iteration number i.e., 176.

5.3.3.7 For heat affected zone:

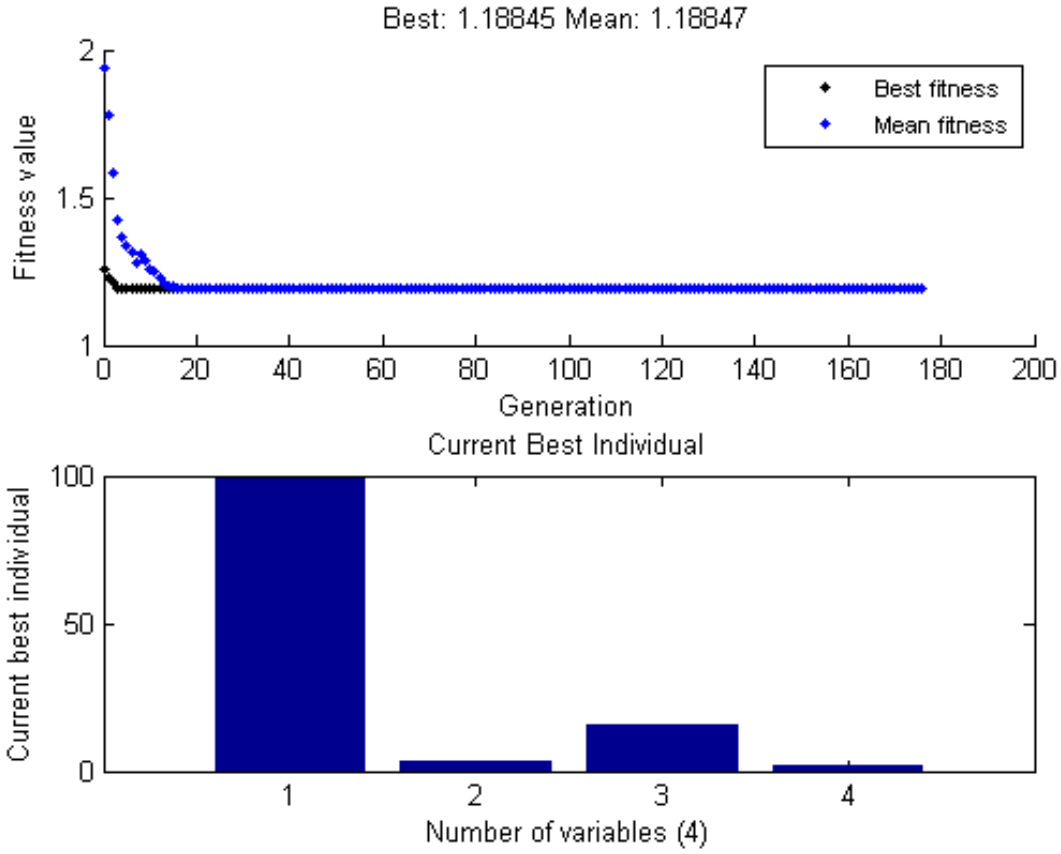

Fig. 249 Results from GA approach for HAZ

Similarly, for the case of HAZ the objective is minimization and the best fitness and individual value plot as given in Fig. 249, where the best and average value of HAZ is found to be 1.18845 mm. The parametric optimal setting is obtained at 100 ampere of cutting current, 2.958 mm/s of cutting speed, 15.504 L/min of gas pressure and 2 mm of stand-off gap. Here, the simulation of genetic algorithm toolbox for all responses stopped at same iteration number i.e., 176.

5.3.4 Particle swarm optimization

5.3.4.1 For material removal rate:

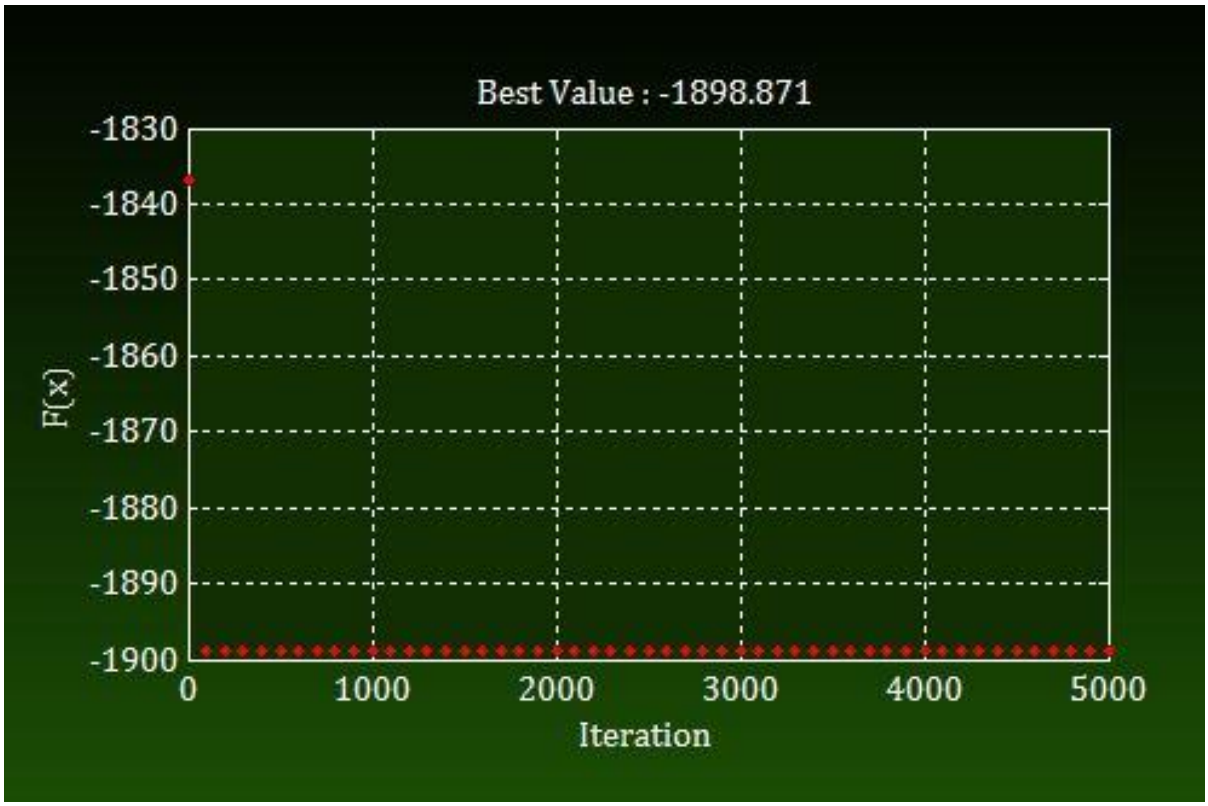

Fig. 250 Results from PSO approach for MRR

The plot of best function value and optimum setting for MRR which was obtained from PSO methodology is shown in Fig. 250. From the graph, it can be seen that the optimum condition for MRR can be found as 100 ampere of cutting current, 4 mm/s of cutting speed, 18 L/min of gas pressure and 2 mm of stand-off gap. The objective function value of MRR utilizing PSO algorithm is calculated as 1898.871 mm^3/min.

5.3.4.2 Mean surface roughness:

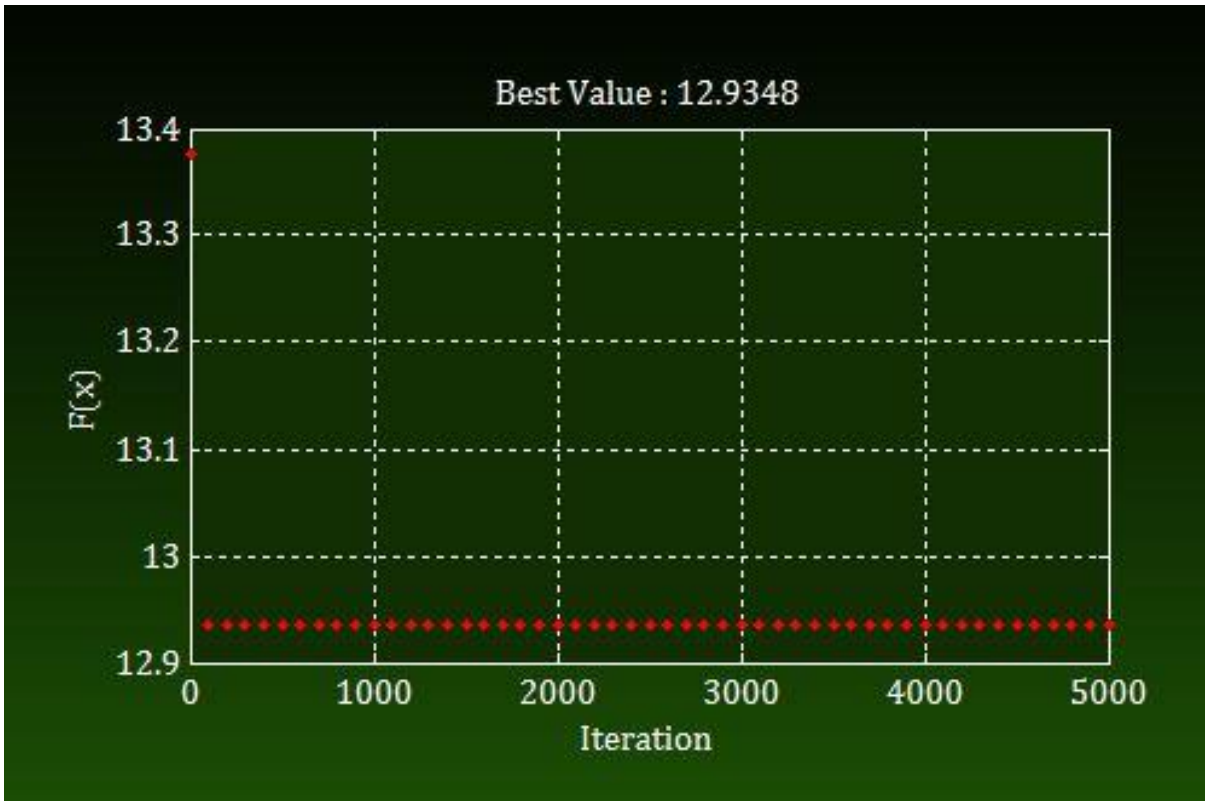

Fig. 251 Results from PSO approach for SR

The plot of best function value and optimum setting for SR which was obtained from PSO methodology is shown in Fig. 251. From the graph, it can be seen that the optimum condition for SR can be found as 200 ampere of cutting current, 2 mm/s of cutting speed, 12 L/min of gas pressure and 2.356 mm of stand-off gap. The best value of objective function for SR using PSO algorithm is obtained as 12.93476 µm.

5.3.4.3 For chamfer:

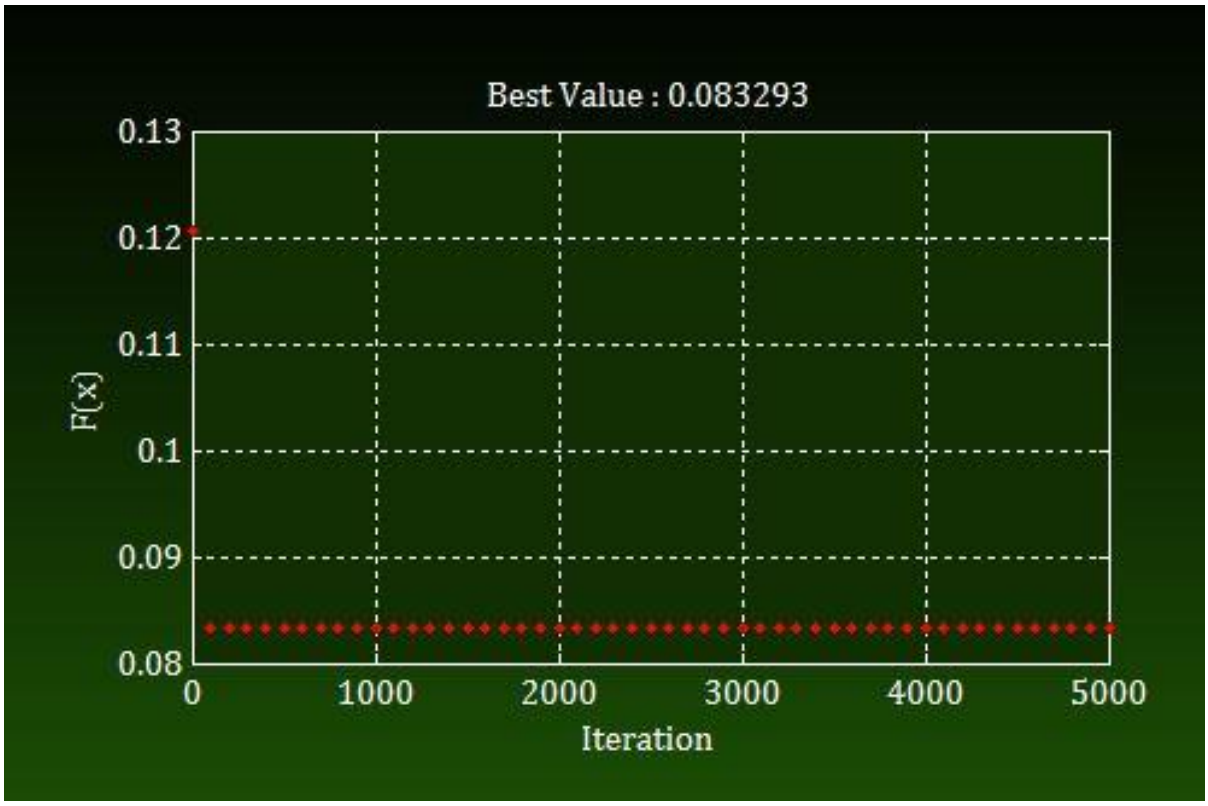

Fig. 252 Results from PSO approach for chamfer

The plot of best function value and optimum setting for chamfer which was obtained from PSO methodology is shown in Fig. 252. From the graph, it can be seen that the optimum condition for chamfer can be found as 200 ampere of cutting current, 2 mm/s of cutting speed, 12 L/min of gas pressure and 2 mm of stand-off gap. The best function value of chamfer using PSO approach is obtained as 0.08329 mm.

5.3.4.4 For dross:

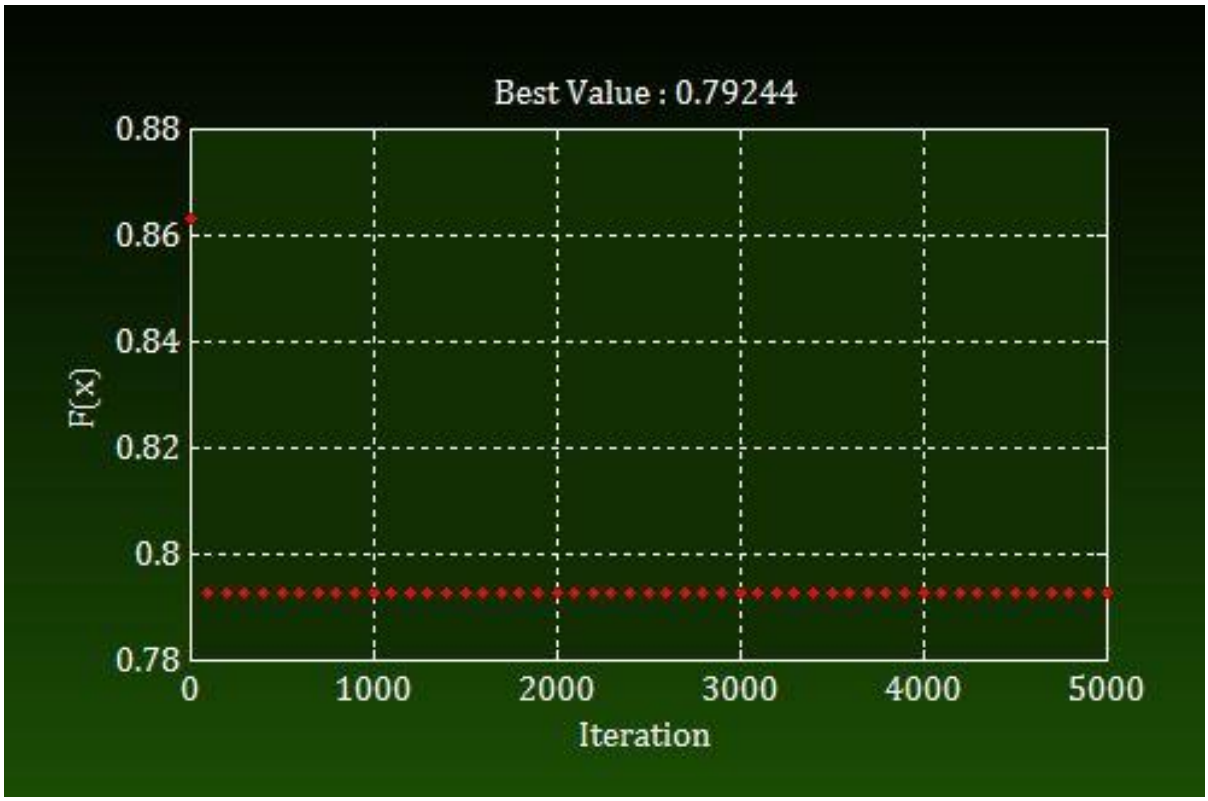

Fig. 253 Results from PSO approach for dross

The plot of best function value and optimum setting for dross which was obtained from PSO methodology is shown in Fig. 253. From the graph, it can be seen that the optimum condition for dross can be found as 200 ampere of cutting current, 2 mm/s of cutting speed, 12.128 L/min of gas pressure and 2 mm of stand-off gap. The optimum value of dross with the help of PSO technique is obtained as 0.79244 mm^2.

5.3.4.5 For right bevel angle:

Fig. 254 Results from PSO approach for right bevel angle

The plot of best function value and optimum setting for right bevel angle which was obtained from PSO methodology is shown in Fig. 254. From the graph, it can be seen that the optimum condition for right bevel angle can be found as 100 ampere of cutting current, 4 mm/s of cutting speed, 18 L/min of gas pressure and 3 mm of stand-off gap. The optimal value of chamfer with the help of PSO technique is obtained as 1.8337°.

5.3.4.6 For kerf:

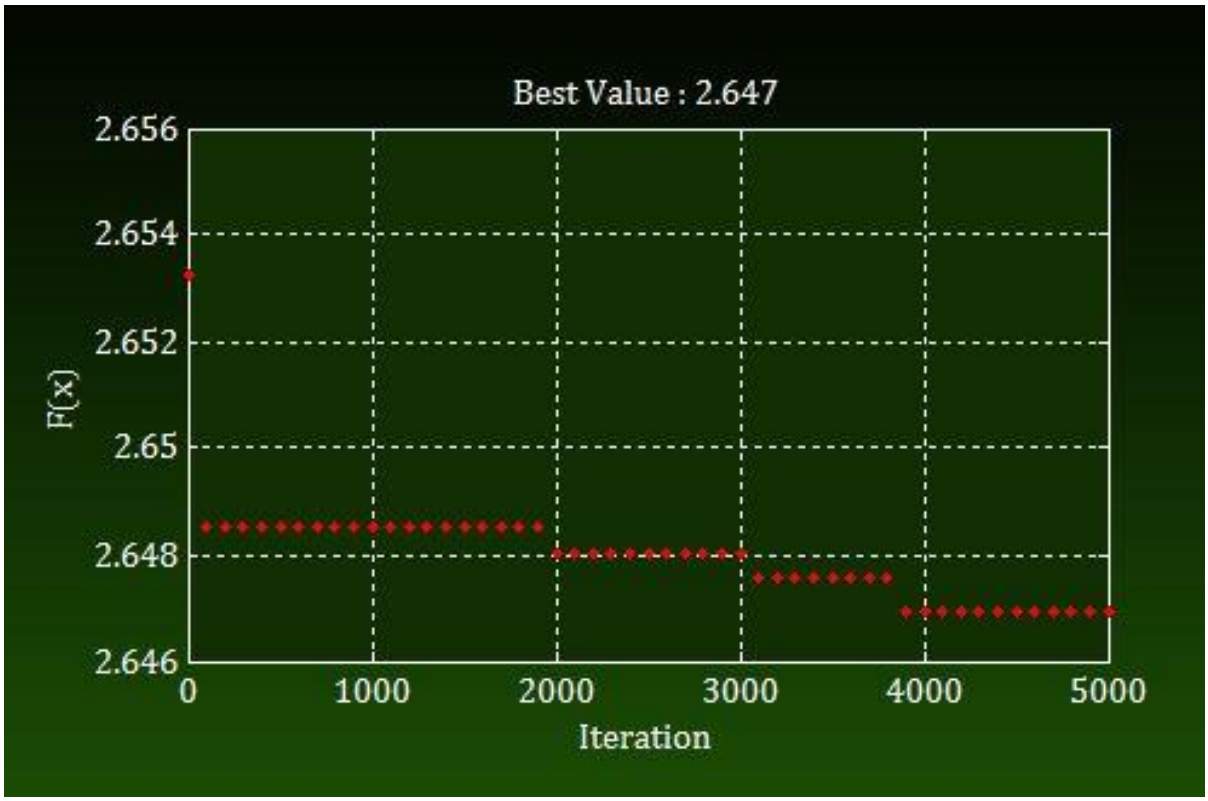

Fig. 255 Results from PSO approach for kerf

The plot of best function value and optimum setting for kerf which was obtained from PSO methodology is shown in Fig. 255. From the graph, it can be seen that the optimum condition for kerf can be found as 167.449 ampere of cutting current, 2 mm/s of cutting speed, 15.153 L/min of gas pressure and 2.659 mm of stand-off gap. The optimal value of kerf using PSO approach is determined as 2.64695 mm.

5.3.4.7 For heat affected zone:

Fig. 256 Results from PSO approach for HAZ

The plot of best function value and optimum setting for HAZ which was obtained from PSO methodology is shown in Fig. 256. From the graph, it can be seen that the optimum condition for HAZ can be found as 100 ampere of cutting current, 2.956 mm/s of cutting speed, 15.506 L/min of gas pressure and 2 mm of stand-off gap. The optimal value of HAZ utilizing PSO technique is found as 2.64695 mm.

5.3.5 Simulated annealing

5.3.5.1 For material removal rate:

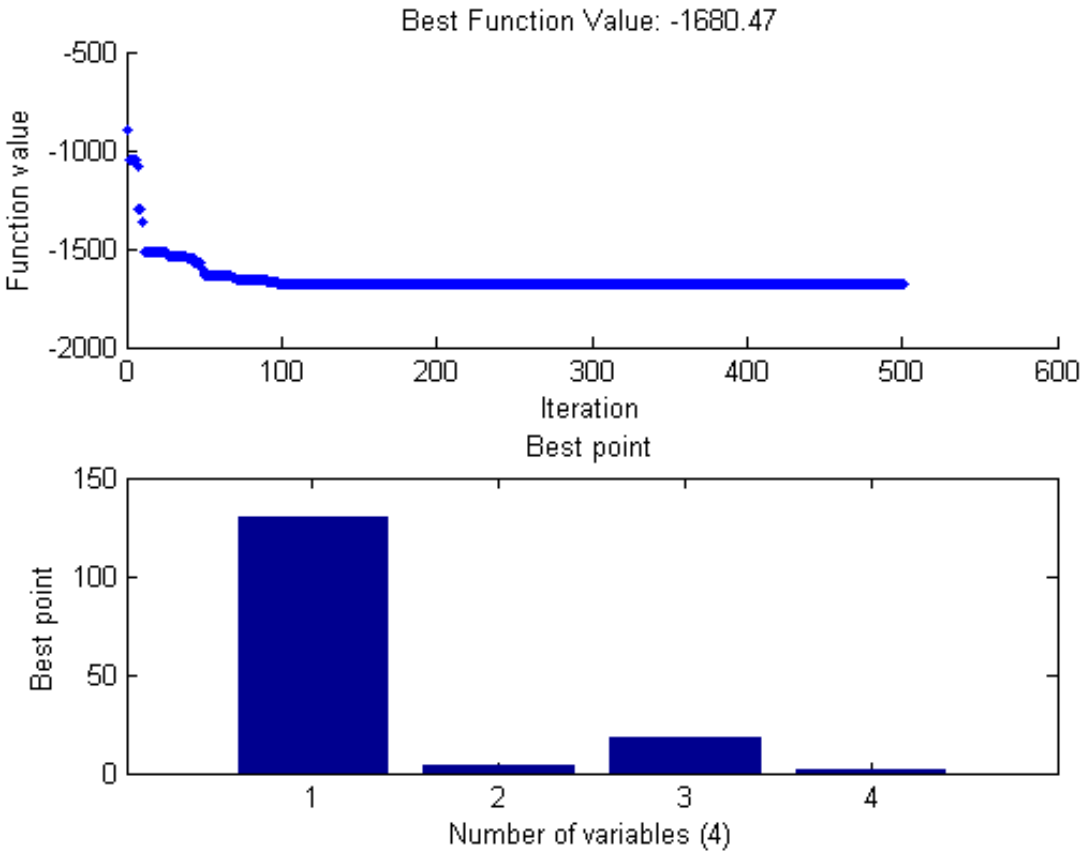

Fig. 257 Results from SA approach for MRR

Nature based novel optimization technique i.e., simulated annealing algorithm is employed to obtain regression equation of MRR from RSM method. By applying Boltzmann annealing approach to the experimental data, the lowest value of MRR is found to be 1680.471 mm^3/min at 130.013 ampere of cutting current, 4 mm/s of cutting speed, 18 L/min of gas pressure and 2 mm of stand-off gap. Fig. 257 shows the best function value and comparative effect of input parameters. Here, the cutting current is the most effective variable. The highest number of iteration for simulating the algorithm is 501, where the minimum value of MRR is found. The best parametric setting of the whole

experimentation as per simulated annealing is shown in Fig. 257 with current iteration number.

5.3.5.2 For surface roughness:

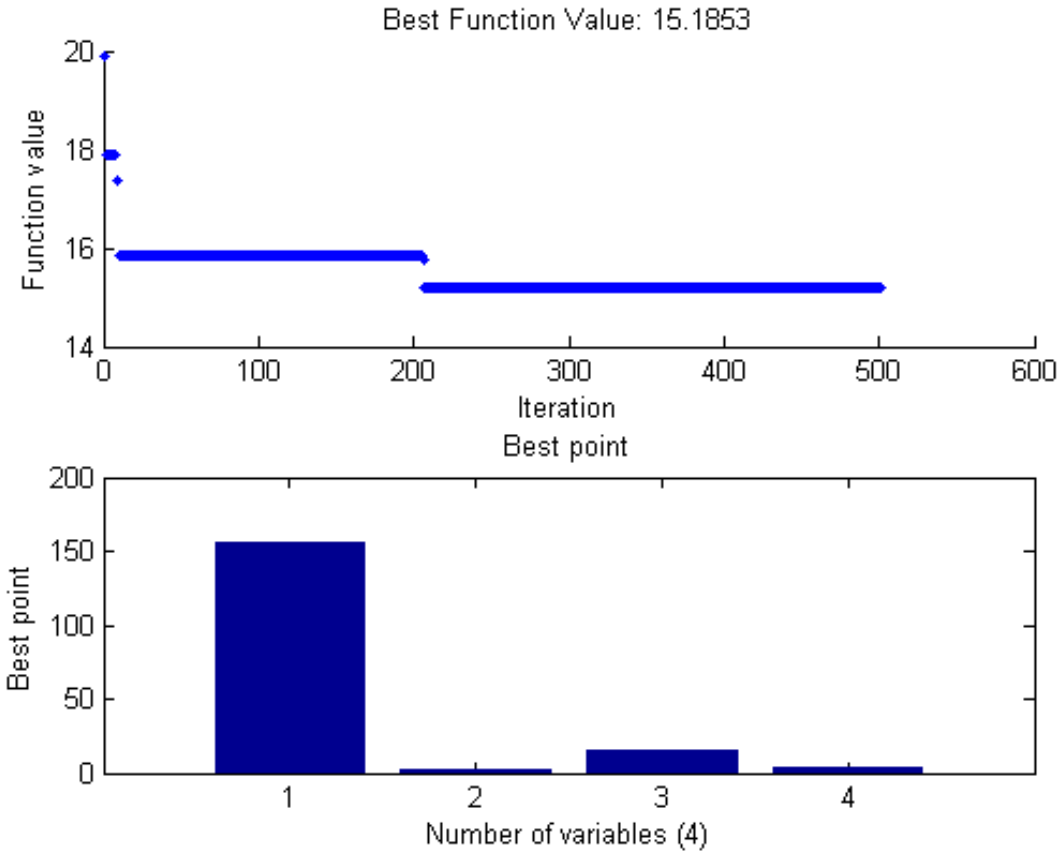

Fig. 258 Results from SA approach for SR

Nature based novel optimization technique i.e., simulated annealing algorithm is employed to obtain regression equation of SR from RSM method. By applying Boltzmann annealing approach to the experimental data, the lowest value of SR is found to be 15.185 µm at 156.375 ampere of cutting current, 2 mm/s of cutting speed, 15.738 L/min of gas pressure and 2.987 mm of stand-off gap. Fig. 258 shows the best function value and comparative effect of input parameters. Here, the cutting current is the most effective variable. The highest number of iteration for simulating the algorithm is 501, where the

minimum value of SR obtained. The best parametric setting of the whole experimentation as per simulated annealing is shown in Fig. 258 with current iteration number.

5.3.5.3 For chamfer:

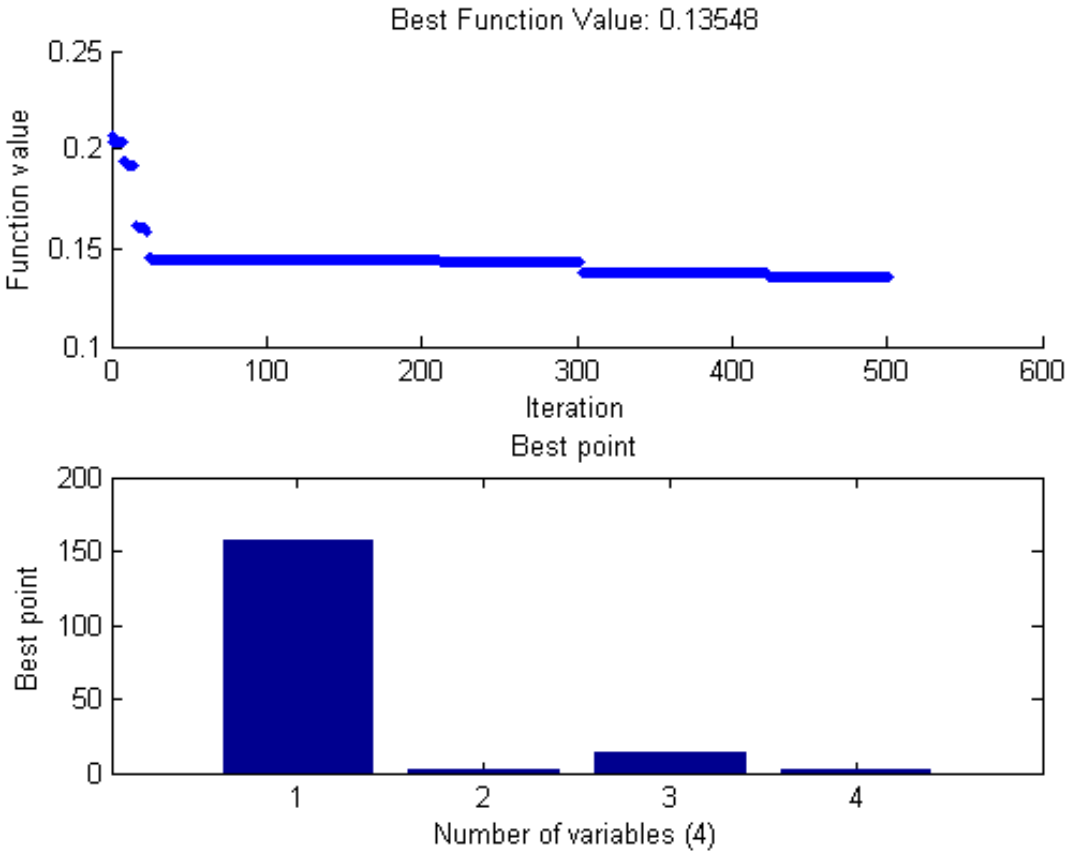

Fig. 259 Results from SA approach for chamfer

Nature based novel optimization technique i.e., simulated annealing algorithm is employed to the obtained regression equation of chamfer from RSM method. By applying Boltzmann annealing approach to the experimental data, the lowest value of chamfer is found to be 0.13547 mm at 156.625 ampere of cutting current, 2.014 mm/s of cutting speed, 13.071 L/min of gas pressure and 2.063 mm of stand-off gap. Fig. 259 shows the best function value and comparative effect of input parameters. Here, the cutting current is the most effective variable. The highest number of iteration for simulating the algorithm is

501, where the minimum value of chamfer can be found. The best parametric setting of the whole experimentation as per simulated annealing is shown in Fig. 259 with current iteration number.

5.3.5.4 For dross:

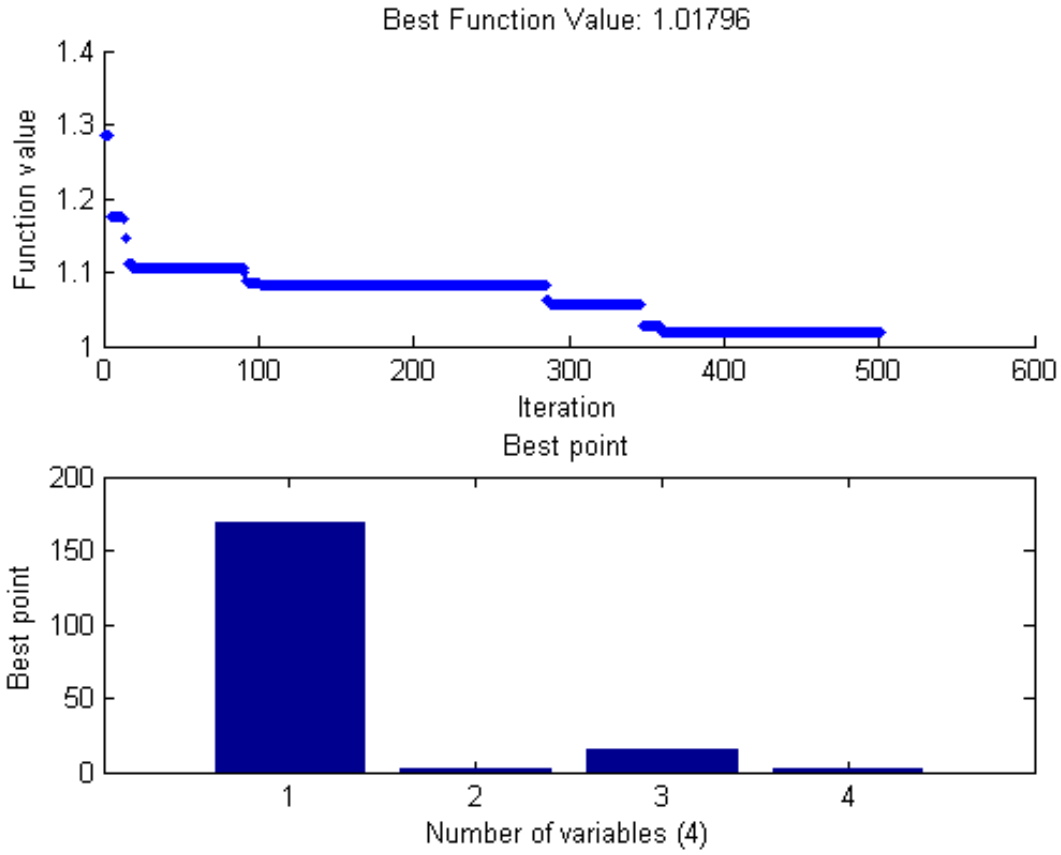

Fig. 260 Results from SA approach for dross

Nature based novel optimization technique i.e., simulated annealing algorithm is employed to the obtained regression equation of dross from RSM method. By applying Boltzmann annealing approach to the experimental data, the lowest value of dross is found to be 1.01796 mm^2 at 168.617 ampere of cutting current, 2 mm/s of cutting speed, 14.858 L/min of gas pressure and 2.554 mm of stand-off gap. Fig. 260 signifies the best function value and comparative effect of input parameters. Here, the cutting current gave

the most effective variable than other two parameters. The highest number of iteration for simulating the algorithm is 501 where the minimum value of dross observed. The best parametric setting of the whole experimentation as per simulated annealing is shown in Fig. 260 with current iteration number.

5.3.5.5 For right bevel angle:

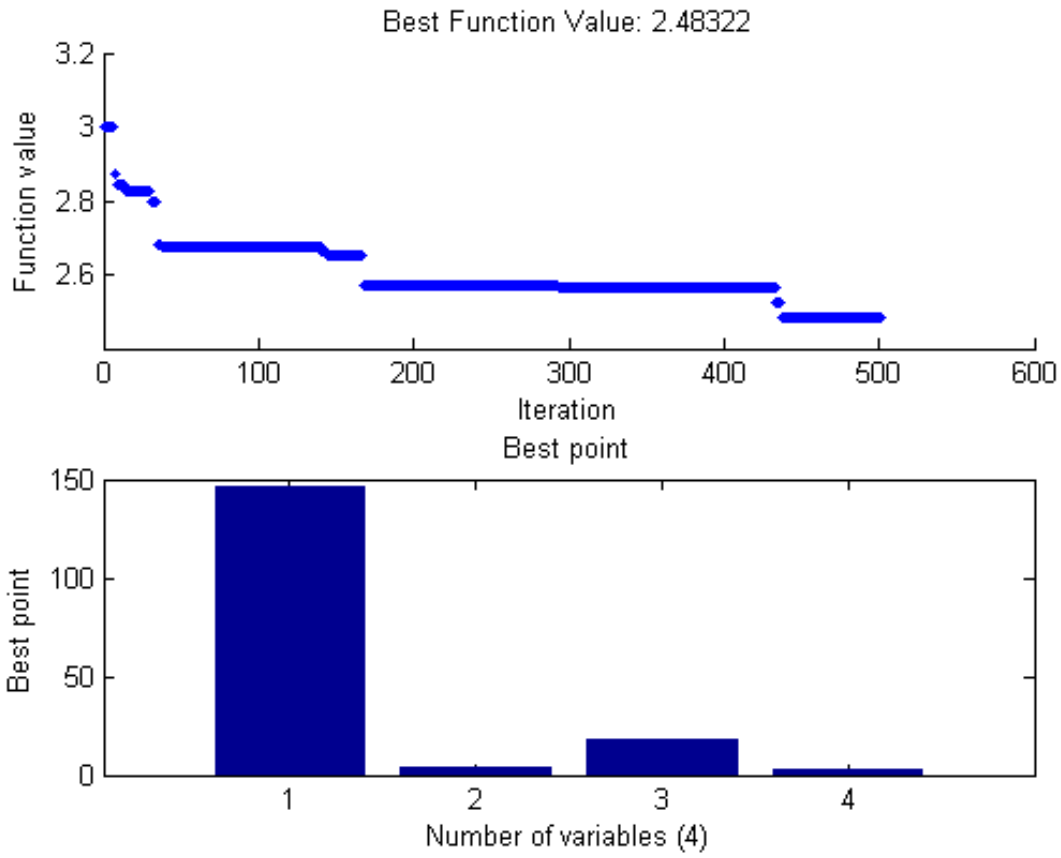

Fig. 261 Results from SA approach for right bevel angle

Nature based novel optimization technique i.e., simulated annealing algorithm is employed to the obtained regression equation of right bevel angle from RSM method. By applying Boltzmann annealing approach to the experimental data, the lowest value of right bevel angle is found to be 2.48322º at 146.557 ampere of cutting current, 3.929

mm/s of cutting speed, 17.787 L/min of gas pressure and 2.898 mm of stand-off gap. Fig. 261 displays the best function value and comparative effect of input parameters. Here, the cutting current is the most effective variable. The highest number of iteration for simulating the algorithm is 501, where the minimum value of right bevel angle observed. The best parametric setting of the whole experimentation as per simulated annealing is shown in Fig. 261 with current iteration number.

5.3.5.6 For kerf:

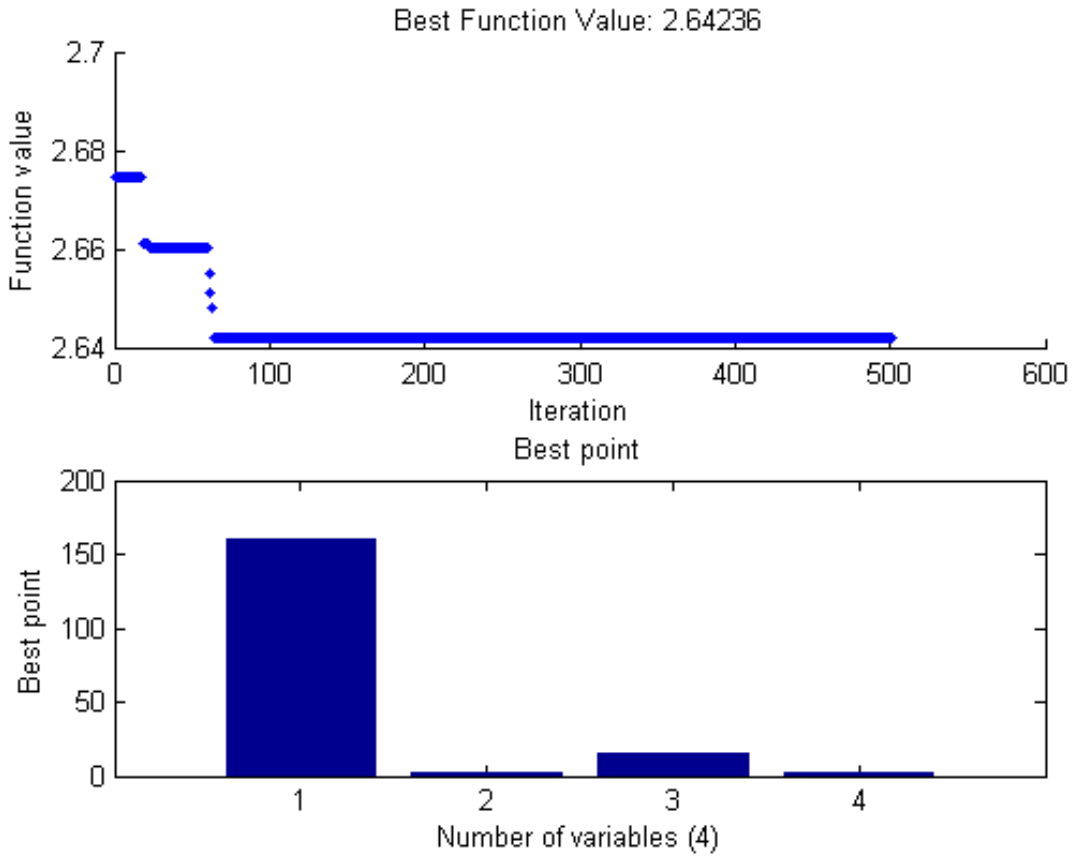

Fig. 262 Results from SA approach for kerf

Nature based novel optimization technique i.e., simulated annealing algorithm is employed to the obtained regression equation of kerf from RSM method. By applying Boltzmann annealing approach to the experimental data, the lowest value of kerf is found

to be 2.64236 mm at 160.635 ampere of cutting current, 2.202 mm/s of cutting speed, 15.279 L/min of gas pressure and 2.683 mm of stand-off gap. Fig. 262 shows the best function value and comparative effect of input parameters. Here, the cutting current is the most effective variable. The highest number of iteration for simulating the algorithm is 501, where the minimum value of kerf observed. The best parametric setting of the whole experimentation as per simulated annealing is shown in Fig. 262 with current iteration number.

5.3.5.7 For heat affected zone:

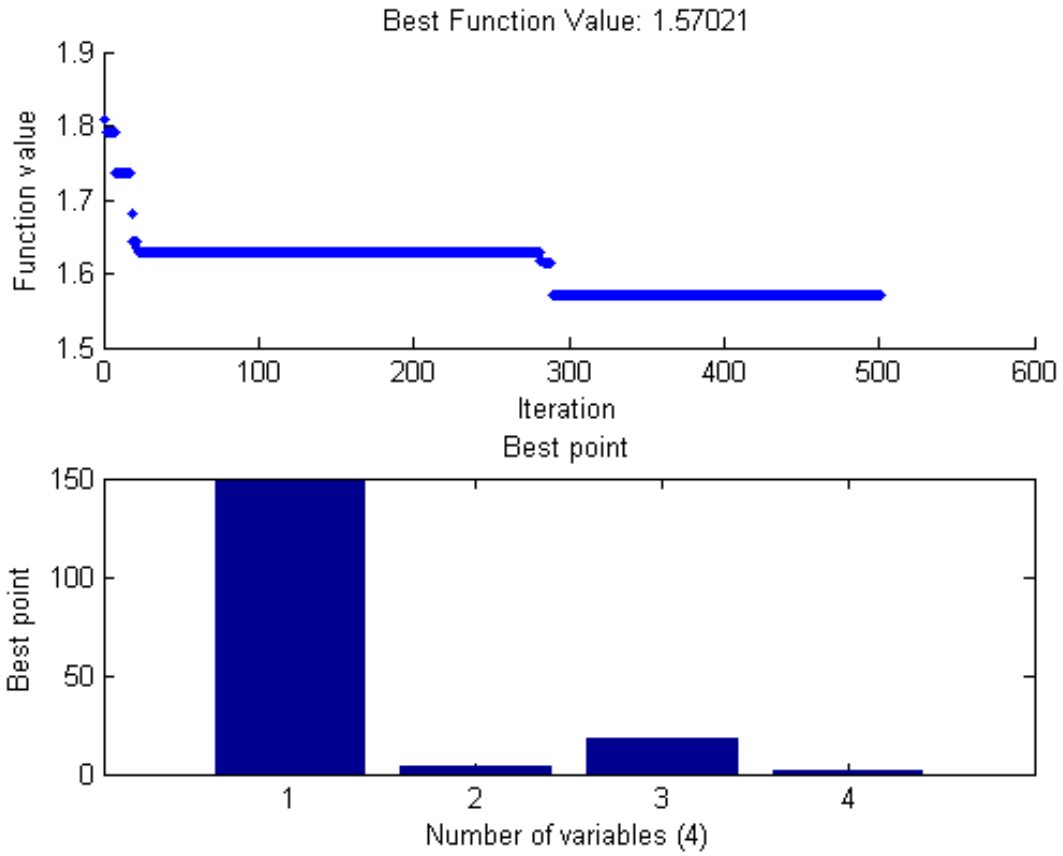

Fig. 263 Results from SA approach for HAZ

Nature based novel optimization technique i.e., simulated annealing algorithm is employed to the obtained regression equation of HAZ from RSM method. By applying

Boltzmann annealing approach to the experimental data, the lowest value of HAZ is found to be 1.57021 mm at 147.874 ampere of cutting current, 3.986 mm/s of cutting speed, 17.535 L/min of gas pressure and 2.003 mm of stand-off gap. Fig. 263 shows the best function value and comparative effect of input parameters. Here, the cutting current is the most effective variable. The highest number of iteration for simulating the algorithm is 501, where the minimum value of HAZ is observed. The best parametric setting of the whole experimentation as per simulated annealing is shown in Fig. 263 with current iteration number.

5.3.6 TLBO results

5.3.6.1 For material removal rate:

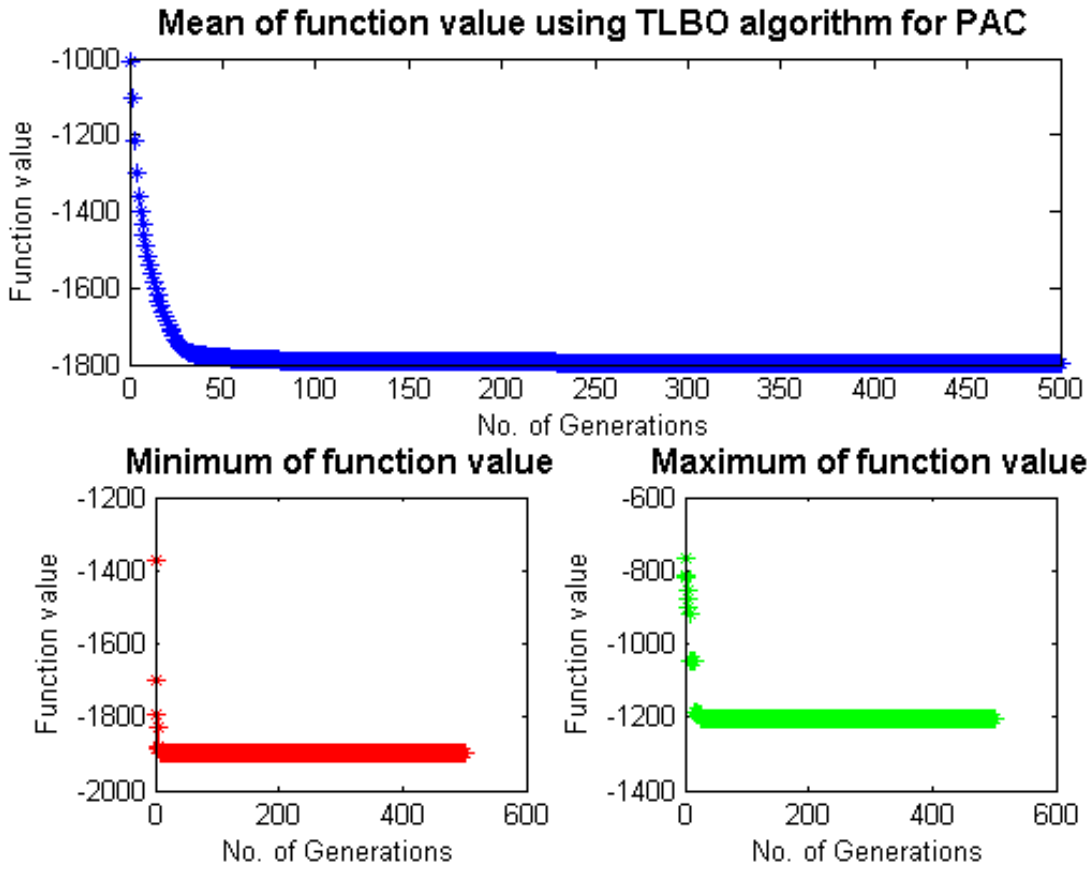

Fig. 264 Obtained plot by TLBO approach for MRR

The TLBO algorithm is run through Matlab R2012b version software by considering 300 as population size and 500 as number of generations. In each run the maximum number of function evaluations N is considered as 750000. Only in the case of MRR response, the theory of negativity is applied because the main objective of this is to convert the maximization type to minimization type problem. Fig. 264 depicts plot of the fitness function value for each generation. It can be observed that it converges to the optimum result in very small population size and less number of generations. From Fig. 264, it can be concluded that the optimal condition for MRR occurred at 112.175 ampere of cutting current, 3.972 mm/s of cutting speed, 17.608 L/min of gas pressure and 2.000 mm of stand-off gap. The objective function value of MRR is found as 1795.06 mm^3/min.

5.3.6.2 For surface roughness:

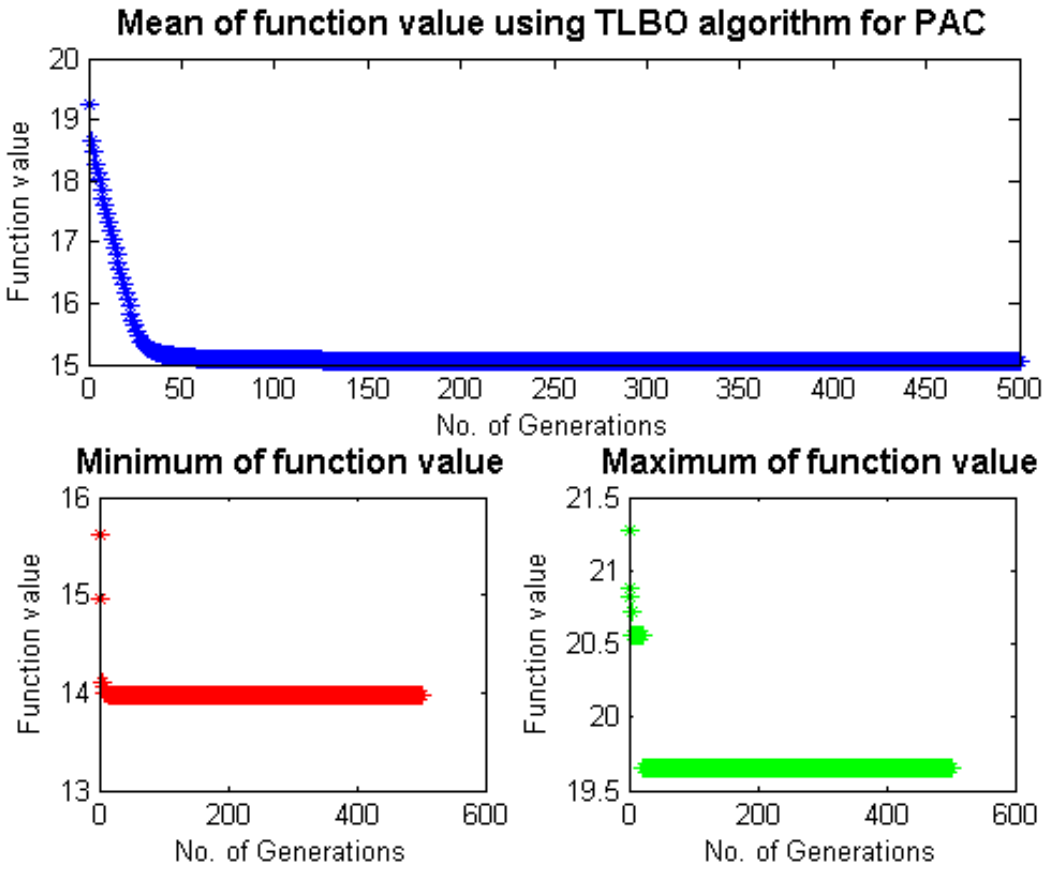

Fig. 265 Obtained plot by TLBO approach for SR

The TLBO algorithm is run through Matlab R2012b version software by considering 300 as population size and 500 as number of generations. In each run the maximum number of function evaluations N is considered as 750000. Fig. 265 depicts plot of the fitness function value for each generation. It can be observed that it converges to the optimum result in very small population size and less number of generations. From Fig. 265, it can be concluded that the optimal condition for SR occurred at 197.273 ampere of cutting current, 2.282 mm/s of cutting speed, 15.754 L/min of gas pressure and 3 mm of stand-off gap. The objective function value of SR is found as 15.061 µm.

5.3.6.3 For chamfer:

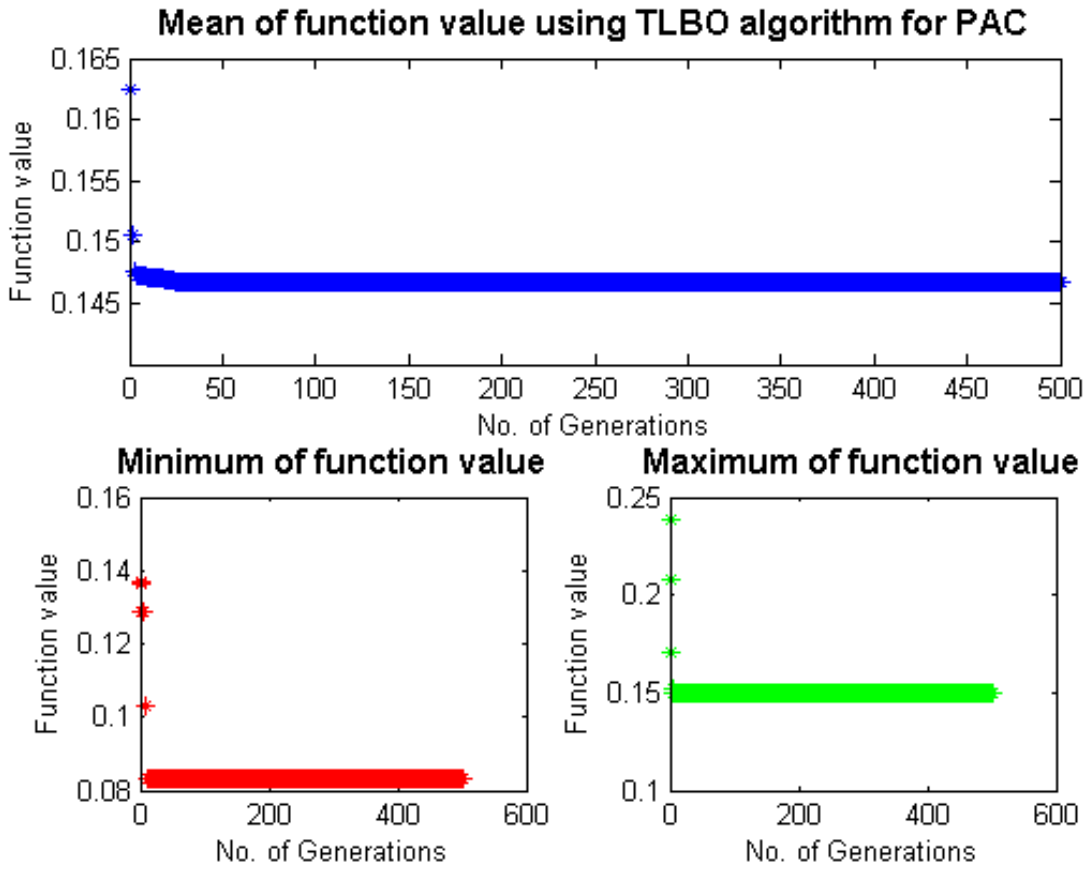

Fig. 266 Obtained plot by TLBO approach for chamfer

The TLBO algorithm is run through Matlab R2012b version software by considering 300 as population size and 500 as number of generations. In each run the maximum number of function evaluations N is considered as 750000. Fig. 266 depicts plot of the fitness function value for each generation. It can be observed that it converges to the optimum result in very small population size and less number of generations. From Fig. 266, it can be concluded that the optimal condition for chamfer occurred at 200.008 ampere of cutting current, 3.797 mm/s of cutting speed, 17.816 L/min of gas pressure and 2.990 mm of stand-off gap. And the objective function value of chamfer is found as 0.14671 mm.

5.3.6.4 For dross:

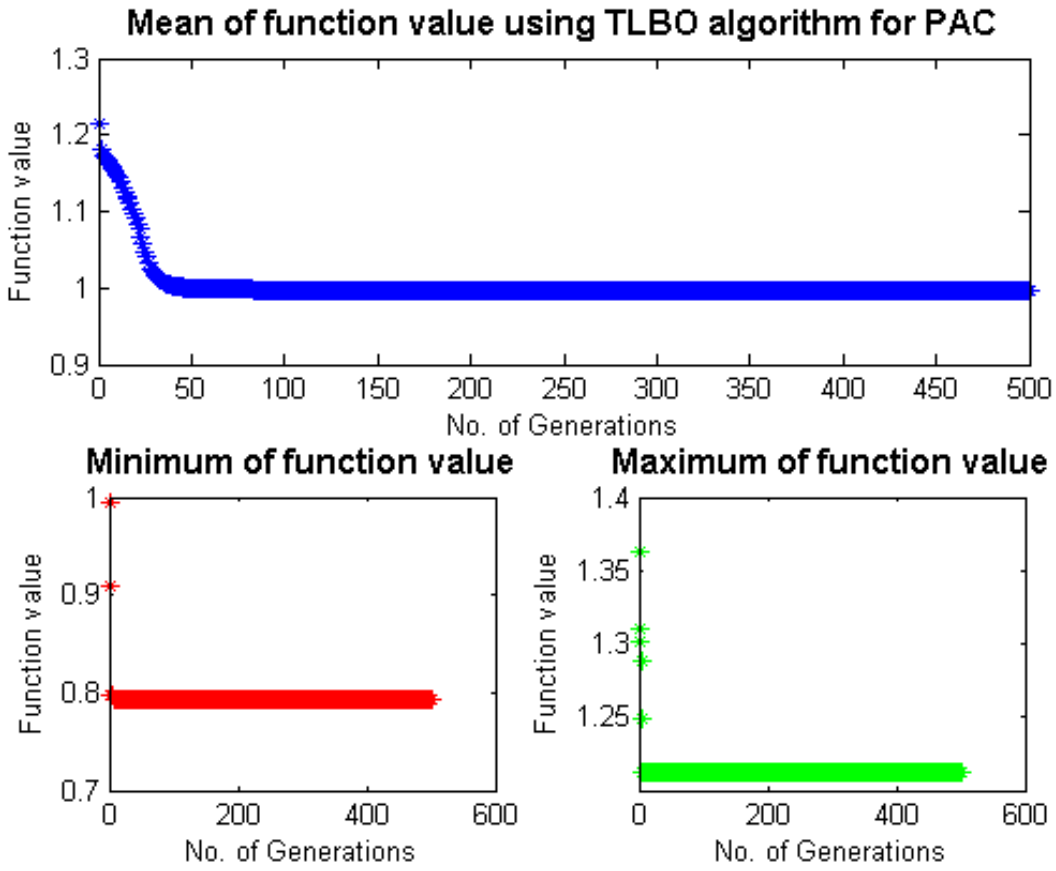

Fig. 267 Obtained plot by TLBO approach for dross

The TLBO algorithm is run through Matlab R2012b version software by considering 300 as population size and 500 as number of generations. In each run the maximum number of function evaluations N is considered as 750000. Fig. 267 depicts plot of the fitness function value for each generation. It can be observed that it converges to the optimum result in very small population size and less number of generations. From Fig. 267, it can be concluded that the optimal condition for dross occurred at 200 ampere of cutting current, 2.812 mm/s of cutting speed, 16.14 L/min of gas pressure and 2.475 mm of stand-off gap. And the objective function value of dross is found as 0.99714 mm^2.

5.3.6.5 For right bevel angle:

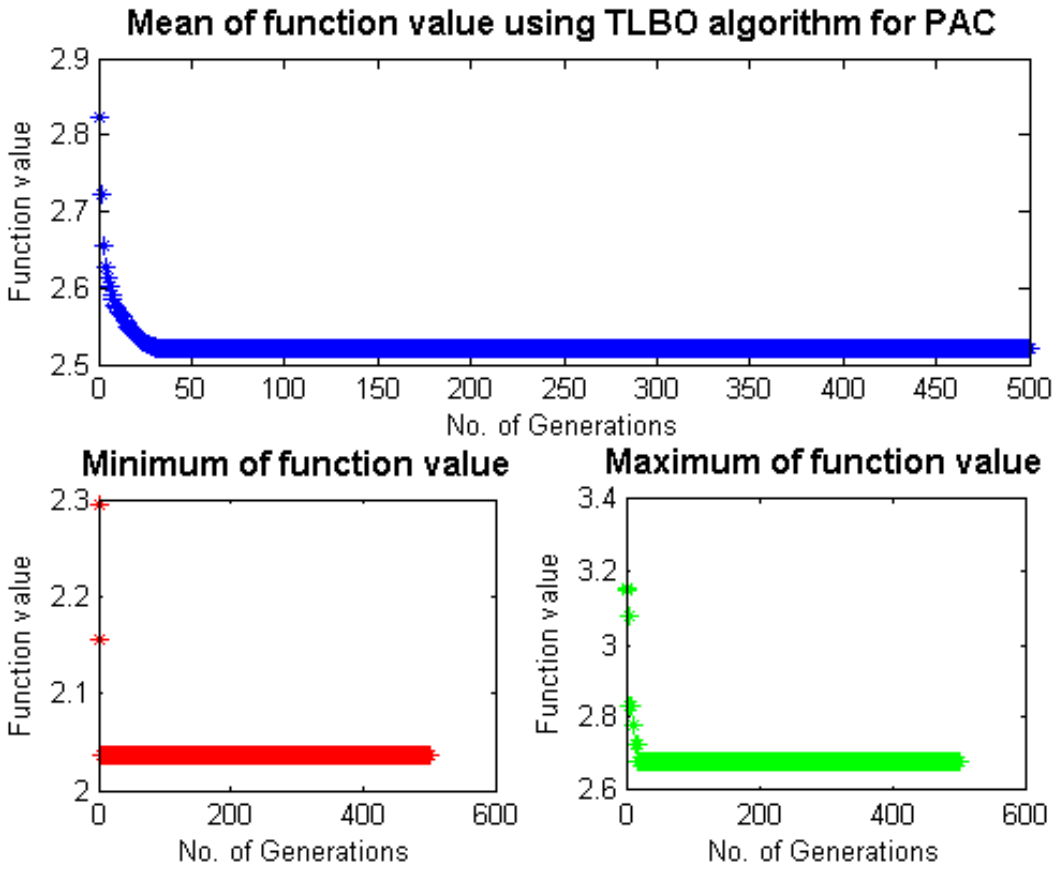

Fig. 268 Obtained plot by TLBO approach for right bevel angle

The TLBO algorithm is run through Matlab R2012b version software by considering 300 as population size and 500 as number of generations. In each run the maximum number of function evaluations N is considered as 750000. Fig. 268 depicts plot of the fitness function value for each generation. It can be observed that it converges to the optimum result in very small population size and less number of generations. From Fig. 268, it can be concluded that the optimal condition for right bevel angle occurred at 164.69 ampere of cutting current, 3.999 mm/s of cutting speed, 17.9956 L/min of gas pressure and 2.84321 mm of stand-off gap. The objective function value of right bevel angle is found as 2.52053º.

5.3.6.6 For kerf:

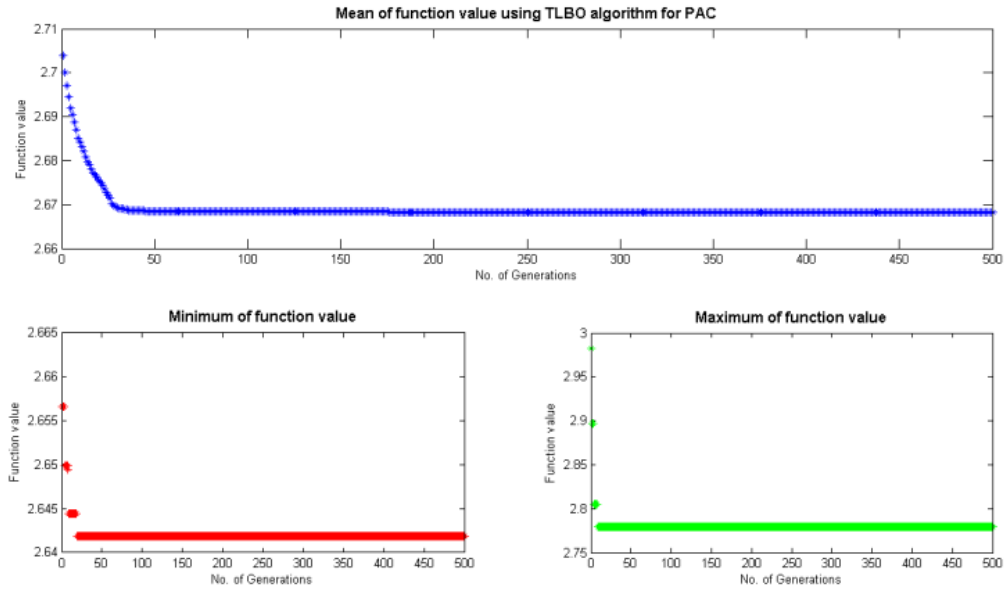

Fig. 269 Obtained plot by TLBO approach for kerf

The TLBO algorithm is run through Matlab R2012b version software by considering 300 as population size and 500 as number of generations along with function evaluation of 750000 in each run. Fig. 269 depicts plot of the fitness function value for each generation. It can be observed that it converges to the optimum result in very small population size and less number of generations. From Fig. 269, it can be concluded that the optimal condition for kerf occurred at 156.816 ampere of cutting current, 2.758 mm/s of cutting speed, 15.515 L/min of gas pressure and 2.721 mm of stand-off gap. And the objective function value of kerf is found as 2.66833 mm.

5.3.6.7 For heat affected zone:

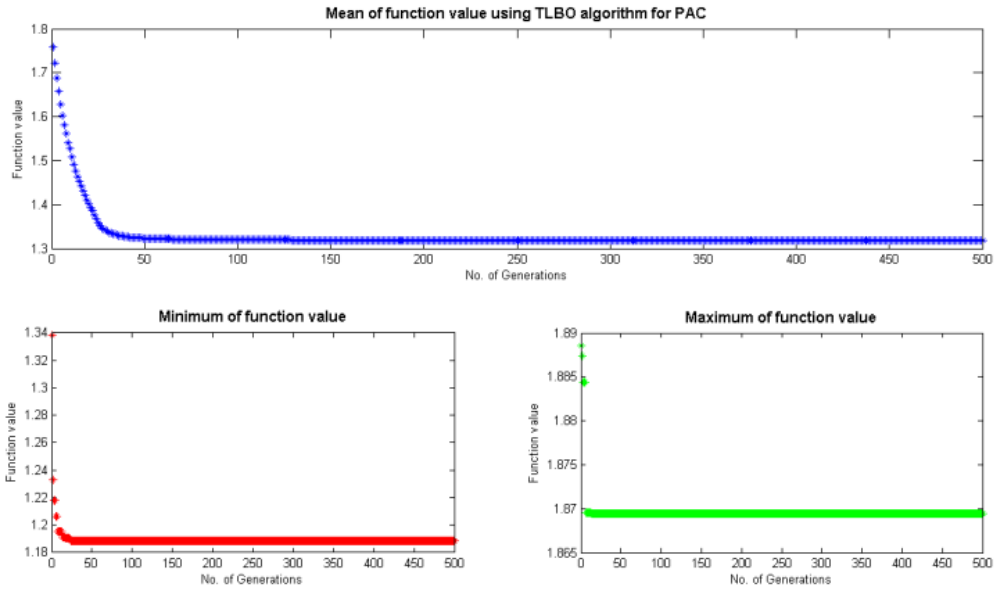

Fig. 270 Obtained plot by TLBO approach for HAZ

The TLBO algorithm is run through Matlab R2012b version software by considering 300 as population size and 500 as number of generations. In each run the maximum number of function evaluations N is considered as 750000. Fig. 270 depicts plot of the fitness function value for each generation. It can be observed that it converges to the optimum result in very small population size and less number of generations. From Fig. 270, it can be concluded that the optimal condition for HAZ occurred at 112.406 ampere of cutting current, 3.102 mm/s of cutting speed, 15.704 L/min of gas pressure and 2.021 mm of stand-off gap. And the best objective function value of HAZ is found as 1.31858 mm.

5.4 CNC Oxy-Fuel Gas Cutting Using DEA Based Taguchi Approach

Experimental layout with output data presented in Table 78 have been analysed by above-mentioned procedure. Data have been normalized first by using Equations 23-24 as

per objective criteria [108]. Normalized data has been tabulated as given in Table 79. Normalized data of bevel angle and dross breadth are considered as input factor, whereas normalized data of dross height have been considered as output factor in Lingo version 14 software for determining the relative efficiency (Table 79). Finally, Taguchi methodology has been applied on relative efficiency for evaluating optimal parametric setting. Nozzle speed, torch height and Oxy-fuel speed at their 3rd, 1st and 1st level respectively, are observed (Fig. 272) as more favourable machining condition. Each normalized data are fed into the Lingo Version 14 software package for determining the relative efficiency. Analysis of variance (ANOVA) of input parameters of the cutting process is shown in Table 81. Fig. 271 gives the percentage contribution chart in 3D pie plot. Table 82 shows the factor ranking in accordance with their degree of significance.

Table 77 Values of Input Process Parameters of CNC Oxy-Fuel Gas Cutting

Process parameters	Units	Code	L(1)	L(2)	L(3)
Nozzle speed	m/min	A	1	1.5	2
Torch height	mm	B	2.0	2.5	3.0
Oxy-fuel speed	mm/min	C	450	550	650

Table 78 Taguchi Design of L_9 with Input and Output Values

Sl. No.	Nozzle speed (m/min)	Torch height (mm)	Oxy-fuel speed (mm/min)	Bevel angle (Degree)	Dross width (mm)	Dross height (mm)
1	1	2.0	450	3	4.53	6.83
2	1	2.5	550	4	6.92	3.58
3	1	3.0	650	4	3.86	6.34
4	1.5	2.0	550	2	4.65	7.56
5	1.5	2.5	650	6	5.61	5.56
6	1.5	3.0	450	5	7.83	4.47
7	2	2.0	650	3	6.79	5.48
8	2	2.5	450	6	5.56	7.64
9	2	3.0	550	4	4.95	5.68

Table 79 Normalized Values, Computed Relative Efficiency and S/N Ratio of Responses

Sl. No.	Norm. 1	Norm. 2	Norm. 3	Relative efficiency	S/N Ratio
1	0.66667	0.85210	0.89398	0.72836	-2.75306
2	0.50000	0.55780	0.46859	0.58321	-4.68352
3	0.50000	1.00000	0.82984	0.57611	-4.78992
4	1.00000	0.83011	0.98953	0.82757	-1.64394
5	0.33333	0.68806	0.72775	0.73429	-2.68269
6	0.40000	0.49298	0.58508	0.82394	-1.68209
7	0.66667	0.56848	0.71728	0.87596	-1.15034
8	0.33333	0.69424	1.00000	1.00000	0.00000
9	0.50000	0.77980	0.74346	0.66189	-3.58432

Table 80 Estimated Model Coefficients for S/N Ratios

Term	Regression Coef.	Std. Err.	T	P
Constant	-2.55221	0.2500	-10.210	0.009
Nozzle speed 1.0	-1.52329	0.3535	-4.309	0.050
Nozzle speed 1.5	0.54930	0.3535	1.554	0.260
Torch height 2.0	0.70310	0.3535	1.989	0.185
Torch height 2.5	0.09681	0.3535	0.274	0.810
Oxy-fuel speed 450	1.07382	0.3535	3.038	0.093
Oxy-fuel speed 550	-0.75172	0.3535	-2.127	0.167

S = 0.7499 R-Sq = 94.6% R-Sq(adj) = 78.3%

Table 81 Analysis Of Variance for Relative Efficiency

Source	DoF	Seq. SS	Adj. SS	Adj. MS	F	Percentage Contribution
Nozzle speed (m/min)	2	10.712	10.712	5.3562	9.53	51.6639
Torch height (mm)	2	3.431	3.431	1.7153	3.05	16.5477
Oxy-fuel speed (mm/min)	2	5.466	5.466	2.7329	4.86	26.3625
Residual Error	2	1.125	1.125	0.5623		5.4259
Total	8	20.734				100

Table 82 Response Table for Signal to Noise Ratios (Larger-Is-Better)

Level	Nozzle speed (m/min)	Torch height (mm)	Oxy-fuel speed (mm/min)
1	-4.076	-1.849	-1.478
2	-2.003	-2.455	-3.304
3	-1.578	-3.352	-2.874
Delta	2.497	1.503	1.826
Rank	1	3	2

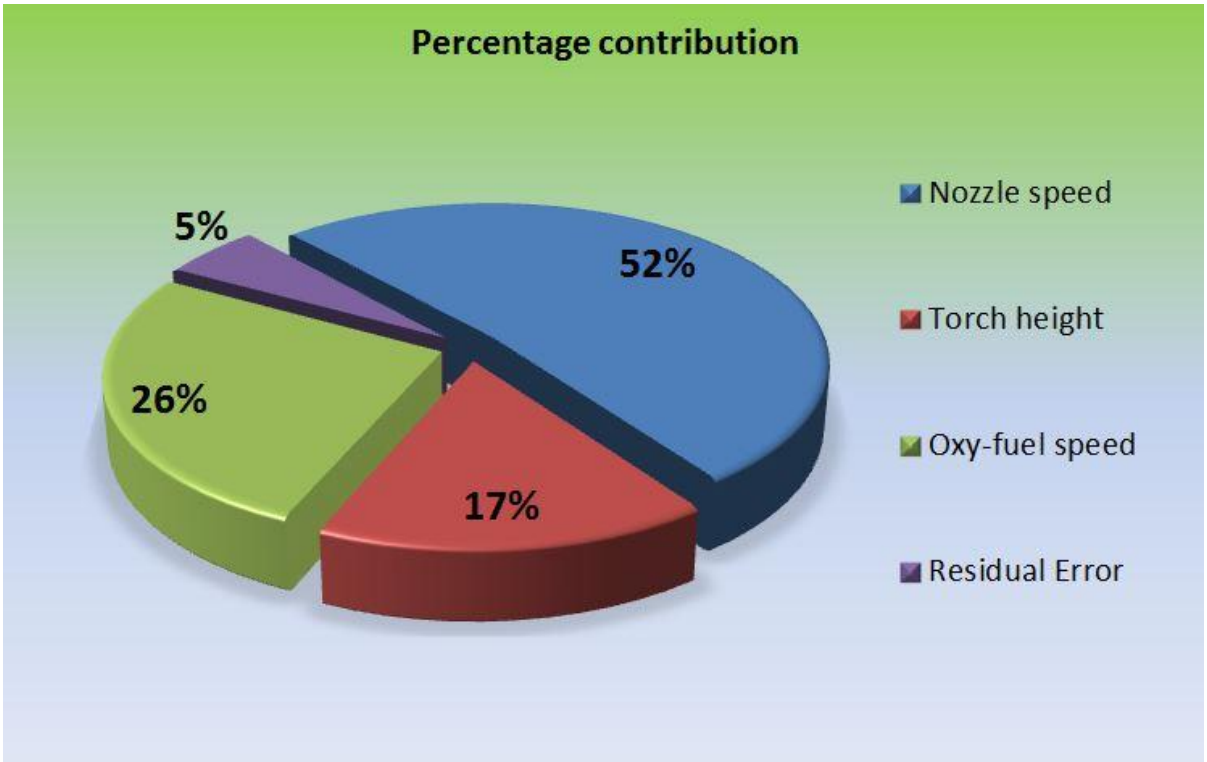

Fig. 271 Percentage contribution of machining parameters

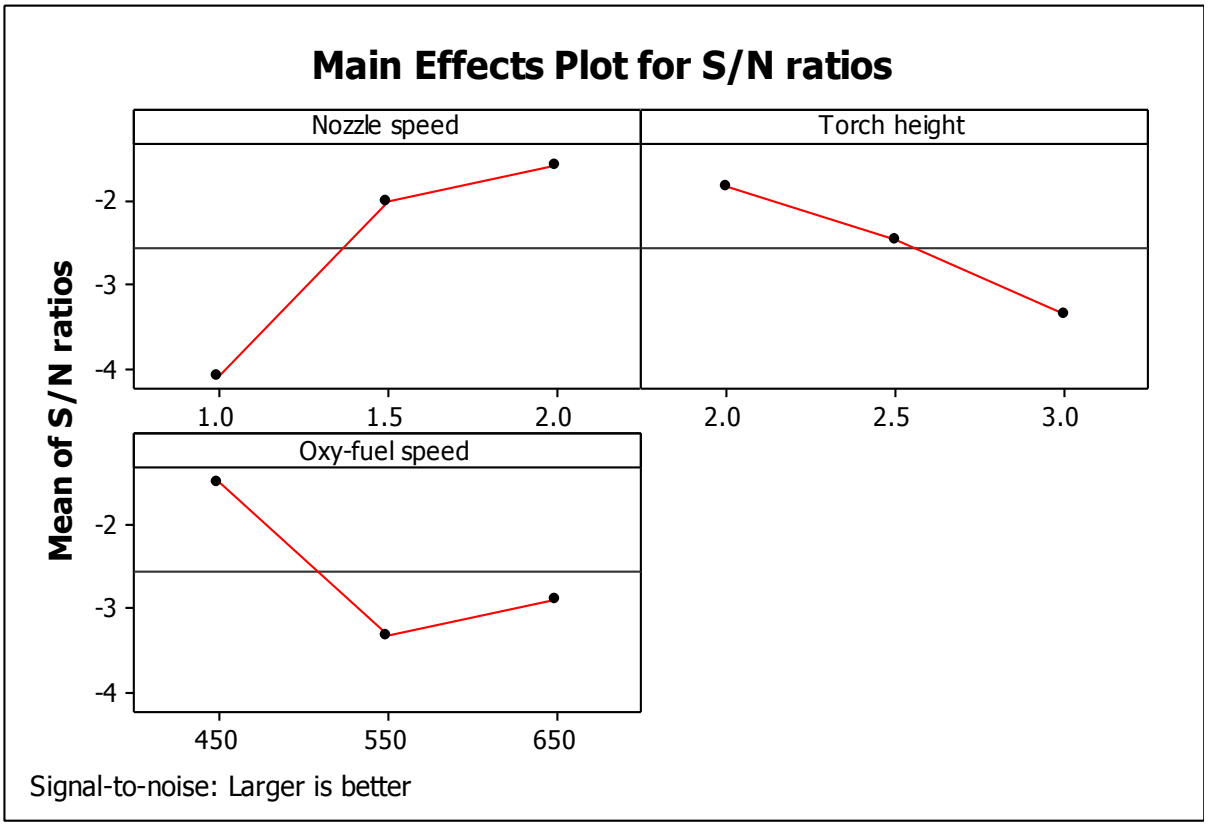

Fig. 272 Main effect plot of Relative efficiency

5.5 CONFIRMATORY TEST

Confirmation testing is necessary to validate the approached model. Once the optimal combination of plasma arc cutting factors is selected, the final step is to predict and verify the expected output response through the confirmatory experiments. So, the confirmatory experiments were conducted using the optimum setting of the machining parameters obtained from desirability function approach coupled with RSM. These experiments were used to predict and validate the improvement in the quality characteristics for plasma arc machining. The estimated desirability function value ($\widetilde{D}$) can be determined by using the optimum parameters as

$$\widetilde{D} = D_m + \sum_{i=1}^{n} (\overline{D_i} - D_m) \tag{29}$$

where D_m is the total mean of the desirability function value at the optimal level [109; 110]. In order to validate the results obtained, three confirmatory experiments were conducted for each of the responses at optimal levels of the process variables. The desirability function value is calculated and compared with the predicted values. Table 83 shows the comparison of estimated values and experimental values of each response obtained from the first case experiment. Similarly, Table 84 demonstrates the comparison of values obtained from various optimization approaches and last confirmatory test results for the second case experiment. Lastly, the comparison of output response of PAC in the third experiment is tabulated in Table 85.

Table 83 Confirmation Test Results of Plasma Arc Cutting for Case 1

Optimization Approach	Feed rate (mm/min)	Cutting current (Ampere)	Voltage (Volt)	Torch height (mm)	MRR (mm^3/min)
RSM	946.5263	50.0868	123.7877	1.4394	0.0256
Desirability	1000	50	150	3	0.598497
GA	1000	50	113.5	3	3.92945
PSO	1000	50	113.499	3	3.92945
SA	934.156	49.874	134.595	2.976	3.2726
TLBO	1000.01	49.9382	147.874	2.9869	3.80718
Experimental value	1000	50	125	3	0.506944
					SR (µm)
RSM	1008.213	49.185	64.548	3.133	3.551
Desirability	900	50	150	3	8.108
GA	1000	40	150	2.082	25.28482
PSO	1000	40	150	2.082	25.28482
SA	965.496	44.99	111.143	2.249	20.7392
TLBO	1000	49.5417	146.63	2.73299	20.7392
Experimental value	1000	50	150	2	3.85
					Right Bevel Angle (Degree)
RSM	1002.465	50.715	114.474	1.727	3.333
Desirability	1000	50	150	3	3.835
GA	1000	50	100	1	48.6317
PSO	1000	50	100	1	48.6317
SA	966.943	49.935	123.613	1.007	44.9597
TLBO	1000	49.9994	114.594	1	48.5337
Experimental value	1000	50	100	1	4

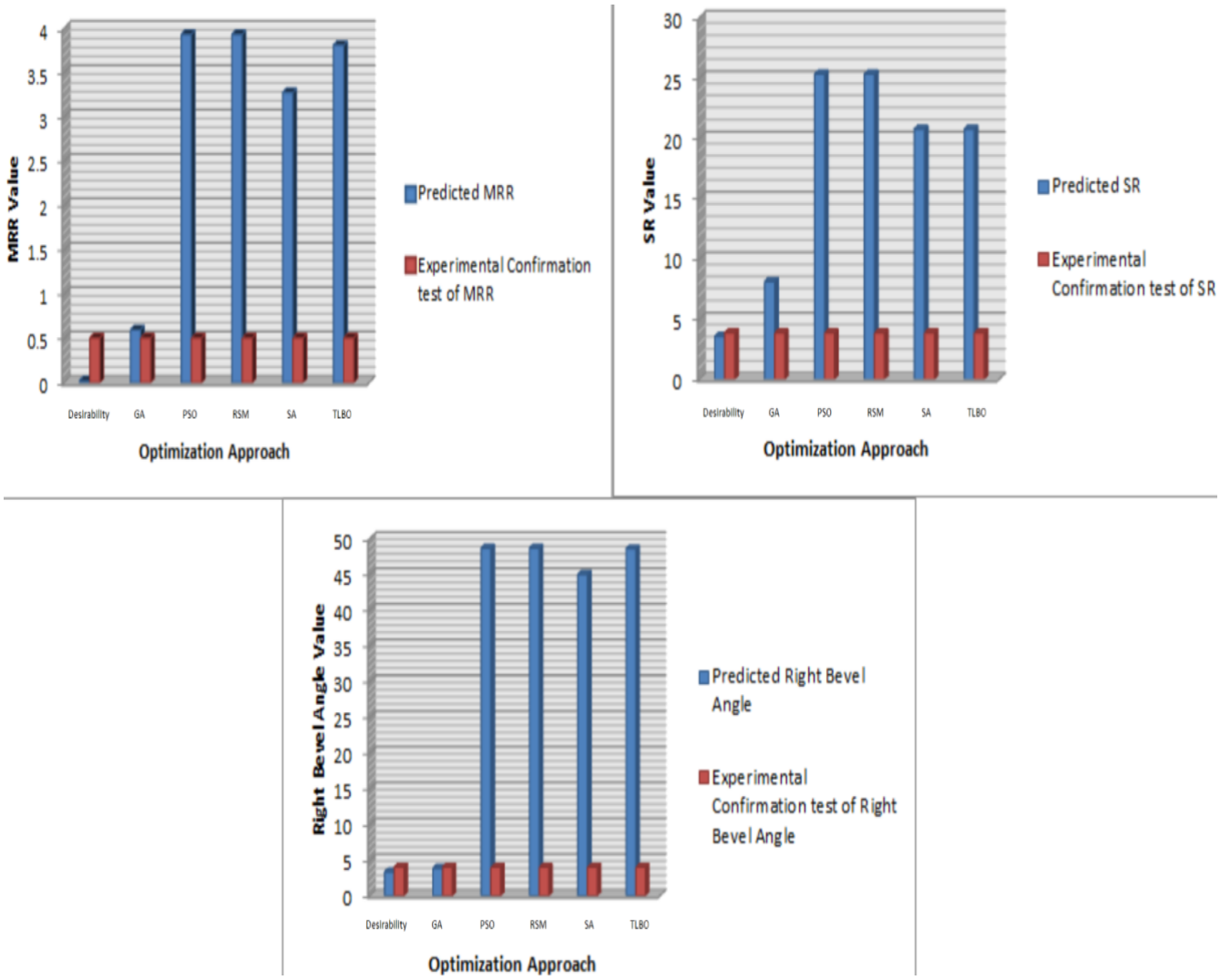

Fig. 273 Comparison of approaches in first phase

Table 84 Confirmation Test Results of Plasma Arc Cutting for Case 2

Optimization Approach	Feed rate (mm/min)	Cutting current (Ampere)	Voltage (Volt)	Torch height (mm)	MRR (mm^3/min)
RSM	951.4757	42.3029	114.3322	2.6301	4734
Desirability	995	47.5	160	3.5	6771.73
GA	920	40	100	2	30207.2
PSO	920	40	100	2	30207.2
SA	920	40	129.869	2	30476.41078
TLBO	924.226	40.6128	105.911	2.97552	31180.1
Experimental value	920	40	100	2	2764.84
					SR (µm)
RSM	908.9561	50.0871	152.9153	2.3686	39.5
Desirability	895	40	140	3.5	75.68
GA	920	45	140	2.367	216.77179
PSO	920	45	140	2.3669	216.7718
SA	922.97	44.149	139.545	2.399	218.75136
TLBO	938.349	43.8974	139.636	3	225.793
Experimental value	920	45	140	2.5	28.62
					Chamfer (mm)
RSM	944.5464	44.4648	78.3166	2.196	1.6156
Desirability	920	40	160	3.5	2.0546
GA	920	40	100	2	38.8355
PSO	920	40	100	2	38.8355
SA	920.011	40.211	101.854	2.001	38.8983
TLBO	924.454	41.8109	105.083	2.97086	39.8281
Experimental value	920	40	100	2	1.29
					Dross (mm^2)
RSM	1055.875	49.929	167.549	3.552	3.521
Desirability	945	47.5	100	3.5	9.901
GA	970	45	100.003	2	29.4362
PSO	970	45	100	2	29.4371
SA	963.512	45	137.263	2	28.717
TLBO	969.999	44.9999	117.292	2	29.2925
Experimental value	970	45	120	2	2.76
					Kerf (mm)
RSM	882.7605	34.9384	133.7895	2.4102	3.151
Desirability	895	47.5	160	3.5	4.065
GA	970	45	140	2	144.3957
PSO	970	45	140	2	144.3957
SA	969.99	44.997	117.413	2	144.30718
TLBO	970.006	45.0006	139.898	2.00345	144.396
Experimental value	970	45	140	2	2.81

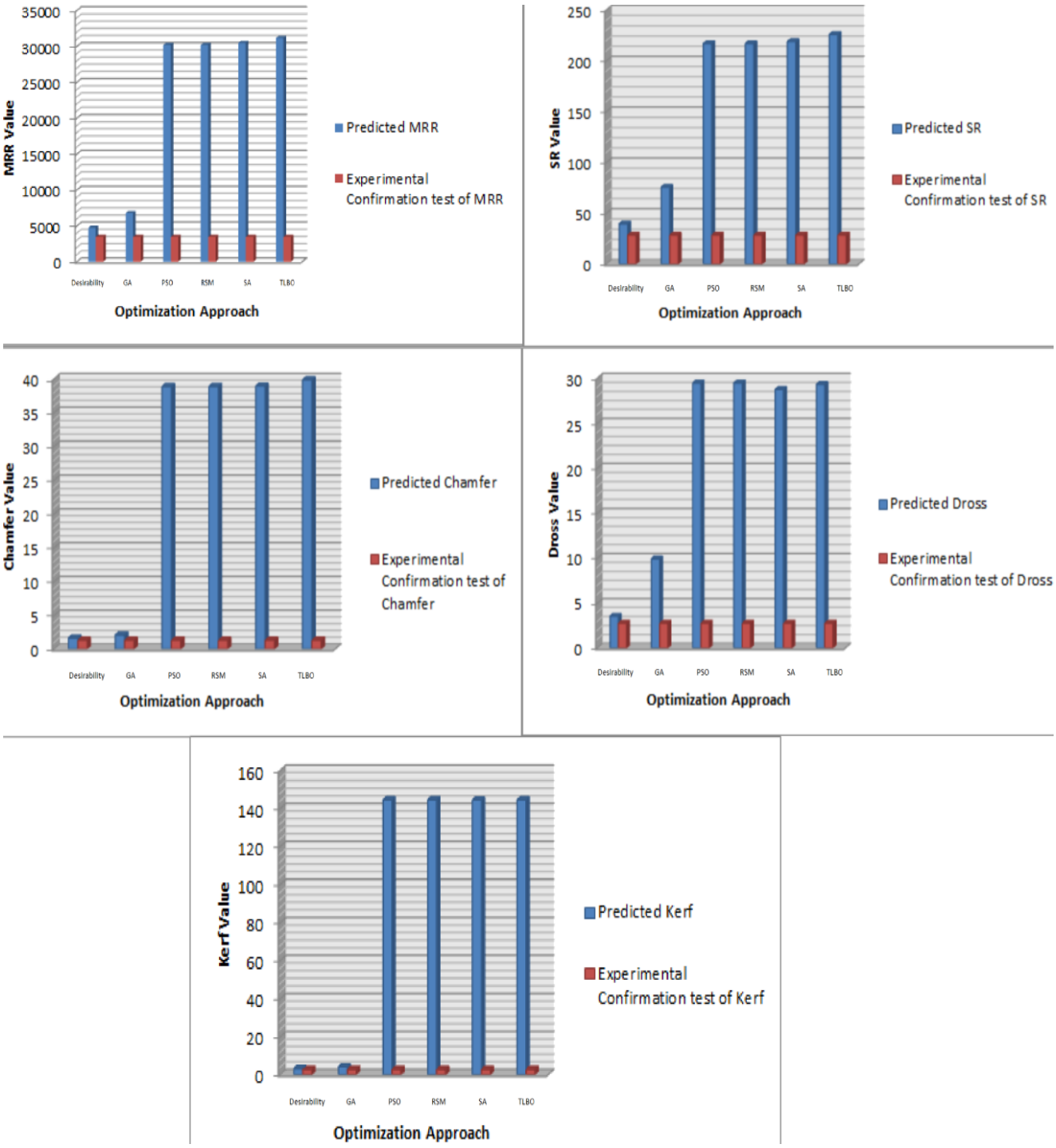

Fig. 274 Comparison of approaches in second phase

Table 85 Confirmation Test Results of Plasma Arc Cutting for Case 3

Optimization Approach	Cutting Current (Ampere)	Cutting Speed (mm/s)	Gas Pressure (L/min)	Stand-off Gap (mm)	MRR (mm^3/min)
RSM	133.08	3.6738	21.1161	3.8056	582.20
Desirability	100	4	12	2.5	1542.82
GA	100	4	18	2	1898.87099
PSO	100	4	18	2	1898.871
SA	130.013	4	18	2	1680.471
TLBO	112.175	3.972	17.608	2	1795.06
Experimental value	100	4	18	2	652.93
					SR (µm)
RSM	185.9596	7.5043	13.789	3.6503	23.4254
Desirability	100	4	18	2.25	30.6972
GA	200	2	12	2.356	12.93477
PSO	200	2	12	2.356	12.93476
SA	156.375	2	15.738	2.987	15.185
TLBO	197.273	2.282	15.754	3	15.061
Experimental value	200	2	15	2.5	24.42
					Chamfer (mm)
RSM	194.3289	2.4226	16.6022	3.0434	0.133
Desirability	100	4	18	2.25	1.475
GA	200	2	12	2	0.083296
PSO	200	2	12	2	0.08329
SA	156.625	2.014	13.071	2.063	0.13547
TLBO	200.008	3.797	17.816	2.99	0.14671
Experimental value	200	2	15	2	0.16
					Dross (mm^2)
RSM	236.4002	4.2987	18.59	4.0965	1.102
Desirability	125	4	18	2.25	1.687
GA	200	2	12.128	2	0.79244
PSO	200	2	12.128	2	0.79244
SA	168.617	2	14.858	2.554	1.01796
TLBO	200	2.812	16.14	2.475	0.99714
Experimental value	200	2	18	2.5	1.23
					Right Bevel Angle (Degree)
RSM	146.9697	2.7576	14.7273	2.4848	3.0051
Desirability	200	2.5	18	3	4.2396
GA	100	4	18	3	1.8337
PSO	100	4	18	3	1.8337
SA	146.557	3.929	17.787	2.898	2.48322
TLBO	164.69	3.999	17.9956	2.84321	2.52053
Experimental value	150	4	18	3	3
					Kerf (mm)
RSM	188.3842	2.3209	14.9168	2.5551	2.498
Desirability	100	4	12	3	3.085
GA	165.73	2.354	15.174	2.618	2.6394

Contd.

Optimization Approach	Cutting Current (Ampere)	Cutting Speed (mm/s)	Gas Pressure (L/min)	Stand-off Gap (mm)	Kerf (mm)
PSO	167.448	2	15.153	2.659	2.64695
SA	160.635	2.202	15.279	2.683	2.64236
TLBO	156.816	2.758	15.515	2.721	2.66833
Experimental value	150	2	15	2.5	2.64
					HAZ (mm)
RSM	179.8258	4.9182	16.5023	2.4575	1.678
Desirability	200	2	18	3	2.898
GA	100	2.958	15.504	2	1.18845
PSO	100	2.956	15.506	2	2.64695
SA	147.874	3.986	17.535	2.003	1.57021
TLBO	112.406	3.102	15.704	2.021	1.31858
Experimental value	150	4	15	2	1.73

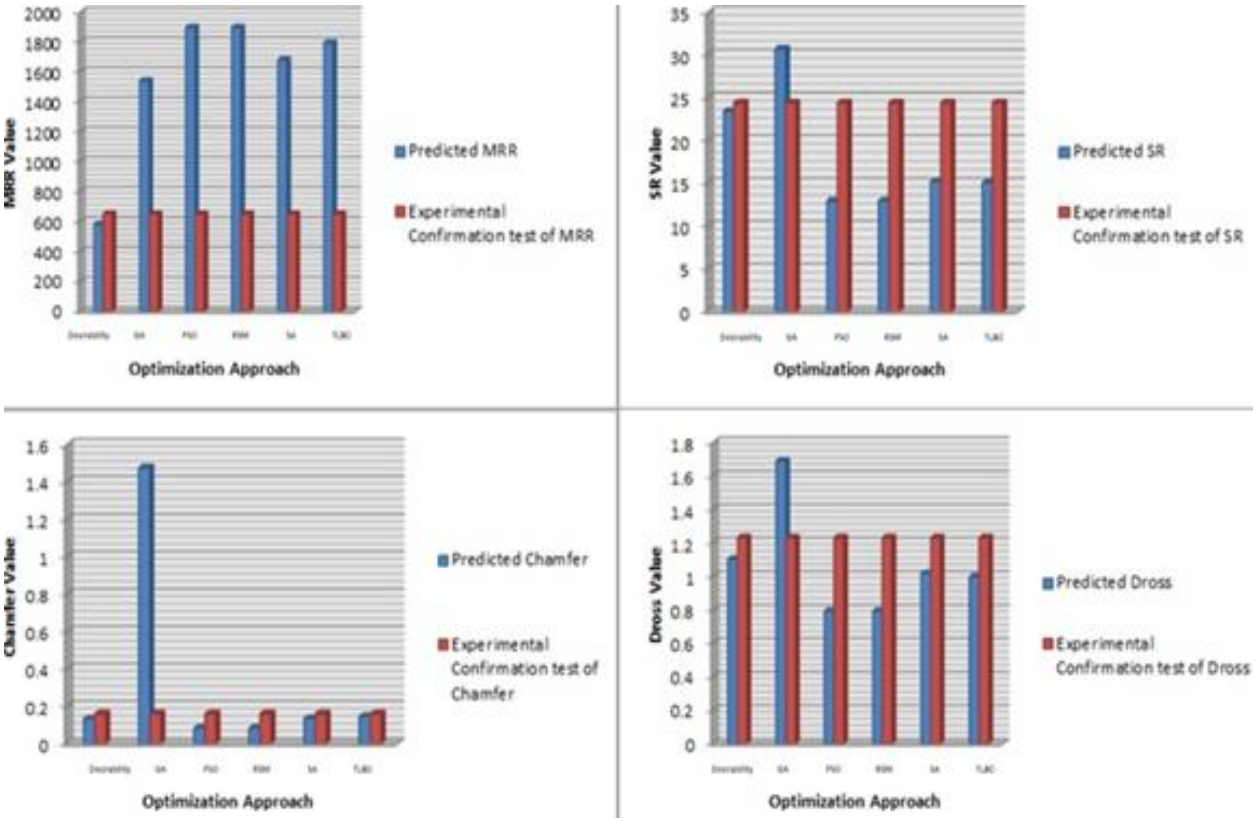

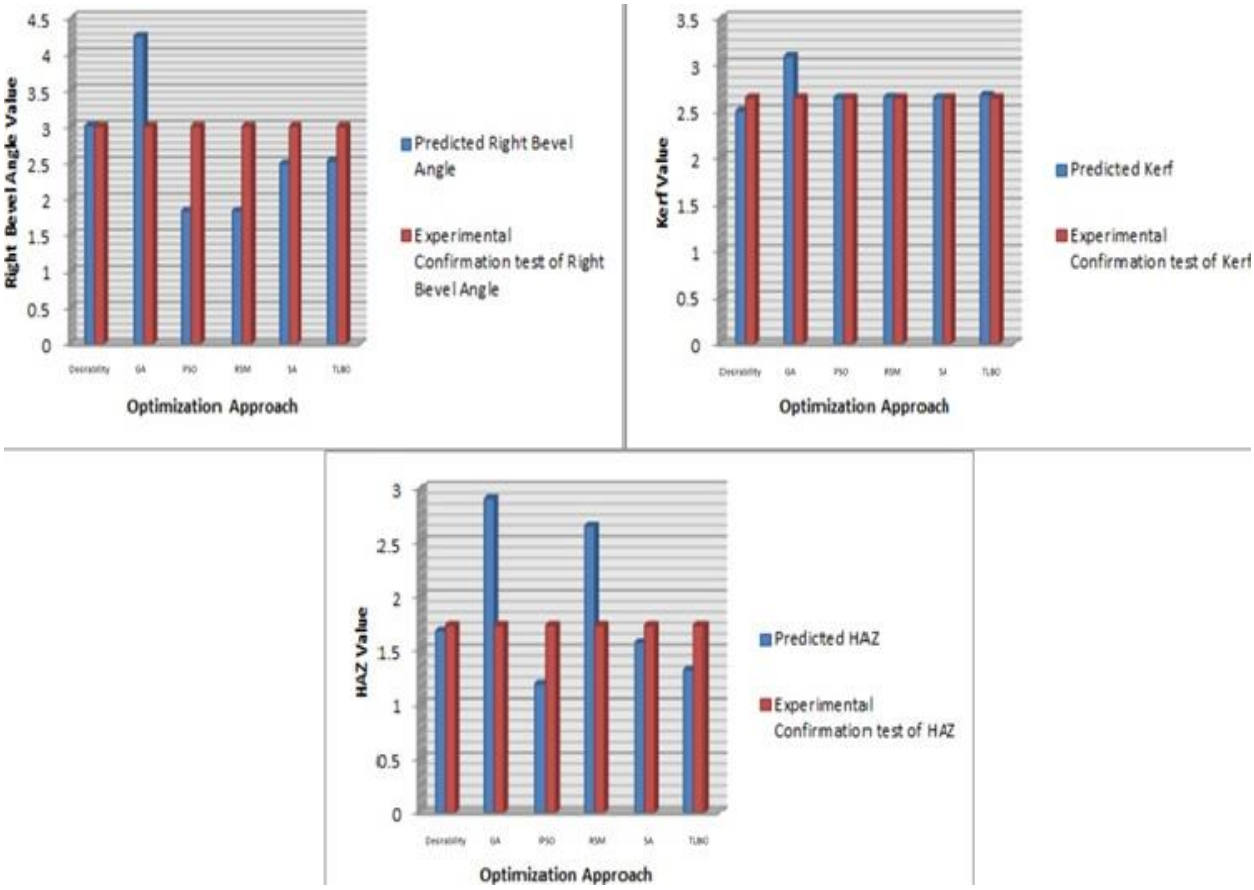

Fig. 275 Comparison of approaches in third phase

The comparison of all approaches for PAC in three different phases of experimentation is tabulated in Tables 83, 84 and 85 respectively. From these tables, it may be noted that there is good agreement between the predicted values and the experimental values for each response in various optimization approaches. Similarly, the comparison plots of optimization techniques on PAC process are plotted in Fig.s 273, 274 and 275 respectively. From the above descriptive analysis, evidently the best design is becoming one primary challenge of technology market. In this paper, the optimal values of process parameters have been numerically found out using the quadratic model of RSM. Since time and cost are comprised while operating the experimental runs, it is relevant to reduce the number of runs while not compromising the quality goals [41].

In 4th phase, confirmation testing is a necessary in final step in Taguchi optimization methodology. Once the optimal combination of Oxy-fuel gas cutting parameters is selected, it is needed to predict and verify the expected response through the confirmation experiments. However, there is no need to run the confirmation test if the optimal Oxy-fuel gas cutting parameter combination is already included in the OA. It can be found that the optimal Oxy-fuel gas cutting levels combination ($A_3B_1C_1$) was not included in the experiment matrix (Table 86). The predicted S/N ratio using the optimal levels of the design factors ($\hat{\eta}_{opt}$) can be calculated as [111]:

$$\hat{\eta}_{opt} = \bar{\eta} + \sum_{i=1}^{p} (\bar{\eta}_{i,opt} - \bar{\eta}) \tag{30}$$

where $\bar{\eta}_{i,opt}$ is the mean S/N ratio for i[th] parameter at the optimal level, p is the number of parameters that significantly affect the quality characteristic. In order to statistically judge the closeness of the predicted ($\bar{\eta}_{i,opt}$) and observed value of S/N ratio (η_{obs}), the k (CIs) were determined. The CI is given by:

$$CI = \sqrt{F_{\alpha;1,\vartheta_e} V_{error} \left[\left(\frac{1}{n_{eff}}\right) + \left(\frac{1}{r}\right)\right]} \tag{31}$$

where $F_{\alpha;1,\vartheta_e}$=18.51 is the F value from statistic table at a 95 % confidence level, ϑ_e=2 is the degrees of freedom for the error, $Verror$=0.5623 is the mean square of error, r=3 is the validation test trial number, and n_{eff} is defined as:

$$n_{eff} = \frac{N}{1 + \vartheta_{total}} \tag{32}$$

where N=9 is the total number of experiments and ϑ_{total}=6 is the total degrees of freedom of all parameters. By substituting these values in Equation 32, n_{eff} value obtained as 1.2857. Similarly CI is obtained as 3.40069 by using Equation 31. If the difference between $\hat{\eta}_{opt}$ and η_{obs} is within the CI value, then the optimum Oxy-fuel

cutting parameter level combinations are valid. Table 87 shows the results of relative efficiency at optimal settings of process parameters. It can be observed that the calculated values of the prediction errors are within the 95 % confidence interval from Table 87.

Table 86 Confirmatory Test Results for Relative Efficiency

No. of experiment	Nozzle speed (m/min)	Torch height (mm)	Oxy-fuel speed (mm/min)	Relative efficiency
1	2	2	450	0.7346
2	2	2	450	0.7189
3	2	2	450	0.7197

Table 87 Analysis of Confirmatory Test

Performance Characteristics	Optimal Setting level	Predicted optimal values	95 % confidence interval	Actual confirmation experimental value
S/N Ratio	A3-B1-C1	0.19942	-3.20127<η_{obs}<3.60011	-2.80043

Chapter 6

CONCLUSION AND SCOPE FOR FUTURE

6 CONCLUSION AND SCOPE FOR FUTURE

6.1 Conclusions

This work furnishes the findings of an experimental investigation on the effect of feed rate, cutting current, cutting speed, gas pressure, voltage and torch height on the characteristic of cut while machining AISI 4140 and AISI 304 stainless steel by plasma arc. Response surface methodology (RSM), desirability function, genetic algorithm (GA), particle swarm optimization (PSO), simulated annealing (SA) and teaching learning based optimization (TLBO) algorithm approaches have been carried out to find optimal condition of input factors on cut attributes of PAC operation. These methodologies are applied as single-objective criteria for each case. A novel approach of response surface method coupled with grey relational analysis and principal component analysis has been carried out to optimize plasma arc cutting processes with multi-objective criteria. The shortened quadratic models developed using the combinatorial plea of RSM and grey relational analysis (GRA) with principle component analysis (PCA) were reasonably accurate and can be used for prediction within the limits of the factors investigated. In the third case, a portable plasma cutting machine is renovated with automatic heating arrangement. The experiments have been conducted to produce slots using L_{27} orthogonal array based on Box-Behnken design. The different responses such as material removal rate, surface roughness, right bevel angle, chamfer, dross, kerf width and heat affected zone are measured in order to determine optimum setting of process parameters. The logic behind the application of various optimization techniques is to compare the results of output responses on input variables. The comparison of the seven optimization methods in plasma arc cutting is not carried out till now. In this present work, the noble advanced

optimization methodologies are applied to optimize the responses of the plasma arc cutting process by taking different design of experiment and optimization techniques on different output variables of plasma arc cutting process.

The conclusions based on the assignment of optimizing process parameters of PAC and Oxy-fuel machining is summarized as follows:

a) The main aim of the optimization process in this project was to study the influence of the machining variables that lead to satisfaction of different conflicting objectives such as material removal rate (MRR) has to be maximized while other responses should be minimized. The single objective as well as multi-objective optimization for output responses has been carried out to achieve the desired optimal settings.

b) The regression coefficient results imply that the predicted and experimental values are in good agreement and the adequacy of the model for cut quality responses of plasma arc cutting process.

c) TLBO approach has been proposed lately as population arranged meta-heuristic optimization technique for tackling optimization issues. Both statistical and nature inspired meta-heuristic approaches are applied on plasma arc cutting process in this study.

d) From results, it was concluded that the use of the hybrid RSM based GRA-PCA and TLBO algorithm which can efficiently search the process parameters for finding optimal machining conditions. Hence, both approaches can be successfully applied as fitting methodology for enhancing the cut quality for industries.

e) Material removal rate (MRR) and surface roughness (SR) responses were best optimized by desirability approach among all the techniques approached according to Box-Behnken design (BBD) with L_{27} orthogonal array. The maximum MRR (0.598497 mm^3/min) was achieved in feed rate = 1000 mm/min, cutting current = 50 ampere, voltage = 150 volt, torch height = 3 mm, and minimum surface roughness (8.108 μm) was achieved in feed rate = 900 mm/min, cutting current = 50 ampere, voltage = 150 volt, torch height = 3 mm utilizing desirability approach. Hence, desirability and RSM approach might be considered for better optimization of MRR and SR respectively.

f) The maximum MRR (30207.2 mm^3/min) was observed equal value in feed rate = 920 mm/min, cutting current = 40 ampere, voltage = 100 volt, torch height = 2 mm using GA and PSO technique. Hence, considering central composite design of L_{30} orthogonal array, GA and PSO approaches gave best optimal results for MRR where as RSM approach contributed the best optimum results for other responses. So, RSM approach might be chosen for better optimization methodology in minimizing responses of PAC process.

g) The maximum MRR (582.20 mm^3/min) was attained equal value in cutting current = 133.08 ampere, cutting speed = 3.6738 mm/s, gas pressure = 21.1161 L/min, stand-off Gap = 3.8056 mm employing RSM technique. RSM approach showed better acceptable results to all responses except MRR whereas both GA and PSO approaches illustrated constant outcome of objective function when BBD with L_{27} orthogonal array was considered.

h) From these three types of layouts on PAC, PSO approach showed the acceptable optimum results for maximizing the MRR response whereas, for minimization of responses such as chamfer, surface roughness and kerf, TLBO approach gave the best optimal results with minimum iterations among all the approaches.

i) Data envelope analysis coupled with Taguchi's optimization technique revealed that nozzle speed was the most influencing parameter in the computer numerical controlled Oxy-fuel gas cutting process as it contributes 51.6639 % towards experiment, which is the maximum as compared to other parameters. The best possible optimum condition of this process is at 2 m/min of nozzle speed, 2.0 mm of torch height and 450 mm/min of Oxy-fuel speed.

j) All confirmatory test results were found in agreement with those of predicted values of the cut responses in the PAC as well as Oxy-fuel gas cutting.

6.2 Scope for Future Work

The following suggestions may be considered to research work in future.

a) Similar kind of comparative study on any machining process can be carried out for optimizing its process parameters.

b) Experimental investigation of plasma machining of other steels can be carried out.

c) Finite element modelling of the plasma arc cutting operation can be carried out to determine temperature distribution.

7 REFERENCES

[1] Hatala M., Orlovský I. Mathematical modelling of plasma arc cutting technological process.

[2] Ramachandran M., Reddy R. G. Thermal plasma synthesis of SiC. *Advances in Manufacturing*, 1 (1) (2013): 50-61.

[3] Rana K., Kaushik P., Chaudhary S. Optimization of plasma arc cutting by applying Taguchi Method. *International Journal of Enhanced Research in Science Technology & Engineering, ISSN* (2013): 2319-7463.

[4] Asiabanpour B., Vejandla D. T., Novoa C., Jimenez J., Fischer R. Optimizing the quality of parts manufactured by the automated plasma cutting process using response surface methodology. *20th Annual International Solid Freeform Fabrication Symposium, SFF 2009* (2009): 47-60.

[5] Aggarwal A., Singh H. Optimization of machining techniques—a retrospective and literature review. *Sadhana*, 30 (6) (2005): 699-711.

[6] Cantoro G., Colombo V., Concetti A., Ghedini E., Sanibondi P., Zinzani F., Rotundo F., Dallavalle S., Vancini M. Plasma arc cutting technology: Simulation and experiments. *11th European Conference on High-Technology Plasma Processes, HTPP 11, June 27, 2010 - July 2, 2010*, 275 (2011). doi:10.1088/1742-6596/275/1/012008.

[7] Colombo V., Concetti A., Ghedini E., Gherardi M., Sanibondi P., Boselli M., Cantoro G. High-speed imaging in pac: multiple view and tomographic reconstruction of pilot arcing transients. *IEEE Transactions on Plasma Science*, 39 (11) (2011): 2916-2917. doi:10.1109/TPS.2011.2146795.

[8] Bhuvenesh R., Saifuldin M. Surface roughness and MRR effect on manual plasma arc cutting machining. (2012).

[9] Kechagias J., Billis M., Maropoulos S. A parameter design of CNC plasma-arc cutting of carbon steel plates using robust design. *International Journal of Experimental Design and Process Optimisation*, 1 (4) (2010): 315-326.

[10] Madić M., Radovanović M. Modeling and analysis of correlations between cutting parameters and cutting force components in turning AISI 1043 steel using ANN. *Journal of the Brazilian Society of Mechanical Sciences and Engineering*, 35 (2) (2013): 111-121. doi:10.1007/s40430-013-0012-3.

[11] Makadia A. J., Nanavati J. Optimisation of machining parameters for turning operations based on response surface methodology. *Measurement*, 46 (4) (2013): 1521-1529.

[12] YUN K.-M., NA S.-J. Real-time control of the plasma arc cutting process by using intensity measurements of ejected plasma. *Welding Journal*, 70 (2) (1991): 43s-48s.

[13] Zhang Y., Zhang S. Observation of the keyhole during plasma arc welding. *Welding Journal-New York*, 78 (1999): 53-s.

[14] Ferreira P., Melo I., Gonçalves-Coelho A., Mourão A. Plasma cutting optimization by using the response surface methodology. *The annals of "DUNĂREA DE JOS" university of Galati fascicle V, technologies in machine building, ISSN* (2009): 1221-4566.

[15] Hatala M., Zajac J., Cep R., Orlovsky I. Research of the technological parameters importance for plasma arc thermal cutting. *2nd International Conference on*

Mechanical and Aerospace Engineering, ICMAE 2011, July 29, 2011 - July 31, 2011, 110-116 (2012): 3742-3749. doi:10.4028/www.scientific.net/AMM.110-116.3742.

[16] Schitsin Y. D., Kuchaev P., Schitsin V. Y. Plasma cutting of metals with reversed polarity and mixed supply of gases. *Welding International*, 27 (11) (2013): 890-892.

[17] Çelik Y. H. Investigating the effects of cutting parameters on materials cut in CNC plasma. *Materials and Manufacturing Processes*, 28 (10) (2013): 1053-1060. doi:10.1080/10426914.2013.773015.

[18] Chakravarty D., Gokhale H., Sundararajan G. Optimizing mechanical properties of spark plasma sintered ZTA using neural network and genetic algorithm. *Materials Science and Engineering: A*, 529 (2011): 492-496.

[19] Bober P. Comparison of different approaches to the cutting plan scheduling. *Quality Innovation Prosperity*, 15 (1) (2011): 47-56.

[20] Lee M.-K., Kwon K.-B. Cutting path optimization in CNC cutting processes using a two-step genetic algorithm. *International Journal of Production Research*, 44 (24) (2006): 5307-5326.

[21] Keraita J. N., Kim K.-H., Stalin N., Prabhu H., Tahera K., Ibrahim R., Lochert P., Alfegi E. M. A., Sopian K., Othman M. Y. H. PC-based low-cost CNC automation of plasma profile cutting of pipes. (2006).

[22] Mikkelsen K. An Experimental investigation of ignition propensity of hot work processes in the nuclear industry. (2014).

[23] Gullu A., Atici U. Investigation of the effects of plasma arc parameters on the structure variation of AISI 304 and St 52 steels. *Materials & Design*, 27 (10) (2006): 1157-1162. doi:http://dx.doi.org/10.1016/j.matdes.2005.02.014.

[24] Ozek C., Caydas U., Unal E. A fuzzy model for predicting surface roughness in plasma arc cutting of AISI 4140 steel. *Materials and Manufacturing Processes*, 27 (1) (2012): 95-102. doi:10.1080/10426914.2011.551952.

[25] Kim S.-I., Kim M.-H. Evaluation of cutting characterization in plasma cutting of thick steel ship plates. *International Journal of Precision Engineering and Manufacturing*, 14 (9) (2013): 1571-1575. doi:10.1007/s12541-013-0212-x.

[26] Boselli M., Colombo V., Ghedini E., Gherardi M., Rotundo F., Sanibondi P. High-speed imaging investigation of transient phenomena impacting plasma arc cutting process optimization. *Journal of Physics D: Applied Physics*, 46 (22) (2013): 224010.

[27] Saravanakumar D., Mohan B., Muthuramalingam T. Application of response surface methodology on finding influencing parameters in servo pneumatic system. *Measurement*, 54 (2014): 40-50.

[28] Ye L., Yang M., Xu L., Guo C., Li L., Wang D. Optimization of inductive angle sensor using response surface methodology and finite element method. *Measurement*, 48 (2014): 252-262.

[29] Asiltürk I., Neşeli S. Multi response optimisation of CNC turning parameters via Taguchi method-based response surface analysis. *Measurement*, 45 (4) (2012): 785-794.

[30] Neşeli S., Yaldız S., Türkeş E. Optimization of tool geometry parameters for turning operations based on the response surface methodology. *Measurement*, 44 (3) (2011): 580-587.

[31] Sankar P. A., Machavaram R., Shankar K. System identification of a composite plate using hybrid response surface methodology and particle swarm optimization in time domain. *Measurement*, 55 (2014): 499-511.

[32] Özek C., Çaydaş U., Ünal E. A Fuzzy model for predicting surface roughness in plasma arc cutting of AISI 4140 steel. *Materials and Manufacturing Processes*, 27 (1) (2012): 95-102. doi:10.1080/10426914.2011.551952.

[33] Kafali M., Ozkok M., Cebi S. Evaluation of pipe cutting technologies in shipbuilding. *Brodogradnja*, 65 (2) (2014): 35-51.

[34] G T., Ivanov M. S. T., Kamberov M. S. K., Romanov M. S. B. Modular conception for high speed cutting machines using laser, plasma or water jet technologies. *VIII International Congress Machines, Technologies, Materials 2011*, 2 (8) (2011): 32-36.

[35] Hung J.-C., Liu H.-K., Chang Y.-S., Hung K.-E., Liu S.-J., Chen H.-Y., Chen P.-Y. Development of electrode insulation layer by using oxygen plasma surface treatment for electrochemical microdrilling. *Procedia CIRP*, 14 (2014): 345-348.

[36] Krajcarz D. Comparison metal water jet cutting with laser and plasma cutting. *Procedia Engineering*, 69 (2014): 838-843.

[37] Zheng M., Zeng M., Jiang C., Chen J., Li S., Wang J. Plasma kinetic resection of prostate combined terazosin for treatment of BPH patient with coexisting hypertension. *Open Journal of Urology*, 4 (05) (2014): 57.

[38] King D. S., Hilmas G. E., Fahrenholtz W. G., Garay J. Plasma arc welding of TiB2-20 vol% TiC. *Journal of the American Ceramic Society*, 97 (1) (2014): 56-59. doi:10.1111/jace.12693.

[39] Bhuvenesh R., Saifuldin M. Surface roughness and MRR effect on manual plasma arc cutting machining. *World Academy of Science, Engineering and Technology*, 6 (2012): 465-468.

[40] Wu C., Wang H., Zhang Y. A new heat source model for keyhole plasma arc welding in FEM analysis of the temperature profile. *Welding Journal-New York*, 85 (12) (2006): 284.

[41] u W., Fang J., Lu Y. Study on ceramic cutting by plasma arc. *Journal of Materials Processing Technology*, 129 (1) (2002): 152-156.

[42] Senthilkumar C., Ganesan G., Karthikeyan R. Parametric optimization of electrochemical machining of Al/15% SiCp composites using NSGA-II. *Transactions of Nonferrous Metals Society of China*, 21 (10) (2011): 2294-2300. doi:10.1016/s1003-6326(11)61010-8.

[43] Dahil L., Dahil İ., Karabulut A. Comparison of advanced cutting techniques on hardox 500 steel material and the effect of structural properties of the material. *Metalurgija*, 53 (3) (2014): 291-294.

[44] Dahil L., Dahil İ. Comparison of heat effects associated with metal cutting method on ST 37 alloy steel. *Metalurgija*, 53 (2) (2014): 235-238.

[45] Salonitis K., Vatousianos S. Experimental investigation of the plasma arc cutting process. *45th CIRP Conference on Manufacturing Systems, CMS 2012, May 16, 2012 - May 18, 2012*, 3 (2012): 287-292. doi:10.1016/j.procir.2012.07.050.

[46] Kumar A., Kumar V., Kumar J. Semi-empirical model on MRR and overcut in WEDM process of pure titanium using multi-objective desirability approach. *Journal of the Brazilian Society of Mechanical Sciences and Engineering* (2014): 1-33. doi:10.1007/s40430-014-0208-1.

[47] Ghodsiyeh D., Golshan A., Izman S. Multi-objective process optimization of wire electrical discharge machining based on response surface methodology. *Journal of the Brazilian Society of Mechanical Sciences and Engineering*, 36 (2) (2014): 301-313. doi:10.1007/s40430-013-0079-x.

[48] Madić M., Radovanović M., Manić M., Trajanović M. Optimization of ANN models using different optimization methods for improving CO_2 laser cut quality characteristics. *Journal of the Brazilian Society of Mechanical Sciences and Engineering*, 36 (1) (2014): 91-99. doi:10.1007/s40430-013-0054-6.

[49] Reddy V. V., Kumar A., Valli P. M., Reddy C. Influence of surfactant and graphite powder concentration on electrical discharge machining of PH17-4 stainless steel. *Journal of the Brazilian Society of Mechanical Sciences and Engineering* (2014): 1-15. doi:10.1007/s40430-014-0193-4.

[50] Lal S., Kumar S., Khan Z. A., Siddiquee A. N. Wire electrical discharge machining of AA7075/SiC/Al2O3 hybrid composite fabricated by inert gas-assisted electromagnetic stir-casting process. *Journal of the Brazilian Society of Mechanical Sciences and Engineering*, 36 (2) (2014): 335-346. doi:10.1007/s40430-013-0087-x.

[51] Molchanova Y. S., Bychkov N. A., Chernyayev S. I. Producing orifices in structural materials by plasma, waterjet and laser cutting and piercing. *Welding International*, 29 (2) (2015): 161-164. doi:10.1080/09507116.2014.897812.

[52] Zhu J., Sun Z., Li Z., Ehn A., Alden M., Salewski M., Leipold F., Kusano Y. Dynamics, OH distributions and UV emission of a gliding arc at various flow-rates investigated by optical measurements. *Journal of Physics D: Applied Physics*, 47 (29) (2014). doi:10.1088/0022-3727/47/29/295203.

[53] Zhang N., Shi N., He M., Yang F., Chen H. Study on wear behavior of plasma arc cladding of tunneling machine pick. *2014 3rd International Conference on Material Science, Environment Science and Computer Science, MSESCS 2014, January 11, 2014 - January 12, 2014*, 886 (2014): 105-108. doi:10.4028/www.scientific.net/AMR.886.105.

[54] Zhang B., Cheng J., Xu B. (CuCoCrFeNi)95B5 high-entropy alloy coatings prepared by plasma transferred arc cladding process. *Xiyou Jinshu Cailiao Yu Gongcheng/Rare Metal Materials and Engineering*, 43 (5) (2014): 1128-1132.

[55] Xu W., Huang S., Chen F., Song J., Liu X. Diamond wear properties in cold plasma jet. *Diamond and Related Materials*, 48 (0) (2014): 96-103. doi:http://dx.doi.org/10.1016/j.diamond.2014.07.008.

[56] Xiaojie T., Yonghong L., Baoping C., Rongju L., Zengkai L., Pengfei S. Experimental investigation on electric arc cutting process for casing. *Materials and Manufacturing Processes*, 29 (2) (2014): 166-174. doi:10.1080/10426914.2013.872255.

[57] Weglowski M. S., Pfeifer T. Influence of cutting technology on properties of the cut edges. *Advances in Manufacturing Science and Technology*, 38 (2) (2014): 63-73. doi:10.2478/amst-2014-0011.

[58] Wang Z., Fang X., Zhang X., Feng Y. Research on a 50kW digital inverter type plasma cutting power supply. *China Welding (English Edition)*, 23 (2) (2014): 51-56.

[59] Vereshchago Y. N., Kostyuchenko V. I. A physical-mathematical model of the power circuit of a plasma torch. *Welding International*, 28 (2) (2014): 133-139. doi:10.1080/09507116.2013.796664.

[60] Tian X., Liu Y., Cai B., Lin R., Liu Z., Sun P. Experimental investigation on electric arc cutting process for casing. *Materials and Manufacturing Processes*, 29 (2) (2014): 166-174. doi:10.1080/10426914.2013.872255.

[61] Thiébaud R., Drezet J.-M., Lebet J.-P. Experimental and numerical characterisation of heat flow during flame cutting of thick steel plates. *Journal of Materials Processing Technology*, 214 (2) (2014): 304-310. doi:http://dx.doi.org/10.1016/j.jmatprotec.2013.09.016.

[62] Tezuka M., Nakamura Y., Iwai H., Sano K., Fukui Y. The development of thermal and mechanical cutting technology for the dismantlement of the internal core of Fukushima Daiichi NPS. *Journal of Nuclear Science and Technology*, 51 (7-8) (2014): 1054-1058. doi:10.1080/00223131.2014.912969.

[63] Sun Q., Chen L., Chen G., Wang H. A novel composite control strategy for plasma cutting power supply based on arc control. *Hanjie Xuebao/Transactions of the China Welding Institution*, 35 (3) (2014): 71-75.

[64] Prevosto L., Kelly H. Diagnostics of cutting arc plasmas. *15th International Congress on Plasma Physics (ICPP 2010) and 13th Latin American Workshop on Plasma Physics (LAWPP 2010), 8-13 Aug. 2010*, 511 (2014): 012065 (012066 pp.). doi:10.1088/1742-6596/511/1/012065.

[65] Nemchinsky V. Erosion of thermionic cathodes in welding and plasma arc cutting systems. *Plasma Science, IEEE Transactions on*, 42 (1) (2014): 199-215. doi:10.1109/TPS.2013.2287794.

[66] Mancinelli B. R., Minotti F. O., Prevosto L., Kelly H. Numerical investigation of the double-arcing phenomenon in a cutting arc torch. *Journal of Applied Physics*, 116 (2) (2014): 023301 (023308 pp.). doi:10.1063/1.4887490.

[67] Kavka T., Tossen S., Maslani A., Konrad M., Pauser H., Stehrer T. Experimental investigation of energy balance in plasma arc cutting process. *15th International Congress on Plasma Physics (ICPP 2010) and 13th Latin American Workshop on Plasma Physics (LAWPP 2010), 8-13 Aug. 2010*, 511 (2014): 012067 (012066 pp.). doi:10.1088/1742-6596/511/1/012067.

[68] Jiajian Z., Zhiwei S., Zhongshan L., Ehn A., Alden M., Salewski M., Leipold F., Kusano Y. Dynamics, OH distributions and UV emission of a gliding arc at various flow-rates investigated by optical measurements. *Journal of Physics D: Applied Physics*, 47 (29) (2014): 295203 (295211 pp.). doi:10.1088/0022-3727/47/29/295203.

[69] Ismail M. I. S., Taha Z. Surface hardening of tool steel by plasma arc with multiple passes. *International Journal of Technology*, 5 (1) (2014): 79. doi:10.14716/ijtech.v5i1.156.

[70] Guo C. T., Ueng H. Y. Improved in dry routing performance with optimized diamond-like carbon films. *Vacuum*, 107 (2014): 304-310. doi:10.1016/j.vacuum.2014.03.012.

[71] Gruber J., onski J., Hlina J. Diagnostics of cathode material loss in cutting plasma torch. *Journal of Physics D: Applied Physics*, 47 (29) (2014). doi:10.1088/0022-3727/47/29/295201.

[72] Farahnakian M., Razfar M. R. Experimental study on hybrid ultrasonic and plasma aided turning of hardened steel AISI 4140. *Materials and Manufacturing Processes*, 29 (5) (2014): 550-556. doi:10.1080/10426914.2014.892612.

[73] Emmelmann C., Kozakov R., Petri N., Schopp H., Steinmeier O. Plasma hybrid welding with an integrated laser and sensor equipment. *Welding and Cutting*, 13 (2) (2014): 116-121.

[74] Das M. K., Kumar K., Barman T. K., Sahoo P. Optimization of MRR and surface roughness in PAC of EN 31 steel using weighted principal component analysis. *Procedia Technology*, 14 (2014): 211-218.

[75] Yoshihiro Y., Yusuke K., Takeru I., Yoshihiko U., Yasunori T., Tatsuo I. Experimental study of magnetic arc blow for plasma arc cutting. *Yosetsu Gakkai Ronbunshu/Quarterly Journal of the Japan Welding Society*, 31 (3) (2013): 193-200. doi:10.2207/qjjws.31.193.

[76] Akkurt A. Surface properties of the cut face obtained by different cutting methods from AISI 304 stainless steel materials. *Indian Journal of Engineering and Materials Sciences*, 16 (6) (2009): 373.

[77] Adelmann B., Hellmann R. Fast laser cutting optimization algorithm. *Physics Procedia*, 12 (2011): 591-598.

[78] Zhou B., Liu Y.-j., Tan S.-K. Efficient simulation of oxygen cutting using a composite heat source model. *International Journal of Heat and Mass Transfer*, 57 (1) (2013): 304-311.

[79] Chen S.-L. The effects of high-pressure assistant-gas flow on high-power CO< sub> 2</sub> laser cutting. *Journal of Materials Processing Technology*, 88 (1) (1999): 57-66.

[80] Ahmadi B., Torkamany M., Jaleh B., Sabaghzadeh J. Theoretical comparison of oxygen assisted cutting by CO_2 and Yb: YAG fiber lasers. *Chinese Journal of Physics*, 47 (4) (2009): 465-475.

[81] Revercomb H., Mason E. A. Theory of plasma chromatography/gaseous electrophoresis. Review. *Analytical Chemistry*, 47 (7) (1975): 970-983.

[82] Eliezer S., Eliezer Y. (2001). *The fourth state of matter: an introduction to plasma science*: CRC Press.

[83] http://strport.ru/instrumenty/printsip-raboty-plazmoreza.

[84] Tripathi D. Solar Physics and Solar System. (2013).

[85] Bouvier M., Braun A., Diels J.-C., Mourou G., Zhao X. M. Apparatus and method for enabling the creation of multiple extended conduction paths in the atmosphere. (1998).

[86] https://www.pinterest.com/laurarbailey/awesome-weather/.

[87] Moarrefzadeh A. Numerical analysis of thermal profile in plasma arc cutting.

[88] Snoeys R., Staelens F., Dekeyser W. Current trends in non-conventional material removal processes. *CIRP Annals-Manufacturing Technology*, 35 (2) (1986): 467-480.

[89] Radovanovic M., Jankovic P., Madic M. Estimate of cutting data by laser cutting, abrasive water jet cutting and plasma cutting.

[90] Hendricks B. R. (1999). *Simulation of plasma arc cutting.*

[91] Vora F. R., Trivedi J. H. CNC profile gas cutting machine – application with nesting software and computer aided programming mechanism. *National Conference on Recent Trends in Engineering & Technology* (2011): 1-4.

[92] Hull F. Delta ferrite and martnesite formation in stainless steels. *Welding Journal*, 52 (5) (1973): 193.

[93] Rao K. S. R. K., Praveena K. Manufacturing of Incoloy-800 tubes nuclear steam generator tubes. *IJSEAT*, 2 (9) (2014): 426-431.

[94] New W. S. Encyclopedia> Stainless steel.

[95] Jeffus L. F. (2002). *Welding: principles and applications*: Cengage Learning.

[96] Gopalakannan S., Senthilvelan T. Application of response surface method on machining of Al–SiC nano-composites. *Measurement*, 46 (8) (2013): 2705-2715.

[97] Del Castillo E., Montgomery D. C., McCarville D. R. Modified desirability functions for multiple response optimization. *Journal of quality technology*, 28 (1996): 337-345.

[98] Khan Z., Prasad B., Singh T. Machining condition optimization by genetic algorithms and simulated annealing. *Computers & Operations Research*, 24 (7) (1997): 647-657.

[99] Vasan A., Raju K. S. Comparative analysis of simulated annealing, simulated quenching and genetic algorithms for optimal reservoir operation. *Applied Soft Computing*, 9 (1) (2009): 274-281. doi:http://dx.doi.org/10.1016/j.asoc.2007.09.002.

[100] Zhang W.-w., Cheng L.-l., Xue H. Research on adjusting height system in NC plasma cutting machine based on complex genetic algorithm. *Modular Machine Tool & Automatic Manufacturing Technique* (10) (2011): 64-68.

[101] Kaya N. Machining fixture locating and clamping position optimization using genetic algorithms. *Computers in Industry*, 57 (2) (2006): 112-120.

[102] Rao R., Savsani V., Vakharia D. Teaching–learning-based optimization: an optimization method for continuous non-linear large scale problems. *Information Sciences*, 183 (1) (2012): 1-15.

[103] Podinovski V. V., Bouzdine-Chameeva T. Weight restrictions and free production in data envelopment analysis. *Operations Research*, 61 (2) (2013): 426-437.

[104] Adler N., Friedman L., Sinuany-Stern Z. Review of ranking methods in the data envelopment analysis context. *European Journal of Operational Research*, 140 (2) (2002): 249-265.

[105] Kechagias J., Pappas M., Karagiannis S., Petropoulos G., Iakovakis V., Maropoulos S. An ANN approach on the optimization of the cutting parameters during CNC plasma-arc cutting. *ASME 2010 10th Biennial Conference on Engineering Systems Design and Analysis, ESDA2010, July 12, 2010 - July 14, 2010*, 4 (2010): 643-649. doi:10.1115/ESDA2010-24225.

[106] Kadirgama K., Noor M., Harun W., Aboue-El-Hossein K. Optimisation of heat affected zone by partial swarm optimisation in air plasma cutting operation. *Journal of Scientific & Industrial Research*, 69 (2010): 439-443.

[107] Salonitis K., Vatousianos S. Experimental Investigation of the plasma arc cutting process. *Procedia CIRP*, 3 (0) (2012): 287-292. doi:http://dx.doi.org/10.1016/j.procir.2012.07.050.

[108] Kumar A., Sahu J., Datta S., Mahapatra S. S. DEA based Taguchi approach for multi-objective optimization in machining polymers: A case study. (2012).

[109] Motorcu A. R., Kus A., Durgun I. The evaluation of the effects of control factors on surface roughness in the drilling of Waspaloy superalloy. *Measurement*, 58 (0) (2014): 394-408. doi:http://dx.doi.org/10.1016/j.measurement.2014.09.012.

[110] Kıvak T. Optimization of surface roughness and flank wear using the Taguchi method in milling of Hadfield steel with PVD and CVD coated inserts. *Measurement*, 50 (0) (2014): 19-28. doi:http://dx.doi.org/10.1016/j.measurement.2013.12.017.

[111] Madić M. J., Radovanović M. R. Identification of the robust conditions for minimization of the HAZ and burr in CO_2 laser cutting. *FME Transactions*, 41 (2) (2013): 130-137.

8 APPENDIX

Regression equations used for optimization

1. Case 1

$$MRR=39.24466-0.06972*A+0.00004*A^2-0.23532*B+0.00193*B^2+0.02407*C-0.00010*C^2-2.53113*D+0.20244*D^2+0.00045*A*D-0.00004*B*C+0.02986*B*D+0.00021*C*D \quad (33)$$

$$SR=220.9933-0.1877*A-5.8032*B+0.0138*B^2-0.0611*C+0.0003*C^2+13.9617*D+1.7333*D^2+0.0045*A*B-0.0003*A*C-0.0209*A*D+0.0044*B*C-0.1120*B*D+0.0280*C*D \quad (34)$$

$$RBA=-72.0417+0.0867*A-0.0001*A^2+2.1833*B-0.0300*B^2-0.1033*C-10.0000*D-0.6250*D^2+0.0050*A*D+0.0020*B*C+0.1500*B*D+0.0100*C*D \quad (35)$$

2. Case 2

$$MRR=318525.8-374.3*A-4590.7*B+7.4*B^2-281.2*C+0.1*C^2-17133.5*D-244.5*D^2+4.6*A*B+0.4*A*C+20.6*A*D-3.0*B*C-29.1*B*D+0.6*C*D \quad (36)$$

$$SR=7607.658-13.943*A+0.007*A^2-65.456*B+0.060*B^2-0.183*C-0.008*C^2+356.262*D+6.566*D^2+0.050*A*B-0.363*A*D+0.077*B*C+1.007*B*D-0.705*C*D \quad (37)$$

$$Chamfer=-68.8627+0.0820*A+0.7669*B-0.0088*B^2-0.0729*C+15.9909*D-0.3004*D^2+0.0003*A*B+0.0001*A*C-0.0102*A*D-0.0001*B*C-0.1215*B*D+0.0041*C*D \quad (38)$$

$$Dross=39.7616+0.2251*A-0.0004*A^2-2.5780*B-0.0711*B^2-0.7803*C+0.0002*C^2-14.2625*D-1.5983*D^2+0.0072*A*B+0.0013*A*C-0.0080*A*D-0.0078*B*C+0.9650*B*D-0.0843*C*D \quad (39)$$

$$Kerf=25.33838-0.15097*A+0.00015*(1)^2+2.42007*B+0.01090*B^2+0.12379*C-0.00010*C^2-5.07050*D+0.10250*D^2-0.00362*A*B-0.00011*A*C+0.00740*A*D+0.00050*B*C-0.02200*B*D-0.00887*C*D \quad (40)$$

3. Case 3

$$MRR=1665.937-19.345*A+0.003*A^2+843.381*B+6.850*B^2+13.781*C+5.289*C^2-275.352*D+149.412*D^2+0.820*A*B+0.041*A*C+3.680*A*D-17.083*B*C-190.275*B*D-48.332*C*D \quad (41)$$

$$SR=60.5500-0.3844*A+0.0005*A^2+6.0058*B-0.2237*B^2-0.2975*C+0.0371*C^2-11.9817*D+3.1750*D^2+0.0022*A*B+0.0045*A*C+0.0348*A*D+0.0967*B*C-1.2000*B*D-0.6283*C*D \quad (42)$$

$$Chamfer=0.093333-0.005800*A+0.000011*A^2+0.281667*B+0.005000*B^2+0.020000*C+0.000833*C^2+0.063333*D+0.040000*D^2-0.000250*A*B+0.000700*A*D-0.000833*B*C-0.080000*B*D-0.015000*C*D \quad (43)$$

$$Dross=2.298333-0.012533*A-0.000002*A^2+0.384167*B-0.007917*B^2-0.046389*C+0.003009*C^2-0.053333*D+0.083333*D^2+0.001000*A*B+0.000067*A*C+0.001900*A*D+0.003333*B*C-0.150000*B*D-0.023333*C*D \quad (44)$$

$$RBA=8.83333-0.03500*A-0.00005*A^2+4.25000*B+0.12500*B^2+0.05556*C+0.02778*C^2-7.66667*D+2.00000*D^2+0.02000*A*D-0.16667*B*C-1.00000*B*D-0.16667*C*D \quad (45)$$

$$Kerf=7.61167-0.01865*A+0.00004*A^2-0.45000*B+0.06000*B^2-0.12222*C+0.00778*C^2-1.50500*D+0.35500*D^2+0.00030*A*B+0.00005*A*C+0.00150*A*D+0.04500*B*D-0.04667*C*D \quad (46)$$

$$HAZ=0.591667+0.042417*A+0.000029*A^2-0.127500*B+0.105417*B^2-0.290833*C+0.008657*C^2-0.011667*D+0.211667*D^2-0.005150*A*B-0.000450*A*C-0.008200*A*D+0.002500*B*C-0.010000*B*D+0.030000*C*D \quad (47)$$

4. Case 4

$$RE=1.07547+0.216722*A-0.123317*B-0.000609915*C \quad (48)$$

9 BIO DATA

Dilip Kumar Bagal

Email: dilipbagal90@gmail.com

Phone (Mob.): 0-9439895073

Personal Details

Father's name: Ganeswar Bagal

Mother's name: Padmabati Bagal

Gender: Male

Date of birth: 29th June 1990

Nationality: Indian

Address for Communication

Dilip Kumar Bagal

Qtr no: D-4/A,

Retang Colony,

AT/PO: Jatni, PS: Jatni,

Dist: Khurda

State-Odisha, India

PIN: 752050

Permanent Address

Vill-Bhupad,

PO-Bangra,

Via-Basipitha,

Dist-Mayurbhanj,

State-Odisha, India

PIN- 757074

Education

- Currently pursuing Master in Technology (Research) in Production Engineering Specialization, Department of Mechanical Engineering, National Institute of Technology, Rourkela. Thesis submitted, awaiting review.
- Completed Bachelor in Technology in Department of Mechanical Engineering, National Institute of Technology, Rourkela in 2012.

10 PUBLICATIONS

10.1 SCI Journals:

1. Maity K. P., Bagal D. K. (2014) "Effect of process parameters on cut quality of stainless steel of plasma arc cutting using hybrid approach". *The International Journal of Advanced Manufacturing Technology*, Volume: 78, Issue: 1-4, Springer Publications, London, pp. 161-175. DOI: 10.1007/s00170-014-6552-6, URL: http://dx.doi.org/10.1007/s00170-014-6552-6 (SCI-Impact Factor = 1.779, Published)
2. Maity K., Bagal D. K. (2014) "Optimization of parameters of plasma arc cutting using desirability function and teacher learning based algorithm". *Journal of the Brazilian Society of Mechanical Sciences and Engineering*, pp. 1-21. Dec 10, 2014 (Communicated)
3. Maity K., Bagal D. K. (2014) "Validation of measuring efficiency of a portable plasma arc cutting system using response surface methodology and desirability function". *Measurement*, Elsevier publications, pp. 1-38. Nov 28, 2014 (Communicated)
4. Maity K., Bagal D. K. (2014) "Multi-objective Optimization of Plasma Arc Cutting using Non-Dominated Sorting Genetic Algorithm". *Journal of Materials Engineering and Performance*, ASM International, pp. 1-17. Sep 07, 2014 (Communicated)
5. Maity K., Bagal D. K. (2014) "Experimental Investigation of CNC Oxy-Fuel Gas Cutting Parameters Using DEA Based Taguchi Method". *Proceedings of the Institution of Mechanical Engineers, Part B: Journal of Engineering Manufacture*, SAGE Journals, pp. 1-14. Oct 17, 2014 (Communicated)
6. Maity K., Bagal D. K. (2014) "Influence of process parameters on chamfer and dross of high tensile alloy steel with CNC Oxy-fuel gas cutting using RSM with Grey-Fuzzy

Logic". *Journal of Materials and Design*, Elsevier publications, pp. 1-14. Feb 18, 2014 (Communicated)

7. Maity K., Bagal D. K. (2014) "Influence of Process Parameters on Bevel Angle and Dross of CNC Oxy-Fuel Gas Cutting by using DEA based Taguchi Method ". *Engineering Optimization*, Taylor & Francis Publications, pp. 1-9. Jan 21, 2014 (Communicated)
8. Maity K., Bagal D. K. (2014) "Minimization of chamfer and dross of CNC gas cutting by hybrid optimization". *Materials and Manufacturing Processes*, Taylor & Francis Publications, pp. 1-23. Apr 25, 2014 (Communicated)
9. Maity K., Bagal D. K. (2014) "Influence of process parameters on bevel angle and dross of high tensile alloy steel of CNC Oxy-fuel gas cutting by using DEA based Taguchi method". *Journal of Mechanical Science and Technology*, Springer Publications, pp. 1-16. May 26, 2014 (Communicated)
10. Maity K., Bagal D. K. (2014) "Analysis of Cut Characteristics of CNC Oxy-Fuel Gas Cutting Using Hybrid DEA Based Taguchi Method". *Journal of Intelligent Manufacturing*, Springer Publications, pp. 1-8. Aug 30, 2014 (Communicated)
11. Maity K., Bagal D. K. (2014) "An Approach for Studying the Effects on Quality of Cut Using Genetic Algorithm for Plasma Arc Cutting". *Journal of Intelligent Manufacturing*, Springer Publications, pp. 1-11. Jul 15, 2014 (Communicated)
12. Maity K., Bagal D. K. (2014) "Investigation of Cut Characteristics of CNC Oxy-Fuel Gas Cutting Using DEA Based Taguchi Method". *Applied Soft Computing*, Elsevier publications, pp. 1-11. Jul 15, 2014 (Communicated)

13. Maity K., Bagal D. K. (2014) "Influence of process parameters on chamfer and dross of high tensile alloy steel of CNC Oxy-fuel gas cutting by using RSM with Grey-Fuzzy logic". *Materials and Manufacturing Processes*, Taylor & Francis Publications pp. 1-29. March 19, 2014 (Communicated)
14. Maity K., Bagal D. K. (2014) "A Study on the Influences of Cut Qualities Using Genetic Algorithm for Plasma Arc Cutting ". *Chinese Journal of Mechanical Engineering*, Springer Publications, pp. 1-11. Dec 26, 2014 (Communicated)
15. Maity K., Bagal D. K. (2014) "Optimization of Parameters of Plasma Arc Cutting Using Statistical and Nature Inspired Algorithms". *Journal of Thermal Spray Technology*, Springer Publications, pp. 1-83. Dec 26, 2014 (Communicated)
16. Maity K., Bagal D. K. (2014) "Combinatorial Approach of RSM with Desirability function, Grey-PCA, GA, PSO, SA and Teacher-Learning-Based-Optimization on Plasma Arc Cutting Process". *International Journal of Mechanical and Materials Engineering*, Springer Publications, pp. 1-103. Dec 26, 2014 (Communicated)

10.2 International Conferences:

1. Maity K. P., Bagal D. K. (2014) "Influence of Process Parameters on Heat Affected Zone and Dross of High Tensile Alloy Steel of CNC Oxy-Fuel Gas Cutting using Taguchi with Grey Fuzzy Logic". Paper presented at the *International Conference on Innovation in Design, Manufacturing and Concurrent Engineering* (IDMC 2014), National Institute of Technology, Rourkela, India, 01-03 March, 2014
2. Maity K. P., Bagal D. K. (2014) "Effect of Process Parameters of Plasma Arc Cutting by Using RSM with Simulated Annealing Algorithm". Paper presented at the *International*

Conference on Innovation in Design, Manufacturing and Concurrent Engineering (IDMC 2014), National Institute of Technology, Rourkela, India, 01-03 March, 2014